Reconstructions paléocéanographiques et paléogéographiques du Canal du Mozambique (Océan Indien) : apport de l'étude isotopique des encroûtements Fe-Mn

Claire Charles

▶ **To cite this version:**

Claire Charles. Reconstructions paléocéanographiques et paléogéographiques du Canal du Mozambique (Océan Indien) : apport de l'étude isotopique des encroûtements Fe-Mn. Sciences de la Terre. Université de Bretagne occidentale - Brest, 2022. Français. NNT : 2022BRES0027 . tel-03858288

HAL Id: tel-03858288

https://theses.hal.science/tel-03858288

Submitted on 17 Nov 2022

HAL is a multi-disciplinary open access archive for the deposit and dissemination of scientific research documents, whether they are published or not. The documents may come from teaching and research institutions in France or abroad, or from public or private research centers.

L'archive ouverte pluridisciplinaire **HAL**, est destinée au dépôt et à la diffusion de documents scientifiques de niveau recherche, publiés ou non, émanant des établissements d'enseignement et de recherche français ou étrangers, des laboratoires publics ou privés.

THESE DE DOCTORAT DE

L'UNIVERSITE
DE BRETAGNE OCCIDENTALE

ECOLE DOCTORALE N° 598
Sciences de la Mer et du littoral
Spécialité : Géosciences Marines

Claire CHARLES

Reconstructions paléocéanographiques et paléogéographiques du Canal du Mozambique (Océan Indien): apport de l'étude isotopique des encroûtements Fe-Mn

Paleoceanographic and paleogeographic reconstructions of the Mozambique Channel (Indian Ocean): contribution of the isotopic study of Fe-Mn crusts

Doctorat présenté et soutenu à l'Institut Universitaire Européen de la Mer, le 29 avril 2022
Unités de recherche :

- Ifremer, Géosciences Marines, Laboratoire des Cycles Géochimiques
- Institut Universitaire Européen de la Mer, Laboratoire Géosciences Océan

Rapporteurs avant soutenance :

Laurie REISBERG	Directrice de recherche, CNRS, CRPG, France
Martin FRANK	Professeur, GEOMAR, Allemagne

Composition du Jury :

Présidente du jury :	**Géraldine SARTHOU**	Directrice de recherche, CNRS, IUEM, France
Rapporteur :	**Laurie REISBERG**	Directrice de recherche, CNRS, CRPG, France
Rapporteur :	**Martin FRANK**	Professeur, GEOMAR, Allemagne
Examinatrice :	**Catherine JEANDEL**	Directrice de recherche, CNRS, LEGOS, France
Examinateur :	**Germain BAYON**	Chercheur, Ifremer, France
Directeur de thèse :	**Jean-Alix BARRAT**	Professeur, IUEM, France

Invités :

Ewan PELLETER	Chercheur, Ifremer, France – Co-encadrant de thèse
Sidonie REVILLON	Chercheuse, SEDISOR, France – Co-encadrante de thèse
Stephan JORRY	Chercheur, Ifremer, France
Jean-Michel KLUSKA	Docteur en géologie, TotalEnergies, France

PREFACE

J'y suis entré tout petit sans le savoir, comme tout le monde
Derrière ses murs, j'ai grandi et j'ai observé chaque seconde
J'y suis entré naturellement, personne m'a demandé mon avis
J'ai étudié son fonctionnement, ça s'appelle l'école de la vie

La vie démarre souvent avec le prof d'insouciance
Il est utile, il t'inspire et puis il te met en confiance
Mais juste après vient le cours des responsabilités
Tu découvres les maux de tête et les premiers contrôles ratés

Le cours de curiosité est un passage important
En le comprenant assez tôt, j'ai gagné pas mal de temps
Puis j'ai promis que je m'inscrirai dans le cours de promesse
Mais j'ai parfois été fort dans le cours de faiblesse

En cours de grosse galère, j'ai eu quelques très bonnes notes
C'est ce genre de résultats, qui te fait connaître tes vrais potes
Ça m'a donné des points d'avance et une sacrée formation
Pour le cours de prise de recul et celui d'adaptation

En cours de solitude, j'avais un bon potentiel
Se satisfaire de soi-même est un atout essentiel
Mais j'aime bien aussi l'ambiance qu'il y avait dans le cours de bordel
J'ai vite compris que l'existence se conjugue mieux au pluriel

C'est qu'en cours d'humanité j'ai eu deux très bons professeurs
On a eu des travaux pratiques tous les jours, moi et ma sœur
J'espère que petit à petit, j'ai bien retenu leurs leçons
Et qu'à l'école d'une autre vie, je transmettrai à ma façon

Au cours de liberté y'avait beaucoup d'élèves en transe
Le cours d'égalité était payant, bravo la France !
Pour la fraternité, y'avait aucun cours officiel
Y'avait que les cours du soir, loin des voies institutionnelles

À l'école de la vie, tout s'apprend, tout s'enseigne
Tout s'entend, on s'entraîne, des matières par centaines
C'est l'école de la vie, j'ai erré dans ses couloirs
J'ai géré dans ses trous noirs, j'essayerai d'aller tout voir…

A l'école de la vie, 3ème temps
Grand Corps Malade

REMERCIEMENTS

J'ai longtemps pensé à la rédaction de mes remerciements, et m'y voilà. La thèse se termine, l'aventure s'achève, et mon premier projet en tant que chercheuse également. Cette expérience m'a beaucoup apporté, elle m'a changée et m'a élevée. Jeune ingénieure dans le monde de la recherche… Un monde où tout reste à faire, où rien n'est acquis, un monde déstabilisant, mais un monde étonnant, passionnant et en constante évolution. Un monde fait tantôt d'incompréhensions tantôt d'émerveillements. Un monde de grandeur, d'aventures, d'amitiés et de collaborations où j'ai fait la connaissance de personnes riches de mille savoirs. En cela, je tiens à remercier toutes les personnes qui ont contribué à cette aventure, à quelque niveau que ce soit.

Tout d'abord, j'adresse tout mon *respect* et ma *gratitude* envers mes deux directeurs, Ewan Pelleter et Jean-Alix Barrat. Je sais que vous n'êtes friands, ni l'un ni l'autre de longs discours alors je tâcherai d'aller à l'essentiel. Merci Ewan d'avoir cru en ce projet et de l'avoir porté pendant des années ainsi que de m'avoir fait confiance pour relever ce défi. Merci à Jean-Alix d'avoir pris part à la thèse et de m'avoir dispensé une formation d'aussi grande qualité. Merci à vous deux de m'avoir écoutée, aidée et accompagnée. Merci d'avoir été présents, tout en restant discrets, merci pour votre énorme générosité et vos qualités *humaines*. C'est un honneur pour moi d'avoir travaillé avec deux scientifiques tels que vous.

Je remercie très chaleureusement Sidonie Révillon. Membre à part entière de mon encadrement, tu m'as été d'une aide immense. Merci pour ta *patience* et la dispense de ta formation depuis mes toutes premières manipulations en salle blanche jusqu'au retraitement interminable de mes résultats. Ton caractère fait de toi quelqu'un d'unique, avec qui j'ai appris à travailler avec grand plaisir. Merci pour ton enthousiasme, ta constante disponibilité et surtout, pour ton *soutien* indéfectible, mois après mois.

Je souhaite ensuite remercier Laurie Reisberg et Martin Frank pour avoir accepté d'être les rapporteurs de mon manuscrit de thèse, mais également Géraldine Sarthou, Catherine Jeandel et Germain Bayon de prendre place dans mon jury final. Je suis très heureuse, et très fière de clôturer ce projet avec vous tous.

Je remercie vivement Catherine Jeandel, François Raisson, Pierre Josso, Jean-Michel Kluska et Stephan Jorry d'avoir accepté de faire partie de mon comité de suivi de thèse. Je garderai toujours de bons souvenirs de nos échanges au cours de ces entretiens. Vous m'avez poussé dans mes retranchements et permis d'améliorer nettement mes réflexions. Je tiens aussi à souligner votre bienveillance et votre gentillesse. Merci particulièrement à toi Stephan, pour ta présence, ton engagement dans le projet, tes conseils, ton accompagnement et tes encouragements, qui m'ont été précieux notamment ces derniers mois.

Ce travail a été possible grâce au financement d'Ifremer et de TotalEnergies dans le cadre du projet PAMELA, et grâce au soutien de l'Unité des Géosciences Marines. C'est pourquoi, je remercie grandement Jean-Marc Daniel, Jean-François Bourillet, François Raisson, Jean-Michel Kluska, et toute l'équipe QEMSCAN de TotalEnergies qui m'a aidée pour les analyses minéralogiques.

J'en profite pour saluer et remercier Marjorie Didier et Cédric Demeurie de Thin Section Lab pour la confection rapide et en totale maîtrise de mes lames minces.

Avec beaucoup d'émotions, je pense à Didier Bourlès qui m'a formée à la cosmogénie et m'a permis de réaliser mes datations à ASTER. Merci Didier d'avoir été si bon, si drôle, si passionnant, si Rock'n'roll, si *solaire*. J'aurais aimé discuter davantage avec toi et finaliser ce projet à tes côtés, mais t'avoir connu va au-

delà de tous mes souhaits. Merci pour tout ce que tu incarnais. Merci à Simon Quentin et Régis Braucher qui ont su prendre la relève et m'aider dans ces derniers mois. Je pense aussi à Georges et Karim, à Coralie et Nouméa. Merci pour votre accueil, votre aide et toutes ces parties de rigolades lors de mes séjours au CEREGE.

Je remercie toute l'équipe du Laboratoire des Cycles Géochimiques qui m'a accueillie dès janvier 2018. Merci notamment à Anne-Sophie Alix, Sandrine Chéron, Yoan Germain, Laëtitia Leroy et Anne Trinquier pour leur accompagnement. Je n'oublie pas Philippe Fernagu et Thierry Dalle Mulle, bien entendu, merci pour votre aide quand il s'agissait de sortir mes échantillons des caisses, merci pour les tours en camion, et avant tout, merci pour votre bonne humeur légendaire !

Et puis, il suffit de passer le portillon – s'il fonctionne – pour découvrir le Laboratoire Géosciences Océan où j'ai été bien entourée, même si je me faisais souvent discrète. Je suis très reconnaissante à Philippe Nonnotte, pour ton aide en salle blanche, pour ton accompagnement toujours bien attentionné, pour ton calme et bien sûr, ta profonde gentillesse. Je remercie également et très chaleureusement Bleuenn Guéguen, Céline Liorzou, Marie-Laure Rouget et Kevin Quessette, que ce soit pour votre aide en analyses ou simplement pour un sourire au coin du couloir. C'était très agréable.

J'en profite pour remercier Gilles Chazot et Arnaud Agranier qui m'ont permis de dispenser des cours à l'Université de Bretagne Occidentale. Grâce à vous, j'ai rencontré des centaines d'étudiants, j'ai découvert des centaines de parcours différents, des centaines de projets merveilleux. La notion de *transmission* m'a toujours été très chère, et je suis heureuse d'y participer, à ma petite échelle.

Avec toute ma reconnaissance, me vient d'ailleurs une pensée très émue pour Léon Jacques, mon professeur d'Histoire-Géographie, qui supervise mon parcours – à Dijon, à Beauvais, à Brest, au Japon, au Canada ou dans l'océan Indien –, et m'encourage depuis mes plus jeunes années. J'en suis extrêmement touchée.

Partons maintenant au large, pour une rencontre inoubliable avec le canal du Mozambique. Je tiens à remercier toutes les équipes scientifiques et les équipes de bord du « Marion Dufresne » de la campagne MAYOBS15. Je pense à tout notre groupe CTD : Cécile Cathalot, Jean-Pierre Donval, Johanne Aube, Jérémie Gouriou, Audrey Boissier; mais aussi à Emmanuel Rinnert notre excellent chef de mission et bien d'autres que je n'oublierai pas. Merci à vous tous de m'avoir fait vivre une expérience inoubliable.

De retour maintenant en France, dans une ville pour le moins exotique, à Beauvais et plus particulièrement, à UniLaSalle, je remercie Sébastien Potel de m'avoir accompagnée très tôt dans ce projet en étant jury de mon mémoire. Et bien sûr, je remercie de tout mon cœur Elsa Ottavi-Pupier, grâce à qui je suis entrée dans le monde de la *recherche*. Merci d'avoir cru en moi, de m'avoir accueillie, conseillée, aiguillée et épaulée. Merci de m'avoir envoyée au Japon, voyage qui n'a fait qu'accroître mon attrait pour ce domaine.

Et puis, que serait ma thèse sans mes compagnons de navire, à amis ifremériens : Thibault et Léa, partis trop tôt vers d'autres horizons ; à Maud, véritable rayon de soleil ; à Ivane, pour notre aventure en camion jaune et à la belle surprise que tu m'as faite ; à Matthieu et Aurélien, mes fidèles amis, à nos galères et à nos rêves de *liberté* ; et à Manon, Kiki, aussi organisée que pipelette, à tous nos partages et à tous nos souvenirs, en mer ou à terre, en Métropole ou à la Réunion, avec un verre ou bien plus.

Je remercie bien entendu tous mes amis et copains, d'enfance, de lycée, de promo, d'ici et d'ailleurs, qui m'ont encouragée, accompagnée et qui ont toujours cru en ma réussite, à défaut d'y croire moi-même.

Enfin, c'est un remerciement tout particulier pour ces personnes qui sont à la base de toute cette aventure. Celles qui ont accepté, respecté et encouragé mes choix, ces personnes qui m'ont tenue à bout de bras et remise sur pied, celles qui m'ont supportée, calmée, raisonnée et épaulée.

À toi, présent dans ma bulle depuis mon premier jour à Brest et dont le destin nous a joué un sacré tour : Johann, merci pour ta douceur, ton calme, ta patience et ta sérénité quand j'en manquais tant. À ton anneau de Bernard Lavilliers, à tes marinières Armor-Lux, à notre échappatoire Plouescat, aux live de The Doors « *because the music is your special friend… until the end* », et « *aux bruits de la ville* » sous le soleil finistérien.

À toi, présente à mes côtés depuis nos plus tendres souvenirs: Mallaury, ma sœur de cœur, membre de ma famille depuis tant d'années, merci. Je reprends Noé Preszow rien que pour tes jolis yeux : « *À nous qui débordons dans les rires et les larmes ; qui ne faisons pas le deuil de nos jours de flamme, quand on avait 10 ans à grandes enjambées, pédalant, pédalant… pour l'éternité* ».

Merci à mes grands-parents pour votre *héritage* ;

Merci à mon frère et ma sœur pour m'avoir soutenue malgré tant de différences, malgré mes silences et malgré mon absence, merci d'avoir toujours été fiers de moi et surtout de me faire rire aux éclats ;

Pour conclure, merci à mes parents, avec qui j'ai découvert la Bretagne il y a des années, sur les routes de Carnac en écoutant les albums de Miossec – papa, discret, réconfortant et fidèle, merci d'avoir toujours cru en mes capacités malgré tes propres combats à mener et maman, mon âme sœur, clairvoyante, compréhensive et bienveillante, merci de me tenir « *éveillée* » …

À Claude,

ACKOWLEDGEMENTS

I have been thinking about writing my thanks for a long time, and here I am. The thesis ends, the adventure ends, and so does my first project as a researcher. This experience has given me a lot, it has changed me and raised me. A world where everything remains to be done, where nothing is taken for granted, a destabilising world, but an astonishing, exciting and constantly evolving world. A world of incomprehension and wonder. A world of greatness, adventures, friendships and collaborations where I have met people who are rich in knowledge. I would like to thank all the people who have contributed to this adventure, at whatever level.

First of all, I would like to express my respect and gratitude to my two directors, Ewan Pelleter and Jean-Alix Barrat. I know that neither of you are fond of long speeches, so I will try to get to the point. Thank you Ewan for believing in this project and for having supported it for years and for having trusted me to take up this challenge. Thank you to Jean-Alix for having taken part in the thesis and for having given me such a high quality training. Thank you both for listening to me, helping me and accompanying me. Thank you for having been present, while remaining discreet, thank you for your enormous generosity and your human qualities. It is an honour for me to have worked with two scientists like you.

I would like to thank Sidonie Révillon most warmly. As a full member of the supervision team, you have been of immense help to me. Thank you for your patience and the training you gave me from my very first manipulations in the clean room to the endless reprocessing of my results. Your character makes you a unique person, with whom I learned to work with great pleasure. Thank you for your enthusiasm, your constant availability and above all, for your unfailing support, month after month.

I would like to thank Laurie Reisberg and Martin Frank for accepting to be the reporters of my thesis manuscript, but also Géraldine Sarthou, Catherine Jeandel and Germain Bayon for being part of my final jury. I am very happy, and very proud to conclude this project with you all.

I would like to thank Catherine Jeandel, François Raisson, Pierre Josso, Jean-Michel Kluska and Stephan Jorry for having accepted to be part of my thesis monitoring committee. I will always have pleasant memories of our exchanges during these meetings. You pushed me to my limits and allowed me to improve my thoughts. I would also like to underline your benevolence and kindness. Special thanks to you, Stephan, for your presence, your commitment to the project, your advice, your support and your encouragement, which have been invaluable to me, especially over the last few months.

This work was made possible thanks to funding from Ifremer and TotalEnergies in the framework of the PAMELA project, and thanks to the support of the Marine Geosciences Unit. Therefore, I would like to thank Jean-Marc Daniel, Jean-François Bourillet, François Raisson, Jean-Michel Kluska, and the whole QEMSCAN team of TotalEnergies who helped me with the mineralogical analyses.

I take this opportunity to salute and thank Marjorie Didier and Cédric Demeurie of Thin Section Lab for the rapid and controlled production of my thin sections.

With a lot of emotions, I think of Didier Bourlès who trained me in cosmogeny and allowed me to carry out my dating at ASTER. Thank you Didier for being so nice, so funny, so fascinating, so rock'n'roll, so "sunny". I would have liked to discuss more with you and to conclude this project by your side, but having known you goes beyond all my wishes. Thank you for everything you embodied. Thank you to Simon

Quentin and Régis Braucher who took over and helped me in these last months. I also think of Georges and Karim, Coralie and Nouméa. Thank you for your hospitality, your help and all the fun during my visits to the CEREGE.

I would like to thank the whole team of the “Laboratoire des Cycles Géochimiques et ressources” who welcomed me in January 2018. Thanks in particular to Anne-Sophie Alix, Sandrine Chéron, Yoan Germain, Laëtitia Leroy and Anne Trinquier for their support. And of course, I can't forget Philippe Fernagu and Thierry Dalle Mulle, thank you for your help when it was necessary to take my samples out of the boxes, thank you for the truck rides, and above all, thank you for your legendary good humour!

And then, you just have to go through the gate - if it works - to discover the “Laboratoire Géosciences Océan” where I was well surrounded, even if I was often very discreet. I am extremely grateful to Philippe Nonnotte, for your help in the clean room, for your always thoughtful guidance, for your calmness and, of course, your profound kindness. I would also like to thank Bleuenn Guéguen, Céline Liorzou, Marie-Laure Rouget and Kevin Quessette very warmly, whether it was for your help in analysis or simply for a smile in the corner of the corridor. It was very pleasant.

I take this occasion to thank Gilles Chazot and Arnaud Agranier who allowed me to teach at the “Université de Bretagne Occidentale”. Thanks to you, I have met hundreds of students, I have discovered hundreds of different career paths, hundreds of wonderful projects. The notion of transmission has always been very dear to me, and I am happy to contribute to it, in my small scale.

With all my gratitude, I have a very emotional thought for Léon Jacques, my History-Geography teacher, who supervises my education - in Dijon, in Beauvais, in Brest, in Japan, in Canada or in the Indian Ocean -, and encourages me since my youngest years. I am extremely touched by this.

Let us now head out to the ocean, for an unforgettable encounter with the Mozambique Channel. I would like to thank all the scientific teams and the teams on board the "Marion Dufresne" for the MAYOBS15 cruise. I am thinking of all our CTD group: Cécile Cathalot, Jean-Pierre Donval, Johanne Aube, Jérémie Gouriou, Audrey Boissier; but also Emmanuel Rinnert, our excellent mission chief, and many others whom I will not forget. Thank you all for giving me an incredible experience.

Now back in France, in Beauvais and more particularly at UniLaSalle, I would like to thank Sébastien Potel for having guided me very early on in this project by being the jury for my master's degree. And of course, I thank Elsa Ottavi-Pupier from the bottom of my heart, thanks to whom I entered the world of research. Thank you for believing in me, for welcoming me, advising me, guiding me and supporting me. Thank you for helping me to travel to Japan, an experience that increased my interest in this field.

And then, what would my thesis be without my shipmates, to my colleagues from Ifremer: Thibault and Léa, who left too soon for other horizons; to Maud, a real ray of sunshine; to Ivane, for our adventure in the yellow truck and the nice surprise you gave me; to Matthieu and Aurélien, my faithful friends, for our galleys and our dreams of freedom; and to Manon, Kiki, who is as organised as she is chatty, for all our sharing and all our memories, at sea or on land, with a drink or much more.

I thank of course all my friends and buddies, from childhood, high school, graduating class, who encouraged me, accompanied me and always believed in my success, for lack of belief myself.

Finally, I would like to say a special thank you to those people who are at the root of this whole adventure. Those who accepted, respected and encouraged my choices, those who held me at arm's length and got me back on my feet, those who supported, calmed, reasoned and supported me.

To you, present in my life since my first day in Brest and whose destiny has played a trick on us: Johann, thank you for your gentleness, your calm, your patience and your serenity when I was so short of it. To your Bernard Lavilliers ring, to your Armor-Lux “marinières”, to our Plouescat escape, to the Doors' live performances "*because the music is your special friend... until the end*", and “aux *bruits de la ville*" under the Finistère sun.

To you, who have been by my side since our fondest memories: Mallaury, my best and intimate friend, my ally, a member of my family for so many years, thank you. I take up Noé Preszow just for your beautiful eyes: “*à nous qui débordons dans les rires et les larmes ; qui ne faisons pas le deuil de nos jours de flamme, quand on avait 10 ans à grandes enjambées, pédalant, pédalant… pour l'éternité*".

Thank you to my grandparents for your cultural legacy;

Thank you to my brother and sister for having supported me despite so many differences, despite my silences and despite my absence, thank you for having always been proud of me and especially for making me laugh out loud;

To conclude, thank you to my parents, with whom I discovered Brittany years ago, on the roads of Carnac while listening to Miossec's albums: Dad, discreet, comforting and faithful, thank you for always believing in my abilities despite your own struggles, and Mom, my soul mate, clear-sighted, understanding and kind, thank you for keeping me "*awake*"...

To Claude,

RÉSUMÉ

Claire Charles – PhD. Thesis – 2022

Le canal du Mozambique représente une zone complexe de mélanges très intenses entre les masses d'eau arrivant au sud, de l'océan Atlantique et, les masses d'eau circulant au nord, de l'océan Indien. Il est également connu et analysé pour son histoire et ses caractéristiques géologiques très intéressantes, liées à sa localisation à l'est du craton africain et à l'ouest de la marge continentale de Madagascar. Ces particularités océanographiques et géologiques ont toujours soulevé des interrogations, à savoir si et comment les courants marins ont pu évoluer et circuler au cours du temps, en s'adaptant à la géodynamique du canal en constant mouvement.

D'origine hydrogénétique et de compositions intermédiaires entre des encroûtements Fe-Mn de marge continentale et d'océan ouvert, les encroûtements Fe-Mn du canal du Mozambique sont de véritables archives de la composition des masses d'eau environnantes. Ainsi, l'analyse géochimique (éléments majeurs, traces ; isotopie Nd, Pb) et la datation absolue (isotopie Be) de 33 encroûtements Fe-Mn, répartis depuis le Plateau des Aiguilles au sud jusqu'au bassin des Comores au nord, permet ici d'établir des séries temporelles jusqu'à 30.7 Ma afin d'étudier l'évolution des courants régionaux depuis l'Oligocène.

Les signatures isotopiques (Nd, Pb) obtenues sur la surface des encroutements Fe-Mn montrent que depuis 80 000 ans, le courant profond Atlantique (NADW) circule avec une forte intensité dans le canal, en arrivant par le Plateau des Aiguilles. Il remonte jusqu'au bassin profond du Mozambique puis aux premières Îles Eparses au centre du canal où son flux diminue progressivement, jusqu'à atteindre la ride de Jeffrey sur la marge ouest de Madagascar. C'est le courant profond Indien (NIDW) qui est majoritaire dans l'archipel des Comores. Cependant, ce modèle de circulation océanographique n'a pas toujours fonctionné ainsi.

Depuis sa mise en place et jusqu'à 11.7 Ma, le NADW avait une forte influence jusqu'aux Îles Glorieuses dans l'extrémité nord du canal. Il dominait le système océanique profond de la région. Cependant, entre le Miocène et le Pliocène (11.7-3.4 Ma), un soulèvement a bouleversé la géodynamique du canal du Mozambique, entrainant une élévation de sa bathymétrie et notamment de la ride de Davie, formée de reliefs sous-marins qui séparent le bassin des Comores du bassin du Mozambique. Face à cet obstacle topographique, le flux du NADW dans le nord du canal a diminué, et ce courant s'est retiré du bassin des Comores, au profit de l'augmentation du NIDW. L'élévation de la ride de Davie n'a cependant pas permis de stopper l'évolution du NADW au nord du canal, avec une présence enregistrée jusqu'à la ride de Jeffrey. Entre le Pliocène et le Pléistocène (5.1-1.6 Ma), c'est une subsidence, enregistrée au centre du canal (banc du Hall), qui a modifié la bathymétrie du secteur. En plus de ces événements régionaux, les courants profonds du canal ont été impactés par des phénomènes mondiaux. Leurs études géochimiques révèlent des apports élémentaires du système téthysien avant sa fermeture (23-14 Ma), transportés par des courants profonds méditerranéens, en direction de l'océan Indien, et du système himalayen dont la forte érosion au Miocène (9.0 Ma) a permis de l'enregistrer à travers les courants indiens.

Ce doctorat vient compléter et affiner les modèles océanographiques pré existants de l'océan Indien, en apportant une étude haute résolution des courants profonds du canal du Mozambique depuis l'Oligocène (30.7 Ma). De plus, l'utilisation des encroûtements Fe-Mn dans l'identification et la caractérisation de mouvements verticaux est une avancée inédite pour les reconstructions géodynamiques.

Mots clés : canal du Mozambique ; encroûtements Fe-Mn ; isotopie Nd, Pb ; NADW ; NIDW ; océan Indien ; uplift

ABSTRACT

Claire Charles – PhD. Thesis – 2022

The Mozambique Channel represents a complex zone of very intense mixing between the water masses arriving in the south, from the Atlantic Ocean and, the water masses circulating to the north, from the Indian Ocean. It is also known and analysed for its history and its very interesting geological characteristics, linked to its location east of the African craton and west of the continental margin of Madagascar. These oceanographic and geological particularities have always raised questions, about whether and how marine currents have been able to evolve and circulate over time adapting to geodynamics of the channel in constant movement.

Of hydrogenetic origin and of intermediate compositions between Fe-Mn crusts of continental margin and open-ocean, the Fe-Mn crusts of the Mozambique Channel are real archives of the geochemical compositions of the surrounding water masses. Geochemical analysis (major and trace elements; Nd and Pb isotopes) and absolute dating (Be isotopes) of 33 Fe-Mn crusts, distributed from the Agulhas Plateau in the south to the Comoros Basin in the north, allows to establish time series up to 30.7 Ma in order to study the evolution of the regional currents since the Oligocene.

The isotopic signatures (Nd, Pb) obtained on the surface of the Fe-Mn crusts show that for 80,000 years, the North Atlantic Deep Water (NADW) has been circulating with high intensity in the channel, arriving via the Agulhas Plateau. It goes up to the deep basin of Mozambique then to the first Îles Eparses in the centre of the channel where its flow gradually decreases, until reaching the Jeffrey Ridge on the west Madagascar margin. The North Indian Deep Water (NIDW) then in the majority in the Comoros archipelago. However, this oceanographic circulation model has not always worked this way.

Since its establishment and until 11.7 Ma, the proto-NADW had a strong influence up to the Îles Glorieuses. It dominated the deep ocean system of the region. However, between the Miocene and Pliocene (11.7-3.4 Ma), a uplift disrupted the geodynamics of the Mozambique Channel, leading to an elevation of its bathymetry and in particular, the Davie Ridge, formed by underwater reliefs that separate the Comoros Basin from the Mozambique Basin. Faced with this topographical obstacle, the flow of NADW in the north of the channel has decreased, and this current has withdrawn from the Comoros basin, in favour of increase of NIDW. The rise of the Davie Ridge did not, however, stop the evolution of NADW to the north of the channel, with a presence recorded up to the Jeffrey Ridge. Between the Pliocene and Pleistocene (5.1-1.6 Ma), it is a subsidence, registered in the centre of the channel (Hall Bank), which modified bathymetry of the area. In addition to these regional events, deep currents of the channel have been impacted by global phenomena. Their geochemical compositions reveal contributions of dissolved elements, coming from the Tethysian system before its closure (23-14 Ma), transported by deep Mediterranean currents, towards the Indian Ocean, and from the Himalayan system, whose strong erosion in the Miocene (9.0 Ma) made it possible to record it through the Indian currents.

This PhD thesis completes and refines the pre-existing oceanographic models of the Indian Ocean, by providing a high-resolution study of the deep currents of Mozambique Channel since the Oligocene. In addition, the use of Fe-Mn crusts in the identification and characterization of vertical movements is an unprecedented advance for paleogeodynamic reconstructions.

Keywords: Fe-Mn crusts; Indian Ocean; Mozambique channel; NADW; NIDW; Nd, Pb isotopes; uplift

TABLE OF CONTENTS

Préface 3

Remerciements 7
Acknowledgements 15

Résumé 23
Abstract 27

Table of contents 31

List of figures 43
List of tables 55
List of appendix 59

Chapitre 1 – Introduction (français) 63

1.1. Cadre général du projet 65
1.1.1. Projet PAMELA 65
1.1.2. Missions océanographiques 66
1.2. Principes géologiques et questionnements scientifiques 68
1.2.1. Caractéristiques générales du Fe et Mn dans les océans 68
1.2.2. Processus de précipitation des dépôts Fe-Mn 69
1.2.2.1. Processus hydrogénétique 69
1.2.2.2. Processus diagénétique 69
1.2.2.3. Processus hydrothermal 70
1.2.3. Encroûtements Fe-Mn 70
1.2.4. Taux de croissance et méthodes de datation 72
1.2.4.1. Chronologie par datation absolue 73
1.2.4.2. Chronologie par datation empirique 73
1.2.4.3. Chronologie par datation indirecte 75
1.2.5. Reconstructions paléocéanographiques 75
1.2.5.1. Le Pb dans les océans 76
1.2.5.2. Le Nd dans les océans 76
1.2.5.3. Précédentes reconstructions paléocéanographiques 76
1.3. Zone d'étude : le canal du Mozambique 78
1.3.1. Contexte et géodynamique 78

1.3.2. Océanographie 82
1.4. Problématiques et méthodes de travail 83
1.5. Structure du manuscrit 85
1.6. Références bibliographiques 86

Chapter 1 – Introduction (english) 95

1.1. General context of the thesis project 97
1.1.1. PAMELA project 97
1.1.2. Oceanographic missions 98
1.2. Geological principles and scientific questioning 100
1.2.1. General characteristics of Fe and Mn in the oceans 100
1.2.2. Precipitation process of Fe-Mn deposits 100
1.2.2.1. Hydrogenetic process 101
1.2.2.2. Diagenetic process 101
1.2.2.3. Hydrothermal process 101
1.2.3. Fe-Mn crusts 102
1.2.4. Growth rates and dating methods 103
1.2.4.1. Chronology by absolute dating 104
1.2.4.2. Chronology by empirical dating 104
1.2.4.3. Chronology by indirect dating 105
1.2.5. Paleoceanographic reconstructions 106
1.2.5.1. Pb in the oceans 106
1.2.5.2. Nd in the oceans 106
1.2.5.3. Previous paleoceanographic reconstructions 108
1.3. Study area : the Mozambique Channel 109
1.3.1. Context and geodynamics 109
1.3.2. Oceanography 112
1.4. Issues and working methods 114
1.5. Structure of the manuscript 115
1.6. Bibliographical references 117

Chapitre 2 – Méthodologie analytique (français) 127

2.1. Introduction 129
2.2. Choix des échantillons et préparation des sous-échantillons 130
2.2.1. Dragages et échantillons 130
2.2.2. Critères de sélection des échantillons 130
2.2.3. Préparation des poudres et des lames minces 131
2.2.3.1. Echantillonnage de la surface – courantologie moderne 131

2.2.3.2. Echantillonnage des séries temporelles – géochronologie du canal du Mozambique 131
2.2.3.3. Confection des lames minces – minéralogie ponctuelle 132
2.3. Caractérisation minéralogique 132
2.3.1. Diffraction par rayons X 132
2.3.1.1. Principes généraux de la DRX 132
2.3.1.2. Conditions d'analyses 133
2.3.2. Evaluation quantitative des minéraux par microscopie électronique à balayage 133
2.4. Mise en solution des éléments 133
2.4.1. Conditions de préparation 133
2.4.2. Protocole d'attaque pour les analyses d'éléments majeurs, traces et isotopies du Nd et Pb 134
2.5. Géochimie élémentaire 135
2.5.1. Caractérisation des éléments majeurs par ICP-OES 135
2.5.1.1. Préparation des solutions à partir des solutions mères 135
2.5.1.2. Principes généraux d'un ICP-OES 135
2.5.1.3. Session d'analyses « type » 136
2.5.2. Analyses des éléments traces par ICP-MS après ajout de Tm 136

❖ ***Papier 1*** *: Charles, C., Barrat, J.A. and Pelleter, E., 2021. Trace element determinations in Fe-Mn oxides by high resolution ICP-MS after Tm addition. Talanta 122446*

2.6. Géochimie isotopique 146
2.6.1. Composition isotopique en Nd par TIMS 146
2.6.1.1. Présentation du Nd 146
2.6.1.2. Séparation du Nd 146
2.6.1.3. Principes généraux d'un TIMS 147
2.6.1.4. Session d'analyses « type » 149
2.6.2. Composition isotopique en Pb par MC-ICP-MS 150
2.6.2.1. Présentation du Pb 150
2.6.2.2. Séparation du Pb 150
2.6.2.3. Principes généraux d'un MC-ICP-MS 150
2.6.2.4. Session d'analyses « type » 150
2.7. Datation absolue par désintégration radioactive du Be 151
2.7.1. Les nucléides cosmogéniques 151
2.7.2. Séparation du Be par chromatographie d'extraction 151
2.7.3. Cathodage des cibles 153
2.7.4. Introduction et analyses par AMS 153
2.7.5. Séquence d'analyses « type » 155

2.7.6. Calculs des concentrations et des âges 156
2.7.7. Extrapolation des âges non mesurés par AMS 157
2.8. Références bibliographiques 157

Chapter 2 – Analytical methodology (english) 163

2.1. Introduction 165
2.2. Selection of samples and preparation of sub-samples 166
2.2.1. Dredges and samples 166
2.2.2. Sample selection criteria 166
2.2.3. Preparation of powders and thin sections 167
2.2.3.1.Surface sampling – modern current patterns 167
2.2.3.2. Sampling of time series – geochronological survey of the Mozambique Channel 167
2.2.3.3. Making thin sections – specific mineralogical study 167
2.3. Mineralogical characterization 168
2.3.1. X-ray diffraction 168
2.3.1.1. General principles of XRD 168
2.3.1.2. Analysis conditions 168
2.3.2. Quantitative assessment of minerals using scanning electron microscopy 169
2.4. Dissolution of elements 169
2.4.1. Conditions of preparation 169
2.4.2. Attack protocol for the analysis of major and trace elements and isotopes of Nd and Pb 169
2.5. Elementary geochemistry 170
2.5.1. Characterization of major elements by ICP-OES 170
2.5.1.1. Preparation of solutions from mother solutions 170
2.5.1.2. General principles of an ICP-OES 170
2.5.1.3. “Typical” analysis session 171
2.5.2. Analysis of trace elements by ICP-MS after addition of Tm 171

❖ ***Paper 1:*** *Charles, C., Barrat, J.A. and Pelleter, E., 2021. Trace element determinations in Fe-Mn oxides by high resolution ICP-MS after Tm addition. Talanta 12244*

2.6. Isotopic geochemistry 181
2.6.1. Isotopic composition in Nd by TIMS 181
2.6.1.1. Presentation of Nd 181
2.6.1.2. Separation of Nd 181
2.6.1.3. General principles of a TIMS 182

2.6.1.4. “Typical” analysis session 184
2.6.2. Isotopic composition in Pb by MC-ICP-MS 184
2.6.2.1. Presentation of Pb 184
2.6.2.2. Separation of Pb 185
2.6.2.3. General principles of a MC-ICP-MS 185
2.6.2.4. “Typical” analysis session 185
2.7. Absolute dating by radioactive decay of Be 186
2.7.1. Cosmogenic nuclides 186
2.7.2. Separation of Be by extraction chromatography 186
2.7.3. Cathoding of targets 188
2.7.4. Introduction and analysis by AMS 188
2.7.5. “Typical” analysis session 190
2.7.6. Calculations of concentrations and dates 190
2.7.7. Extrapolations of dates not measured by AMS 191
2.8. Bibliographical references 192

Chapter 3 – Modern isotopic records of the regional water masses 197

3.1. Introduction (français) 199
3.1. Introduction (english) 199
3.2. Nd isotopic signatures of the channel water masses and new 2D circulation model 200

❖ ***Paper 2*** *: Charles, C., Pelleter, E., Révillon, S., Nonnotte, P., Jorry, S.J., Kluska, J.-M., 2020. Intermediate and deep ocean current circulation in the Mozambique Channel: New insights from ferromanganese crust Nd isotopes. Marine Geology. 430, 106356.*

3.3. Contribution de l’étude isotopique du Pb, apports détritiques et circulation océanique 214
3.3.1. Encroûtements Fe-Mn et méthodologie 214
3.3.2. Distribution isotopique du Pb dans l’océan Indien 214
3.3.2.1. Tendances isotopiques du Pb 217
3.3.2.2. Réseau de domaines isotopiques 217
3.3.3. Résultats des compositions isotopiques du Pb 218
3.3.3.1. $^{206}Pb/^{204}Pb$ 218
3.3.3.2. $^{207}Pb/^{204}Pb$ 218
3.3.3.3. $^{208}Pb/^{204}Pb$ 218
3.3.3.4. $^{208}Pb/^{206}Pb$ 220
3.3.3.5. Influence de la profondeur 220
3.3.4. Discussion 220

3.3.4.1. Caractérisation des signatures isotopiques du Pb 220
3.3.4.2. Signature antarctique au Plateau des Aiguilles 223
3.3.4.3. Forte influence du NADW au sud-ouest du canal du Mozambique 223
3.3.4.4. Propagation du NADW en direction du bassin des Comores 225
3.3.5. Résumé et conclusion 226
3.3.6. Références bibliographiques 226
3.4. Conclusion (français) 228
3.4. Conclusion (english) 228

Chapter 4 – Fe-Mn crusts: archives of vertical paleogeodynamic movements 229

❖ ***Paper 3*** *: Charles, C., Pelleter, E., Révillon, S., Jorry, S.J., Kluska, J.-M., Bourlès, D., Quentin, S., Braucher, R., Nonnotte, P., Liorzou, C., Chéron, S., Germain, Y., Barrat, J.A., in prep. Fe-Mn crusts as archives of vertical movements: new insights for the geodynamic reconstruction of the Mozambique Channel over the past 30 Ma, in prep.*

4.1. Abstract 233
4.2. Introduction 234
4.3. Geological settings 235
4.4. Oceanography 237
4.5. Samples and analytical methods 238
4.5.1. Fe-Mn crusts 238
4.5.2. Stratigraphic layers 240
4.5.3. X-ray diffraction mineralogy 240
4.5.4. Major, trace elements and isotopic compositions 241
4.5.5. Be dating 242
4.6. Results 242
4.6.1. Characterization of the studied Fe-Mn crusts 242
4.6.1.1. X-ray diffraction mineralogy 242
4.6.1.2. Major and minor elements 242
4.6.1.3. Metal and trace concentrations 245
4.6.1.4. Rare earth elements + Y 246
4.6.2. Age-depth modelling 247
4.6.3. Nd and Pb isotope compositions 248
4.6.3.1. Nd isotope data 250
4.6.3.2. Pb isotope data 250
4.6.3.3. Resume 251
4.7. Discussion 256
4.7.1. Characterization of the εNd records 256

4.7.1.1. Phosphatisation and detrital contaminations 256
4.7.1.2. Impact of the glacial/interglacial cycles 258
4.7.1.3. Influence of the unradiogenic African margin 258
4.7.2. Interpretation of the εNd records 261
4.7.2.1. Physical-chemical changes of the water masses 261
Tasman strait and Drake passage 261
High intensity of Himalayan weathering 262
Tethys seaway closure 263
Indonesian seaway closure 264
NADW export during the Miocene 264
Panama isthmus closure 265
Northern hemisphere glaciation 265
4.7.2.2. Vertically movements of the Fe-Mn crusts 266
Uplift phenomenon 266
Subsidence event 271
4.8. Conclusion 272
4.9. Acknowledgements 273
4.10. Bibliographical references 273

Chapter 5 – Deep paleoceanography of the channel of the last 20 Ma 291

5.1. Résumé (français) 293
5.1. Abstract (english) 293
5.2. Introduction 294
5.3. Geological context 296
5.4. Materials 297
5.5. Methods 298
5.5.1. Mineralogy 298
5.5.2. Geochemistry 299
5.6. Results 299
5.6.1. Petrology and mineralogy 299
5.6.2. Age-depth modelling 300
5.6.2.1. $^{10}Be/^{9}Be$ extrapolated 300
5.6.2.2. Other methods 303
5.6.3. Major and minor elements 305
5.6.4. Metal and trace elements 308
5.6.5. Rare earth elements + Y 308
5.6.6. Nd and Pb isotope compositions 309
5.6.6.1. Nd 309

5.6.6.2. Pb 313
$^{206}Pb/^{204}Pb$ and $^{208}Pb/^{204}Pb$ 313
$^{207}Pb/^{204}Pb$ 313
$^{208}Pb/^{206}Pb$ 313
5.7. Discussion 314
5.7.1. South of the channel : Agulhas Plateau 314
5.7.2. North of the channel : Glorieuses Islands 318
5.7.3. Paleocirculation of the deep currents 319
5.8. Conclusion 322
5.9. Acknowledgements 322
5.10. Bibliographical references 323

Chapitre 6 – Synthèse, conclusions et perspectives (français) 333

6.1. Introduction 335
6.2. Que reflète la signature géochimique des encroûtements Fe-Mn ? 336
6.3. Identification et modèle de circulation des masses d'eau subactuelles dans le canal du Mozambique 336
6.3.1. Quelles sont les principales masses d'eau dans la région et quelles sont leurs signatures isotopiques en Nd ? 336
6.3.2. Quelle est la circulation moderne des courants profonds ? 338
6.3.3. La ride de Davie joue-t-elle un rôle de barrière topographique dans l'évolution des masses d'eau profondes ? 338
6.4. Géodynamique du canal du Mozambique : identification et datation de mouvements verticaux à partir de 12 Ma 338
6.4.1. Quelle est la résolution temporelle des encroûtements Fe-Mn étudiés pour les reconstructions géodynamiques ? 339
6.4.2. Des bouleversements géographiques ont-ils été enregistrés dans le canal du Mozambique ? Si oui, lesquels ? 340
6.4.3. Quelle pourrait être l'incidence de tels mouvements verticaux sur la circulation des masses d'eau régionales au cours du temps ? 342
6.5. Reconstruction océanographique des courants profonds du canal du Mozambique : un modèle évolutif sur 20 Ma 342
6.5.1. Quelle est la résolution temporelle des encroûtements Fe-Mn étudiés pour les reconstructions océanographiques ? 342
6.5.2. Comment ont évolué les signatures isotopiques des courants profonds au cours des 20 derniers Ma ? 343
6.5.3. Quelles sont les conséquences de l'uplift sur le transport des masses d'eau profondes au cours des 12 derniers Ma ? 344
6.6. Perspectives 345
6.6.1. Etendre la fiabilité des modèles d'âge des encroûtements Fe-Mn étudiés au-delà de 12 Ma 345
6.6.1.1. Chronologie par datation empirique 345

6.6.1.2. Chronologie par datation indirecte 346
6.6.2. Identifier des événements locaux par étude minéralogique et géochimique haute résolution de deux encroûtements Fe-Mn 346
6.6.2.1. Encroûtement Fe-Mn MOZ1-DR04-23 : événements volcaniques 349
6.6.2.2. Encroûtement Fe-Mn MOZ5-DR03-01 : « boundary exchanges » 350
6.6.3. Modélisation océanographique 353
6.7. Références bibliographiques 356

Chapter 6 – Summary, conclusions and perspectives (english) 361

6.1. Introduction 363
6.2. What does the geochemical signature of Fe-Mn crusts reflect? 363
6.3. Identification and circulation model of modern water masses in the Mozambique Channel 364
6.3.1. What are the main water masses in the Mozambique Channel and what are their Nd isotope signatures? 364
6.3.2. What is the modern circulation of deep currents in the Mozambique Channel? 364
6.3.3. Does the Davie Ridge act as a topographic barrier in the modern evolution of deep water masses? 366
6.4. Geodynamics of the Mozambique Channel: recording and identification of vertical movements from 12 Ma 366
6.4.1. What is the temporal resolution of Fe-Mn crusts studied for paleogeodynamic reconstructions? 366
6.4.2. Have geographic changes been recorded in the Mozambique Channel? If yes, which ones? 367
6.4.3. What might be the impact of such vertical movements on the circulation of regional water masses? 368
6.5. Paleoceanographic reconstruction of the deep currents of Mozambique Channel: an evolutionary model over 30 Ma 370
6.5.1. What is the temporal resolution of Fe-Mn crusts studied for paleoceanographic reconstructions? 370
6.5.2. How did the isotopic signatures of the deep currents of the Mozambique Channel evolve during the 20 Ma? 371
6.5.3. What are the consequences of the uplift on the transport of deep water masses in the Mozambique Channel during the last 12 Ma? 372
6.6. Perspectives 372
6.6.1. Improve the reliability of age models of Fe-Mn crusts studied beyond 12 Ma 372
6.6.1.1. Chronology by empirical dating 372
6.6.1.2. Chronology by indirect dating 373
6.6.2. Identify local events by high resolution mineralogical and geochemical study of two Fe-Mn crusts 373
6.6.2.1. Fe-Mn crust MOZ1-DR04-23: volcanic events 376
6.6.2.2. Fe-Mn crust MOZ5-DR03-01: « boundary exchanges » 377
6.6.3. Oceanographic modelling 380
6.7. Bibliographical references 382

Appendices 389

Appendix 1. Details of the oceanographic cruises 391
Appendix 2. List and details of the 33 Fe-Mn crusts of this study 395
Appendix 3. Presentation of the sampled and analysed time series 399
MOZ1-DR04-023 400
MOZ1-DR10-05 402
MOZ1-DR11-01 404
MOZ1-DR17-01 406
MOZ1-DR22-01 408
DR75-0012 410
DR84-0026 412
MOZ5-DR03-01 414
Appendix 4. Locations of the 8 thin sections sampled on the Fe-Mn crusts MOZ1-DR04-23 and MOZ5-DR03-01 417
Appendix 5. XRD patterns of the sample MOZ1-DR04-23 419
Appendix 6. XRD patterns of the sample MOZ5-DR03-01 423
Appendix 7. Mineralogical results of the 4 thin sections from the Fe-Mn crusts MOZ1-DR04-23 and MOZ5-DR03-01 427
Appendix 8. C. CHARLES *et al.,* 2019. Paleoceanographic and paleogeographic reconstruction of the Mozambique Channel through geochemical study of Fe-Mn crusts. *Seminar PAMELA.* November 2019, Pau, France. Poster 433
Appendix 9. C. CHARLES *et al.,* 2019. Paleoceanographic and paleogeographic reconstruction of the Mozambique Channel through geochemical study of Fe-Mn crusts. *Seminar PAMELA.* November 2019, Pau, France. Oral presentation 435
Appendix 10. C. CHARLES *et al.,* 2019. Paleoceanographic and paleogeodynamic reconstruction of the Mozambique Channel – Contribution of Nd isotopes in ferromanganese crusts. *European Geosciences Union.* April 2019, Vienna, Austria. Oral presentation 441
Appendix 11. C. CHARLES *et al.,* 2020. Paleoceanographic reconstruction of the Mozambique Channel through the Fe-Mn crusts geochemical study. *Goldschmidt Conference.* June 2020, Honolulu, Hawaii, USA. Oral presentation 449
Appendix 12. C. CHARLES *et al.,* 2021. Vertical movements recorded in Fe-Mn crusts: what interest in resource exploration? *Goldschmidt Conference.* July 2021, Lyon, France. Oral presentation 457

LIST OF FIGURES

Chapitre 1 – Introduction (français)

Figure 1.1. *Localisation du site d'étude à l'ouest de l'océan Indien. Le canal du Mozambique est situé entre les marges continentales africaines et malgaches (©NASA).* 66

Figure 1.2. *Bathymétrie de l'est de l'océan Indien (GEBCO et campagnes PAMELA) avec les navigations des missions océanographiques PAMELA-MOZ1 et PAMELA-MOZ5 menés par le projet PAMELA ainsi que les campagnes MD-06 Nosicaa et MD-39 Rida dirigées par le MNHN. Les points représentent les positions des 17 dragues respectives dont proviennent les échantillons de cette thèse (Annexe 1).* 67

Figure 1.3. *Concentration de l'oxygène, manganèse et fer dissous dans l'océan Indien selon la profondeur (d'après Saager et al., 1989 ; Chinni et al., 2019).* 68

Figure 1.4. *Classifications des différents processus de formation des dépôts Fe-Mn : hydrogénétique, diagénétique et hydrothermal, selon (A) l'étude de Bonatti (1972) et d'après (B) Josso et al., 2017 (modifiés).* 69

Figure 1.5. *Processus hydrogénétique de formation à grande échelle des encroûtements Fe-Mn (modifiée, d'après Koschinsky, Halbach, 1995).* 71

Figure 1.6. *(A) Structure minéralogique en tunnel de la todorokite et (B) en feuillets de la vernadite montrant les sites H20 en jaune (modifiée, d'après Post 1999).* 71

Figure 1.7. *Encroûtement Fe-Mn MOZ5-DR03-01 dont différentes périodes temporelles sont visibles grâce à la présence de lamines. PAMELA MOZ5 (Moulin, Evain, 2016).* 72

Figure 1.8. *Courbe du ratio $^{187}Os/^{188}Os$ de l'eau de mer d'après Ravizza, Peucker-Ehrenbrink (2003) (A). Comparaison avec la courbe de l'osmium enregistrée dans l'encroûtement CD29-2 (gris) et ajustement à la signature de l'eau de mer (noir). Les tirets et les rectangles noirs montrent les périodes d'érosion et de lacune de l'échantillon, modifiée, d'après Klemm et al. (2005) (B).* 74

Figure 1.9. *Localisation des encroûtements Fe-Mn dont les études temporelles ont été réalisées à partir des isotopes du Nd, Pb et Be (A). Événements paléogéographiques majeurs au cours des 50 Ma qui ont influencé la circulation des océans et valeurs isotopiques en Nd des grands domaines océaniques. Les rectangles noirs correspondent aux fermetures alors que les blancs montrent les ouvertures. Les flèches indiquent les directions générales des plaques tectoniques. (B) D'après Frank (2002).* 75

Figure 1.10. *Comparaison et variations des signatures isotopiques en Nd des séries temporelles analysées dans les différents domaines océaniques (modifié, d'après Frank (2002).* 77

Figure 1.11. *Reconstruction des différents stades de la dislocation du Gondwana et de la mise en place du canal du Mozambique (rectangle rouge) depuis le Jurassique supérieur avec la séparation de l'Afrique et de la structure « Madagascar-Antarctique » jusqu'à l'émersion de la ride de Davie à l'Éocène marquant le début de la stabilité géodynamique du canal. La DFZ est notée en pointillés noirs et la ride de Davie d'un trait plein noir (modifié, d'après Thompson (2017)).* 79

***Figure 1.12**. Synthèse de la structuration du canal du Mozambique et des évènements magmatiques / géodynamiques majeurs ayant eu lieu depuis sa mise en place.* 80

***Figure 1.13.** Bathymétrie du canal du Mozambique (GEBCO et campagnes PAMELA) avec ses principales structures géologiques. Les monts sous-marins ponctuant le long de la ride de Davie sont entourés en blanc et les courants océaniques présents dans le canal sont indiqués par des flèches.* 81

Chapter 1 – Introduction (english)

***Figure 1.1.** Location of the study site to the west of the Indian Ocean. The Mozambique Channel is located between the African and Malagasy continental margins (©NASA).* 98

***Figure 1.2.** Bathymetry of the eastern Indian Ocean (GEBCO and PAMELA campaigns) with the navigations of PAMELA-MOZ1 and PAMELA-MOZ5 oceanographic missions led by the PAMELA project as well as the MD-06 Nosicaa and MD-39 Rida campaigns led by the MNHN. The points represent the positions of the 17 respective dredges from which the samples from this thesis come (Appendix 1).* 99

***Figure 1.3.** Concentration of dissolved oxygen, manganese and iron in the Indian Ocean according to depth (after Saager and al., 1989 ; Chinni and al., 2019).* 100

***Figure 1.4.** Classifications of the different processes of formation of Fe-Mn deposits: hydrogenetic, diagenetic and hydrothermal, according to (A) the study by Bonatti (1972) and (B) Josso and al., 2017 (modified).* 101

***Figure 1.5.** Hydrogenetic process of large-scale formation of Fe-Mn crusts (modified from Koschinsky, Halbach, 1995).* 103

***Figure 1.6.** (A) Mineralogical tunnel structure of todorokite and (B) in layers of vernadite showing H20 sites in yellow (modified, after Post 1999).* 103

***Figure 1.7.** Fe-Mn crust MOZ5-DR03-01 of which different periods are visible thanks to the laminations. PAMELA-MOZ5 (Moulin, Evain, 2016).* 104

***Figure 1.8.** Curve of the $^{187}Os/^{188}Os$ ratio of seawater according to Ravizza, Peucker-Ehrenbrink (2003) (A). Comparison with the osmium curve recorded in CD29-2 (grey) and adjustment to the seawater signature (black). Black dashes and rectangles show erosion and gap periods of the sample from Klemm and al. (2005) (B).* 105

***Figure 1.9.** Location of Fe-Mn crusts whose temporal studies were carried out using isotopes of Nd, Pb and Be (A). Major paleogeographic events during the 50 Ma which influenced the circulation of the oceans and isotopic values in Nd of the large oceanic domains. The black rectangles correspond to the closures while the white shows the openings. Arrows indicate general directions of tectonic plates. (B) According to Frank (2002).* 107

***Figure 1.10.** Comparison and variations of the Nd isotope signatures of time series analyzed in the different oceanic domains (modified, from Frank (2002)).* 109

Figure 1.11. *Reconstruction of the different stages of the dislocation of Gondwana and the establishment of the Mozambique Channel (red rectangle) from the Upper Jurassic with the separation of Africa and the "Madagascar-Antarctic" structure until the emergence of the Davie ridge in the Eocene marking the beginning of the geodynamic stability of the canal. Black dotted lines denote the DFZ and the Davie ridge with a solid black line (modified, after Thompson (2017)).* 110

Figure 1.12*. Summary of the structuring of Mozambique Channel and major magmatic / geodynamic events that have taken place since its establishment.* 111

Figure 1.13. *Bathymetry of the Mozambique Channel (GEBCO and PAMELA cruises) with its main geological structures. Seamounts along Davie ridge are circled in white and ocean currents in the channel are indicated by arrows.* 113

Chapitre 2 – Méthodologie analytique (français)

Figure 2.1. *Encroûtement Fe-Mn MOZ1-DR11-01 après avoir été échantillonné et dont toute la stratigraphie réalisée est visible. PAMELA MOZ1 (Olu, 2014).* 131

Figure 2.2*. Schéma du rayonnement incident et diffracté par une maille cristalline selon la loi de Bragg.* 132

Figure 2.3. *Schéma simplifié du principe d'analyse élémentaire par le biais d'un ICP-AES (d'après la documentation du constructeur Horiba (2021) et Levine (2021)).* 135

Figure 2.4*. Schéma simplifié d'un TIMS Thermo Scientific ™ Triton depuis la source primaire jusqu'à l'obtention des intensités en sortie, d'après la documentation du constructeur.* 148

Figure 2.5. *Schéma explicatif de la production du ^{10}Be atmosphérique et du ^{10}Be in situ à partir des rayons cosmiques et des multiples réactions de nucléosynthèse dans l'atmosphère et dans la lithosphère.* 152

Figure 2.6. *Schéma et photo de l'instrument national ASTER - Spectromètre de masse par accélérateur situé au LN2C - CEREGE (d'après Delunel (2010)).* 154

Figure 2.7. *Photo de la série temporelle MOZ-DR22-01 et ses nombreuses lamines illustrant le calcul des taux de croissance.* 157

Chapter 2 – Analytical methodology (english)

Figure 2.1. *Fe-Mn crust MOZ1-DR11-01 after having been sampled and of which all the stratigraphy carried out is visible. PAMELA MOZ1 (Olu, 2014).* 167

Figure 2.2*. Scheme of incident and diffracted radiation by a crystal lattice according to Bragg law.* 168

Figure 2.3. *Simplified scheme of the principle of elemental analysis by means of an ICP-AES (according to the manufacturer's documentation Horiba (2021) and Levine (2021).* 171

Figure 2.4*. Simplified diagram of a TIMS Thermo Scientific ™ Triton from primary source to output intensities, based on manufacturer documentation.* 183

Figure 2.5. *Explanatory diagram of the production of atmospheric ^{10}Be and ^{10}Be in situ from cosmic rays and the multiple nucleosynthesis reactions in the atmosphere and in the lithosphere.* 187

Figure 2.6. *Diagram and photo of the national ASTER instrument - Accelerator mass spectrometer located at LN2C - CEREGE (from Delunel (2010)).* 189

Figure 2.7. *Photo of the MOZ-DR22-01 time serie and its many laminae illustrating the calculation of growth rates.* 191

Chapter 3 – Modern isotopic records of the regional water masses

Figure 3.1. *Localisation des échantillons analysés par Vlastélic et al. (2001) ainsi que les grands domaines isotopiques définis. Les flèches montrent les voies de circulation principales des masses d'eau profondes comme définies par Mantyla et Reid (1995). Figure modifiée d'après Vlastélic et al. (2001).* 215

Figure 3.2. *Variations des rapports isotopiques $^{207}Pb/^{204}Pb$ vs. $^{206}Pb/^{204}Pb$ et, $^{208}Pb/^{204}Pb$ vs. $^{206}Pb/^{204}Pb$ issues Vlastélic et al. (2001). Trois lignées (N-Indian, A-Indian, SW-Indian) et un groupe de points (S-Indian) y sont définis et correspondent à différents secteurs géographiques de l'océan Indien.* 216

Figure 3.3. *(A) Rapport isotopique $^{208}Pb/^{206}Pb$ en fonction de la latitude montrant une tendance avec des rapports plus élevés (> 2.0707) dans le nord du canal du Mozambique. Les deux encroutements MOZ1-DR22-06 et DR75-0012 se trouvent en dehors de cette corrélation. (B) Profondeur maximale de prélèvement des échantillons en fonction du rapport isotopique $^{206}Pb/^{204}Pb$ ne présentant pas de relation directe mais plusieurs tendances distinctes. Dans les deux graphiques, les points blancs non inclus dans un champ proviennent de la région de Bassas da India et Europa.* 221

Figure 3.4. *(A) Rapport isotopique $^{207}Pb/^{204}Pb$ en fonction du rapport $^{206}Pb/^{204}Pb$. (B) Rapport isotopique $^{208}Pb/^{204}Pb$ en fonction du rapport $^{206}Pb/^{204}Pb$. Les lignées en gris sont définies d'après Vlastélic et al. (2001). Les échantillons de PAMELA-MOZ1 forment un cluster de points entre plusieurs lignées alors que les encroûtements Fe-Mn de PAMELA-MOZ5 s'alignent sur la tendance « SW-Indian ».* 222

Figure 3.5. *Zoom du rapport isotopique $^{208}Pb/^{204}Pb$ en fonction du rapport $^{206}Pb/^{204}Pb$. Les lignées en gris sont définies d'après Vlastélic et al. (2001). Les échantillons de PAMELA-MOZ1 s'étendent entre plusieurs lignées alors que les encroûtements Fe-Mn de PAMELA-MOZ5 s'alignent sur la tendance « SW-Indian ». Les points verts sont issus de la drague DR11 de la ride de Jeffrey, au nord de la ride de Davie.* 224

Chapter 4 – Fe-Mn crusts: archives of vertical paleogeodynamic movements

Figure 4.1. *Bathymetry of the Mozambique Channel (data from GEBCO and PAMELA cruises) with the limits of the tectonic plates of the region (dashed black lines) from Lemoine et al. (2020), Michon (2016), Saria et al. (2014), Stamps et al. (2021, 2018, 2008). The samples are represented by the purple dot (DR84-0026), the blue square (MOZ1-DR10-05), the pink diamond (MOZ1-DR17-01) and the yellow triangle (MOZ1-DR22-01).* 234

Figure 4.2. *Salinity section of the Mozambique Channel showing the distribution of its main water masses, the bathymetry is represented in grey, and T-S diagram, based on Conductivity Temperature Depth (CTD) profiles. AABW: Antarctic Bottom Water; AAIW: Antarctic Intermediate Water; NADW: North Atlantic Deep Water; NIDW: North Indian Deep Water; RSW; Red Sea Water; SICW: South Indian Centre Water; STSW; Sub-Tropical Surface Water; TSW; Tropical Surface Water.* 238

Figure 4.3. *Images of the four selected Fe-Mn crusts. They all present a planar shape and two of them (MOZ1-DR17-01; DR84-0026) show carbonate substrate.* 239

Figure 4.4. *PAAS-normalised (Taylor and McLennan, 1985) REY compositions of the four studied Fe-Mn crusts with all their respective layers (n).* 246

Figure 4.5. *Ternary discriminative diagrams for oceanic deposits highlighting the hydrogenetic nature of all the layers (n) from each Fe-Mn crust of this work. The diagram on the left is from Bonatti et al. (1972) and the one on the right from Josso et al. (2017).* 247

Figure 4.6. *The $^{10}Be/^{9}Be$ ratios in the crusts MOZ1-DR17-01, MOZ1-DR10-05, MOZ1-DR22-01 and DR84-0026 versus depth beneath the growth surface. The ages have been calculated from the radioactive decay of the Be in the samples. The growth rates and ages beyond the age range covered by $^{10}Be/^{9}Be$ data have been calculated using the extrapolation of the growth rates of the deepest layers whose $^{10}Be/^{9}Be$ values were measured.* 248

Figure 4.7. *Time series of $\varepsilon_{Nd\,(T)}$ and $^{206}Pb/^{204}Pb$, $^{207}Pb/^{204}Pb$, $^{208}Pb/^{204}Pb$, $^{208}Pb/^{206}Pb$ versus age derived from $^{10}Be/^{9}Be$ dating (**Figure 4.6**) for the four analysed Fe-Mn crusts. Error bars are included in the sample points. The time series values from the literature are shown for comparisons with SS663 isotope values from O'Nions et al. (1998) and Frank and O'Nions (1998), 109 D-C and ALV539 data from O'Nions et al. (1998) and BM 1969.5 values from Burton et al. (1997) and O'Nions et al. (1998).* 249

Figure 4.8. *The diagram on the top represents the Nd isotope signatures (εNd) vs. the sum of the major elements commonly associated with detrital components, normalised by Fe and Mn (due to the matrix of the Fe-Mn crusts). No correlation is visible expect for the sample DR84-0026. The diagram on the bottom illustrates a mixing calculation curve and highlights that the DR84-0026 composition shows too weak Al contents to be significantly impacted by a geochemical mixing with low radiogenic sediments containing high contents of Al.* 257

Figure 4.9. *Map of the Mozambique Channel (data from GEBCO and PAMELA cruises) showing the locations of the four Fe-Mn crusts of this study. In blue, Nd isotope signature (εNd) are presented for the main very low radiogenic formations surrounding the channel (De Waele et al., 2006; Grantham et al., 2011; Jelsma et al., 1996; Kröner et al., 2018; Möller et al., 1998; Paquette et al., 1994). The black pentagons correspond to the core tops analysed by van der Lubbe et al. (2016). The two darkest stars are surface water samples : VM 19-214 from Franzese et al. (2006) and GIK 16152 from Rahlf et al. (2020) whereas the two other stars correspond to the cores DSDP 25 Site 242 from Roddaz et al. (2020) and 64EP304-80 from van der Lubbe et al. (2016). The Mozambique Fan is represented by the blue area with dotted outline (Droz and Mougenot et al., 1987).* 259

Figure 4.10. *Latitude (data from PAMELA cruises) vs. Nd isotope signatures (εNd) of all the layers of the four studied Fe-Mn crusts showing there is no linear correlation from low radiogenic values in the south (e.g. MOZ1-DR17-01) to more radiogenic values in the north of the Mozambique Channel (e.g. DR84-0026).* 261

Figure 4.11. *Periods of main Nd and Pb isotope variations identified in the four time series. The arrows represent the increases (more radiogenic) and decreases (less radiogenic) in compositions. P1 is from 30.6 to 11.4 Ma; P2 from 11.4 to 5.1; P3 from 5.1 to 1.6 and P4 from 1.6 to modern time. Recent changes (P4 and P3) show more decoupled variations in the records of the four Fe-Mn crusts whereas old changes (P2, P1) are homogenous in the four samples.* 263

Figure 4.12. *Schematic propositions of the uplift event appeared between 11.1-11.7 and 5.7-3.4 Ma and the subsidence movement observed between 5.1 and 1.6 Ma in the Mozambique Channel. The figure is based on the examples of the sample MOZ1-DR10-05 (Macua Mount, north of the Davie Ridge) for the uplift demonstration and of the Fe-Mn crust MOZ1-DR17-01 (Hall Bank, south of the Davie Ridge) for the subsidence explanation. The colours of the water masses are identical to that on the* ***figure 4.2*** *corresponding to salinity values acquired from Conductivity Temperature Depth (CTD) profiles.* 267

Chapter 5 – Deep paleoceanography of the channel over the last 20 Ma

Figure 5.1. *Map of localisations of the samples 232D and 13KD-1 from Frank et al. (2006), SS663 and 109D-C from O'Nions et al. (1998) and, the Fe-Mn crusts studied in this work: MOZ1-DR04-23, MOZ1-DR11-01 and DR75-0012 dredged in the Mozambique Channel (SW Indian Ocean). The arrows indicate the main deep-water flow patterns according to Mantyla and Reid (1995).* 295

Figure 5.2. *Images of the three selected Fe-Mn crusts. They all present a planar shape and two of them (MOZ1-DR04-23, DR75-0012) show polygenic breach substrates.* 297

Figure 5.3. *The $^{10}Be/^{9}Be$ ratios in the crusts MOZ1-DR04-23, MOZ1-DR11-01 and DR75-0012 versus depth beneath the growth surfaces. The ages have been calculated from the radioactive decay of the Be in the samples. The growth rates and ages beyond the age ranges covered by $^{10}Be/^{9}Be$ values were calculated using the extrapolation of the growth rates of the deepest layers whose $^{10}Be/^{9}Be$ values were measured.* 302

Figure 5.4. *Evaluation of the relationship between the ages (Ma) and the depths (mm) for the studied Fe-Mn crusts presenting a combination of $^{10}Be/^{9}Be$ and Co based calculations. The dashed line corresponds to the chronology acquired by extrapolation of the last growth rate from $^{10}Be/^{9}Be$ measurements, whereas the solid line is the $^{10}Be/^{9}Be$ calibrated Co chronology. The other data are Co chronology established with different equations from Frank et al. (1999), Manheim (1986) and Manheim and Lane-Bostwick (1988).* 304

Figure 5.5. *Ternary discriminative diagrams for oceanic deposits highlighting the hydrogenetic nature of all the layers (n) from each Fe-Mn crust of this work. The diagram on the left is from Bonatti et al. (1972) and the one on the right is from Josso et al. (2017).* 307

Figure 5.6. *PAAS-normalised (Pourmand et al., 2012; Taylor and McLennan, 1985) REY compositions of the three studied Fe-Mn crusts with all their respective layers (n).* 309

Figure 5.7. *Time series of $\varepsilon_{Nd\,(T)}$ and $^{206}Pb/^{204}Pb$, $^{207}Pb/^{204}Pb$, $^{208}Pb/^{204}Pb$, $^{208}Pb/^{206}Pb$ versus ages derived from $^{10}Be/^{9}Be$ dating (**Figure 5.3**) for the three analysed Fe-Mn crusts. Error bars are included in the sample points. The time series values from the literature are shown for comparisons with SS663 isotope values from O'Nions et al. (1998) and Frank and O'Nions (1998); 109 D-C and ALV539 data from O'Nions et al. (1998); and BM 1969.5 values from Burton et al. (1997) and O'Nions et al. (1998).* 312

Figure 5.8. *Comparison of the Pb isotope ratios of crusts MOZ1-DR04-23, MOZ1-DR11-01 and DR75-0012 with other available Fe-Mn crusts time series results and the isotopic composition of the Himalayan Belt composed of granites. Defined domains are from Abouchami et al. (1997), Burton et al. (1997), Frank and O'Nions (1998), Frank et al. (2002), Ling et al. (1997) and O'Nions et al. (1998). The dashed lines and black area (S-Indian) represent also oceanographic domains from Vlastélic et al. (2001).* 317

Figure 5.9. *Paleoceanographic reconstruction of the deep-water masses (NADW, NIDW) in the Mozambique Channel before the major uplift event appeared during the Middle Miocene (11.7-11.1 Ma) and identified near Europa island (MOZ1-DR22-01) and in the northern part of the Davie ridge (DR84-0026 and MOZ1-DR10-05) according to Charles et al. (in prep.).* 320

Figure 5.10. *Paleoceanographic reconstruction of the deep-water masses (NADW, NIDW) in the Mozambique Channel from the Early Pliocene (5.7-3.4 Ma), after the major geodynamic uplift identified near Europa island (MOZ1-DR22-01) and in the northern part of the Davie ridge (DR84-0026 and MOZ1-DR10-05) according to Charles et al. (in prep.).* 321

Chapitre 6 – Synthèse, conclusions et perspectives (français)

Figure 6.1. *Bathymétrie du canal du Mozambique (données issues de GEBCO et des missions océanographiques PAMELA) montrant les estimations de contributions du NADW et sa circulation dans le canal du Mozambique. Les flèches en pointillés représentes les potentiels passages topographiques de la ride de Davie permettant la propagation du NADW dans le bassin des Comores. Il s'agit d'une figure synthèse issue du papier Charles et al. (2020), modifiée et replacée ici par souci de confort pour le lecteur.* 337

Figure 6.2. *Figure synthétique présentant les quatre encroûtements Fe-Mn utilisés dans la reconstruction paléogéodynamique du canal du Mozambique et leurs principales caractéristiques (épaisseur, taux de croissance, nombre de lamines prélevées et âge).* 339

Figure 6.3. *Figure synthétique des signatures isotopiques $\varepsilon_{Nd\,(T)}$ et $^{208}Pb/^{206}Pb$ en fonction du temps. La marge d'erreur est incluse dans les points. Des signatures provenant d'études précédentes ont été ajoutées pour comparaisons : SS663 de O'Nions et al. (1998) et Frank, O'Nions (1998); 109 D-C et ALV539 de O'Nions et al. (1998) et, BM 1969.5 de Burton et al. (1997) and O'Nions et al. (1998).* 341

Figure 6.4. *Figure synthétique présentant les trois encroûtements Fe-Mn utilisés dans la reconstruction paléocéanographiques du canal du Mozambique et leurs principales caractéristiques (épaisseur, taux de croissance, nombre de lamines prélevées et âge).* 343

Figure 6.5. *Reconstruction paléocéanographique des courants profonds Atlantique (NADW) et Indien (NIDW) du canal du Mozambique. La figure (A) illustre la situation au Pliocène (3.4 Ma), après la mise en place de l'uplift généralisé dans la région, alors que la figure B correspond à la reconstruction paléocourantologique au Miocène (11.7 Ma), avant ce bouleversement géodynamique. Il s'agit d'une figure synthèse issue du chapitre 5 et modifiée.* 344

Figure 6.6. *Bathymétrie du canal du Mozambique (données issues de GEBCO et des missions océanographiques PAMELA) présentant la localisation des encroûtements Fe-Mn MOZ1-DR04-23 (Îles Glorieuses, 16.2 Ma) et MOZ5-DR03-01 (Vallée de Natal, 19.7 Ma) ainsi que les zones d'influence de potentiels phénomènes locaux enregistrés dans leurs compositions minéralogiques et géochimiques.* 347

Figure 6.7. *Images et cartographies minéralogiques de la lame mince MOZ1-DR04-23 E réalisées avec le FEG-SEM Qemscan ®. a) acquisition BSE ; b) acquisition EDS montrant les principales phases minéralogiques (Nanomin - FEI, Hillsboro, OR, USA) ; c) acquisition BSE et les oxydes Mn ; d) acquisition BSE et les oxydes Fe.* 348

Figure 6.8. *Graphique des concentrations en Al en fonction des concentrations en Ti dans l'encroûtement Fe-Mn MOZ1-DR04-23. Les numéros au niveau de chaque point correspondent à la profondeur (mm) de la lamine prélevée dans l'encroûtement Fe-Mn, ceux en gras et en couleurs correspondent aux lamines dont les datations sont indiquées. Les deux flèches indiquent de potentiels influences de phénomènes volcaniques et/ou d'apports sédimentaires, et les âges associés.* 349

Figure 6.9. *Synthèse des phénomènes volcaniques (barres noires) dans l'archipel des Comores et dans les régions environnantes. Les barres blanches représentent les activités nouvellement estimées. Les numéros 1, 2 et 3 correspondent aux différentes périodes de volcanisme. Les encadrés représentent de potentiels phénomènes volcaniques enregistrés dans l'encroûtement Fe-Mn MOZ1-DR04-23, provenant de la région des Îles Glorieuses (**Figure 6.8**). Image modifiée, d'après Michon (2016).* 350

Figure 6.10. *Images et cartographies minéralogiques de la lame mince MOZ5-DR03-01 B réalisées avec le FEG-SEM Qemscan ®. a) acquisition BSE ; b) acquisition EDS montrant les principales phases minéralogiques (Nanomin - FEI, Hillsboro, OR, USA) ; c) acquisition BSE et les oxydes Mn ; d) acquisition BSE et les oxydes Fe.* 351

Figure 6.11. *Signature isotopique en Nd ($\varepsilon_{Nd\ (T)}$) en fonction de l'âge, acquis à partir du rapport isotopique $^{10}Be/^{9}Be$, des encroûtements Fe-Mn MOZ5-DR03-01 et DR75-0012 issus de cette étude. Les données des encroûtements Fe-Mn ALV539 et BM 1969.05 proviennent des travaux de Burton et al. (1997) et de O'Nions et al. (1998).* 352

Figure 6.12. *Sections correspondantes à la distribution des principales masses d'eau du canal du Mozambique, d'après les profils Conductivité-Température-Profondeur (CTD). A : Données de température (°C) ; B : Données de salinité (psu) ; C : Données en oxygène dissous (ml/l). La bathymétrie du canal du Mozambique est issue des données GEBCO 2014 et des campagnes PAMELA)* 355

Chapter 6 – Synthesis, conclusions and perspectives (english)

Figure 6.1. *Mozambique Channel bathymetry (data from GEBCO and PAMELA oceanographic missions) showing estimated contributions from NADW and its circulation in the Mozambique Channel. The dotted arrows represent the potential topographic passages of the Davie Ridge allowing the propagation of NADW in the Comoros Basin. This is a summary figure from the paper Charles et al. (2020), modified and relocated here for the convenience of the reader.* 365

Figure 6.2. *Synthetic figure showing the four Fe-Mn crusts used in the paleogeodynamic reconstruction of the Mozambique Channel and their main characteristics (thickness, growth rate, number of laminae sampled and ages* 367

Figure 6.3. *Synthetic figure of the isotopic signatures εNd (T) and 208Pb/206Pb over time. The margin of error is included in the points. Signatures from previous studies have been added for comparison: SS663 from O'Nions et al. (1998) and Frank, O'Nions (1998); 109 D-C and ALV539 from O'Nions et al. (1998) and, BM 1969.5 from Burton et al. (1997) and O'Nions et al. (1998).* 369

Figure 6.4. *Synthetic figure presenting the four Fe-Mn crusts used in the paleogeodynamic reconstruction of the Mozambique Channel and their main characteristics (thickness, growth rate, number of laminae sampled and age).* 370

Figure 6.5. *Palaeoceanographic reconstruction of the deep Atlantic (NADW) and Indian (NIDW) currents of the Mozambique Channel. Figure (A) illustrates the situation in the Pliocene (3.4 Ma), after the establishment of the generalized uplift in the region, while figure B corresponds to the current reconstruction in the Miocene (11.7 Ma), before this geodynamic upheaval. This is a summary figure from chapter 5 and modified.* 371

Figure 6.6. *Bathymetry of the Mozambique Channel (data from GEBCO and PAMELA oceanographic missions) showing the location of Fe-Mn crusts MOZ1-DR04-23 (Glorious Islands, 16.2 Ma) and MOZ5-DR03-01 (Natal Valley, 19.7 Ma) as well as the zones of influence of potential local phenomena recorded in their mineralogical and geochemical compositions.* 374

Figure 6.7. *Images and mineralogical maps of the MOZ1-DR04-23 E thin section made with the FEG-SEM Qemscan ®. a) BSE acquisition; b) EDS acquisition showing the main mineralogical phases (Nanomin - FEI, Hillsboro, OR, USA); c) BSE acquisition and Mn oxides; d) BSE acquisition and Fe oxides.* 375

Figure 6.8. *Plot of Al concentrations versus Ti concentrations in the Fe-Mn crust MOZ1-DR04-23. The numbers at each point correspond to the depth (mm) of the lamina sampled on the Fe-Mn crust, those in bold and in colour correspond to the laminae with the dates indicated. The two arrows indicate potential volcanic and/or sedimentary influences and associated ages.* 376

Figure 6.9. *Synthesis of volcanic phenomena (black bars) in the Comoros archipelago and in the surrounding regions. White bars represent newly estimated activities. Numbers 1, 2 and 3 correspond to the different periods of volcanism. The boxes represent potential volcanic phenomena recorded in the Fe-Mn crust MOZ1-DR04-23, from the Glorious Islands region (**Figure 6.8**). Modified image, according to Michon (2016).* 377

Figure 6.10. *Images and mineralogical maps of the MOZ5-DR03-01 B thin section produced with the FEG-SEM Qemscan ®. a) BSE acquisition; b) EDS acquisition showing the main mineralogical phases (Nanomin - FEI, Hillsboro, OR, USA) ; c) BSE acquisition and Mn oxides; d) BSE acquisition and Fe oxides.* 378

Figure 6.11. *Nd isotopic signature ($\varepsilon_{Nd\,(T)}$) according to the age, acquired from the $^{10}Be/^{9}Be$, isotopic ratio, of the Fe-Mn crusts MOZ5-DR03-01 and DR75-0012 from this study. The data for the Fe-Mn ALV539 and BM 1969.05 crusts come from the work of Burton et al. (1997) and of O'Nions et al. (1998).* 379

Figure 6.12. *Sections corresponding to distribution of the main water masses of Mozambique Channel, according to the Conductivity-Temperature-Depth (CTD) profiles. A: Temperature data (°C); B: Salinity data (psu) ; C: Dissolved oxygen data (ml/l). The bathymetry of Mozambique Channel is taken from GEBCO 2014 data and PAMELA campaigns.* 381

LIST OF TABLES

Chapitre 1 – Introduction (français)

Tableau 1.1. *Abréviations des principales masses d'eau présentes dans le canal du Mozambique, leurs profondeurs et leurs signatures isotopiques εNd respectives.* 82

Chapter 1 – Introduction (english)

Table 1.1. *Abbreviations of the main water masses present in the Mozambique Channel, their depths and their respective εNd isotopic signatures.* 112

Chapitre 2 – Méthodologie analytique (français)

Tableau 2.1. *Profil d'élution du Pb et du Nd selon les acides et les résines utilisés.* 147

Chapter 2 – Analytical methodology (english)

Table 2.1. *Elution profile of Pb and Nd according to the used acids and resins.* 182

Chapter 3 – Modern isotopic records of the regional water masses

Tableau 3.1. *Numéro international (IGSN), localisation, profondeur et valeurs des isotopes de Pb des encroûtements de Fe-Mn étudiés provenant des expéditions océanographiques PAMELA-MOZ1 (Olu, 2014), PAMELA-MOZ5 (Moulin, Evain, 2016), MD-06 Nosicaa (Leclaire, 1975) et MD-39 Rida (Leclaire, 1984).* 219

Chapter 4 – Fe-Mn crusts: an archive of vertical paleogeodynamic movements

Table 4.1. *International Geo Sample Number (IGSN), location, depth and major characteristics of the four studied Fe-Mn crusts from the PAMELA-MOZ1 (Olu, 2014) and MD39-Rida (Leclaire, 1984). The water masses correspond to the modern records of the samples, the * corresponds to the transition depth defined between the intermediate and deep water by Charles et al. (2020) and GR for "Growth rate".* 240

Table 4.2. *Major and trace elements mean compositions of the four studied Fe-Mn crusts.* 243

Table 4.3. *Be, Nd and Pb isotope compositions of all layers of the four studied Fe-Mn crusts from the PAMELA-MOZ1 (Olu, 2014) and MD39-Rida (Leclaire, 1984). –S corresponds to the surface (top of the Fe-Mn crust) and the other numbers are related to their depth on the Fe-Mn crust slice. The * indicate the ^{10}Be dated layers.* 253

Table 4.4. *Amplitudes and vertical rate movements of the identified uplift (from 11.1-11.7 to 5.7-3.4 Ma) and subsidence (from 5.1 to 1.6 Ma) events in the Mozambique Channel. All the parameters are detailed in the text.* [a]*Mean modern depth (mbsl);* [b]*Estimated depth;* [c]*Drowning amplitude estimated from growth rates between 11 and 15 m/Ma in the north and between 29 and 39 m/Ma in the south of the channel (Courgeon 2017; Courgeon et al., 2018).* 269

Chapter 5 – Deep paleoceanography of the channel of the last 20 Ma

Table 5.1. *International Geo Sample Number (IGSN), location, depth and major characteristics of the studied Fe-Mn crusts from the PAMELA-MOZ1 (Olu, 2014) and MD-06 Nosicaa (Leclaire, 1975). The water masses correspond to the modern records of the analysed samples by Charles et al. (2020).* 298

Table 5.2. *Results of* $^{10}Be/^{9}Be$ *isotope analyses and age determination with the extrapolation of the last measured growth rate (GR) for the three studied Fe-Mn crusts. –S indicates the surface layer and the other numbers are related to their depths on the Fe-Mn crust slice. The * show the layers whose Be isotopes have been measured.* 300

Table 5.3. *Chemical characterisation of the three studied Fe-Mn crusts. The data correspond to the means of the elements. The standard deviations (SD) are also provided to represent a complete vision of the ranges.* 306

Table 5.4. *Nd and Pb isotope compositions of all the layers of the three studied Fe-Mn crusts from the PAMELA-MOZ1 (Olu, 2014) and MD06-Nosicaa (Leclaire, 1975). -S corresponds to the surface (top of the Fe-Mn crust) and the other numbers are related to their depth on the Fe-Mn crust slice. The * indicate the* ^{10}Be *dated layers.* 310

Table 5.5. *Calculations of the NADW and the NIDW inputs at three different locations of the Mozambique Channel (Glorieuses Islands, Jeffrey Ridge and Agulhas Plateau) over time. Numbers are percentages of NADW calculated with Pacific water mass end-member values of* $\varepsilon Nd = -4$ *and -6 (Frank et al., 2002).* 315

LIST OF APPENDICES

Appendices

Appendix 1. *Details of the oceanographic cruises* 391

Appendix 2. *List and details of the 33 Fe-Mn crusts of this study* 395

Appendix 3. *Presentation of the sampled and analysed time series* 399

MOZ1-DR04-023 400

MOZ1-DR10-05 402

MOZ1-DR11-01 404

MOZ1-DR17-01 406

MOZ1-DR22-01 408

DR75-0012 410

DR84-0026 412

MOZ5-DR03-01 414

Appendix 4. *Locations of the 8 thin sections sampled on the Fe-Mn crusts MOZ1-DR04-23 and MOZ5-DR03-01* 417

Appendix 5. *XRD patterns of the sample MOZ1-DR04-23* 419

Appendix 6. *XRD patterns of the sample MOZ5-DR03-01* 423

Appendix 7. *Mineralogical results of the 4 thin sections from the Fe-Mn crusts MOZ1-DR04-23 and MOZ5-DR03-01* 427

Appendix 8. *C. CHARLES et al., 2019. Paleoceanographic and paleogeographic reconstruction of the Mozambique Channel through geochemical study of Fe-Mn crusts. Seminar PAMELA. November 2019, Pau, France. Poster* 433

Appendix 9. *C. CHARLES et al., 2019. Paleoceanographic and paleogeographic reconstruction of the Mozambique Channel through geochemical study of Fe-Mn crusts. Seminar PAMELA. November 2019, Pau, France. Oral presentation* 435

Appendix 10. *C. CHARLES et al., 2019. Paleoceanographic and paleogeodynamic reconstruction of the Mozambique Channel – Contribution of Nd isotopes in ferromanganese crusts. European 1Geosciences Union. April 2019, Vienna, Austria. Oral presentation* 441

Appendix 11. *C. CHARLES et al., 2020. Paleoceanographic reconstruction of the Mozambique Channel through the Fe-Mn crusts geochemical study. Goldschmidt Conference. June 2020, Honolulu, Hawaii, USA. Oral presentation* 449

Appendix 12. *C. CHARLES et al., 2021. Vertical movements recorded in Fe-Mn crusts: what interest in resource exploration? Goldschmidt Conference. July 2021, Lyon, France. Oral presentation* 457

CHAPITRE 1 : INTRODUCTION

1.1. Cadre général du projet de thèse

Le canal du Mozambique est issu de la séparation de l'Afrique et de Madagascar entre 180 Ma et 80 Ma (Coffin, Rabinowitz, 1987 ; Eagles, König, 2008 ; Gaina et al., 2013 ; Heirtzler, Burroughs, 1971). Depuis, la tectonique régionale a peu évolué à l'exception de mouvements verticaux (entre 35 et 25 Ma, puis entre 15 et 2 Ma) et de phénomènes volcaniques à partir de 30 Ma et encore présents aujourd'hui. Sa localisation entre l'océan Atlantique et l'océan Indien en fait une zone stratégique de mélange de masses d'eau (Collins et al., 2016 ; de Ruijter et al., 2002 ; DiMarco et al., 2002 ; Flemming, Kudrass, 2018 ; van Aken et al., 2004 ; You, 2000), principalement connue pour le courant des Aiguilles, essentiel à la régulation de la chaleur entre les deux hémisphères (Gordon, 1986 ; Weijer, 1999 ; Lutjeharms, 2006).

La circulation océanique du canal reste aujourd'hui encore largement méconnue notamment en ce qui concerne l'impact des événements géologiques régionaux et locaux sur l'évolution des courants profonds et intermédiaires. C'est dans ce contexte, que les missions PAMELA-MOZ1 et PAMELA-MOZ5 (paragraphe 1.1.1 – Projet PAMELA) ont été proposées et réalisées respectivement en 2014 et 2016, dans le but d'identifier et de comprendre les interactions entre les masses d'eau et les systèmes sédimentaires profonds, notamment dans la région sud-ouest du canal, dans le nord de la vallée de Natal. L'enjeu portait également sur l'étude de l'origine de la mise en place des plates-formes carbonatées et des grands événements volcaniques du canal du Mozambique.

Les deux campagnes ont permis de réunir une collection unique d'encroûtements ferromanganésifères (Fe-Mn) dans le canal du Mozambique. Ces concrétions géologiques sont utilisées depuis les années 1980 dans des travaux de reconstructions paléocéanographiques et paléogéographiques à partir de leurs études minéralogiques et, géochimiques élémentaires et isotopiques (Albarède et al., 1997 ; Christensen et al., 1997 ; Frank et al., 1999 ; Josso et al., 2020 ; Mizell et al., 2020).

En intégrant les données bathymétriques des deux missions océanographiques et, l'étude minéralogique et géochimique approfondie des encroûtements Fe-Mn, cette thèse a pour objectifs de (1) caractériser les masses d'eau présentes dans le canal du Mozambique et leurs voies de circulation, (2) retracer l'évolution courantologique de cette zone de mélange au cours des derniers 30 Ma et (3) comprendre l'impact des bouleversements climatiques et géographiques mondiaux et régionaux (e.g. volcanisme, subsidence, uplift) sur la composition géochimique des masses d'eau et sur leur circulation.

1.1.1. Projet PAMELA

Le projet PAMELA (PA*ssive* M*argin* E*xploration* LA*boratory*) vient d'une étroite collaboration scientifique entre l'Institut Français de la Recherche pour l'Exploitation de la Mer (IFREMER) et Total dans le but d'établir un modèle d'évolution de marge passive, dans une démarche de « source to sink ». Ce programme, porté entre 2013 et 2019, inclut un nombre important de partenaires tels que l'Institut Français du Pétrole et des Énergies Nouvelles (IFPEN), l'Université de Bretagne Occidentale (UBO), l'Université de Pierre et Marie Curie (UPMC), l'Université de Rennes et le Centre National de la Recherche Scientifique (CNRS). Cinq thèmes de recherche ont été principalement abordés : l'évolution géodynamique, les systèmes sédimentaires, les aléas géologiques, l'étude des courants et l'étude des écosystèmes marins. Il

s'agit d'une collaboration d'envergure qui offre la possibilité de développer d'importantes avancées scientifiques par l'acquisition de données novatrices sur des zones stratégiques pour la compréhension des marges continentales. Quatre zones de recherche ont été sélectionnées pour leur représentativité de multiples contextes : le golfe de Gascogne, la marge est de la Corse, le golfe d'Aden et le canal du Mozambique (Figure 1.1).

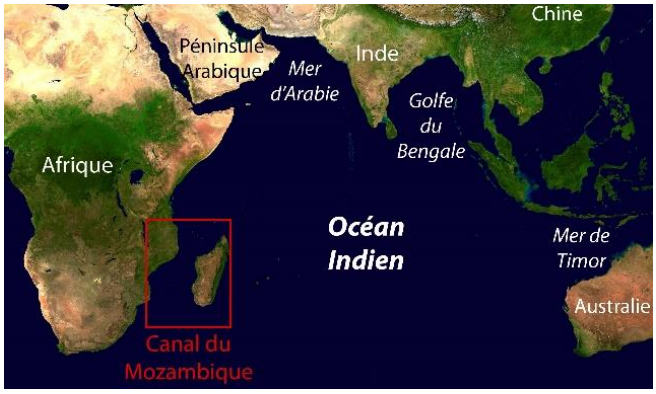

Figure 1.1. *Localisation du site d'étude à l'ouest de l'océan Indien. Le canal du Mozambique est situé entre les marges continentales africaines et malgaches (©NASA).*

Ce dernier correspond au plus grand chantier scientifique du projet depuis 2014 en raison de son remarquable intérêt géologique et océanographique. Dans ce cadre, 7 campagnes océanographiques ont été réalisées afin de caractériser (1) sa structure crustale et sédimentaire, (2) sa genèse, son évolution verticale ainsi que sa déformation associée à la cinématique des plaques, (3) l'ensemble des systèmes sédimentaires, du delta aux lobes turbiditiques profonds, et (4) leurs interactions avec les variations paléocourantologiques et paléoclimatiques.

1.1.2. Missions océanographiques

Ce travail de thèse s'appuie sur des échantillons prélevés lors de 4 campagnes océanographiques. La plupart des échantillons proviennent de 2 campagnes réalisées dans le cadre du projet PAMELA, les deux autres ont été réalisées par le Muséum National d'Histoire Naturelle de Paris (MNHN) en 1975 et 1984. Nous présenterons ici succinctement ces campagnes.

PAMELA-MOZ1 a eu lieu en 2014, à bord du N/O L'Atalante (Olu, 2014). Cette campagne s'est intéressée à 11 secteurs clefs du canal du Mozambique, depuis le lobe du Zambèze au sud jusqu'à la région des îles Glorieuses au nord (Figure 1.2). Les objectifs des opérations de dragages étaient de (1) se renseigner sur l'âge de mise en place du volcanisme de l'arc des Comores, de la ride de Davie ainsi que des monts sous-marins de la région de Bassas da India, (2) de caractériser la nature des encroûtements Fe-Mn échantillonnés préalablement le long de la ride de Davie et (3) d'identifier leur potentiel métallogénique. Finalement, 22 opérations de dragages ont été réalisées sur les flancs des monts sous-marins et des édifices volcaniques, depuis l'Île Europa au sud jusqu'aux îles Glorieuses au nord. Un total de 186 échantillons a été récupéré dont 74 encroûtements Fe-Mn.

PAMELA-MOZ5 a été réalisée en 2016 à bord du « Pourquoi pas ? » (Moulin, Evain, 2016). L'étude crustale des marges passives bordant le bassin est Limpopo et la vallée de Natal était le but principal de cette mission océanographique (Figure 1.2), par le biais d'une acquisition sismique réflexion multitraces et sismique grand-angle important. Cependant, 8 opérations de dragages ont été également réalisées, et 5 ont rapporté des encroûtements Fe-Mn à caractère exceptionnel.

MD-06 Nosicaa (Leclaire, 1975) et MD-39 Rida (Leclaire, 1984) sont deux campagnes océanographiques dirigées par MNHN. La première MD-06 Nosicaa s'est intéressée à l'origine et à la nature des sédiments dans l'Océan

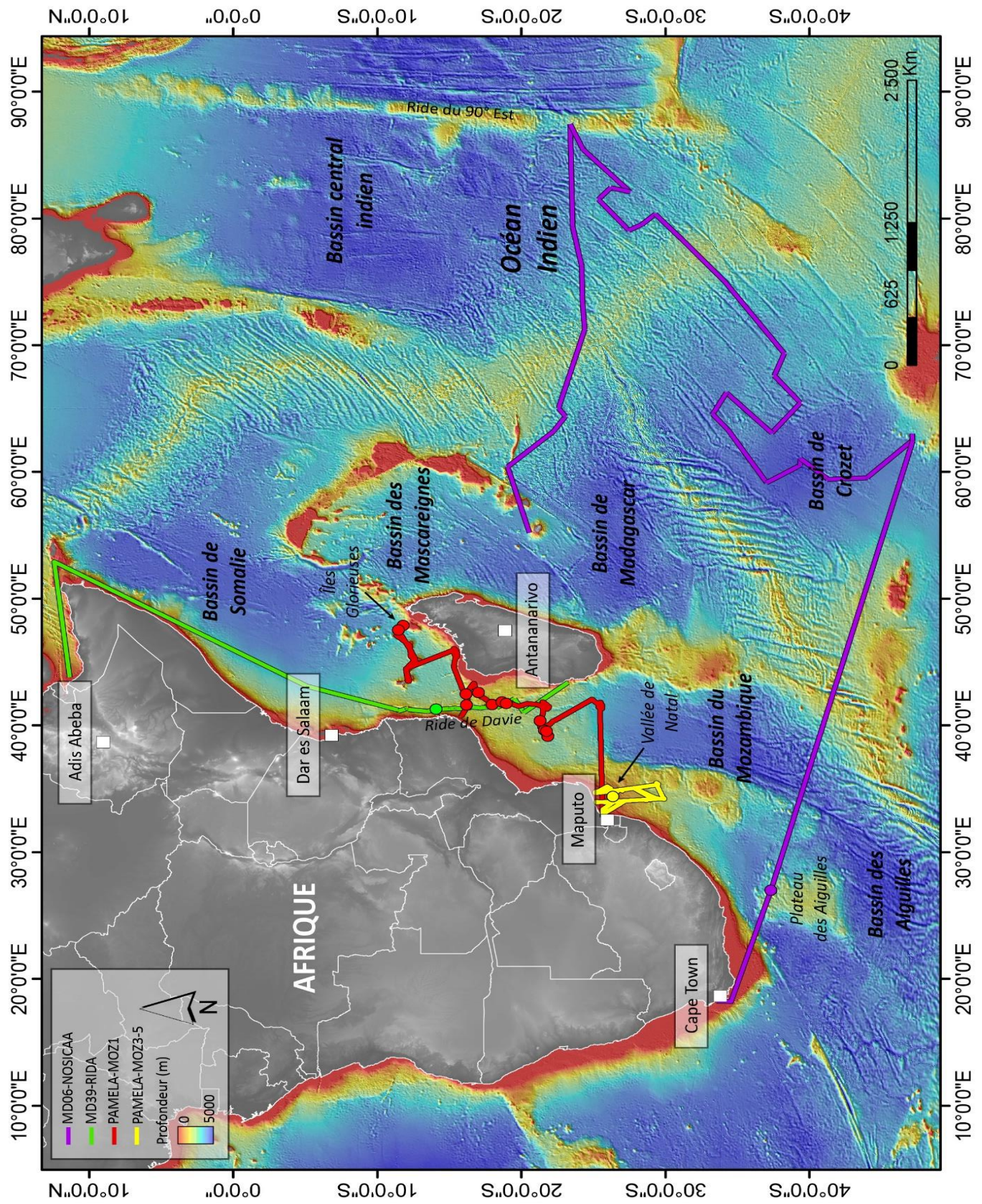

Figure 1.2. *Bathymétrie de l'est de l'océan Indien (GEBCO et campagnes PAMELA) avec les navigations des missions océanographiques PAMELA-MOZ1 et PAMELA-MOZ5 menés par le projet PAMELA ainsi que les campagnes MD-06 Nosicaa et MD-39 Rida dirigées par le MNHN. Les points représentent les positions des 17 dragues respectives dont proviennent les échantillons de cette thèse (**Annexe 1**).*

Indien central et austral (Figure 1.2) alors que la deuxième MD39-Rida visait à étudier la structure de la ride de Davie (Figure 1.2) et la dynamique des masses d'eau du canal du Mozambique sous l'influence des changements météorologiques. Cette campagne océanographique est à l'origine des premiers encroûtements Fe-Mn découverts dans ce secteur. Au cours de cette thèse, un échantillon de chacune de ces campagnes est étudié. L'un provenant du Plateau des Aiguilles et faisant office d'un jalon primordial au sud du canal. L'autre venant de la pente ouest de la ride de Davie, dans la région du mont Paisley.

1.2. Principes géologiques et questionnements scientifiques

1.2.1. Caractéristiques générales du Fe et Mn dans les océans

Le fer (Fe) et le manganèse (Mn) sont des métaux très présents dans l'océan où ils jouent un rôle essentiel dans les cycles biogéochimiques. Ce sont des éléments sensibles aux conditions oxydo-réductrices, ce qui leur permet de migrer sous formes dissoutes et de précipiter en fonction des modifications des conditions physico-chimiques de l'environnement. Les cycles biogéochimiques des métaux dans les océans sont contrôlés par des sources et des puits qui varient selon les métaux considérés (Frank, 2002).

Dans le cas du Mn, l'hydrothermalisme est la source principale de ce métal, avec des concentrations chimiques au niveau des fumeurs noirs parfois un million de fois plus fortes que celles présentes dans l'eau de mer (Elderfield et al., 1996). Cependant, d'autres sources de Mn existent telles que les apports terrigènes par voie fluviatile et éolienne, ou le volcanisme sous-marin. Ainsi, la répartition du Mn dans la colonne d'eau est très variable, comme le montre la figure 1.3. Le Mn est un élément métastable avec :

(1) des concentrations élevées depuis la surface des océans, sous forme Mn^{2+}, jusque dans la Zone Minimum d'Oxygène (OMZ), qui est une zone entre 700 et 2000 mètres de profondeur où la cinétique d'oxydation du Mn est très lente et ses concentrations peuvent atteindre près de 4 nmol/kg (Klinkhammer, Bender, 1980),

(2) des concentrations devenant nettement plus faibles en profondeur à cause de la précipitation des oxy-hydroxydes et favorisées par l'activité bactériologique.

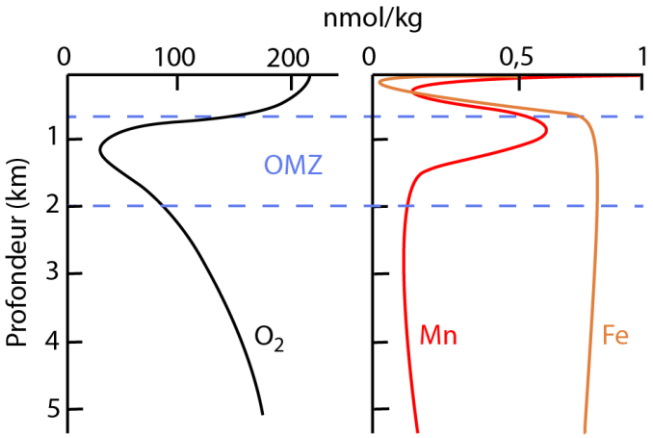

Figure 1.3. *Concentration de l'oxygène, manganèse et fer dissous dans l'océan Indien selon la profondeur (d'après Saager et al., 1989 ; Chinni et al., 2019).*

Le Fe, quant à lui, provient principalement des apports atmosphériques, sédimentaires, hydrothermaux et des rivières. Il est majoritairement présent sous forme particulaire (>1 µm). Sa concentration dans la colonne d'eau suit une distribution moins variable que le Mn, comme le montre la figure 1.3. En surface sa concentration est très élevée, avec une moyenne de 70 pmol/kg, due aux apports éoliens. Il est rapidement consommé et ses concentrations diminuent intensément en surface avant d'être rejeté. À partir de l'OMZ, il existe une stabilité des concentrations en profondeur.

1.2.2. Processus de précipitation des dépôts Fe-Mn

Différents processus de précipitations sont à l'origine de la grande variété de minéralisations Fe-Mn. Ils varient selon des facteurs définis, liés à l'environnement géodynamique, l'activité hydrothermale, la bathymétrie du fond marin ou encore l'intensité des courants. Ainsi, les trois processus principaux impliqués dans la croissance des dépôts Fe-Mn profonds sont : le processus hydrogénétique, le processus diagénétique et le processus hydrothermal, et plusieurs classifications, présentées ci-après permettent de les caractériser (Figure 1.4 ; Bonatti, 1972 ; Josso et al., 2017).

1.2.2.1. Processus hydrogénétique

Ce processus correspond à la précipitation d'oxydes métalliques sous forme colloïdale depuis la solution marine en milieu oxydant (Dymond et al., 1984). En effet, dans l'eau océanique, les éléments peuvent être présents sous forme élémentaire ou constituer des complexes (organiques ou inorganiques). Ces derniers formeront des colloïdes pouvant alors interagir avec les métaux dissous (Hein et al., 1997 ; Koschinsky, 1994 ; Koschinsky, Halbach, 1995).

Plusieurs facteurs importants tels que (1) la concentration initiale de l'élément dans l'eau de mer, (2) le degré d'oxydation et le pH dans la colonne d'eau (Hein et al., 1997) ou encore, (3) l'apport d'éléments par processus de dissolution et de dilution des éléments détritiques contrôlent la concentration des éléments dans les dépôts hydrogénés. Enfin, il est essentiel de noter que le taux de précipitation lié à ce processus est très faible. Il varie entre 0,5 et 15 mm/Ma ce qui nécessite un environnement de dépôt calme, à très faible taux de sédimentation (Hein et al., 1997).

1.2.2.2. Processus diagénétique

Le processus diagénétique dépend des conditions d'oxydation de la colonne sédimentaire, de son

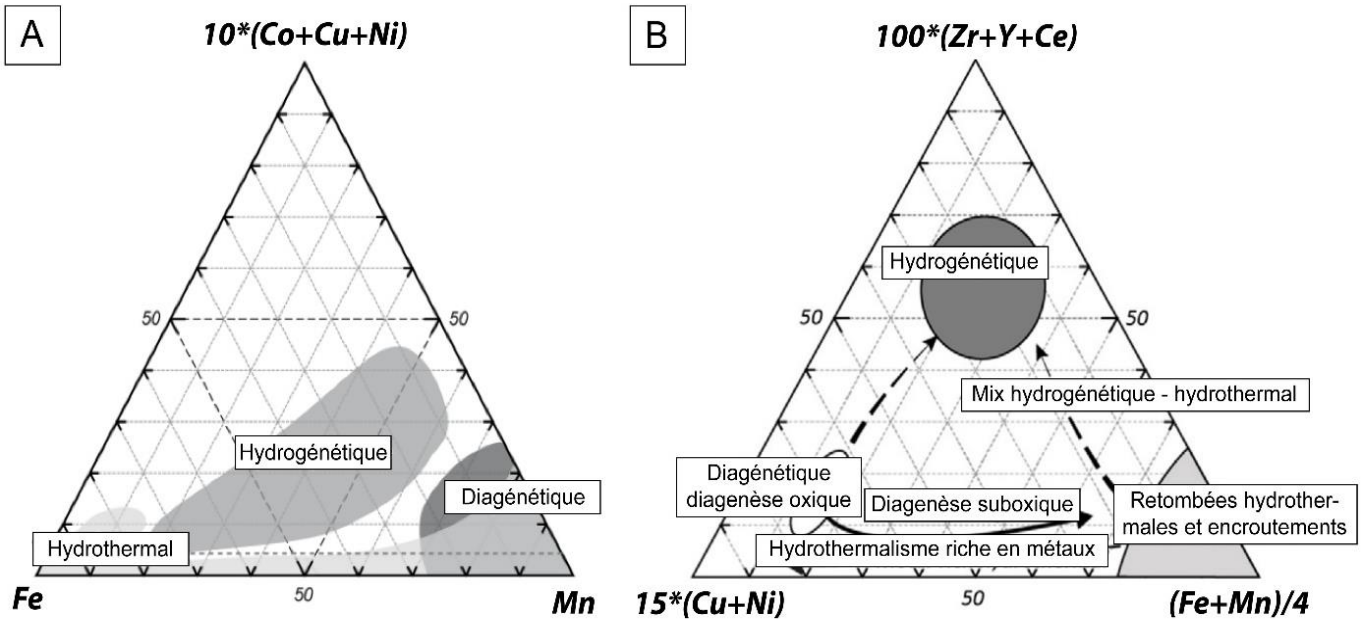

Figure 1.4. *Classifications des différents processus de formation des dépôts Fe-Mn : hydrogénétique, diagénétique et hydrothermal, selon (A) l'étude de Bonatti (1972) et d'après (B) Josso et al., 2017 (modifiés).*

épaisseur, du taux de sédimentation et de l'activité biologique. Ainsi, les formations diagénétiques sont issues de deux conditions distinctes : avec et sans oxygène.

Dans le cas d'une diagénèse avec présence d'oxygène, les éléments métalliques sont remobilisés par les eaux interstitielles sous la faible épaisseur de sédiments, où ils sont alors reprécipités (Dymond, Eklund, 1978 ; Jung, Lee, 1999). Dans le cas d'un processus sans oxygène, l'élément stable est réduit sous sa forme mobile. Il va alors migrer jusqu'à la profondeur de nouvelles conditions oxydo-réductrices et précipiter de nouveau.

1.2.2.3. Processus hydrothermal

Ce dernier processus est lié directement à la précipitation de la solution hydrothermale proche des sources d'émissions d'importants flux thermiques, comme au niveau des dorsales ou arcs océaniques, et au niveau des points chauds. Cependant, plus le fluide hydrothermal émis va s'éloigner de sa source et se mélanger avec l'eau de mer plus les précipités auront la composition des dépôts hydrogénétiques (Hein et al., 1997).

Les trois processus ici présentés ont d'abord été illustrés dans le diagramme ternaire de Bonatti, 1972 (Figure 1.4). Il s'agit d'un diagramme visant à classifier ces trois modes de précipitations des dépôts Fe-Mn par le biais d'un pôle Mn, d'un pôle Fe et d'un pôle correspondant à la somme des teneurs en nickel (Ni), cuivre (Cu) et cobalt (Co).

Ainsi, chaque processus de formation occupe une place précise du diagramme avec un rapport Fe/Mn très variable et des teneurs en métaux Co, Cu et Ni relativement faibles. Josso et al. (2017) propose un second diagramme de classification intégrant les métaux, le rapport Fe/Mn, mais également l'yttrium (Y) et le cérium (Ce) faisant partie des terres rares (REY) et le zirconium (Zr) qui est un élément fortement chargé (HSFE ; Figure 1.5). Ces derniers sont généralement présents en faibles concentrations dans les dépôts diagénétiques et hydrothermaux, ce qui permet de distinguer les apports hydrogénétiques des apports diagénétiques.

1.2.3. Encroûtements Fe-Mn

Les encroûtements Fe-Mn sont des dépôts métallifères océaniques sous forme d'oxy-hydroxydes de Fe (FeOOH.nH2O) et de Mn (MnOOH.nH2O), enrichis en métaux de transitions (Hein et al., 2013 ; Li, Schoonmaker, 2003) au même titre que les nodules polymétalliques ou les sulfures hydrothermaux (Cronan, 1980). Dans les cas des encroûtements, le processus de formation dans la colonne d'eau océanique a lieu par le biais de formation de colloïdes puis par l'adsorption de métaux (processus hydrogénétique ; Figure 1.5).

En effet, la phase réduite Mn^{2+}, enrichie dans l'OMZ (Klinkhammer, Bender, 1980) se retrouve oxydée lorsqu'elle est mélangée avec des eaux profondes plus riches en oxygène. À ce stade, le Mn et les Fe à l'origine d'oxy-hydroxydes forment des colloïdes qui en fonction de leur charge surfacique, peuvent devenir des colloïdes mixtes (Koschinsky, Halbach, 1995). Les colloïdes d'oxy-hydroxydes de Fe (FeO(OH)) ayant des charges surfaciques positives piègent les éléments anioniques et les larges complexes. À l'inverse, les colloïdes d'oxydes de Mn (MnOOH), ayant une surface chargée négativement, attirent les cations (Hein et al., 2013 ; Koschinsky, Halbach, 1995 ; Koschinsky et al., 1997 ; Yuan-Hui, 1982). Les éléments tels que le phosphore (P), le thorium (Th), les terres rares lourdes (HREE), l'arsenic (As), le titane (Ti) et le vanadium (V) sont incorporés à FeO(OH) (Figure 1.5). Alors que les éléments comme le Co,

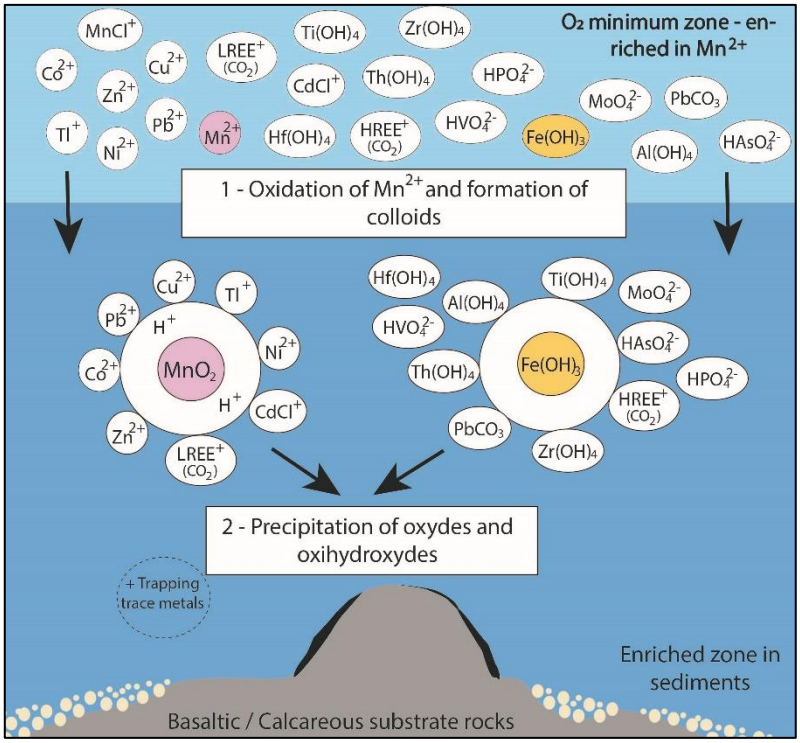

Figure 1.5. *Processus hydrogénétique de formation à grande échelle des encroûtements Fe-Mn (modifiée, d'après Koschinsky, Halbach, 1995).*

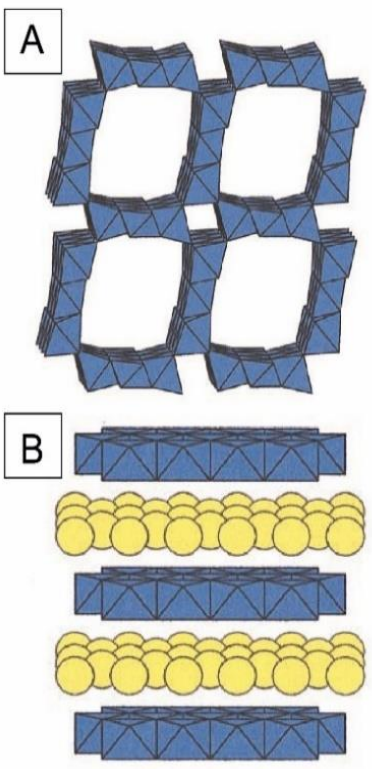

Figure 1.6. *(A) Structure minéralogique en tunnel de la todorokite et (B) en feuillets de la vernadite montrant les sites H20 en jaune (modifiée, d'après Post 1999).*

le Ni, le Cu, le zinc (Zn), le thallium (Tl) et les terres rares légères (LREE) se retrouvent préférentiellement sur la phase MnOOH (Bau, 1996 ; Koschinsky, Hein, 2003). Les colloïdes précipitent ensuite sur les substrats durs, dans des zones à très faibles taux de sédimentation (Craig et al., 1982 ; Halbach et al., 1983), et piègent les métaux traces dissous (Figure 1.5).

À ce stade, le Fe précipite principalement sous forme amorphe (FeO(OH)) alors que les trois états d'oxydation du Mn : Mn^{2+}, Mn^{3+} et Mn^{4+} lui permettent de s'associer à une multitude d'éléments et de former de nombreuses phases multivalentes (Post, 1999). Cette large variété de valence électronique lui permet d'accommoder de nombreuses architectures cristallines intégrant aisément d'autres cations sur la base cristallographique d'octaèdres MnO_6. Deux structures minéralogiques principales se dégagent en contexte océanique selon les arrangements qu'adoptent ces octaèdres par jonction des angles ou de leurs bordures (Post 1999).

Les deux minéraux principaux formés à partir du Mn sont chacun associés à une structure particulière (Figure 1.6). La vernadite ou δ-MnO2, « manganate z-désordonné », « manganate désordonné » ou « manganate turbostratique » présente une structure en feuillets. Alors que la todorokite (Ca, Na, K)3-5[Mn(IV), Mn(III), Mg]60123-4.5H20, « manganate à 10 Å » ou encore « manganite à 10 Å » est un polymorphe possédant une structure en tunnel (Figure 1.6 ; Aplin, Cronan, 1985 ; Hein et al., 2016 ; Kuhn et al., 1998 ; Post, 1999), cependant elle ne figure quasiment jamais dans les encroûtements hydrogénétiques, à moins d'une remobilisation secondaire. Des minéraux

secondaires tels que du quartz, des feldspaths, de la carbonate-fluorapatite (CFA) ou d'autres minéraux détritiques sont également identifiables dans ces dépôts hydrogénés et proviennent principalement de l'érosion de sources continentales environnantes (Guan et al., 2017 ; Hein et al., 2013, 1997).

1.2.4. Taux de croissance et méthodes de datation

Les encroûtements se trouvent dans tous les océans à des profondeurs entre 400 et 7000 mètres de profondeur où ils s'accumulent sur des substrats indurés comme des monts sous-marins ou des plateaux pauvres en sédiments (Figure 1.5 ; Josso et al., 2017 ; Koschinsky, Hein, 2017). Formés directement à partir de la précipitation des éléments chimiques de l'eau de mer environnante, ces dépôts hydrogénés présentent des taux de croissance très lents, de l'ordre 1 à 10 mm/Ma en moyenne (Frank et al., 1999 ; Josso et al., 2019 ; Putenaus, Halbach, 1988). C'est pourquoi, les croûtes les plus épaisses peuvent atteindre 80 Ma (Frank et al., 1999). Ce taux de précipitation très faible permet une adsorption efficace des éléments dissous dans l'eau de mer sur des périodes de temps très larges conduisant à des enrichissements importants en métaux de base (e.g. Cu, Ni) et en métaux critiques (e.g. Co, REE, Zr, Nb, Y, Te et Pt ; Hein et al., 2010 ; Koschinsky, Hein, 2017 ; Lusty et al., 2018 ; Piper, 1974). Les encroûtements Fe-Mn contiennent donc des enregistrements des cycles des métaux dans les océans (Cronan, 2017 ; Koschinsky, Halbach, 1995 ; Koschinsky et al., 1997) avec chaque millimètre d'épaisseur correspondant à une période temporelle précise (Figure 1.7).

Ils constituent ainsi de véritables archives condensées de l'évolution géochimique des océans au cours du temps, enregistrant les changements climatiques et géomorphologiques tels que les périodes d'érosion glaciaire, les intempéries tropicales ou encore les ouvertures et les fermetures des grands domaines océaniques (Albarède et al., 1997 ; Frank et al., 2002 ; Josso et al., 2020 ; Rehkämper et al., 2004).

Figure 1.7. *Encroûtement Fe-Mn MOZ5-DR03-01 dont différentes périodes temporelles sont visibles grâce à la présence de lamines. PAMELA MOZ5 (Moulin, Evain, 2016).*

Depuis leurs découvertes, ces dépôts sont nettement étudiés pour les reconstructions paléocéanographiques utilisant différents proxys isotopiques comme le strontium (Sr), le néodyme (Nd), le plomb (Pb ; Christensen et al., 1997 ; Frank et al., 2002), mais également l'osmium (Os) et l'hafnium (Hf ; Burton et al., 1999 ; David et al., 2001 ; Klemm et al., 2005 ; Piotrowski et al., 2000). Cependant, la datation des encroûtements reste un enjeu majeur pour leur utilisation en tant qu'archives. Leur taux de croissance très faibles limite la résolution temporelle à un échantillonnage stratigraphique par micro forages qui intègrent entre 20 000 et 80 000 ans en moyenne par prélèvement (Charles et al., 2020 ; Josso et al., 2019). De plus, leur minéralogie et leur structure très poreuse (Hein et al., 2000) engendrent un contact quasi constant entre les couches des encroûtements et l'eau de mer, ce qui induit des rééquilibrages élémentaires et des

échanges non négligeables avec la signature géochimique de l'océan en temps réel (Josso et al., 2019).

Ces conditions rendent impossible l'utilisation de la datation absolue U-Pb en raison de la diffusion de l'uranium (U) dans les oxydes Fe-Mn bien qu'elle puisse être utilisée pour dater les substrats carbonatés et donner une contrainte temporelle de début de formation de l'encroûtement (Claude et al., 2005 ; Goto et al., 2014). Il est donc primordial d'établir une chronologie fiable et absolue pour les études stratigraphiques des encroûtements Fe-Mn, afin de corréler les variations géochimiques des océans avec des événements paléoclimatiques et paléocéanographiques identifiés.

1.2.4.1. Chronologie par datation absolue

Dans une étude haute résolution des premières structures, une chronologie absolue peut être effectuée utilisant ($^{230}Th_{ex}$) et ($^{230}Th_{ex}/^{232}Th$) jusqu'à 1 Ma (Claude et al., 2005). Au-delà de cette période, l'utilisation d'une autre méthode est requise. Le ^{10}Be est un isotope cosmogénique instable dont la demi-vie est suffisamment longue (1,387 ± 0,012 Ma) pour couvrir une plage temporelle jusqu'à 12 Ma (Chmeleff et al., 2010 ; Korschinek et al., 2010).

Une fois formé dans l'atmosphère terrestre, le ^{10}Be est rapidement (3 ans, selon Baroni et al., 2011) transféré à la surface du globe par le biais des précipitations. À ce stade, il est soit absorbé sur des particules et déposé sur des sédiments marins, soit contenu à la surface des sédiments continentaux. Plus de 99% du ^{10}Be se retrouve dans les dépôts sédimentaires. Ainsi, immobilisé et isolé des facteurs d'échange extérieurs, ce nucléide permet de dater efficacement les sédiments accumulés.

1.2.4.2. Chronologie par datation empirique

Un autre système de datation est proposé par Puteanus, Halbach (1988) partant du principe que le flux de Co sur un oxyde de Mn est uniquement lié au processus hydrogénétique et donc constant (Halbach et al., 1983). Si le flux du Co est constant alors la concentration en Co sera directement dépendante du taux de croissance de l'échantillon. Pour mesurer un taux de croissance (mm/Ma), il en résulte l'équation empirique suivante, avec la concentration en %wt :

$$\frac{1{,}28}{([Co] - 0{,}24)} \qquad (1)$$

Une approche similaire est réalisée par Manheim, Lane-Bostwick (1988) prenant en considération un large panel d'oxyde Fe-Mn tel que des dépôts hydrothermaux ou des sédiments pélagiques. L'équation initiale est alors dérivée pour obtenir la formule suivante, qui intègre les concentrations de Fe et de Mn, constituants principaux des oxy-hydroxydes Fe-Mn hydrogénétiques, avec les concentrations en %wt :

$$\frac{0{,}68}{\left([Co] \times \left(\frac{50}{[Fe] + [Mn]}\right)\right)^{1{,}67}} \qquad (2)$$

Bien que les âges acquis par ces deux équations soient des âges minimums, car ces techniques ne prennent pas en compte les lacunes et les surfaces érodées des dépôts de Fe-Mn, les deux méthodes sont utilisées fréquemment et indépendamment afin d'apporter une résolution temporelle aux données géochimiques dans les reconstitutions paléocéanographiques (David et al., 2001 ; Frank

et al., 1999 ; Hu et al., 2012 ; Ling et al., 2005 ; Marino et al., 2017).

1.2.4.3. Chronologie par datation indirecte

Dans la mesure où l'utilisation du Co en tant que géochronomètre présente plusieurs limites (e.g. identification des lacunes), une méthode indirecte a été considérée à travers l'étude isotopique de l'Os.

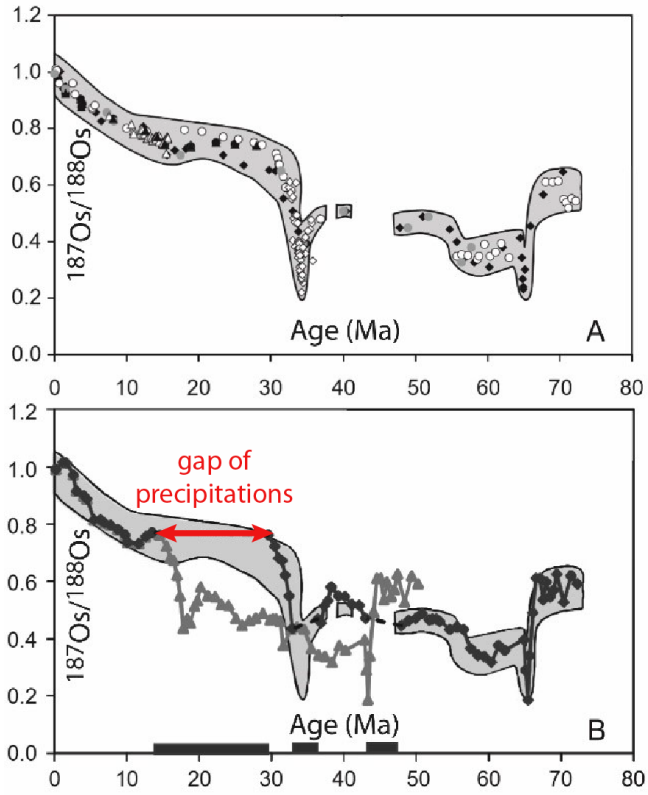

Figure 1.8. *Courbe du ratio $^{187}Os/^{188}Os$ de l'eau de mer d'après Ravizza, Peucker-Ehrenbrink (2003) (A). Comparaison avec la courbe de l'osmium enregistrée dans l'encroûtement CD29-2 (gris) et ajustement à la signature de l'eau de mer (noir). Les tirets et les rectangles noirs montrent les périodes d'érosion et de lacune de l'échantillon, modifiée, d'après Klemm et al. (2005) (B).*

En effet, le taux de diffusion de l'Os post-dépôt est très faible (de l'ordre de 3×10^{-8} cm²/an selon Henderson, Burton, 1999), ce qui ne perturbe pas la composition isotopique de l'Os dans les encroûtements Fe-Mn au cours du temps. Cette caractéristique permet de comparer les variations du ratio $^{187}Os/^{188}Os$ dans les encroûtements à l'évolution globale de ce ratio isotopique dans l'eau de mer, dont le profil a été établi et daté jusqu'à la fin du Cénozoique (Figure 1.8 ; Burton et al., 1999 ; Klemm et al., 2005 ; Peucker-Ehrenbrink, Ravizza, 2000, 2012).

Cette approche permet ainsi de faire correspondre une valeur isotopique à un âge précis pour chaque lamine d'un échantillon.

L'échantillon CD29-2 de l'océan Pacifique a déjà fait l'objet de cette approche (Christensen et al., 1997 ; Frank et al., 1999 ; Lee et al., 1999 ; Ling et al., 1997 ; Ling et al., 2005) et les âges acquis ont été comparés aux datations issues de la méthode empirique par le flux de Co. Cette comparaison montre des taux de croissance similaires mais souligne aussi que les datations issues de la méthode par flux de Co sont inexactes en raison des lacunes identifiables avec la datation indirecte par l'isotopie de l'Os (Figure 1.8 ; Klemm et al., 2005).

1.2.5. Reconstructions paléocéanographiques

Les encroûtements Fe-Mn, par leur statut d'archives des océans ont fait l'objet de nombreuses études géochimiques pour des reconstructions paléocéanographiques, mais également paléogéographiques.

Depuis les années 1980, les auteurs se sont majoritairement intéressés aux compositions géochimiques des éléments majeurs et aux compositions isotopiques du Pb et du Nd sur une vingtaine d'encroûtements répartis dans les océans Atlantique, Indien et Pacifique (Figure 1.9 ; Albarède et al., 1997 ; Christensen et al., 1997 ; Frank, 2002 ; Frank et al., 2002

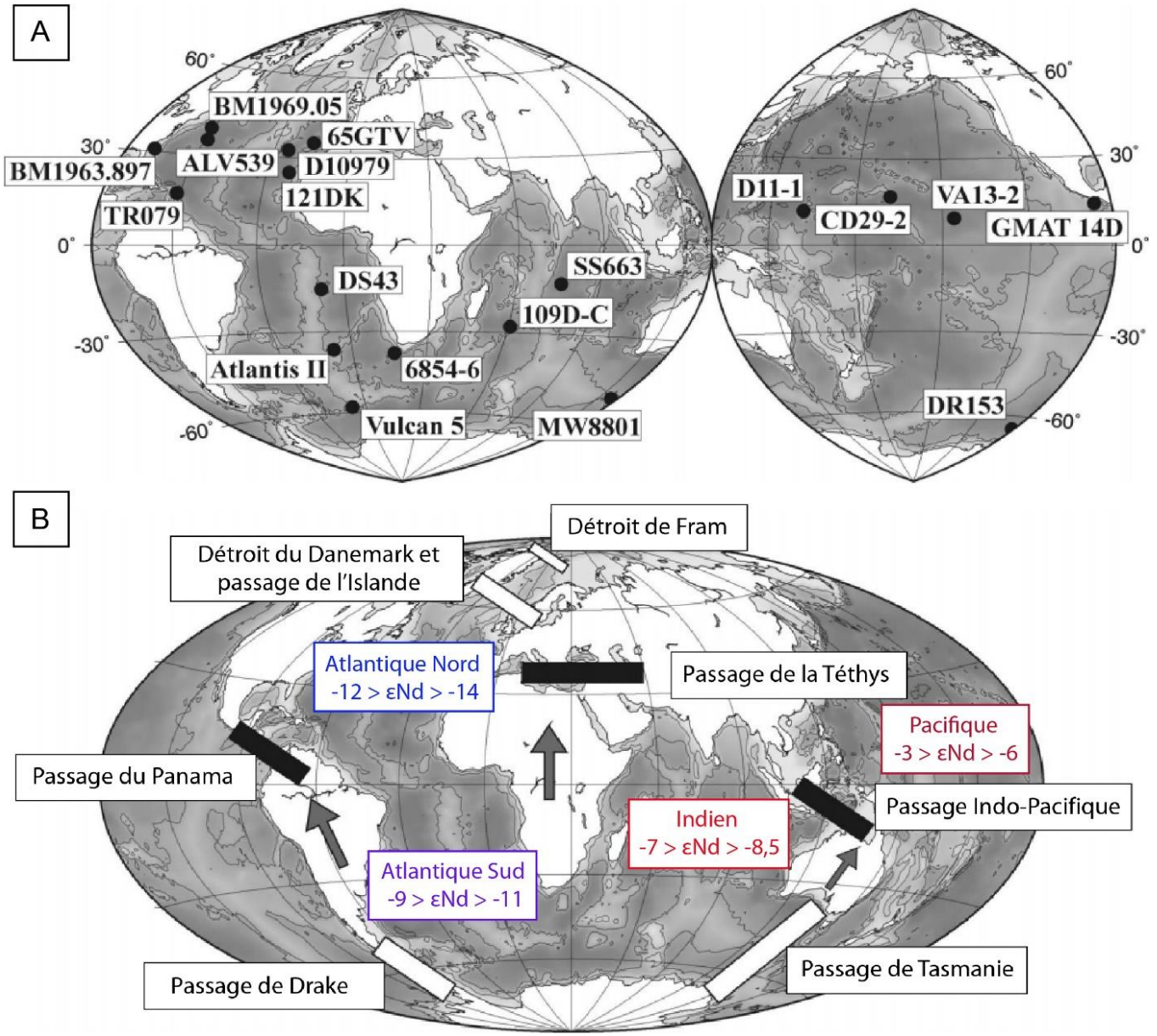

Figure 1.9. *Localisation des encroûtements Fe-Mn dont les études temporelles ont été réalisées à partir des isotopes du Nd, Pb et Be (A). Événements paléogéographiques majeurs au cours des 50 Ma qui ont influencé la circulation des océans et valeurs isotopiques en Nd des grands domaines océaniques. Les rectangles noirs correspondent aux fermetures alors que les blancs montrent les ouvertures. Les flèches indiquent les directions générales des plaques tectoniques. (B) d'après Frank (2002).*

Frank, O'nions, 1998 ; Ling et al., 1997 ; O'nions et al., 1998 ; Rehkämper et al., 2004 ; Segl et al., 1984).

1.2.5.1. Le Pb dans les océans

Le Pb des océans provient principalement des apports continentaux par le biais des apports fluviaux issus de l'érosion continentale. L'apport éolien, notamment des poussières volcaniques, n'explique que 10 % à 12 % du bilan du Pb dans les océans (Chow, Patterson, 1962) et l'apport hydrothermal demeure peu présent (<2 %) et très localisé (Chen et al., 1986). Concernant le temps de résidence du Pb, celui-ci est nettement inférieur (80 ans à 100 ans) à celui du Nd et inférieur au temps de mélange des océans (Frank et al., 2002). Cependant, il est suffisamment grand (> 20 ans) pour que le Pb constitue un traceur majeur des phénomènes océaniques et atmosphériques sur de très courtes échelles de temps.

1.2.5.2. Le Nd dans les océans

Dans les océans, le Nd provient majoritairement des apports éoliens et continentaux, par le biais des rivières et fleuves (Bayon et al., 2015; Elderfield et al., 1990; Goldstein, Jacobsen, 1988; Ingri et al., 2000; Tachikawa et al., 1997 ; van der Lubbe et al., 2016). Cependant, la contribution relative de chacun de ses apports dans le bilan global du Nd est encore discutée selon les zones géographiques (Jones et al., 1994). Concernant son temps de résidence dans les océans, il est estimé entre 600 ans et 2000 ans (Arsouze et al., 2009 ; Jeandel et al., 1995 ; Rempfer et al., 2011 ; Tachikawa et al., 2003) alors que le temps de mélange des océans est de l'ordre du millier d'années (Broecker et al., 1982). Le Nd constitue donc un traceur quasi-conservateur de la chimie des masses d'eau particulièrement intéressant et exploité pour les études paléocéanographiques (Frank, 2002; Goldstein, Hemming, 2003).

Les variations de valeurs de εNd sont liées à l'érosion et à la dissolution des roches dans les régions sources des masses d'eau. Par exemple, l'érosion des roches continentales du vieux bouclier canadien est à l'origine de valeurs εNd extrêmement peu radiogéniques. Les masses d'eau de l'Atlantique Nord présentent donc des valeurs εNd entre -12 et -14 alors que celles de l'Atlantique Sud montrent des valeurs εNd entre -9 et -11, liées au mélange entre les valeurs très peu radiogéniques de l'Atlantique Nord et plus radiogéniques du Pacifique (Jeandel, 1993; Piepgras, Wasserburg, 1987, 1982). Les valeurs εNd de l'océan Pacifique sont très radiogéniques (entre 0 et -6) de par l'érosion des roches volcaniques très jeunes dérivées du manteau (Piepgras, Jacobsen, 1988 ; Shimizu et al., 1994). Enfin, la composition isotopique en Nd de l'océan Indien résulte du mélange entre les valeurs peu radiogéniques de l'Atlantique et plus radiogéniques du Pacifique. Ses valeurs εNd varient entre -7 et -8,5 (Arsouze et al., 2007; Bertram, Elderfield, 1993; Wilson et al., 2012).

1.2.5.3. Précédentes reconstructions paléocéanographiques

Des analyses isotopiques réalisées à partir de la surface de plusieurs centaines d'encroûtements à travers le globe ont mis en évidence des grandes tendances isotopiques en Nd dans tous les domaines océaniques (Albarède et al., 1997). Ceci a permis de choisir des échantillons clés pour réaliser des études temporelles afin d'identifier et de confirmer des événements géodynamiques majeurs (Figure 1.9) à travers des changements de compositions isotopiques en Nd des masses d'eau.

Parmi eux, la séparation de l'Australie et de l'Antarctique qui entraîna à l'Oligocène (30-25 Ma) l'ouverture du passage de Tasmanie (Figure 1.9) et l'établissement du courant Antarctique Circumpolaire Current (ACC) qui a été enregistré dès l'Éocène (Kennett, 1977). Puis, l'ouverture du passage de Drake, entre l'Amérique du Sud et l'Antarctique, qui date la fin de l'Oligocène (23 Ma), a permis la circulation totale des masses d'eau autour de l'Antarctique (Barker, Burrell, 1977). D'autres événements ont été mis en évidence, notamment entre 20 Ma et 13 Ma avec la fermeture du passage de la Téthys au niveau de l'Europe (Bialik et al., 2019 ; Sun et al., 2021) et entre 25 Ma et 6 Ma qui représente la période totale de fermeture du passage Indo-Pacifique (Figure 1.9; Ali et al., 1994 ; Hall et al., 2011 ; Srinivasan, Sinha, 1998).

D'autres événements géodynamiques majeurs, plus récents, ont été étudiés, notamment par Burton et al. (1997) à travers l'isotopie du Nd et du Pb sur les échantillons CD29-2, de l'océan Pacifique, et BM1969.05 de l'océan Atlantique (Figure 1.9). Les résultats isotopiques du Nd ont notamment montré un changement brutal de valeurs de moins en moins radiogéniques des courants profonds de l'océan Atlantique (εNd passant de -11 à -13 ; Figure 1.10) à partir de la fin du Pliocène (3,5 Ma) directement liés à une hausse de la contribution des masses d'eau de la mer du Labrador par rapport aux masses d'eau du Pacifique nettement plus radiogéniques (εNd entre -3 et -4 ; Figure 1.10; Piepgras, Jacobsen, 1988). Ces observations sont en lien avec la fermeture du passage du Panama empêchant ainsi la rencontre des océans Pacifique et Atlantique (Figure 1.9 ; Keigwin, 1982 ; Nisancioglu, 2003). Ce changement majeur est notamment visible à partir de l'encroûtement BM1963.897 qui se situe sur le Plateau de Blake, au large de la côte sud-est des États-Unis. Sa signature géochimique montre une chute des compositions isotopiques de Nd à partir de 10 Ma, passant de -7,5 avant la fermeture de l'isthme à -10,5 après la fermeture totale du passage du Panama (Figure 1.9). Ces observations ont également été faites à partir des données isotopiques du Pb et de l'étude des rapports $^{206}Pb/^{204}Pb$ et $^{207}Pb/^{204}Pb$ (Burton et al., 1997).

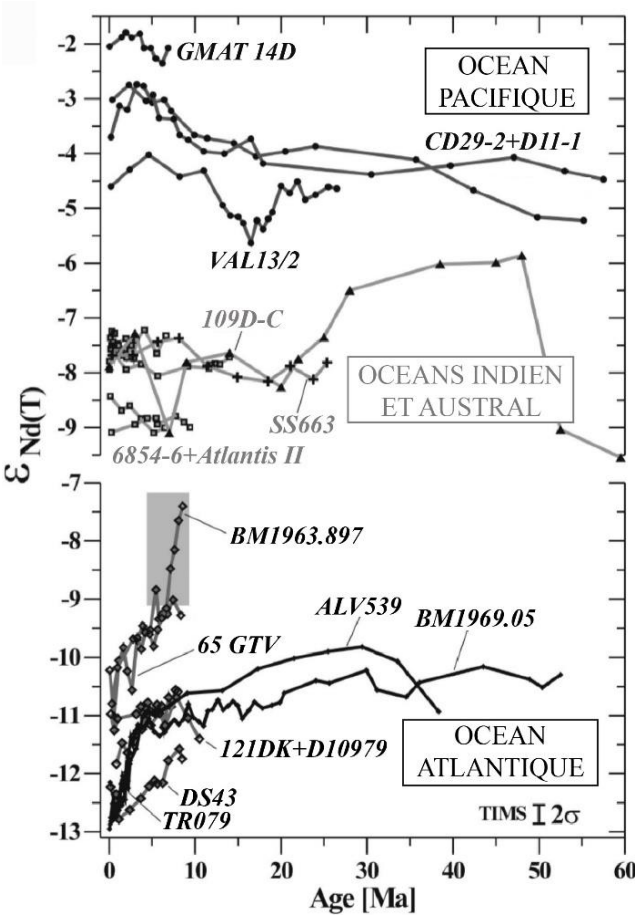

Figure 1.10. *Comparaison et variations des signatures isotopiques en Nd des séries temporelles analysées dans les différents domaines océaniques (modifié, d'après Frank (2002).*

L'étude de Frank (2002) s'est également intéressée à des phénomènes de grande ampleur à l'échelle de l'océan Atlantique et de l'océan Austral. Elle révèle aussi une augmentation de différences entre les signatures isotopiques en Nd et en Pb enregistrées dans des encroûtements de ces deux domaines océaniques à partir de 3,5 Ma. Les compositions isotopiques des masses d'eau du nord de l'Atlantique enregistrées dans les échantillons ALV539 et BM1969.05 ont

fortement diminué à partir de 3 Ma (εNd passant de -11 à -13 ; Figure 1.10) alors que celles des masses d'eau des océans Austral (Atlantis II) et Indien (109D-C) sont restées constantes (εNd respectivement entre -8,5 et -9,5 et, entre -7 et -8 ; Figure 1.10). Ces observations viennent appuyer les conclusions de Burton et al. (1997). De plus, elles indiquent une réduction des apports des masses d'eau profondes de l'Atlantique vers le sud en raison de la grande glaciation de l'hémisphère nord (NHG ; Raymo, 1994 ; Shackleton et al., 1984). Cette baisse d'apport des courants profonds de l'Atlantique dans l'hémisphère sud est estimée entre 14% et 37% entre 3,5 Ma et 0 Ma. Ces estimations sont effectuées à partir d'un calcul de mélange de pôles entre l'Atlantique nord (εNd fixé à -13 d'après Jeandel, 1993 ; Piepgras, Wasserburg, 1987, 1982) et l'océan Pacifique (εNd fixé entre -4 et -6 d'après Piepgras, Jacobsen, 1988 ; Rutberg et al., 2000 ; Shimizu et al., 1994).

Malgré un nombre important d'encroûtements Fe-Mn déjà analysés (Figure 1.9a), notamment en haute résolution par le biais de stratigraphies, les dépôts Fe-Mn du canal du Mozambique demeurent peu connus et aucune étude temporelle n'a été réalisée dans cette zone géographique alors que la localisation du canal, à l'ouest de l'océan Indien et proche des marges continentales (Figure 1.1), représente un intérêt majeur pour des études paléocéanographiques et paléogéographiques.

En effet, le canal du Mozambique joue un rôle essentiel dans le mélange des océans Atlantique et Indien et aucune extension latérale significative liée à la tectonique des plaques n'a été enregistrée depuis près de 80 Ma. Il se distingue donc des domaines océaniques ouverts où les encroûtements Fe-Mn peuvent dériver sur des milliers de kilomètres, passant de l'influence d'une masse d'eau à une autre modifiant de facto leurs signatures isotopiques (Meynadier et al., 2008).

Ainsi, en s'affranchissant des corrections de dérive inhérentes à certaines études d'encroûtements, nous serons en mesure d'étudier et de comprendre l'évolution de la courantologie du canal du Mozambique au cours du temps et l'impact de la géodynamique mondiale et régionale sur celle-ci à travers une étude minéralogique et géochimique d'encroûtements Fe-Mn.

1.3. Zone d'étude : le canal du Mozambique

1.3.1 Contexte et géodynamique

Le canal du Mozambique est localisé au sud-ouest de l'océan Indien, entre la marge continentale est-Africaine du Mozambique et Madagascar (Figure 1.1). Il est issu du démantèlement de la partie Est (Madagascar, Inde, Antarctique et Australie, appelée ici « Madagascar-Antarctique ») et de la partie Ouest (Afrique et Amérique du Sud) du Gondwana (McElhinny, 1970 ; McKenzie, Sclater, 1971). Le rift a commencé au Jurassique inférieur (Eagles, König, 2008) entraînant l'ouverture progressive du nord du Bassin du Mozambique à partir du Jurassique supérieur (Figure 1.11, 1.12; Jokat et al., 2003 ; König et Jokat, 2010 ; Leinweber, Jokat, 2012 ; Leinweber et al., 2013).

Il s'accentua avec l'ouverture sud du Bassin du Mozambique et de la Vallée de Natal à partir du Crétacé inférieur (Figure 1.12; Goodlad et al., 1982 ; Gradstein et al., 2012 ; Watkeys, Sokoutis, 1998) avant le déplacement de la structure Madagascar-Antarctique vers le Sud le long d'une zone transformante majeure appelée la Zone de Fracture de Davie (DFZ) jusqu'au Crétacé

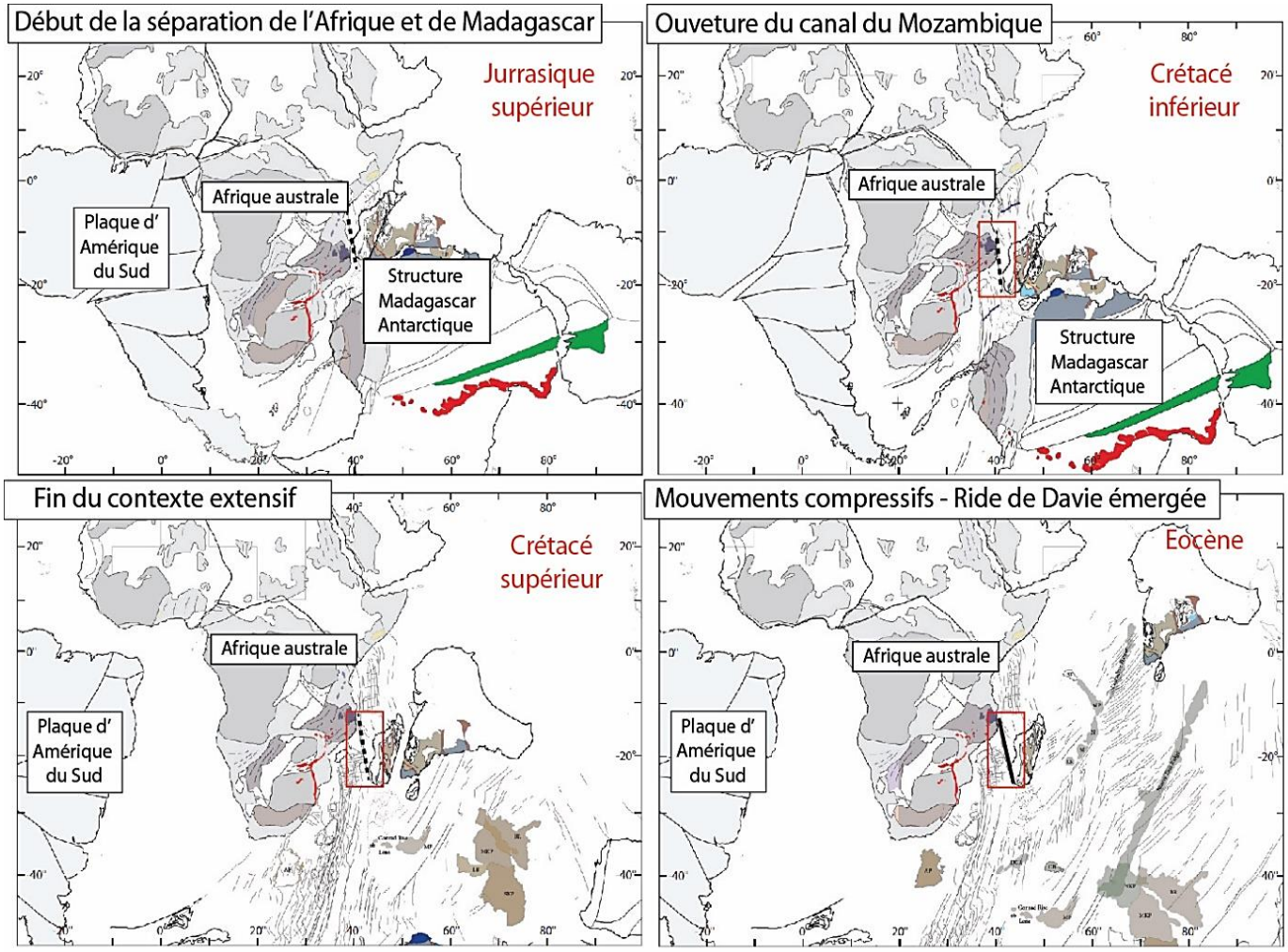

Figure 1.11. *Reconstruction des différents stades de la dislocation du Gondwana et de la mise en place du canal du Mozambique (rectangle rouge) depuis le Jurassique supérieur avec la séparation de l'Afrique et de la structure « Madagascar-Antarctique » jusqu'à l'émersion de la ride de Davie à l'Éocène marquant le début de la stabilité géodynamique du canal. La DFZ est notée en pointillés noirs et la ride de Davie d'un trait plein noir (modifié, d'après Thompson (2017)).*

supérieur marquant la fin du contexte extensif de la zone (Figure 1.11; Coffin, Rabinowitz, 1987 ; Gaina et al., 2013 ; Heirtzler, Burroughs, 1971). À partir du Crétacé supérieur, le bloc Antarctique-Inde s'est séparé de Madagascar, événement à l'origine d'une grande activité volcanique sur l'île de Madagascar, mais également au niveau des bassins Morondava et Mahajanga situés à l'ouest de l'île (Figure 1.12, 1.13; Bassias, 1992 ; Rogers et al., 2000 ; Storey et al., 1995 ; Torsvik et al., 2000).

Les îles Eparses (Bassas Da India, Europa, Juan de Nova, et les îles Glorieuses) sont des témoins de cette activité volcanique depuis leur formation à partir du Paléocène jusqu'à l'Oligocène. Elles sont issues de deux grands phénomènes d'uplift : le premier au Paléocène et le second, d'au moins 200 m (Leroux et al., 2020) de l'Éocène supérieur jusqu'à l'Oligocène étroitement lié à des pulses magmatiques engendrés par le développement du Système de Rift Est-Africain (EARS ; Chorowicz, 2005 ; Courgeon et al., 2017, 2016 ; Franke et al., 2015 ; Leroux et al., 2019 ; MacGregor, 2015 ; Masters et al., 2021 ; Walford et al., 2005).

Les îles ont ensuite été structurées par l'installation de plateformes carbonatées jusqu'au Miocène avant qu'une phase de subsidence (entre 221 et 663 m) marque l'arrêt de fonctionnement de ces plateformes carbonatées (Courgeon et al., 207, 2016 ; Leroux et al., 2020 ; McGrew, 1983). À la suite de cet épisode d'affaissement, un troisième uplift régional, (425 m ; Leroux et al., 2020) entraînant une déformation lithosphérique à l'origine d'une forte activité magmatique encore présente aujourd'hui (Emerick, Ducan, 1982 ; Michon, 2016 ; Pelleter et al., 2014), a été mise en évidence jusqu'au début du Pliocène avant un nouvel et dernier épisode de subsidence à partir du Pliocène (Courgeon et al., 2018 ; Delaunay,

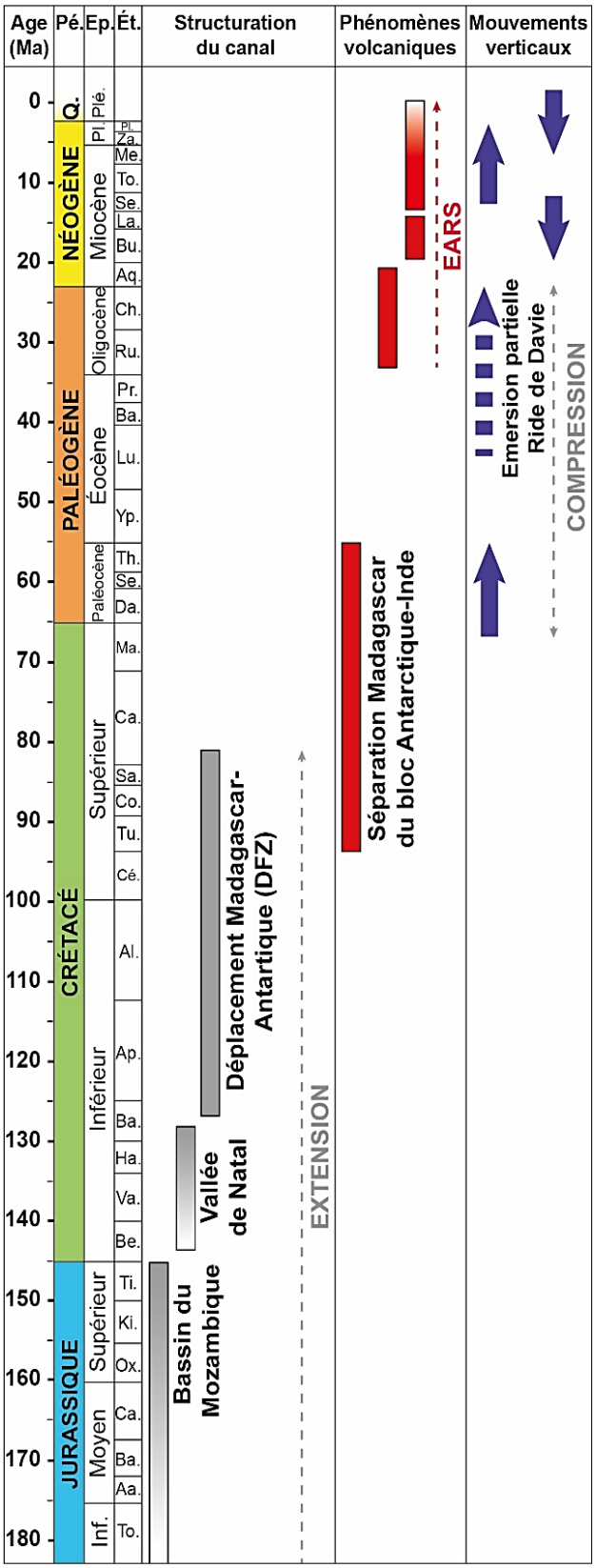

***Figure 1.12**. Synthèse de la structuration du canal du Mozambique et des évènements magmatiques / géodynamiques majeurs ayant eu lieu depuis sa mise en place.*

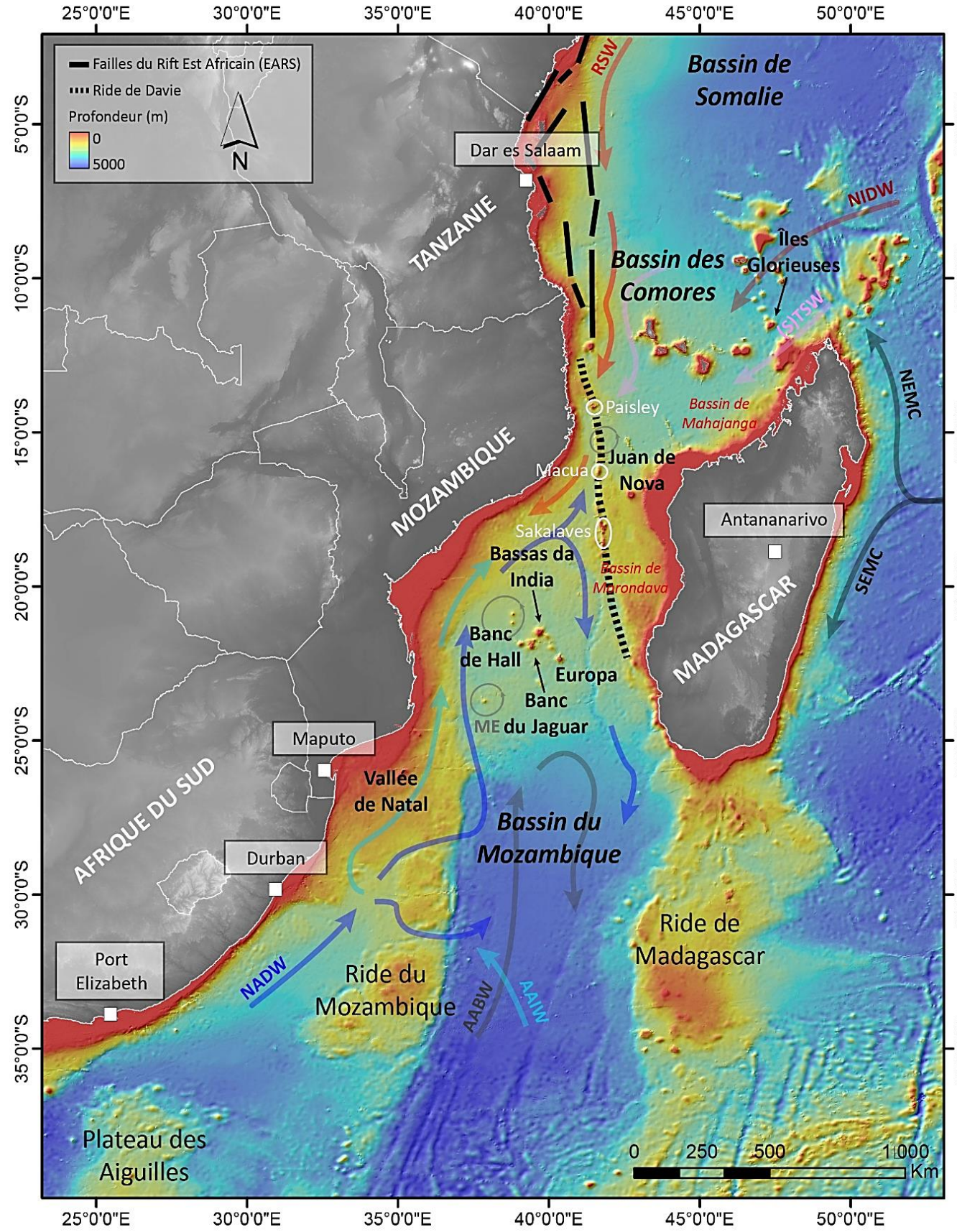

Figure 1.13. *Bathymétrie du canal du Mozambique (GEBCO et campagnes PAMELA) avec ses principales structures géologiques. Les monts sous-marins ponctuant le long de la ride de Davie sont entourés en blanc et les courants océaniques présents dans le canal sont indiqués par des flèches.*

2018 ; Leroux et al., 2020; Nicholas et al., 2007 ; Walford et al., 2005).

La ride de Davie, qui est une structure héritée de la DFZ et ponctuée de plusieurs monts sous-marins tels que le mont Paisley, le mont Macua et les monts Sakalaves, a ainsi été partiellement émergée de l'Éocène à l'Oligocène avant d'être majoritairement immergée à partir du Miocène (Ponte, 2018). Elle est aujourd'hui orientée N170 et s'étend sur 1200 km de l'est de la marge africaine (13°S) au sud-ouest de Madagascar (23°S) séparant le bassin des Comores au nord-est, du bassin profond du Mozambique au sud-ouest (Figure 1.13).

1.3.2. Océanographie

La localisation du canal du Mozambique fait de lui une zone d'échange complexe entre les masses d'eau des océans Indien et Atlantique (Figure 1.13) qui présentent des signatures isotopiques en Nd différentes. Comme vu précédemment, l'océan Atlantique étant peu radiogénique par rapport à l'océan Indien qui résulte d'un mélange les masses d'eau atlantiques et pacifiques. Ces dernières étant très radiogéniques. Actuellement, le canal du Mozambique correspond à un conduit à travers lequel les masses d'eaux superficielles indiennes, chaudes et radiogéniques, sont entraînées en direction du Sud dans le courant du Mozambique (MC ; Di Marco et al., 2002 ; Flemming, Kudrass, 2018 ; Quartly et al., 2013) alors que les eaux atlantiques peu radiogéniques circulent dans le courant profond du Mozambique (MUC), du sud vers le nord (De Ruijter et al., 2002).

Le tableau 1.1 présente une synthèse des valeurs isotopiques en Nd propres aux principales masses d'eau présentes dans le canal et présentées dans les paragraphes suivants.

Tableau 1.1. *Abréviations des principales masses d'eau présentes dans le canal du Mozambique, leurs profondeurs et leurs signatures isotopiques εNd respectives.*

Abréviations	Profondeur (m)	εNd
SICW	200-700	-8.5 à -7[a]
RSW	800-1400	-8.5 à -7[a]
AAIW	800-1500	-9 à -8[b]
NIDW	2000-3000	-8.5 à -7[a]
NADW	1500-3500	-13 à -9[c]

[a]*Bertram, Elderfield (1993), Arsouze et al. (2007)*
[b]*Piepgras, Wasserburg (1982), Jeandel (1993), Arsouze et al. (2007), Amakawa et al. (2013)*
[c]*Piepgras, Wasserburg (1987), Jeandel (1993), Rickli et al. (2009), Tachikawa et al. (2017)*

Le MC fait partie du courant des Aiguilles (AC), qui constitue un lien essentiel dans les échanges de chaleur et de sel entre les océans Indien et Atlantique (Gordon, 1986 ; Weijer et al., 1999). Il est également caractérisé par des tourbillons anticycloniques (ME) de diamètres atteignant 300 km et pouvant affecter toute la colonne d'eau (Figure 1.13; De Ruijter et al., 2002 ; Halo et al., 2014). La formation de ces anticyclones est liée au courant Sud Equatorial (SEC) qui arrive à l'est de Madagascar (17°S) et se divise en deux : le courant nord-est de Madagascar (NEMC) et le courant sud-est de Madagascar (SEMC ; Schott et al., 2009). Le MC transporte des eaux superficielles, jusqu'à 200 m de profondeur, composées des eaux de Surface Tropicales (TSW) et des eaux de Surface Subtropicales (STSW), mais également les eaux Centrales du Sud de l'océan Indien (SICW) présentes entre 200 m et 600 m de profondeur. Les eaux intermédiaires du MC sont principalement composées des masses d'eau de la mer Rouge (RSW) entre 900 m et 1200 m de profondeur, qui entrent au nord du canal du Mozambique en longeant la côte est-africaine (Figure 1.13).

Le MUC et le courant profond des Aiguilles (AUC) transportent les eaux Intermédiaires Antarctiques (AAIW) entre 800 m et 1500 m de profondeur (Ullgren et al., 2012). Ce dernier arrive de l'est de la ride du Mozambique puis circule le long de la côte mozambicaine (Figure 1.13; Fine, 1993). Les eaux profondes Nord Atlantiques (NADW) font aussi partie du MUC, entre 2000 m et 3500 m de profondeur. Elles arrivent du sud de l'Afrique et entrent dans le canal du Mozambique par la vallée de Natal (Toole, Warren, 1993). La partie superficielle du NADW circule vers le nord du bassin du Mozambique jusqu'à l'ouest de la ride de Davie. Le reste du NADW se replie vers le Sud en suivant la bordure ouest de la ride (Figure 1.13 ; Ullgren et al., 2012 ; van Aken et al., 2004). Enfin, à plus de 4000 m de profondeur, le courant profond Antarctique (AABW) circule à l'est de la ride du Mozambique jusqu'au bassin du Mozambique. Il est ensuite dévié, avant de repartir vers le Sud longeant la ride de Madagascar (Figure 1.13 ; Kolla et al., 1980).

Enfin, au nord du canal du Mozambique, le courant profond Nord Indien (NIDW) circule à plus de 2000 m de profondeur (Collins et al., 2016). Il est transporté depuis l'océan Indien et est très présent dans le nord du canal, au niveau des îles Glorieuses (Di Marco et al., 2002). Très peu d'études se sont intéressées à la circulation du NIDW après son arrivée au nord de Madagascar et son passage au niveau des îles Glorieuses (Figure 1.13). Les résultats existants indiquent que la ride de Davie formerait un obstacle à la circulation des courants profonds dans le canal du Mozambique (Mantyla, Reid, 1995 ; Toole, Warren, 1993 ; You, 2000).

Cependant, de nouvelles données hydrographiques, basées sur des mesures de conductivité, température, pression, oxygène dissous et salinité, ont identifié la présence des courants AAIW et NADW au-delà de la ride et ont proposé de nouvelles routes de circulation (Collins et al., 2016 ; Di Marco et al., 2002 ; van Aken, 2004). Ces nouveaux résultats permettent aujourd'hui de remettre en question l'évolution des courants profonds dans le canal du Mozambique et le rôle de la géodynamique locale sur la répartition de ces masses d'eau.

1.4. Problématiques et méthodes de travail

Comme présenté, le canal du Mozambique, situé entre l'est de l'Afrique et la marge continentale de Madagascar, représente un couloir maritime encore très peu connu de l'océan Indien. Il est parcouru de courants superficiels, intermédiaires et profonds dont les paramètres physico-chimiques ont été étudiés et sont dorénavant connus, mais dont le modèle de circulation demeure incompris. L'objectif global de cette thèse est donc d'identifier, d'étudier et de comprendre l'évolution de la courantologie du canal du Mozambique au cours du temps et l'impact de la géodynamique mondiale et régionale sur celle-ci à travers une étude minéralogique et géochimique d'encroûtements Fe-Mn.

Alors que les techniques analytiques et les données seront présentées dans les chapitres suivants, cette partie vise à présenter la méthodologie générale suivie au cours de cette thèse selon les différentes problématiques posées.

Dans un premier temps, il s'agit d'identifier les signatures géochimiques des masses d'eau de l'océan Atlantique et de l'océan Indien présentes dans la zone d'étude. Ce premier axe repose sur 33 encroûtements Fe-Mn répartis de manière homogène dans le canal, du Plateau des Aiguilles au sud, jusqu'aux îles Glorieuses au nord. La partie superficielle des échantillons, correspondant aux derniers dépôts élémentaires, est échantillonnée avant de procéder aux analyses

isotopiques en Nd reflétant la signature des domaines océaniques, et en Pb pouvant indiquer des apports élémentaires de sources secondaires. L'objectif de cet axe est d'identifier les masses d'eau présentes dans le canal et de comprendre leurs voies de circulation afin de proposer un modèle 2D de circulation subactuelle des courants dans le canal du Mozambique, en prenant en compte la ride de Davie. Le rôle de cette structure géologique sera hautement discuté puisqu'elle sépare actuellement le canal en deux bassins, pouvant ainsi s'apparenter à une barrière bloquant l'évolution des courants profonds.

Le deuxième aspect a pour objectif de créer un modèle 3D de la courantologie passée du canal du Mozambique. Cette étude paléocéanographique repose sur 4 encroûtements Fe-Mn dragués entre 800 m et 1700 m de profondeur, susceptibles d'avoir changé de masse d'eau au cours du temps, et donc de signature géochimique, et 3 encroûtements Fe-Mn profonds (>1780 m) afin de cibler les courants profonds. Les épaisseurs importantes des échantillons permettront de réaliser un échantillonnage haute résolution sous forme de stratigraphies et une géochronologie au $^{10}Be/^{9}Be$. Les âges mesurés apporteront une dimension temporelle aux résultats.

Une corrélation entre l'évolution géographique mondiale, la géodynamique du canal (e.g. uplift, subsidence) et des variations de signatures des masses d'eau permettra de comprendre l'impact des mouvements tectoniques, identifiés lors du travail de 3D et par d'autres auteurs, sur la circulation des courants profonds. L'objectif final sera d'associer ces résultats à de la modélisation afin de développer un modèle 4D de la circulation des courants intermédiaires et profonds au cours des 30 derniers Ma.

Enfin, d'autres facteurs peuvent impacter et influencer les signatures géochimiques des encroûtements Fe-Mn (e.g. volcanisme, échanges continent/océans, fluides interstitiels) au cours du temps. Dans ces cas précis, les variations enregistrées ne reflètent pas les signatures pures des masses d'eau. C'est pourquoi un axe exploratoire de la 4D sera présenté dans les perspectives et consacré aux phénomènes locaux enregistrés dans 2 échantillons clés. Un intérêt particulier sera porté sur l'identification et les conséquences directes d'événements volcaniques sur les compositions minéralogiques et géochimiques d'un encroûtement localisé au niveau des Îles Glorieuses. Ce travail s'intéressera notamment à l'isotopie du Pb et de l'Os. Alors que l'étude géochimique d'un encroûtement proche d'une zone de décharges continentales se focalisera sur les échanges élémentaires et isotopiques entre le socle africain et les masses d'eau environnantes.

1.5. Structure du manuscrit

Ce manuscrit de thèse est divisé en 6 chapitres. Les chapitres 2, 3 et 4 sont associés à des articles (publiés, soumis ou en préparation). Les références bibliographiques sont systématiquement citées à la fin de chaque chapitre.

Chapitre 1 - Introduction (ce chapitre)

Cette partie introductive sert de base au manuscrit. Ses objectifs sont multiples :

(1) définir le cadre général de la thèse et du projet dans lequel elle s'inscrit,

(2) présenter la zone d'étude,

(3) exposer les différentes problématiques scientifiques,

(4) présenter la méthodologie suivie afin de répondre à ces dernières et,

(5) donner une vision générale du manuscrit.

Chapitre 2 – Méthodologie analytique

Le chapitre 2 vise à expliquer les méthodes et les appareils analytiques utilisés au cours de la thèse, depuis l'échantillonnage jusqu'à l'acquisition des données. Il inclut un papier publié dans Talanta en avril 2021 présentant la mise au point d'une méthode pour déterminer les éléments traces dans les oxydes Fe-Mn (Charles et al., 2021).

- ***Charles, C.**, Barrat, J.-A., Pelleter, E., 2021. Trace Element Determinations in Fe-Mn Oxides by High Resolution ICP-MS after Tm Addition. Talanta 122446.*

Chapitre 3 – Enregistrements isotopiques modernes des masses d'eau régionales

Le chapitre 3 se concentre sur la caractérisation isotopique (Nd, Pb) des masses d'eau intermédiaires et profondes et l'impact de la ride de Davie sur leur évolution spatiale au cours des derniers 20 à 80 000 ans. Les résultats permettent d'identifier de nouvelles voies de circulation des courants grâce à leurs signatures isotopiques et de mesurer leur intensité de propagation avec des calculs de contribution qui pourront être applicables à des études temporelles par la suite (voir chapitres 4 et 5). Ce chapitre inclut un papier publié dans une édition spéciale de Marine Geology en septembre 2020 (Charles et al., 2020).

- ***Charles, C.,** Pelleter, E., Révillon, S., Nonnotte, P., Jorry, S.J., Kluska, J.-M., 2020. Intermediate and deep ocean current circulation in the Mozambique Channel: New insights from ferromanganese crust Nd isotopes. Marine Geology. 430, 106356.*

Chapitre 4 – Encroûtements Fe-Mn : archives des mouvements verticaux

Le chapitre 4 étudie la géodynamique du canal au cours du temps et vise à établir une chronologie des phénomènes tectoniques enregistrés au sein des encroûtements Fe-Mn à partir de leurs signatures isotopiques de Nd. Les résultats mettent en évidence que les échantillons ont changé de masses d'eau en raison d'un uplift identifié à partir de 11.7 Ma suivi d'une subsidence à partir de 5.1 Ma. Ces phénomènes sont la cause directe de variations de concentrations élémentaires au sein des échantillons et permettront de discuter de leur impact sur la circulation des courants profonds (voir chapitre 5). Ce chapitre est un papier qui sera soumis dans *Earth and Planetary Science Letters* après le dépôt du manuscrit.

- ***Charles, C.,** Pelleter, E., Révillon, S., Jorry, S.J., Kluska, J.-M., Bourlès, D., Quentin, S., Braucher, R., Nonnotte, P., Liorzou, C., Chéron, S., Germain, Y., Barrat, J.-A., in prep. Fe-Mn crusts as archives of vertical movements: new insights for the geodynamic reconstruction of the Mozambique Channel over the past 12 Ma.*

Chapitre 5 – Reconstruction océanographique du canal du Mozambique : un modèle évolutif sur 20 Ma

Le chapitre 5 s'intéresse à la paléocirculation des courants profonds. Il fait le lien avec les événements géodynamiques mis en évidence dans le chapitre 4 et leur impact direct sur l'évolution des courants dans le canal du Mozambique au cours du temps. Afin de quantifier ce phénomène, cet axe de la thèse est appuyé par des calculs de contributions des courants profonds comme présentés dans le chapitre 3. Un modèle évolutif de la circulation des masses d'eau présente une

synthèse des résultats obtenus et des phénomènes mis en évidence. Ce chapitre est un papier en préparation.

Chapitre 6 – Synthèse, conclusions et perspectives

Le 6ème chapitre de ce manuscrit synthétise les différents résultats présentés dans cette thèse au cours des chapitres précédents et conclut l'étude. Il vise également à discuter des potentielles perspectives pour de futurs projets et questionnements scientifiques tels que l'influence de phénomènes locaux (e.g. volcanisme, boundary exchanges) sur les signatures des masses d'eau enregistrées dans les encroûtements Fe-Mn.

1.6. Références bibliographiques

Abouchami, W., Goldstein, S.L., Gazer, S.J.G., Eisenhauer, A., Mangini, A., 1997. Secular changes of lead and neodymium in central Pacific seawater recorded by a Fe-Mn crust. Geochim. Cosmochim. Acta 61, 3957–3974.

Albarède, F., Goldstein, S.L., Dautel, D., 1997. The neodymium isotopic composition of manganese nodules from the Southern and Indian oceans, the global oceanic neodymium budget, and their bearing on deep ocean circulation. Geochim. Cosmochim. Acta 61, 1277–1291.

Ali, J., Roberts, S., Hall, R., 1994. The closure of the Indo-Pacific Gateway: a new plate tectonic perspective. pp. 10–20.

Amakawa, H., Tazoe, H., Obata, H., Gamo, T., Sano, Y., Shen, C.-C., 2013. Neodymium isotopic composition and concentration in the Southwest Pacific Ocean. Geochem. J. 47, 409–422.

Aplin, A., Cronan, D., 1985. Ferromanganese oxide deposits from the Central Pacific Ocean, I. Encrustations from the Line Islands Archipelago. Geochim. Cosmochim. Acta 49, 427–436.

Arsouze, T., Dutay, J.-C., Lacan, F., Jeandel, C., 2007. Modeling the neodymium isotopic composition with a global ocean circulation model. Chem. Geol. 239, 165–177.

Barker, P.F., Burrell, J., 1977. The opening of Drake Passage. Mar. Geol., Circum-Antartic Marine Geology 25, 15–34.

Baroni, M., Bard, E., Petit, J.-R., Magand, O., Bourlès, D., 2011. Volcanic and solar activity, and atmospheric circulation influences on cosmogenic 10Be fallout at Vostok and Concordia (Antarctica) over the last 60 years. Geochim. Cosmochim. Acta 75, 7132–7145.

Bassias, Y., 1992. Petrological and geochemical investigation of rocks from the Davie fracture zone (Mozambique Channel) and some tectonic implications. J. Afr. Earth Sci. Middle East 15, 321–339.

Bau, M., 1996. Controls on the fractionation of isovalent trace elements in magmatic and aqueous systems: evidence from Y/Ho, Zr/Hf, and lanthanide tetrad effect. Contrib. Mineral. Petrol. 123, 323–333.

Bertram, C.J., Elderfield, H., 1993. The geochemical balance of the rare earth elements and neodymium isotopes in the oceans. Geochim. Cosmochim. Acta 57, 1957–1986.

Bialik, O.M., Frank, M., Betzler, C., Zammit, R., Waldmann, N.D., 2019. Two-step closure of the Miocene Indian Ocean Gateway to the Mediterranean. Sci. Rep. 9, 8842.

Bonatti, E., 1972. Classification and genesis of submarine iron-manganese deposits. Ferromanganese Depos. Ocean Floor.

Bourlès, D., Raisbeck, G.M., Yiou, F., 1989. 10Be and 9Be in marine sediments and their potential for dating. Geochim. Cosmochim. Acta 53, 443–452.

Burton, K.W., Bourdon, B., Birck, J.-L., Allègre, C.J., Hein, J.R., 1999. Osmium isotope variations in the oceans recorded by FeMn crusts. Earth Planet. Sci. Lett. 171, 185–197.

Burton, K.W., Ling, H.-F., O'Nions, R.K., 1997. Closure of the Central American Isthmus and its effect on deep-water formation in the North Atlantic. Nature 386, 382.

Charles, C., Barrat, J.-A., Pelleter, E., 2021. Trace Element Determinations in Fe-Mn Oxides by High Resolution ICP-MS after Tm Addition. Talanta 122446.

Charles, C., Pelleter, E., Révillon, S., Nonnotte, P., Jorry, S.J., Kluska, J.-M., 2020. Intermediate and deep ocean current circulation in the Mozambique Channel: New insights from ferromanganese crust Nd isotopes. Mar. Geol. 430, 106356.

Chinni, V., Singh, S.K., Bhushan, R., Rengarajan, R., Sarma, V.V.S.S., 2019. Spatial variability in dissolved iron concentrations in the marginal and open waters of the Indian Ocean. Mar. Chem. 208, 11–28.

Chmeleff, J., von Blanckenburg, F., Kossert, K., Jakob, D., 2010. Determination of the 10Be half-life by multicollector ICP-MS and liquid scintillation counting. Nucl. Instrum. Methods Phys. Res. B 268, 192–199.

Chorowicz, J., 2005. The East African rift system. J. Afr. Earth Sci., Phanerozoic Evolution of Africa 43, 379–410.

Christensen, J.N., Halliday, A.N., Godfrey, L.V., Hein, J.R., Rea, D.K., 1997. Climate and Ocean Dynamics and the Lead Isotopic Records in Pacific Ferromanganese Crusts. Science 277, 913–918.

Claude, C., Suhr, G., Hofmann, A.W., Koschinsky, A., 2005. U-Th chronology and paleoceanographic record in a Fe-Mn crust from the NE Atlantic over the last 700 ka. Geochim. Cosmochim. Acta 69, 4845–4854.

Coffin, M.F., Rabinowitz, P.D., 1987. Reconstruction of Madagascar and Africa: Evidence from the Davie Fracture Zone and Western Somali Basin. J. Geophys. Res. Solid Earth 92, 9385–9406.

Collins, C., Hermes, J.C., Roman, R.E., Reason, C.J.C., 2016. First dedicated hydrographic survey of the Comoros Basin. J. Geophys. Res. Oceans 121, 1291–1305.

Courgeon, S., Bachèlery, P., Jouet, G., Jorry, S.J., Bou, E., BouDagher-Fadel, M.K., Révillon, S., Camoin, G., Poli, E., 2018. The offshore east African rift system: new insights from the Sakalaves seamounts (Davie Ridge, SW Indian Ocean). Terra Nova 30, 380–388.

Courgeon, S., Jorry, S.J., Camoin, G.F., BouDagher-Fadel, M.K., Jouet, G., Révillon, S., Bachèlery, P., Pelleter, E., Borgomano, J., Poli, E., Droxler, A.W., 2016. Growth and demise of Cenozoic isolated carbonate platforms: New insights from the Mozambique Channel seamounts (SW Indian Ocean). Mar. Geol. 380, 90–105.

Courgeon, S., Jorry, S.J., Jouet, G., Camoin, G., BouDagher-Fadel, M.K., Bachèlery, P., Caline, B., Boichard, R., Révillon, S., Thomas, Y., Thereau, E., Guérin, C., 2017. Impact of tectonic and volcanism on the Neogene evolution of isolated carbonate platforms (SW Indian Ocean). Sediment. Geol. 355, 114–131.

Craig, J.D., Andrews, J.E., Meylan, M.A., 1982. Ferromanganese deposits in the Hawaiian Archipelago. Mar. Geol. 45, 127–157.

Cronan, D.S., 1980. Metallogenesis at oceanic spreading centres. J. Geol. Soc. 137, 369–371.

Cronan, D.S., 2017. Handbook of Marine Mineral Deposits. Routledge.

David, K., Frank, M., O'Nions, R.K., Belshaw,

N.S., Arden, J.W., 2001. The Hf isotope composition of global seawater and the evolution of Hf isotopes in the deep Pacific Ocean from Fe–Mn crusts. Chem. Geol. 178, 23–42.

Delaunay, A., 2018. Madagascar vertical movements (90 - 0 Ma): a double approach including onshore geomorphology and Madagascar western margins sedimentary record (phdthesis). Université Rennes 1.

de Ruijter, W.P.M., Ridderinkhof, H., Lutjeharms, J.R.E., Schouten, M.W., Veth, C., 2002. Observations of the flow in the Mozambique Channel: OBSERVATIONS IN THE MOZAMBIQUE CHANNEL. Geophys. Res. Lett. 29, 140-1-140–3.

DiMarco, S.F., Chapman, P., Nowlin, W.D., Hacker, P., Donohue, K., Luther, M., Johnson, G.C., Toole, J., 2002. Volume transport and property distributions of the Mozambique Channel. Deep Sea Res. Part II Top. Stud. Oceanogr. 49, 1481–1511.

Dymond, J., Eklund, W., 1978. A microprobe study of metalliferous sediment components. Earth Planet. Sci. Lett. 40, 243–251.

Dymond, J., Lyle, M., Finney, B., Piper, D.Z., Murphy, K., Conard, R., Pisias, N., 1984. Ferromanganese nodules from MANOP Sites H, S, and R—Control of mineralogical and chemical composition by multiple accretionary processes. Geochim. Cosmochim. Acta 48, 931–949.

Eagles, G., König, M., 2008. A model of plate kinematics in Gondwana breakup. Geophys. J. Int. 173, 703–717.

Elderfield, H., Bertram, C.J., Erez, J., 1996. A biomineralization model for the incorporation of trace elements into foraminiferal calcium carbonate. Earth Planet. Sci. Lett. 142, 409–423.

Fine, R.A., 1993. Circulation of Antarctic intermediate water in the South Indian Ocean. Deep Sea Res. Part Oceanogr. Res. Pap. 40, 2021–2042.

Flemming, B.W., Kudrass, H.-R., 2018. Large dunes on the outer shelf off the Zambezi Delta, Mozambique: evidence for the existence of a Mozambique Current. Geo-Mar. Lett. 38, 95–106.

Frank, M., 2002. Radiogenic isotopes: tracers of past ocean circulation and erosional input. Rev. Geophys. 40, 1–1.

Frank, M., O'Nions, R.K., 1998. Sources of Pb for Indian Ocean ferromanganese crusts: a record of Himalayan erosion? Earth Planet. Sci. Lett. 158, 121–130.

Frank, M., O'Nions, R.K., Hein, J.R., Banakar, V.K., 1999. 60 Myr records of major elements and Pb–Nd isotopes from hydrogenous ferromanganese crusts: reconstruction of seawater paleochemistry. Geochim. Cosmochim. Acta 63, 1689–1708.

Frank, M., Whiteley, N., Kasten, S., Hein, J.R., O'Nions, K., 2002. North Atlantic Deep Water export to the Southern Ocean over the past 14 Myr: Evidence from Nd and Pb isotopes in ferromanganese crusts. Paleoceanography 17, 12-1-12–9.

Franke, D., Jokat, W., Ladage, S., Stollhofen, H., Klimke, J., Lutz, R., Mahanjane, E.S., Ehrhardt, A., Schreckenberger, B., 2015. The offshore East African Rift System: Structural framework at the toe of a juvenile rift. Tectonics 34, 2086–2104.

Gaina, C., Torsvik, T.H., van Hinsbergen, D.J.J., Medvedev, S., Werner, S.C., Labails, C., 2013. The African Plate: A history of oceanic crust accretion and subduction since the Jurassic. Tectonophysics, Progress in understanding the South Atlantic margins 604, 4–25.

Goodlad, S.W., Martin, A.K., Hartnady, C.J.H., 1982. Mesozoic magnetic anomalies in the southern Natal Valley. Nature 295, 686.

Gordon, A.L., 1986. Interocean exchange of thermocline water. J. Geophys. Res. Oceans 91, 5037–5046.

Goto, K.T., Anbar, A.D., Gordon, G.W., Romaniello, S.J., Shimoda, G., Takaya, Y., Tokumaru, A., Nozaki, T., Suzuki, K., Machida, S., Hanyu, T., Usui, A., 2014. Uranium isotope systematics of ferromanganese crusts in the Pacific Ocean: Implications for the marine 238U/235U isotope system. Geochim. Cosmochim. Acta 146, 43–58.

Gradstein, F.M., Ogg, J., G., Schmitz, M., Ogg, G., 2012. The Geologic Time Scale. Elsevier.

Guan, Y., Sun, X., Ren, Y., Jiang, X., 2017. Mineralogy, geochemistry and genesis of the polymetallic crusts and nodules from the South China Sea. Ore Geol. Rev. 89, 206–227.

Halbach, P., Segl, M., Puteanus, D., Mangini, A., 1983. Co-fluxes and growth rates in ferromanganese deposits from central Pacific seamount areas. Nature 304, 716.

Hall, R., Cottam, M.A., Wilson, M.E.J., 2011. The SE Asian gateway: history and tectonics of the Australia–Asia collision. Geol. Soc. Lond. Spec. Publ. 355, 1–6.

Halo, I., Backeberg, B., Penven, P., Ansorge, I., Reason, C., Ullgren, J.E., 2014. Eddy properties in the Mozambique Channel: A comparison between observations and two numerical ocean circulation models. Deep Sea Res. Part II Top. Stud. Oceanogr. 100, 38–53.

Hein, J.R., Conrad, T., Mizell, K., Banakar, V.K., Frey, F.A., Sager, W.W., 2016. Controls on ferromanganese crust composition and reconnaissance resource potential, Ninetyeast Ridge, Indian Ocean. Deep Sea Res. Part Oceanogr. Res. Pap. 110, 1–19.

Hein, J.R., Conrad, T.A., Staudigel, H., 2010. Seamount Mineral Deposits: A Source Of Rare Metals For High-Technology Industries. Oceanography 23, 184–189.

Hein, J.R., Koschinsky, A., Bau, M., Manheim, F.T., Kang, J.-K., and Roberts, L., 2000. Cobalt-rich ferromanganese crusts in the Pacific. In: Cronan, D.S. (ed), Handbook of marine minerals. CRC Press, Boca Raton, Florida, pp. 239-279.

Hein, J.R., Koschinsky, A., Halbach, P., Manheim, F.T., Bau, M., Kang, J.-K., Lubick, N., 1997. Iron and manganese oxide mineralization in the Pacific. Geol. Soc. Lond. Spec. Publ. 119, 123–138.

Hein, J.R., Mizell, K., Koschinsky, A., Conrad, T.A., 2013. Deep-ocean mineral deposits as a source of critical metals for high- and green-technology applications: Comparison with land-based resources. Ore Geol. Rev. 51, 1–14.

Heirtzler, J.R., Burroughs, R.H., 1971. Madagascar's Paleoposition: New Data from the Mozambique Channel. Science 174, 488–490.

Henderson, G.M., Burton, K.W., 1999. Using (234U/238U) to assess diffusion rates of isotope tracers in ferromanganese crusts. Earth Planet. Sci. Lett. 170, 169–179.

Hu, R., Chen, T., Ling, H., 2012. Late Cenozoic history of deep water circulation in the western North Pacific: Evidence from Nd isotopes of ferromanganese crusts. Chin. Sci. Bull. 57, 4077–4086.

Jeandel, C., 1993. Concentration and isotopic composition of Nd in the South Atlantic Ocean. Earth Planet. Sci. Lett. 117, 581–591.

Jokat, W., Boebel, T., König, M., Meyer, U., 2003. Timing and geometry of early Gondwana breakup. J. Geophys. Res. Solid Earth 108.

Josso, P., Parkinson, I., Horstwood, M., Lusty, P., Chenery, S., Murton, B., 2019. Improving confidence in ferromanganese crust age models: A composite geochemical approach. Chem. Geol. 513, 108–119.

Josso, P., Pelleter, E., Pourret, O., Fouquet, Y., Etoubleau, J., Cheron, S., Bollinger, C., 2017. A new discrimination scheme for oceanic ferromanganese deposits using high field strength and rare earth elements. Ore Geol. Rev., SI:Marine mineral deposits: New resources for base, precious, and critical metals 87, 3–15.

Josso, P., Rushton, J., Lusty, P., Matthews, A., Chenery, S., Holwell, D., Kemp, S.J., Murton, B., 2020. Late Cretaceous and Cenozoic paleoceanography from north-east Atlantic ferromanganese crust microstratigraphy. Mar. Geol. 422, 106122.

Jung, H.-S., Lee, C.-B., 1999. Growth of diagenetic ferromanganese nodules in an oxic deep-sea sedimentary environment, northeast equatorial Pacific. Mar. Geol. 157, 127–144.

Keigwin, L., 1982. Isotopic Paleoceanography of the Caribbean and East Pacific: Role of Panama Uplift in Late Neogene Time. Science 217, 350–353.

Kennett, J.P., 1977. Cenozoic evolution of Antarctic glaciation, the circum-Antarctic Ocean, and their impact on global paleoceanography. J. Geophys. Res. 1896-1977 82, 3843–3860.

Klemm, V., Levasseur, S., Frank, M., Hein, J.R., Halliday, A.N., 2005. Osmium isotope stratigraphy of a marine ferromanganese crust. Earth Planet. Sci. Lett. 238, 42–48.

Klinkhammer, G.P., Bender, M.L., 1980. The distribution of manganese in the Pacific Ocean. Earth Planet. Sci. Lett. 46, 361–384.

Kolla, V., Eittreim, S., Sullivan, L., Kostecki, J.A., Burckle, L.H., 1980. Current-controlled, abyssal microtopography and sedimentation in Mozambique Basin, southwest Indian Ocean. Mar. Geol. 34, 171–206.

König, M., Jokat, W., 2010. Advanced insights into magmatism and volcanism of the Mozambique Ridge and Mozambique Basin in the view of new potential field data. Geophys. J. Int. 180, 158–180.

Korschinek, G., Bergmaier, A., Faestermann, T., Gerstmann, U.C., Knie, K., Rugel, G., Wallner, A., Dillmann, I., Dollinger, G., von Gostomski, Ch.L., Kossert, K., Maiti, M., Poutivtsev, M., Remmert, A., 2010. A new value for the half-life of 10Be by Heavy-Ion Elastic Recoil Detection and liquid scintillation counting. Nucl. Instrum. Methods Phys. Res. Sect. B Beam Interact. Mater. At. 268, 187–191.

Koschinsky, A., 1994. Geochemische Krustenprofile und sequentielle Laugungsversuche an Manganerzkrusten aus dem Zentralpazifik zur Klärung von Genese und Elementassoziationen. Reimer.

Koschinsky, A., Halbach, P., 1995. Sequential leaching of marine ferromanganese precipitates: Genetic implications. Geochim. Cosmochim. Acta 59, 5113–5132.

Koschinsky, A., Hein, J.R., 2003. Uptake of elements from seawater by ferromanganese crusts: solid-phase associations and seawater speciation. Mar. Geol. 198, 331–351.

Koschinsky, A., Hein, J.R., 2017. Marine ferromanganese encrustations: Archives of changing oceans. Elements.

Koschinsky, A., Stascheit, A., Bau, M., Halbach, P., 1997. Effects of phosphatization on the geochemical and mineralogical composition of marine ferromanganese crusts. Geochim. Cosmochim. Acta 61, 4079–4094.

Kuhn, T., Bau, M., Blum, N., Halbach, P., 1998. Origin of negative Ce anomalies in mixed hydrothermal–hydrogenetic Fe–Mn crusts from the Central Indian Ridge. Earth Planet. Sci. Lett. 163, 207–220.

Leclaire, L., 1984. RIDA - MD39 cruise, Marion Dufresne R/V. https://doi.org/10.17600/84010511

Leclaire, L., 1975. NOSICAA - MD 06 cruise, Marion Dufresne R/V. https://doi.org/10.17600/75010711

Lee, D.-C., Halliday, A.N., Hein, J.R., Burton, K.W., Christensen, J.N., Günther, D., 1999. Hafnium Isotope Stratigraphy of Ferromanganese Crusts. Science 285, 1052–1054.

Leinweber, V.T., Jokat, W., 2012. The Jurassic history of the Africa–Antarctica corridor — new constraints from magnetic data on the conjugate continental margins. Tectonophysics 530–531, 87–101.

Leinweber, V.T., Klingelhoefer, F., Neben, S., Reichert, C., Aslanian, D., Matias, L., Heyde, I., Schreckenberger, B., Jokat, W., 2013. The crustal structure of the Central Mozambique continental margin — Wide-angle seismic, gravity and magnetic study in the Mozambique Channel, Eastern Africa. Tectonophysics 599, 170–196.

Leroux, E., Counts, J., Jorry, S., Jouet, G., Révillon, S., BouDagher-Fadel, M.K., Courgeon, S., Berthod, C., Ruffet, G., Bachèlery, P., Grenard-Grand, E., 2020. Evolution of the Glorieuses seamount in the SW Indian Ocean and surrounding deep Somali Basin since the Cretaceous. Mar. Geol. 106202.

Li, Y.-H., Schoonmaker, J.E., 2003. 7.01 - Chemical Composition and Mineralogy of Marine Sediments, in: Holland, H.D., Turekian, K.K. (Eds.), Treatise on Geochemistry. Pergamon, Oxford, pp. 1–35.

Ling, H.F., Burton, K.W., O'Nions, R.K., Kamber, B.S., von Blanckenburg, F., Gibb, A.J., Hein, J.R., 1997. Evolution of Nd and Pb isotopes in Central Pacific seawater from ferromanganese crusts. Earth Planet. Sci. Lett. 146, 1–12.

Ling, H.-F., Jiang, S.-Y., Frank, M., Zhou, H.-Y., Zhou, F., Lu, Z.-L., Chen, X.-M., Jiang, Y.-H., Ge, C.-D., 2005. Differing controls over the Cenozoic Pb and Nd isotope evolution of deepwater in the central North Pacific Ocean. Earth Planet. Sci. Lett. 232, 345–361.

Lusty, P.A.J., Hein, J.R., Josso, P., 2018. Formation and Occurrence of Ferromanganese Crusts: Earth's Storehouse for Critical Metals. Elements 14, 313–318.

Lutjeharms, J.R.E., 2006. The Agulhas Current. Springer-Verlag, Berlin Heidelberg.

Macgregor, D., 2015. History of the development of the East African Rift System: A series of interpreted maps through time. J. Afr. Earth Sci. 101, 232–252.

Manheim, F.T., Lane-Bostwick, C.M., 1988. Cobalt in ferromanganese crusts as a monitor of hydrothermal discharge on the Pacific sea floor. Nature 335, 59.

Mantyla, A.W., Reid, J.L., 1995. On the origins of deep and bottom waters of the Indian Ocean. J. Geophys. Res. Oceans 100, 2417–2439.

Marino, E., González, F.J., Somoza, L., Lunar, R., Ortega, L., Vázquez, J.T., Reyes, J., Bellido, E., 2017. Strategic and rare elements in Cretaceous-Cenozoic cobalt-rich ferromanganese crusts from seamounts in the Canary Island Seamount Province (northeastern tropical Atlantic). Ore Geol. Rev., SI:Marine mineral deposits: New resources for base, precious, and critical metals 87, 41–61.

Masters, J.C., Génin, F., Zhang, Y., Pellen, R., Huck, T., Mazza, P.P.A., Rabineau, M., Doucouré, M., Aslanian, D., 2021. Biogeographic mechanisms involved in the colonization of Madagascar by African vertebrates: Rifting, rafting and runways. J. Biogeogr. 48, 492–510.

McElhinny, M.W., 1970. Formation of the Indian Ocean. Nature 228, 977.

McKenzie, D., Sclater, J.G., 1971. The Evolution of the Indian Ocean since the Late Cretaceous. Geophys. J. Int. 24, 437–528.

McGrew, H.J., 1983. Oil and gas developments in central and southern Africa in 1982. Am Assoc Pet Geol Bull U. S. 67:10.

Meynadier, L., Allègre, C., O'Nions, R.K., 2008. Plate tectonics, radiogenic isotopic tracers and paleoceanography: The case of the manganese crusts in the Pacific. Earth Planet. Sci. Lett. 272, 513–522.

Mizell, K., Hein, J.R., Lam, P.J., Koppers, A.A.P., Staudigel, H., 2020. Geographic and Oceanographic Influences on Ferromanganese Crust Composition Along a Pacific Ocean Meridional Transect, 14 N to 14S. Geochem. Geophys. Geosystems 21, e2019GC008716.

Moulin, M., Evain, M., 2016. PAMELA-MOZ05 cruise, Pourquoi pas ? R/V.

Nicholas, C.J., Pearson, P.N., McMillan, I.K., Ditchfield, P.W., Singano, J.M., 2007. Structural evolution of southern coastal Tanzania since the Jurassic. J. Afr. Earth Sci. 48, 273–297.

Nisancioglu, K.H., Raymo, M.E., Stone, P.H., 2003. Reorganization of Miocene deep water circulation in response to the shoaling of the Central American Seaway: Reorganization of Miocene Deep Water Circulation. Paleoceanography 18, n/a-n/a.

O'Nions, R.K., Frank, M., von Blanckenburg, F., Ling, H.-F., 1998. Secular variation of Nd and Pb isotopes in ferromanganese crusts from the Atlantic, Indian and Pacific Oceans. Earth Planet. Sci. Lett. 155, 15–28.

Olu Karine, 2014. PAMELA-MOZ01 cruise,L'Atalante R/V.

Peucker-Ehrenbrink, B., Ravizza, G., 2000. The marine osmium isotope record. Terra Nova 12, 205–219.

Peucker-Ehrenbrink, B., Ravizza, G., 2012. Chapter 8 - Osmium Isotope Stratigraphy, in: Gradstein, F.M., Ogg, J.G., Schmitz, M.D., Ogg, G.M. (Eds.), The Geologic Time Scale. Elsevier, Boston, pp. 145–166.

Piepgras, D.J., Jacobsen, S.B., 1988. The isotopic composition of neodymium in the North Pacific. Geochim. Cosmochim. Acta 52, 1373–1381.

Piepgras, D.J., Wasserburg, G.J., 1982. Isotopic Composition of Neodymium in Waters from the Drake Passage. Science 217, 207–214

Piepgras, D.J., Wasserburg, G.J., 1987. Rare earth element transport in the western North Atlantic inferred from Nd isotopic observations. Geochim. Cosmochim. Acta 51, 1257–1271.

Piotrowski, A.M., Lee, D.-C., Christensen, J.N., Burton, K.W., Halliday, A.N., Hein, J.R., Günther, D., 2000. Changes in erosion and ocean circulation recorded in the Hf isotopic compositions of North Atlantic and Indian Ocean ferromanganese crusts. Earth Planet. Sci. Lett. 181, 315–325.

Piper, D.Z., 1974. Rare earth elements in ferromanganese nodules and other marine phases. Geochim. Cosmochim. Acta 38, 1007–1022.

Ponte, J.-P., 2018. La marge africaine du canal du Mozambique, le système turbiditique du Zambèze : une approche « Source to Sink » au Méso – Cénozoïque (phdthesis). Université Rennes 1.

Post, J.E., 1999. Manganese oxide minerals: Crystal structures and economic and environmental significance. Proc. Natl. Acad. Sci. U. S. A. 96, 3447–3454.

Puteanus, D., Halbach, P., 1988. Correlation of Co concentration and growth rate — A method for age determination of ferromanganese crusts. Chem. Geol. 69, 73–85.

Quartly, G.D., de Cuevas, B.A., Coward, A.C., 2013. Mozambique Channel eddies in GCMs: A question of resolution and slippage. Ocean Model. 63, 56–67.

Ravizza, G.E., Peucker-Ehrenbrink, B., 2003. The marine 187Os/188Os record of the Eocene-Oligocene transition: the interplay of weathering and glaciation. Earth and Planetary Science Letters, 210(1-2), 151-165.

Raymo, M.E., 1994. The initiation of northern hemisphere glaciation. Annu. Rev. Earth Planet. Sci. 22, 353–383.

Rehkämper, M., Frank, M., Hein, J.R., Halliday, A., 2004. Cenozoic marine geochemistry of thallium deduced from isotopic studies of ferromanganese crusts and pelagic sediments. Earth Planet. Sci. Lett. 219, 77–91.

Reynolds, B.C., Frank, M., O'Nions, R.K., 1999. Nd- and Pb-isotope time series from Atlantic ferromanganese crusts: implications for changes in provenance and paleocirculation over the last 8 Myr. Earth Planet. Sci. Lett. 173, 381–396.

Rickli, J., Frank, M., Halliday, A.N., 2009. The hafnium–neodymium isotopic composition of Atlantic seawater. Earth Planet. Sci. Lett. 280, 118–127.

Rogers, W.E., Hartman, W.D., Krause, K.S.K., 2000. Stratigraphic Analysis of Upper Cretaceous Rocks in the Mahajanga Basin, Northwestern Madagascar: Implications for Ancient and Modern Faunas. J. Geol. 108, 275–301.

Saager, P.M., De Baar, H.J.W., Burkill, P.H., 1989. Manganese and iron in Indian Ocean waters. Geochim. Cosmochim. Acta 53, 2259–2267.

Schott, F.A., Xie, S.-P., McCreary, J.P., 2009. Indian Ocean circulation and climate variability. Rev. Geophys. 47, RG1002.

Segl, M., Mangini, A., Bonani, G., Hofmann, H.J., Nessi, M., Suter, M., Wölfli, W., Friedrich, G., Plüger, W.L., Wiechowski, A., Beer, J., 1984. 10 Be-dating of a manganese crust from Central North Pacific and implications for ocean palaeocirculation. Nature 309, 540.

Shackleton, N.J., Backman, J., Zimmerman, H., Kent, D.V., Hall, M.A., Roberts, D.G., Schnitker, D., Baldauf, J.G., Desprairies, A., Homrighausen, R., Huddlestun, P., Keene, J.B., Kaltenback, A.J., Krumsiek, K. a. O., Morton, A.C., Murray, J.W., Westberg-Smith, J., 1984. Oxygen isotope calibration of the onset of ice-rafting and history of glaciation in the North Atlantic region. Nature 307, 620–623.

Srinivasan, M.S., Sinha, D.K., 1998. Early Pliocene closing of the Indonesian Seaway: evidence from north-east Indian Ocean and Tropical Pacific deep sea cores. J. Asian Earth Sci. 16, 29–44.

Storey, M., Mahoney, J.J., Saunders, A.D., Duncan, R.A., Kelley, S.P., Coffin, M.F., 1995. Timing of Hot Spot—Related Volcanism and the Breakup of Madagascar and India. Science 267, 852–855.

Sun, J., Sheykh, M., Ahmadi, N., Cao, M., Zhang, Z., Tian, S., Sha, J., Jian, Z., Windley, B.F., Talebian, M., 2021. Permanent closure of the Tethyan Seaway in the northwestern Iranian Plateau driven by cyclic sea-level fluctuations in the late Middle Miocene. Palaeogeogr. Palaeoclimatol. Palaeoecol. 564, 110172.

Tachikawa, K., Arsouze, T., Bayon, G., Bory, A., Colin, C., Dutay, J.-C., Frank, N., Giraud, X., Gourlan, A.T., Jeandel, C., Lacan, F., Meynadier, L., Montagna, P., Piotrowski, A.M., Plancherel, Y., Pucéat, E., Roy-Barman, M., Waelbroeck, C., 2017. The large-scale evolution of neodymium isotopic composition in the global modern and Holocene ocean revealed from seawater and archive data. Chem. Geol. 457, 131–148.

Thompson, J. O., 2017. The opening of the Indian Ocean : what is the impact on the East African, Madagascar and Antarctic margins, and what are the origins of the aseismic ridges ? PhD Thesis, Université de Rennes.

Toole, J.M., Warren, B.A., 1993. A hydrographic

section across the subtropical South Indian Ocean. Deep Sea Res. Part Oceanogr. Res. Pap. 40, 1973–2019.

Torsvik, T.H., Tucker, R.D., Ashwal, L.D., Carter, L.M., Jamtveit, B., Vidyadharan, K.T., Venkataramana, P., 2000. Late Cretaceous India-Madagascar fit and timing of break-up related magmatism. Terra Nova 12, 220–224.

Ullgren, J.E., van Aken, H.M., Ridderinkhof, H., de Ruijter, W.P.M., 2012. The hydrography of the Mozambique Channel from six years of continuous temperature, salinity, and velocity observations. Deep Sea Res. Part Oceanogr. Res. Pap. 69, 36–50.

van Aken, H.M., Ridderinkhof, H., de Ruijter, W.P.M., 2004. North Atlantic deep water in the south-western Indian Ocean. Deep Sea Res. Part Oceanogr. Res. Pap. 51, 755–776.

Walford, H.L., White, N.J., Sydow, J.C., 2005. Solid sediment load history of the Zambezi Delta. Earth Planet. Sci. Lett. 238, 49–63.

Watkeys, M.K., Sokoutis, D., 1998. Transtension in southeastern Africa associated with Gondwana break-up. Geol. Soc. Lond. Spec. Publ. 135, 203–214.

Weijer, W., 1999. Impact of Interbasin Exchange on the Atlantic Overturning Circulation. J. Phys. Oceanogr. 29, 19.

You, Y., 2000. Implications of the deep circulation and ventilation of the Indian Ocean on the renewal mechanism of North Atlantic Deep Water. J. Geophys. Res. Oceans 105, 23895–23926.

Yuan-Hui, L., 1982. Interelement relationship in abyssal Pacific ferromanganese nodules and associated pelagic sediments. Geochim. Cosmochim. Acta 46.

CHAPTER 1 : INTRODUCTION

1.1. General context of the thesis project

The Mozambique Channel originated from the separation of Africa and Madagascar between 180 Ma and 80 Ma (Coffin, Rabinowitz, 1987 ; Eagles, König, 2008 ; Gaina et al., 2013; Heirtzler, Burroughs, 1971). Since then, regional tectonics have little changed with the exception of vertical movements (between 35 and 25 Ma, then between 15 and 2 Ma) and volcanic phenomena from 30 Ma and still present today. Its location between Atlantic Ocean and Indian Ocean makes it a strategic zone for mixing water masses (Collins et al., 2016 ; de Ruijter et al., 2002 ; DiMarco et al., 2002 ; Flemming, Kudrass, 2018 ; van Aken et al., 2004 ; You, 2000), mainly known for the Agulhas current, essential for regulation of heat between the two hemispheres (Gordon, 1986 ; Weijer, 1999 ; Lutjeharms, 2006).

The oceanic circulation of the Channel remains largely unknown today, particularly with regard to the impact of regional and local geological events on the evolution of deep and intermediate currents. It is in this context that PAMELA-MOZ1 et PAMELA-MOZ5 missions (paragraph 1.1.1 – PAMELA project) were proposed and carried out in 2014 and 2016 respectively, with the aim of identifying and understanding the interactions between water masses and deep sedimentary systems, especially in the southwestern region of the Channel, in the north of Natal valley. The issue was also to study the origin of the creation of carbonate platforms and major volcanic events in the Mozambique Channel.

Both campaigns revealed a unique collection of ferromanganese (Fe-Mn) crusts in Mozambique Channel. These geological concretions have been used since the 1980s in paleoceanographic and paleogeographic reconstructions from their mineralogical and, elementary and isotopic geochemical studies. (Albarède et al., 1997 ; Christensen et al., 1997 ; Frank et al., 1999 ; Josso et al., 2020 ; Mizell et al., 2020).

By integrating bathymetric data from the two oceanographic missions and the in-depth mineralogical and geochemical study of Fe-Mn crusts, this thesis aims to (1) characterize the water masses present in Mozambique Channel and their circulation routes, (2) retrace currentological evolution of this mixing zone over the last 30 Ma and (3) understand the impact of regional geodynamic phenomena (e.g. volcanism, subsidence, uplift) on the geochemical composition of water masses and on their circulation.

1.1.1. PAMELA project

The PAMELA project (PA*ssive* M*argin* E*xploration* LA*boratory*) comes from a close scientific collaboration between the Institut Français de la Recherche pour l'Exploitation de la Mer (IFREMER) and Total with the aim of establishing a model of evolution of passive margin, in a " source to sink " approach. This program, carried between 2013 and 2019, includes a large number of partners such as the Institut Français du Pétrole et des Énergies Nouvelles (IFPEN), the Université de Bretagne Occidentale (UBO), the Université de Pierre et Marie Curie (UPMC), the Université de Rennes and Centre National de la Recherche Scientifique (CNRS). Five research themes were mainly addressed: geodynamic evolution, sedimentary systems, geological hazards, the study of currents and study of marine ecosystems. This is a large-scale collaboration that offers the possibility of developing important scientific advances through the acquisition of innovative data on strategic areas for the understanding of continental margins.

Four research areas were selected for their representativeness of multiple contexts: the Bay of Biscay, the eastern margin of Corsica, the Gulf of Aden and the Mozambique Channel (Figure 1.1).

Figure 1.1. *Location of the study site to the west of the Indian Ocean. The Mozambique Channel is located between the African and Malagasy continental margins (©NASA).*

The latter corresponds to the project's largest scientific worksite since 2014 due to its remarkable geological and oceanographic interest. In this context, 7 oceanographic campaigns were carried out in order to characterize (1) its crustal and sedimentary structure, (2) its genesis, its vertical evolution as well as its deformation associated with the kinematics of plates, (3) all the sedimentary systems, from delta to deep turbiditic lobes, and (4) their interactions with paleocurrent and paleoclimatic variations.

1.1.2. Oceanographic missions

This thesis work is based on samples taken during 4 oceanographic campaigns. Most of the samples come from 2 campaigns carried out as part of PAMELA project, the other two were carried out by the Muséum National d'Histoire Naturelle de Paris (MNHN) in 1975 and 1984. We will briefly present these campaigns here.

PAMELA-MOZ1 took place in 2014, aboard the N/O L'Atalante (Olu, 2014). This campaign focused on 11 key sectors of Mozambique Channel, from the Zambezi lobe in the south to the îles Glorieuses region in the north (Figure 1.2). The objectives of the dredging operations were to (1) learn about the age of volcanism of the Comoros Arc, the Davie ridge as well as the seamounts of Bassas da India region, (2) characterize the nature of Fe-Mn crusts previously sampled along the Davie ridge and (3) identify their metallogenic potential. Finally, 22 dredging operations were carried out on the sides of seamounts and volcanic structures, from Île Europa in the south to the îles Glorieuses in the north. A total of 186 samples were recovered including 74 Fe-Mn crusts.

PAMELA-MOZ5 was carried out in 2016 aboard the " Pourquoi pas ?" (Moulin, Evain, 2016). The crustal study of passive margins bordering the eastern Limpopo basin and Natal valley was the main purpose of this oceanographic mission (Figure 1.2), through a multi-trace seismic reflection acquisition and an important wide-angle seismic. However, 8 dredging operations were also carried out, and 5 reported Fe-Mn crusts of an exceptional nature.

MD-06 Nosicaa (Leclaire, 1975) and MD-39 Rida (Leclaire, 1984) are two oceanographic campaigns directed by MNHN which took place respectively in 1975 and 1984. The first MD-06 Nosicaa looked at the origin and nature of sediments in the central and southern Indian Ocean (Figure 1.2) while the second MD-39 Rida aimed to study the structure of the Davie ridge (Figure 1.2) and the dynamics of water masses in Mozambique Channel under the influence of meteorological changes. This oceanographic campaign is the source of the first Fe-Mn crusts discovered in this sector. During this thesis, a sample of each of these campaigns is studied. One from the Plateau des Aiguilles and serving as a

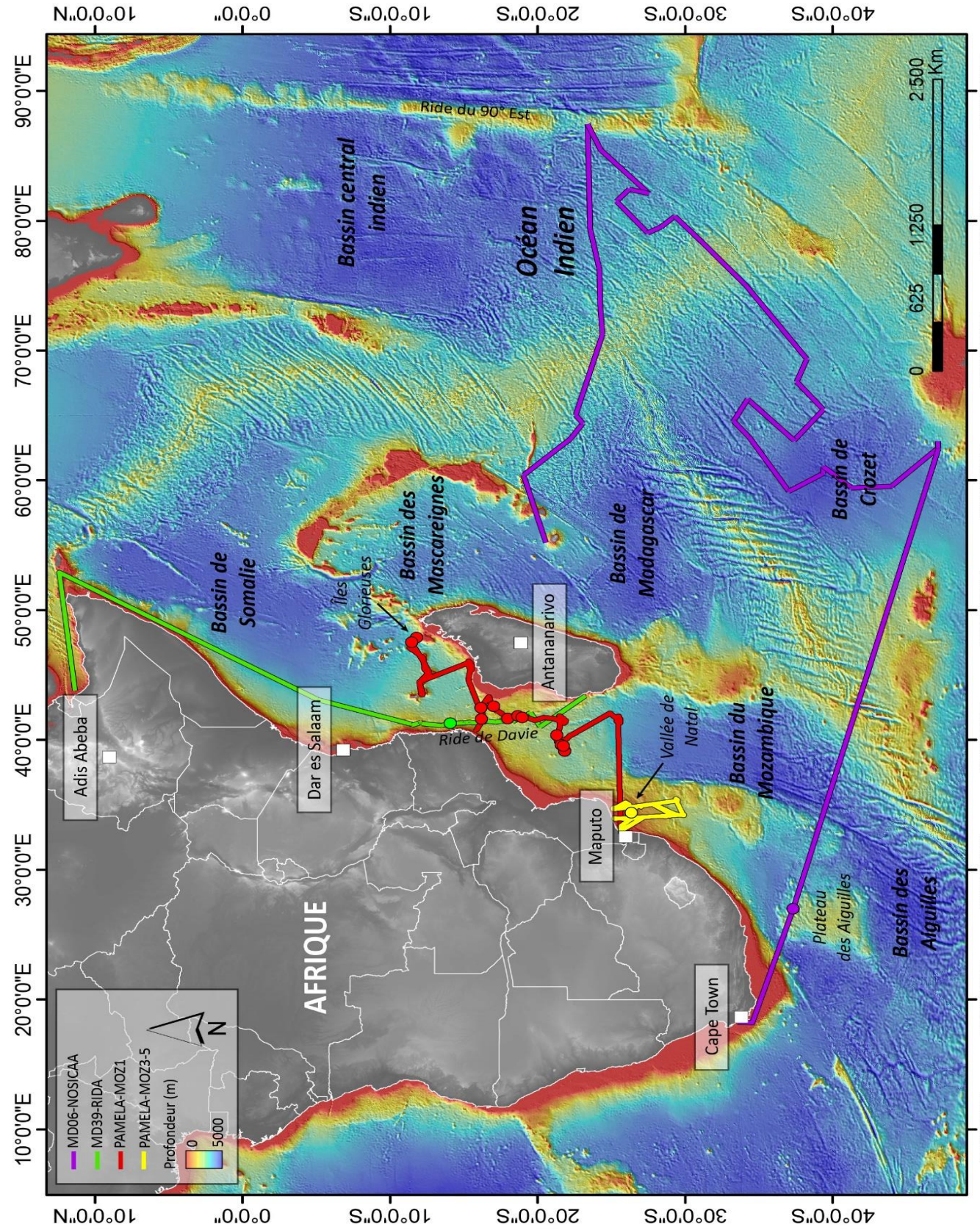

Figure 1.2. *Bathymetry of the eastern Indian Ocean (GEBCO and PAMELA campaigns) with the navigations of PAMELA-MOZ1 and PAMELA-MOZ5 oceanographic missions led by the PAMELA project as well as the MD-06 Nosicaa and MD-39 Rida campaigns led by the MNHN. The points represent the positions of the 17 respective dredges from which the samples from this thesis come (**Appendix 1**).*

major landmark to the south of the Channel. The other coming from the western slope of the Davie Ridge, in the area of Mount Paisley.

1.2. Geological principles and scientific questioning

1.2.1. General characteristics of Fe and Mn in the oceans

Iron (Fe) and manganese (Mn) are metals very present in the ocean where they play an essential role in biogeochemical cycles. They are elements sensitive to oxidation-reduction conditions, which allows them to migrate in dissolved forms and precipitate according to changes in the physico-chemical conditions of the environment. Biogeochemical cycles of metals in oceans are controlled by sources and shafts that vary according to the metals considered (Frank, 2002).

In the case of Mn, hydrothermalism is the main source of this metal, with chemical concentrations in black smokers sometimes a million times higher than those present in seawater (Elderfield et al., 1996). However, other sources of Mn exist such as terrigenous inputs by fluvial and wind routes, or underwater volcanism. Thus, distribution of Mn in the water column is very variable, as shown in figure 1.3. Mn is a metastable element with:

(1) high concentrations from the ocean surface, in the form of Mn^{2+}, up to the Minimum Oxygen Zone (OMZ), which is an area between 700 and 2000 metres deep where oxidation kinetics of Mn is very slow and its concentrations can reach close to 4 nmol/kg (Klinkhammer, Bender, 1980),

(2) concentrations becoming significantly lower in depth due to precipitation of oxy-hydroxides and favored by bacteriological activity.

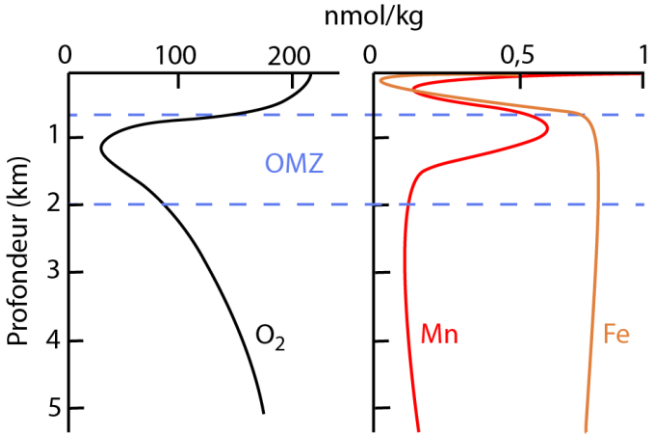

Figure 1.3. *Concentration of dissolved oxygen, manganese and iron in the Indian Ocean according to depth (after Saager and al., 1989 ; Chinni and al., 2019).*

The Fe, on the other hand, comes mainly from atmospheric, sedimentary, hydrothermal and river inputs. It is mainly present in particulate form (>1 µm). Its concentration in the water column follows a less variable distribution than Mn, as shown in figure 1.3. On the surface, its concentration is very high, with an average of 70pmol/kg, due to wind inputs. It is quickly consumed and its concentrations decrease sharply on the surface before being released. From the OMZ, there is a stability of concentrations at depth.

1.2.2. Precipitation process of Fe-Mn deposits

Different precipitation processes are responsible for the wide variety of Fe-Mn mineralization. They vary according to defined factors, related to the geodynamic environment, hydrothermal activity, bathymetry of the seabed or intensity of currents. Thus, the three main processes involved in the growth of deep Fe-Mn deposits are: the hydrogenetic process, diagenetic process and hydrothermal process, and several classifications, presented below allow to characterize them. (Figure 1.4 ; Bonatti, 1972 ; Josso et al., 2017).

1.2.2.1. Hydrogenetic process

This process corresponds to the precipitation of metal oxides in colloidal form from marine solution in an oxidizing medium (Dymond et al., 1984). In fact, in ocean water, the elements can be present in elemental form or constitute complexes (organic or inorganic). The latter will form colloids which can then interact with the dissolved metals (Hein et al., 1997; Koschinsky, 1994; Koschinsky, Halbach, 1995,).

Several important factors such as (1) the initial concentration of the element in seawater, (2) degree of oxidation and pH in the water column (Hein et al., 1997) or (3) the addition of elements by process of dissolution and dilution of detrital elements control the concentration of elements in hydrogen deposits. Finally, it is essential to note that the rate of precipitation associated with this process is very low. It varies between 0.5 and 15 mm/Ma which requires a calm deposition environment, with a very low sedimentation rate (Hein et al., 1997).

1.2.2.2. Diagenetic process

The diagenetic process depends on oxidation conditions of the sediment column, its thickness, the rate of sedimentation and biological activity. Thus, diagenetic formations arise from two distinct conditions: with and without oxygen.

In the case of a diagenesis with the presence of oxygen, metallic elements are remobilized by interstitial water under the small thickness of sediments, where they are then reprecipitated (Dymond, Eklund, 1978 ; Jung, Lee, 1999). In the case of a process without oxygen, the stable element is reduced in its mobile form. It will then migrate to the depth of new oxy-reducing conditions and precipitate again.

1.2.2.3. Hydrothermal process

This latter process is directly related to the precipitation of hydrothermal solution close to the sources of emissions of significant thermal fluxes,

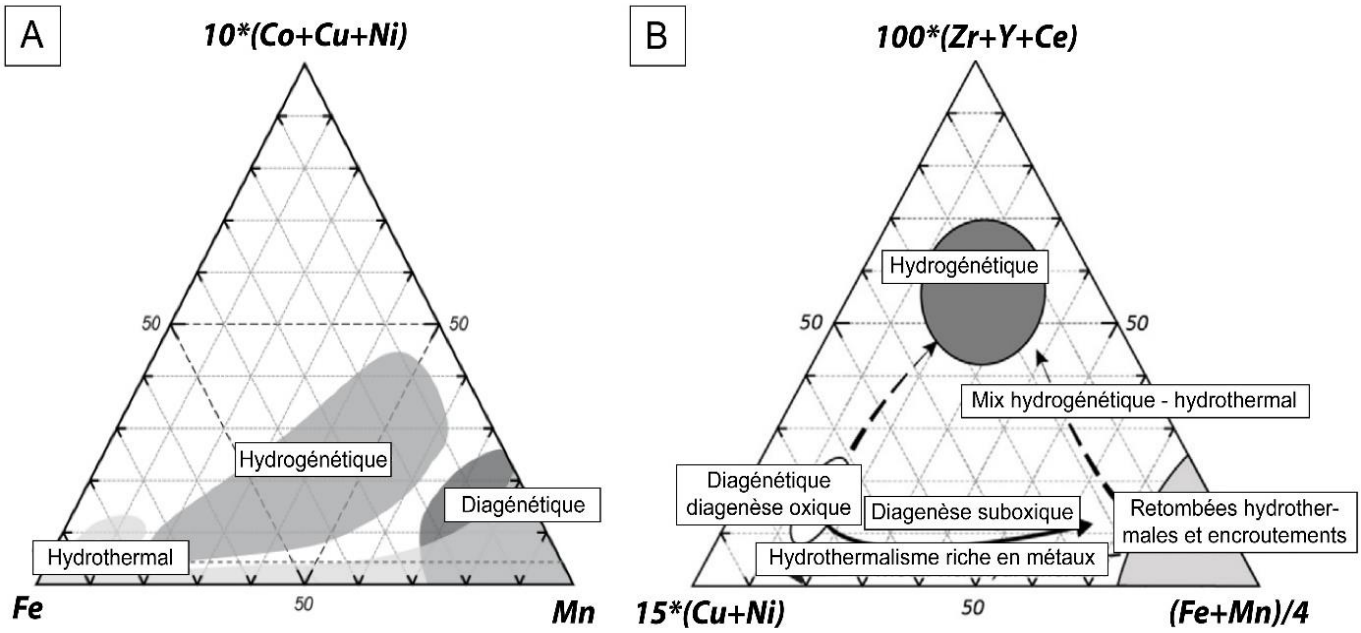

Figure 1.4. *Classifications of the different processes of formation of Fe-Mn deposits: hydrogenetic, diagenetic and hydrothermal, according to (A) the study by Bonatti (1972) and (B) Josso et al., 2017 (modified).*

such as at the level of ridges or oceanic arcs, and at the level of hot spots. However, the further hydrothermal fluid emitted will move away from its source and mix with seawater, the more the precipitates will have the composition of hydrogen deposits (Hein et al., 1997).

The three processes presented here were first illustrated in the ternary diagram of Bonatti, 1972 (Figure 1.4). This is a diagram aiming to classify these three modes of precipitation of Fe-Mn deposits by means of an Mn pole, an Fe pole and a pole corresponding to the sum of contents in nickel (Ni), copper (Cu) et cobalt (Co). Thus, each formation process occupies a precise place in the diagram with a very variable Fe / Mn ratio and relatively low levels of metals Co, Cu and Ni. Josso et al. (2017) proposes a second classification diagram integrating metals, the Fe / Mn ratio, but also yttrium (Y) and cerium (Ce) being part of the rare earths (REY) and zirconium (Zr) which is a strongly charged element (HSFE ; Figure 1.5). The latter are generally present in low concentrations in diagenetic and hydrothermal deposits, which makes it possible to distinguish the hydro-genetic inputs from the diagenetic contributions.

1.2.3. Fe-Mn crusts

Fe-Mn crusts are oceanic metalliferous deposits in the form of Fe (FeOOH.nH2O) and Mn (MnOOH.nH2O) oxy-hydroxides, enriched with transition metals (Hein et al., 2013 ; Li, Schoonmaker, 2003) in the same way as polymetallic nodules or hydrothermal sulphides (Cronan, 1980). In the case of crusts the formation process in oceanic water column takes place through the formation of colloids and then through adsorption of metals (hydrogenetic process; Figure 1.5).

Indeed, the reduced phase Mn^{2+}, enriched in the OMZ (Klinkhammer, Bender, 1980) is oxidized when mixed with deeper waters richer in oxygen. At this stage, the Mn and Fe, the source of oxy-hydroxides, form colloids, which, depending on their surface charge density, can become mixed colloids (Koschinsky, Halbach, 1995). Fe (FeO(OH)) oxyhydroxide colloids with positive surface charges trap anionic elements and large complexes. Conversely, Mn oxide colloids (MnOOH) having a negatively charged surface, attract cations (Hein et al., 2013; Koschinsky, Halbach, 1995 ; Koschinsky et al., 1997 ; Yuan-Hui, 1982). Elements such as phosphorus (P), thorium (Th), heavy rare earths (HREE), arsenic (As), titanium (Ti) and vanadium (V) are incorporated into FeO (OH) (Figure 1.5). While elements such as Co, Ni, Cu, zinc (Zn), thallium (Tl) and light rare earths (LREE) are found preferentially on the MnOOH phase (Bau, 1996 ; Koschinsky, Hein, 2003). Colloids then precipitate on hard substrates in areas with very low sedimentation rates (Craig et al., 1982 ; Halbach et al., 1983), and trap dissolved trace metals (Figure 1.5).

At this stage, Fe precipitates mainly in amorphous form (FeO (OH)) while the three oxidation states of Mn : Mn^{2+}, Mn^{3+} et Mn^{4+} allow it to associate with a multitude of elements and form many multivalent phases (Post, 1999). This wide variety of electronic valence allows it to accommodate many crystal architectures easily integrating other cations on the crystallographic basis of MnO_6 octahedra. Two main mineralogical structures emerge in an oceanic context according to the arrangements adopted by these octahedra by junction of angles or their borders. (Post 1999).

The two main minerals formed from Mn are each associated with a particular structure (Figure 1.6). Vernadite or δ-MnO2, "z-disordered manganate", "disordered manganate" or "turbostratic manganate" has a layered structure. While

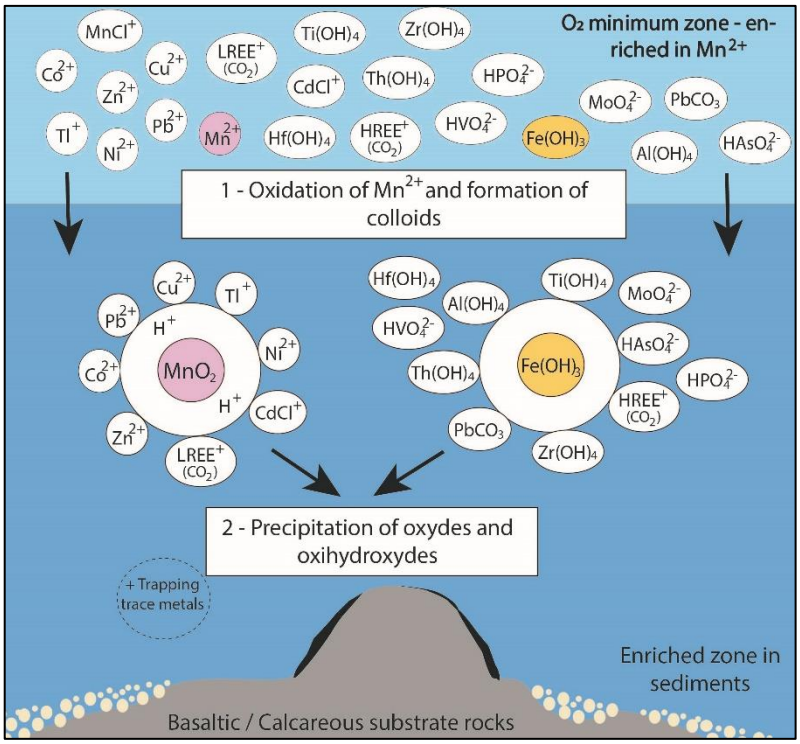

Figure 1.5. *Hydrogenetic process of large-scale formation of Fe-Mn crusts (modified from Koschinsky, Halbach, 1995).*

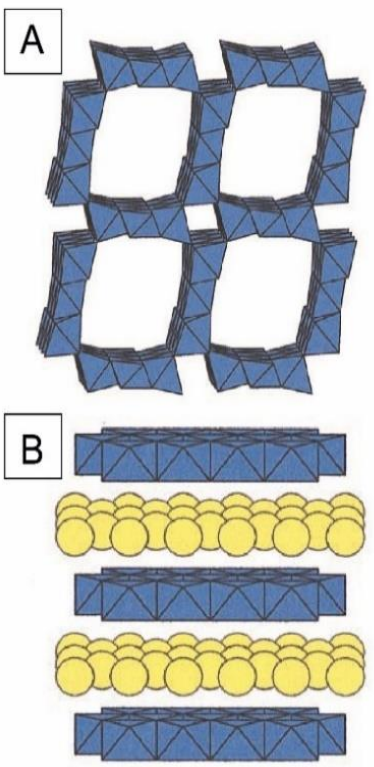

Figure 1.6. *(A) Mineralogical tunnel structure of todorokite and (B) in layers of vernadite showing H20 sites in yellow (modified, after Post 1999).*

todorokite (Ca, Na, K)3-5[Mn(IV), Mn(III), Mg]60123-4.5H20, " 10 Å manganate " or " 10 Å manganite " is a polymorph with a tunnel structure (Figure 1.6 ; Aplin, Cronan, 1985; Hein et al., 2016; Kuhn et al., 1998 ; Post, 1999), however it almost never appears in hydrogenetic crusts, unless secondary remobilization. Secondary minerals such as quartz, feldspar, carbonate-fluorapatite (CFA) or other detritic minerals are also identifiable in these hydrogenated deposits and are mainly due to erosion from surrounding continental sources (Guan et al., 2017; Hein et al., 2013, 1997).

1.2.4. Growth rates and dating methods

Crusts are found in all oceans at depths between 400 and 7000 meters where they accumulate on hard substrates such as seamounts or low sediment plateaus (Figure 1.5 ; Josso et al., 2017 ; Koschinsky, Hein, 2017). Formed directly from the precipitation of chemical elements from surrounding seawater, these hydrogen deposits show very slow growth rates, of the order of 1 to 10 mm / Ma on average (Frank et al., 1999 ; Josso et al., 2019 ; Putenaus, Halbach, 1988). Therefore, the thickest crusts can reach 80 Ma (Frank et al., 1999). This very low precipitation rate allows efficient adsorption of elements dissolved in seawater over very long periods of time leading to significant enrichments in base metals (e.g. Cu, Ni) and critical metals (e.g. Co, REE, Zr, Nb, Y, Te et Pt ; Hein et al., 2010 ; Koschinsky, Hein, 2017 ; Lusty et al., 2018; Piper, 1974). Fe-Mn crusts therefore contain records of the cycles of metals in oceans. (Cronan, 2017; Koschinsky, Halbach, 1995; Koschinsky et al., 1997) with each millimeter of thickness corresponding to a specific time period (Figure 1.7). They thus

constitute a true condensed archive of the geochemical evolution of oceans over time, recording climatic and geomorphological changes such as periods of glacial erosion, tropical bad weather or even the openings and closings of large oceanic areas (Albarède et al., 1997; Frank et al., 2002; Josso et al., 2020; Rehkämper et al., 2004).

Figure 1.7. *Fe-Mn crust MOZ5-DR03-01 of which different periods are visible thanks to the laminations. PAMELA-MOZ5 (Moulin, Evain, 2016).*

Since their discoveries, these deposits have been clearly studied for paleoceanographic reconstructions using different isotopic proxies such as strontium (Sr), neodymium (Nd), lead (Pb; Christensen et al., 1997; Frank et al., 2002), but also osmium (Os) and hafnium (Hf ; Burton et al., 1999 ; David et al., 2001 ; Klemm et al., 2005 ; Piotrowski et al., 2000). However, the dating of crusts remains a major issue for their use as archives. Their very low growth rate limits temporal resolution to a stratigraphic sampling by micro-boreholes which integrate between 20,000 and 80,000 years on average per sample (Charles et al., 2020; Josso et al., 2019 ;). In addition, their mineralogy and their very porous structure (Hein et al., 2000) generate almost constant contact between layers of crusts and seawater, which induces elementary rebalancing and significant exchanges with the geochemical signature of ocean in real time (Josso et al., 2019).

These conditions make it impossible to use absolute U-Pb dating due to the diffusion of uranium (U) in Fe-Mn oxides although it can be used to date carbonate substrates and give a time constraint of the beginning of crust formation (Claude et al., 2005 ; Goto et al., 2014). It is therefore essential to establish a reliable and absolute chronology for the stratigraphic studies of Fe-Mn crusts, in order to correlate the geochemical variations of oceans with identified paleoclimatic and paleoceanographic events.

1.2.4.1. Chronology by absolute dating

In a high resolution study of early structures, an absolute timeline can be performed using ($^{230}Th_{ex}$) and ($^{230}Th_{ex}/^{232}Th$) up to 1 Ma (Claude et al., 2005). Beyond this period, the use of another method is required. The ^{10}Be is an unstable cosmogenic isotope with a sufficiently long half-life (1,387 ± 0,012 Ma) to cover a time range up to 12 Ma (Chmeleff et al., 2010; Korschinek et al., 2010). Once formed in the Earth's atmosphere, ^{10}Be is rapidly (3 years, according to Baroni et al., 2011) transferred to the surface of the globe through precipitation. At this stage, it is either absorbed on particles and deposited on marine sediments, or contained on the surface of continental sediments. More than 99% of ^{10}Be is found in sedimentary deposits. Thus, immobilized and isolated from external exchange factors, this nuclide makes it possible to date the accumulated sediments effectively.

1.2.4.2. Chronology by empirical dating

Puteanus, Halbach (1988) on the assumption that the Co flux on a Mn oxide is solely related to the hydrogenetic process and therefore constant,

propose another dating system (Halbach et al., 1983). If the Co flux is constant then the Co concentration will be directly dependent on the growth rate of the sample. To measure a growth rate (mm/Ma), the following empirical equation results, with the concentration of %wt:

$$\frac{1{,}28}{([Co] - 0{,}24)} \qquad (1)$$

A similar approach is carried out by Manheim, Lane-Bostwick (1988) taking into consideration a large panel of Fe-Mn oxides such as hydrothermal deposits or pelagic sediments. The initial equation is then derived to obtain the following formula, which integrates the concentrations of Fe and Mn, main components of hydrogenetic Fe-Mn oxy-hydroxides, with the concentrations in %wt :

$$\frac{0{,}68}{\left([Co] \times \left(\frac{50}{[Fe] + [Mn]}\right)\right)^{1{,}67}} \qquad (2)$$

Although the ages acquired by these two equations are minimum ages, as these techniques do not take into account the gaps and eroded of Fe-Mn deposits, the two methods are used frequently and independently in order to provide a temporal resolution to geochemical data in paleoceanographic reconstructions (David et al., 2001 ; Frank et al., 1999 ; Hu et al., 2012 ; Ling et al., 2005 ; Marino et al., 2017).

1.2.4.3. Chronology by indirect dating

Since the use of Co as a geochronometer has several limitations (e.g. identification of gaps), an indirect method was considered through the isotopic study of Os.

Indeed, the rate of diffusion of the post-deposition Os is very low (of the order of 3×10^{-8} cm²/ year according to Henderson, Burton, 1999), which does not disturb the Os isotopic composition in Fe-Mn crusts over time. This characteristic makes it possible to compare the variations of $^{187}Os/^{188}Os$ ratio in crusts to the overall evolution of this isotopic ratio in seawater, the profile of which was established and dated until the end of the Cenozoic (Figure 1.8 ; Burton et al., 1999 ; Klemm et al., 2005 ; Peucker-Ehrenbrink, Ravizza, 2000, 2012).

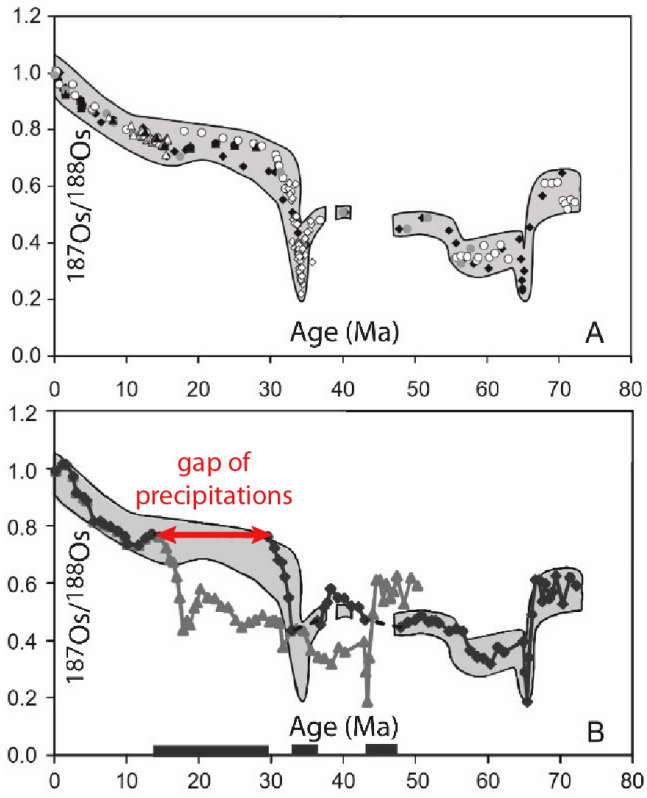

Figure 1.8. *Curve of the $^{187}Os/^{188}Os$ ratio of seawater according to Ravizza, Peucker-Ehrenbrink (2003) (A). Comparison with the osmium curve recorded in CD29-2 (grey) and adjustment to the seawater signature (black). Black dashes and rectangles show erosion and gap periods of the sample from Klemm and al. (2005) (B).*

This approach thus makes it possible to match an isotopic value to a specific age for each laminae in a sample. The CD29-2 sample from the Pacific Ocean has already been the subject of this approach and the acquired ages were compared to dating from the empirical Co flux method.

(Christensen et al., 1997; Frank et al., 1999; Lee et al., 1999; Ling et al., 2005, 1997). This comparison shows similar growth rates but also highlights that the Co flux method dates are inaccurate due to gaps identifiable with indirect Os (Figure 1.8; Klemm et al., 2005).

1.2.5. Paleoceanographic reconstructions

Fe-Mn crusts, by their status as ocean archives, have been the subject of numerous geochemical studies for paleoceanographic reconstructions, but also paleogeographic.

Since the 1980s, the authors have mainly been interested in the geochemical compositions of the major elements and in isotopic compositions of Nd and Pb over some twenty crusts distributed in the Atlantic, Indian and Pacific Oceans (Figure 1.9 ; Albarède et al., 1997 ; Christensen et al., 1997 ; Frank, 2002 ; Frank et al., 2002 ; Frank, O'nions, 1998 ; Ling et al., 1997 ; O'Nions et al., 1998; Rehkämper et al., 2004; Segl et al., 1984).

1.2.5.1. Pb in the oceans

The Pb of the oceans comes mainly from continental inputs through river inputs from continental erosion. Wind input, especially volcanic dust, explains only 10% to 12% of the Pb balance in the oceans (Chow, Patterson, 1962) and hydrothermal input remains low (<2 %) and very localized (Chen et al., 1986). Regarding the residence time of Pb, this is clearly less (80 years to 100 years) than that of Nd and less than the mixing time of the oceans (Frank et al., 2002). However, it is long enough (> 20 years) for Pb to constitute a major tracer of oceanic and atmospheric phenomena over very short time scales.

1.2.5.2. Nd in the oceans

In the oceans, Nd mainly comes from wind and continental inputs, via rivers and streams (Bayon et al., 2015; Elderfield et al., 1990; Goldstein, Jacobsen, 1988; Ingri et al., 2000; Tachikawa et al., 1997; van der Lubbe et al., 2016). However, the relative input of each of its contributions in the overall balance sheet of Nd is still debated according to the geographical areas. (Jones et al., 1994). Regarding its residence time in the oceans, it is estimated between 600 years and 2000 years (Arsouze et al., 2009 ; Jeandel et al., 1995 ; Rempfer et al., 2011 ; Tachikawa et al., 2003) while the mixing time of the oceans is of the order of a thousand years (Broecker et al., 1982). Nd therefore constitutes a quasi-conservative tracer of the chemistry of water masses, which is particularly interesting and exploited for paleoceanographic studies. (Frank, 2002; Goldstein, Hemming, 2003).

The variations in values of εNd are linked to the erosion and dissolution of rocks in the source regions of water masses. For example, erosion of the continental rocks of the old Canadian Shield is responsible for extremely low radiogenic εNd values. The water mass of the North Atlantic therefore show εNd values between -12 and -14 while those of the South Atlantic show εNd values between -9 and -11, linked to the mixing between the very little radiogenic values of North Atlantic and high radiogenic values of the Pacific (Jeandel, 1993; Piepgras, Wasserburg, 1987, 1982).

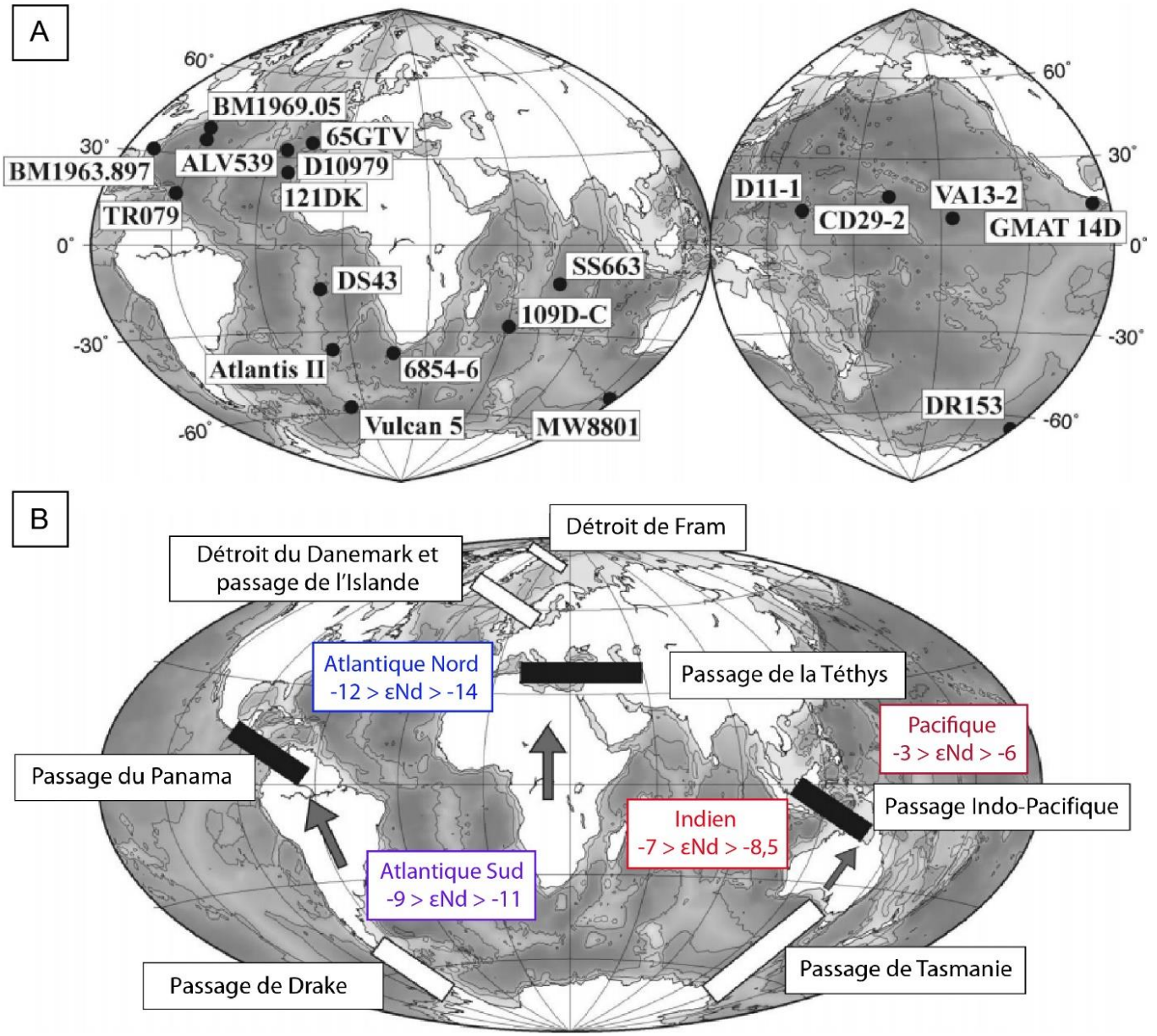

Figure 1.9. *Location of Fe-Mn crusts whose temporal studies were carried out using isotopes of Nd, Pb and Be (A). Major paleogeographic events during the 50 Ma which influenced the circulation of the oceans and isotopic values in Nd of the large oceanic domains. The black rectangles correspond to the closures while the white shows the openings. Arrows indicate general directions of tectonic plates. (B) According to Frank (2002).*

The εNd values of Pacific Ocean are very radiogenic (between 0 and -6) due to erosion of very young volcanic rocks derived from the mantle (Piepgras, Jacobsen, 1988 ; Shimizu et al., 1994). Finally, the Nd isotopic composition of the Indian Ocean results from the mixing between low radiogenic values of the Atlantic and very radiogenic values of the Pacific. Its εNd values vary between -7 and -8.5 (Arsouze et al., 2007; Bertram, Elderfield, 1993; Wilson et al., 2012).

1.2.5.3. Previous paléocéanographiques reconstructions

Isotopic analyzes carried out from the surface of several hundred crusts across the globe have revealed major isotopic trends in Nd in all oceanic domains (Albarède et al., 1997). This allowed the selection of key samples for temporal studies to identify and confirm major geodynamic events (Figure 1.9) through changes in the Nd isotopic composition of water masses.

Among them, the separation of Australia and Antarctica which led at the Oligocene (30-25 Ma) the opening of the Tasmanian passage (Figure 1.9) and the establishment of the Antarctic Circumpolar Current (ACC) which has been recorded as early as the Eocene (Kennett, 1977). Then, the opening of the Drake Passage, between South America and Antarctica, dating from the end of the Oligocene (23 Ma), allowed the total circulation of water masses around Antarctica (Barker, Burrell, 1977). Other events have been highlighted, in particular between 20 Ma and 13 Ma with the closure of the Tethys passage at European level (Bialik et al., 2019 ; Sun et al., 2021) and between 25 Ma and 6 Ma which represents the total period of closure of the Indo-Pacific passage (Figure 1.9 ; Ali et al., 1994 ; Hall et al., 2011 ; Srinivasan, Sinha, 1998).

Other major, more recent geodynamic events have been studied, notably by Burton et al. (1997) through isotopy of Nd and Pb on samples CD29-2, from Pacific Ocean, and BM1969.05 from Atlantic Ocean (Figure 1.9). The isotopic results of Nd in particular showed a sudden change in less and less radiogenic values of the deep currents of Atlantic Ocean (εNd going from -11 to -13; Figure 1.10) from the end of the Pliocene (3,5 Ma) directly related to an increase in contribution of water masses of the Labrador Sea compared to the much more radiogenic water masses of the Pacific (εNd between -3 and -4 ; Figure 1.10; Piepgras, Jacobsen, 1988). These observations are related to the closure of the Panama passage preventing the meeting of Pacific and Atlantic oceans (Figure 1.9 ; Keigwin, 1982 ; Nisancioglu, 2003). This major change is particularly visible from crust BM1963.897 which is located on the Blake Plateau, off the southeast coast of the United States. Its geochemical signature shows a drop in isotopic values in Nd from 10 Ma, going from -7.5 before the closure of the isthmus to -10.5 after the complete closure of the Panama passage (Figure 1.9). These observations were also made from Pb isotopic data and from the study of $^{206}Pb/^{204}Pb$ et $^{207}Pb/^{204}Pb$ (Burton et al., 1997).

The study by Frank (2002) also looked at large-scale phenomena across the Atlantic and Southern Oceans. It also reveals an increase in differences between the isotopic signatures in Nd and in Pb recorded in crusts of these two oceanic domains from 3.5 Ma. The isotopic compositions of the water masses of North Atlantic recorded in the samples ALV539 and BM1969.05 strongly decreased from 3 Ma (εNd going from -11 to -13 ; Figure 1.10) while those of the water masses of Southern (Atlantis II) and Indian (109D-C) oceans remained constant (εNd respectively between -8.5 and -9.5 and, between -7 and -8 ; Figure 1.10). These observations support the conclusions of Burton et al. (1997). In addition, they indicate a reduction in the inflow of deep Atlantic water masses to the south due to the great

glaciation of the northern hemisphere (NHG ; Raymo, 1994; Shackleton et al., 1984). This decrease in the contribution of deep Atlantic currents in southern hemisphere is estimated between 14% and 37% between 3.5 Ma and 0 Ma. These estimates are based on a calculation of mixing of poles between the North Atlantic (εNd fixed at -13 according to Jeandel (1993); Piepgras, Wasserburg (1987, 1982)) and Pacific Ocean (εNd fixed between -4 and -6 according to Piepgras, Jacobsen (1988) ; Rutberg et al. (2000); Shimizu et al. (1994)).

Despite a large number of Fe-Mn crusts already analyzed (Figure 1.9a), in particular in high resolution through stratigraphies, Fe-Mn deposits of Mozambique Channel remain little known and no temporal study has been carried out in this geographical area while the location of the channel, west of the Indian Ocean and close to continental margins (Figure 1.1), is of major interest for paleoceanographic and paleogeographic studies. Indeed, the Mozambique Channel plays an essential role in the mixing of the Atlantic and Indian Oceans and no significant lateral extension related to plate tectonics has been recorded since nearly 80 Ma. It is therefore distinguished from open oceanic domains where Fe-Mn crusts can drift over thousands of kilometers, passing from the influence of one masse of water to another modifying de facto their isotopic signatures (Meynadier and al., 2008).

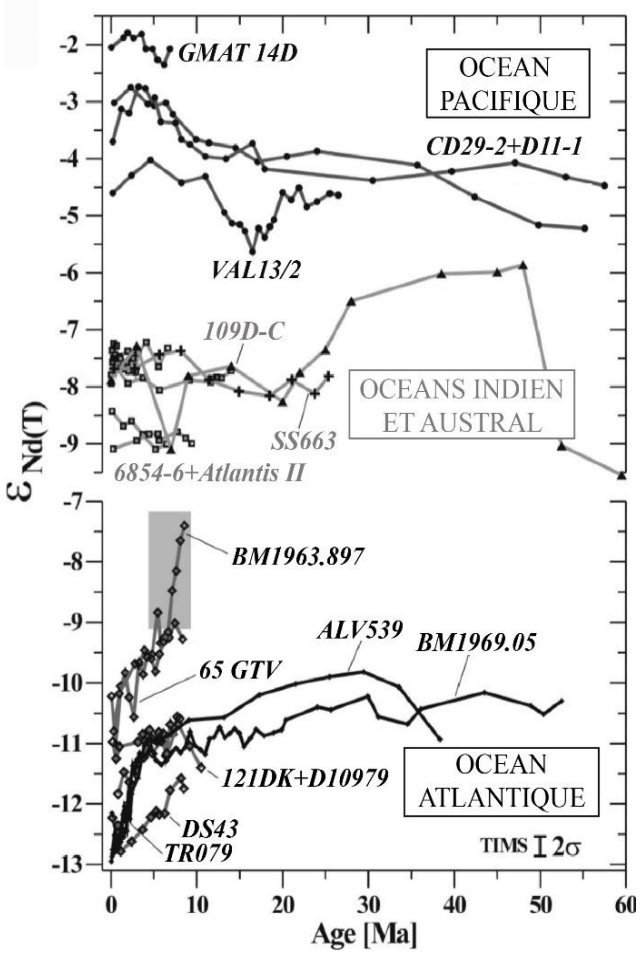

Figure 1.10. *Comparison and variations of the Nd isotope signatures of time series analyzed in the different oceanic domains (modified, from Frank (2002)).*

Thus, by freeing ourselves from the drift corrections inherent in certain crusts studies, we will be able to study and understand the evolution of the Mozambique Channel currentology over time and the impact of regional geodynamics on it through a mineralogical and geochemical study of Fe-Mn crusts.

1.3. Study area: the Mozambique Channel

1.3.1 Context and geodynamics

The Mozambique Channel is located southwest of the Indian Ocean, between the East African continental margin of Mozambique and Madagascar (Figure 1.1). It originated from the dismantling of the eastern part (Madagascar, India, Antarctica and Australia, here referred to as "Madagascar-Antarctica") and the western part

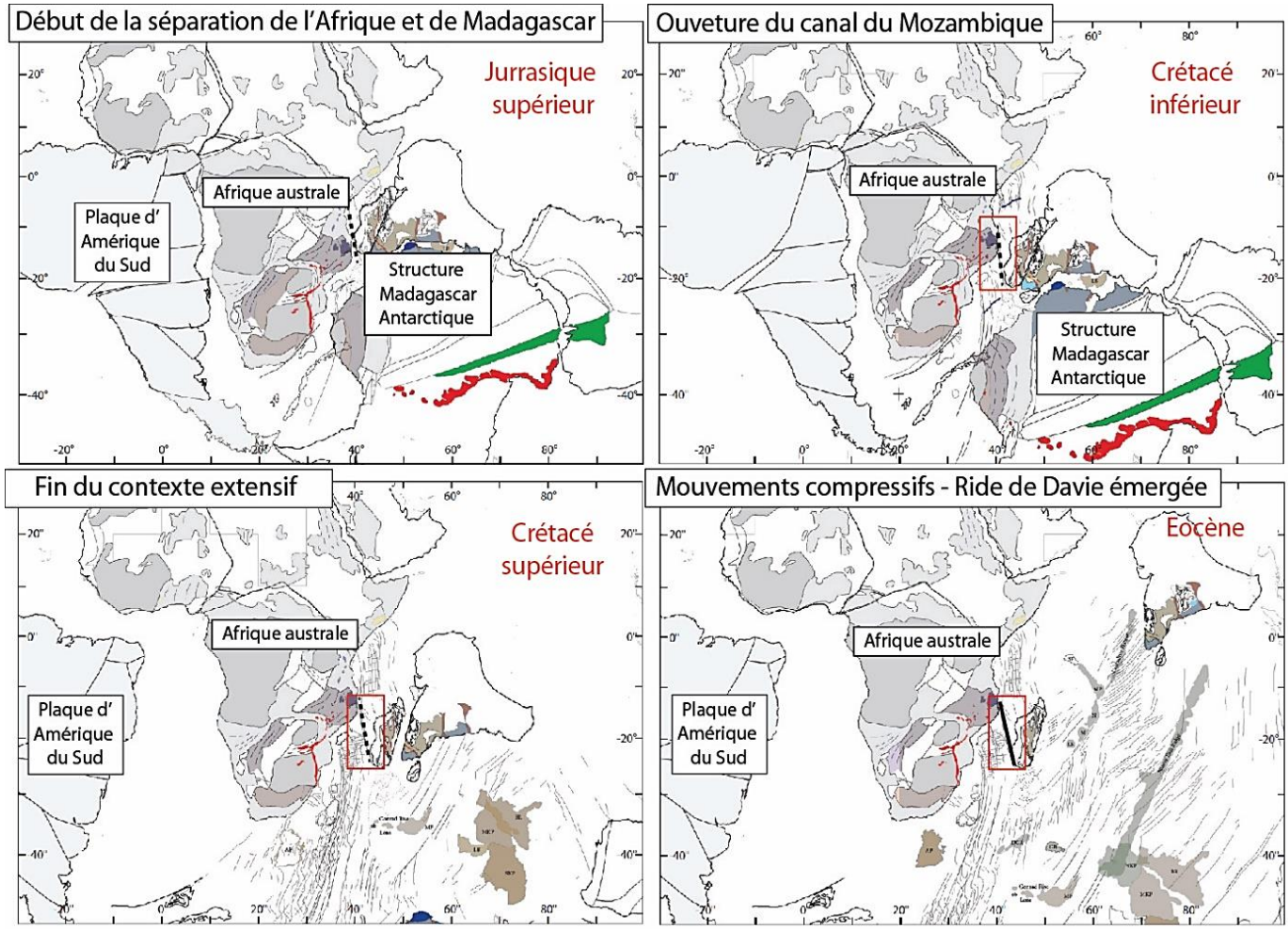

Figure 1.11. *Reconstruction of the different stages of the dislocation of Gondwana and the establishment of the Mozambique Channel (red rectangle) from the Upper Jurassic with the separation of Africa and the "Madagascar-Antarctic" structure until the emergence of the Davie ridge in the Eocene marking the beginning of the geodynamic stability of the canal. Black dotted lines denote the DFZ and the Davie ridge with a solid black line (modified, after Thompson (2017)).*

(Africa and South America) of the Gondwana McElhinny, 1970 ; McKenzie, Sclater, 1971). The rift began in the Lower Jurassic (Eagles, König, 2008) leading to the progressive opening of the northern Mozambique Basin from the Upper Jurassic (Figure 1.11, 1.12; Jokat et al., 2003 ; König et Jokat, 2010 ; Leinweber, Jokat, 2013, 2012). It increased with the southern opening of the Mozambique Basin and the Natal Valley from the Lower Cretaceous (Figure 1.12; Goodlad et al., 1982 ; Gradstein et al., 2012; Watkeys, Sokoutis, 1998) before the movement of the Madagascar-Antarctic structure southward along a major transformation zone called the Davie Fracture Zone (DFZ) to the upper Cretaceous marking the end of the extensive context of the zone (Figure 1.11; Coffin, Rabinowitz, 1987 ; Heirtzler, Burroughs, 1971 ; Gaina et al., 2013).

From the Upper Cretaceous, the Antarctic-India block separated from Madagascar, an event at the origin of a great volcanic activity on the island of Madagascar, but also at the level of the Morondava and Mahajanga basins located to the west of the island (Figure 1.12, 1.13; Bassias, 1992 ; Rogers et al., 2000 ; Storey et al., 1995 ; Torsvik et al., 2000).

The Scattered Islands (Bassas Da India, Europa, Juan de Nova, and îles Glorieuses) are witnesses of this volcanic activity since their formation from the Paleocene to the Oligocene. They result from two major uplift phenomena: the first in the Paleocene and the second, of at least 200m (Leroux and al., 2020) from the Upper Eocene to the Oligocene closely linked to magmatic pulses generated by the development of the East African Rift System (EARS ; Chorowicz, 2005 ; Courgeon et al., 2017, 2016 ; Franke et al., 2015 ; Leroux et al., 2020 ; MacGregor, 2015 ; Masters et al., 2021 ; Walford et al., 2005).

The islands were then structured by the installation of carbonate platforms until the

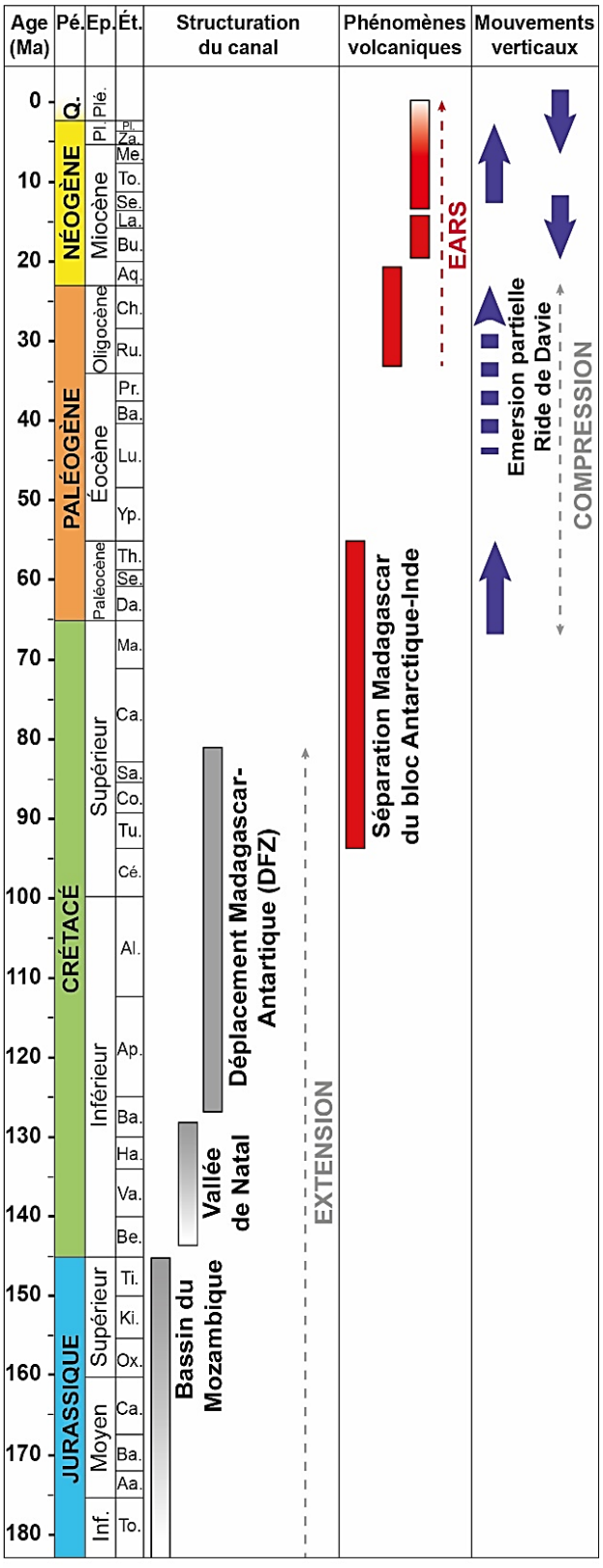

***Figure 1.12**. Summary of the structuring of Mozambique Channel and major magmatic / geodynamic events that have taken place since its establishment.*

Miocene before a phase of subsidence marked the shutdown of these carbonate platforms. (Courgeon et al., 2017, 2016 ; Leroux et al., 2020 ; McGrew, 1983). Following this subsidence episode, a third regional uplift, (425 m ; Leroux et al., 2020) causing lithospheric deformation at the origin of a strong magmatic activity still present today (Emerick, Ducan, 1982 ; Michon, 2016 ; Pelleter et al., 2014), has been demonstrated until the beginning of the Pliocene before a new and last episode of subsidence from the Pliocene (Courgeon et al., 2018 ; Delaunay, 2018 ; Leroux et al., 2020 ; Nicholas et al., 2007 ; Walford et al., 2005).

The Davie Ridge, which is a structure inherited from the DFZ and punctuated by several seamounts such as Mount Paisley, Mount Macua and the Sakalava Mountains, was thus partially emerged from the Eocene to the Oligocene before being mainly submerged from the Miocene (Ponte, 2018). It is today oriented N170 and extends over 1200 km from the east of the African margin (13 ° S) to the southwest of Madagascar (23 ° S) separating the Comoros basin to the northeast, from the deep basin of Mozambique to the southwest (Figure 1.13).

1.3.2. Oceanography

The location of the Mozambique Channel makes it an area of complex exchange between water masses of the Indian and Atlantic Oceans (Figure 1.13) which have different Nd isotopic signatures.

As seen previously, the Atlantic Ocean being not very radiogenic compared to Indian Ocean which results from a mixture of Atlantic and Pacific water masses. The latter being very radiogenic. Currently, the Mozambique Channel corresponds to a conduit through which the Indian surface water masses, hot and radiogenic, are drawn in a southerly direction in the Mozambique Current (MC ; Di Marco et al., 2002 ; Flemming, Kudrass, 2018; Quartly et al., 2013) while the low radiogenic Atlantic waters flow in the deep Mozambique Current (MUC), from south to north (De Ruijter et al., 2002).

Table 1.1 presents a summary of the isotopic values in Nd specific to the main water masses present in the channel and presented in the following paragraphs.

Table 1.1. *Abbreviations of the main water masses present in the Mozambique Channel, their depths and their respective εNd isotopic signatures.*

Abbreviations	Depth (m)	εNd
SICW	200-700	-8.5 to -7[a]
RSW	800-1400	-8.5 to -7[a]
AAIW	800-1500	-9 to -8[b]
NIDW	2000-3000	-8.5 to -7[a]
NADW	1500-3500	-13 to -9[c]

[a]*Bertram, Elderfield (1993), Arsouze and al. (2007)*
[b]*Piepgras, Wasserburg (1982), Jeandel (1993), Arsouze and al. (2007), Amakawa and al. (2013)*
[c]*Piepgras, Wasserburg (1987), Jeandel (1993), Rickli and al. (2009), Tachikawa and al. (2017)*

Le MC fait partie du courant des Aiguilles (AC), which is an essential link in the exchange of heat and salt between the Indian and Atlantic oceans (Gordon, 1986 ; Weijer et al., 1999), and is characterized by anticyclonic eddies (ME) with diameters up to 300km that can affect the entire water column (Figure 1.13; De Ruijter et al., 2002 ; Halo et al., 2014). The formation of these anticyclones is linked to the South Equatorial Current (SEC) which arrives in the east of Madagascar (17 ° S) and is divided into two: the North-East Current of Madagascar (NEMC) and the South-East Current of Madagascar (SEMC ; Schott et al., 2009).

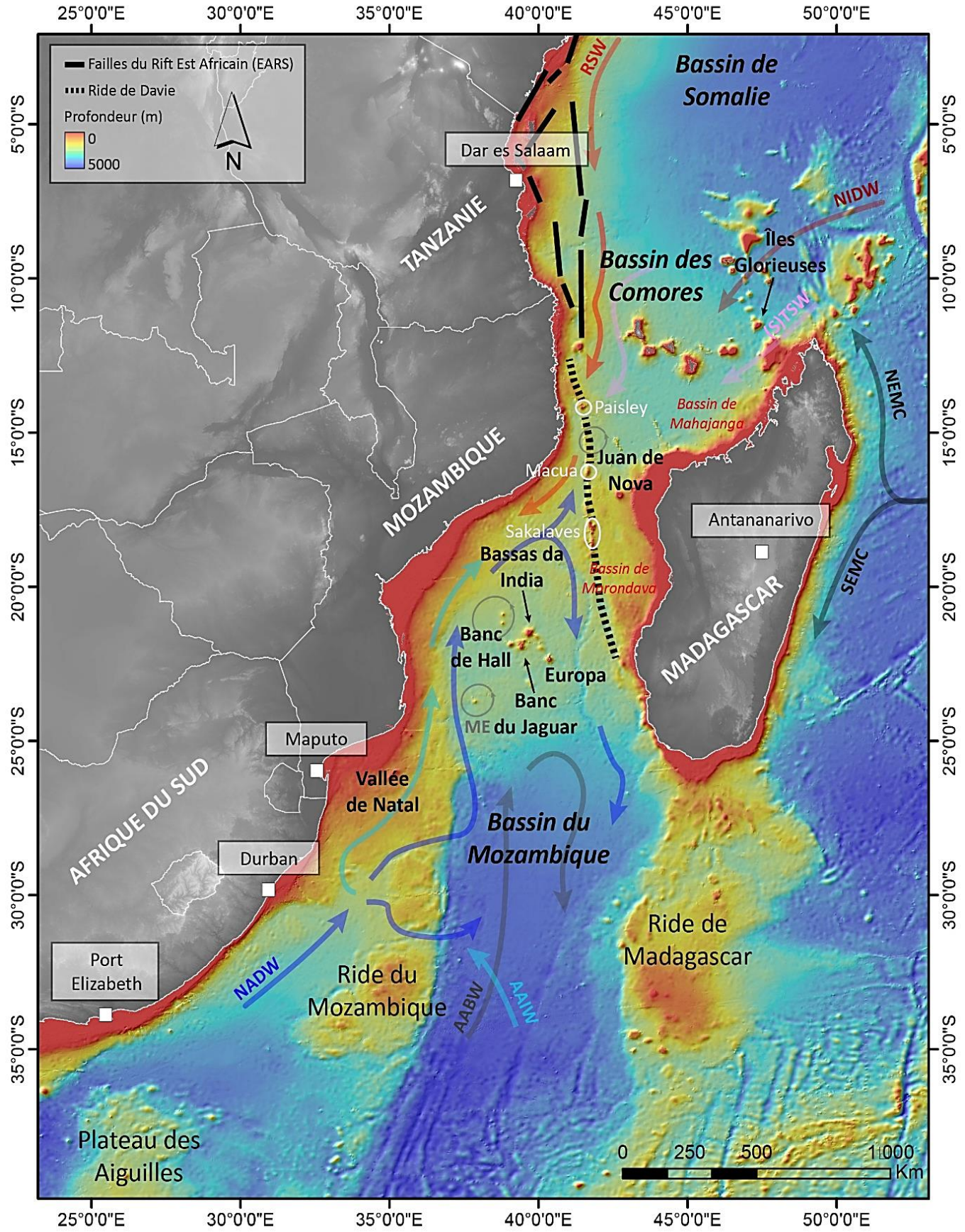

Figure 1.13. *Bathymetry of the Mozambique Channel (GEBCO and PAMELA cruises) with its main geological structures. Seamounts along Davie ridge are circled in white and ocean currents in the channel are indicated by arrows.*

The MC carries surface water up to 200m deep, composed of Tropical Surface Waters (TSW) and Subtropical Surface Waters (STSW), but also Central Waters of the South Indian Ocean (SICW) present between 200m and 600m deep. The intermediate waters of the MC are mainly composed of water masses of the Red Sea (RSW) between 900m and 1200m deep, which enter north of the Mozambique Channel along the East African coast. (Figure 1.13).

The MUC and the deep current of Aiguilles (AUC) carry the Antarctic Intermediate Waters (AAIW) between 800m and 1500m deep (Ullgren et al., 2012). The latter arrives from the east of the Mozambique Ridge and then circulates along the Mozambican coast (Figure 1.13; Fine, 1993). The North Atlantic deep waters (NADW) are also part of the MUC, between 2000m and 3500m deep. They arrive from southern Africa and enter the Mozambique Channel through the Natal Valley (Toole, Warren, 1993). The surface part of the NADW flows north of the Mozambique Basin to the west of the Davie Ridge. The rest of NADW retreats to the south following the western edge of the ridge (Figure 1.13; Ullgren et al., 2012; van Aken et al., 2004). Finally, at a depth of more than 4000m, the Antarctic Deep Current (AABW) circulates east of the Mozambique Ridge to the Mozambique Basin. It is then deviated, before heading south along the Madagascar ridge (Figure 1.13; Kolla et al., 1980).

Finally, to the north of the Mozambique Channel, the North Indian Deep Current (NIDW) circulates at a depth of more than 2000m (Collins et al., 2016). It is transported from the Indian Ocean and is very present in the north of the channel, at the level of the Îles Glorieuses (Di Marco et al., 2002). Very few studies have investigated the circulation of NIDW after its arrival north of Madagascar and its passage to the Îles Glorieuses (Figure 1.13). Existing results indicate that the Davie ridge would form an obstacle to the circulation of deep currents in the Mozambique Channel (Mantyla, Reid, 1995; Toole, Warren, 1993; You, 2000).

However, new hydrographic data, based on measurements of conductivity, temperature, pressure, dissolved oxygen and salinity, identified the presence of AAIW and NADW currents beyond the ridge and proposed new circulation routes (Collins et al., 2016 ; Di Marco et al., 2002; van Aken, 2004). These new results now allow to question the evolution of deep currents in the Mozambique Channel and the role of local geodynamics on the distribution of these water masses.

1.4. Issues and working methods

As presented, the Mozambique Channel, located between eastern Africa and continental margin of Madagascar, represents a still little known sea corridor in the Indian Ocean. It is traversed by superficial, intermediate and deep currents, whose physicochemical parameters have been studied and are now known, but whose circulation model remains misunderstood. The overall objective of this thesis is therefore identify, study and understand the evolution of the currentology of the Mozambique Channel over time and the impact of regional geodynamics on it through a mineralogical and geochemical study of Fe-Mn crusts.

While the analytical techniques and the data will be presented in the following chapters, this part aims to present the general methodology followed during this thesis according to the different issues raised.

The first step is to identify the geochemical signatures of the Atlantic Ocean and Indian Ocean water masses present in the study area. This first axis is based on 29 Fe-Mn crusts distributed

homogeneously in the channel, from the Plateau des Aiguilles in the south, to the Îles Glorieuses in the north. The surface part of the samples, corresponding to the last elemental deposits, is sampled before proceeding with isotopic analyzes in Nd reflecting the signature of the oceanic domains, and in Pb which can indicate elemental inputs from secondary sources. The objective of this axis is to identify the water masses present in the channel and to understand their circulation routes in order to propose a 2D model of modern circulation of currents in the Mozambique Channel, taking into account the Davie ridge. The role of this geological structure will be highly discussed since it currently separates the channel into two basins, thus being able to appear as a barrier blocking the evolution of deep currents.

The second aspect aims to create a 3D model of the past currentology of the Mozambique Channel. This paleoceanographic study is based on 7 Fe-Mn crusts dredged between 800m and 2000m deep, likely to have changed water mass over time, and therefore geochemical signature, and 2 deep Fe-Mn crusts (>2000min order to target deep currents. The large thicknesses of samples will allow high-resolution sampling in the form of stratigraphies and a $^{10}Be/^{9}Be$ geochronology. Measured ages will bring a temporal dimension to the results. A correlation between the geodynamic evolution of the channel (e.g. uplift, subsidence) and variations in signatures of water masses will make it possible to understand the impact of tectonic movements, identified during the 3D work and by other authors, on the circulation of intermediate and deep currents.

The final objective will be to associate these results with modelling in order to develop 4D a 4D model of the circulation of intermediate and deep currents during the last 30 Ma.

Finally, other factors can impact and influence the geochemical signatures of Fe-Mn crusts (e.g. volcanism, continent / ocean exchanges, and interstitial fluids) over time. In these specific cases, recorded variations do not reflect the pure signatures of water masses. This is why an exploratory axis of 4D will be devoted to local phenomena recorded in 2 key samples. Particular interest will be focused on the identification and direct consequences of magmatic events on the mineralogical and geochemical compositions of a crust located at the Îles Glorieuses. This work will focus on the isotopy of Pb and Os. While geochemical study of a crust near an area of continental discharges will focus on elementary and isotopic exchanges between the African basement and the surrounding water masses.

1.5. Structure of the manuscript

This thesis manuscript is divided into 6 chapters. Chapters 2, 3 and 4 are associated with articles (published, submitted or in prep.). Bibliographical references are systematically cited at the end of each chapter.

Chapter 1 - Introduction (this chapter)

This introductory part serves as the basis of the manuscript. Its objectives are multiple:

(1) define the general framework of the thesis and the project in which it is part,

(2) present the study area,

(3) expose the various scientific issues,

(4) present the methodology followed in order to respond to these and,

(5) give a general vision of the manuscript.

Chapter 2 - Analytical methodology

The purpose of Chapter 2 is to explain the methods and analytical devices used during the thesis, from sampling to data acquisition. It includes a paper published in Talanta in April 2021 presenting the development of a method to determine trace elements in Fe-Mn oxides (Charles and al., 2021).

- ***Charles, C.**, Barrat, J.-A., Pelleter, E., 2021. Trace Element Determinations in Fe-Mn Oxides by High Resolution ICP-MS after Tm Addition. Talanta 122446.*

Chapter 3 - Modern circulation of intermediate and deep currents in the Mozambique Channel

Chapter 3 focuses on the isotopic (Nd, Pb) characterization of intermediate and deep-water masses and the impact of the Davie Ridge on their spatial evolution over the past 20 to 80,000 years. The results make it possible to identify new circulation routes of currents thanks to their isotopic signatures and to measure their propagation intensity with contribution calculations that could be applicable to temporal studies subsequently (see chapters 4 and 5). This chapter includes a paper published in Marine Geology in September 2020 (Charles and al., 2020).

- *Charles, C., Pelleter, E., Révillon, S., Nonnotte, P., Jorry, S.J., Kluska, J.-M., 2020. Intermediate and deep ocean current circulation in the Mozambique Channel: New insights from ferromanganese crust Nd isotopes. Marine Geology. 430, 106356.*

Chapter 4 - Geodynamics of the Mozambique Channel: identification of vertical movements from 12 Ma

Chapter 4 studies the geodynamics of the channel over time and aims to establish a chronology of the tectonic phenomena recorded within the crusts from their isotopic signatures in Nd. The results show that the samples changed water masses due to an uplift identified from 11.7 Ma followed by subsidence from 5.7 Ma. These phenomena are the direct cause of variations in elemental concentrations within the samples and will allow discussing their impact on the circulation of deep currents (see Chapter 5). This chapter is a paper that will be submitted to *Earth and Planetary Science Letters* after the manuscript submission.

- ***Charles, C.,** Pelleter, E., Révillon, S., Jorry, S.J., Kluska, J.-M., Bourlès, D., Quentin, S., Braucher, R., Nonnotte, P., Liorzou, C., Chéron, S., Germain, Y., Barrat, J.-A., in prep. Fe-Mn crusts as archives of vertical movements: new insights for the geodynamic reconstruction of the Mozambique Channel over the past 12 Ma.*

Chapter 5 - Paleocirculation of currents in the Mozambique Channel: an evolutionary model from 20 Ma

Chapter 5 focuses on the past circulation of currents. It makes the link with the geodynamic events highlighted in Chapter 4 and their direct impact on the evolution of currents in the Mozambique Channel over time. In order to quantify this phenomenon, this axis of the thesis is supported by calculations of contributions of currents as presented in chapter 3. An evolutionary model of the circulation of water masses presents a synthesis of the results obtained and the phenomena highlighted. This chapter is a paper in prep. to be submitted in 2022.

Chapter 6 - Summary, conclusions and perspectives

The 6th chapter of this manuscript summarises the various results presented in this thesis in the previous chapters and concludes the study. It also aims to discuss potential perspectives for future projects and scientific questions such as the influence of local phenomena (e.g. volcanism, boundary exchanges) on the water mass signatures recorded in Fe-Mn crusts.

1.6. Bibliographical references

Abouchami, W., Goldstein, S.L., Gazer, S.J.G., Eisenhauer, A., Mangini, A., 1997. Secular changes of lead and neodymium in central Pacific seawater recorded by a Fe-Mn crust. Geochim. Cosmochim. Acta 61, 3957–3974.

Albarède, F., Goldstein, S.L., Dautel, D., 1997. The neodymium isotopic composition of manganese nodules from the Southern and Indian oceans, the global oceanic neodymium budget, and their bearing on deep ocean circulation. Geochim. Cosmochim. Acta 61, 1277–1291.

Ali, J., Roberts, S., Hall, R., 1994. The closure of the Indo-Pacific Gateway: a new plate tectonic perspective. pp. 10–20.

Amakawa, H., Tazoe, H., Obata, H., Gamo, T., Sano, Y., Shen, C.-C., 2013. Neodymium isotopic composition and concentration in the Southwest Pacific Ocean. Geochem. J. 47, 409–422.

Aplin, A., Cronan, D., 1985. Ferromanganese oxide deposits from the Central Pacific Ocean, I. Encrustations from the Line Islands Archipelago. Geochim. Cosmochim. Acta 49, 427–436.

Arsouze, T., Dutay, J.-C., Lacan, F., Jeandel, C., 2007. Modeling the neodymium isotopic composition with a global ocean circulation model. Chem. Geol. 239, 165–177.

Barker, P.F., Burrell, J., 1977. The opening of Drake Passage. Mar. Geol., Circum-Antartic Marine Geology 25, 15–34.

Baroni, M., Bard, E., Petit, J.-R., Magand, O., Bourlès, D., 2011. Volcanic and solar activity, and atmospheric circulation influences on cosmogenic 10Be fallout at Vostok and Concordia (Antarctica) over the last 60 years. Geochim. Cosmochim. Acta 75, 7132–7145.

Bassias, Y., 1992. Petrological and geochemical investigation of rocks from the Davie fracture zone (Mozambique Channel) and some tectonic implications. J. Afr. Earth Sci. Middle East 15, 321–339.

Bau, M., 1996. Controls on the fractionation of isovalent trace elements in magmatic and aqueous systems: evidence from Y/Ho, Zr/Hf, and lanthanide tetrad effect. Contrib. Mineral. Petrol. 123, 323–333.

Bertram, C.J., Elderfield, H., 1993. The geochemical balance of the rare earth elements and neodymium isotopes in the oceans. Geochim. Cosmochim. Acta 57, 1957–1986.

Bialik, O.M., Frank, M., Betzler, C., Zammit, R., Waldmann, N.D., 2019. Two-step closure of the Miocene Indian Ocean Gateway to the Mediterranean. Sci. Rep. 9, 8842.

Bonatti, E., 1972. Classification and genesis of submarine iron-manganese deposits. Ferromanganese Depos. Ocean Floor.

Bourlès, D., Raisbeck, G.M., Yiou, F., 1989. 10Be and 9Be in marine sediments and their potential for dating. Geochim. Cosmochim. Acta 53, 443–452.

Burton, K.W., Bourdon, B., Birck, J.-L., Allègre, C.J., Hein, J.R., 1999. Osmium isotope variations in the oceans recorded by FeMn crusts. Earth Planet. Sci. Lett. 171, 185–197.

Burton, K.W., Ling, H.-F., O'Nions, R.K., 1997.

Closure of the Central American Isthmus and its effect on deep-water formation in the North Atlantic. Nature 386, 382.

Charles, C., Barrat, J.-A., Pelleter, E., 2021. Trace Element Determinations in Fe-Mn Oxides by High Resolution ICP-MS after Tm Addition. Talanta 122446.

Charles, C., Pelleter, E., Révillon, S., Nonnotte, P., Jorry, S.J., Kluska, J.-M., 2020. Intermediate and deep ocean current circulation in the Mozambique Channel: New insights from ferromanganese crust Nd isotopes. Mar. Geol. 430, 106356.

Chinni, V., Singh, S.K., Bhushan, R., Rengarajan, R., Sarma, V.V.S.S., 2019. Spatial variability in dissolved iron concentrations in the marginal and open waters of the Indian Ocean. Mar. Chem. 208, 11–28.

Chmeleff, J., von Blanckenburg, F., Kossert, K., Jakob, D., 2010. Determination of the 10Be half-life by multicollector ICP-MS and liquid scintillation counting. Nucl. Instrum. Methods Phys. Res. B 268, 192–199.

Chorowicz, J., 2005. The East African rift system. J. Afr. Earth Sci., Phanerozoic Evolution of Africa 43, 379–410.

Christensen, J.N., Halliday, A.N., Godfrey, L.V., Hein, J.R., Rea, D.K., 1997. Climate and Ocean Dynamics and the Lead Isotopic Records in Pacific Ferromanganese Crusts. Science 277, 913–918.

Claude, C., Suhr, G., Hofmann, A.W., Koschinsky, A., 2005. U-Th chronology and paleoceanographic record in a Fe-Mn crust from the NE Atlantic over the last 700 ka. Geochim. Cosmochim. Acta 69, 4845–4854.

Coffin, M.F., Rabinowitz, P.D., 1987. Reconstruction of Madagascar and Africa: Evidence from the Davie Fracture Zone and Western Somali Basin. J. Geophys. Res. Solid Earth 92, 9385–9406.

Collins, C., Hermes, J.C., Roman, R.E., Reason, C.J.C., 2016. First dedicated hydrographic survey of the Comoros Basin. J. Geophys. Res. Oceans 121, 1291–1305.

Courgeon, S., Bachèlery, P., Jouet, G., Jorry, S.J., Bou, E., BouDagher-Fadel, M.K., Révillon, S., Camoin, G., Poli, E., 2018. The offshore east African rift system: new insights from the Sakalaves seamounts (Davie Ridge, SW Indian Ocean). Terra Nova 30, 380–388.

Courgeon, S., Jorry, S.J., Camoin, G.F., BouDagher-Fadel, M.K., Jouet, G., Révillon, S., Bachèlery, P., Pelleter, E., Borgomano, J., Poli, E., Droxler, A.W., 2016. Growth and demise of Cenozoic isolated carbonate platforms: New insights from the Mozambique Channel seamounts (SW Indian Ocean). Mar. Geol. 380, 90–105.

Courgeon, S., Jorry, S.J., Jouet, G., Camoin, G., BouDagher-Fadel, M.K., Bachèlery, P., Caline, B., Boichard, R., Révillon, S., Thomas, Y., Thereau, E., Guérin, C., 2017. Impact of tectonic and volcanism on the Neogene evolution of isolated carbonate platforms (SW Indian Ocean). Sediment. Geol. 355, 114–131.

Craig, J.D., Andrews, J.E., Meylan, M.A., 1982. Ferromanganese deposits in the Hawaiian Archipelago. Mar. Geol. 45, 127–157.

Cronan, D.S., 1980. Metallogenesis at oceanic spreading centres. J. Geol. Soc. 137, 369–371.

Cronan, D.S., 2017. Handbook of Marine Mineral Deposits. Routledge.

David, K., Frank, M., O'Nions, R.K., Belshaw, N.S., Arden, J.W., 2001. The Hf isotope composition of global seawater and the evolution of Hf isotopes in the deep Pacific Ocean from Fe–Mn crusts. Chem. Geol. 178, 23–42.

Delaunay, A., 2018. Madagascar vertical

movements (90 - 0 Ma): a double approach including onshore geomorphology and Madagascar western margins sedimentary record (phdthesis). Université Rennes 1.

de Ruijter, W.P.M., Ridderinkhof, H., Lutjeharms, J.R.E., Schouten, M.W., Veth, C., 2002. Observations of the flow in the Mozambique Channel: OBSERVATIONS IN THE MOZAMBIQUE CHANNEL. Geophys. Res. Lett. 29, 140-1-140–3.

DiMarco, S.F., Chapman, P., Nowlin, W.D., Hacker, P., Donohue, K., Luther, M., Johnson, G.C., Toole, J., 2002. Volume transport and property distributions of the Mozambique Channel. Deep Sea Res. Part II Top. Stud. Oceanogr. 49, 1481–1511.

Dymond, J., Eklund, W., 1978. A microprobe study of metalliferous sediment components. Earth Planet. Sci. Lett. 40, 243–251.

Dymond, J., Lyle, M., Finney, B., Piper, D.Z., Murphy, K., Conard, R., Pisias, N., 1984. Ferromanganese nodules from MANOP Sites H, S, and R—Control of mineralogical and chemical composition by multiple accretionary processes. Geochim. Cosmochim. Acta 48, 931–949.

Eagles, G., König, M., 2008. A model of plate kinematics in Gondwana breakup. Geophys. J. Int. 173, 703–717.

Elderfield, H., Bertram, C.J., Erez, J., 1996. A biomineralization model for the incorporation of trace elements into foraminiferal calcium carbonate. Earth Planet. Sci. Lett. 142, 409–423.

Fine, R.A., 1993. Circulation of Antarctic intermediate water in the South Indian Ocean. Deep Sea Res. Part Oceanogr. Res. Pap. 40, 2021–2042.

Flemming, B.W., Kudrass, H.-R., 2018. Large dunes on the outer shelf off the Zambezi Delta, Mozambique: evidence for the existence of a Mozambique Current. Geo-Mar. Lett. 38, 95–106.

Frank, M., 2002. Radiogenic isotopes: tracers of past ocean circulation and erosional input. Rev. Geophys. 40, 1–1.

Frank, M., O'Nions, R.K., 1998. Sources of Pb for Indian Ocean ferromanganese crusts: a record of Himalayan erosion? Earth Planet. Sci. Lett. 158, 121–130.

Frank, M., O'Nions, R.K., Hein, J.R., Banakar, V.K., 1999. 60 Myr records of major elements and Pb–Nd isotopes from hydrogenous ferromanganese crusts: reconstruction of seawater paleochemistry. Geochim. Cosmochim. Acta 63, 1689–1708.

Frank, M., Whiteley, N., Kasten, S., Hein, J.R., O'Nions, K., 2002. North Atlantic Deep Water export to the Southern Ocean over the past 14 Myr: Evidence from Nd and Pb isotopes in ferromanganese crusts. Paleoceanography 17, 12-1-12–9.

Franke, D., Jokat, W., Ladage, S., Stollhofen, H., Klimke, J., Lutz, R., Mahanjane, E.S., Ehrhardt, A., Schreckenberger, B., 2015. The offshore East African Rift System: Structural framework at the toe of a juvenile rift. Tectonics 34, 2086–2104.

Gaina, C., Torsvik, T.H., van Hinsbergen, D.J.J., Medvedev, S., Werner, S.C., Labails, C., 2013. The African Plate: A history of oceanic crust accretion and subduction since the Jurassic. Tectonophysics, Progress in understanding the South Atlantic margins 604, 4–25.

Goodlad, S.W., Martin, A.K., Hartnady, C.J.H., 1982. Mesozoic magnetic anomalies in the southern Natal Valley. Nature 295, 686.

Gordon, A.L., 1986. Interocean exchange of thermocline water. J. Geophys. Res. Oceans 91, 5037–5046.

Goto, K.T., Anbar, A.D., Gordon, G.W., Romaniello, S.J., Shimoda, G., Takaya, Y.,

Tokumaru, A., Nozaki, T., Suzuki, K., Machida, S., Hanyu, T., Usui, A., 2014. Uranium isotope systematics of ferromanganese crusts in the Pacific Ocean: Implications for the marine 238U/235U isotope system. Geochim. Cosmochim. Acta 146, 43–58.

Gradstein, F.M., Ogg, J., G., Schmitz, M., Ogg, G., 2012. The Geologic Time Scale. Elsevier.

Guan, Y., Sun, X., Ren, Y., Jiang, X., 2017. Mineralogy, geochemistry and genesis of the polymetallic crusts and nodules from the South China Sea. Ore Geol. Rev. 89, 206–227.

Halbach, P., Segl, M., Puteanus, D., Mangini, A., 1983. Co-fluxes and growth rates in ferromanganese deposits from central Pacific seamount areas. Nature 304, 716.

Hall, R., Cottam, M.A., Wilson, M.E.J., 2011. The SE Asian gateway: history and tectonics of the Australia–Asia collision. Geol. Soc. Lond. Spec. Publ. 355, 1–6.

Halo, I., Backeberg, B., Penven, P., Ansorge, I., Reason, C., Ullgren, J.E., 2014. Eddy properties in the Mozambique Channel: A comparison between observations and two numerical ocean circulation models. Deep Sea Res. Part II Top. Stud. Oceanogr. 100, 38–53.

Hein, J.R., Conrad, T., Mizell, K., Banakar, V.K., Frey, F.A., Sager, W.W., 2016. Controls on ferromanganese crust composition and reconnaissance resource potential, Ninetyeast Ridge, Indian Ocean. Deep Sea Res. Part Oceanogr. Res. Pap. 110, 1–19.

Hein, J.R., Conrad, T.A., Staudigel, H., 2010. Seamount Mineral Deposits: A Source Of Rare Metals For High-Technology Industries. Oceanography 23, 184–189.

Hein, J.R., Koschinsky, A., Bau, M., Manheim, F.T., Kang, J.-K., and Roberts, L., 2000. Cobalt-rich ferromanganese crusts in the Pacific. In: Cronan, D.S. (ed), Handbook of marine minerals. CRC Press, Boca Raton, Florida, pp. 239-279.

Hein, J.R., Koschinsky, A., Halbach, P., Manheim, F.T., Bau, M., Kang, J.-K., Lubick, N., 1997. Iron and manganese oxide mineralization in the Pacific. Geol. Soc. Lond. Spec. Publ. 119, 123–138.

Hein, J.R., Mizell, K., Koschinsky, A., Conrad, T.A., 2013. Deep-ocean mineral deposits as a source of critical metals for high- and green-technology applications: Comparison with land-based resources. Ore Geol. Rev. 51, 1–14.

Heirtzler, J.R., Burroughs, R.H., 1971. Madagascar's Paleoposition: New Data from the Mozambique Channel. Science 174, 488–490.

Henderson, G.M., Burton, K.W., 1999. Using (234U/238U) to assess diffusion rates of isotope tracers in ferromanganese crusts. Earth Planet. Sci. Lett. 170, 169–179.

Hu, R., Chen, T., Ling, H., 2012. Late Cenozoic history of deep water circulation in the western North Pacific: Evidence from Nd isotopes of ferromanganese crusts. Chin. Sci. Bull. 57, 4077–4086.

Jeandel, C., 1993. Concentration and isotopic composition of Nd in the South Atlantic Ocean. Earth Planet. Sci. Lett. 117, 581–591.

Jokat, W., Boebel, T., König, M., Meyer, U., 2003. Timing and geometry of early Gondwana breakup. J. Geophys. Res. Solid Earth 108.

Josso, P., Parkinson, I., Horstwood, M., Lusty, P., Chenery, S., Murton, B., 2019. Improving confidence in ferromanganese crust age models: A composite geochemical approach. Chem. Geol. 513, 108–119.

Josso, P., Pelleter, E., Pourret, O., Fouquet, Y., Etoubleau, J., Cheron, S., Bollinger, C., 2017. A new discrimination scheme for oceanic ferromanganese deposits using high field strength and rare earth elements. Ore Geol. Rev.,

SI:Marine mineral deposits: New resources for base, precious, and critical metals 87, 3–15.

Josso, P., Rushton, J., Lusty, P., Matthews, A., Chenery, S., Holwell, D., Kemp, S.J., Murton, B., 2020. Late Cretaceous and Cenozoic paleoceanography from north-east Atlantic ferromanganese crust microstratigraphy. Mar. Geol. 422, 106122.

Jung, H.-S., Lee, C.-B., 1999. Growth of diagenetic ferromanganese nodules in an oxic deep-sea sedimentary environment, northeast equatorial Pacific. Mar. Geol. 157, 127–144.

Keigwin, L., 1982. Isotopic Paleoceanography of the Caribbean and East Pacific: Role of Panama Uplift in Late Neogene Time. Science 217, 350–353.

Kennett, J.P., 1977. Cenozoic evolution of Antarctic glaciation, the circum-Antarctic Ocean, and their impact on global paleoceanography. J. Geophys. Res. 1896-1977 82, 3843–3860.

Klemm, V., Levasseur, S., Frank, M., Hein, J.R., Halliday, A.N., 2005. Osmium isotope stratigraphy of a marine ferromanganese crust. Earth Planet. Sci. Lett. 238, 42–48.

Klinkhammer, G.P., Bender, M.L., 1980. The distribution of manganese in the Pacific Ocean. Earth Planet. Sci. Lett. 46, 361–384.

Kolla, V., Eittreim, S., Sullivan, L., Kostecki, J.A., Burckle, L.H., 1980. Current-controlled, abyssal microtopography and sedimentation in Mozambique Basin, southwest Indian Ocean. Mar. Geol. 34, 171–206.

König, M., Jokat, W., 2010. Advanced insights into magmatism and volcanism of the Mozambique Ridge and Mozambique Basin in the view of new potential field data. Geophys. J. Int. 180, 158–180.

Korschinek, G., Bergmaier, A., Faestermann, T., Gerstmann, U.C., Knie, K., Rugel, G., Wallner, A., Dillmann, I., Dollinger, G., von Gostomski, Ch.L., Kossert, K., Maiti, M., Poutivtsev, M., Remmert, A., 2010. A new value for the half-life of 10Be by Heavy-Ion Elastic Recoil Detection and liquid scintillation counting. Nucl. Instrum. Methods Phys. Res. Sect. B Beam Interact. Mater. At. 268, 187–191.

Koschinsky, A., 1994. Geochemische Krustenprofile und sequentielle Laugungsversuche an Manganerzkrusten aus dem Zentralpazifik zur Klärung von Genese und Elementassoziationen. Reimer.

Koschinsky, A., Halbach, P., 1995. Sequential leaching of marine ferromanganese precipitates: Genetic implications. Geochim. Cosmochim. Acta 59, 5113–5132.

Koschinsky, A., Hein, J.R., 2003. Uptake of elements from seawater by ferromanganese crusts: solid-phase associations and seawater speciation. Mar. Geol. 198, 331–351.

Koschinsky, A., Hein, J.R., 2017. Marine ferromanganese encrustations: Archives of changing oceans. Elements.

Koschinsky, A., Stascheit, A., Bau, M., Halbach, P., 1997. Effects of phosphatization on the geochemical and mineralogical composition of marine ferromanganese crusts. Geochim. Cosmochim. Acta 61, 4079–4094.

Kuhn, T., Bau, M., Blum, N., Halbach, P., 1998. Origin of negative Ce anomalies in mixed hydrothermal–hydrogenetic Fe–Mn crusts from the Central Indian Ridge. Earth Planet. Sci. Lett. 163, 207–220.

Leclaire, L., 1984. RIDA - MD39 cruise, Marion Dufresne R/V. https://doi.org/10.17600/84010511

Leclaire, L., 1975. NOSICAA - MD 06 cruise, Marion Dufresne R/V. https://doi.org/10.17600/75010711

Lee, D.-C., Halliday, A.N., Hein, J.R., Burton, K.W., Christensen, J.N., Günther, D., 1999. Hafnium Isotope Stratigraphy of Ferromanganese Crusts. Science 285, 1052–1054.

Leinweber, V.T., Jokat, W., 2012. The Jurassic history of the Africa–Antarctica corridor — new constraints from magnetic data on the conjugate continental margins. Tectonophysics 530–531, 87–101.

Leinweber, V.T., Klingelhoefer, F., Neben, S., Reichert, C., Aslanian, D., Matias, L., Heyde, I., Schreckenberger, B., Jokat, W., 2013. The crustal structure of the Central Mozambique continental margin — Wide-angle seismic, gravity and magnetic study in the Mozambique Channel, Eastern Africa. Tectonophysics 599, 170–196.

Leroux, E., Counts, J., Jorry, S., Jouet, G., Révillon, S., BouDagher-Fadel, M.K., Courgeon, S., Berthod, C., Ruffet, G., Bachèlery, P., Grenard-Grand, E., 2020. Evolution of the Glorieuses seamount in the SW Indian Ocean and surrounding deep Somali Basin since the Cretaceous. Mar. Geol. 106202.

Li, Y.-H., Schoonmaker, J.E., 2003. 7.01 - Chemical Composition and Mineralogy of Marine Sediments, in: Holland, H.D., Turekian, K.K. (Eds.), Treatise on Geochemistry. Pergamon, Oxford, pp. 1–35.

Ling, H.F., Burton, K.W., O'Nions, R.K., Kamber, B.S., von Blanckenburg, F., Gibb, A.J., Hein, J.R., 1997. Evolution of Nd and Pb isotopes in Central Pacific seawater from ferromanganese crusts. Earth Planet. Sci. Lett. 146, 1–12.

Ling, H.-F., Jiang, S.-Y., Frank, M., Zhou, H.-Y., Zhou, F., Lu, Z.-L., Chen, X.-M., Jiang, Y.-H., Ge, C.-D., 2005. Differing controls over the Cenozoic Pb and Nd isotope evolution of deepwater in the central North Pacific Ocean. Earth Planet. Sci. Lett. 232, 345–361.

Lusty, P.A.J., Hein, J.R., Josso, P., 2018. Formation and Occurrence of Ferromanganese Crusts: Earth's Storehouse for Critical Metals. Elements 14, 313–318.

Lutjeharms, J.R.E., 2006. The Agulhas Current. Springer-Verlag, Berlin Heidelberg.

Macgregor, D., 2015. History of the development of the East African Rift System: A series of interpreted maps through time. J. Afr. Earth Sci. 101, 232–252.

Manheim, F.T., Lane-Bostwick, C.M., 1988. Cobalt in ferromanganese crusts as a monitor of hydrothermal discharge on the Pacific sea floor. Nature 335, 59.

Mantyla, A.W., Reid, J.L., 1995. On the origins of deep and bottom waters of the Indian Ocean. J. Geophys. Res. Oceans 100, 2417–2439.

Marino, E., González, F.J., Somoza, L., Lunar, R., Ortega, L., Vázquez, J.T., Reyes, J., Bellido, E., 2017. Strategic and rare elements in Cretaceous-Cenozoic cobalt-rich ferromanganese crusts from seamounts in the Canary Island Seamount Province (northeastern tropical Atlantic). Ore Geol. Rev., SI:Marine mineral deposits: New resources for base, precious, and critical metals 87, 41–61.

Masters, J.C., Génin, F., Zhang, Y., Pellen, R., Huck, T., Mazza, P.P.A., Rabineau, M., Doucouré, M., Aslanian, D., 2021. Biogeographic mechanisms involved in the colonization of Madagascar by African vertebrates: Rifting, rafting and runways. J. Biogeogr. 48, 492–510.

McElhinny, M.W., 1970. Formation of the Indian Ocean. Nature 228, 977.

McKenzie, D., Sclater, J.G., 1971. The Evolution of the Indian Ocean since the Late Cretaceous. Geophys. J. Int. 24, 437–528.

McGrew, H.J., 1983. Oil and gas developments in central and southern Africa in 1982. Am Assoc Pet Geol Bull U. S. 67:10.

Meynadier, L., Allègre, C., O'Nions, R.K., 2008. Plate tectonics, radiogenic isotopic tracers and paleoceanography: The case of the manganese crusts in the Pacific. Earth Planet. Sci. Lett. 272, 513–522.

Mizell, K., Hein, J.R., Lam, P.J., Koppers, A.A.P., Staudigel, H., 2020. Geographic and Oceanographic Influences on Ferromanganese Crust Composition Along a Pacific Ocean Meridional Transect, 14 N to 14S. Geochem. Geophys. Geosystems 21, e2019GC008716.

Moulin, M., Evain, M., 2016. PAMELA-MOZ05 cruise, Pourquoi pas ? R/V.

Nicholas, C.J., Pearson, P.N., McMillan, I.K., Ditchfield, P.W., Singano, J.M., 2007. Structural evolution of southern coastal Tanzania since the Jurassic. J. Afr. Earth Sci. 48, 273–297.

Nisancioglu, K.H., Raymo, M.E., Stone, P.H., 2003. Reorganization of Miocene deep water circulation in response to the shoaling of the Central American Seaway: Reorganization of Miocene Deep Water Circulation. Paleoceanography 18, n/a-n/a.

O'Nions, R.K., Frank, M., von Blanckenburg, F., Ling, H.-F., 1998. Secular variation of Nd and Pb isotopes in ferromanganese crusts from the Atlantic, Indian and Pacific Oceans. Earth Planet. Sci. Lett. 155, 15–28.

Olu Karine, 2014. PAMELA-MOZ01 cruise,L'Atalante R/V.

Peucker-Ehrenbrink, B., Ravizza, G., 2000. The marine osmium isotope record. Terra Nova 12, 205–219.

Peucker-Ehrenbrink, B., Ravizza, G., 2012. Chapter 8 - Osmium Isotope Stratigraphy, in: Gradstein, F.M., Ogg, J.G., Schmitz, M.D., Ogg, G.M. (Eds.), The Geologic Time Scale. Elsevier, Boston, pp. 145–166.

Piepgras, D.J., Jacobsen, S.B., 1988. The isotopic composition of neodymium in the North Pacific. Geochim. Cosmochim. Acta 52, 1373–1381.

Piepgras, D.J., Wasserburg, G.J., 1982. Isotopic Composition of Neodymium in Waters from the Drake Passage. Science 217, 207–214

Piepgras, D.J., Wasserburg, G.J., 1987. Rare earth element transport in the western North Atlantic inferred from Nd isotopic observations. Geochim. Cosmochim. Acta 51, 1257–1271.

Piotrowski, A.M., Lee, D.-C., Christensen, J.N., Burton, K.W., Halliday, A.N., Hein, J.R., Günther, D., 2000. Changes in erosion and ocean circulation recorded in the Hf isotopic compositions of North Atlantic and Indian Ocean ferromanganese crusts. Earth Planet. Sci. Lett. 181, 315–325.

Piper, D.Z., 1974. Rare earth elements in ferromanganese nodules and other marine phases. Geochim. Cosmochim. Acta 38, 1007–1022.

Ponte, J.-P., 2018. La marge africaine du canal du Mozambique, le système turbiditique du Zambèze : une approche « Source to Sink » au Méso – Cénozoïque (phdthesis). Université Rennes 1.

Post, J.E., 1999. Manganese oxide minerals: Crystal structures and economic and environmental significance. Proc. Natl. Acad. Sci. U. S. A. 96, 3447–3454.

Puteanus, D., Halbach, P., 1988. Correlation of Co concentration and growth rate — A method for age determination of ferromanganese crusts. Chem. Geol. 69, 73–85.

Quartly, G.D., de Cuevas, B.A., Coward, A.C., 2013. Mozambique Channel eddies in GCMs: A question of resolution and slippage. Ocean Model. 63, 56–67.

Ravizza, G.E., Peucker-Ehrenbrink, B., 2003. The marine 187Os/188Os record of the Eocene-Oligocene transition: the interplay of weathering

and glaciation. Earth and Planetary Science Letters, 210(1-2), 151-165.

Raymo, M.E., 1994. The initiation of northern hemisphere glaciation. Annu. Rev. Earth Planet. Sci. 22, 353–383.

Rehkämper, M., Frank, M., Hein, J.R., Halliday, A., 2004. Cenozoic marine geochemistry of thallium deduced from isotopic studies of ferromanganese crusts and pelagic sediments. Earth Planet. Sci. Lett. 219, 77–91.

Reynolds, B.C., Frank, M., O'Nions, R.K., 1999. Nd- and Pb-isotope time series from Atlantic ferromanganese crusts: implications for changes in provenance and paleocirculation over the last 8 Myr. Earth Planet. Sci. Lett. 173, 381–396.

Rickli, J., Frank, M., Halliday, A.N., 2009. The hafnium–neodymium isotopic composition of Atlantic seawater. Earth Planet. Sci. Lett. 280, 118–127.

Rogers, W.E., Hartman, W.D., Krause, K.S.K., 2000. Stratigraphic Analysis of Upper Cretaceous Rocks in the Mahajanga Basin, Northwestern Madagascar: Implications for Ancient and Modern Faunas. J. Geol. 108, 275–301.

Saager, P.M., De Baar, H.J.W., Burkill, P.H., 1989. Manganese and iron in Indian Ocean waters. Geochim. Cosmochim. Acta 53, 2259–2267.

Schott, F.A., Xie, S.-P., McCreary, J.P., 2009. Indian Ocean circulation and climate variability. Rev. Geophys. 47, RG1002.

Segl, M., Mangini, A., Bonani, G., Hofmann, H.J., Nessi, M., Suter, M., Wölfli, W., Friedrich, G., Plüger, W.L., Wiechowski, A., Beer, J., 1984. 10 Be-dating of a manganese crust from Central North Pacific and implications for ocean palaeocirculation. Nature 309, 540.

Shackleton, N.J., Backman, J., Zimmerman, H., Kent, D.V., Hall, M.A., Roberts, D.G., Schnitker, D., Baldauf, J.G., Desprairies, A., Homrighausen, R., Huddlestun, P., Keene, J.B., Kaltenback, A.J., Krumsiek, K. a. O., Morton, A.C., Murray, J.W., Westberg-Smith, J., 1984. Oxygen isotope calibration of the onset of ice-rafting and history of glaciation in the North Atlantic region. Nature 307, 620–623.

Srinivasan, M.S., Sinha, D.K., 1998. Early Pliocene closing of the Indonesian Seaway: evidence from north-east Indian Ocean and Tropical Pacific deep sea cores. J. Asian Earth Sci. 16, 29–44.

Storey, M., Mahoney, J.J., Saunders, A.D., Duncan, R.A., Kelley, S.P., Coffin, M.F., 1995. Timing of Hot Spot—Related Volcanism and the Breakup of Madagascar and India. Science 267, 852–855.

Sun, J., Sheykh, M., Ahmadi, N., Cao, M., Zhang, Z., Tian, S., Sha, J., Jian, Z., Windley, B.F., Talebian, M., 2021. Permanent closure of the Tethyan Seaway in the northwestern Iranian Plateau driven by cyclic sea-level fluctuations in the late Middle Miocene. Palaeogeogr. Palaeoclimatol. Palaeoecol. 564, 110172.

Tachikawa, K., Arsouze, T., Bayon, G., Bory, A., Colin, C., Dutay, J.-C., Frank, N., Giraud, X., Gourlan, A.T., Jeandel, C., Lacan, F., Meynadier, L., Montagna, P., Piotrowski, A.M., Plancherel, Y., Pucéat, E., Roy-Barman, M., Waelbroeck, C., 2017. The large-scale evolution of neodymium isotopic composition in the global modern and Holocene ocean revealed from seawater and archive data. Chem. Geol. 457, 131–148.

Thompson, J. O., 2017. The opening of the Indian Ocean : what is the impact on the East African, Madagascar and Antarctic margins, and what are the origins of the aseismic ridges ? PhD Thesis, Université de Rennes.

Toole, J.M., Warren, B.A., 1993. A hydrographic section across the subtropical South Indian Ocean. Deep Sea Res. Part Oceanogr. Res. Pap.

40, 1973–2019.

Torsvik, T.H., Tucker, R.D., Ashwal, L.D., Carter, L.M., Jamtveit, B., Vidyadharan, K.T., Venkataramana, P., 2000. Late Cretaceous India-Madagascar fit and timing of break-up related magmatism. Terra Nova 12, 220–224.

Ullgren, J.E., van Aken, H.M., Ridderinkhof, H., de Ruijter, W.P.M., 2012. The hydrography of the Mozambique Channel from six years of continuous temperature, salinity, and velocity observations. Deep Sea Res. Part Oceanogr. Res. Pap. 69, 36–50.

van Aken, H.M., Ridderinkhof, H., de Ruijter, W.P.M., 2004. North Atlantic deep water in the south-western Indian Ocean. Deep Sea Res. Part Oceanogr. Res. Pap. 51, 755–776.

Walford, H.L., White, N.J., Sydow, J.C., 2005. Solid sediment load history of the Zambezi Delta. Earth Planet. Sci. Lett. 238, 49–63.

Watkeys, M.K., Sokoutis, D., 1998. Transtension in southeastern Africa associated with Gondwana break-up. Geol. Soc. Lond. Spec. Publ. 135, 203–214.

Weijer, W., 1999. Impact of Interbasin Exchange on the Atlantic Overturning Circulation. J. Phys. Oceanogr. 29, 19.

You, Y., 2000. Implications of the deep circulation and ventilation of the Indian Ocean on the renewal mechanism of North Atlantic Deep Water. J. Geophys. Res. Oceans 105, 23895–23926.

Yuan-Hui, L., 1982. Interelement relationship in abyssal Pacific ferromanganese nodules and associated pelagic sediments. Geochim. Cosmochim. Acta 46, 1053–1

CHAPITRE 2 : METHODOLOGIE ANALYTIQUE

2.1. Introduction (français)

Ce second chapitre est dédié aux méthodes d'échantillonnages ainsi qu'aux techniques et protocoles expérimentales et analytiques développés et employés au cours de cette thèse.

En effet, pour l'étude géochimique et minéralogique des encroûtements Fe-Mn, il est nécessaire de mettre au point un protocole particulier - qui s'étend de l'échantillonnage des roches au traitement des résultats obtenus - tout en tenant compte des caractéristiques physico-chimiques particulières et uniques de ces oxydes (Hein, Koschinsky, 2014).

Cet axe de la thèse porte d'une part sur le protocole de sélection et de caractérisation minéralogique des échantillons. Et d'autre part, sur tous les protocoles géochimiques utilisés depuis la mise en solution des échantillons et obtention des solutions mères, jusqu'aux analyses, afin de garantir des résultats précis et de qualité. Il s'agit notamment de faire un point sur les différents protocoles chimiques mis au point pour la mesure des éléments traces (Charles et al., 2021), des éléments majeurs et des compositions isotopiques. Les instruments utilisés sont également présentés.

En fin de chapitre, une attention toute particulière est portée sur la géochronologie. Il s'agit d'un axe primordial sur lequel repose 52 analyses du rapport isotopique $^{10}Be/^{9}Be$. Ces analyses fournissent une résolution temporelle aux reconstructions océanographiques et géodynamiques. La datation absolue par étude des nucléides cosmogéniques est donc présentée dans cette partie ainsi que les appareils de pointe utilisés en collaboration avec le CEREGE à Aix-en-Provence.

2.1. Introduction (english)

This second chapter focusses on sampling methods as well as experimental and analytical techniques and protocols developed and employed during this PhD project, taking into account the particular physicochemical characteristics of the Fe-Mn crusts (Hein, Koschinsky, 2014),

This part of the thesis focuses on the protocol for the selection and mineralogical characterisation of samples. And on the other hand, on all the geochemical protocols used from the dissolution of the samples and obtaining the mother solutions, to the analyses, in order to guarantee accurate and high quality results. The different chemical procedures developed for the analyses of trace elements (Charles et al., 2021), major elements and isotopic compositions will be described in parallel with the rapid presentation of the analytical instruments.

At the end of the chapter, a particular attention is given to the geochronology acquired by studying cosmogenic isotopes in order to obtain absolute data. It provides oceanographic and geodynamic reconstructions with a temporal resolution. This is an essential part of the PhD project, with 52 analyses of the $^{10}Be/^{9}Be$ isotopic ratio. The application of this methodology on Fe-Mn crusts is presented in this section, as well as the highly specialized and advanced equipment used in collaboration with the CEREGE – Aix en Provence.

2.2. Choix des échantillons et préparation des sous-échantillons

2.2.1. Dragages et échantillons

Les encroûtements ferromanganésifères ici étudiés proviennent de 15 opérations de dragages différentes, effectuées lors de 4 missions océanographiques présentées précédemment (voir Chapitre 1). Lors des missions PAMELA, la cartographie précise de plusieurs zones clés du canal du Mozambique (i.e., archipel des îles éparses françaises, ride de Davie) a été obtenue par l'utilisation du sondeur multi-faisceaux grands fonds Seabat 7150 (Reson) qui équipe le « Pourquoi pas ?». Le suivi topographique du fond sous-marin et de ses structures (bathymétrie) ainsi que son imagerie détaillée a permis de récolter un maximum d'informations sur les morphologies profondes, et ainsi, de cibler des zones optimales de dragages. La localisation des différentes dragues est visible sur la figure 1.2 (Chapitre 1). Les coordonnées GPS ainsi que les longueurs de tracés de dragues sont disponibles en annexe 1.

Dans cette étude, 27 échantillons sont issus de la première mission PAMELA dans le canal du Mozambique, PAMELA-MOZ1 (Olu, 2014) et 4 échantillons proviennent de la campagne océanographique PAMELA-MOZ5 (Moulin, Evain, 2016). Parallèlement, 2 échantillons ont été dragués par le MNHN et ajoutés à la collection de cette thèse, afin d'enrichir les analyses du projet avec un jalon au sud du canal (mission MD-06 Nosicaa ; DR75-0012 ; Leclaire, 1975) et un jalon tout au nord de la ride de Davie (mission MD-39 Rida ; DR84-0026 ; Leclaire, 1984). Ainsi, les encroûtements ferromanganésifères étudiés durant cette thèse se répartissent sur un transect de plus de 3500 km depuis le Plateau des Aiguilles, au sud, jusqu'aux Îles Glorieuses, au nord du canal, et couvrent les masses d'eau superficielles, intermédiaires et profondes du secteur, avec des dragues comprises entre 170 m et 2650 m de profondeur.

Parmi ces encroûtements ferromanganésifères, 33 ont été sélectionnés pour l'étude de la circulation moderne des courants intermédiaires et profonds du canal du Mozambique. L'étude de l'évolution temporelle des courants repose quant à elle sur 3 encroûtements Fe-Mn (pour un total de 52 lamines). Quatre autres encroûtements Fe-Mn (pour un total de 61 lamines) ont été choisis pour réaliser l'étude des événements paléogéographiques. Enfin, un encroûtement se situant à moins de 300 km des côtes a été choisi pour évaluer l'influence de la marge continentale sur les compositions isotopiques comme évoqué par certains auteurs dans leurs études (Conrad et al., 2017; Guan et al., 2017; Hein et al., 2013, 1997).

2.2.2. Critères de sélection des échantillons

Tous ces encroûtements ont été choisis et intégrés à ce projet de recherche en raison de plusieurs critères morphologiques, s'ajoutant aux critères de localisation et de profondeur. Premièrement, ce sont des encroûtements suffisamment indurés, non altérés, qui ne s'effritent pas au toucher et qui ne présentent pas non plus d'altération secondaire (e.g. carbonates, phosphates) remplissant les vacuoles et zones fracturées, pouvant influencer fortement leurs signatures géochimiques (Hein et al., 2016; Koschinsky et al., 1997; Mizell et al., 2020; Sousa et al., 2021).

Cette première discrimination macroscopique est réalisée directement à bord, sur échantillons mouillés mais doit être refaite en laboratoire, après débarquement, sur échantillons complètement secs. Les encroûtements ainsi sélectionnés présentent des surfaces non (ou peu) érodées. L'échantillonnage de la partie

superficielle, correspondant aux derniers dépôts, est possible.

Ensuite, et c'est particulièrement le cas pour les séries temporelles, les échantillons correspondent aux encroûtements les plus épais (Figure 2.1) que les dragues ont permis de récolter au cours des campagnes océanographiques. Leur épaisseur est un atout essentiel pour établir une géochronologie précise et suffisamment étendue pour comprendre la courantologie et la géodynamique du canal du Mozambique au cours du temps. Elles varient entre 10 mm et 100 mm. La profondeur des échantillons est également essentielle afin de cibler toutes les masses d'eau du canal. Elles varient entre 170 m et 2650 m. Enfin, les lamines des échantillons, issues du processus de précipitation des oxy-hydroxydes Fe-Mn, doivent être visibles macroscopiquement afin de distinguer et de réaliser des prélèvements qui correspondent à des stratigraphies temporelles « haute-résolution » (1 lamine tous les 2 à 5 mm).

Figure 2.1. *Encroûtement Fe-Mn MOZ1-DR11-01 après avoir été échantillonné et dont toute la stratigraphie réalisée est visible. PAMELA MOZ1 (Olu, 2014).*

Les 33 encroûtements ferromanganésifères retenus pour ce projet sont nommés selon les dragues et les missions océanographiques dont ils sont issus. Toutes les informations sont présentées en annexe 2.

2.2.3. Préparation des poudres et des lames minces

2.2.3.1. Échantillonnage de la surface – courantologie moderne

Une fois les échantillons sélectionnés, la surface des encroûtements (i.e., les derniers dépôts accumulés) est prélevée à l'aide d'une microforeuse afin d'obtenir au minimum entre 100 et 200 mg de poudre qui servira pour la totalité des analyses géochimiques et géochronologiques. La microforeuse est composée d'une pointe en diamant de 1 mm de diamètre. En passant délicatement sur la partie superficielle de l'échantillon, il est possible de récupérer de la poudre correspondant aux 100 µm d'encroûtement dernièrement déposés. Les 33 encroutements Fe-Mn de ce projet sont traités et autant de prélèvements sont réalisés.

2.2.3.2. Échantillonnage des séries temporelles – géochronologique du canal du Mozambique

Concernant les 8 séries temporelles, présentées et détaillées en annexe 3, les stratigraphies sont également réalisées par microforeuse, lamine après lamine (Figure 2.1), tout en évitant le plus possible les minéraux allochtones (e.g. carbonates, clastes volcaniques, phosphates). La quantité prélevée est de 200 mg par lamine. Les épaisseurs de forage sont de 1 mm (± 0,25 à 1 mm) selon la cohésion de la roche. Un total de 129 prélèvements est réalisé.

La pointe de la microforeuse est nettoyée entre chaque échantillonnage afin de limiter toute contamination externe et intra échantillon. Elle est rincée à l'eau distillée, séchée à l'air comprimé et nettoyée par friction contre du quartz pur pour éliminer tous les résidus. Elle est ensuite placée au bain à ultrasons pendant 3 minutes avant d'être rincée, séchée et utilisée de nouveau.

2.2.3.3. Confection des grandes lames minces – étude minéralogique ponctuelle

Deux échantillons faisant partie des séries temporelles ont été sélectionnés pour des analyses minéralogiques approfondies en raison de leurs localisations particulières. Il s'agit de l'encroûtement MOZ-DR04-23, dragué au large de l'archipel des Îles Glorieuses, dont l'étude des minéraux permettra d'appréhender les événements volcaniques de cette zone au cours du temps, et de l'encroutement MOZ5-DR03-01, initialement situé sur le plateau du Mozambique (au nord de la vallée de Natal) à 200 km des côtes africaines, dont l'étude minéralogique permettra de qualifier et de quantifier les apports détritiques du continent enregistrés dans l'échantillon.

Des grandes lames minces de 60 mm par 45 mm ont pu être réalisées sur la moitié non échantillonnée des deux encroûtements. Elles ont été confectionnées à partir de sucres de 10 cm de haut par 5 cm de large. La découpe des sucres est réalisée de manière à ce que plusieurs sucres recoupent les mêmes structures afin de pouvoir faciliter l'identification des structures et donc, des lamines analysées. Cinq grandes lames minces polies sont confectionnées sur l'encroûtement MOZ1-DR04-23 et 3 sur l'encroûtement MOZ5-DR03-01. Les 8 lames minces sont présentées en annexe 4, et leur minéralogie sera analysée avec le FEG-SEM Qemscan ® (CSTJF TotalEnergies, Pau).

2.3. Caractérisation minéralogique

La minéralogie de certaines poudres a été étudiée afin de faire des liens pertinents avec des résultats de géochimie. La diffraction par rayon X (DRX) a été utilisée. Elle a permis d'obtenir des résultats fiables et rapides donnant un premier aperçu de la composition des poudres. Parallèlement, une méthode de microscopie électronique à balayage (MEB) a été utilisée sur les lames minces des échantillons MOZ1-DR04-23 et MOZ5-DR03-01 (voir paragraphe 2.3.2). Les microstructures de ces deux échantillons ont ainsi été détaillées au MEB couplé avec le logiciel QemSCAN® qui est un acronyme anglais signifiant évaluation quantitative des matériaux au moyen de la microscopie électronique à balayage. Ces deux méthodes analytiques sont présentées dans cette partie.

2.3.1. Diffraction par rayons X

2.3.1.1. Principes généraux de la DRX

La diffraction par rayons X (DRX) permet d'obtenir la composition, en pourcentage, des différents minéraux présents dans les poudres échantillonnées. Cette méthode consiste à irradier l'échantillon d'un faisceau monochromatique de rayons X primaires afin de générer différentes interactions avec la matière. Les plans réticulaires, composant les différents réseaux cristallins des minéraux, vont alors diffracter les rayons X incidents selon la loi de Bragg (Figure 2.2).

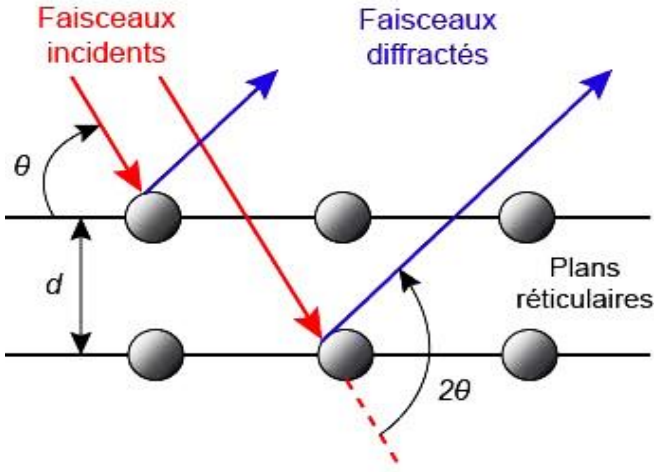

***Figure 2.2**. Schéma du rayonnement incident et diffracté par une maille cristalline selon la loi de Bragg.*

Cette loi empirique mesure la distance séparant deux plans réticulaires, propre à chaque maille cristalline d'un minéral :

$$2\,d\,\sin\theta = n\lambda \qquad (1)$$

Avec d, la distance inter-réticulaire séparant 2 plans de la même famille ; θ, l'angle du rayonnement émis entre le faisceau incident et le plan réticulaire ; n, l'ordre de diffraction et λ, la longueur d'onde du rayonnement diffracté. Les rayons diffractés sont ensuite analysés par un détecteur. Les résultats sont obtenus sous forme de spectres des angles de diffraction, appelé diffractogramme.

2.3.1.2. Conditions d'analyses

Le jour des analyses, un volume de poudre est placé en excès sur un porte-échantillon circulaire en silice amorphe. La surface se doit d'être lisse, sans rugosité ni relief afin d'éviter tout décalage angulaire. Les échantillons sont analysés avec un diffractomètre Bruker D8 Advance. Cet appareil est de type Bragg-Brentano à montage $\theta - 2\theta$, c'est-à-dire que le tube à rayons X reste fixe alors que l'échantillon et le détecteur peuvent être en mouvement. Le plan de l'échantillon fait un angle θ avec le faisceau incident, et le détecteur fait un angle de 2θ avec le faisceau diffracté. L'acquisition du spectre est effectuée sur une plage angulaire de 5° à 70° avec un pas d'échantillonnage de 0.01° et un temps d'analyse par pas de 1s.

Les diffractogrammes acquis sont regardés méticuleusement avec le logiciel d'interprétation 'EVA' et sa base de données minéralogiques. Chaque pic correspond à un ou plusieurs minéraux qu'il est alors possible d'identifier et de quantifier.

2.3.2. Évaluation quantitative des minéraux au moyen de la microscopie électronique à balayage

La technologie du Qemscan ® (QUANTA 650, FEI) consiste à mesurer la variabilité minéralogique d'échantillons à partir de sa composition chimique, à l'échelle du micromètre. C'est un système entièrement automatisé et non-destructif. Cette méthode est basée sur la microscopie électronique à balayage (MEB) couplée la spectroscopie de rayons X à dispersion d'énergie (SDE) pour produire des cartes élémentaires en 2D, ici de lames minces.

Les cartes élémentaires 2D sont post-traitées à l'aide d'un logiciel appelé Nanomin (FEI, Hillsboro, OR, USA). Il permet la quantification automatique de la minéralogie par la déconvolution des spectres de rayons X de chaque pixel analysé. Ces analyses ont été réalisées à TotalEnergies – Centre Scientifique et Technique Jean Féger (CSTJF) à Pau, où les spectres de références sont sélectionnés dans une base de données de spectres mesurés sur des minéraux purs ou créés synthétiquement.

L'un des grands avantages du MEB-SDE Qemscan ® est qu'il produit à la fois un ensemble de données sur la composition minéralogique globale mais aussi un flux d'images 2D de chaque lame mince étudiées : cartes chimiques (éléments majeurs et certains éléments traces), cartes minéralogiques et images acquises par détecteurs d'électrons rétrodiffusés (BSE). Les cartes minéralogiques peuvent être combinées avec l'imagerie BSE sous le logiciel Nanomin. Les images BSE peuvent être acquises à une résolution nanométrique, permettant de visualiser et d'identifier les principales phases détritiques, dont des minéraux allochtones, présents dans les encroûtements analysés (Fialips et al., 2018).

2.4. Mise en solution des éléments

2.4.1. Conditions de préparation

La chimie est effectuée au Laboratoire Géosciences Océan – UMR 6538 de l'Institut Universitaire Européen de la Mer (IUEM). La salle blanche utilisée est classée 1000 (ISO 6) selon la norme ISO 14644-1 qui spécifie la

classification de la propreté particulaire de l'air (ISO, 2015b).

De l'eau déminéralisée avec un système Milli-Q (Millipore ®) à 18.2 MΩ est utilisée pour le nettoyage du matériel et la préparation des acides. Les réactifs utilisés tels que l'acide nitrique (HNO_3) et chlorhydrique (HCl ; grade commercial, Merck, Darmstadt, Allemagne) et l'acide fluorhydrique (HF) ultra-pur (Hiperpur-plus ®, Panreac, Barcelone, Espagne) sont purifiés au laboratoire par un système de distillation par ébullition.

2.4.2. Protocole d'attaque pour les analyses d'éléments majeurs, traces et isotopies du Nd et Pb

A l'exception des poudres utilisées pour la datation au Be (Chapitres 4 et 5), nous avons choisi de réaliser une attaque totale sur les poudres prélevées, ce qui induit la dissolution et la mise en solution de toutes les phases présentes dans les prélèvements, y compris les oxydes métalliques et les silicates.

Ce choix d'attaque permet dans un premier temps de minimiser le temps de préparation des solutions mères (une solution mère pour toutes les analyses élémentaires (traces, majeurs) et isotopiques (Nd, Pb)) en faveur d'une quantité importante de sous-échantillons.

En effet, à partir des 33 encroûtements échantillonnés, il résulte un total de 162 sous-échantillons auxquels s'ajoutent 10 blancs de chimie (c.-à-d. des béchers sans poudre ayant subi l'ensemble du protocole de manière à contrôler la qualité des manipulations et des réactifs utilisés) et 10 standards très utilisés par la communauté scientifique dont 8 d'oxydes Fe-Mn (Fe-Mn-1, GSMC-1, GSMC-2, GSMC-3, GSPN-2, GSPN-3, NOD-A-1, NOD-P-1) et 2 basaltes (BEN, BHVO-2).

Cependant, il fallait vérifier que cette attaque totale ne risquait pas de générer des contaminations des signatures isotopiques par dissolution de clastes détritiques.

Après examinations minéralogiques des échantillons par Diffraction au Rayon X (DRX), il résulte un degré de cristallinité des encroûtements très faible (moyenne de 8%) et correspondant à des phases détritiques de type quartz et feldspaths en très faible quantité. Or, les concentrations en Nd (élément majoritairement étudié ici) liées à ces phases sont extrêmement faibles et ne sont pas censées impacter de manière significative les signatures géochimiques des échantillons. Le choix d'une attaque totale a ainsi été validé.

Pour la préparation des solutions mères utilisées pour les analyses élémentaires (traces, majeurs) et isotopiques (Nd, Pb), environ 100 mg de poudre est placé à l'étuve à 60 °C pendant 24 heures. Ils sont dissous dans 2 ml d'HF 32N et 2 ml d'HNO3 14N dans des Savillex ® en Teflon à 120 °C pendant 24 heures. Les solutions qui en résultent sont ensuite mises à évaporer à 110 °C sur plaque chauffante. Après évaporation, 2 ml d'HNO3 14N sont ajoutés et les Savillex ® sont remis sur plaque chauffante à 120 °C pendant 12 heures. Les échantillons sont ensuite évaporés une seconde fois et repris dans 20 ml d'HCl Quartex 6N pour préparer les solutions finales.

Aucune particule résiduelle est observée dans les solutions mères qui sont transférées et stockées dans bouteilles en polypropylène, préalablement lavées à l'HNO3.

2.5. Géochimie élémentaire

2.5.1. Caractérisation des éléments majeurs par ICP-OES

2.5.1.1. Préparation des solutions à partir des solutions mères

Pour l'analyse des éléments majeurs par Spectromètre à Émission Atomique (avec plasma couplé par induction) ou ICP-OES, les concentrations en éléments majeurs des solutions mères sont mesurées dans un premier temps afin de calculer les taux de dilution. Puis, les volumes calculés de solutions sont évaporés sur plaque chauffante à 110 °C et reprises en HNO_3 0,3N pour les mesures, afin d'avoir des facteurs totaux de dilution compris entre 1.10^{-6}g et 10.10^{-6}g d'échantillon par g de solution ICP-OES. Un standard interne de bore est utilisé, comme spécifié dans le protocole de Cotten et al. (1995), afin de certifier une bonne reproductibilité des mesures.

Les standards internationaux (cités dans le paragraphe 2.4.2) sont également préparés et analysés dans les mêmes conditions que les échantillons afin de réaliser une gamme de calibration.

2.5.1.2. Principes généraux d'un ICP-OES

Les mesures sont réalisées sur un ICP-OES de type Horiba Jobin Yvon® Ultima 2, au sein de l'IUEM. L'échantillon en solution est disposé au niveau du système d'introduction d'échantillon puis dispersé en fines gouttelettes à l'aide d'un nébuliseur (Figure 2.3). Ce fluide est ensuite amené au plasma où tous les éléments présents sont atomisés puis excités. Un spectromètre mesure alors le rayonnement électromagnétique émis, et plus précisément l'ensemble des photons émis aux différentes longueurs d'onde par retour des éléments excités à leurs états fondamentaux. Les photons émis aux différentes longueurs

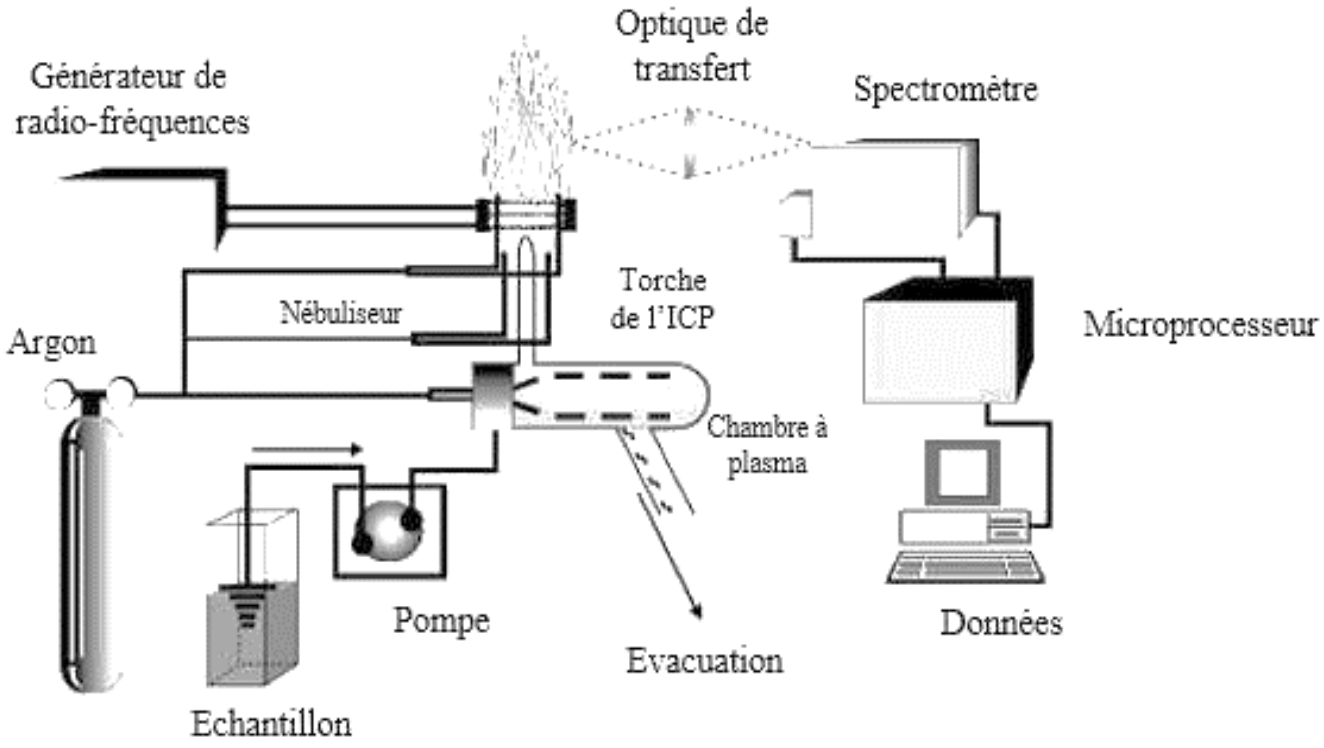

Figure 2.3. *Schéma simplifié du principe d'analyse élémentaire par le biais d'un ICP-AES (d'après la documentation du constructeur Horiba (2021) et Levine (2021)).*

d'onde sont caractéristiques pour chaque élément chimique et l'intensité d'émission est proportionnelle à la quantité de l'élément dans l'échantillon. Ainsi, l'appareil permet une analyse qualitative et quantitative des éléments présents en solution.

Cependant, l'émission atomique n'est pas une méthode absolue. Une étape d'étalonnage est nécessaire afin de calculer la relation entre l'intensité émise par une raie d'émission et la concentration de l'élément associé. Les standards d'oxydes Fe-Mn et de basaltes utilisés comme étalons permettent d'obtenir des courbes d'étalonnage linéaires sur plusieurs ordres de grandeurs permettant des analyses sur une gamme étendue de concentrations.

2.5.1.3. Session d'analyses « type »

Une séquence de mesure commence par une étape de calibration de la machine avec le standard interne. Puis, les premières analyses sont effectuées sur 3 blancs de manière à vérifier la qualité du travail réalisé en salle blanche et à corriger les résultats acquis de potentiels apports extérieurs liés aux manipulations et aux réactifs. La séquence est ensuite établie avec le passage de 5 standards puis une alternance de 1 standard BHVO-2 avec 10 échantillons puis 5 standards pour conclure.

Les mesures de standards permettent de calculer la dérive instrumentale lors des analyses. La déviation standard relative par rapport aux valeurs recommandées est inférieure à 3 % pour tous les éléments majeurs. Les détails techniques et conditions exactes de mesures ont été présentés dans Cotten et al. (1995).

2.5.2. Analyse des éléments traces par ICP-MS après ajout de Tm

- ***Papier 1** : Charles, C., Barrat, J.A. and Pelleter, E., 2021. Trace element determinations in Fe-Mn oxides by high resolution ICP-MS after Tm addition. Talanta 122446.*

Talanta 233 (2021) 122446

Contents lists available at ScienceDirect

Talanta

journal homepage: www.elsevier.com/locate/talanta

Review

Trace element determinations in Fe–Mn oxides by high resolution ICP-MS after Tm addition

Claire Charles [a,b,*], Jean-Alix Barrat [b,c], Ewan Pelleter [a]

[a] IFREMER, Unité Géosciences Marines, Laboratoire Cycles Géochimiques (LCG), 29280, Plouzané, France
[b] Univ Brest, CNRS, UMR 6538 (Laboratoire Géosciences Océan), Institut Universitaire Européen de La Mer (IUEM), Place Nicolas Copernic, 29280, Plouzané, France
[c] Univ Brest, CNRS, UMR 6539 (Laboratoire des Sciences de L'Environnement Marin), LIA BeBEST, Institut Universitaire Européen de La Mer (IUEM), Place Nicolas Copernic, 29280, Plouzané, France

ARTICLE INFO

Keywords:
ICP-MS
Fe–Mn oxides
Trace elements
Rare earth elements
High-resolution
Tm spike

ABSTRACT

In order to propose an optimal analytical procedure specific to ferromanganese (Fe–Mn) oxides, we investigated different modes of data acquisition using inductively coupled plasma mass spectrometry (ICP-MS). The results of trace element and Rare Earth Element (REE) determination in eight Fe–Mn nodules and crusts (FeMn-1, GSMC-1, GSMC-2, GSMC-3, GSPN-2, GSPN-3, NOD-A-1 and NOD-P-1) are presented here. The analytical procedure involves chemical dissolution of the Fe–Mn oxides and addition of a thulium (Tm) spike. The correction of measured values from potential isobaric interferences was investigated using both corrections based on mono-elemental solutions, and data acquisition in the high-resolution mode. The obtained results show that the high-resolution acquisition mode is unnecessary to achieve high quality data for REE in Fe–Mn oxides. Using our revised method, we provide a consistent set of precise and accurate values for eight widely used but poorly characterized certified reference materials.

1. Introduction

Fe–Mn oxides are ubiquitous in the ocean and are produced by three main processes or combination of these [1–3]: (1) precipitation of Fe–Mn oxyhydroxide colloids from cold ambient seawater, (2) precipitation from pore water and (3) precipitation from hydrothermal fluids. Whereas Fe–Mn mineralizations that precipitate from the third process are mainly composed of Fe or Mn and Si, polymetallic nodules and Fe–Mn crusts that form from the two other mechanisms can be enriched in base metals (e.g., Cu, Ni) and critical metals (e.g., Co, REE, Zr, Nb, Y, Te and Pt) [4–6]. Consequently, Fe–Mn crusts and polymetallic nodules are now seen as a potential mineral resource and recent studies highlight the growing interest for REE and Y (REY) [e.g., [7]].

Besides their economic potential, REY can be used as geochemical proxies for deciphering between the different types of Fe–Mn oxides, and REY are now widely used in recently published discrimination diagrams [2,8]. Normalized REY patterns (e.g., Post-Archean Australian Shale; Mud of Queensland) [9,10] is an easy way to visualize anomalies for redox-sensitive elements (e.g., Ce ± Eu) as well as non-redox-sensitive elements (e.g., La, Gd, Y) which are linked to the behavior of REY during geochemical processes [2,11]. For example, as a redox-sensitive element and part of the REY suite [12,13], Ce (and its anomaly) can provide insights to identify the distinct water mass layers in the oceans [14–16]. Even though REE fractionation during surface-complexation on Mn and Fe oxides must be carefully assessed when studying Fe–Mn oxides [13], crucial information can be gleaned from comparative studies of REE and Y [12]. Apart from these anomalies (i.e., Ce, Eu, La, Gd, Y), normalized REY patterns are smooth functions of ionic radius and can be used to estimate the analytical quality of the data [2].

Therefore, it is of prime importance to establish a precise and time-effective method to quantify trace elements abundances, especially the REY, in Fe–Mn oxides. The most widely technique used for determining trace element concentrations is inductively coupled plasma mass spectrometry (ICP-MS). This technique offers several advantages such as very low limits of detection and high data accuracy. Moreover, ICP-MS is powerful in rapidly and simultaneously determining numerous trace elements. However, the presence of isobaric interferences, a common issue in mass spectrometry, can affect the results, as exemplified for REE [17–20]. Three alternatives exist to overcome isobaric interferences: (a) the purification of samples, (b) the correction of interferences using solutions of pure elements to estimate their contributions, and (c) data acquisition in high-resolution mode. The first is not suitable for our case:

* Corresponding author. IFREMER, Unité Géosciences Marines, Laboratoire Cycles Géochimiques (LCG), 29280, Plouzané, France.
E-mail address: claire.charles@ifremer.fr (C. Charles).

https://doi.org/10.1016/j.talanta.2021.122446
Received 8 January 2021; Received in revised form 14 April 2021; Accepted 18 April 2021
Available online 30 April 2021
0039-9140/© 2021 The Author(s). Published by Elsevier B.V. This is an open access article under the CC BY-NC-ND license (http://creativecommons.org/licenses/by-nc-nd/4.0/).

Table 1
ICP-MS operating conditions and measurement parameters.

RF power	1200 W
Sample uptake rate	100 μL/min
Coolant argon flow rates	16 L/min
Auxiliary argon flow rates	0.9 L/min
Nebuliser argon flow rates	1.031 L/min
Torch	Quartz
Nebuliser	PFA ST micro-flow
Spray chamber	Quartz cyclonic
Cones	Nickel
Low resolution mode (LRM)	^{9}Be, ^{89}Y, ^{90}Zr, ^{93}Nb, ^{133}Cs, ^{135}Ba, ^{139}La, ^{140}Ce, ^{141}Pr, $^{143,146}Nd$, $^{147,149}Sm$, ^{151}Eu, ^{157}Gd, ^{159}Tb, ^{163}Dy, ^{165}Ho, ^{167}Er, ^{169}Tm, ^{174}Yb, ^{175}Lu, $^{177,178}Hf$, ^{181}Ta, ^{232}Th, ^{238}U
Medium resolution mode (MRM)	^{31}P, ^{45}Sc, ^{47}Ti, ^{51}V, ^{52}Cr, ^{66}Zn, ^{69}Ga, ^{85}Rb, ^{88}Sr, ^{90}Zr, ^{93}Nb, ^{111}Cd, ^{133}Cs, ^{181}Ta,
High resolution mode (HRM)	^{39}K, ^{43}Ca, ^{45}Sc, ^{52}Cr, ^{139}La, ^{140}Ce, ^{141}Pr, $^{143,146}Nd$, $^{147,149}Sm$, $^{151,153}Eu$, $^{155,157}Gd$, ^{159}Tb, ^{163}Dy, ^{165}Ho, ^{167}Er, ^{169}Tm, ^{174}Yb, ^{175}Lu
Acquisition mode	Mass Accuracy
Number of scans	3*2
Ion lens settings	Acquisition to obtain maximum signal intensity
Wash time	100 s

purifying the sample would add extra workload with the separation of elements. Consequently, fewer elements per run would be acquired (e.g., Eu without Ba) for a higher degree of work.

The main goal of this study is to compare the two other possibilities to correct measured abundances from potential isobaric interferences: the use of mono-elemental solutions and data acquisition using the high-resolution mode. The use of this latter method appeared to be well suited considering the typically high trace element and REE content in Fe–Mn oxides. To process, we decide to follow a well-established analytical procedure for trace element determination by ICP-MS based on the addition of Tm spike [21–23]. The addition of Tm spike in the samples before ICP-MS measurements produces a positive Tm anomaly in the resulting REE patterns, which can be used to calculate trace element abundances in the sample solutions. This procedure was initially developed to allow the determination of REE abundances after separation and concentration and intensively described [21,24–26]. We subsequently systematized this technique for all our samples because it simplifies the preparation of solutions [e.g., [22, 27]], and largely reduces the errors associated with the correction of signal drift during analytical sessions.

The resulting data produced in both low and high-resolution modes will be compared and a new set of reference values for a suite of commonly-used certified reference materials will be proposed.

2. Standards and analytical method

Eight certified reference materials of Fe–Mn oxides were analyzed in this study. They correspond to some of the most widely used Fe–Mn standards by the scientific community for the characterization of major and trace elements (FeMn-1, GSMC-1, GSMC-2, GSMC-3, GSPN-2, GSPN-3, NOD-A-1, NOD-P-1). Additionally, two other certified reference materials were also used to validate our ICP-MS measurements (BE-N and BCR-2, two well-characterized basalts). Another certified reference material (basalt BHVO-2) was analyzed to correct measured values from instrumental drift and for calibration purposes.

All sample preparations were conducted in a Class 1000 (ISO 6) clean laboratory. Deionized water purified with a Milli-Q system (Millipore®) at 18.2 MΩ was used for material cleaning and preparation of acid solutions. The following reagents were used: nitric and hydrochloric acid solutions (commercial grade, Merck, Darmstadt, Germany), and ultra-pure hydrofluoric acid solution (HIPERPUR-PLUS®, Panreac, Barcelona, Spain), all of them were purified by sub-boiling. About 1 g of each Fe–Mn certified reference materials was dried in an oven at about 60 °C for a period of one day. One hundred mg of powder were dissolved in closed screw-top Teflon vessels (Savillex®) at about 120 °C for one day with 2 ml of 32 N HF and 2 ml of 14 N HNO_3. The vessels were then opened for evaporation at about 110 °C. After evaporation to dryness, 2 ml of 14 N HNO_3 was added. The vessels were capped and put back on the hotplate for 12 h at about 120 °C. The samples were dried a second time and taken up in about 20 ml of Quartex 6 M HCl to prepare the "mother solutions". No residual particles were observed in the mother solutions. The solutions were then transferred to acid cleaned polypropylene bottles. For analysis, aliquots of each mother solution were spiked with a Tm solution (30 ng of Tm per mg of sample) and then evaporated to dryness. Finally, a few hours before measurements, the residues were taken up in 0.4 N HNO_3 containing traces of HF (6 drops of 32 N HF/l). The total dilution factors are comprised between 0.05 and 0.06 mg of sample per g of solution.

Trace element abundances were determined with a high-resolution inductively coupled plasma mass spectrometry (HR-ICP-MS) Thermo Electron Element XR (Thermo Scientific, Bremen, Germany) at the PSO ("Pôle Spectrométrie Océan") in Plouzané, France. This instrument can be operated in low (LRM, m/Δm approx. 300), medium (MRM, m/Δm = 4500) and high (HRM, m/Δm = 9200) resolution modes, depending on the required sensitivity and potential interferences for each element. Basic operating conditions and measuring parameters are summarized in Table 1. The REE were determined (a) in low-resolution mode to enhance sensitivity and were corrected for oxide and hydroxide interferences by analyzing solutions of ultra-pure water, Ba + Ce, Pr + Nd and Sm + Eu + Gd + Tb at the beginning of the measurement cycle, and (b) in high-resolution mode. A solution prepared with BHVO-2 was run after every three samples and used for both calibration and instrumental drift corrections following the procedure of Barrat et al. [21–24].

The raw data were first corrected for drift, procedural blank and interferences. Raw elemental concentrations were then calculated from corrected data, but these concentrations do not correspond to absolute abundances. At this stage, the Er and Yb measured concentrations were used to interpolate the content of Tm in the sample solutions. From these

Table 2
BHVO-2 working values used in this study, abundances (oxides in wt%, other elements in µg/g) and relative standard deviations (in italic) for the certified reference materials.

	Be	P_2O_5	K_2O	CaO	Sc	TiO_2	V	Cr	Zn	Ga	Rb	Sr	Y	Zr	Nb	Cs	Ba	Hf	Ta	Pb	Th	U
BHVO-2, working values																						
Barrat et al. (2012)	1.1	0.27	0.52	11.4	32.3	2.73	317	280	101	20.6	9.08	396	27.6	164.9	16.82	0.096	131	4.474	1.1	1.51	1.21	0.41
BE-N (n = 6)	**1.95**	**1.10**	**1.42**	**14.04**	**22.64**	**2.58**	**231**	**342**	**118**	**16.73**	**47.57**	**1409**	**30.90**	**260**	**103.0**	**0.75**	**1055**	**5.81**	**5.13**	**4.22**	**10.61**	**2.45**
RSD %	***2.12***	***2.02***	***2.77***	***1.57***	***1.32***	***3.04***	***1.60***	***1.37***	***1.87***	***1.78***	***3.58***	***1.80***	***0.83***	***1.79***	***1.72***	***3.47***	***1.52***	***1.90***	***6.57***	***3.82***	***1.59***	***1.16***
Jochum et al. (2016)	1.9	1.04	1.42	13.99	22.55	2.612	231.9	353.1	122.9	17.20	47.61	1392	29.44	272.9	113.2	0.73	1039	5.72	5.64	4.081	10.58	2.44
BCR-2 (n = 5)	**2.37**	**0.356**	**1.82**	**7.15**	**33.93**	**2.27**	**418**	**15.01**	**132**	**21.46**	**47.04**	**344**	**38.15**	**180**	**11.44**	**1.13**	**676**	**4.95**	**0.747**	**9.47**	**5.889**	**1.652**
RSD %	***3.48***	***1.44***	***0.98***	***2.18***	***1.34***	***1.18***	***0.93***	***1.85***	***2.87***	***1.10***	***0.63***	***1.00***	***0.76***	***0.75***	***0.83***	***1.08***	***0.48***	***0.80***	***0.95***	***3.98***	***0.65***	***0.44***
Jochum et al. (2016)	2.17	0.359	1.774	7.11	33.53	2.265	417.6	15.85	129.5	22.07	46.02	337.4	36.07	186.5	12.44	1.160	683.9	4.972	0.785	10.59	5.828	1.683
NOD-A-1 (n = 6)	**5.45**	**1.19**	**0.55**	**14.57**	**11.36**	**0.444**	**562**	**20.82**	**539**	**5.31**	**9.79**	**1472**	**128**	**289**	**42.61**	**0.58**	**1451**	**6.14**	**0.73**		**22.80**	**6.90**
RSD %	***2.44***	***1.77***	***1.04***	***1.93***	***1.53***	***1.35***	***1.44***	***5.66***	***1.32***	***2.17***	***1.32***	***1.90***	***1.82***	***1.22***	***1.07***	***2.23***	***1.48***	***1.74***	***1.09***		***1.70***	***1.80***
Flanagan and Gottfried (1980)		1.40	0.60	15.40		0.53	770		590			1750					1670					
Dulski (2001)											9.7	1467	116	233		0.56	1352	4			23.4	7
Axelsson et al. (2002)	5.60	1.36	0.60	16.06	12.4	0.51	660	20.9	800	6.30	10.6	1630	120	310	43.1	0.61	1530	5.80	0.76		25.1	7.00
Bau et al. (2014)													117									
Laurila et al. (2014)					12.1		614						122.6	321.5			1479	6.2			23.9	
NOD-P-1 (n = 6)	**2.21**	**0.44**	**1.15**	**2.86**	**9.67**	**0.429**	**446**	**14.21**	**1479**	**24.24**	**23.89**	**630**	**96.99**	**263**	**20.06**	**1.66**	**2537**	**4.13**	**0.35**		**15.63**	**4.03**
RSD %	***1.41***	***1.20***	***0.99***	***1.40***	***0.79***	***0.96***	***0.96***	***1.78***	***1.16***	***1.08***	***0.65***	***1.10***	***0.98***	***0.35***	***0.43***	***1.44***	***0.46***	***1.00***	***1.05***		***0.45***	***0.55***
Flanagan and Gottfried (1980)		0.46	1.20	3.10		0.50	570		1600			649					3350					
Dulski (2001)											24.5	680	91	298			2453				16.6	4.21
Axelsson et al. (2002)	2.30	0.47	1.20	3.15	9.70	0.45	510	13.3	2020	28.1	23.7	670	90.0	280	21.3	1.80	2690	4.20	0.33		16.7	4.00
Bau et al. (2014)													88.9									
Laurila et al. (2014)					10.25		492.5						93	287			2611	4			16.4	
FeMn-1 (n = 5)	**1.57**	**0.33**	**0.92**	**2.35**	**7.98**	**0.257**	**426**	**8.22**	**1742**	**23.16**	**12.01**	**682**	**73.76**	**298**	**12.34**	**0.78**	**3012**	**4.67**	**0.21**		**6.70**	**4.17**
RSD %	***2.72***	***2.90***	***5.69***	***4.64***	***2.86***	***3.46***	***2.15***	***8.47***	***1.57***	***1.63***	***2.99***	***2.80***	***1.93***	***1.50***	***2.23***	***3.65***	***1.85***	***1.63***	***3.33***		***1.80***	***1.46***
Webb et al. (2008)		0.352*		2.50	8.095*	0.29*	468.5*		1845		12.5*	683.3	69.11	325	13.4	0.85*	3158*	4.74	0.26*		6.87	4.39
Kricte (2011)	1.66	0.356	0.911	2.53	9.31	0.297	483		1821	31	12.9	683	69.1	326	13.8	0.822	3176	4.89	0.252		7.12	4.39
Bau et al. (2014)													66.7									
GSPN-2 (n = 5)	**3.53**	**0.49**	**0.994**	**2.44**	**14.08**	**1.19**	**423**	**13.53**	**809**	**20.42**	**15.24**	**835**	**149**	**558**	**45.65**	**0.83**	**1693**	**9.93**	**0.64**		**24.23**	**6.51**
RSD %	***0.44***	***1.22***	***0.91***	***1.10***	***0.91***	***1.29***	***0.81***	***4.66***	***2.43***	***1.34***	***1.18***	***0.90***	***0.80***	***0.68***	***0.88***	***0.85***	***0.69***	***0.74***	***0.92***		***0.77***	***0.98***
Wang et al. (1998)		0.58	1.08	2.67	13.7	1.37	425.9	17	918	27	16	869	133	618		0.84	1800	10			26	6.2
Dulski (2001)											16.2	875	144	614		0.89	1716	9.8			26.5	6.98
Laurila et al. (2014)					14.1		439.1						139.5	610			1729	9.55			25.1	
GSPN-3 (n = 5)	**1.75**	**0.32**	**1.094**	**2.09**	**10.03**	**0.47**	**403**	**11.03**	**1522**	**32.12**	**18.07**	**547**	**92.6**	**239**	**19.09**	**1.12**	**2370**	**3.90**	**0.31**		**15.34**	**3.77**
RSD %	***1.17***	***3.40***	***6.75***	***5.71***	***3.11***	***1.90***	***1.64***	***3.78***	***1.87***	***1.91***	***3.05***	***1.34***	***1.34***	***0.96***	***0.61***	***13.12***	***0.46***	***1.14***	***5.83***		***1.14***	***1.62***
Wang et al. (1998)		0.37	1.14	2.25	9.4	0.54	442	18	1600	38	17	561	84	256	21	1.2	2400	3.9	0.31		15	3.8
Dulski (2001)											18.8	565	87.4	274		1.26	2323	4.1			16.2	3.99
Bau et al. (2014)													83.3									
GSMC-1 (n = 5)	**5.35**	**1.45**	**0.70**	**4.34**	**11.56**	**1.93**	**574**	**14.11**	**618**	**2.93**	**9.72**	**1449**	**259**	**597**	**58.75**	**0.63**	**1745**	**10.27**	**1.17**		**20.12**	**12.07**
RSD %	***4.18***	***3.09***	***2.41***	***1.75***	***1.73***	***1.52***	***1.53***	***7.16***	***4.75***	***2.52***	***1.77***	***1.37***	***0.76***	***0.92***	***1.32***	***1.61***	***1.23***	***0.30***	***1.04***		***0.88***	***0.90***

(*continued on next page*)

Table 2 (*continued*)

	Be	P_2O_5	K_2O	CaO	Sc	TiO_2	V	Cr	Zn	Ga	Rb	Sr	Y	Zr	Nb	Cs	Ba	Hf	Ta	Pb	Th	U
Wang et al. (2003)		1.59	0.76	4.6		2.2	617		676		11	1481	239	656	58	0.6	1847	9.3	1.1		25	12
Bau et al. (2014)													244									
GSMC-2 (n = 5)	**5.27**	**3.08**	**0.67**	**7.09**	**10.60**	**1.68**	**586**	**12.58**	**547**	**3.03**	**9.01**	**1518**	**273**	**533**	**50.25**	**0.63**	**1852**	**8.78**	**0.97**		**15.16**	**11.60**
RSD %	***0.81***	***0.48***	***0.81***	***1.61***	***0.90***	***0.39***	***0.43***	***6.20***	***0.42***	***1.22***	***0.68***	***0.64***	***0.56***	***0.59***	***0.52***	***0.61***	***0.48***	***0.43***	***0.81***		***0.54***	***0.49***
Wang et al. (2003)		3.3	0.71	7.4	13	1.9	617		606		12	1551	251	602	53	0.9	1840	10.1			16.2	11
GSMC-3 (n = 5)	**4.86**	**3.48**	**0.79**	**7.55**	**10.70**	**1.72**	**524**	**12.48**	**538**	**4.05**	**10.59**	**1426**	**267**	**578**	**50.23**	**0.58**	**2029**	**9.62**	**1.12**		**14.19**	**11.25**
RSD %	***0.73***	***1.00***	***0.77***	***1.59***	***0.38***	***0.60***	***0.69***	***18.24***	***1.15***	***0.84***	***1.19***	***0.90***	***0.65***	***0.84***	***0.76***	***1.01***	***1.00***	***0.49***	***0.69***		***0.59***	***0.44***
Wang et al. (2003)		3.7	0.83	7.8	12.4	1.9	556		592		12	1466	247	642	53	0.5	2066	10			17	11

*Provisional.

abundances and the amount of Tm added during the chemical procedure, it was possible to calculate the element concentrations in the samples. The advantage of this calculations is that possible effects of the signal drift have no or negligible impact here [21,23]. Each solution was analyzed in triplicate and the results were averaged. The concentrations are provided in Tables 2 and 3, relative to our working values for the USGS basalt BHVO-2 [22]. In the event of future change to these BHVO-2 values, the data need only to be corrected by the ratio of the new and old values.

3. Results and discussion

The results and precision of the measurements as the relative standard deviation (RSD) are provided in Tables 2 and 3 For basalt standards BE-N and BCR-2, precisions are generally better than 4% for most elements and typically below 1.5% for the REE. Our data are in excellent agreement with the recommended values [28].

The eight Fe–Mn certified reference materials display high abundances of trace elements and REE. The results are also shown in Tables 2 and 3, while corresponding patterns are presented in Fig. 1. A Queensland alluvial sediment composite (MUQ) was used for normalization [9, 29] since it presents many well-characterized elements. Precision is mostly better than 4% for most elements and typically below 2.5% for the REE. Although the majority of our results are highly comparable to those obtained previously in the literature [2,30–37], important differences (>10%) exist between some of our data. For example, this is the cases for V (e.g., NOD-P-1 : 614 μg/g [37] vs. 562 μg/g in this study) and Zr (e.g., GSMC-2 : 602 μg/g [32] vs. 533 μg/g in this study). These variations are systematic for the eight Fe–Mn certified reference materials as illustrated in Fig. 2. Results from the other laboratories are higher than our data. Whereas the results obtained in this study for the basalt standards are in perfect agreement with the data published by Jochum et al. (2016) and used in the geochemical database GeoReM (Geological and Environmental Reference Materials). Our values are perfectly aligned on the x = y line (Fig. 2). These observations show the main differences between our data and those from previous studies come from a calibration bias and also confirm the high quality of our instrument calibration and the analytical procedure from homogeneous powder.

Comparisons between low-resolution and high-resolution REE results are provided in Table 4. The patterns and concentrations of REE are very similar whether in low or high-resolution modes. The Eu anomalies are calculated as the ratio of the normalized values of the element by the interpolation of the adjacent elements such as:

$$Eu\,/\,Eu^{*} = Eu_{MUQ}/(Sm_{MUQ} \times Gd_{MUQ})^{1/2} \quad (1)$$

and determined after data acquisition in low and high-resolution modes were also compared and appear to be very similar, within 3%, as well as in the basaltic certified references materials (Fig. 3). The isobaric interferences normally generated on Eu (BaO+, BaOH+) and on Gd (CeOH+, PrO+) are therefore well corrected in low-resolution mode. The RSD are generally less than 2% for the nodules and less than 1.5% for the crusts. The patterns are smooth (Fig. 1), which indicate excellent analytical quality [2]. The elementary ratios such as Zr/Hf [$(Zr/Hf)_{MUQ}$ = 1.25–1.71], La/Sm [$(La/Sm)_{MUQ}$ = 0.64–1.36] and Gd/Yb [$(Gd/Yb)_{MUQ}$ = 0.81–1.22] are characteristic of marine Fe–Mn oxides [2,8,38] and the well-known anomalies such as positive Ce anomalies (average Ce/Ce* = 1.73) and negative Y anomalies (average $(Y/Ho)_{MUQ}$ = 0.86) are clearly apparent [12,39–42]. The Ce anomaly is calculated using the same procedure as for the Eu anomaly calculation, such as:

$$Ce\,/\,Ce^{*} = Ce_{MUQ}/(La_{MUQ} \times Pr_{MUQ})^{1/2} \quad (2)$$

Although RSD from analyses obtained in high-resolution mode are generally better than 5%, they are nevertheless 1.5 to 14.5 times greater than those obtained in low-resolution mode. Results with RSD as low as

Table 3
BHVO-2 working values used in this study, REE abundances (μg/g) and relative standard deviations (in italic) for the certified reference materials.

	La	Ce	Pr	Nd	Sm	Eu	Gd	Tb	Dy	Ho	Er	Yb	Lu
BHVO-2, working values													
Barrat et al. (2012)	15.2	37.5	5.31	24.5	6.07	2.07	6.24	0.94	5.31	1.00	2.54	2.00	0.27
BE-N (n = 6)	**83.05**	**153.4**	**17.30**	**66.85**	**12.17**	**3.69**	**10.17**	**1.305**	**6.46**	**1.108**	**2.58**	**1.85**	**0.242**
RSD %	***0.88***	***0.79***	***1.12***	***0.90***	***1.02***	***1.04***	***2.07***	***1.28***	***0.77***	***0.44***	***0.76***	***0.88***	***0.35***
Jochum et al. (2016)	82.55	153.00	17.39	66.35	12.03	3.68	10.09	1.30	6.48	1.08	2.61	1.82	0.249
BCR-2 (n = 5)	**24.99**	**52.98**	**6.80**	**28.78**	**6.57**	**1.93**	**6.68**	**1.048**	**6.39**	**1.322**	**3.68**	**3.38**	**0.491**
RSD %	***0.72***	***0.79***	***0.67***	***0.71***	***0.54***	***0.82***	***0.67***	***0.44***	***0.75***	***0.73***	***0.76***	***0.49***	***0.95***
Jochum et al. (2016)	25.08	53.12	6.83	28.26	6.55	1.99	6.81	1.08	6.42	1.31	3.67	3.39	0.50
NOD-A-1 (n = 6)	**111.2**	**745**	**23.85**	**99.55**	**21.79**	**5.28**	**24.28**	**3.84**	**23.08**	**4.96**	**14.31**	**13.48**	**2.08**
RSD %	***1.68***	***1.75***	***1.74***	***1.70***	***1.81***	***2.29***	***2.08***	***1.63***	***1.68***	***1.73***	***1.93***	***1.69***	***1.79***
Flanagan and Gottfried (1980)	120	730		94	21	5	26		23		12	14	2.2
Dulski (2001)	112	743	24.3	93	19.8	5.4	24.9	3.9	23.5	4.9	14.6	13.7	2.2
Axelsson et al. (2002)	115	720	25.0	98.0	21.9	5.20	25.4	4.00	23.8	5.00	14.4	13.9	2.10
Bau et al. (2014)	115	792	24.8	103	22.3	5.51	26.1	3.98	24	5.06	15.1	14.1	2.27
Laurila et al. (2014)	115.4	750	25.1	104.3	22.8	5.5	25	4	24.1	5	14.2	14	2.2
NOD-P-1 (n = 6)	**106.4**	**319**	**31.40**	**132.2**	**31.87**	**7.68**	**30.28**	**4.71**	**26.29**	**5.00**	**13.42**	**12.70**	**1.82**
RSD %	***0.35***	***0.55***	***0.32***	***0.46***	***0.54***	***1.31***	***1.40***	***0.83***	***0.51***	***0.61***	***0.76***	***0.69***	***0.69***
Flanagan and Gottfried (1980)	104	290		120	30	7.5	28		27		12	13	1.8
Dulski (2001)	110	329	33	128	30	8	31.7	4.8	27.5	5.13	14.15	13.3	1.99
Axelsson et al. (2002)	105	305	31.0	130	31.0	7.60	30.4	4.90	27.1	5.00	13.6	12.9	1.80
Bau et al. (2014)	104	322	31.5	127	31.9	7.97	32.2	4.89	27.9	5.01	14	13.4	1.96
Laurila et al. (2014)	110.5	325	33	138	33.2	7.9	30.95	4.9	27.3	5.05	13.2	13.15	1.93
FeMn-1 (n = 6)	**66.69**	**107.8**	**14.22**	**62.62**	**13.65**	**3.53**	**15.68**	**2.48**	**15.81**	**3.37**	**9.77**	**9.90**	**1.49**
RSD %	***1.80***	***1.99***	***1.57***	***2.05***	***0.61***	***0.97***	***2.31***	***2.39***	***2.28***	***0.91***	***1.45***	***1.96***	***1.52***
Webb et al. (2008)	68.22	110	14.11*	62.95	14.03	3.8	15.63	2.52	15.8	3.42	9.80	10	1.59*
Kriete (2010)	68.2	109	14.3	63	14.1	3.75	15.6	2.53	15.8	3.44	9.81	9.88	1.57
Bau et al. (2014)	65	108	14.3	59.5	13.7	3.61	16.1	2.5	16.5	3.38	10.1	10.3	1.58
GSPN-2 (n = 5)	**175**	**617**	**49.19**	**201**	**47.07**	**11.60**	**47.33**	**7.42**	**41.81**	**8.00**	**21.47**	**20.22**	**2.97**
RSD %	***1.01***	***0.93***	***1.22***	***0.79***	***0.83***	***0.74***	***0.74***	***0.86***	***0.91***	***0.78***	***0.78***	***0.88***	***0.52***
Wang et al. (1998)	184	620	49	198	46	11	48	7.6	42	8.2	21	20	2.9
Dulski (2001)	191	657	53	201	46	12.5	50.6	7.82	44.7	8.4	23.2	21.7	3.3
Laurila et al. (2014)	180.1	607.05	49.5	204.3	47.6	11.6	46.55	7.45	42.15	7.85	20.65	20.35	3
GSPN-3 (n = 5)	**92.20**	**252**	**29.06**	**123**	**30.54**	**7.42**	**29.21**	**4.67**	**26.11**	**4.93**	**13.16**	**12.47**	**1.79**
RSD %	***0.36***	***0.75***	***0.44***	***1.03***	***1.08***	***1.01***	***1.59***	***1.17***	***1.74***	***1.71***	***1.91***	***0.76***	***0.95***
Wang et al. (1998)	96	249	29	121	31	7.6	28	4.6	27	5.1	13	12	1.8
Dulski (2001)	97	262	30.9	120	29	7.95	30.8	4.87	27.4	5	13.9	13.2	1.95
Bau et al. (2014)	95.9	267	29.1	124	31	7.46	29.6	4.68	26.8	4.92	13.8	12.9	1.9
GSMC-1 (n = 5)	**326**	**1246**	**68.74**	**283**	**58.40**	**14.36**	**61.68**	**9.53**	**56.48**	**11.58**	**31.93**	**29.20**	**4.26**
RSD %	***1.76***	***1.73***	***0.84***	***1.16***	***0.80***	***0.99***	***1.08***	***0.70***	***0.51***	***0.65***	***0.47***	***0.57***	***0.18***
Wang et al. (2003)	352	1315	72	293	61	15	65	9.5	58	11.3	32	31	4.5
Bau et al. (2014)	349	1370	71			15.2	68.4	10.3	60.1	12.1	34.1	30.9	4.68
GSMC-2 (n = 5)	**317**	**1134**	**60.52**	**249**	**49.31**	**12.12**	**54.34**	**8.28**	**49.98**	**10.55**	**29.70**	**27.28**	**4.10**
RSD %	***0.49***	***1.40***	***0.53***	***0.48***	***0.44***	***0.49***	***0.63***	***0.58***	***0.60***	***0.55***	***0.53***	***0.46***	***0.57***
Wang et al. (2003)	323	989	63	246	49	12	58	8.1	52	10.5	30	28	4.2
GSMC-3 (n = 5)	**289**	**1014**	**58.06**	**240**	**49.27**	**12.19**	**54.53**	**8.24**	**48.95**	**10.24**	**28.49**	**26.34**	**3.91**
RSD %	***0.78***	***1.01***	***0.91***	***0.84***	***0.69***	***0.64***	***1.34***	***0.56***	***0.74***	***0.56***	***0.86***	***0.72***	***0.47***
Wang et al. (2003)	306	1080	62	246	51	12	55	8	51	10.2	29	27.4	4.2

*Provisional.

those acquired in low-resolution are conceivable in high-resolution provided exclusive usage of more concentrated solutions to enhance the entering signal. However, such protocol would generate an important risk of saturation of the collector in low-resolution requiring a substantial increase of the rinse time and overall cleaning procedure between each analytical session. Therefore, the high-resolution acquisition seems not to be relevant for REE characterization in Fe–Mn oxides.

4. Conclusion

In this study, the determination by ICP-MS of REE and other trace element abundances in eight certified reference materials of Fe–Mn oxides (FeMn-1, GSMC-1, GSMC-2, GSMC-3, GSPN-2, GSPN-3, NOD-A-1 and NOD-P-1) was investigating, using a Tm addition analytical procedure. Two different approaches were investigated for the correction of

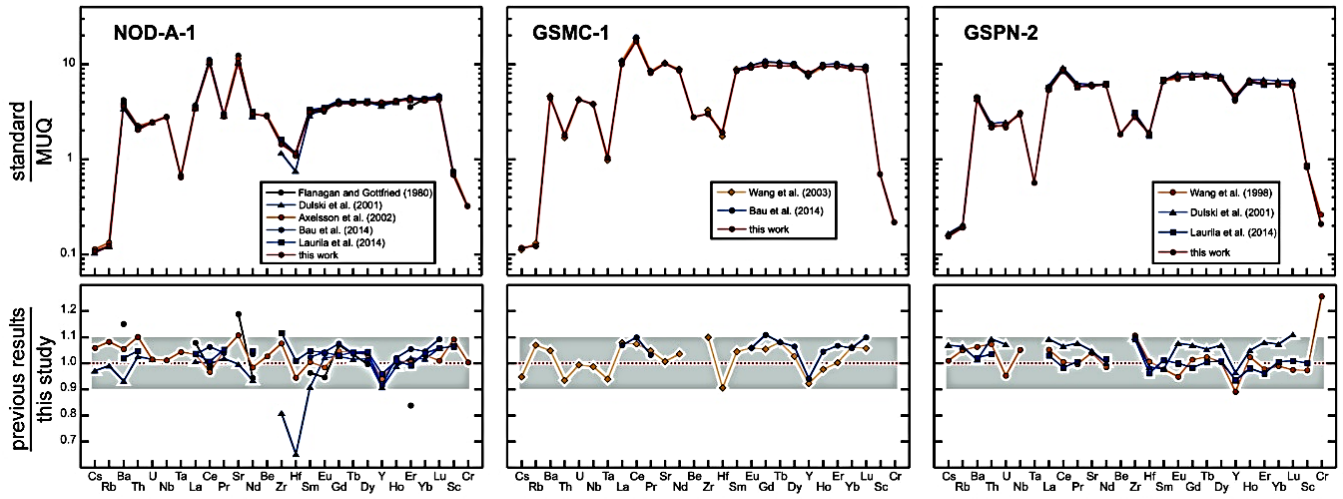

Fig. 1. MUQ normalized trace elements and REE patterns measured in LR mode from the certified reference materials NOD-A-1, GSMC-1 and GSPN-2.

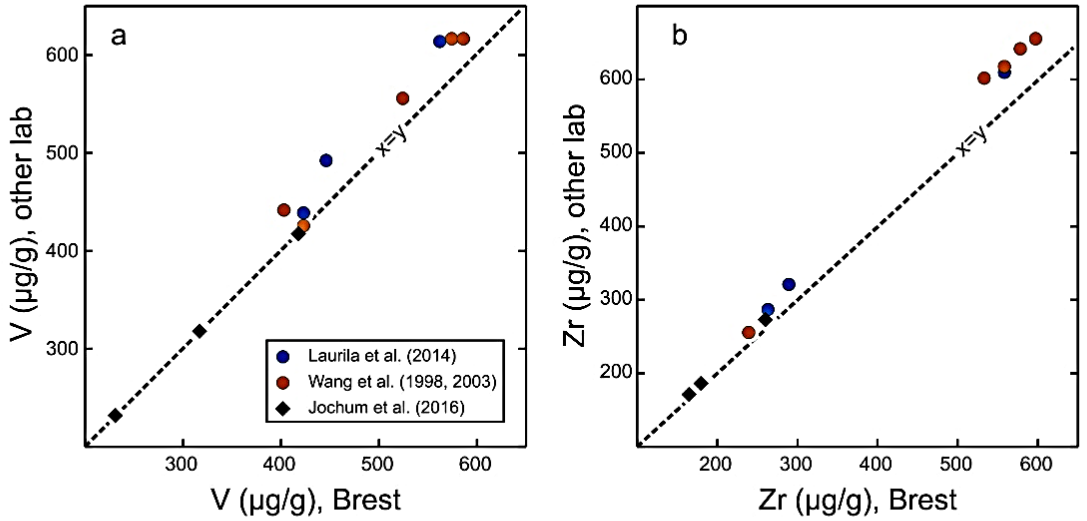

Fig. 2. A comparison of the V (µg/g) and the Zr (µg/g) values obtained in LR mode in this study and from literature studies showing a calibration bias. The black diamonds represent the basalt standards (including BHVO-2) and the points correspond to the Fe–Mn oxides.

isobaric interferences that can significantly affect measured concentrations during ICP-MS analyses: the use of mono-elemental solutions and the data acquisition in high-resolution mode. Our data demonstrate that the high-resolution acquisition mode is not the preferred choice for REE measurements in Fe–Mn oxides. Indeed, despite accurate data, the RSD are greater (<6.5%) than those obtained with the low resolution mode after correction of interferences using mono-elemental solutions (RSD < 2.5%).

The procedure was developed and validated using two silicate reference materials (BCR-2, BEN) providing precise and accurate data, before being applied to Fe–Mn oxides and calibrated with a silicate standard (BHVO-2). Although notable differences exist between our values and some data of the literature, the obtained results for two silicate certified reference materials (BCR-2 and BEN) are in excellent agreement with published reference values demonstrating the high-quality calibration of our analytical procedure. Using our revised protocol, we propose a new set of fair and accurate reference values for eight Fe–Mn certified reference materials that are widely used, but which were so far poorly characterized for trace elements.

As tracers of processes, sources and physicochemical parameters, REE and Y can provide crucial information concerning the mechanisms of formation of Fe–Mn oxides. REE and Y are also essential for deciphering between the different types of Fe–Mn oceanic deposits. Quantifying them precisely is a key step to discriminate mineral resources before targeting deposits and driving deep-sea exploration. Thus, this new set of data will serve as useful reference values for studies aiming at precisely quantifying REE (and other trace element) abundances in Fe–Mn oxides.

Declaration of competing interest

The authors declare that they have no known competing financial

Table 4
Comparisons between low and high-resolution REE values for the certified reference materials.

	La	Ce	Pr	Nd	Sm	Eu	Gd	Tb	Dy	Ho	Er	Yb	Lu
Basalts													
BE-N													
LR, n = 6 (*RSD%*)	83.1 (*0.88*)	153 (*0.79*)	17.30 (*1.12*)	66.85 (*0.90*)	12.17 (*1.02*)	3.69 (*1.04*)	10.17 (*2.07*)	1.305 (*1.28*)	6.46 (*0.77*)	1.108 (*0.44*)	2.58 (*0.76*)	1.85 (*0.88*)	0.242 (*0.35*)
HR, n = 6 (*RSD%*)	83.0 (*4.39*)	152 (*5.51*)	17.09 (*5.72*)	66.53 (*5.77*)	12.22 (*6.26*)	3.66 (*6.41*)	9.81 (*5.22*)	1.299 (*7.74*)	6.59 (*6.09*)	1.115 (*6.20*)	2.61 (*4.41*)	1.81 (*5.35*)	0.232 (*6.56*)
HR/LR	0.999	0.993	0.988	0.995	1.004	0.990	0.965	0.995	1.021	1.006	1.008	0.977	0.958
BCR-2													
LR, n = 5 (*RSD%*)	24.99 (*0.72*)	52.98 (*0.79*)	6.80 (*0.67*)	28.78 (*0.71*)	6.57 (*0.54*)	1.93 (*0.82*)	6.68 (*0.67*)	1.048 (*0.44*)	6.39 (*0.75*)	1.322 (*0.73*)	3.68 (*0.76*)	3.38 (*0.48*)	0.491 (*0.95*)
HR, n = 5 (*RSD%*)	24.50 (*1.33*)	52.83 (*3.04*)	6.77 (*3.60*)	28.61 (*2.99*)	6.45 (*3.35*)	1.97 (*1.51*)	6.70 (*2.38*)	1.036 (*5.95*)	6.31 (*2.22*)	1.304 (*2.24*)	3.67 (*3.83*)	3.35 (*5.97*)	0.480 (*4.20*)
HR/LR	0.980	0.997	0.996	0.994	0.980	1.021	1.003	0.989	0.987	0.987	0.998	0.991	0.977
Nodules													
NOD-A-1													
LR, n = 6 (*RSD%*)	111.2 (*1.68*)	745 (*1.74*)	23.85 (*1.74*)	99.55 (*1.70*)	21.79 (*1.81*)	5.28 (*2.29*)	24.28 (*2.08*)	3.84 (*1.63*)	23.08 (*1.68*)	4.96 (*1.73*)	14.31 (*1.93*)	13.48 (*1.69*)	2.08 (*1.79*)
HR, n = 6 (*RSD%*)	110.0 (*3.03*)	740 (*2.38*)	23.79 (*2.18*)	99.45 (*1.77*)	21.73 (*3.37*)	5.41 (*2.70*)	24.75 (*2.54*)	3.90 (*2.12*)	22.92 (*2.18*)	5.02 (*2.83*)	14.52 (*5.22*)	13.69 (*3.09*)	2.14 (*5.37*)
HR/LR	0.989	0.994	0.997	0.999	0.997	1.024	1.019	1.015	0.993	1.013	1.015	1.016	1.029
NOD-P-1													
LR, n = 6 (*RSD%*)	106.4 (*0.35*)	319 (*0.55*)	31.40 (*0.32*)	132.2 (*0.46*)	31.87 (*0.54*)	7.68 (*1.31*)	30.28 (*1.40*)	4.71 (*0.83*)	26.29 (*0.51*)	5.00 (*0.61*)	13.42 (*0.76*)	12.70 (*0.69*)	1.82 (*0.69*)
HR, n = 6 (*RSD%*)	107.1 (*3.02*)	321 (*2.20*)	31.84 (*2.38*)	134.5 (*2.14*)	32.41 (*2.63*)	7.97 (*3.30*)	30.85 (*2.35*)	4.74 (*3.75*)	27.03 (*4.00*)	5.16 (*3.14*)	13.58 (*4.33*)	13.08 (*4.61*)	1.93 (*5.73*)
HR/LR	1.006	1.005	1.014	1.018	1.017	1.037	1.019	1.007	1.028	1.031	1.012	1.030	1.058
FeMn-1													
LR, n = 6 (*RSD%*)	66.69 (*1.80*)	107.8 (*1.99*)	14.22 (*1.57*)	62.62 (*2.05*)	13.65 (*0.61*)	3.53 (*0.97*)	15.68 (*2.31*)	2.48 (*2.39*)	15.81 (*2.28*)	3.37 (*0.91*)	9.77 (*1.45*)	9.90 (*1.96*)	1.49 (*1.52*)
HR, n = 6 (*RSD%*)	65.43 (*6.05*)	106.0 (*4.78*)	14.20 (*4.02*)	62.63 (*3.20*)	13.75 (*4.85*)	3.64 (*3.75*)	15.44 (*2.85*)	2.48 (*4.72*)	15.74 (*5.68*)	3.36 (*4.57*)	9.89 (*5.42*)	10.07 (*2.03*)	1.51 (*3.98*)
HR/LR	0.981	0.983	0.999	1.000	1.008	1.029	0.985	0.999	0.995	0.996	1.012	1.017	1.014
GSPN-2													
LR, n = 5 (*RSD%*)	175 (*1.01*)	617 (*0.93*)	49.19 (*1.22*)	201 (*0.79*)	47.07 (*0.83*)	11.60 (*0.74*)	47.33 (*0.74*)	7.42 (*0.86*)	41.81 (*0.91*)	8.00 (*0.78*)	21.47 (*0.78*)	20.22 (*0.88*)	2.97 (*0.52*)
HR, n = 5 (*RSD%*)	174 (*2.44*)	609 (*2.86*)	47.81 (*2.47*)	199 (*1.87*)	46.31 (*2.37*)	11.62 (*2.51*)	46.82 (*1.62*)	7.27 (*2.45*)	41.61 (*2.68*)	7.85 (*2.52*)	21.85 (*2.38*)	19.74 (*1.85*)	2.87 (*4.45*)
HR/LR	0.997	0.986	0.972	0.990	0.984	1.002	0.989	0.980	0.995	0.981	1.018	0.976	0.964
GSPN-3													
LR, n = 5 (*RSD%*)	92.19 (*0.36*)	251 (*0.75*)	29.06 (*0.44*)	123 (*1.03*)	30.54 (*1.08*)	7.42 (*1.01*)	29.21 (*1.59*)	4.67 (*1.17*)	26.11 (*1.74*)	4.93 (*1.71*)	13.16 (*1.91*)	12.47 (*0.76*)	1.79 (*0.95*)
HR, n = 5 (*RSD%*)	90.19 (*5.24*)	245 (3.41)	28.51 (*3.93*)	122 (*3.28*)	30.32 (*3.59*)	7.37 (*2.78*)	28.60 (*2.50*)	4.63 (*3.05*)	25.57 (3.76)	4.81 (*4.76*)	13.47 (*4.47*)	12.40 (*4.43*)	1.81 (*6.17*)
HR/LR	0.978	0.974	0.981	0.995	0.993	0.993	0.979	0.991	0.979	0.977	1.024	0.994	1.016
Crusts													
GSMC-1													
LR, n = 5 (*RSD%*)	326 (*1.76*)	1245 (*1.73*)	68.74 (*0.84*)	283 (*1.16*)	58.40 (*0.80*)	14.36 (*0.99*)	61.68 (*1.08*)	9.53 (*0.70*)	56.48 (*0.51*)	11.58 (*0.65*)	31.93 (*0.47*)	29.20 (*0.57*)	4.26 (*0.18*)
HR, n = 5 (*RSD%*)	331 (*4.09*)	1237 (*3.19*)	67.41 (*3.80*)	283 (*3.14*)	58.54 (*3.69*)	14.45 (*3.03*)	63.71 (*3.91*)	9.32 (*3.45*)	56.53 (*2.89*)	11.60 (*3.60*)	32.32 (*3.54*)	29.16 (*4.07*)	4.21 (*3.65*)
HR/LR	1.015	0.994	0.981	1.000	1.002	1.006	1.033	0.978	1.001	1.002	1.012	0.999	0.988
GSMC-2													
LR, n = 5 (*RSD%*)	317 (*0.49*)	1134 (*1.40*)	60.52 (*0.53*)	249 (*0.48*)	49.31 (*0.44*)	12.12 (*0.49*)	54.34 (*0.63*)	8.28 (*0.58*)	49.98 (*0.60*)	10.55 (*0.55*)	29.70 (*0.53*)	27.28 (*0.46*)	4.10 (*0.57*)
HR, n = 5 (*RSD%*)	312 (*2.57*)	1117 (*1.97*)	59.64 (*2.78*)	246 (*2.56*)	49.54 (*1.11*)	12.25 (*2.70*)	54.64 (*3.18*)	8.16 (*2.58*)	49.78 (*1.71*)	10.55 (*2.85*)	29.75 (*2.37*)	27.32 (*3.18*)	4.11 (*3.98*)
HR/LR	0.986	0.986	0.986	0.988	1.005	1.011	1.006	0.986	0.996	0.999	1.002	1.002	1.004
GSMC-3													
LR, n = 5 (*RSD%*)	289 (*0.78*)	1014 (*1.01*)	58.06 (*0.91*)	240 (*0.84*)	49.27 (*0.69*)	12.19 (*0.64*)	54.53 (*1.34*)	8.24 (*0.56*)	48.95 (*0.74*)	10.24 (*0.56*)	28.49 (*0.86*)	26.34 (*0.72*)	3.91 (*0.47*)
HR, n = 5 (*RSD%*)	300 (*2.21*)	1042 (*1.19*)	59.98 (*1.46*)	249 (*1.56*)	51.09 (*1.01*)	12.62 (*2.21*)	56.64 (*2.50*)	8.58 (*0.76*)	50.24 (*1.71*)	10.53 (*0.76*)	29.24 (*2.08*)	27.33 (*1.88*)	4.04 (*2.71*)
HR/LR	1.039	1.028	1.033	1.038	1.037	1.035	1.039	1.042	1.026	1.028	1.027	1.038	1.032

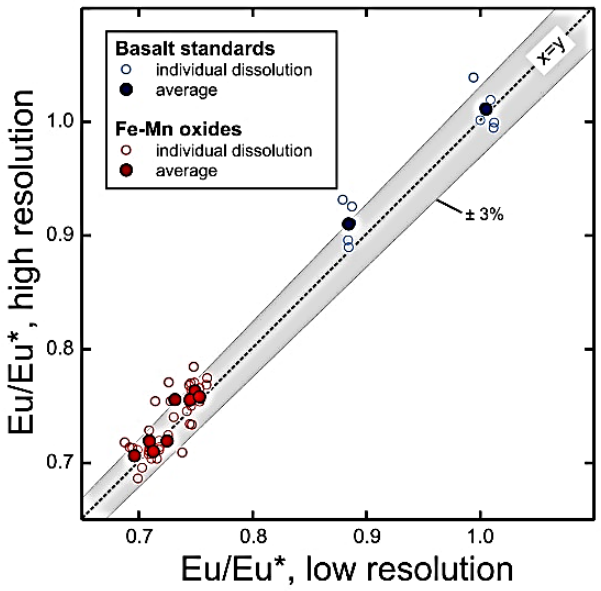

Fig. 3. A comparison of measured Eu/Eu* ratio in LR and HR modes for the basalt standards and the studied Fe–Mn oxides.

interests or personal relationships that could have appeared to influence the work reported in this paper.

Acknowledgements

We would like to thank Bleuenn GUEGUEN for her precious help during data acquisition. Claire CHARLES PhD is co-funded by TOTAL and IFREMER as part of the PAMELA (Passive Margin Exploration Laboratories) scientific project. We gratefully acknowledge Editor-in-Chief Jean-Michel KAUFFMANN, the two anonymous reviewers and Germain BAYON for thorough and thoughtful comments that significantly improved the manuscript. The PAMELA project is a scientific project led by Ifremer and TOTAL in collaboration with the Université de Bretagne Occidentale, Université Rennes 1, Université Pierre and Marie Curie, CNRS and IFPEN.

References

[1] J.R. Hein, A. Koschinsky, P. Halbach, F.T. Manheim, M. Bau, J.-K. Kang, N. Lubick, Iron and manganese oxide mineralization in the Pacific, Geol. Soc. Lond. Spec. Publ. 119 (1997) 123–138, https://doi.org/10.1144/GSL.SP.1997.119.01.09.
[2] M. Bau, K. Schmidt, A. Koschinsky, J.R. Hein, T. Kuhn, A. Usui, Discriminating between different genetic types of marine ferro manganese crusts and nodules based on rare earth elements and yttrium, Chem. Geol. 381 (2014) 1–9, https://doi.org/10.1016/j.chemgeo.2014.05.004.
[3] K. Schmidt, M. Bau, J.R. Hein, A. Koschinsky, Fractionation of the geochemical twins Zr–Hf and Nb–Ta during scavenging from seawater by hydrogenetic ferromanganese crusts, Geochem. Cosmochim. Acta 140 (2014) 468–487, https://doi.org/10.1016/j.gca.2014.05.036.
[4] D.Z. Piper, Rare earth elements in ferromanganese nodules and other marine phases, Geochem. Cosmochim. Acta 38 (1974) 1007–1022, https://doi.org/10.1016/0016-7037(74)90002-7.
[5] J.R. Hein, T.A. Conrad, H. Staudigel, Seamount Mineral Deposits: a source of rare metals for high technology industries, Oceanography 23 (2010) 184–189.
[6] A. Koschinsky, J.R. Hein, Marine ferromanganese encrustations: archives of changing oceans, Elements 13 (2017) 177–182, https://doi.org/10.2113/gselements.13.3.177.
[7] Y. Zhong, Z. Chen, F.J. Gonzalez, X. Zheng, G. Li, Y. Luo, A. Mo, A. Xu, S. Wang, Rare earth elements and yttrium in ferromanganese deposits from the South China Sea: distribution, composition and resource considerations, Acta Oceanol. Sin. 37 (2018) 41–54, https://doi.org/10.1007/s13131-018-1205-5.
[8] P. Josso, E. Pelleter, O. Pourret, Y. Fouquet, J. Etoubleau, S. Cheron, C. Bollinger, A new discrimination scheme for oceanic ferromanganese deposits using high field strength and rare earth elements, Ore Geol. Rev. 87 (2017) 3–15, https://doi.org/10.1016/j.oregeorev.2016.09.003.
[9] A. Pourmand, N. Dauphas, T.J. Ireland, A novel extraction chromatography and MC-ICP-MS technique for rapid analysis of REE, Sc and Y: revising CI-chondrite and Post-Archean Australian Shale (PAAS) abundances, Chem. Geol. 291 (2012) 38–54, https://doi.org/10.1016/j.chemgeo.2011.08.011.
[10] B.S. Kamber, A. Greig, K.D. Collerson, A new estimate for the composition of weathered young upper continental crust from alluvial sediments, Queensland, Australia, Geochem. Cosmochim. Acta 69 (2005) 1041–1058, https://doi.org/10.1016/j.gca.2004.08.020.
[11] P. Lusty, J.R. Hein, P. Josso, Formation and occurrence of ferromanganese crusts: earth's storehouse for critical metals, Elements 14 (2018) 313–318, https://doi.org/10.2138/gselements.14.5.313.
[12] T. Kuhn, M. Bau, N. Blum, P. Halbach, Origin of negative Ce anomalies in mixed hydrothermal–hydrogenetic Fe–Mn crusts from the Central Indian Ridge, Earth Planet Sci. Lett. 163 (1998) 207–220, https://doi.org/10.1016/S0012-821X(98)00188-5.
[13] M. Bau, A. Koschinsky, Oxidative scavenging of cerium on hydrous Fe oxide: evidence from the distribution of rare earth elements and yttrium between Fe oxides and Mn oxides in hydrogenetic ferromanganese crusts, Geochem. J. 43 (2009) 37–47, https://doi.org/10.2343/geochemj.1.0005.
[14] Y.G. Liu, M.R.U. Miah, R.A. Schmitt, Cerium: a chemical tracer for paleo-oceanic redox conditions, Geochem. Cosmochim. Acta 52 (1988) 1361–1371, https://doi.org/10.1016/0016-7037(88)90207-4.
[15] C.R. German, T. Masuzawa, M.J. Greaves, H. Elderfield, J.M. Edmond, Dissolved rare earth elements in the Southern Ocean: cerium oxidation and the influence of hydrography, Geochem. Cosmochim. Acta 59 (1995) 1551–1558, https://doi.org/10.1016/0016-7037(95)00061-4.
[16] Y. Dou, S. Yang, C. Li, X. Shi, J. Liu, L. Bi, Deepwater redox changes in the southern Okinawa Trough since the last glacial maximum, Prog. Oceanogr. 135 (2015) 77–90, https://doi.org/10.1016/j.pocean.2015.04.007.
[17] E.H. Evans, J.J. Giglio, Interferences in inductively coupled plasma mass spectrometry, A review, J. Anal. At. Spectrom. 8 (1993) 1–18, https://doi.org/10.1039/JA9930800001.
[18] P. Dulski, Interferences of oxide, hydroxide and chloride analyte species in the determination of rare earth elements in geological samples by inductively coupled plasma mass spectrometry, Fresenius' J. Anal. Chem. 350 (1994) 194–203, https://doi.org/10.1007/BF00322470.
[19] S.M. Eggins, J.D. Woodhead, L.P.J. Kinsley, G.E. Mortimer, P. Sylvester, M. T. McCulloch, J.M. Hergt, M.R. Handler, A simple method for the precise determination of N= 40 trace elements in geological samples by ICPMS using enriched isotope internal standardisation, Chem. Geol. 134 (1997) 311–326, https://doi.org/10.1016/S0009-2541(96)00100-3.
[20] N.M. Raut, L.-S. Huang, S.K. Aggarwal, K.-C. Lin, Determination of lanthanides in rock samples by inductively coupled plasma mass spectrometry using thorium as oxide and hydroxide correction standard, Spectrochim. Acta Part B At. Spectrosc. 58 (2003) 809–822, https://doi.org/10.1016/S0584-8547(03)00016-8.
[21] J.A. Barrat, F. Keller, J. Amossé, R.N. Taylor, R.W. Nesbitt, T. Hirata, Determination of rare earth elements in sixteen silicate reference samples by icp-ms after Tm addition and ion exchange separation, Geostand. Newsl. 20 (1996) 133–139, https://doi.org/10.1111/j.1751-908X.1996.tb00177.x.
[22] J.A. Barrat, B. Zanda, F. Moynier, C. Bollinger, C. Liorzou, G. Bayon, Geochemistry of CI chondrites: major and trace elements, and Cu and Zn Isotopes, Geochem. Cosmochim. Acta 83 (2012) 79–92, https://doi.org/10.1016/j.gca.2011.12.011.
[23] J.A. Barrat, N. Dauphas, P. Gillet, C. Bollinger, J. Etoubleau, A. Bischoff, A. Yamaguchi, Evidence from Tm anomalies for non-CI refractory lithophile element proportions in terrestrial planets and achondrites, Geochem. Cosmochim. Acta 176 (2016) 1–17, https://doi.org/10.1016/j.gca.2015.12.004.
[24] J.A. Barrat, G. Bayon, X. Wang, S. Le Goff, M.L. Rouget, B. Gueguen, D. Ben Salem, A new chemical separation procedure for the determination of rare earth elements and yttrium abundances in carbonates by ICP-MS, Talanta 219 (2020) 121244, https://doi.org/10.1016/j.talanta.2020.121244.
[25] G. Bayon, J.A. Barrat, J. Etoubleau, M. Benoit, C. Bollinger, S. Révillon, Determination of rare earth elements, Sc, Y, Zr, Ba, Hf and Th in geological samples by ICP-ms after Tm addition and alkaline fusion, Geostand. Geoanal. Res. 33 (2009) 51–62, https://doi.org/10.1111/j.1751-908X.2008.00880.x.
[26] N. Freslon, G. Bayon, D. Birot, C. Bollinger, J.A. Barrat, Determination of rare earth elements and other trace elements (Y, Mn, Co, Cr) in seawater using Tm addition and Mg(OH)2 co-precipitation, Talanta 85 (2011) 582–587, https://doi.org/10.1016/j.talanta.2011.04.023.
[27] D. Ben Salem, J.A. Barrat, Determination of rare earth elements in gadolinium-based contrast agents by ICP-MS, Talanta 221 (2021) 121589, https://doi.org/10.1016/j.talanta.2020.121589.
[28] K.P. Jochum, U. Weis, B. Schwager, B. Stoll, S.A. Wilson, G.H. Haug, M.O. Andreae, J. Enzweiler, Reference values following ISO guidelines for frequently requested rock reference materials, Geostand. Geoanal. Res. 40 (2016) 333–350, https://doi.org/10.1111/j.1751-908X.2015.00392.x.
[29] M.G. Lawrence, B.S. Kamber, The behaviour of the rare earth elements during estuarine mixing—revisited, Mar. Chem. 100 (2006) 147–161, https://doi.org/10.1016/j.marchem.2005.11.007.
[30] F.J. Flanagan, D. Gottfried, USGS Rock Standards; III, Manganese-Nodule Reference Samples USGS-Nod-A-1 and USGS-Nod-P-1, USGS Numbered Series No. 1155, Professional Paper, U.S. Govt. Print Off., Washington, 1980, https://doi.org/10.3133/pp1155.
[31] Y. Wang, D. Luo, Y. Gao, H. Song, J. Li, W. Chen, Y. Teng, S. Zhou, A preliminary study on the preparation of four pacific ocean polymetallic nodule and sediment reference materials: GSPN-2, GSPN-3, GSMS-2 and GSMS-3, geostand, Newsl. 22 (1998) 247–254, https://doi.org/10.1111/j.1751-908X.1998.tb00697.x.

[32] X. Wang, Y. Gao, Y. Wang, S.I. Andreev, Three cobalt-rich seamount crust reference materials: GSMC-1 to 3, geostand, Newsl. 27 (2003) 251–257, https://doi.org/10.1111/j.1751-908X.2003.tb00726.x.

[33] P. Dulski, Reference materials for geochemical studies: new analytical data by ICP-ms and critical discussion of reference values, Geostand. Newsl. 25 (2001) 87–125, https://doi.org/10.1111/j.1751-908X.2001.tb00790.x.

[34] M. Axelsson, I. Rodushkin, J. Ingri, B. Öhlander, Multielemental analysis of Mn–Fe nodules by ICP-MS : optimisation of analytical method, Analyst 127 (2002) 76–82, https://doi.org/10.1039/B105706P.

[35] P.C. Webb, M. Thompson, P.J. Potts, J.S. Watson, C. Kriete, GeoPT23 - an International Proficiency Test for Analytical Geochemistry Laboratories - Report on Round 23 (Separation Lake Pegmatite, OU-9) and 23A (Manganese Nodule, FeMn-1), International Association of Geoanalysts: Unpublished report, 2008.

[36] C. Kriete, An evaluation of the inter-method discrepancies in ferromanganese nodule proficiency test GeoPT 23A, geostand, Geoanalytical Res 35 (2011) 319–340, https://doi.org/10.1111/j.1751-908X.2010.00055.x.

[37] T.E. Laurila, M.D. Hannington, S. Petersen, D. Garbe-Schönberg, Early depositional history of metalliferous sediments in the Atlantis II Deep of the Red Sea: evidence from rare earth element geochemistry, Geochem. Cosmochim. Acta 126 (2014) 146–168, https://doi.org/10.1016/j.gca.2013.11.001.

[38] J.R. Hein, T.A. Conrad, K. Mizell, V.K. Banakar, F.A. Frey, W.W. Sager, Controls on ferromanganese crust composition and reconnaissance resource potential, Ninetyeast Ridge, Indian Ocean, Deep Sea Research Part I: Oceanographic Research Papers 110 (2016) 1–19, https://doi.org/10.1016/j.dsr.2015.11.006.

[39] M.I. Leybourne, K.H. Johannesson, Rare earth elements (REE) and yttrium in stream waters, stream sediments, and Fe–Mn oxyhydroxides: fractionation, speciation, and controls over REE+Y patterns in the surface environment, Geochem. Cosmochim. Acta 72 (2008) 5962–5983, https://doi.org/10.1016/j.gca.2008.09.022.

[40] J.N. Pattan, G. Parthiban, Geochemistry of ferromanganese nodule–sediment pairs from Central Indian Ocean Basin, J. Asian Earth Sci. 40 (2011) 569–580, https://doi.org/10.1016/j.jseaes.2010.10.010.

[41] L. Surya Prakash, D. Ray, A.L. Paropkari, A.V. Mudholkar, M. Satyanarayanan, B. Sreenivas, D. Chandrasekharam, D. Kota, K.A. Kamesh Raju, S. Kaisary, V. Balaram, T. Gurav, Distribution of REEs and yttrium among major geochemical phases of marine Fe–Mn-oxides: comparative study between hydrogenous and hydrothermal deposits, Chem. Geol. 312 (2012) 127–137, https://doi.org/10.1016/j.chemgeo.2012.03.024, 313.

[42] Y. Ren, X. Sun, Y. Guan, Z. Xiao, Y. Liu, J. Liao, Z. Guo, Distribution of rare earth elements plus yttrium among major mineral phases of marine Fe–Mn crusts from the south China sea and western pacific ocean: a comparative study, Minerals 9 (2019) 8, https://doi.org/10.3390/min9010008.

2.6. Géochimie isotopique

2.6.1. Composition isotopique en Nd par TIMS

2.6.1.1. Présentation du Nd

Le néodyme (Nd) fait partie des terres rares (en anglais, Rare Earth Elements ; REE) intermédiaires et possède de nombreux isotopes dont seulement cinq sont stables dans la nature (^{142}Nd, ^{143}Nd, ^{145}Nd, ^{146}Nd et ^{148}Nd) avec des abondances entre 27,1 % et 5,7 %. Deux de ses isotopes possèdent des demi-vies très longues (^{144}Nd, ^{150}Nd) avec des abondances respectives de 23,9 % et 5,6 %. Les autres ont des demi-vies très courtes et sont donc moins abondants dans la nature. L'isotope ^{143}Nd provient pour partie de la désintégration du samarium (Sm), et plus précisément de son isotope radiogénique ^{147}Sm, par radioactivité.

Les variations isotopiques en Nd étant très faibles (par la demi-vie très longue de ^{147}Sm), la notation εNd est utilisée. Cette dernière correspond à l'écart mesuré entre la valeur du rapport ^{143}Nd/^{144}Nd dans la roche analysée et la valeur du rapport ^{143}Nd/^{144}Nd du modèle Réservoir Chondritique Uniforme (CHUR) au même âge dont la valeur est estimée à 0.512638 (Jacobsen, Wasserburg, 1980) :

$$\varepsilon\mathrm{Nd} = \left(\frac{^{143}Nd/^{144}Nd\ (mesuré)}{^{143}Nd/^{144}Nd\ (CHUR)}\right) \times 10^4 \qquad (2)$$

Cette mesure d'écart rend les comparaisons plus faciles. Les εNd peuvent être négatifs ou positifs correspondant, respectivement, à un système peu radiogénique ou à un système plus radiogénique.

2.6.1.2. Séparation du Nd

À partir des solutions mères et donc de la quantité de poudre initialement prélevée, une concentration minimum en Nd de 115 µg/g d'échantillon a été mesurée et a permis de calculer le volume d'aliquote à prélever afin d'atteindre une détection minimum de 0,5 µg lors de l'analyse au Spectromètre de Masse à Thermo-Ionisation (TIMS). C'est entre 2 ml et 21 ml de solution mère qui ont été prélevés.

Les prélèvements sont purifiés en laboratoire de chimie par séparation élémentaire. Cette technique consiste à éliminer tous les éléments, sauf celui dont on veut connaître la composition isotopique et qui sera analysé au spectromètre. Cette étape est primordiale afin que d'autres éléments ne puissent pas nuire à l'émission de l'élément analysé. La procédure de séparation du Nd se déroule en 2 étapes par chromatographie d'extraction (Tableau 2.1).

La première étape consiste à séparer les REE des autres éléments présents dans la matrice. Pour cela, des colonnes en téflon contenant une résine macroporeuse échangeuse de cations de type TRU-Spec sont utilisées. Cette résine permet de fixer les lanthanides et les actinides complexés en HNO_3 1N mais pas les éléments majeurs. Ensuite, l'élution des REE se fait en HCl. Après passage sur la colonne, et récupération des REE en phase aqueuse, la solution est de nouveau évaporée sur une plaque chauffante à environ 90 °C.

La seconde étape consiste à séparer le Nd des autres REE. La méthode la plus utilisée est l'extraction sur une colonne en téflon contenant une autre résine chromatographique de type Ln. Cette résine à la particularité de permettre la migration des REE légères avant les REE lourds grâce à sa constante de stabilité qui augmente

Tableau 2.1. *Profil d'élution du Pb et du Nd selon les acides et les résines utilisés.*

Etape	Acide et quantité	Colonne et résine
Conditionnement	*3ml HNO3 1M*	*Sr-Spec*
Conditionnement	*3ml HNO3 1M*	*TRU-Spec*
	Positionner Sr-Spec sur TRU-Spec	
Chargement de l'échantillon	*1 ml HNO3 1M*	*Sr-Spec et TRU-Spec*
Piégeage	*1 ml HNO3 1M*	*Sr-Spec et TRU-Spec*
	Désassembler les colonnes	
Poubelle (traces)	*3 ml HCl 2N*	*Sr-Spec*
Elution et récupération du Pb	3 ml HCl 6N	Sr-Spec
Conditionnement	*6 ml HCl 0,2N*	*Ln*
Poubelle (majeurs)	*2 ml HNO3 1M*	*TRU-Spec*
	Positionner TRU-Spec sur Ln	
Piégeage des REE	*3 ml HCl 0,2 N*	*TRU-Spec et Ln*
	Désassembler les colonnes	
Poubelle (Ce, La)	*9.5 ml HCl 0.2N*	*Ln*
Elution et récupération du Nd	5 ml HCl 0.3N	Ln

avec le numéro atomique des éléments (Peppard et al., 1957).

Ainsi, avec de l'HCl normalisé à 0,2N, il est possible de séparer le lanthane (La) et le cérium (Ce) des autres REE. Puis, avec de l'HCl 0,3N, le Nd est élué et récupéré. Cette méthode permet d'obtenir une séparation complète des pics d'élution des différentes REE lors de l'élution. Après cette dernière étape de séparation, l'échantillon est amené à sec. Il est ensuite repris dans 3 µl d'HNO_3 1N et prêt à être déposé sur filament pour introduction dans le spectromètre.

Il est important de noter que la résine Ln n'est pas changée après chaque session d'extraction, contrairement à la résine TRU-Spec. La résine Ln se change après 6 mois d'utilisation. Une calibration des colonnes est alors obligatoire par méthode colorimétrique. Elle consiste à prélever des fractions successives au cours de l'élution et à y ajouter du noir d'ériochrome. La fraction caractéristique du Nd passe du bleu au rose lorsque l'élément est présent en solution. Cette technique permet ainsi d'établir un profil précis de l'élution du Nd comme présenté dans le tableau 2.1.

2.6.1.3. Principes généraux d'un TIMS

Les mesures sont effectuées sur un TIMS Thermo Scientific ™ Triton (Figure 2.4) au sein de l'IUEM. La thermo-ionisation ou ionisation de surface, est la technique employée pour produire des faisceaux d'ions dans les sources des spectromètres de masse TIMS. Dans notre cas, l'acquisition se fait en double filament avec un évaporant (portant l'échantillon) et un ionisant. Elle consiste à évaporer et ioniser par chauffage l'élément chimique à analyser, déposé préalablement sur le filament évaporant. Les

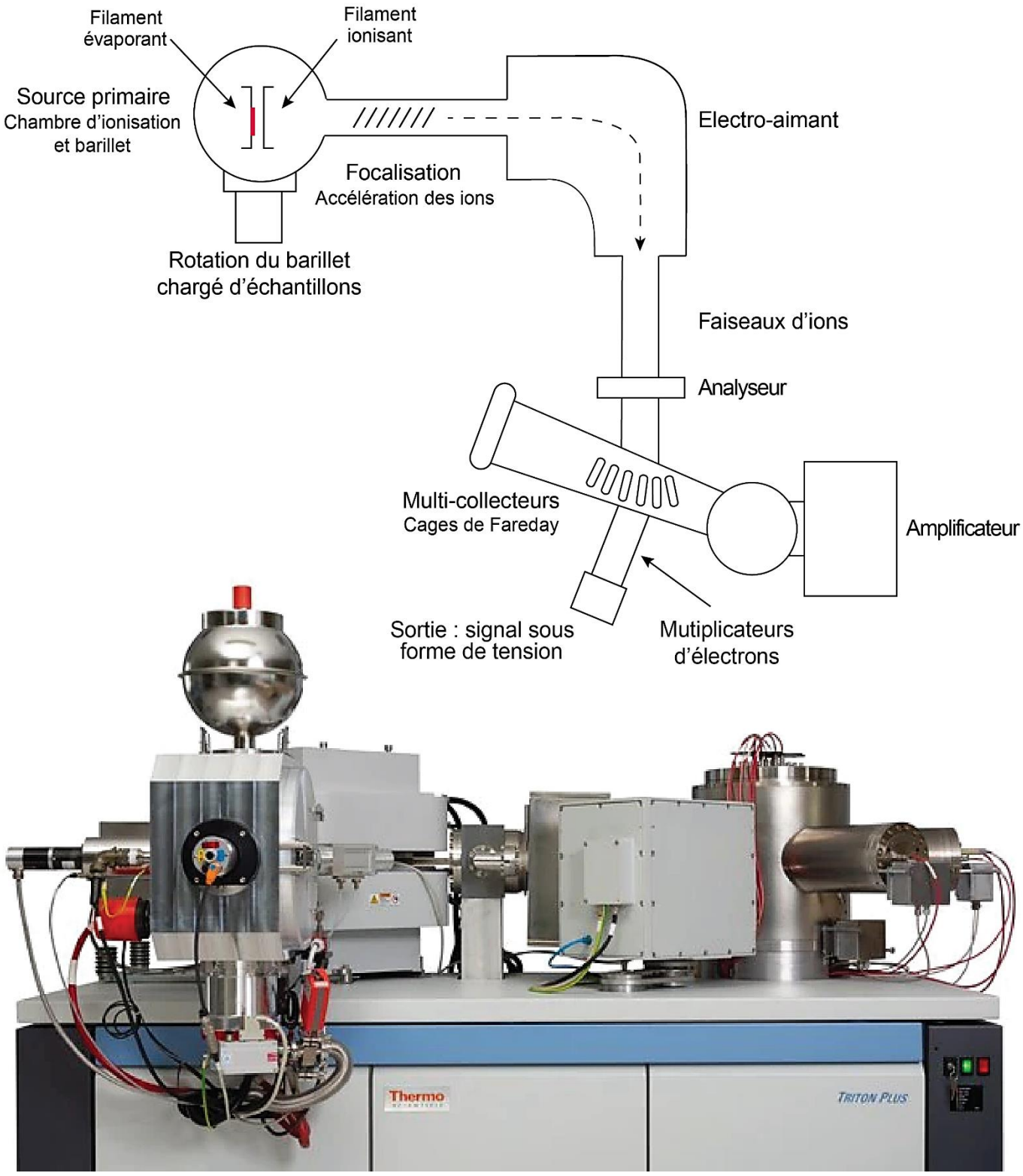

***Figure 2.4**. Schéma simplifié d'un TIMS Thermo Scientific ™ Triton depuis la source primaire jusqu'à l'obtention des intensités en sortie, d'après la documentation du constructeur.*

pieds de filaments sont installés dans la chambre primaire et qui effectuera des rotations afin de placer l'échantillon à analyser en face des lentilles de focalisation (Figure 2.4). Après mise en pompage, les filaments sont parcourus sous vide par un courant électrique qui provoque leur échauffement par effet Joule. L'échantillon alors chauffé s'évapore et s'ionise selon la loi de Saha Langmuir :

$$\frac{N_+}{N_0} = exp\left[\frac{(W-I)}{kT}\right] \qquad (3)$$

Avec N_+, la quantité d'ions créés ; N_0, la quantité d'atomes qui s'échappent de l'échantillon ; W, la fonction de travail du métal qui constitue le filament ; I, le potentiel d'ionisation de l'élément analysé ; k, la constante de Boltzmann (~ 8.62×10^{-5} eV/°K) et T, la température de chauffage. Les ions sont ensuite focalisés et accélérés pour former un faisceau d'ions. Ce dernier passe par un champ électrostatique, généré par un électro-aimant, qui va dévier les ions selon leurs masses, d'après la force de Lorentz :

$$F = qvB = \frac{mv^2}{r} \qquad (4)$$

Avec F, la force de Lorentz ; q, v, et m respectivement la charge, la vitesse et la masse de la particule ; B, le champ magnétique et r, le rayon de courbure de la trajectoire de la particule. Ces nouveaux faisceaux d'ions (autant de faisceaux qu'il y a de type d'isotopes) sont ensuite captés dans les collecteurs et analysés dans le spectromètre. Les résultats sont exprimés sous forme de rapports isotopiques, donnés par les intensités relatives mesurées des différents faisceaux d'ions.

2.6.1.4. Session d'analyses « type »

Les solutions reprises en HNO_3 0,25N sont chargées sur des filaments de rhénium (Re). Le séchage du dépôt est effectué à l'aide d'un courant de 0,8 A. Pour améliorer la fixation du dépôt sur le filament évaporant, ce dernier est flashé à 2A avant de l'éteindre immédiatement.

Les supports de filaments sont alors montés sur un barillet porte-échantillons, ils sont positionnés de manière à ce que le filament évaporant se trouve en face du filament ionisant. Le barillet est monté dans la source primaire du TIMS avant que le pompage en ultravide soit lancé. Une fois l'ultravide atteint, il est possible de démarrer le paramétrage de la séquence et les analyses. La dérive instrumentale est mesurée par le biais du standard externe JNdi (Tanaka et al., 2020).

Le Nd ayant une température d'émission proche de 1550 °C, les filaments sont chauffés par courants électriques allant de 1A à plus de 4A, jusqu'à obtenir la température idéale d'émission. Ensuite, le faisceau d'ions est focalisé en ajustant notamment la position des lentilles de focalisation. Enfin, les mesures peuvent être réalisées manuellement ou automatiquement.

Au cours de la thèse, les deux modes de mesures ont été réalisés. La séquence type programmée consiste en 15 blocs d'analyses avec 20 scans par bloc. Ce qui représente 300 mesures moyennées pour un échantillon, donnant une bonne représentativité statistique. Les rapports isotopiques $^{143}Nd/^{144}Nd$ obtenus en sortie sont normalisés par la valeur du CHUR comme expliqué dans le paragraphe 2.6.1.1, et ainsi notées εNd.

2.6.2. Composition isotopique en Pb par MC-ICP-MS

2.6.2.1. Présentation du Pb

Le plomb (Pb) possède 38 isotopes connus et seulement quatre isotopes ont été observés stables dans la nature (^{204}Pb, ^{206}Pb, ^{207}Pb, ^{208}Pb) avec des abondances respectives de 1,4% ; 24,1% ; 22,1% et 52,4%. Parmi eux, uniquement l'isotope ^{204}Pb n'est pas radiogénique. ^{208}Pb qui est l'isotope majoritaire est issu de la désintégration du thorium (^{232}Th) alors que le ^{206}Pb et ^{207}Pb sont issus de la désintégration de l'uranium (respectivement ^{238}U et ^{235}U). Les quantités relatives de ces isotopes ont donc évolué au cours du temps, c'est pourquoi étudier les rapports isotopiques ^{206}Pb/^{204}Pb, ^{207}Pb/^{204}Pb et ^{208}Pb/^{204}Pb met en évidence des variations isotopiques au cours du temps, essentielles aux reconstructions paléocéanographiques et paléogéologiques.

2.6.2.2. Séparation du Pb

Le Pb étant très concentré dans les encroûtements Fe-Mn, il ne nécessite pas de précautions analytiques particulières. De ce fait, toutes les séparations de Pb sont réalisées sur les mêmes aliquotes prélevées pour les séparations du Nd (voir le paragraphe 2.6.1.2).

Préalablement à la première étape de séparation du Nd, qui consiste à isoler les REE du reste de la matrice, des colonnes remplies de résine macroporeuse échangeuse de cations de type Sr-Spec sont positionnées sur les colonnes TRU-Spec. La résine Sr-Spec permet alors de retenir le Sr et le Pb en HNO_3 1N alors que le reste de l'échantillon coulera directement dans la colonne TRU-Spec pour la séparation du Nd. Les colonnes sont alors désassemblées l'une de l'autre (Tableau 2.1).

Une fois le Sr et le Pb captés sur la résine Sr-Spec, la fraction de Sr est éluée en HCl normalisé 2N et mise à la poubelle. Le Pb, quant à lui, est récupéré avec de l'HCl normalisé 6N (Horwitz et al., 1994 ; Vajda et al., 1997). L'échantillon est ensuite amené à sec sur plaque chauffante et stocké.

2.6.2.3. Principes généraux d'un MC-ICP-MS

Le MC-ICP-MS est un instrument de mesures multi-élémentaires tout comme l'ICP-MS (voir le paragraphe 2.5.2 ; Charles et al., 2021). L'échantillon est introduit dans une chambre de nébulisation. L'aérosol produit est injecté dans le plasma à 8000 °C. Les éléments sont atomisés et ionisés avant d'être séparés par l'association d'un filtre magnétique et d'un filtre électrostatique. La différence réside dans le fait qu'un MC-ICP-MS permet de collecter les ions sur plusieurs détecteurs simultanément. Les faisceaux d'ions créés arrivent dans 9 cages de Faraday où les ions d'un élément donné frappent le fond, s'accumulent et sont mesurés simultanément avant de retrouver leurs neutralités. En sortie, les résultats sont présentés sous forme de rapports isotopiques issus des intensités relatives mesurées. Les rapports ici utilisés sont le ^{206}Pb/^{204}Pb, le ^{207}Pb/^{204}Pb, et le ^{208}Pb/^{204}Pb.

Cette technique d'analyse isotopique diffère de celle choisie pour l'isotopie du Nd. En effet, le MC-ICP-MS présente une efficacité d'ionisation proche de 100 %, ce qui permet d'analyser la plupart des éléments, y compris ceux plus compliqués à mesurer par TIMS, comme le Pb.

2.6.2.4. Session d'analyses « type »

Quelques jours avant la session d'analyse, le résidu est repris avec 0,5 ml d'HNO_3 normalisé 0,3N et prêt à être mesuré avec un Spectromètre de Masse à Plasma à Couplage Inductif Multi-Collection (MC-ICP-MS) de type Thermo

Scientific ™ Neptune présent au département des Géosciences Marines de l'IFREMER.

L'appareil est paramétré comme un ICP-MS : il faut d'abord laisser l'instrument chauffer, puis régler la torche à plasma et les calibrations pour les résolutions. La première étape analytique est de mesurer les concentrations en Pb des échantillons afin de préparer les dilutions des solutions à analyser.

Notre session d'analyse est basée sur l'étude de White et al. (2000). Une concentration connue de thallium est également ajoutée afin de mesurer et de corriger le biais en masse instrumental. Lors des analyses, le standard externe NIST NBS 981 est mesuré (Yuan et al., 2016). Les valeurs du standard serviront dans le traitement des données afin d'interpoler les mesures de façon précise et juste. La séquence type est paramétrée de façon à passer 1 standard tous les deux échantillons. Elle consiste en 6 blocs d'analyses avec 5 scans par bloc soit 30 mesures moyennées pour un échantillon. Les données acquises sont sous forme d'intensité enregistrée pour chaque rapport isotopique. Elles sont ensuite corrigées des potentielles interférences entre le mercure (Hg) et le Pb, du biais en masse calculé à partir du Tl et normalisées grâce à l'interpolation du NIST NBS 981 et des valeurs certifiées de Todt et al. (2013).

2.7. Datation absolue par désintégration radioactive du Be

Les 8 séries temporelles de la thèse ont été datées selon deux méthodes différentes. L'une relève d'une équation empirique à partir de la concentration en cobalt (Co) des encroûtements. L'autre méthode est directement héritée de la décroissance radioactive des nucléides cosmogéniques et fournit des datations absolues. Cette seconde technique a été retenue, afin d'apporter une échelle temporelle suffisamment fine et précise à cette étude, pour mettre en évidence des phénomènes géologiques majeurs.

2.7.1. Les nucléides cosmogéniques

Afin de dater les séries temporelles d'encroûtements de ce projet, c'est la datation absolue par désintégration radioactive du Be produit *in situ* qui a été retenue. Dans cette partie, il s'agit d'expliquer les grands principes de la cosmogénie. Les nucléides (ou noyaux) cosmogéniques, tels que le ^{10}Be, représentent tous les isotopes formés dans la haute atmosphère ou dans la lithosphère par réactions nucléaires des particules issues des rayons cosmiques. Ces derniers proviennent de deux composantes : solaire et galactique. La première a une intensité faible et variable alors que la seconde est plus importante, de par son origine qui est la voie lactée, avec une intensité relativement constante.

Une fois dans la haute atmosphère, les rayons cosmiques interagissent avec des éléments déjà présents dans l'atmosphère. C'est le rayonnement primaire (Figure 2.5). Les isotopes radioactifs de ^{10}Be sont produits par nucléosynthèse et plus précisément, par un processus de spallation des atomes d'oxygène (O) et d'azote (N). Le rayonnement secondaire résulte des impacts du rayonnement primaire entraînant la formation de gerbes cosmiques faites de neutrons et de muons (Figure 2.5).

Le flux et l'énergie des particules primaires et des particules secondaires produites dans les cascades nucléaires décroissent de manière exponentielle fonction de l'épaisseur d'atmosphère traversée. Seulement environ ~0,1 % des particules secondaires atteignent la lithosphère. À ce stade, les nucléides cosmogéniques restant vont principalement interagir avec le silicium. Le minéral cible des isotopes ^{10}Be est donc le quartz (SiO_2), minéral hautement présent dans les sédiments. C'est la production de nucléides cosmogéniques *in situ* (Figure 2.5).

Ainsi, plus de 99 % du ^{10}Be se retrouve piégé dans les dépôts sédimentaires qui s'accumulent au

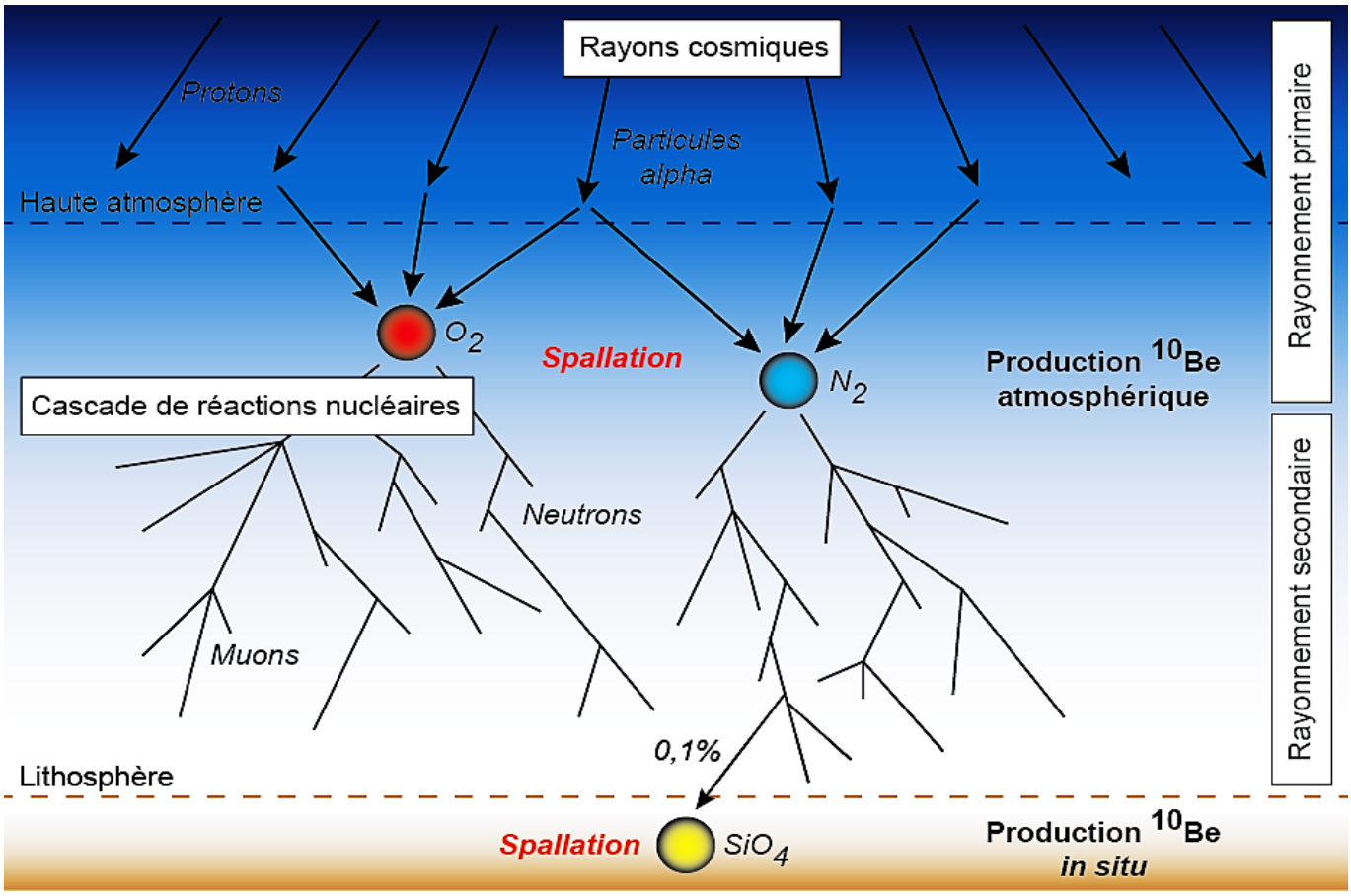

Figure 2.5. *Schéma explicatif de la production du ^{10}Be atmosphérique et du ^{10}Be in situ à partir des rayons cosmiques et des multiples réactions de nucléosynthèse dans l'atmosphère et dans la lithosphère.*

cours du temps (Lebatard, Bourlès, 2015). Le temps de demi-vie du ^{10}Be est relativement long ($T_{1/2}$ = 1,387 ± 0,012 Ma d'après Chmeleff et al. (2010) ; Korschinek et al. (2010) ; Nishiizumi (2007)), ce qui permet de dater des échantillons par désintégration radioactive jusqu'à 10 Ma de manière efficace.

Cependant, l'utilisation de cet isotope en tant qu'outil de datation nécessite de s'affranchir des variations des conditions physico-chimique environnementales. C'est pourquoi la concentration en ^{10}Be doit être normalisée par celle de l'isotope stable ^{9}Be (Bourlès et al., 1989).

2.7.2. Séparation du Be par chromatographie d'extraction

Les datations au ^{10}Be se sont déroulées au Centre Européen de Recherche et de l'Enseignement en Géosciences de l'Environnement (CEREGE) au sein du Laboratoire National des Nucléides Cosmogéniques (LN2C). Le protocole qui suit repose sur 100 mg de poudre par échantillon et a été initié par D. Bourlès en 1989. Il doit être réalisé dans une unité dédiée à la préparation d'échantillons pour les mesures de la concentration du ^{10}Be atmosphérique afin de proscrire toute contamination d'échantillons analysés pour la mesure du ^{10}Be in-situ. Le protocole est décrit pour une solution mais plusieurs échantillons sont traités simultanément ainsi que des blancs.

La première étape est la lixiviation des échantillons. Elle permet le lessivage total de la poudre par une solution de lixiviation composée d'acide acétique (CH_3CO_2H) et de chlorhydrate d'hydroxylamine (NH_2OH, HCl). Ce dernier va dissoudre la phase inorganique de l'encroûtement et solubiliser les oxy-hydroxydes de Fe et Mn, phases principales du Be authigénique (Bourlès et al., 1989; Ku et al., 1982; von Blanckenburg et al., 1996). L'acide acétique mettra en solution le Be absorbé par la phase inorganique (Bourlès et al., 1989b).

Une fois le mélange de l'échantillon avec la solution de lixiviation (20 mL/g) réalisé, il est placé dans un bain-marie de sable pendant 7 heures à 100 °C ± 2 °C. À la suite du temps de chauffe, la solution est séparée du résidu solide par une série de centrifugation et de récupération du surnageant. La solution finale est pesée puis un aliquote de 2 ml est prélevé et pesé pour effectuer les mesures de la concentration en ^{9}Be. Ces analyses sont effectuées par Spectrométrie d'Absorption Atomique sans flamme (AAS).

Le reste de la solution est pesé et une solution enrichie en ^{9}Be (3×10^{-4}g de ^{9}Be) est ajoutée. Ce spike va agir comme un entraîneur. Son ajout en quantité très supérieur au ^{9}Be naturel (insignifiant) va permettre d'avoir une cible suffisamment abondante pour la mesure du rapport ^{9}Be/^{10}Be.

L'échantillon est ensuite repris dans de l'eau acidifiée (50 % H_2O, 50 % HNO_3), évaporé et rincé à l'HCl. La solution est alors amenée à un pH de 8,5 à l'aide d'ammoniac (NH_3 ; 1 ml/10 ml de solution) afin de précipiter de l'hydroxyde de Be ($Be(OH_2)$). L'échantillon est centrifugé et le surnageant est jeté avant de reprendre le résidu dans de l'HCl.

La phase d'extraction du Be peut commencer. L'échantillon est injecté dans une colonne à résine échangeuse d'ions avec de l'HCl. Cette première résine (Dowex 1 × 8) permet de séparer le Be du Fe et du Mn dissous sous formes Fe^{2+} et Mn^{2+}. Cette étape est réalisée deux fois compte tenu de la forte concentration en Fe et Mn dans les encroûtements ferromanganésifères. Quand la colonne a fini de s'éluer, l'échantillon subit de nouveau une précipitation en milieu alcalin avant d'être injecté dans une seconde résine.

La résine (Dowex 50 × 8) permet alors de séparer le Be du bore (B). Une fois cette étape terminée, la solution est de nouveau amenée à un pH de 8,5 puis centrifugée. Le précipité est dissous avec de l'HNO_3 et transféré dans un creuset pour être oxydé dans un four à 800 °C pendant 1h. L'oxyde de béryllium (BeO) est prêt pour être cathodé.

2.7.3. Cathodage des cibles

Pour le cathodage, il s'agit de préparer un mélange avec le BeO et de la poudre de niobium (Nb). Celle-ci est utilisée comme conducteur afin de faciliter l'ionisation de l'échantillon dans la source du spectromètre et d'améliorer le rendement d'extraction des ions. Le mélange est introduit par entonnoir dans une cathode de molybdène. Celle-ci est ensuite placée sous presse quelques secondes pour compacter la poudre. Chaque cathode est finalement chargée sur le carrousel qui sera introduit dans la source du Spectromètre de Masse par Accélérateur de particules (AMS).

2.7.4. Introduction et analyses par AMS

Le but de l'AMS est de compter le nombre d'atomes d'un élément caractérisé par une masse et un numéro atomique. Dans le cas de la thèse, c'est le rapport isotopique ^{9}Be/^{10}Be qui est mesuré. Il permet de déduire la concentration en ^{10}Be. Ces analyses ont été réalisées sur

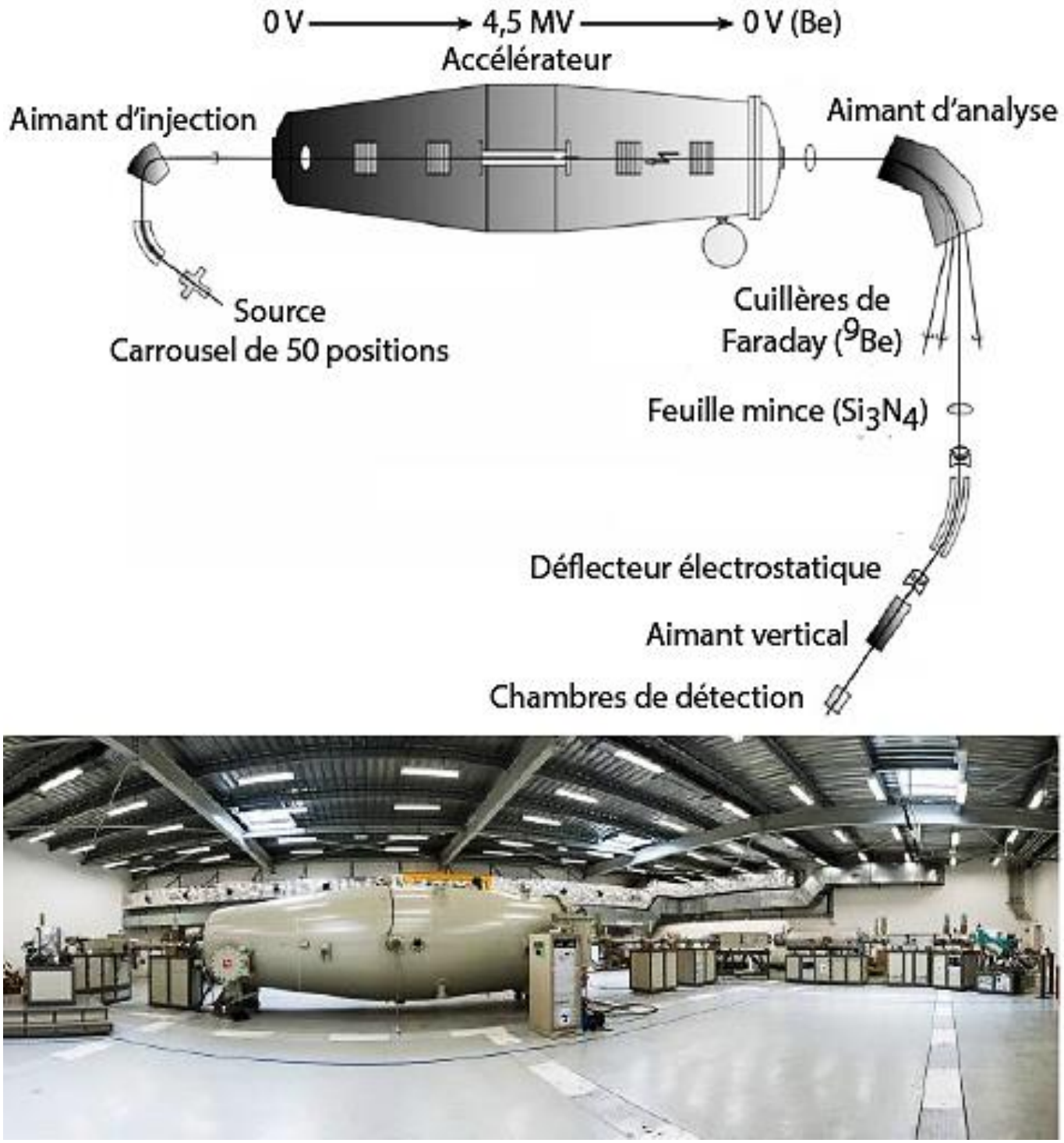

Figure 2.6. *Schéma et photo de l'instrument national ASTER - Spectromètre de masse par accélérateur situé au LN2C - CEREGE (d'après Delunel (2010)).*

l'accélérateur tandem ASTER (Accélérateur pour les Sciences de la Terre, Environnement, Risques) de 5MV au CEREGE. Le principe de la spectrométrie de masse par accélérateur est similaire à celui de la spectrométrie de masse conventionnelle. Il s'agit des mêmes étapes fondamentales telles que l'ionisation de l'échantillon, l'accélération du faisceau ionique, la séparation des ions sous champ magnétique en fonction de leurs masses et de leurs charges, et la détection. La différence se trouve au niveau de l'accélération des ions qui peut aller jusqu'à des énergies cinétiques extraordinairement hautes (dizaine de MeV), grâce à un accélérateur de type tandem. Cela permet de mesurer des radionucléides longue période tels que des nucléides cosmologiques ^{10}Be, ^{14}C, ^{26}Al, ou ^{36}Cl. Ces nucléides ont des temps de demi-vie trop longs pour être mesurés par comptage, et trop courts pour être suffisamment abondants lors des mesures par spectrométrie de masse classique.

Pour le cas du ^{10}Be, le facteur limitant à la séparation en champ magnétique est la résolution en masse et le niveau de séparation de l'aimant. C'est-à-dire que la différence de masse entre le ^{10}Be et son isobare ^{10}B (qui lui est 108 à 1015 fois plus abondant), est trop faible pour qu'ils soient séparés par spectrométrie de masse classique. Grâce à l'accélérateur Tandréton de l'instrument, les ions sont accélérés une première fois de 0 à 4,5 V puis de 4,5 V à la masse de sortie de l'accélérateur. La séparation du ^{10}Be et du ^{10}B se fait selon le numéro atomique, par l'intermédiaire de la loi de Bethe-Bloch. Cette loi décrit la perte d'énergie d'une particule chargée rapide traversant la matière :

$$-\frac{dE}{dx} = K\frac{z^2}{v^2} \qquad (5)$$

Avec E, l'énergie de la particule ; x, la distance parcourue ; z, le numéro atomique de la particule ; et v, sa vitesse. K est une constante qui dépend du matériau traversé par la particule. La quantité d'énergie perdue est donc proportionnelle au numéro atomique. Ainsi, la perte d'énergie du ^{10}B (z = 5) en sortie de la matière sera plus importante que celle du ^{10}Be (z = 4), et sera donc plus déviée en champ magnétique. Cette caractéristique de perte d'énergie, dans une faible épaisseur de matière, suivie directement d'une étape de détection, ne sont possibles que si l'atome analysé présente une énergie suffisamment élevée pour que ces deux étapes soient réalisées séquentiellement. C'est en cela que l'accélération des ions, entre la partie source et la partie analytique par spectrométrie de masse classique, est une étape cruciale.

En sortie de l'accélérateur, les faisceaux d'ions sont dirigés vers l'aimant qui se charge de dévier les ions selon leurs masses. Les ions fortement déviés $^{9}Be^{2+}$ sont interceptés par une cuillère de Faraday alors que les ions $^{10}Be^{2+}$ restant traversent une feuille de nitrure de silicium (Si_3N_4). Cette feuille favorise la sélection des cations de Be de charge 4+ et réduit les cations de B. Le faisceau final, ainsi épuré, circule jusqu'au détecteur final. Celui-ci est composé de 4 chambres dont la pression interne est réglée de manière à ce que seuls les ions Be puissent traverser chacune des chambres. Ainsi, le signal électrique est analysé et comptabilisé.

2.7.5. Séquence d'analyses « type »

Le carrousel sur lequel sont positionnés les échantillons présente 50 positions. Une cible de graphite est chargée et utilisée lors du nettoyage après le passage des échantillons. Environ 3 standards NIST SRM 4325 sont également ajoutés ainsi qu'un blanc machine (solution commerciale de ^{9}Be). Le reste des positions est

dédié aux échantillons d'encroûtements et aux blancs de chimie.

Le rapport ^{10}Be/^{9}Be, obtenu en sortie, est corrigé à partir au rapport ^{10}Be/^{9}Be mesurés plusieurs fois sur un standard connu. Cette correction est effectuée à partir de l'étalon certifié NIST SRM 4325 dont les valeurs du rapport et la période de demi-vie du ^{10}Be ont été corrigées par Nishiizumu et al. (2007).

L'incertitude relative du rapport isotopique est calculée selon le principe de propagation des erreurs et selon le nombre de coups acquis dans le détecteur final. À cela s'ajoute également l'erreur analytique issue du rapport mesuré à partir du standard (<1 %) :

$$\sigma_{ech} = \sqrt{\left(\frac{\sqrt{n}}{n}\right)^2 + (\sigma_{std})^2} \qquad (6)$$

Avec n, le nombre de coups acquis dans le détecteur final et σ_{std} l'erreur analytique relative issue du standard.

2.7.6. Calculs des concentrations et des âges

Enfin, le rapport ^{10}Be/^{9}Be mesuré va permettre de calculer les concentrations de l'isotope cosmogénique ^{10}Be produit in situ. Il s'agit dans un premier temps de trouver la quantité d'atomes $n\ ^{9}Be$ qui a été ajoutée dans l'échantillon lors du protocole de chimie (voir paragraphe 2.7.2.) :

$$n\ ^{9}Be = \frac{m_{spike} \times N}{M\ ^{9}Be} \qquad (7)$$

Avec, m_{spike} la masse de spike (solution enrichie) ajoutée ; *N*, la constante d'Avogadro (6,022 × 10^{23}) et $M\ ^{9}Be$ la masse molaire du ^{9}Be. Il est alors possible de déterminer la concentration du ^{10}Be. Elle correspond au nombre d'atomes $n\ ^{9}Be$ par gramme de quartz dissous noté m_{Qz}, à partir de l'équation suivante :

$$[^{10}Be] = \frac{\left(^{10}Be/^{9}Be_{ech} - \ ^{10}Be/^{9}Be_{blc}\right) \times \ n\ ^{9}Be}{m_{Qz}} \qquad (8)$$

Avec, $^{10}Be/^{9}Be_{ech}$ le rapport isotopique mesuré et $^{10}Be/^{9}Be_{blc}$ le rapport isotopique mesuré du blanc.

Les concentrations obtenues permettent ainsi de calculer un nouveau rapport authigénique ^{10}Be/^{9}Be juste et précis. La dernière étape consiste donc à calculer l'âge des échantillons à partir de l'équation classique de la décroissance radioactive suivante :

$$\left(\frac{^{10}\mathrm{Be}}{^{9}\mathrm{Be}}\right)_{(t)} = \left(\frac{^{10}\mathrm{Be}}{^{9}\mathrm{Be}}\right)_{(0)}^{-\lambda t} \qquad (9)$$

Où, ^{10}Be/^{9}Be$_{(t)}$ correspond au rapport authigène mesuré au temps t ; ^{10}Be/^{9}Be$_{(0)}$ le rapport authigène initial mesuré au sommet de l'échantillon où débutent les pertes dues à la décroissance radioactive ; λ, la constante de décroissance radioactive du Be mesurée à partir de son temps de demi-vie ($T_{1/2}$ = 1,387 ± 0,012 Ma ; voir paragraphe 2.7.1.) et donc t, l'âge de l'échantillon en Ma. En fonction de l'âge obtenu et de la profondeur des lamines échantillonnées sur les séries temporelles, il est également possible de calculer les taux de croissance des encroûtements.

2.7.7. Extrapolation des âges non mesurés par AMS

Pour chaque série temporelle, entre 3 et 9 datations ont été réalisées, soit un total de 52 datations à partir du rapport isotopique $^{10}Be/^{9}Be$. Cependant, ces 52 mesures ne permettent pas de dater toutes les lamines des 8 séries temporelles. De plus, comme vu précédemment, cette méthode de datation ne peut pas couvrir jusqu'à plus de 10 Ma.

C'est pourquoi, l'âge des lamines non datées par l'AMS et la résolution temporelle au-delà de 10 Ma ont été élaborées à partir de l'extrapolation des taux de croissance (GR ; growth rate en anglais) acquis à partir de la datation absolue au Be. Le taux de croissance d'une lamine, ici *b*, est calculé de manière très simple :

$$GR_b = \frac{Prof_b - Prof_a}{\hat{A}ge_b - \hat{A}ge_a} \qquad (10)$$

Avec $Prof$ la profondeur en mm de la lamine sur l'échantillon et $\hat{A}ge$ l'âge mesuré à partir de l'AMS ; *b* correspond à la lamine dont on cherche le taux de croissance et *a* la lamine précédente. La figure 2.7 illustre les paramètres de ce calcul.

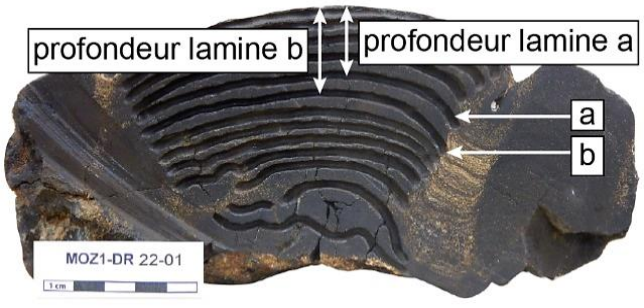

Figure 2.7. *Photo de la série temporelle MOZ-DR22-01 et ses nombreuses lamines illustrant le calcul des taux de croissance.*

Une fois les taux de croissance calculé pour chacune des lamines dont l'âge a été mesuré, il est possible d'extrapoler l'âge non calculé des autres lamines.

Deux méthodes sont possibles : soit le calcul prend en considération la moyenne des taux de croissance calculés, soit il dépend du dernier taux de croissance calculé. Il a été choisi de fonder le calcul sur le dernier taux de croissance calculé. Ce choix est motivé d'après l'observation d'une certaine stabilité des taux de croissance en profondeur des échantillons (donc avec le temps) alors que certains taux de croissance plus récents sont complètement différents. Ce choix n'impacte en rien les résultats dont les variations, selon la méthode préférée, sont inférieures à l'erreur associée.

L'âge extrapolé d'une lamine, ici noté *c*, est donc calculé d'après l'équation suivante, avec les mêmes paramètres que ceux présentés pour l'équation 10 précédemment vue :

$$\hat{A}ge_c = \frac{Prof_c - Prof_b}{GR_b} + \hat{A}ge_b \qquad (11)$$

Ainsi, toutes les lamines des 8 séries temporelles étudiées dans ce projet ont pu être datées. Cependant, un regard critique devra être apporté sur les datations supérieures à 10 Ma dans la mesure où elles ne sont pas absolues et ne tiennent donc pas compte des potentielles lacunes sédimentaires ou périodes d'érosion des encroutements.

2.8. Références bibliographiques

Arsouze, T., Dutay, J.-C., Lacan, F., Jeandel, C., 2009. Reconstructing the Nd oceanic cycle using a coupled dynamical – biogeochemical model.

Biogeosciences 6, 2829–2846. https://doi.org/10.5194/bg-6-2829-2009

Arsouze, T., Dutay, J.-C., Lacan, F., Jeandel, C., 2007. Modeling the neodymium isotopic composition with a global ocean circulation model. Chem. Geol. 239, 165–177. https://doi.org/10.1016/j.chemgeo.2006.12.006

Bayon, G., Toucanne, S., Skonieczny, C., André, L., Bermell, S., Cheron, S., Dennielou, B., Etoubleau, J., Freslon, N., Gauchery, T., Germain, Y., Jorry, S.J., Ménot, G., Monin, L., Ponzevera, E., Rouget, M.-L., Tachikawa, K., Barrat, J.A., 2015. Rare earth elements and neodymium isotopes in world river sediments revisited. Geochim. Cosmochim. Acta 170, 17–38. https://doi.org/10.1016/j.gca.2015.08.001

Bertram, C.J., Elderfield, H., 1993. The geochemical balance of the rare earth elements and neodymium isotopes in the oceans. Geochim. Cosmochim. Acta 57, 1957–1986. https://doi.org/10.1016/0016-7037(93)90087-D

Bourlès, D., Raisbeck, G.M., Yiou, F., 1989. 10Be and 9Be in marine sediments and their potential for dating. Geochim. Cosmochim. Acta 53, 443–452. https://doi.org/10.1016/0016-7037(89)90395-5

Bourlès, D.L., Klinkhammer, G., Campbell, A.C., Measures, C.I., Brown, E.T., Edmond, J.M., 1989b. Beryllium in marine pore waters: geochemical and geochronological implications. Nature 341, 731–733. https://doi.org/10.1038/341731a0

Broecker, W.S., Peng, T., Beng, Z., 1982. Tracers in the sea. Lamont-Doherty Geological Observatory, Columbia University.

Charles, C., Barrat, J.-A., Pelleter, E., 2021. Trace Element Determinations in Fe-Mn Oxides by High Resolution ICP-MS after Tm Addition. Talanta 122446. https://doi.org/10.1016/j.talanta.2021.122446

Chen, J.H., Lawrence Edwards, R., Wasserburg, G.J., 1986. 238U,234U and232Th in seawater. Earth Planet. Sci. Lett. 80, 241–251. https://doi.org/10.1016/0012-821X(86)90108-1

Chmeleff, J., von Blanckenburg, F., Kossert, K., Jakob, D., 2010. Determination of the 10Be half-life by multicollector ICP-MS and liquid scintillation counting. Nucl. Instrum. Methods Phys. Res. B 268, 192–199. https://doi.org/10.1016/j.nimb.2009.09.012

Chow, T.J., Patterson, C.C., 1962. The occurrence and significance of lead isotopes in pelagic sediments. Geochim. Cosmochim. Acta 26, 263–308. https://doi.org/10.1016/0016-7037(62)90016-9

Conrad, T., Hein, J.R., Paytan, A., Clague, D.A., 2017. Formation of Fe-Mn crusts within a continental margin environment. Ore Geol. Rev., SI:Marine mineral deposits: New resources for base, precious, and critical metals 87, 25–40. https://doi.org/10.1016/j.oregeorev.2016.09.010

Cotten, J., Le Dez, A., Bau, M., Caroff, M., Maury, R.C., Dulski, P., Fourcade, S., Bohn, M., Brousse, R., 1995. Origin of anomalous rare-earth element and yttrium enrichments in subaerially exposed basalts: Evidence from French Polynesia. Chem. Geol. 119, 115–138. https://doi.org/10.1016/0009-2541(94)00102-E

Delunel, R., 2010. Evolution géomorphologique du massif des Ecrins-Pelvoux depuis le Dermier Maximum Glaciaire – Apports des nucléides cosmogéniques produits in-stu. Thèse de doctorat, Université Joseph-Fourier, Grenoble I. ⟨tel-00511048⟩

DiMarco, S.F., Chapman, P., Nowlin, W.D., Hacker, P., Donohue, K., Luther, M., Johnson, G.C., Toole, J., 2002. Volume transport and property distributions of the Mozambique Channel. Deep Sea Res. Part II Top. Stud. Oceanogr. 49, 1481–1511. https://doi.org/10.1016/S0967-0645(01)00159-X

Elderfield, H., Upstill-Goddard, R., Sholkovitz, E.R., 1990. The rare earth elements in rivers, estuaries, and coastal seas and their significance to the composition of ocean waters. Geochim.

Cosmochim. Acta 54, 971–991. https://doi.org/10.1016/0016-7037(90)90432-K

Fialips, C.I., Labeyrie, B., Burg, V., Mazière, V., Munerel, Y., Haurie, H., Jolivet, I., Lasnel, R., Laurent, J.-P., Lambert, L., Jacquelin-Vallée, L., 2018. Quantitative Mineralogy of Vaca Muerta and Alum Shales From Core Chips and Drill Cuttings by Calibrated SEM-EDS Mineralogical Mapping. Presented at the SPE/AAPG/SEG Unconventional Resources Technology Conference, OnePetro. https://doi.org/10.15530/URTEC-2018-2902304

Fine, R.A., 1993. Circulation of Antarctic intermediate water in the South Indian Ocean. Deep Sea Res. Part Oceanogr. Res. Pap. 40, 2021–2042. https://doi.org/10.1016/0967-0637(93)90043-3

Frank, M., 2002. Radiogenic isotopes: tracers of past ocean circulation and erosional input. Rev. Geophys. 40, 1–1. https://doi.org/10.1029/2000RG000094

Frank, M., Whiteley, N., Kasten, S., Hein, J.R., O'Nions, K., 2002. North Atlantic Deep Water export to the Southern Ocean over the past 14 Myr: Evidence from Nd and Pb isotopes in ferromanganese crusts. Paleoceanography 17, 12-1-12–9. https://doi.org/10.1029/2000PA000606

Goldstein, S.J., Jacobsen, S.B., 1988. Rare earth elements in river waters. Earth Planet. Sci. Lett. 89, 35–47. https://doi.org/10.1016/0012-821X(88)90031-3

Goldstein, S.L., Hemming, S.R., 2003. 6.17 - Long-lived Isotopic Tracers in Oceanography, Paleoceanography, and Ice-sheet Dynamics, in: Holland, H.D., Turekian, K.K. (Eds.), Treatise on Geochemistry. Pergamon, Oxford, pp. 453–489. https://doi.org/10.1016/B0-08-043751-6/06179-X

Guan, Y., Sun, X., Ren, Y., Jiang, X., 2017. Mineralogy, geochemistry and genesis of the polymetallic crusts and nodules from the South China Sea. Ore Geol. Rev. 89, 206–227. https://doi.org/10.1016/j.oregeorev.2017.06.020

Hein, J.R., Conrad, T., Mizell, K., Banakar, V.K., Frey, F.A., Sager, W.W., 2016. Controls on ferromanganese crust composition and reconnaissance resource potential, Ninetyeast Ridge, Indian Ocean.

Hein, J.R., Koschinsky, A., Halbach, P., Manheim, F.T., Bau, M., Kang, J.-K., Lubick, N., 1997. Iron and manganese oxide mineralization in the Pacific. Geol. Soc. Lond. Spec. Publ. 119, 123–138. https://doi.org/10.1144/GSL.SP.1997.119.01.09

Hein, J.R., Mizell, K., Koschinsky, A., Conrad, T.A., 2013. Deep-ocean mineral deposits as a source of critical metals for high- and green-technology applications: Comparison with land-based resources. Ore Geol. Rev. 51, 1–14. https://doi.org/10.1016/j.oregeorev.2012.12.001

HORIBA (2021). ICP-OES spectrometers [en ligne]. Horiba [consulté le 31 août 2021]. Disponible sur : https://www.horiba.com/fra/products/scientific/elemental-analysis/icp-oes-spectrometers/

Horwitz, E.P., Dietz, M.L., Rhoads, S., Felinto, C., Gale, N.H., Houghton, J., 1994. A lead-selective extraction chromatographic resin and its application to the isolation of lead from geological samples. Anal. Chim. Acta 292, 263–273. https://doi.org/10.1016/0003-2670(94)00068-9

Ingri, J., Widerlund, A., Land, M., Gustafsson, Ö., Andersson, P., Öhlander, B., 2000. Temporal variations in the fractionation of the rare earth elements in a boreal river; the role of colloidal particles. Chem. Geol. 166, 23–45. https://doi.org/10.1016/S0009-2541(99)00178-3

ISO (2015b) ISO 14644-1/2015 Salles propres et environnements maitrisés apparentés – Partie 1 : classification de la propreté particulaire de l'air [en ligne]. ISO- Organisation internationale de normalisation [consulté le 27 avril 2018]. Disponible sur: https://www.iso.org/fr/standard/53394.html

Jacobsen, S.B., Wasserburg, G.J., 1980. Sm-Nd isotopic evolution of chondrites. Earth Planet. Sci. Lett. 50, 139–155. https://doi.org/10.1016/0012-821X(80)90125-9

Jeandel, C., 1993. Concentration and isotopic composition of Nd in the South Atlantic Ocean. Earth Planet. Sci. Lett. 117, 581–591. https://doi.org/10.1016/0012-821X(93)90104-H

Jeandel, C., Bishop, J.K., Zindler, A., 1995. Exchange of neodymium and its isotopes between seawater and small and large particles in the Sargasso Sea. Geochim. Cosmochim. Acta 59, 535–547. https://doi.org/10.1016/0016-7037(94)00367-U

Jones, C.E., Halliday, A.N., Rea, D.K., Owen, R.M., 1994. Neodymium isotopic variations in North Pacific modern silicate sediment and the insignificance of detrital REE contributions to seawater. Earth Planet. Sci. Lett. 127, 55–66. https://doi.org/10.1016/0012-821X(94)90197-X

Korschinek, G., Bergmaier, A., Faestermann, T., Gerstmann, U.C., Knie, K., Rugel, G., Wallner, A., Dillmann, I., Dollinger, G., von Gostomski, Ch.L., Kossert, K., Maiti, M., Poutivtsev, M., Remmert, A., 2010. A new value for the half-life of 10Be by Heavy-Ion Elastic Recoil Detection and liquid scintillation counting. Nucl. Instrum. Methods Phys. Res. Sect. B Beam Interact. Mater. At. 268, 187–191. https://doi.org/10.1016/j.nimb.2009.09.020

Koschinsky, A., Stascheit, A., Bau, M., Halbach, P., 1997. Effects of phosphatization on the geochemical and mineralogical composition of marine ferromanganese crusts. Geochim. Cosmochim. Acta 61, 4079–4094. https://doi.org/10.1016/S0016-7037(97)00231-7

Ku, T.L., Kusakabe, M., Nelson, D.E., Southern, J.R., Korteling, R.G., Vogel, J., Nowikow, I., 1982. Constancy of oceanic deposition of 10 Be as recorded in manganese crusts. Nature 299, 240. https://doi.org/10.1038/299240a0

Lebatard, A.-E., Bourlès, D., 2015. Quantification des processus superficiels et datation par les radionucléides cosmogéniques 10Be, 26Al et 36Cl. Quat. Rev. Assoc. Fr. Pour Létude Quat. 193–213. https://doi.org/10.4000/quaternaire.7339

Leclaire, L., 1984. RIDA - MD39 Cruise. Marion Dufresne R/V. https://doi.org/10.17600/84010511

Leclaire, L., 1975. NOSICAA - MD 06 Cruise. Marion Dufresne R/V. https://doi.org/10.17600/75010711

Levine, M. (2021) ICP-OES-ICP Chemistry, ICP-OES analysis, strengths and limitations [en ligne]. Technology Networks [consulté le 31 août 2021]. Disponible sur: https://www.technologynetworks.com/analysis/articles/icp-oes-icp-chemistry-icp-oes-analysis-strengths-and-limitations-342265#D3

Lubbe, H.J.L. van der, Frank, M., Tjallingii, R., Schneider, R.R., 2016. Neodymium isotope constraints on provenance, dispersal, and climate-driven supply of Zambezi sediments along the Mozambique Margin during the past ~45,000 years. Geochem. Geophys. Geosystems 17, 181–198. https://doi.org/10.1002/2015GC006080

Mizell, K., Hein, J.R., Koschinsky, A., Hayes, S.M., 2020. Effects of Phosphatization on the Mineral Associations and Speciation of Pb in Ferromanganese Crusts. ACS Earth Space Chem. 4, 1515–1526. https://doi.org/10.1021/acsearthspacechem.0c00037

Moulin, M., Evain, M., 2016. PAMELA-MOZ05 cruise, Pourquoi pas ? R/V.

Nishiizumi, K., Imamura, M., Caffee, M.W., Southon, J.R., Finkel, R.C., McAninch, J., 2007. Absolute calibration of 10Be AMS standards. Nucl. Inst Methods Phys. Res. B 2, 403–413. https://doi.org/10.1016/j.nimb.2007.01.297

Nishiizumi, K., Winterer, E.L., Kohl, C.P., Klein, J., Middleton, R., Lal, D., Arnold, J.R., 1989. Cosmic ray production rates of 10Be and 26Al in quartz from glacially polished rocks. J. Geophys.

Res. Solid Earth 94, 17907–17915. https://doi.org/10.1029/JB094iB12p17907

Olu Karine, 2014. PAMELA-MOZ01 cruise,L'Atalante R/V.

Peppard, D.F., Mason, G.W., Maier, J.L., Driscoll, W.J., 1957. Fractional extraction of the lanthanides as their di-alkyl orthophosphates. J. Inorg. Nucl. Chem. 4, 334–343. https://doi.org/10.1016/0022-1902(57)80016-5

Piepgras, D.J., Jacobsen, S.B., 1988. The isotopic composition of neodymium in the North Pacific. Geochim. Cosmochim. Acta 52, 1373–1381. https://doi.org/10.1016/0016-7037(88)90208-6

Piepgras, D.J., Wasserburg, G.J., 1987. Rare earth element transport in the western North Atlantic inferred from Nd isotopic observations. Geochim. Cosmochim. Acta 51, 1257–1271. https://doi.org/10.1016/0016-7037(87)90217-1

Piepgras, D.J., Wasserburg, G.J., 1982. Isotopic Composition of Neodymium in Waters from the Drake Passage. Science 217, 207–214.

Rempfer, J., Stocker, T.F., Joos, F., Dutay, J.-C., Siddall, M., 2011. Modelling Nd-isotopes with a coarse resolution ocean circulation model: Sensitivities to model parameters and source/sink distributions. Geochim. Cosmochim. Acta 75, 5927–5950. https://doi.org/10.1016/j.gca.2011.07.044

Shimizu, H., Tachikawa, K., Masuda, A., Nozaki, Y., 1994. Cerium and neodymium isotope ratios and REE patterns in seawater from the North Pacific Ocean. Geochim. Cosmochim. Acta 58, 323–333. https://doi.org/10.1016/0016-7037(94)90467-7

Sousa, I.M.C., Santos, R.V., Koschinsky, A., Bau, M., Wegorzewski, A.V., Cavalcanti, J.A.D., Dantas, E.L., 2021. Mineralogy and chemical composition of ferromanganese crusts from the Cruzeiro do Sul Lineament - Rio Grande Rise, South Atlantic. J. South Am. Earth Sci. 108, 103207. https://doi.org/10.1016/j.jsames.2021.103207

Tachikawa, K., Athias, V., Jeandel, C., 2003. Neodymium budget in the modern ocean and paleo-oceanographic implications. J. Geophys. Res. Oceans 108. https://doi.org/10.1029/1999JC000285

Tachikawa, K., Handel, C., Dupré, B., 1997. Distribution of rare earth elements and neodymium isotopes in settling particulate material of the tropical Atlantic Ocean (EUMELI site). Deep Sea Res. Part Oceanogr. Res. Pap. 44, 1769–1792. https://doi.org/10.1016/S0967-0637(97)00057-5

Tanaka, T., Togashi, S., Kamioka, H., Amakawa, H., Kagami, H., Hamamoto, T., Yuhara, M., Orihashi, Y., Yoneda, S., Shimizu, H., Kunimaru, T., Takahashi, K., Yanagi, T., Nakano, T., Fujimaki, H., Shinjo, R., Asahara, Y., Tanimizu, M., Dragusanu, C., 2000. JNdi-1: a neodymium isotopic reference in consistency with LaJolla neodymium. Chem. Geol. 168, 279–281. https://doi.org/10.1016/S0009-2541(00)00198-4

Todt, W., Cliff, R.A., Hanser, A., Hofmann, A.W., 2013. Evaluation of a 202Pb–205Pb Double Spike for High - Precision Lead Isotope Analysis.*, in: Earth Processes: Reading the Isotopic Code. American Geophysical Union (AGU), pp. 429–437. https://doi.org/10.1029/GM095p0429

Toole, J.M., Warren, B.A., 1993. A hydrographic section across the subtropical South Indian Ocean. Deep Sea Res. Part Oceanogr. Res. Pap. 40, 1973–2019. https://doi.org/10.1016/0967-0637(93)90042-2

Ullgren, J.E., van Aken, H.M., Ridderinkhof, H., de Ruijter, W.P.M., 2012. The hydrography of the Mozambique Channel from six years of continuous temperature, salinity, and velocity observations. Deep Sea Res. Part Oceanogr. Res. Pap. 69, 36–50. https://doi.org/10.1016/j.dsr.2012.07.003

Vajda, N., LaRosa, J., Zeisler, R., Danesi, P., Kis-Benedek, Gy., 1997. A novel technique for the simultaneous determination of 210Pb and 210Po

using a crown ether. J. Environ. Radioact. 37, 355–372. https://doi.org/10.1016/S0265-931X(95)00059-J

von Blanckenburg, F., Belshaw, N.S., O'Nions, R.K., 1996. Separation of 9Be and cosmogenic 10Be from environmental materials and SIMS isotope dilution analysis. Chem. Geol. 129, 93–99. https://doi.org/10.1016/0009-2541(95)00157-3

White, W.M., Albarède, F., Télouk, P., 2000. High-precision analysis of Pb isotope ratios by multi-collector ICP-MS. Chem. Geol. 167, 257–270. https://doi.org/10.1016/S0009-2541(99)00182-5

Wilson, D.J., Piotrowski, A.M., Galy, A., McCave, I.N., 2012. A boundary exchange influence on deglacial neodymium isotope records from the deep western Indian Ocean. Earth Planet. Sci. Lett. 341–344, 35–47. https://doi.org/10.1016/j.epsl.2012.06.009

Yuan, H., Yuan, W., Cheng, C., Liang, P., Liu, X., Dai, M., Bao, Z., Zong, C., Chen, K., Lai, S., 2016. Evaluation of lead isotope compositions of NIST NBS 981 measured by thermal ionization mass spectrometer and multiple-collector inductively coupled plasma mass spectrometer. Solid Earth Sci. 1, 74–78. https://doi.org/10.1016/j.sesci.2016.04.001

CHAPTER 2 : ANALYTICAL METHODOLOGY

2.1. Introduction (french)

Ce second chapitre est dédié aux méthodes d'échantillonnages ainsi qu'aux techniques et protocoles expérimentales et analytiques développés et employés au cours de cette thèse.

En effet, pour l'étude géochimique et minéralogique des encroûtements Fe-Mn, il est nécessaire de mettre au point un protocole particulier - qui s'étend de l'échantillonnage des roches au traitement des résultats obtenus - tout en tenant compte des caractéristiques physico-chimiques particulières et uniques de ces oxydes (Hein, Koschinsky, 2014).

Cet axe de la thèse porte d'une part sur le protocole de sélection et de caractérisation minéralogique des échantillons. Et d'autre part, sur tous les protocoles géochimiques utilisés depuis la mise en solution des échantillons et obtention des solutions mères, jusqu'aux analyses, afin de garantir des résultats précis et de qualité. Il s'agit notamment de faire un point sur les différents protocoles chimiques mis au point pour la mesure des éléments traces (Charles et al., 2021), des éléments majeurs et des compositions isotopiques. Les instruments utilisés sont également présentés.

En fin de chapitre, une attention toute particulière est portée sur la géochronologie. Il s'agit d'un axe primordial sur lequel repose 52 analyses du rapport isotopique $^{10}Be/^{9}Be$. Ces analyses fournissent une résolution temporelle aux reconstructions océanographiques et géodynamiques. La datation absolue par étude des nucléides cosmogéniques est donc présentée dans cette partie ainsi que les appareils de pointe utilisés en collaboration avec le CEREGE à Aix-en-Provence.

2.1. Introduction (english)

This second chapter focusses on sampling methods as well as experimental and analytical techniques and protocols developed and employed during this PhD project, taking into account the particular physicochemical characteristics of the Fe-Mn crusts (Hein, Koschinsky, 2014),

This part of the thesis focuses on the protocol for the selection and mineralogical characterisation of samples. And on the other hand, on all the geochemical protocols used from the dissolution of the samples and obtaining the mother solutions, to the analyses, in order to guarantee accurate and high quality results. The different chemical procedures developed for the analyses of trace elements (Charles et al., 2021), major elements and isotopic compositions will be described in parallel with the rapid presentation of the analytical instruments.

At the end of the chapter, a particular attention is given to the geochronology acquired by studying cosmogenic isotopes in order to obtain absolute data. It provides oceanographic and geodynamic reconstructions with a temporal resolution. This is an essential part of the PhD project, with 52 analyses of the $^{10}Be/^{9}Be$ isotopic ratio. The application of this methodology on Fe-Mn crusts is presented in this section, as well as the highly specialized and advanced equipment used in collaboration with the CEREGE – Aix en Provence.

2.2. Selection of samples and preparation of sub-samples

2.2.1. Dredges and samples

The ferromanganese crusts studied here come from 15 different dredging operations, carried out during 4 oceanographic missions presented above (see Chapter 1). During the PAMELA missions, a precise mapping of several key areas of the Mozambique Channel (i.e., archipelago of French scattered islands, Davie Ridge) was obtained by using the Seabat 7150 (Reson) deep sea multibeam sounder equipped on the "Pourquoi pas?". The topographic monitoring of the seabed and its structures (bathymetry) as well as its detailed imagery made it possible to collect as much information as possible on the deep morphologies, and thus, to target optimal dredging areas. The location of the different dredges can be seen in figure 1.2 (Chapter 1). The GPS coordinates as well as the lengths of dredger tracks are available in appendix 1.

In this study, 27 samples are from the first PAMELA mission in the Mozambique Channel, PAMELA-MOZ1 (Olu, 2014) and 4 samples came from the PAMELA-MOZ5 oceanographic campaign (Moulin, Evain, 2016). At the same time, 2 samples were dredged by the MNHN and added to the collection of this thesis, in order to enrich the analyzes of the project with a milestone to the south of the canal (MD-06 Nosicaa; DR75-0012; Leclaire, 1975) and a milestone in the north of the Davie ridge (MD-39 Rida; DR84-0026. Leclaire, 1984). The ferromanganese crusts studied during this phD are distributed over a transect of more than 3,500 km from the Plateau des Aiguilles, in the south, to the Îles Glorieuses, to the north of the canal, and cover the surface, intermediate and deep-water masses of the sector, with dredges between 170 and 2650 m deep.

Of these ferromanganese crusts, 33 were selected for the study of modern circulation of intermediate and deep currents of Mozambique Channel. The study of the temporal evolution of currents is based on three Fe-Mn crusts (for 52 layers). Four other Fe-Mn crusts (for 61 layers) were selected for the study of paleogeographic events. Finally, a crust located less than 300 km from the coast was retained to evaluate the influence of the continental margin on the isotopic compositions as mentioned by some authors in their studies (Conrad et al., 2017; Guan et al., 2017; Hein et al., 2013, 1997).

2.2.2. Sample selection criteria

All these Fe-Mn crusts were chosen and incorporated into this research project because of several morphological criteria, in addition to the criteria of location and depth. First, these are sufficiently hardened, unaltered crusts which do not crumble to the touch and which also do not have secondary alteration (e.g. carbonates, phosphates) filling vacuoles and fractured areas, which can strongly influence their geochemical signatures (Hein et al., 2016; Koschinsky et al., 1997; Mizell et al., 2020; Sousa et al., 2021).

This first macroscopic discrimination is carried out directly on board, on wet samples but must be redone in laboratory, after landing, on completely dry samples. The crusts thus selected have non (or little) eroded surfaces. Sampling of the superficial part, corresponding to the last deposits, is possible.

Then, and this is particularly the case for time series, the samples correspond to the thickest crusts (Figure 2.1) that the dredges allowed to collect during the oceanographic campaigns. Their thickness is an essential asset to establish a precise geochronology and sufficiently extensive to understand the currentology and geodynamics

of Mozambique Channel over time. They range from 10 mm to 100 mm. The depth of the samples is also essential in order to target all water masses in the channel. They vary between 170 m and 2650 m. Finally, the laminae of samples, resulting from the process of precipitation of the Fe-Mn oxy-hydroxides, must be visible macroscopically in order to distinguish and take samples, which correspond to "high-resolution" temporal stratigraphies (1 layer every 2 to 5 mm).

Figure 2.1. *Fe-Mn crust MOZ1-DR11-01 after having been sampled and of which all the stratigraphy carried out is visible. PAMELA MOZ1 (Olu, 2014).*

The 33 ferromanganese crusts selected for this project are named according to the dredges and oceanographic missions from which they originate. All the information is presented in appendix 2.

2.2.3. Preparation of powders and thin sections

2.2.3.1. Surface sampling – modern current patterns

Once the samples have been selected, the surface of crusts (the last accumulated deposits) is taken using a micro drill to obtain at least 100 to 200 mg of powder, which will be used for all geochemical, and geochronological analyzes. The micro drill consists of a 1 mm diameter diamond tip. By gently passing over the surface part of the sample, it is possible to recover powder corresponding to the 100 µm of crust recently deposited. The 33 Fe-Mn crusts of this project are treated and as many samples are taken.

2.2.3.2. Sampling of time series - geochronological survey of the Mozambique Channel

For the 8 time series (presentation and details in appendix 3), stratigraphies are also carried out by micro drill, laminae after laminae (Figure 2.1), while avoiding as much as possible allochthonous minerals (e.g. carbonates, volcanic clasts, phosphates). The sampled quantity is about 200 mg of each powder. The drilling thicknesses are 1 mm (± 0.25 to 1 mm) depending on cohesion of the rock.

The tip of the micro drill is cleaned between each sampling in order to limit any external and intra-sample contamination. It is rinsed with distilled water, dried with compressed air and scraped against pure quartz to remove any residue. It is then placed in an ultrasonic bath for 3 minutes before being rinsed, dried and used again.

2.2.3.3. Making thin sections – specific mineralogical study

Two samples from the time series were selected for in-depth mineralogical analyzes because of their particular locations. These are the MOZ-DR04-23, dredged off the Îles Glorieuses archipelago, whose study of minerals will make it possible to understand the volcanic events in this area over time, and the MOZ5-DR03-01, initially located on the Mozambique plateau (north of the Natal Valley) 200 km from the African coast, whose mineralogical study will allow to qualify

and quantify the detrital inputs from the continent recorded in the sample.

Large thin sections of 60 mm by 45 mm could be made on the unsampled half of the two crusts. They were made from sections of 10 cm high by 5 cm wide. The cutting of sections is carried out so that several thin sections overlap the same structures in order to facilitate the identification of structures and therefore of the analyzed layers. Five large polished thin sections are made on the MOZ1-DR04-23 crust and 3 on the MOZ5-DR03-01 crust. The 8 thin sections are presented in appendix 4, and will be analyzed for mineralogical observations with the FEG-SEM Qemscan ® (CSTJF TotalEnergies, Pau).

2.3. Mineralogical characterization

The mineralogy of some powders has been studied in order to make relevant links with geochemical results. X-ray diffraction (XRD) was used. It allowed to obtain reliable and fast results giving a first insight into the composition of the powders. At the same time, a scanning electron microscopy (SEM) method was used on the thin sections of samples MOZ1-DR04-23 and MOZ5-DR03-01 (see paragraph 2.3.2). The microstructures of these two samples were thus detailed with SEM coupled with the QemSCAN® software which is an English acronym meaning quantitative evaluation of materials by means of scanning electron microscopy. These two analytical methods are presented in this part.

2.3.1. X-ray diffraction

2.3.1.1. General principles of XRD

X-ray diffraction (XRD) makes it possible to obtain the composition, in percentage, of various minerals present in the powders sampled. This method involves irradiating the sample with a monochromatic beam of primary X-rays to generate different interactions with matter. The reticular planes, making up the various crystal lattices of minerals, will then diffract the incident X-rays according to Bragg law (Figure 2.2). This empirical law measures the distance separating two reticular planes, specific to each crystal cell of a mineral:

$$2\,d\,\sin\theta = n\lambda \qquad (1)$$

With d, the inter-reticular distance separating 2 planes of the same family; θ, the angle of the radiation emitted between the incident beam and the reticular plane; n, the order of diffraction and λ, the wavelength of the diffracted radiation. The diffracted rays are then analyzed by a detector. The results are obtained in the form of diffraction angle spectra, called a diffractogram.

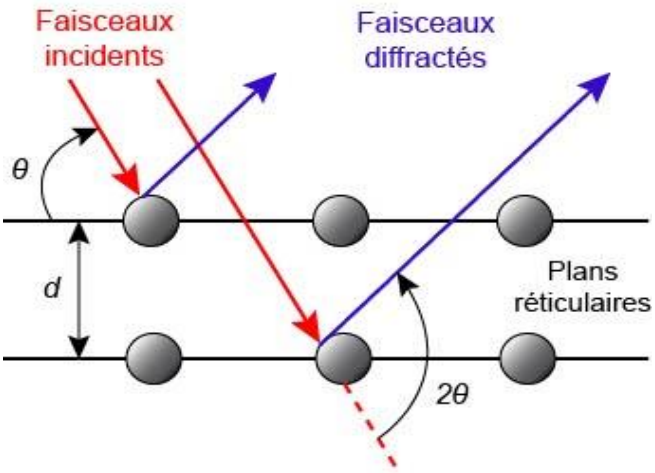

***Figure 2.2**. Diagram of incident and diffracted radiation by a crystal lattice according to Bragg law.*

2.3.1.2. Analysis conditions

On the day of analyzes, an excess volume of powder is placed on a circular amorphous silica sample holder. The surface must be smooth, without roughness or relief to avoid any angular shift.

The samples are analyzed with a Bruker D8 Advance diffractometer. This is a Bragg-Brentano type with θ-2θ mounting, that is to say that the x-ray tube remains stationary while the sample and the detector may be in motion. The plane of the sample has an angle θ with the incident beam, and the detector has an angle of 2θ with the diffracted beam. The spectrum is acquired over an angular range of 5 ° to 70 ° with a sampling step of 0.01 ° and an analysis time in steps of 1s.

The acquired diffractograms are looked at meticulously with the interpretation software "EVA" and its mineralogical database. Each peak corresponds to one or more minerals that can be identified and quantified.

2.3.2. Quantitative assessment of minerals using scanning electron microscopy

Qemscan ® (QUANTA 650, FEI) consists of measuring the mineralogical variability of samples from their chemical composition, at micrometer scale. It is a fully automated and non-destructive system. This method is based on scanning electron microscopy (SEM) coupled with energy dispersive X-ray spectroscopy (EDS) to produce elementary 2D maps, here of thin sections. 2D elementary maps are post-processed using software called Nanomin (FEI, Hillsboro, OR, USA). It allows automatic quantification of mineralogy by deconvoluting the X-ray spectra of each pixel analyzed. These analyzes were carried out at TotalEnergies – Centre Scientifique et Technique Jean Féger (CSTJF) in Pau, where the reference spectra are selected from a database of spectra measured on pure or synthetically created minerals.

One of the great advantages of MEB-SDE Qemscan ® is that it produces both a set of data on the overall mineralogical composition but also a stream of 2D images of each thin section studied: chemical maps (major elements and some trace elements), mineralogical maps and images acquired by backscattered electron detectors (BSD). Mineralogical maps can be combined with BSE imaging under the Nanomin software. BSE images can be acquired at nanometric resolution, allowing visualization and identification of the main detrital phases, including allochthonous minerals, present in the crusts analyzed. (Fialips et al., 2018).

2.4. Dissolution of elements

2.4.1. Conditions of preparation

The chemistry is carried out at the Laboratoire Géosciences Océan – UMR 6538 at the Institut Universitaire Européen de la Mer (IUEM). The clean room used is classified 1000 (ISO 6) according to ISO 14644-1 which specifies the classification of particulate air cleanliness (ISO, 2015b).

Demineralized water with a Milli-Q (Millipore ®) system at 18.2 MΩ is used for equipment cleaning and acid preparation. The reagents used such as nitric (HNO3) and hydrochloric acid (HCl; commercial grade, Merck, Darmstadt, Germany) and ultra-pure hydrofluoric acid (HF) (Hiperpur-plus ®, Panreac, Barcelona, Spain) are purified in the laboratory by a boiling distillation system.

2.4.2. Attack protocol for the analysis of major and trace elements and isotopes of Nd and Pb

With the exception of the powders used for Be dating (Chapters 4 and 5), we have chosen to carry out a total attack on the collected powders, which induces dissolution and the placing in solution of all the phases present in the samples, including metal oxides and silicates.

This choice of attack allows firstly minimizing the preparation time of the mother solutions (one

mother solution for all the analyses of trace elements, major elements and Nd, Pb isotopes) in favor of a large quantity of sub-samples. Indeed, from the 33 Fe-Mn crusts, a total of 162 samples is obtained, to which are added 10 chemistry blanks (powder-free beakers that have undergone the entire protocol in order to control the quality of the manipulations and reagents used) and 10 standards widely used by the scientific community including 8 of Fe-Mn oxides (Fe-Mn-1, GSMC-1, GSMC-2, GSMC-3, GSPN-2, GSPN-3, NOD-A-1, NOD-P-1) and 2 basalts (BEN, BHVO-2).

However, it was necessary to check that this total attack did not risk generating contamination of the isotopic signatures by dissolution of detrital clasts. After mineralogical examinations of the samples by X-ray Diffraction (XRD), the degree of crystallinity of the crusts is very low (average of 8%) and corresponds to detrital phases of the quartz and feldspar type in very small quantities. However, the Nd concentrations (the main element studied here) linked to these phases are extremely low and are not expected to have a significant impact on the geochemical signatures of the samples. The choice of a total attack was thus validated.

For the preparation of mother solutions used for elementary (trace, major) and isotopic (Nd, Pb) analyses, approximately 100 mg of powder is placed in an oven at 60°C for 24 hours. They are dissolved in 2 ml of 32N HF and 2 ml of 14N HNO3 in Savillex ® in Teflon at 120 ° C for 24 hours. The resulting solutions are then evaporated at 110 ° C. on a hot plate. After evaporation, 2 ml of 14N HNO3 are added and the Savillex ® are put back on a hotplate at 120 ° C for 12 hours. The samples are then evaporated a second time and taken up in 20 ml of 6N Quartex HCl to prepare the final solutions. No residual particles are observed in the mother solutions, which are transferred and stored in polypropylene bottles, previously washed with HNO3.

2.5. Elementary geochemistry

2.5.1. Characterization of major elements by ICP-OES

2.5.1.1. Preparation of solutions from mother solutions

For the analysis of major elements by Atomic Emission Spectrometer (with induction-coupled plasma) or ICP-AES, the concentrations of major elements in the mother solutions are first measured in order to calculate the dilution rates. Then, the calculated volumes of solutions are evaporated on a hot plate at 110 ° C and retaken in 0.3N HNO3 for measurements, in order to have total dilution factors of between 1.10^{-6}g and 10.10^{-6}g of sample per g of ICP-AOS solution. An internal boron standard is used, as specified in the protocol of Cotten et al. (1995), in order to certify a good reproducibility of the measurements.

The international standards (cited in the section 2.4.2) are also prepared and analyzed under the same conditions as the samples in order to create a calibration range.

2.5.1.2. General principles of an ICP-OES

Measurements are carried out on an ICP-OES of Horiba Jobin Yvon® Ultima 2 type, within the IUEM. The sample in solution is placed at the level of the sample introduction system and then dispersed into fine droplets using a nebulizer (Figure 2.3).

This fluid is then brought to the plasma where all elements present are atomized and then excited. A spectrometer then measures the electromagnetic radiation emitted, and more precisely all photons

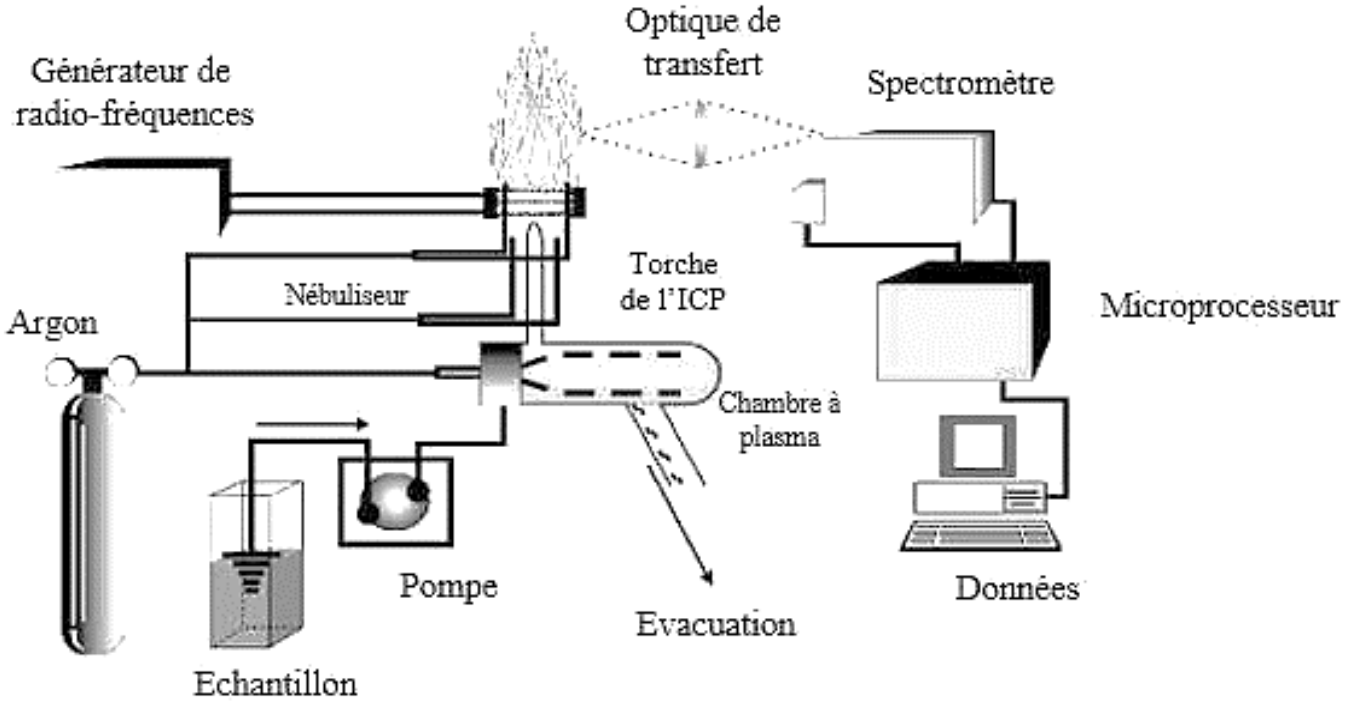

Figure 2.3. *Simplified scheme of the principle of elemental analysis by means of an ICP-AES (according to the manufacturer's documentation Horiba (2021) and Levine (2021).*

emitted at different wavelengths by return of the excited elements to their fundamental states. The photons emitted at different wavelengths are characteristic for each chemical element and the emission intensity is proportional to the amount of the element in the sample. Thus, the device allows a qualitative and quantitative analysis of the elements present in solution.

However, atomic emission is not an absolute method. A calibration step is required in order to calculate the relationship between the intensity emitted by an emission line and the concentration of associated element. The Fe-Mn and basalt oxide used as standards provide linear calibration curves over several orders of magnitude allowing analyzes over a wide range of concentrations.

2.5.1.3. "Typical" analysis session

A measurement sequence begins with a step of calibrating the machine with internal standard. Then, the first analyzes are carried out on 3 blanks in order to check quality of the work done in the clean room and to correct the results acquired from potential external inputs related to manipulations and reagents. The sequence is then established with the passage of 5 standards then an alternation of 1 BHVO-2 standard with 10 samples then 5 standards to conclude.

Standard measurements are used to calculate instrument drift during the analyzes. The relative standard deviation from recommended values is less than 3% for all major elements. Technical details and exact measurement conditions have been presented in Cotten et al. (1995).

2.5.2. Analyze of trace elements by ICP-MS after addition of Tm

- ***Paper 1*** *: Charles, C., Barrat, J.A. and Pelleter, E., 2021. Trace element determinations in Fe-Mn oxides by high resolution ICP-MS after Tm addition. Talanta 122446*

Talanta 233 (2021) 122446

Contents lists available at ScienceDirect

Talanta

journal homepage: www.elsevier.com/locate/talanta

Review

Trace element determinations in Fe–Mn oxides by high resolution ICP-MS after Tm addition

Claire Charles [a,b,*], Jean-Alix Barrat [b,c], Ewan Pelleter [a]

[a] IFREMER, Unité Géosciences Marines, Laboratoire Cycles Géochimiques (LCG), 29280, Plouzané, France
[b] Univ Brest, CNRS, UMR 6538 (Laboratoire Géosciences Océan), Institut Universitaire Européen de La Mer (IUEM), Place Nicolas Copernic, 29280, Plouzané, France
[c] Univ Brest, CNRS, UMR 6539 (Laboratoire des Sciences de L'Environnement Marin), LIA BeBEST, Institut Universitaire Européen de La Mer (IUEM), Place Nicolas Copernic, 29280, Plouzané, France

ARTICLE INFO

Keywords:
ICP-MS
Fe–Mn oxides
Trace elements
Rare earth elements
High-resolution
Tm spike

ABSTRACT

In order to propose an optimal analytical procedure specific to ferromanganese (Fe–Mn) oxides, we investigated different modes of data acquisition using inductively coupled plasma mass spectrometry (ICP-MS). The results of trace element and Rare Earth Element (REE) determination in eight Fe–Mn nodules and crusts (FeMn-1, GSMC-1, GSMC-2, GSMC-3, GSPN-2, GSPN-3, NOD-A-1 and NOD-P-1) are presented here. The analytical procedure involves chemical dissolution of the Fe–Mn oxides and addition of a thulium (Tm) spike. The correction of measured values from potential isobaric interferences was investigated using both corrections based on mono-elemental solutions, and data acquisition in the high-resolution mode. The obtained results show that the high-resolution acquisition mode is unnecessary to achieve high quality data for REE in Fe–Mn oxides. Using our revised method, we provide a consistent set of precise and accurate values for eight widely used but poorly characterized certified reference materials.

1. Introduction

Fe–Mn oxides are ubiquitous in the ocean and are produced by three main processes or combination of these [1–3]: (1) precipitation of Fe–Mn oxyhydroxide colloids from cold ambient seawater, (2) precipitation from pore water and (3) precipitation from hydrothermal fluids. Whereas Fe–Mn mineralizations that precipitate from the third process are mainly composed of Fe or Mn and Si, polymetallic nodules and Fe–Mn crusts that form from the two other mechanisms can be enriched in base metals (e.g., Cu, Ni) and critical metals (e.g., Co, REE, Zr, Nb, Y, Te and Pt) [4–6]. Consequently, Fe–Mn crusts and polymetallic nodules are now seen as a potential mineral resource and recent studies highlight the growing interest for REE and Y (REY) [e.g., [7]].

Besides their economic potential, REY can be used as geochemical proxies for deciphering between the different types of Fe–Mn oxides, and REY are now widely used in recently published discrimination diagrams [2,8]. Normalized REY patterns (e.g., Post-Archean Australian Shale; Mud of Queensland) [9,10] is an easy way to visualize anomalies for redox-sensitive elements (e.g., Ce ± Eu) as well as non-redox-sensitive elements (e.g., La, Gd, Y) which are linked to the behavior of REY during geochemical processes [2,11]. For example, as a redox-sensitive element and part of the REY suite [12,13], Ce (and its anomaly) can provide insights to identify the distinct water mass layers in the oceans [14–16]. Even though REE fractionation during surface-complexation on Mn and Fe oxides must be carefully assessed when studying Fe–Mn oxides [13], crucial information can be gleaned from comparative studies of REE and Y [12]. Apart from these anomalies (i.e., Ce, Eu, La, Gd, Y), normalized REY patterns are smooth functions of ionic radius and can be used to estimate the analytical quality of the data [2].

Therefore, it is of prime importance to establish a precise and time-effective method to quantify trace elements abundances, especially the REY, in Fe–Mn oxides. The most widely technique used for determining trace element concentrations is inductively coupled plasma mass spectrometry (ICP-MS). This technique offers several advantages such as very low limits of detection and high data accuracy. Moreover, ICP-MS is powerful in rapidly and simultaneously determining numerous trace elements. However, the presence of isobaric interferences, a common issue in mass spectrometry, can affect the results, as exemplified for REE [17–20]. Three alternatives exist to overcome isobaric interferences: (a) the purification of samples, (b) the correction of interferences using solutions of pure elements to estimate their contributions, and (c) data acquisition in high-resolution mode. The first is not suitable for our case:

* Corresponding author. IFREMER, Unité Géosciences Marines, Laboratoire Cycles Géochimiques (LCG), 29280, Plouzané, France.
E-mail address: claire.charles@ifremer.fr (C. Charles).

https://doi.org/10.1016/j.talanta.2021.122446
Received 8 January 2021; Received in revised form 14 April 2021; Accepted 18 April 2021
Available online 30 April 2021
0039-9140/© 2021 The Author(s). Published by Elsevier B.V. This is an open access article under the CC BY-NC-ND license (http://creativecommons.org/licenses/by-nc-nd/4.0/).

Table 1
ICP-MS operating conditions and measurement parameters.

RF power	1200 W
Sample uptake rate	100 µL/min
Coolant argon flow rates	16 L/min
Auxiliary argon flow rates	0.9 L/min
Nebuliser argon flow rates	1.031 L/min
Torch	Quartz
Nebuliser	PFA ST micro-flow
Spray chamber	Quartz cyclonic
Cones	Nickel
Low resolution mode (LRM)	$^{9}Be, ^{89}Y, ^{90}Zr, ^{93}Nb, ^{133}Cs, ^{135}Ba, ^{139}La, ^{140}Ce, ^{141}Pr, ^{143,146}Nd, ^{147,149}Sm, ^{151}Eu, ^{157}Gd, ^{159}Tb, ^{163}Dy, ^{165}Ho, ^{167}Er, ^{169}Tm, ^{174}Yb, ^{175}Lu, ^{177,178}Hf, ^{181}Ta, ^{232}Th, ^{238}U$
Medium resolution mode (MRM)	$^{31}P, ^{45}Sc, ^{47}Ti, ^{51}V, ^{52}Cr, ^{66}Zn, ^{69}Ga, ^{85}Rb, ^{88}Sr, ^{90}Zr, ^{93}Nb, ^{111}Cd, ^{133}Cs, ^{181}Ta,$
High resolution mode (HRM)	$^{39}K, ^{43}Ca, ^{45}Sc, ^{52}Cr, ^{139}La, ^{140}Ce, ^{141}Pr, ^{143,146}Nd, ^{147,149}Sm, ^{151,153}Eu, ^{155,157}Gd, ^{159}Tb, ^{163}Dy, ^{165}Ho, ^{167}Er, ^{169}Tm, ^{174}Yb, ^{175}Lu$
Acquisition mode	Mass Accuracy
Number of scans	3*2
Ion lens settings	Acquisition to obtain maximum signal intensity
Wash time	100 s

purifying the sample would add extra workload with the separation of elements. Consequently, fewer elements per run would be acquired (e.g., Eu without Ba) for a higher degree of work.

The main goal of this study is to compare the two other possibilities to correct measured abundances from potential isobaric interferences: the use of mono-elemental solutions and data acquisition using the high-resolution mode. The use of this latter method appeared to be well suited considering the typically high trace element and REE content in Fe–Mn oxides. To process, we decide to follow a well-established analytical procedure for trace element determination by ICP-MS based on the addition of Tm spike [21–23]. The addition of Tm spike in the samples before ICP-MS measurements produces a positive Tm anomaly in the resulting REE patterns, which can be used to calculate trace element abundances in the sample solutions. This procedure was initially developed to allow the determination of REE abundances after separation and concentration and intensively described [21,24–26]. We subsequently systematized this technique for all our samples because it simplifies the preparation of solutions [e.g., [22, 27]], and largely reduces the errors associated with the correction of signal drift during analytical sessions.

The resulting data produced in both low and high-resolution modes will be compared and a new set of reference values for a suite of commonly-used certified reference materials will be proposed.

2. Standards and analytical method

Eight certified reference materials of Fe–Mn oxides were analyzed in this study. They correspond to some of the most widely used Fe–Mn standards by the scientific community for the characterization of major and trace elements (FeMn-1, GSMC-1, GSMC-2, GSMC-3, GSPN-2, GSPN-3, NOD-A-1, NOD-P-1). Additionally, two other certified reference materials were also used to validate our ICP-MS measurements (BE-N and BCR-2, two well-characterized basalts). Another certified reference material (basalt BHVO-2) was analyzed to correct measured values from instrumental drift and for calibration purposes.

All sample preparations were conducted in a Class 1000 (ISO 6) clean laboratory. Deionized water purified with a Milli-Q system (Millipore®) at 18.2 MΩ was used for material cleaning and preparation of acid solutions. The following reagents were used: nitric and hydrochloric acid solutions (commercial grade, Merck, Darmstadt, Germany), and ultra-pure hydrofluoric acid solution (HIPERPUR-PLUS®, Panreac, Barcelona, Spain), all of them were purified by sub-boiling. About 1 g of each Fe–Mn certified reference materials was dried in an oven at about 60 °C for a period of one day. One hundred mg of powder were dissolved in closed screw-top Teflon vessels (Savillex®) at about 120 °C for one day with 2 ml of 32 N HF and 2 ml of 14 N HNO_3. The vessels were then opened for evaporation at about 110 °C. After evaporation to dryness, 2 ml of 14 N HNO_3 was added. The vessels were capped and put back on the hotplate for 12 h at about 120 °C. The samples were dried a second time and taken up in about 20 ml of Quartex 6 M HCl to prepare the "mother solutions". No residual particles were observed in the mother solutions. The solutions were then transferred to acid cleaned polypropylene bottles. For analysis, aliquots of each mother solution were spiked with a Tm solution (30 ng of Tm per mg of sample) and then evaporated to dryness. Finally, a few hours before measurements, the residues were taken up in 0.4 N HNO_3 containing traces of HF (6 drops of 32 N HF/l). The total dilution factors are comprised between 0.05 and 0.06 mg of sample per g of solution.

Trace element abundances were determined with a high-resolution inductively coupled plasma mass spectrometry (HR-ICP-MS) Thermo Electron Element XR (Thermo Scientific, Bremen, Germany) at the PSO ("Pôle Spectrométrie Océan") in Plouzané, France. This instrument can be operated in low (LRM, m/Δm approx. 300), medium (MRM, m/Δm = 4500) and high (HRM, m/Δm = 9200) resolution modes, depending on the required sensitivity and potential interferences for each element. Basic operating conditions and measuring parameters are summarized in Table 1. The REE were determined (a) in low-resolution mode to enhance sensitivity and were corrected for oxide and hydroxide interferences by analyzing solutions of ultra-pure water, Ba + Ce, Pr + Nd and Sm + Eu + Gd + Tb at the beginning of the measurement cycle, and (b) in high-resolution mode. A solution prepared with BHVO-2 was run after every three samples and used for both calibration and instrumental drift corrections following the procedure of Barrat et al. [21–24].

The raw data were first corrected for drift, procedural blank and interferences. Raw elemental concentrations were then calculated from corrected data, but these concentrations do not correspond to absolute abundances. At this stage, the Er and Yb measured concentrations were used to interpolate the content of Tm in the sample solutions. From these

Table 2
BHVO-2 working values used in this study, abundances (oxides in wt%, other elements in µg/g) and relative standard deviations (in italic) for the certified reference materials.

	Be	P_2O_5	K_2O	CaO	Sc	TiO_2	V	Cr	Zn	Ga	Rb	Sr	Y	Zr	Nb	Cs	Ba	Hf	Ta	Pb	Th	U
BHVO-2, working values																						
Barrat et al. (2012)	1.1	0.27	0.52	11.4	32.3	2.73	317	280	101	20.6	9.08	396	27.6	164.9	16.82	0.096	131	4.474	1.1	1.51	1.21	0.41
BE-N (n = 6)	**1.95**	**1.10**	**1.42**	**14.04**	**22.64**	**2.58**	**231**	**342**	**118**	**16.73**	**47.57**	**1409**	**30.90**	**260**	**103.0**	**0.75**	**1055**	**5.81**	**5.13**	**4.22**	**10.61**	**2.45**
RSD %	***2.12***	***2.02***	***2.77***	***1.57***	***1.32***	***3.04***	***1.60***	***1.37***	***1.87***	***1.78***	***3.58***	***1.80***	***0.83***	***1.79***	***1.72***	***3.47***	***1.52***	***1.90***	***6.57***	***3.82***	***1.59***	***1.16***
Jochum et al. (2016)	1.9	1.04	1.42	13.99	22.55	2.612	231.9	353.1	122.9	17.20	47.61	1392	29.44	272.9	113.2	0.73	1039	5.72	5.64	4.081	10.58	2.44
BCR-2 (n = 5)	**2.37**	**0.356**	**1.82**	**7.15**	**33.93**	**2.27**	**418**	**15.01**	**132**	**21.46**	**47.04**	**344**	**38.15**	**180**	**11.44**	**1.13**	**676**	**4.95**	**0.747**	**9.47**	**5.889**	**1.652**
RSD %	***3.48***	***1.44***	***0.98***	***2.18***	***1.34***	***1.18***	***0.93***	***1.85***	***2.87***	***1.10***	***0.63***	***1.00***	***0.76***	***0.75***	***0.83***	***1.08***	***0.48***	***0.80***	***0.95***	***3.98***	***0.65***	***0.44***
Jochum et al. (2016)	2.17	0.359	1.774	7.11	33.53	2.265	417.6	15.85	129.5	22.07	46.02	337.4	36.07	186.5	12.44	1.160	683.9	4.972	0.785	10.59	5.828	1.683
NOD-A-1 (n = 6)	**5.45**	**1.19**	**0.55**	**14.57**	**11.36**	**0.444**	**562**	**20.82**	**539**	**5.31**	**9.79**	**1472**	**128**	**289**	**42.61**	**0.58**	**1451**	**6.14**	**0.73**		**22.80**	**6.90**
RSD %	***2.44***	***1.77***	***1.04***	***1.93***	***1.53***	***1.35***	***1.44***	***5.66***	***1.32***	***2.17***	***1.32***	***1.90***	***1.82***	***1.22***	***1.07***	***2.23***	***1.48***	***1.74***	***1.09***		***1.70***	***1.80***
Flanagan and Gottfried (1980)		1.40	0.60	15.40		0.53	770		590			1750					1670					
Dulski (2001)											9.7	1467	116	233		0.56	1352	4			23.4	7
Axelsson et al. (2002)	5.60	1.36	0.60	16.06	12.4	0.51	660	20.9	800	6.30	10.6	1630	120	310	43.1	0.61	1530	5.80	0.76		25.1	7.00
Bau et al. (2014)													117									
Laurila et al. (2014)					12.1		614						122.6	321.5			1479	6.2			23.9	
NOD-P-1 (n = 6)	**2.21**	**0.44**	**1.15**	**2.86**	**9.67**	**0.429**	**446**	**14.21**	**1479**	**24.24**	**23.89**	**630**	**96.99**	**263**	**20.06**	**1.66**	**2537**	**4.13**	**0.35**		**15.63**	**4.03**
RSD %	***1.41***	***1.20***	***0.99***	***1.40***	***0.79***	***0.96***	***0.96***	***1.78***	***1.16***	***1.08***	***0.65***	***1.10***	***0.98***	***0.35***	***0.43***	***1.44***	***0.46***	***1.00***	***1.05***		***0.45***	***0.55***
Flanagan and Gottfried (1980)		0.46	1.20	3.10		0.50	570		1600			649					3350					
Dulski (2001)											24.5	680	91	298			2453				16.6	4.21
Axelsson et al. (2002)	2.30	0.47	1.20	3.15	9.70	0.45	510	13.3	2020	28.1	23.7	670	90.0	280	21.3	1.80	2690	4.20	0.33		16.7	4.00
Bau et al. (2014)													88.9									
Laurila et al. (2014)					10.25		492.5						93	287			2611	4			16.4	
FeMn-1 (n = 5)	**1.57**	**0.33**	**0.92**	**2.35**	**7.98**	**0.257**	**426**	**8.22**	**1742**	**23.16**	**12.01**	**682**	**73.76**	**298**	**12.34**	**0.78**	**3012**	**4.67**	**0.21**		**6.70**	**4.17**
RSD %	***2.72***	***2.90***	***5.69***	***4.64***	***2.86***	***3.46***	***2.15***	***8.47***	***1.57***	***1.63***	***2.99***	***2.80***	***1.93***	***1.50***	***2.23***	***3.65***	***1.85***	***1.63***	***3.33***		***1.80***	***1.46***
Webb et al. (2008)		0.352*		2.50	8.095*	0.29*	468.5*		1845		12.5*	683.3	69.11	325	13.4	0.85*	3158*	4.74	0.26*		6.87	4.39
Kricte (2011)	1.66	0.356	0.911	2.53	9.31	0.297	483		1821	31	12.9	683	69.1	326	13.8	0.822	3176	4.89	0.252		7.12	4.39
Bau et al. (2014)													66.7									
GSPN-2 (n = 5)	**3.53**	**0.49**	**0.994**	**2.44**	**14.08**	**1.19**	**423**	**13.53**	**809**	**20.42**	**15.24**	**835**	**149**	**558**	**45.65**	**0.83**	**1693**	**9.93**	**0.64**		**24.23**	**6.51**
RSD %	***0.44***	***1.22***	***0.91***	***1.10***	***0.91***	***1.29***	***0.81***	***4.66***	***2.43***	***1.34***	***1.18***	***0.90***	***0.80***	***0.68***	***0.88***	***0.85***	***0.69***	***0.74***	***0.92***		***0.77***	***0.98***
Wang et al. (1998)		0.58	1.08	2.67	13.7	1.37	425.9	17	918	27	16	869	133	618		0.84	1800	10			26	6.2
Dulski (2001)											16.2	875	144	614		0.89	1716	9.8			26.5	6.98
Laurila et al. (2014)					14.1		439.1						139.5	610			1729	9.55			25.1	
GSPN-3 (n = 5)	**1.75**	**0.32**	**1.094**	**2.09**	**10.03**	**0.47**	**403**	**11.03**	**1522**	**32.12**	**18.07**	**547**	**92.6**	**239**	**19.09**	**1.12**	**2370**	**3.90**	**0.31**		**15.34**	**3.77**
RSD %	***1.17***	***3.40***	***6.75***	***5.71***	***3.11***	***1.90***	***1.64***	***3.78***	***1.87***	***1.91***	***3.05***	***1.34***	***1.34***	***0.96***	***0.61***	***13.12***	***0.46***	***1.14***	***5.83***		***1.14***	***1.62***
Wang et al. (1998)		0.37	1.14	2.25	9.4	0.54	442	18	1600	38	17	561	84	256	21	1.2	2400	3.9	0.31		15	3.8
Dulski (2001)											18.8	565	87.4	274		1.26	2323	4.1			16.2	3.99
Bau et al. (2014)													83.3									
GSMC-1 (n = 5)	**5.35**	**1.45**	**0.70**	**4.34**	**11.56**	**1.93**	**574**	**14.11**	**618**	**2.93**	**9.72**	**1449**	**259**	**597**	**58.75**	**0.63**	**1745**	**10.27**	**1.17**		**20.12**	**12.07**
RSD %	***4.18***	***3.09***	***2.41***	***1.75***	***1.73***	***1.52***	***1.53***	***7.16***	***4.75***	***2.52***	***1.77***	***1.37***	***0.76***	***0.92***	***1.32***	***1.61***	***1.23***	***0.30***	***1.04***		***0.88***	***0.90***

(*continued on next page*)

Table 2 (*continued*)

	Be	P_2O_5	K_2O	CaO	Sc	TiO_2	V	Cr	Zn	Ga	Rb	Sr	Y	Zr	Nb	Cs	Ba	Hf	Ta	Pb	Th	U
Wang et al. (2003)		1.59	0.76	4.6		2.2	617		676		11	1481	239	656	58	0.6	1847	9.3	1.1		25	12
Bau et al. (2014)													244									
GSMC-2 (n = 5)	**5.27**	**3.08**	**0.67**	**7.09**	**10.60**	**1.68**	**586**	**12.58**	**547**	**3.03**	**9.01**	**1518**	**273**	**533**	**50.25**	**0.63**	**1852**	**8.78**	**0.97**		**15.16**	**11.60**
RSD %	***0.81***	***0.48***	***0.81***	***1.61***	***0.90***	***0.39***	***0.43***	***6.20***	***0.42***	***1.22***	***0.68***	***0.64***	***0.56***	***0.59***	***0.52***	***0.61***	***0.48***	***0.43***	***0.81***		***0.54***	***0.49***
Wang et al. (2003)		3.3	0.71	7.4	13	1.9	617		606		12	1551	251	602	53	0.9	1840	10.1			16.2	11
GSMC-3 (n = 5)	**4.86**	**3.48**	**0.79**	**7.55**	**10.70**	**1.72**	**524**	**12.48**	**538**	**4.05**	**10.59**	**1426**	**267**	**578**	**50.23**	**0.58**	**2029**	**9.62**	**1.12**		**14.19**	**11.25**
RSD %	***0.73***	***1.00***	***0.77***	***1.59***	***0.38***	***0.60***	***0.69***	***18.24***	***1.15***	***0.84***	***1.19***	***0.90***	***0.65***	***0.84***	***0.76***	***1.01***	***1.00***	***0.49***	***0.69***		***0.59***	***0.44***
Wang et al. (2003)		3.7	0.83	7.8	12.4	1.9	556		592		12	1466	247	642	53	0.5	2066	10			17	11

*Provisional.

abundances and the amount of Tm added during the chemical procedure, it was possible to calculate the element concentrations in the samples. The advantage of this calculations is that possible effects of the signal drift have no or negligible impact here [21,23]. Each solution was analyzed in triplicate and the results were averaged. The concentrations are provided in Tables 2 and 3, relative to our working values for the USGS basalt BHVO-2 [22]. In the event of future change to these BHVO-2 values, the data need only to be corrected by the ratio of the new and old values.

3. Results and discussion

The results and precision of the measurements as the relative standard deviation (RSD) are provided in Tables 2 and 3 For basalt standards BE-N and BCR-2, precisions are generally better than 4% for most elements and typically below 1.5% for the REE. Our data are in excellent agreement with the recommended values [28].

The eight Fe–Mn certified reference materials display high abundances of trace elements and REE. The results are also shown in Tables 2 and 3, while corresponding patterns are presented in Fig. 1. A Queensland alluvial sediment composite (MUQ) was used for normalization [9, 29] since it presents many well-characterized elements. Precision is mostly better than 4% for most elements and typically below 2.5% for the REE. Although the majority of our results are highly comparable to those obtained previously in the literature [2,30–37], important differences (>10%) exist between some of our data. For example, this is the cases for V (e.g., NOD-P-1 : 614 μg/g [37] vs. 562 μg/g in this study) and Zr (e.g., GSMC-2 : 602 μg/g [32] vs. 533 μg/g in this study). These variations are systematic for the eight Fe–Mn certified reference materials as illustrated in Fig. 2. Results from the other laboratories are higher than our data. Whereas the results obtained in this study for the basalt standards are in perfect agreement with the data published by Jochum et al. (2016) and used in the geochemical database GeoReM (Geological and Environmental Reference Materials). Our values are perfectly aligned on the x = y line (Fig. 2). These observations show the main differences between our data and those from previous studies come from a calibration bias and also confirm the high quality of our instrument calibration and the analytical procedure from homogeneous powder.

Comparisons between low-resolution and high-resolution REE results are provided in Table 4. The patterns and concentrations of REE are very similar whether in low or high-resolution modes. The Eu anomalies are calculated as the ratio of the normalized values of the element by the interpolation of the adjacent elements such as:

$$Eu\,/\,Eu^{*} = Eu_{MUQ}/(Sm_{MUQ} \times Gd_{MUQ})^{1/2} \quad (1)$$

and determined after data acquisition in low and high-resolution modes were also compared and appear to be very similar, within 3%, as well as in the basaltic certified references materials (Fig. 3). The isobaric interferences normally generated on Eu (BaO+, BaOH+) and on Gd (CeOH+, PrO+) are therefore well corrected in low-resolution mode. The RSD are generally less than 2% for the nodules and less than 1.5% for the crusts. The patterns are smooth (Fig. 1), which indicate excellent analytical quality [2]. The elementary ratios such as Zr/Hf [$(Zr/Hf)_{MUQ}$ = 1.25–1.71], La/Sm [$(La/Sm)_{MUQ}$ = 0.64–1.36] and Gd/Yb [$(Gd/Yb)_{MUQ}$ = 0.81–1.22] are characteristic of marine Fe–Mn oxides [2,8,38] and the well-known anomalies such as positive Ce anomalies (average Ce/Ce* = 1.73) and negative Y anomalies (average $(Y/Ho)_{MUQ}$ = 0.86) are clearly apparent [12,39–42]. The Ce anomaly is calculated using the same procedure as for the Eu anomaly calculation, such as:

$$Ce\,/\,Ce^{*} = Ce_{MUQ}/(La_{MUQ} \times Pr_{MUQ})^{1/2} \quad (2)$$

Although RSD from analyses obtained in high-resolution mode are generally better than 5%, they are nevertheless 1.5 to 14.5 times greater than those obtained in low-resolution mode. Results with RSD as low as

Table 3
BHVO-2 working values used in this study, REE abundances (μg/g) and relative standard deviations (in italic) for the certified reference materials.

	La	Ce	Pr	Nd	Sm	Eu	Gd	Tb	Dy	Ho	Er	Yb	Lu
BHVO-2, working values													
Barrat et al. (2012)	15.2	37.5	5.31	24.5	6.07	2.07	6.24	0.94	5.31	1.00	2.54	2.00	0.27
BE-N (n = 6)	**83.05**	**153.4**	**17.30**	**66.85**	**12.17**	**3.69**	**10.17**	**1.305**	**6.46**	**1.108**	**2.58**	**1.85**	**0.242**
RSD %	***0.88***	***0.79***	***1.12***	***0.90***	***1.02***	***1.04***	***2.07***	***1.28***	***0.77***	***0.44***	***0.76***	***0.88***	***0.35***
Jochum et al. (2016)	82.55	153.00	17.39	66.35	12.03	3.68	10.09	1.30	6.48	1.08	2.61	1.82	0.249
BCR-2 (n = 5)	**24.99**	**52.98**	**6.80**	**28.78**	**6.57**	**1.93**	**6.68**	**1.048**	**6.39**	**1.322**	**3.68**	**3.38**	**0.491**
RSD %	***0.72***	***0.79***	***0.67***	***0.71***	***0.54***	***0.82***	***0.67***	***0.44***	***0.75***	***0.73***	***0.76***	***0.49***	***0.95***
Jochum et al. (2016)	25.08	53.12	6.83	28.26	6.55	1.99	6.81	1.08	6.42	1.31	3.67	3.39	0.50
NOD-A-1 (n = 6)	**111.2**	**745**	**23.85**	**99.55**	**21.79**	**5.28**	**24.28**	**3.84**	**23.08**	**4.96**	**14.31**	**13.48**	**2.08**
RSD %	***1.68***	***1.75***	***1.74***	***1.70***	***1.81***	***2.29***	***2.08***	***1.63***	***1.68***	***1.73***	***1.93***	***1.69***	***1.79***
Flanagan and Gottfried (1980)	120	730		94	21	5	26		23		12	14	2.2
Dulski (2001)	112	743	24.3	93	19.8	5.4	24.9	3.9	23.5	4.9	14.6	13.7	2.2
Axelsson et al. (2002)	115	720	25.0	98.0	21.9	5.20	25.4	4.00	23.8	5.00	14.4	13.9	2.10
Bau et al. (2014)	115	792	24.8	103	22.3	5.51	26.1	3.98	24	5.06	15.1	14.1	2.27
Laurila et al. (2014)	115.4	750	25.1	104.3	22.8	5.5	25	4	24.1	5	14.2	14	2.2
NOD-P-1 (n = 6)	**106.4**	**319**	**31.40**	**132.2**	**31.87**	**7.68**	**30.28**	**4.71**	**26.29**	**5.00**	**13.42**	**12.70**	**1.82**
RSD %	***0.35***	***0.55***	***0.32***	***0.46***	***0.54***	***1.31***	***1.40***	***0.83***	***0.51***	***0.61***	***0.76***	***0.69***	***0.69***
Flanagan and Gottfried (1980)	104	290		120	30	7.5	28		27		12	13	1.8
Dulski (2001)	110	329	33	128	30	8	31.7	4.8	27.5	5.13	14.15	13.3	1.99
Axelsson et al. (2002)	105	305	31.0	130	31.0	7.60	30.4	4.90	27.1	5.00	13.6	12.9	1.80
Bau et al. (2014)	104	322	31.5	127	31.9	7.97	32.2	4.89	27.9	5.01	14	13.4	1.96
Laurila et al. (2014)	110.5	325	33	138	33.2	7.9	30.95	4.9	27.3	5.05	13.2	13.15	1.93
FeMn-1 (n = 6)	**66.69**	**107.8**	**14.22**	**62.62**	**13.65**	**3.53**	**15.68**	**2.48**	**15.81**	**3.37**	**9.77**	**9.90**	**1.49**
RSD %	***1.80***	***1.99***	***1.57***	***2.05***	***0.61***	***0.97***	***2.31***	***2.39***	***2.28***	***0.91***	***1.45***	***1.96***	***1.52***
Webb et al. (2008)	68.22	110	14.11*	62.95	14.03	3.8	15.63	2.52	15.8	3.42	9.80	10	1.59*
Kriete (2010)	68.2	109	14.3	63	14.1	3.75	15.6	2.53	15.8	3.44	9.81	9.88	1.57
Bau et al. (2014)	65	108	14.3	59.5	13.7	3.61	16.1	2.5	16.5	3.38	10.1	10.3	1.58
GSPN-2 (n = 5)	**175**	**617**	**49.19**	**201**	**47.07**	**11.60**	**47.33**	**7.42**	**41.81**	**8.00**	**21.47**	**20.22**	**2.97**
RSD %	***1.01***	***0.93***	***1.22***	***0.79***	***0.83***	***0.74***	***0.74***	***0.86***	***0.91***	***0.78***	***0.78***	***0.88***	***0.52***
Wang et al. (1998)	184	620	49	198	46	11	48	7.6	42	8.2	21	20	2.9
Dulski (2001)	191	657	53	201	46	12.5	50.6	7.82	44.7	8.4	23.2	21.7	3.3
Laurila et al. (2014)	180.1	607.05	49.5	204.3	47.6	11.6	46.55	7.45	42.15	7.85	20.65	20.35	3
GSPN-3 (n = 5)	**92.20**	**252**	**29.06**	**123**	**30.54**	**7.42**	**29.21**	**4.67**	**26.11**	**4.93**	**13.16**	**12.47**	**1.79**
RSD %	***0.36***	***0.75***	***0.44***	***1.03***	***1.08***	***1.01***	***1.59***	***1.17***	***1.74***	***1.71***	***1.91***	***0.76***	***0.95***
Wang et al. (1998)	96	249	29	121	31	7.6	28	4.6	27	5.1	13	12	1.8
Dulski (2001)	97	262	30.9	120	29	7.95	30.8	4.87	27.4	5	13.9	13.2	1.95
Bau et al. (2014)	95.9	267	29.1	124	31	7.46	29.6	4.68	26.8	4.92	13.8	12.9	1.9
GSMC-1 (n = 5)	**326**	**1246**	**68.74**	**283**	**58.40**	**14.36**	**61.68**	**9.53**	**56.48**	**11.58**	**31.93**	**29.20**	**4.26**
RSD %	***1.76***	***1.73***	***0.84***	***1.16***	***0.80***	***0.99***	***1.08***	***0.70***	***0.51***	***0.65***	***0.47***	***0.57***	***0.18***
Wang et al. (2003)	352	1315	72	293	61	15	65	9.5	58	11.3	32	31	4.5
Bau et al. (2014)	349	1370	71			15.2	68.4	10.3	60.1	12.1	34.1	30.9	4.68
GSMC-2 (n = 5)	**317**	**1134**	**60.52**	**249**	**49.31**	**12.12**	**54.34**	**8.28**	**49.98**	**10.55**	**29.70**	**27.28**	**4.10**
RSD %	***0.49***	***1.40***	***0.53***	***0.48***	***0.44***	***0.49***	***0.63***	***0.58***	***0.60***	***0.55***	***0.53***	***0.46***	***0.57***
Wang et al. (2003)	323	989	63	246	49	12	58	8.1	52	10.5	30	28	4.2
GSMC-3 (n = 5)	**289**	**1014**	**58.06**	**240**	**49.27**	**12.19**	**54.53**	**8.24**	**48.95**	**10.24**	**28.49**	**26.34**	**3.91**
RSD %	***0.78***	***1.01***	***0.91***	***0.84***	***0.69***	***0.64***	***1.34***	***0.56***	***0.74***	***0.56***	***0.86***	***0.72***	***0.47***
Wang et al. (2003)	306	1080	62	246	51	12	55	8	51	10.2	29	27.4	4.2

*Provisional.

those acquired in low-resolution are conceivable in high-resolution provided exclusive usage of more concentrated solutions to enhance the entering signal. However, such protocol would generate an important risk of saturation of the collector in low-resolution requiring a substantial increase of the rinse time and overall cleaning procedure between each analytical session. Therefore, the high-resolution acquisition seems not to be relevant for REE characterization in Fe–Mn oxides.

4. Conclusion

In this study, the determination by ICP-MS of REE and other trace element abundances in eight certified reference materials of Fe–Mn oxides (FeMn-1, GSMC-1, GSMC-2, GSMC-3, GSPN-2, GSPN-3, NOD-A-1 and NOD-P-1) was investigating, using a Tm addition analytical procedure. Two different approaches were investigated for the correction of

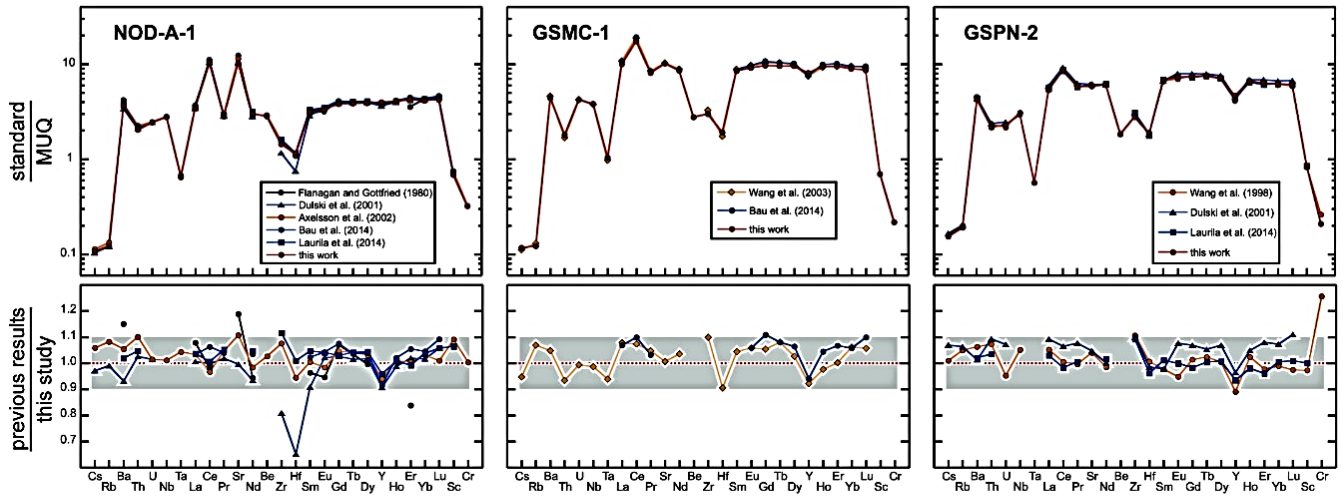

Fig. 1. MUQ normalized trace elements and REE patterns measured in LR mode from the certified reference materials NOD-A-1, GSMC-1 and GSPN-2.

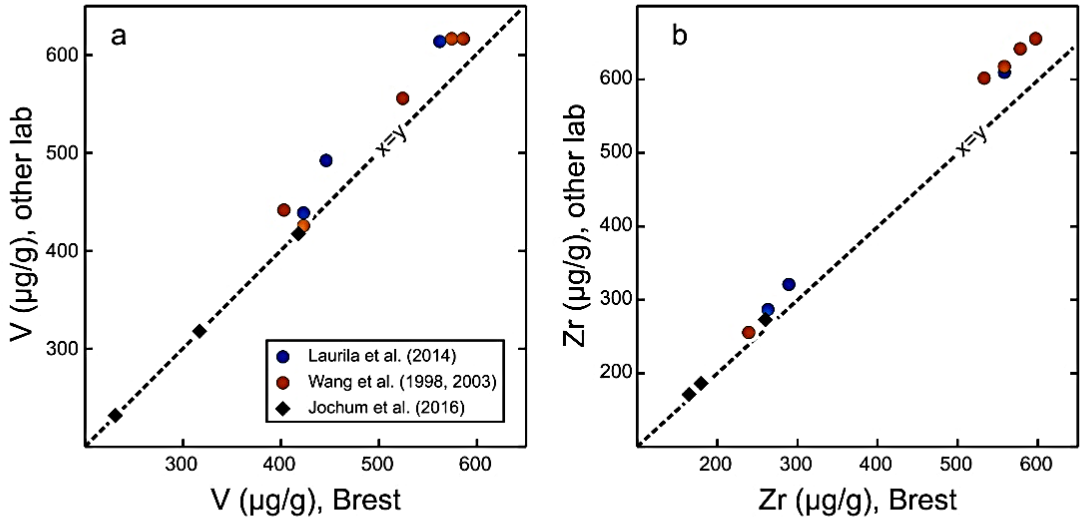

Fig. 2. A comparison of the V (µg/g) and the Zr (µg/g) values obtained in LR mode in this study and from literature studies showing a calibration bias. The black diamonds represent the basalt standards (including BHVO-2) and the points correspond to the Fe–Mn oxides.

isobaric interferences that can significantly affect measured concentrations during ICP-MS analyses: the use of mono-elemental solutions and the data acquisition in high-resolution mode. Our data demonstrate that the high-resolution acquisition mode is not the preferred choice for REE measurements in Fe–Mn oxides. Indeed, despite accurate data, the RSD are greater (<6.5%) than those obtained with the low resolution mode after correction of interferences using mono-elemental solutions (RSD < 2.5%).

The procedure was developed and validated using two silicate reference materials (BCR-2, BEN) providing precise and accurate data, before being applied to Fe–Mn oxides and calibrated with a silicate standard (BHVO-2). Although notable differences exist between our values and some data of the literature, the obtained results for two silicate certified reference materials (BCR-2 and BEN) are in excellent agreement with published reference values demonstrating the high-quality calibration of our analytical procedure. Using our revised protocol, we propose a new set of fair and accurate reference values for eight Fe–Mn certified reference materials that are widely used, but which were so far poorly characterized for trace elements.

As tracers of processes, sources and physicochemical parameters, REE and Y can provide crucial information concerning the mechanisms of formation of Fe–Mn oxides. REE and Y are also essential for deciphering between the different types of Fe–Mn oceanic deposits. Quantifying them precisely is a key step to discriminate mineral resources before targeting deposits and driving deep-sea exploration. Thus, this new set of data will serve as useful reference values for studies aiming at precisely quantifying REE (and other trace element) abundances in Fe–Mn oxides.

Declaration of competing interest

The authors declare that they have no known competing financial

Table 4
Comparisons between low and high-resolution REE values for the certified reference materials.

	La	Ce	Pr	Nd	Sm	Eu	Gd	Tb	Dy	Ho	Er	Yb	Lu
Basalts													
BE-N													
LR, n = 6 (*RSD%*)	83.1 (*0.88*)	153 (*0.79*)	17.30 (*1.12*)	66.85 (*0.90*)	12.17 (*1.02*)	3.69 (*1.04*)	10.17 (*2.07*)	1.305 (*1.28*)	6.46 (*0.77*)	1.108 (*0.44*)	2.58 (*0.76*)	1.85 (*0.88*)	0.242 (*0.35*)
HR, n = 6 (*RSD%*)	83.0 (*4.39*)	152 (*5.51*)	17.09 (*5.72*)	66.53 (*5.77*)	12.22 (*6.26*)	3.66 (*6.41*)	9.81 (*5.22*)	1.299 (*7.74*)	6.59 (*6.09*)	1.115 (*6.20*)	2.61 (*4.41*)	1.81 (*5.35*)	0.232 (*6.56*)
HR/LR	0.999	0.993	0.988	0.995	1.004	0.990	0.965	0.995	1.021	1.006	1.008	0.977	0.958
BCR-2													
LR, n = 5 (*RSD%*)	24.99 (*0.72*)	52.98 (*0.79*)	6.80 (*0.67*)	28.78 (*0.71*)	6.57 (*0.54*)	1.93 (*0.82*)	6.68 (*0.67*)	1.048 (*0.44*)	6.39 (*0.75*)	1.322 (*0.73*)	3.68 (*0.76*)	3.38 (*0.48*)	0.491 (*0.95*)
HR, n = 5 (*RSD%*)	24.50 (*1.33*)	52.83 (*3.04*)	6.77 (*3.60*)	28.61 (*2.99*)	6.45 (*3.35*)	1.97 (*1.51*)	6.70 (*2.38*)	1.036 (*5.95*)	6.31 (*2.22*)	1.304 (*2.24*)	3.67 (*3.83*)	3.35 (*5.97*)	0.480 (*4.20*)
HR/LR	0.980	0.997	0.996	0.994	0.980	1.021	1.003	0.989	0.987	0.987	0.998	0.991	0.977
Nodules													
NOD-A-1													
LR, n = 6 (*RSD%*)	111.2 (*1.68*)	745 (*1.74*)	23.85 (*1.74*)	99.55 (*1.70*)	21.79 (*1.81*)	5.28 (*2.29*)	24.28 (*2.08*)	3.84 (*1.63*)	23.08 (*1.68*)	4.96 (*1.73*)	14.31 (*1.93*)	13.48 (*1.69*)	2.08 (*1.79*)
HR, n = 6 (*RSD%*)	110.0 (*3.03*)	740 (*2.38*)	23.79 (*2.18*)	99.45 (*1.77*)	21.73 (*3.37*)	5.41 (*2.70*)	24.75 (*2.54*)	3.90 (*2.12*)	22.92 (*2.18*)	5.02 (*2.83*)	14.52 (*5.22*)	13.69 (*3.09*)	2.14 (*5.37*)
HR/LR	0.989	0.994	0.997	0.999	0.997	1.024	1.019	1.015	0.993	1.013	1.015	1.016	1.029
NOD-P-1													
LR, n = 6 (*RSD%*)	106.4 (*0.35*)	319 (*0.55*)	31.40 (*0.32*)	132.2 (*0.46*)	31.87 (*0.54*)	7.68 (*1.31*)	30.28 (*1.40*)	4.71 (*0.83*)	26.29 (*0.51*)	5.00 (*0.61*)	13.42 (*0.76*)	12.70 (*0.69*)	1.82 (*0.69*)
HR, n = 6 (*RSD%*)	107.1 (*3.02*)	321 (*2.20*)	31.84 (*2.38*)	134.5 (*2.14*)	32.41 (*2.63*)	7.97 (*3.30*)	30.85 (*2.35*)	4.74 (*3.75*)	27.03 (*4.00*)	5.16 (*3.14*)	13.58 (*4.33*)	13.08 (*4.61*)	1.93 (*5.73*)
HR/LR	1.006	1.005	1.014	1.018	1.017	1.037	1.019	1.007	1.028	1.031	1.012	1.030	1.058
FeMn-1													
LR, n = 6 (*RSD%*)	66.69 (*1.80*)	107.8 (*1.99*)	14.22 (*1.57*)	62.62 (*2.05*)	13.65 (*0.61*)	3.53 (*0.97*)	15.68 (*2.31*)	2.48 (*2.39*)	15.81 (*2.28*)	3.37 (*0.91*)	9.77 (*1.45*)	9.90 (*1.96*)	1.49 (*1.52*)
HR, n = 6 (*RSD%*)	65.43 (*6.05*)	106.0 (*4.78*)	14.20 (*4.02*)	62.63 (*3.20*)	13.75 (*4.85*)	3.64 (*3.75*)	15.44 (*2.85*)	2.48 (*4.72*)	15.74 (*5.68*)	3.36 (*4.57*)	9.89 (*5.42*)	10.07 (*2.03*)	1.51 (*3.98*)
HR/LR	0.981	0.983	0.999	1.000	1.008	1.029	0.985	0.999	0.995	0.996	1.012	1.017	1.014
GSPN-2													
LR, n = 5 (*RSD%*)	175 (*1.01*)	617 (*0.93*)	49.19 (*1.22*)	201 (*0.79*)	47.07 (*0.83*)	11.60 (*0.74*)	47.33 (*0.74*)	7.42 (*0.86*)	41.81 (*0.91*)	8.00 (*0.78*)	21.47 (*0.78*)	20.22 (*0.88*)	2.97 (*0.52*)
HR, n = 5 (*RSD%*)	174 (*2.44*)	609 (*2.86*)	47.81 (*2.47*)	199 (*1.87*)	46.31 (*2.37*)	11.62 (*2.51*)	46.82 (*1.62*)	7.27 (*2.45*)	41.61 (*2.68*)	7.85 (*2.52*)	21.85 (*2.38*)	19.74 (*1.85*)	2.87 (*4.45*)
HR/LR	0.997	0.986	0.972	0.990	0.984	1.002	0.989	0.980	0.995	0.981	1.018	0.976	0.964
GSPN-3													
LR, n = 5 (*RSD%*)	92.19 (*0.36*)	251 (*0.75*)	29.06 (*0.44*)	123 (*1.03*)	30.54 (*1.08*)	7.42 (*1.01*)	29.21 (*1.59*)	4.67 (*1.17*)	26.11 (*1.74*)	4.93 (*1.71*)	13.16 (*1.91*)	12.47 (*0.76*)	1.79 (*0.95*)
HR, n = 5 (*RSD%*)	90.19 (*5.24*)	245 (3.41)	28.51 (*3.93*)	122 (*3.28*)	30.32 (*3.59*)	7.37 (*2.78*)	28.60 (*2.50*)	4.63 (*3.05*)	25.57 (3.76)	4.81 (*4.76*)	13.47 (*4.47*)	12.40 (*4.43*)	1.81 (*6.17*)
HR/LR	0.978	0.974	0.981	0.995	0.993	0.993	0.979	0.991	0.979	0.977	1.024	0.994	1.016
Crusts													
GSMC-1													
LR, n = 5 (*RSD%*)	326 (*1.76*)	1245 (*1.73*)	68.74 (*0.84*)	283 (*1.16*)	58.40 (*0.80*)	14.36 (*0.99*)	61.68 (*1.08*)	9.53 (*0.70*)	56.48 (*0.51*)	11.58 (*0.65*)	31.93 (*0.47*)	29.20 (*0.57*)	4.26 (*0.18*)
HR, n = 5 (*RSD%*)	331 (*4.09*)	1237 (*3.19*)	67.41 (*3.80*)	283 (*3.14*)	58.54 (*3.69*)	14.45 (*3.03*)	63.71 (*3.91*)	9.32 (*3.45*)	56.53 (*2.89*)	11.60 (*3.60*)	32.32 (*3.54*)	29.16 (*4.07*)	4.21 (*3.65*)
HR/LR	1.015	0.994	0.981	1.000	1.002	1.006	1.033	0.978	1.001	1.002	1.012	0.999	0.988
GSMC-2													
LR, n = 5 (*RSD%*)	317 (*0.49*)	1134 (*1.40*)	60.52 (*0.53*)	249 (*0.48*)	49.31 (*0.44*)	12.12 (*0.49*)	54.34 (*0.63*)	8.28 (*0.58*)	49.98 (*0.60*)	10.55 (*0.55*)	29.70 (*0.53*)	27.28 (*0.46*)	4.10 (*0.57*)
HR, n = 5 (*RSD%*)	312 (*2.57*)	1117 (*1.97*)	59.64 (*2.78*)	246 (*2.56*)	49.54 (*1.11*)	12.25 (*2.70*)	54.64 (*3.18*)	8.16 (*2.58*)	49.78 (*1.71*)	10.55 (*2.85*)	29.75 (*2.37*)	27.32 (*3.18*)	4.11 (*3.98*)
HR/LR	0.986	0.986	0.986	0.988	1.005	1.011	1.006	0.986	0.996	0.999	1.002	1.002	1.004
GSMC-3													
LR, n = 5 (*RSD%*)	289 (*0.78*)	1014 (*1.01*)	58.06 (*0.91*)	240 (*0.84*)	49.27 (*0.69*)	12.19 (*0.64*)	54.53 (*1.34*)	8.24 (*0.56*)	48.95 (*0.74*)	10.24 (*0.56*)	28.49 (*0.86*)	26.34 (*0.72*)	3.91 (*0.47*)
HR, n = 5 (*RSD%*)	300 (*2.21*)	1042 (*1.19*)	59.98 (*1.46*)	249 (*1.56*)	51.09 (*1.01*)	12.62 (*2.21*)	56.64 (*2.50*)	8.58 (*0.76*)	50.24 (*1.71*)	10.53 (*0.76*)	29.24 (*2.08*)	27.33 (*1.88*)	4.04 (*2.71*)
HR/LR	1.039	1.028	1.033	1.038	1.037	1.035	1.039	1.042	1.026	1.028	1.027	1.038	1.032

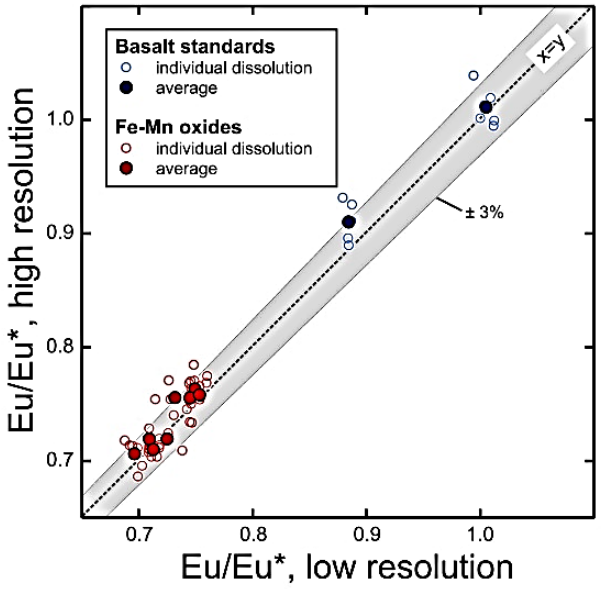

Fig. 3. A comparison of measured Eu/Eu* ratio in LR and HR modes for the basalt standards and the studied Fe–Mn oxides.

interests or personal relationships that could have appeared to influence the work reported in this paper.

Acknowledgements

We would like to thank Bleuenn GUEGUEN for her precious help during data acquisition. Claire CHARLES PhD is co-funded by TOTAL and IFREMER as part of the PAMELA (Passive Margin Exploration Laboratories) scientific project. We gratefully acknowledge Editor-in-Chief Jean-Michel KAUFFMANN, the two anonymous reviewers and Germain BAYON for thorough and thoughtful comments that significantly improved the manuscript. The PAMELA project is a scientific project led by Ifremer and TOTAL in collaboration with the Université de Bretagne Occidentale, Université Rennes 1, Université Pierre and Marie Curie, CNRS and IFPEN.

References

[1] J.R. Hein, A. Koschinsky, P. Halbach, F.T. Manheim, M. Bau, J.-K. Kang, N. Lubick, Iron and manganese oxide mineralization in the Pacific, Geol. Soc. Lond. Spec. Publ. 119 (1997) 123–138, https://doi.org/10.1144/GSL.SP.1997.119.01.09.

[2] M. Bau, K. Schmidt, A. Koschinsky, J.R. Hein, T. Kuhn, A. Usui, Discriminating between different genetic types of marine ferro manganese crusts and nodules based on rare earth elements and yttrium, Chem. Geol. 381 (2014) 1–9, https://doi.org/10.1016/j.chemgeo.2014.05.004.

[3] K. Schmidt, M. Bau, J.R. Hein, A. Koschinsky, Fractionation of the geochemical twins Zr–Hf and Nb–Ta during scavenging from seawater by hydrogenetic ferromanganese crusts, Geochem. Cosmochim. Acta 140 (2014) 468–487, https://doi.org/10.1016/j.gca.2014.05.036.

[4] D.Z. Piper, Rare earth elements in ferromanganese nodules and other marine phases, Geochem. Cosmochim. Acta 38 (1974) 1007–1022, https://doi.org/10.1016/0016-7037(74)90002-7.

[5] J.R. Hein, T.A. Conrad, H. Staudigel, Seamount Mineral Deposits: a source of rare metals for high technology industries, Oceanography 23 (2010) 184–189.

[6] A. Koschinsky, J.R. Hein, Marine ferromanganese encrustations: archives of changing oceans, Elements 13 (2017) 177–182, https://doi.org/10.2113/gselements.13.3.177.

[7] Y. Zhong, Z. Chen, F.J. Gonzalez, X. Zheng, G. Li, Y. Luo, A. Mo, A. Xu, S. Wang, Rare earth elements and yttrium in ferromanganese deposits from the South China Sea: distribution, composition and resource considerations, Acta Oceanol. Sin. 37 (2018) 41–54, https://doi.org/10.1007/s13131-018-1205-5.

[8] P. Josso, E. Pelleter, O. Pourret, Y. Fouquet, J. Etoubleau, S. Cheron, C. Bollinger, A new discrimination scheme for oceanic ferromanganese deposits using high field strength and rare earth elements, Ore Geol. Rev. 87 (2017) 3–15, https://doi.org/10.1016/j.oregeorev.2016.09.003.

[9] A. Pourmand, N. Dauphas, T.J. Ireland, A novel extraction chromatography and MC-ICP-MS technique for rapid analysis of REE, Sc and Y: revising CI-chondrite and Post-Archean Australian Shale (PAAS) abundances, Chem. Geol. 291 (2012) 38–54, https://doi.org/10.1016/j.chemgeo.2011.08.011.

[10] B.S. Kamber, A. Greig, K.D. Collerson, A new estimate for the composition of weathered young upper continental crust from alluvial sediments, Queensland, Australia, Geochem. Cosmochim. Acta 69 (2005) 1041–1058, https://doi.org/10.1016/j.gca.2004.08.020.

[11] P. Lusty, J.R. Hein, P. Josso, Formation and occurrence of ferromanganese crusts: earth's storehouse for critical metals, Elements 14 (2018) 313–318, https://doi.org/10.2138/gselements.14.5.313.

[12] T. Kuhn, M. Bau, N. Blum, P. Halbach, Origin of negative Ce anomalies in mixed hydrothermal–hydrogenetic Fe–Mn crusts from the Central Indian Ridge, Earth Planet Sci. Lett. 163 (1998) 207–220, https://doi.org/10.1016/S0012-821X(98)00188-5.

[13] M. Bau, A. Koschinsky, Oxidative scavenging of cerium on hydrous Fe oxide: evidence from the distribution of rare earth elements and yttrium between Fe oxides and Mn oxides in hydrogenetic ferromanganese crusts, Geochem. J. 43 (2009) 37–47, https://doi.org/10.2343/geochemj.1.0005.

[14] Y.G. Liu, M.R.U. Miah, R.A. Schmitt, Cerium: a chemical tracer for paleo-oceanic redox conditions, Geochem. Cosmochim. Acta 52 (1988) 1361–1371, https://doi.org/10.1016/0016-7037(88)90207-4.

[15] C.R. German, T. Masuzawa, M.J. Greaves, H. Elderfield, J.M. Edmond, Dissolved rare earth elements in the Southern Ocean: cerium oxidation and the influence of hydrography, Geochem. Cosmochim. Acta 59 (1995) 1551–1558, https://doi.org/10.1016/0016-7037(95)00061-4.

[16] Y. Dou, S. Yang, C. Li, X. Shi, J. Liu, L. Bi, Deepwater redox changes in the southern Okinawa Trough since the last glacial maximum, Prog. Oceanogr. 135 (2015) 77–90, https://doi.org/10.1016/j.pocean.2015.04.007.

[17] E.H. Evans, J.J. Giglio, Interferences in inductively coupled plasma mass spectrometry, A review, J. Anal. At. Spectrom. 8 (1993) 1–18, https://doi.org/10.1039/JA9930800001.

[18] P. Dulski, Interferences of oxide, hydroxide and chloride analyte species in the determination of rare earth elements in geological samples by inductively coupled plasma mass spectrometry, Fresenius' J. Anal. Chem. 350 (1994) 194–203, https://doi.org/10.1007/BF00322470.

[19] S.M. Eggins, J.D. Woodhead, L.P.J. Kinsley, G.E. Mortimer, P. Sylvester, M. T. McCulloch, J.M. Hergt, M.R. Handler, A simple method for the precise determination of N= 40 trace elements in geological samples by ICPMS using enriched isotope internal standardisation, Chem. Geol. 134 (1997) 311–326, https://doi.org/10.1016/S0009-2541(96)00100-3.

[20] N.M. Raut, L.-S. Huang, S.K. Aggarwal, K.-C. Lin, Determination of lanthanides in rock samples by inductively coupled plasma mass spectrometry using thorium as oxide and hydroxide correction standard, Spectrochim. Acta Part B At. Spectrosc. 58 (2003) 809–822, https://doi.org/10.1016/S0584-8547(03)00016-8.

[21] J.A. Barrat, F. Keller, J. Amossé, R.N. Taylor, R.W. Nesbitt, T. Hirata, Determination of rare earth elements in sixteen silicate reference samples by icp-ms after Tm addition and ion exchange separation, Geostand. Newsl. 20 (1996) 133–139, https://doi.org/10.1111/j.1751-908X.1996.tb00177.x.

[22] J.A. Barrat, B. Zanda, F. Moynier, C. Bollinger, C. Liorzou, G. Bayon, Geochemistry of CI chondrites: major and trace elements, and Cu and Zn Isotopes, Geochem. Cosmochim. Acta 83 (2012) 79–92, https://doi.org/10.1016/j.gca.2011.12.011.

[23] J.A. Barrat, N. Dauphas, P. Gillet, C. Bollinger, J. Etoubleau, A. Bischoff, A. Yamaguchi, Evidence from Tm anomalies for non-CI refractory lithophile element proportions in terrestrial planets and achondrites, Geochem. Cosmochim. Acta 176 (2016) 1–17, https://doi.org/10.1016/j.gca.2015.12.004.

[24] J.A. Barrat, G. Bayon, X. Wang, S. Le Goff, M.L. Rouget, B. Gueguen, D. Ben Salem, A new chemical separation procedure for the determination of rare earth elements and yttrium abundances in carbonates by ICP-MS, Talanta 219 (2020) 121244, https://doi.org/10.1016/j.talanta.2020.121244.

[25] G. Bayon, J.A. Barrat, J. Etoubleau, M. Benoit, C. Bollinger, S. Révillon, Determination of rare earth elements, Sc, Y, Zr, Ba, Hf and Th in geological samples by ICP-ms after Tm addition and alkaline fusion, Geostand. Geoanal. Res. 33 (2009) 51–62, https://doi.org/10.1111/j.1751-908X.2008.00880.x.

[26] N. Freslon, G. Bayon, D. Birot, C. Bollinger, J.A. Barrat, Determination of rare earth elements and other trace elements (Y, Mn, Co, Cr) in seawater using Tm addition and Mg(OH)2 co-precipitation, Talanta 85 (2011) 582–587, https://doi.org/10.1016/j.talanta.2011.04.023.

[27] D. Ben Salem, J.A. Barrat, Determination of rare earth elements in gadolinium-based contrast agents by ICP-MS, Talanta 221 (2021) 121589, https://doi.org/10.1016/j.talanta.2020.121589.

[28] K.P. Jochum, U. Weis, B. Schwager, B. Stoll, S.A. Wilson, G.H. Haug, M.O. Andreae, J. Enzweiler, Reference values following ISO guidelines for frequently requested rock reference materials, Geostand. Geoanal. Res. 40 (2016) 333–350, https://doi.org/10.1111/j.1751-908X.2015.00392.x.

[29] M.G. Lawrence, B.S. Kamber, The behaviour of the rare earth elements during estuarine mixing—revisited, Mar. Chem. 100 (2006) 147–161, https://doi.org/10.1016/j.marchem.2005.11.007.

[30] F.J. Flanagan, D. Gottfried, USGS Rock Standards; III, Manganese-Nodule Reference Samples USGS-Nod-A-1 and USGS-Nod-P-1, USGS Numbered Series No. 1155, Professional Paper, U.S. Govt. Print Off., Washington, 1980, https://doi.org/10.3133/pp1155.

[31] Y. Wang, D. Luo, Y. Gao, H. Song, J. Li, W. Chen, Y. Teng, S. Zhou, A preliminary study on the preparation of four pacific ocean polymetallic nodule and sediment reference materials: GSPN-2, GSPN-3, GSMS-2 and GSMS-3, geostand, Newsl. 22 (1998) 247–254, https://doi.org/10.1111/j.1751-908X.1998.tb00697.x.

[32] X. Wang, Y. Gao, Y. Wang, S.I. Andreev, Three cobalt-rich seamount crust reference materials: GSMC-1 to 3, geostand, Newsl. 27 (2003) 251–257, https://doi.org/10.1111/j.1751-908X.2003.tb00726.x.
[33] P. Dulski, Reference materials for geochemical studies: new analytical data by ICP-ms and critical discussion of reference values, Geostand. Newsl. 25 (2001) 87–125, https://doi.org/10.1111/j.1751-908X.2001.tb00790.x.
[34] M. Axelsson, I. Rodushkin, J. Ingri, B. Öhlander, Multielemental analysis of Mn–Fe nodules by ICP-MS : optimisation of analytical method, Analyst 127 (2002) 76–82, https://doi.org/10.1039/B105706P.
[35] P.C. Webb, M. Thompson, P.J. Potts, J.S. Watson, C. Kriete, GeoPT23 - an International Proficiency Test for Analytical Geochemistry Laboratories - Report on Round 23 (Separation Lake Pegmatite, OU-9) and 23A (Manganese Nodule, FeMn-1), International Association of Geoanalysts: Unpublished report, 2008.
[36] C. Kriete, An evaluation of the inter-method discrepancies in ferromanganese nodule proficiency test GeoPT 23A, geostand, Geoanalytical Res 35 (2011) 319–340, https://doi.org/10.1111/j.1751-908X.2010.00055.x.
[37] T.E. Laurila, M.D. Hannington, S. Petersen, D. Garbe-Schönberg, Early depositional history of metalliferous sediments in the Atlantis II Deep of the Red Sea: evidence from rare earth element geochemistry, Geochem. Cosmochim. Acta 126 (2014) 146–168, https://doi.org/10.1016/j.gca.2013.11.001.
[38] J.R. Hein, T.A. Conrad, K. Mizell, V.K. Banakar, F.A. Frey, W.W. Sager, Controls on ferromanganese crust composition and reconnaissance resource potential, Ninetyeast Ridge, Indian Ocean, Deep Sea Research Part I: Oceanographic Research Papers 110 (2016) 1–19, https://doi.org/10.1016/j.dsr.2015.11.006.
[39] M.I. Leybourne, K.H. Johannesson, Rare earth elements (REE) and yttrium in stream waters, stream sediments, and Fe–Mn oxyhydroxides: fractionation, speciation, and controls over REE+Y patterns in the surface environment, Geochem. Cosmochim. Acta 72 (2008) 5962–5983, https://doi.org/10.1016/j.gca.2008.09.022.
[40] J.N. Pattan, G. Parthiban, Geochemistry of ferromanganese nodule–sediment pairs from Central Indian Ocean Basin, J. Asian Earth Sci. 40 (2011) 569–580, https://doi.org/10.1016/j.jseaes.2010.10.010.
[41] L. Surya Prakash, D. Ray, A.L. Paropkari, A.V. Mudholkar, M. Satyanarayanan, B. Sreenivas, D. Chandrasekharam, D. Kota, K.A. Kamesh Raju, S. Kaisary, V. Balaram, T. Gurav, Distribution of REEs and yttrium among major geochemical phases of marine Fe–Mn-oxides: comparative study between hydrogenous and hydrothermal deposits, Chem. Geol. 312 (2012) 127–137, https://doi.org/10.1016/j.chemgeo.2012.03.024, 313.
[42] Y. Ren, X. Sun, Y. Guan, Z. Xiao, Y. Liu, J. Liao, Z. Guo, Distribution of rare earth elements plus yttrium among major mineral phases of marine Fe–Mn crusts from the south China sea and western pacific ocean: a comparative study, Minerals 9 (2019) 8, https://doi.org/10.3390/min9010008.

2.6. Isotopic geochemistry

2.6.1. Isotopic composition in Nd by TIMS

2.6.1.1. Presentation of Nd

Neodymium (Nd) is one of the intermediate rare earth elements (REE) and has many isotopes of which only five are stable in nature (^{142}Nd, ^{143}Nd, ^{145}Nd, ^{146}Nd and ^{148}Nd) with abundances between 27,1 % et 5,7 %. Two of its isotopes have very long half-lives (^{144}Nd, ^{150}Nd) with respective abundances of 23,9 % et 5,6 %. The others have very short half-lives and are therefore less abundant in nature. The ^{143}Nd isotope comes in part from the decay of samarium (Sm), and more precisely of its radiogenic isotope ^{147}Sm, by radioactivity.

The Nd isotope variations being very small (due to the very long half-life of ^{147}Sm), the notation εNd is used. The latter corresponds to the difference measured between the value of ^{143}Nd/^{144}Nd ratio in the analyzed rock and the value of ^{143}Nd/^{144}Nd ratio of the Uniform Chondritic Reservoir (CHUR) model at the same age, the value of which is estimated at 0.512638 (Jacobsen and Wasserburg, 1980) :

$$\varepsilon Nd = \left(\frac{^{143}Nd/^{144}Nd\ (mesuré)}{^{143}Nd/^{144}Nd\ (CHUR)} \right) \times 10^4 \qquad (2)$$

This difference measure makes comparisons easier. The εNd can be negative or positive, corresponding to a less radiogenic or a more radiogenic system, respectively.

2.6.1.2. Separation of the Nd

From the stock solutions and therefore from the quantity of powder initially taken, a minimum Nd concentration of 115 µg / g of sample was measured and allowed to calculate the volume of aliquot to be taken in order to achieve minimum detection of 0.5 µg during analysis with a Thermo-Ionization Mass Spectrometer (TIMS). Between 2 ml and 21 ml of stock solution were collected.

The samples are purified in a chemical laboratory by elementary separation. This technique consists of eliminating all the elements, except the one whose isotopic composition we want to know and which will be analyzed with the spectrometer. This step is essential so that other elements cannot interfere with the emission of the analyzed element. The Nd separation procedure takes place in 2 steps by extraction chromatography (Table 2.1).

The first step is to separate the REEs from other elements present in the matrix. For this, Teflon columns containing a TRU-Spec type cation-exchange macroporous resin are used. This resin makes it possible to fix the lanthanides and the actinides complexed in HNO_3 1N but not the major elements. Then, the elution of REEs is done in HCl. After passing through the column, and recovery of REEs in aqueous phase, the solution is again evaporated on a hot plate at approximately 90 ° C.

The second step is to separate the Nd from the other REEs. The most commonly used method is extraction on a Teflon column containing another Ln-type chromatographic resin. This resin has the particularity of allowing migration of light REEs before heavy REEs thanks to its constant stability, which increases with the atomic number of the elements (Peppard et al., 1957).

Table 2.1. *Elution profile of Pb and Nd according to the used acids and resins.*

Etape	Acide et quantité	Colonne et résine
Conditionnement	*3ml HNO3 1M*	*Sr-Spec*
Conditionnement	*3ml HNO3 1M*	*TRU-Spec*
	Positionner Sr-Spec sur TRU-Spec	
Chargement de l'échantillon	*1 ml HNO3 1M*	*Sr-Spec et TRU-Spec*
Piégeage	*1 ml HNO3 1M*	*Sr-Spec et TRU-Spec*
	Désassembler les colonnes	
Poubelle (traces)	*3 ml HCl 2N*	*Sr-Spec*
Elution et récupération du Pb	3 ml HCl 6N	Sr-Spec
Conditionnement	*6 ml HCl 0,2N*	*Ln*
Poubelle (majeurs)	*2 ml HNO3 1M*	*TRU-Spec*
	Positionner TRU-Spec sur Ln	
Piégeage des REE	*3 ml HCl 0,2 N*	*TRU-Spec et Ln*
	Désassembler les colonnes	
Poubelle (Ce, La)	*9.5 ml HCl 0.2N*	*Ln*
Elution et récupération du Nd	5 ml HCl 0.3N	Ln

Thus, with HCl normalized to 0.2N, it is possible to separate lanthanum (La) and cerium (Ce) from other REEs. Then, with 0.3N HCl, the Nd is eluted and recovered. This method allows a complete separation of the elution peaks of different REEs during elution. After this last separation step, the sample is brought to dryness. It is then taken up in 3 µl of 1N HNO3 and ready to be deposited on a filament for introduction into the spectrometer.

It is important to note that the Ln resin is not changed after each extraction session, unlike the TRU-Spec resin. Ln resin can be changed after 6 months of use. A calibration of the columns is then compulsory by colorimetric method. It consists of taking successive fractions during the elution and adding erochromic black to it. The characteristic fraction of Nd changes from blue to pink when the element is present in solution. This technique thus makes it possible to establish a precise profile of the elution of Nd as presented in table 2.1.

2.6.1.3. General principles of a TIMS

The measurements are performed on a Thermo Scientific ™ Triton TIMS (Figure 2.4) within the IUEM. Thermo-ionization, or surface ionization, is the technique used to produce ion beams in the sources of TIMS mass spectrometers. In our case, the acquisition is done in double filament with an evaporator (carrying a sample) and an ionizer. It consists of evaporating and ionizing by heating chemical element to be analyzed, previously deposited on the evaporator filament. The filament feet are installed in the primary chamber and which will rotate in order to place the sample to be analyzed in front of the focusing lenses (Figure 2.4). After pumping, the filaments are traversed under vacuum by an electric current,

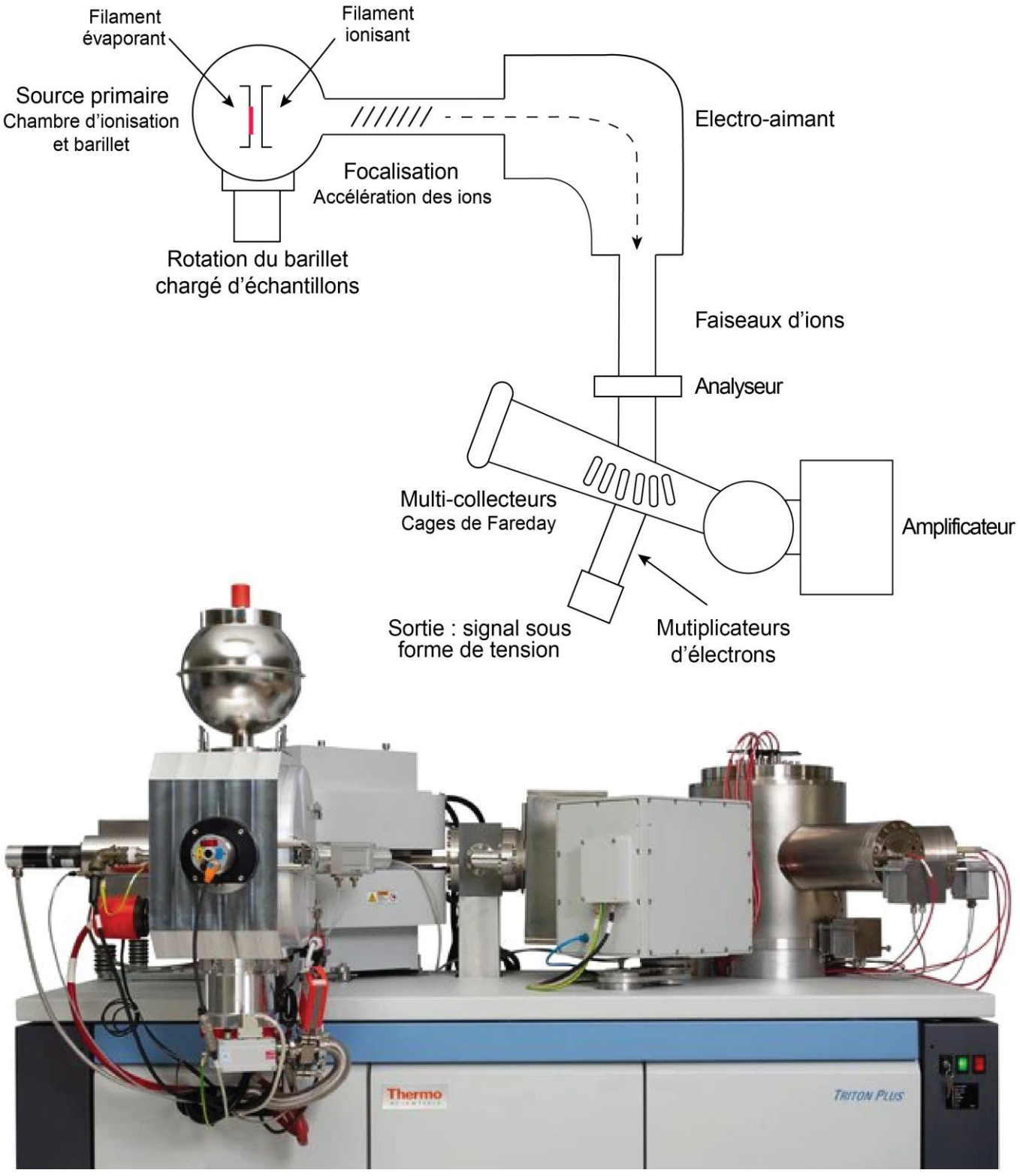

***Figure 2.4**. Simplified diagram of a TIMS Thermo Scientific ™ Triton from primary source to output intensities, based on manufacturer documentation.*

which causes them to heat up by the Joule effect. The heated sample evaporates and ionizes according to the law of Saha Langmuir:

$$\frac{N_+}{N_0} = exp\left[\frac{(W-I)}{kT}\right] \quad (3)$$

With N +, the amount of ions created; N_0, the amount of atoms escaping from the sample; W, the working function of the metal that makes up the filament; I, the ionization potential of the analyzed element; k, the Boltzmann constant (~ 8.62 × 10-5 eV / ° K) and T, the heating temperature. The ions are then focused and accelerated to form an ion beam. The latter passes through an electrostatic field, generated by an electromagnet, which will deflect the ions according to their masses, according to the Lorentz force:

$$F = qvB = \frac{mv^2}{r} \quad (4)$$

With F, the Lorentz force; q, v, and m respectively the charge, the speed and the mass of the particle; B, the magnetic field and r, the radius of curvature of the trajectory of the particle. These new ion beams (as many beams as there are types of isotopes) are then captured in the collectors and analyzed in the spectrometer. The results are expressed as isotope ratios, given by the measured relative intensities of the different ion beams.

2.6.1.4. "Typical" analysis session

The solutions taken up in 0,25N HNO_3 are loaded onto rhenium (Re) filaments. The deposit is dried using a current of 0.8 A. To improve the attachment of deposit on the evaporator filament, the latter is flashed at 2A before turning it off immediately. The filament holders are then installed on a barrel and positioned so that the evaporating filament faces the ionizing filament. The barrel is positioned in the TIMS primary source before ultra-high vacuum pumping is initiated. Once ultravacuum is reached, it is possible to start the sequence setting and the analyzes. Instrument drift is measured using the JNdi external standard (Tanaka et al., 2020).

With the Nd having an emission temperature close to 1550 ° C, the filaments are heated by electric currents ranging from 1A to more than 4A, until obtaining the ideal emission temperature. Then, the ion beam is focused, in particular by adjusting the position of the focusing lenses. Finally, measurements can be performed manually or automatically. During the thesis, both measurement modes were performed. The typical programmed sequence consists of 15 analysis blocks with 20 scans per block. This represents 300 averaged measurements for a sample, giving good statistical representativeness. The $^{143}Nd/^{144}Nd$ isotope ratios obtained at the output are normalized by the value of the CHUR as explained in paragraph 2.6.1.1, and thus noted εNd.

2.6.2. Isotopic composition in Pb by MC-ICP-MS

2.6.2.1. Presentation of Pb

Lead (Pb) has 38 known isotopes and only four isotopes have been observed to be stable in nature (^{204}Pb, ^{206}Pb, ^{207}Pb, ^{208}Pb) with respective abundances of 1,4%; 24,1%; 22,1% and 52,4%. Of these, only the ^{204}Pb isotope is not radiogenic. ^{208}Pb which is the major isotope, comes from the decay of thorium (^{232}Th) while ^{206}Pb and ^{207}Pb comes from the decay of uranium (^{238}U and ^{235}U respectively). The relative quantities of these

isotopes have therefore evolved over time, which is why studying the isotopic ratios $^{206}Pb/^{204}Pb$, $^{207}Pb/^{204}Pb$ and $^{208}Pb/^{204}Pb$ shows isotopic variations over time, essential for for paleoceanographic and paleogeological reconstructions.

2.6.2.2. Separation of the Pb

As Pb is highly concentrated in Fe-Mn crusts, it does not require any special analytical precautions. Therefore, all the Pb separations are carried out on the same aliquots taken for Nd separations (see paragraph 2.6.1.2).

Prior to the first Nd separation step, which consists in isolating the REEs from the rest of the matrix, columns filled with Sr-Spec type macroporous cation exchange resin are positioned on the TRU-Spec columns. The Sr-Spec resin then allows the Sr and Pb to be retained in 1N HNO_3 while the rest of the sample will flow directly into the TRU-Spec column for the separation of Nd. The columns are then disassembled from each other (Table 2.1).

Once the Sr and Pb are captured on the Sr-Spec resin, the Sr fraction is eluted in 2N standardized HCl and discarded. Pb, on the other hand, is recovered with standard 6N HCl (Horwitz and al., 1994 ; Vajda and al., 1997). The sample is then brought to dryness on a hotplate and stored.

2.6.2.3. General principles of a MC-ICP-MS

The MC-ICP-MS is a multi-element measuring instrument just like the ICP-MS (see paragraph 2.5.2; Charles and al., 2021). The sample is introduced into a nebulization chamber. The aerosol produced is injected into the plasma at 8000 ° C. The elements are atomized and ionized before being separated by the combination of a magnetic filter and an electrostatic filter. The difference is that an MC-ICP-MS allows ions to be collected on several detectors simultaneously. The ion beams created arrive in 9 Faraday cages where the ions of a given element hit the bottom, accumulate and are measured simultaneously before regaining their neutrality. At the output, the results are presented as isotope ratios resulting from the relative intensities measured. The ratios used here are $^{206}Pb/^{204}Pb$, $^{207}Pb/^{204}Pb$, and $^{208}Pb/^{204}Pb$.

This isotopic analysis technique differs from the one chosen for the isotopy of Nd. Indeed, the MC-ICP-MS has an ionization efficiency close to 100%, which allows the analysis of most elements, including those more complicated to measure by TIMS, such as Pb.

2.6.2.4. "Typical" analysis session

A few days before the analysis session, the residue is taken up with 0.5 ml of normalized 0.3N HNO3 and ready to be measured with a Multi-Collector Inductively Coupled Plasma Mass Spectrometer (MC-ICP-MS) Thermo Scientific ™ Neptune type present at the Department of Marine Geosciences of IFREMER

The device is set up as an ICP-MS: you must first let the instrument warm up, then set the plasma torch and calibrations for the resolutions. The first analytical step is to measure the Pb concentrations of samples in order to prepare the dilutions of the solutions to be analyzed.

Our analysis session is based on the study of White et al. (2000). A known concentration of thallium is also added in order to measure and correct instrumental mass bias. During the analyzes, the NIST NBS 981 external standard is measured (Yuan et al., 2016). The values of the standard will be used in data processing in order to interpolate measurements precisely and accurately. The typical sequence is set to pass 1 standard every two samples. It consists of 6 analysis blocks with 5 scans per block, so 30

averaged measurements for a sample. The data acquired are in the form of recorded intensity for each isotope ratio. They are then corrected for potential interferences between mercury (Hg) and Pb, the mass bias calculated from Tl and normalized through interpolation of NIST NBS 981 and certified values of Todt and al. (2013).

2.7. Absolute dating by radioactive decay of Be

The 8 time series of the thesis were dated according to two different methods. One is based on an empirical equation based on the concentration of cobalt (Co) in crusts. The other method is directly inherited from the radioactive decay of cosmogenic nuclides and provides absolute dating. This second technique was chosen, in order to bring a sufficiently fine and precise time scale to this study, to highlight major geological phenomena.

2.7.1. Cosmogenic nuclides

In order to date the crusts time series of this project, absolute dating by radioactive decay of the Be produced in situ was used. In this part, the main principles of cosmogeny are explained. Cosmogenic nuclides (or nuclei), such as ^{10}Be, represent all the isotopes formed in the upper atmosphere or in the lithosphere by nuclear reactions of particles originating from cosmic rays. These originate from two components: solar and galactic. The first has a weak and variable intensity while the second is more important, because of its origin, which is the Milky Way galaxy, with a relatively constant intensity.

Once in the upper atmosphere, cosmic rays interact with elements already in the atmosphere. This is the primary radiation (Figure 2.5). The radioactive isotopes of ^{10}Be are produced by nucleosynthesis and more specifically, by a process of spallation of oxygen (O) and nitrogen (N) atoms. Secondary radiation results from the impacts of primary radiation resulting in the formation of cosmic showers made up of neutrons and muons (Figure 2.5). The flux and energy of primary particles and secondary particles produced in nuclear cascades decrease exponentially depending on the thickness of the atmosphere traversed. Only about ~0,1 % of the secondary particles reach the lithosphere. At this point, the remaining cosmogenic nuclides will mainly interact with the silicon. The target mineral for ^{10}Be isotopes is therefore quartz (SiO2), a mineral highly present in sediments. It is the production of cosmogenic nuclides *in situ* (Figure 2.5).

Thus, more than 99% of ^{10}Be is found trapped in sedimentary deposits that accumulate over time (Lebatard, Bourlès, 2015). The half-life of ^{10}Be is relatively long ($T_{1/2}$ = 1,387 ± 0,012 Ma according to Chmeleff and al. (2010) ; Korschinek and al. (2010); Nishiizumi (2007)), which makes it possible to date samples by radioactive decay up to 10 Ma efficiently. However, the use of this isotope as a dating tool requires overcoming variations in environmental physicochemical conditions. Therefore, the ^{10}Be concentration should be normalized that of the stable isotope ^{9}Be (Bourlès et al., 1989).

2.7.2. Separation of Be by extraction chromatography

The ^{10}Be dating took place at the Centre Européen de Recherche et de l'Enseignement en Géosciences de l'Environnement (CEREGE) within the Laboratoire National des Nucléides Cosmogéniques (LN2C). The following protocol is based on 100 mg of powder per sample and was initiated by D. Bourlès in 1989. It must be carried out in a unit dedicated to preparation of samples for measurements of the concentration of atmospheric ^{10}Be in order to prohibit any contamination of samples analyzed

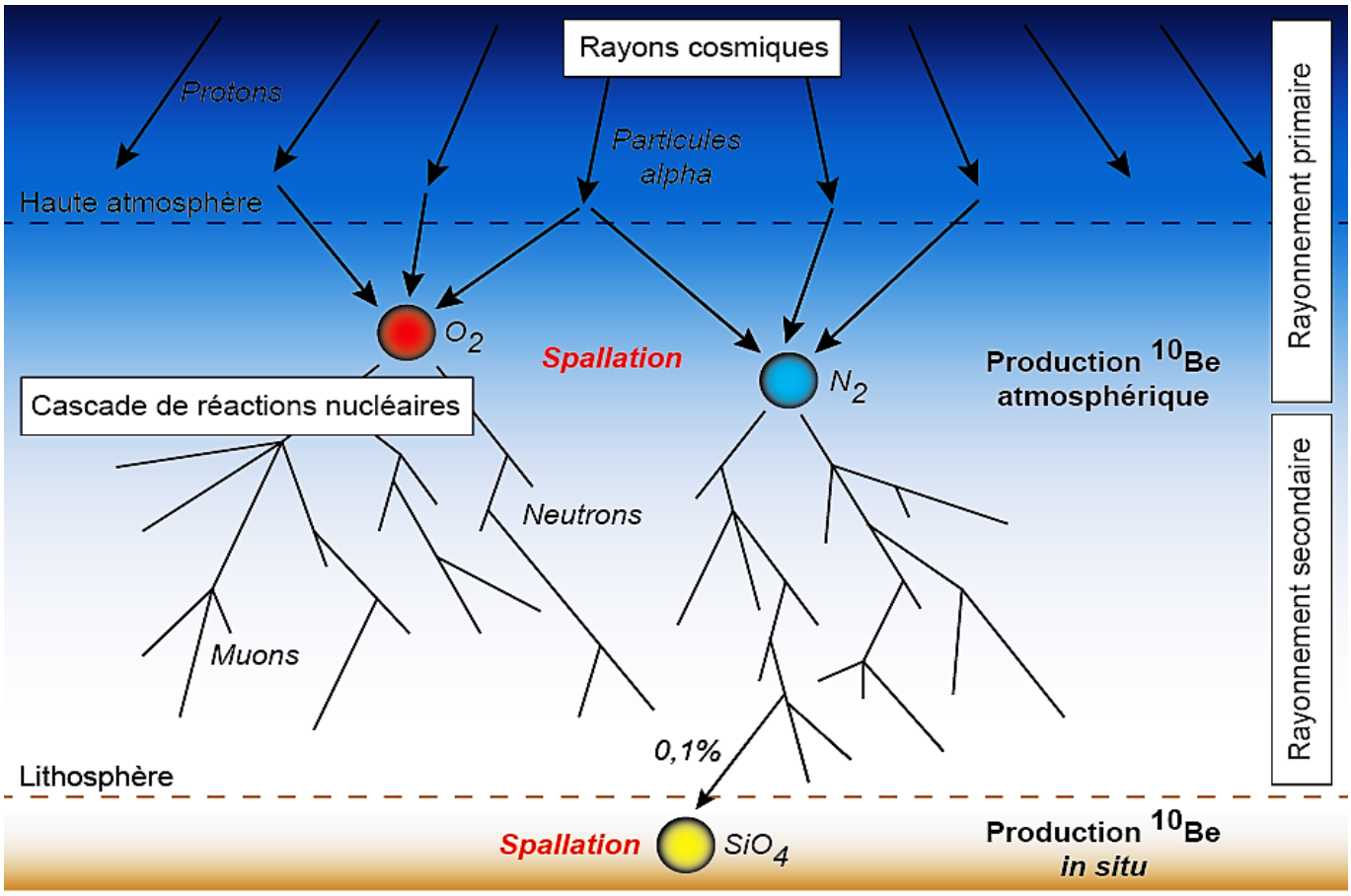

Figure 2.5. *Explanatory diagram of the production of atmospheric ^{10}Be and ^{10}Be in situ from cosmic rays and the multiple nucleosynthesis reactions in the atmosphere and in the lithosphere.*

for the measurement of ^{10}Be in-situ. The protocol is described for one solution but several samples are processed simultaneously as well as blanks.

The first step is the leaching of samples. It allows the total leaching of the powder by a leaching solution composed of acetic acid (CH3CO2H) and hydroxylamine hydrochloride (NH2OH, HCl). The latter will dissolve the inorganic phase of the crust and solubilize the oxy-hydroxides of Fe and Mn, main phases of authigenic Be (Bourlès et al., 1989; Ku et al., 1982; von Blanckenburg et al., 1996). The acetic acid will dissolve the Be absorbed by the inorganic phase (Bourlès et al., 1989b).

Once the sample has been mixed with the leaching solution (20 mL / g), it is placed in a sand water bath for 7 hours at 100 ° C ± 2 ° C. Following the heating time, the solution is separated from the solid residue by a series of centrifugation and collection of the supernatant. The final solution is weighed then an aliquot of 2 ml is taken and weighed in order to carry out the measurements of ^{9}Be concentration. These analyzes are carried out by Flameless Atomic Absorption Spectrometry (AAS)

The rest of the solution is weighed and a solution enriched in ^{9}Be (3×10^{-4}g of ^{9}Be) is added. This spike will act as a trainer. Its addition in a quantity much greater than the natural ^{9}Be (insignificant) will provide a sufficiently abundant target for the measurement of ^{9}Be/^{10}Be ratio.

The sample is then taken up in acidified water (50 % H_2O, 50 % HNO_3), evaporated and rinsed with HCl. The solution is then brought to a pH of 8.5

using ammonia (NH_3; 1 ml/10 ml of solution) in order to precipitate Be hydroxide ($Be(OH_2)$). The sample is centrifuged and the supernatant is discarded before taking up the residue in HCl.

The Be extraction phase can begin. The sample is injected into an ion exchange resin column with HCl. This first resin (Dowex 1 × 8) makes it possible to separate Be from Fe and Mn dissolved in Fe^{2+} et Mn^{2+} forms. This step is carried out twice given the high concentration of Fe and Mn in the ferromanganese crusts. When the column has finished eluting, the sample is again precipitated in an alkaline medium before being injected into a second resin. The resin (Dowex 50 × 8) then makes it possible to separate the Be from the boron (B). Once this step is completed, the solution is again brought to a pH of 8.5 and then centrifuged. The precipitate is dissolved with l'HNO_3 and transferred to a crucible to be oxidized in an oven at 800 ° C for 1 hour. Beryllium oxide (BeO) is ready to be cathoded.

2.7.3. Cathoding of targets

For cathoding, a mixture is made with BeO and niobium powder (Nb). It is used as a conductor to facilitate ionization of the sample in the spectrometer source and improve ion extraction efficiency. The mixture is funneled into a molybdenum cathode. It is then pressed for a few seconds to compact the powder. Each cathode is finally loaded onto the carousel which will be introduced into the source of the Particle Accelerator Mass Spectrometer (AMS).

2.7.4. Introduction and analysis by AMS

The purpose of AMS is to count the number of atoms of an element characterized by mass and atomic number. In the case of the thesis, it is the isotope ratio $^{9}Be/^{10}Be$ which is measured. It allows to deduce the concentration in ^{10}Be. These analyzes were carried out on the ASTER tandem accelerator (Accelerator for Earth Sciences, Environment, Risks) of 5MV at CEREGE. The principle of accelerator mass spectrometry is similar to that of conventional mass spectrometry. These are the same basic steps such as ionization of the sample, acceleration of the ion beam, separation of ions under a magnetic field according to their masses and charges, and detection. The difference is in the acceleration of the ions, which can go up to extraordinarily high kinetic energies (around ten MeV), thanks to a tandem type accelerator. This allows long-lived radionuclides such as cosmological nuclides ^{10}Be, ^{14}C, ^{26}Al, ou ^{36}Cl to be measured. These nuclides have half-lives that are too long to be measured by counting and too short to be sufficiently abundant during measurements by conventional mass spectrometry.

In the case of ^{10}Be, the limiting factor for magnetic field separation is the mass resolution and the level of separation of the magnet. That is, the mass difference between ^{10}Be and its isobar ^{10}B (which is 108 to 1015 times more abundant), is too small for them to be separated by conventional mass spectrometry. Thanks to the instrument's Tandreton accelerator, the ions are accelerated a first time from 0 to 4.5 V and then from 4.5 V to the output mass of the accelerator. The separation of ^{10}Be and of ^{10}B is done according to atomic number, through the Bethe-Bloch law. This law describes the energy loss of a fast charged particle passing through matter:

$$-\frac{dE}{dx} = K\frac{z^2}{v^2} \quad (5)$$

With E, the energy of the particle; x, the distance traveled; z, the atomic number of the particle; and

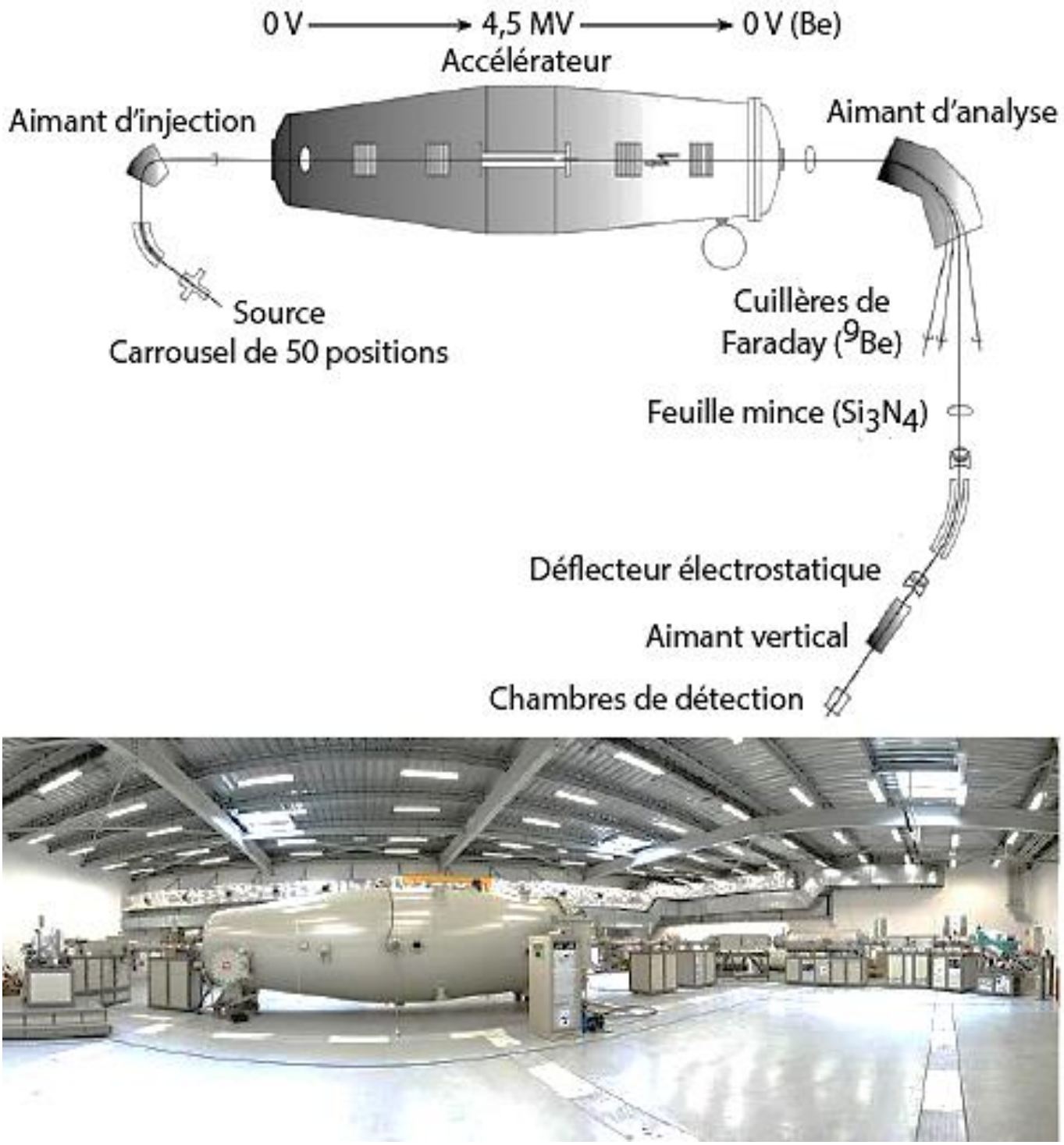

Figure 2.6. *Diagram and photo of the national ASTER instrument - Accelerator mass spectrometer located at LN2C - CEREGE (from Delunel (2010)).*

v, its speed. K is a constant, which depends on the material passed through by the particle. The amount of energy lost is therefore proportional to the atomic number. Thus, the energy loss of ^{10}B (z = 5) at the output of the material will be greater than that of ^{10}Be (z = 4) and will therefore be more deflected in the magnetic field. This characteristic of energy loss, in a small thickness of material, followed directly by a detection step, are only possible if the analyzed atom has a sufficiently high energy for these two steps to be carried out sequentially. It is in this respect that the acceleration of ions, between the source part and the analytical part by conventional mass spectrometry, is a crucial step.

At the exit of the accelerator, the ion beams are directed towards the magnet, which is responsible for deflecting the ions according to their masses. The strongly deflected $^{9}Be^{2+}$ are intercepted by a Faraday spoon while the remaining $^{10}Be^{2+}$ ions pass through a sheet of silicon nitride (Si_3N_4). This sheet favors the selection of Be cations of charge 4+ and reduces the cations of B. The final beam, thus cleaned, circulates to the final detector. It consists of 4 chambers whose internal pressure is regulated so that only Be ions can pass through each chamber. Thus, the electrical signal is analyzed and recorded.

2.7.5. "Typical" analysis session

The carousel on which the samples are positioned has 50 positions. A graphite target is loaded and used for cleaning after the samples have passed. About 3 NIST SRM 4325 standards are also added as well as a machine blank (^{9}Be commercial solution). The rest of the positions are dedicated to crust samples and chemical blanks.

The $^{10}Be/^{9}Be$, obtained at the output, is corrected from the $^{10}Be/^{9}Be$ ratio measured several times on a known standard. This correction is made using the NIST SRM 4325 certified standard, whose ratio values and the half-life of ^{10}Be have been corrected by Nishiizumu et al. (2007).

The relative uncertainty of the isotopic ratio is calculated according to the error propagation principle and the number of hits acquired in the final detector. To this is also added the analytical error resulting from the report measured from the standard (<1 %) :

$$\sigma_{ech} = \sqrt{\left(\frac{\sqrt{n}}{n}\right)^2 + (\sigma_{std})^2} \qquad (6)$$

With n, the number of hits acquired in the final detector and σ_{std} the relative analytical error resulting from the standard.

2.7.6. Calculations of concentrations and dates

Finally, the measured $^{10}Be/^{9}Be$ ratio will allow to calculate the concentrations of the cosmogenic isotope ^{10}Be produced in situ. The first step is to find the quantity of $n\ ^{9}Be$ atoms that was added to the sample during the chemistry protocol (see paragraph 2.7.2.):

$$n\ ^{9}Be = \frac{m_{spike} \times N}{M\ ^{9}Be} \qquad (7)$$

With, m_{spike} the spike mass (enriched solution) added; N, the Avogadro constant ($6{,}022 \times 10^{23}$) and $M\ ^{9}Be$ the molar mass of ^{9}Be. It is then possible to determine the concentration of ^{10}Be. It corresponds to the number of atoms $n\ ^{9}Be$ per gram of dissolved quartz noted m_{Qz}, from the following equation:

$$[^{10}Be] = \frac{\left(^{10}Be/^{9}Be_{ech} - {}^{10}Be/^{9}Be_{blc}\right) \times n\ {}^{9}Be}{m_{Qz}} \quad (8)$$

With, $^{10}Be/^{9}Be_{ech}$ the measured isotope ratio and $^{10}Be/^{9}Be_{blc}$ the measured isotope ratio of the blank.

The concentrations obtained thus allow a new accurate ^{10}Be/^{9}Be authigenic ratio to be calculated. The last step therefore consists in calculating the age of the samples from the following classical equation of radioactive decay:

$$\left(\frac{^{10}\mathrm{Be}}{^{9}\mathrm{Be}}\right)_{(t)} = \left(\frac{^{10}\mathrm{Be}}{^{9}\mathrm{Be}}\right)_{(0)}^{-\lambda t} \quad (9)$$

Where, $^{10}\mathrm{Be}/^{9}\mathrm{Be}_{(t)}$ corresponds to the authigenic ratio measured at time t; $^{10}\mathrm{Be}/^{9}\mathrm{Be}_{(0)}$ the initial authigenic ratio measured at the top of the sample where the losses due to radioactive decay begin; λ, the radioactive decay constant of Be measured from its half-life time ($T_{1/2}$ = 1,387 ± 0,012 Ma ; see paragraph 2.7.1.) and therefore t, the age of the sample in Ma. Depending on the age obtained and the depth of the laminae sampled over the time series, it is also possible to calculate the growth rates of the crusts.

2.7.7. Extrapolation of ages not measured by AMS

For each time series, between 3 and 9 dating were performed, for a total of 52 dating from the isotopic ratio ^{10}Be/^{9}Be. However, these 52 measurements do not allow us to date all the laminae of the 8 time series. In addition, as seen previously, this dating method cannot cover up to more than 10 Ma.

This is why the age of the laminae not dated by AMS and the temporal resolution beyond 10 Ma were developed from extrapolation of the growth rates (GR) acquired from absolute dating of Be. The growth rate of a laminae, here *b*, is calculated in a very simple way:

$$GR_b = \frac{Prof_b - Prof_a}{\hat{A}ge_b - \hat{A}ge_a} \quad (10)$$

With $Prof$ the depth in mm of the laminae on the sample and $\hat{A}ge$ the age measured from the AMS; *b* corresponds to the laminae for which the growth rate is being sought and *a* the previous laminae. Figure 2.7 illustrates the parameters of this calculation.

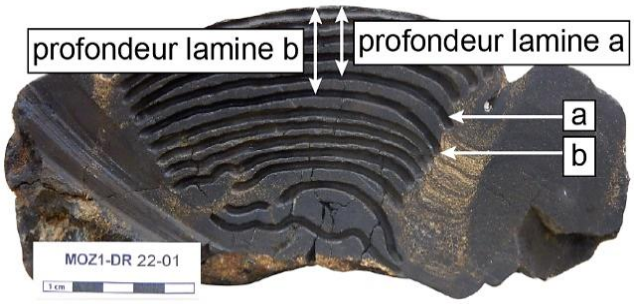

Figure 2.7. *Photo of the MOZ-DR22-01 time serie and its many laminae illustrating the calculation of growth rates.*

Once the growth rates have been calculated for each lamina whose age has been measured, it is possible to extrapolate the uncalculated age of the other laminae.

Two methods are possible: either the calculation takes into account the average of the calculated growth rates, or it depends on the last calculated growth rate. It was chosen to base the calculation on the last calculated growth rate. This choice is

motivated by the observation of a certain stability of growth rates at depth of the samples (therefore with time) while some more recent growth rates are completely different. This choice does not affect the results whose variations, according to the preferred method, are lower than the associated error.

The extrapolated age of a laminae, here noted c, is therefore calculated using the following equation, with the same parameters as presented for equation 10 previously seen:

$$\hat{A}ge_c = \frac{Prof_c - Prof_b}{GR_b} + \hat{A}ge_b \qquad (11)$$

Thus, all the laminae of the 8 time series studied in this project could be dated. However, a critical look should be made on dating greater than 10 Ma as they are not absolute and therefore do not take into account potential sedimentary gaps or erosion periods of crusts.

2.8. Bibliographical references

Arsouze, T., Dutay, J.-C., Lacan, F., Jeandel, C., 2009. Reconstructing the Nd oceanic cycle using a coupled dynamical – biogeochemical model. Biogeosciences 6, 2829–2846. https://doi.org/10.5194/bg-6-2829-2009

Arsouze, T., Dutay, J.-C., Lacan, F., Jeandel, C., 2007. Modeling the neodymium isotopic composition with a global ocean circulation model. Chem. Geol. 239, 165–177. https://doi.org/10.1016/j.chemgeo.2006.12.006

Bayon, G., Toucanne, S., Skonieczny, C., André, L., Bermell, S., Cheron, S., Dennielou, B., Etoubleau, J., Freslon, N., Gauchery, T., Germain, Y., Jorry, S.J., Ménot, G., Monin, L., Ponzevera, E., Rouget, M.-L., Tachikawa, K., Barrat, J.A., 2015. Rare earth elements and neodymium isotopes in world river sediments revisited. Geochim. Cosmochim. Acta 170, 17–38. https://doi.org/10.1016/j.gca.2015.08.001

Bertram, C.J., Elderfield, H., 1993. The geochemical balance of the rare earth elements and neodymium isotopes in the oceans. Geochim. Cosmochim. Acta 57, 1957–1986. https://doi.org/10.1016/0016-7037(93)90087-D

Bourlès, D., Raisbeck, G.M., Yiou, F., 1989. 10Be and 9Be in marine sediments and their potential for dating. Geochim. Cosmochim. Acta 53, 443–452. https://doi.org/10.1016/0016-7037(89)90395-5

Bourlès, D.L., Klinkhammer, G., Campbell, A.C., Measures, C.I., Brown, E.T., Edmond, J.M., 1989b. Beryllium in marine pore waters: geochemical and geochronological implications. Nature 341, 731–733. https://doi.org/10.1038/341731a0

Broecker, W.S., Peng, T., Beng, Z., 1982. Tracers in the sea. Lamont-Doherty Geological Observatory, Columbia University.

Charles, C., Barrat, J.-A., Pelleter, E., 2021. Trace Element Determinations in Fe-Mn Oxides by High Resolution ICP-MS after Tm Addition. Talanta 122446. https://doi.org/10.1016/j.talanta.2021.122446

Chen, J.H., Lawrence Edwards, R., Wasserburg, G.J., 1986. 238U,234U and232Th in seawater. Earth Planet. Sci. Lett. 80, 241–251. https://doi.org/10.1016/0012-821X(86)90108-1

Chmeleff, J., von Blanckenburg, F., Kossert, K., Jakob, D., 2010. Determination of the 10Be half-life by multicollector ICP-MS and liquid scintillation counting. Nucl. Instrum. Methods Phys. Res. B 268, 192–199. https://doi.org/10.1016/j.nimb.2009.09.012

Chow, T.J., Patterson, C.C., 1962. The occurrence and significance of lead isotopes in pelagic sediments. Geochim. Cosmochim. Acta 26, 263–308. https://doi.org/10.1016/0016-7037(62)90016-9

Conrad, T., Hein, J.R., Paytan, A., Clague, D.A., 2017. Formation of Fe-Mn crusts within a continental margin environment. Ore Geol. Rev., SI:Marine mineral deposits: New resources for base, precious, and critical metals 87, 25–40. https://doi.org/10.1016/j.oregeorev.2016.09.010

Cotten, J., Le Dez, A., Bau, M., Caroff, M., Maury, R.C., Dulski, P., Fourcade, S., Bohn, M., Brousse, R., 1995. Origin of anomalous rare-earth element and yttrium enrichments in subaerially exposed basalts: Evidence from French Polynesia. Chem. Geol. 119, 115–138. https://doi.org/10.1016/0009-2541(94)00102-E

Delunel, R., 2010. Evolution géomorphologique du massif des Ecrins-Pelvoux depuis le Dermier Maximum Glaciaire – Apports des nucléides cosmogéniques produits in-stu. Thèse de doctorat, Université Joseph-Fourier, Grenoble I. ⟨tel-00511048⟩

DiMarco, S.F., Chapman, P., Nowlin, W.D., Hacker, P., Donohue, K., Luther, M., Johnson, G.C., Toole, J., 2002. Volume transport and property distributions of the Mozambique Channel. Deep Sea Res. Part II Top. Stud. Oceanogr. 49, 1481–1511. https://doi.org/10.1016/S0967-0645(01)00159-X

Elderfield, H., Upstill-Goddard, R., Sholkovitz, E.R., 1990. The rare earth elements in rivers, estuaries, and coastal seas and their significance to the composition of ocean waters. Geochim. Cosmochim. Acta 54, 971–991. https://doi.org/10.1016/0016-7037(90)90432-K

Fialips, C.I., Labeyrie, B., Burg, V., Mazière, V., Munerel, Y., Haurie, H., Jolivet, I., Lasnel, R., Laurent, J.-P., Lambert, L., Jacquelin-Vallée, L., 2018. Quantitative Mineralogy of Vaca Muerta and Alum Shales From Core Chips and Drill Cuttings by Calibrated SEM-EDS Mineralogical Mapping. Presented at the SPE/AAPG/SEG Unconventional Resources Technology Conference, OnePetro. https://doi.org/10.15530/URTEC-2018-2902304

Fine, R.A., 1993. Circulation of Antarctic intermediate water in the South Indian Ocean. Deep Sea Res. Part Oceanogr. Res. Pap. 40, 2021–2042. https://doi.org/10.1016/0967-0637(93)90043-3

Frank, M., 2002. Radiogenic isotopes: tracers of past ocean circulation and erosional input. Rev. Geophys. 40, 1–1. https://doi.org/10.1029/2000RG000094

Frank, M., Whiteley, N., Kasten, S., Hein, J.R., O'Nions, K., 2002. North Atlantic Deep Water export to the Southern Ocean over the past 14 Myr: Evidence from Nd and Pb isotopes in ferromanganese crusts. Paleoceanography 17, 12-1-12–9. https://doi.org/10.1029/2000PA000606

Goldstein, S.J., Jacobsen, S.B., 1988. Rare earth elements in river waters. Earth Planet. Sci. Lett. 89, 35–47. https://doi.org/10.1016/0012-821X(88)90031-3

Goldstein, S.L., Hemming, S.R., 2003. 6.17 - Long-lived Isotopic Tracers in Oceanography, Paleoceanography, and Ice-sheet Dynamics, in: Holland, H.D., Turekian, K.K. (Eds.), Treatise on Geochemistry. Pergamon, Oxford, pp. 453–489. https://doi.org/10.1016/B0-08-043751-6/06179-X

Guan, Y., Sun, X., Ren, Y., Jiang, X., 2017. Mineralogy, geochemistry and genesis of the polymetallic crusts and nodules from the South China Sea. Ore Geol. Rev. 89, 206–227. https://doi.org/10.1016/j.oregeorev.2017.06.020

Hein, J.R., Conrad, T., Mizell, K., Banakar, V.K., Frey, F.A., Sager, W.W., 2016. Controls on ferromanganese crust composition and reconnaissance resource potential, Ninetyeast Ridge, Indian Ocean.

Hein, J.R., Koschinsky, A., Halbach, P., Manheim, F.T., Bau, M., Kang, J.-K., Lubick, N., 1997. Iron and manganese oxide mineralization in the Pacific. Geol. Soc. Lond. Spec. Publ. 119, 123–138. https://doi.org/10.1144/GSL.SP.1997.119.01.09

Hein, J.R., Mizell, K., Koschinsky, A., Conrad, T.A., 2013. Deep-ocean mineral deposits as a source of critical metals for high- and green-technology applications: Comparison with land-based resources. Ore Geol. Rev. 51, 1–14. https://doi.org/10.1016/j.oregeorev.2012.12.001

HORIBA (2021). ICP-OES spectrometers [en ligne]. Horiba [consulté le 31 août 2021]. Disponible sur : https://www.horiba.com/fra/products/scientific/elemental-analysis/icp-oes-spectrometers/

Horwitz, E.P., Dietz, M.L., Rhoads, S., Felinto, C., Gale, N.H., Houghton, J., 1994. A lead-selective extraction chromatographic resin and its application to the isolation of lead from geological samples. Anal. Chim. Acta 292, 263–273. https://doi.org/10.1016/0003-2670(94)00068-9

Ingri, J., Widerlund, A., Land, M., Gustafsson, Ö., Andersson, P., Öhlander, B., 2000. Temporal variations in the fractionation of the rare earth elements in a boreal river; the role of colloidal particles. Chem. Geol. 166, 23–45. https://doi.org/10.1016/S0009-2541(99)00178-3

ISO (2015b) ISO 14644-1/2015 Salles propres et environnements maitrisés apparentés – Partie 1 : classification de la propreté particulaire de l'air [en ligne]. ISO- Organisation internationale de normalisation [consulté le 27 avril 2018]. Disponible sur: https://www.iso.org/fr/standard/53394.html

Jacobsen, S.B., Wasserburg, G.J., 1980. Sm-Nd isotopic evolution of chondrites. Earth Planet. Sci. Lett. 50, 139–155. https://doi.org/10.1016/0012-821X(80)90125-9

Jeandel, C., 1993. Concentration and isotopic composition of Nd in the South Atlantic Ocean. Earth Planet. Sci. Lett. 117, 581–591. https://doi.org/10.1016/0012-821X(93)90104-H

Jeandel, C., Bishop, J.K., Zindler, A., 1995. Exchange of neodymium and its isotopes between seawater and small and large particles in the Sargasso Sea. Geochim. Cosmochim. Acta 59, 535–547. https://doi.org/10.1016/0016-7037(94)00367-U

Jones, C.E., Halliday, A.N., Rea, D.K., Owen, R.M., 1994. Neodymium isotopic variations in North Pacific modern silicate sediment and the insignificance of detrital REE contributions to seawater. Earth Planet. Sci. Lett. 127, 55–66. https://doi.org/10.1016/0012-821X(94)90197-X

Korschinek, G., Bergmaier, A., Faestermann, T., Gerstmann, U.C., Knie, K., Rugel, G., Wallner, A., Dillmann, I., Dollinger, G., von Gostomski, Ch.L., Kossert, K., Maiti, M., Poutivtsev, M., Remmert, A., 2010. A new value for the half-life of 10Be by Heavy-Ion Elastic Recoil Detection and liquid scintillation counting. Nucl. Instrum. Methods Phys. Res. Sect. B Beam Interact. Mater. At. 268, 187–191. https://doi.org/10.1016/j.nimb.2009.09.020

Koschinsky, A., Stascheit, A., Bau, M., Halbach, P., 1997. Effects of phosphatization on the geochemical and mineralogical composition of marine ferromanganese crusts. Geochim. Cosmochim. Acta 61, 4079–4094. https://doi.org/10.1016/S0016-7037(97)00231-7

Ku, T.L., Kusakabe, M., Nelson, D.E., Southern, J.R., Korteling, R.G., Vogel, J., Nowikow, I., 1982. Constancy of oceanic deposition of 10 Be as recorded in manganese crusts. Nature 299, 240. https://doi.org/10.1038/299240a0

Lebatard, A.-E., Bourlès, D., 2015. Quantification des processus superficiels et datation par les radionucléides cosmogéniques 10Be, 26Al et 36Cl. Quat. Rev. Assoc. Fr. Pour Létude Quat. 193–213. https://doi.org/10.4000/quaternaire.7339

Leclaire, L., 1984. RIDA - MD39 Cruise. Marion Dufresne R/V. https://doi.org/10.17600/84010511

Leclaire, L., 1975. NOSICAA - MD 06 Cruise. Marion Dufresne R/V. https://doi.org/10.17600/75010711

Levine, M. (2021) ICP-OES-ICP Chemistry, ICP-OES analysis, strengths and limitations [en ligne]. Technology Networks [consulté le 31 août 2021]. Disponible sur: https://www.technologynetworks.com/analysis/articles/icp-oes-icp-chemistry-icp-oes-analysis-strengths-and-limitations-342265#D3

Lubbe, H.J.L. van der, Frank, M., Tjallingii, R., Schneider, R.R., 2016. Neodymium isotope constraints on provenance, dispersal, and climate-driven supply of Zambezi sediments along the Mozambique Margin during the past ~45,000 years. Geochem. Geophys. Geosystems 17, 181–198. https://doi.org/10.1002/2015GC006080

Mizell, K., Hein, J.R., Koschinsky, A., Hayes, S.M., 2020. Effects of Phosphatization on the Mineral Associations and Speciation of Pb in Ferromanganese Crusts. ACS Earth Space Chem. 4, 1515–1526. https://doi.org/10.1021/acsearthspacechem.0c00037

Moulin, M., Evain, M., 2016. PAMELA-MOZ05 cruise, Pourquoi pas ? R/V.

Nishiizumi, K., Imamura, M., Caffee, M.W., Southon, J.R., Finkel, R.C., McAninch, J., 2007. Absolute calibration of 10Be AMS standards. Nucl. Inst Methods Phys. Res. B 2, 403–413. https://doi.org/10.1016/j.nimb.2007.01.297

Nishiizumi, K., Winterer, E.L., Kohl, C.P., Klein, J., Middleton, R., Lal, D., Arnold, J.R., 1989. Cosmic ray production rates of 10Be and 26Al in quartz from glacially polished rocks. J. Geophys. Res. Solid Earth 94, 17907–17915. https://doi.org/10.1029/JB094iB12p17907

Olu Karine, 2014. PAMELA-MOZ01 cruise,L'Atalante R/V.

Peppard, D.F., Mason, G.W., Maier, J.L., Driscoll, W.J., 1957. Fractional extraction of the lanthanides as their di-alkyl orthophosphates. J. Inorg. Nucl. Chem. 4, 334–343. https://doi.org/10.1016/0022-1902(57)80016-5

Piepgras, D.J., Jacobsen, S.B., 1988. The isotopic composition of neodymium in the North Pacific. Geochim. Cosmochim. Acta 52, 1373–1381. https://doi.org/10.1016/0016-7037(88)90208-6

Piepgras, D.J., Wasserburg, G.J., 1987. Rare earth element transport in the western North Atlantic inferred from Nd isotopic observations. Geochim. Cosmochim. Acta 51, 1257–1271. https://doi.org/10.1016/0016-7037(87)90217-1

Piepgras, D.J., Wasserburg, G.J., 1982. Isotopic Composition of Neodymium in Waters from the Drake Passage. Science 217, 207–214.

Rempfer, J., Stocker, T.F., Joos, F., Dutay, J.-C., Siddall, M., 2011. Modelling Nd-isotopes with a coarse resolution ocean circulation model: Sensitivities to model parameters and source/sink distributions. Geochim. Cosmochim. Acta 75, 5927–5950. https://doi.org/10.1016/j.gca.2011.07.044

Shimizu, H., Tachikawa, K., Masuda, A., Nozaki, Y., 1994. Cerium and neodymium isotope ratios and REE patterns in seawater from the North Pacific Ocean. Geochim. Cosmochim. Acta 58, 323–333. https://doi.org/10.1016/0016-7037(94)90467-7

Sousa, I.M.C., Santos, R.V., Koschinsky, A., Bau, M., Wegorzewski, A.V., Cavalcanti, J.A.D., Dantas, E.L., 2021. Mineralogy and chemical composition of ferromanganese crusts from the Cruzeiro do Sul Lineament - Rio Grande Rise, South Atlantic. J. South Am. Earth Sci. 108, 103207. https://doi.org/10.1016/j.jsames.2021.103207

Tachikawa, K., Athias, V., Jeandel, C., 2003. Neodymium budget in the modern ocean and paleo-oceanographic implications. J. Geophys. Res. Oceans 108. https://doi.org/10.1029/1999JC000285

Tachikawa, K., Handel, C., Dupré, B., 1997. Distribution of rare earth elements and neodymium isotopes in settling particulate material of the tropical Atlantic Ocean (EUMELI site). Deep Sea Res. Part Oceanogr. Res. Pap. 44,

1769–1792. https://doi.org/10.1016/S0967-0637(97)00057-5

Tanaka, T., Togashi, S., Kamioka, H., Amakawa, H., Kagami, H., Hamamoto, T., Yuhara, M., Orihashi, Y., Yoneda, S., Shimizu, H., Kunimaru, T., Takahashi, K., Yanagi, T., Nakano, T., Fujimaki, H., Shinjo, R., Asahara, Y., Tanimizu, M., Dragusanu, C., 2000. JNdi-1: a neodymium isotopic reference in consistency with LaJolla neodymium. Chem. Geol. 168, 279–281. https://doi.org/10.1016/S0009-2541(00)00198-4

Todt, W., Cliff, R.A., Hanser, A., Hofmann, A.W., 2013. Evaluation of a 202Pb–205Pb Double Spike for High - Precision Lead Isotope Analysis.*, in: Earth Processes: Reading the Isotopic Code. American Geophysical Union (AGU), pp. 429–437. https://doi.org/10.1029/GM095p0429

Toole, J.M., Warren, B.A., 1993. A hydrographic section across the subtropical South Indian Ocean. Deep Sea Res. Part Oceanogr. Res. Pap. 40, 1973–2019. https://doi.org/10.1016/0967-0637(93)90042-2

Ullgren, J.E., van Aken, H.M., Ridderinkhof, H., de Ruijter, W.P.M., 2012. The hydrography of the Mozambique Channel from six years of continuous temperature, salinity, and velocity observations. Deep Sea Res. Part Oceanogr. Res. Pap. 69, 36–50. https://doi.org/10.1016/j.dsr.2012.07.003

Vajda, N., LaRosa, J., Zeisler, R., Danesi, P., Kis-Benedek, Gy., 1997. A novel technique for the simultaneous determination of 210Pb and 210Po using a crown ether. J. Environ. Radioact. 37, 355–372. https://doi.org/10.1016/S0265-931X(95)00059-J

von Blanckenburg, F., Belshaw, N.S., O'Nions, R.K., 1996. Separation of 9Be and cosmogenic 10Be from environmental materials and SIMS isotope dilution analysis. Chem. Geol. 129, 93–99. https://doi.org/10.1016/0009-2541(95)00157-3

White, W.M., Albarède, F., Télouk, P., 2000. High-precision analysis of Pb isotope ratios by multi-collector ICP-MS. Chem. Geol. 167, 257–270. https://doi.org/10.1016/S0009-2541(99)00182-5

Wilson, D.J., Piotrowski, A.M., Galy, A., McCave, I.N., 2012. A boundary exchange influence on deglacial neodymium isotope records from the deep western Indian Ocean. Earth Planet. Sci. Lett. 341–344, 35–47. https://doi.org/10.1016/j.epsl.2012.06.009

Yuan, H., Yuan, W., Cheng, C., Liang, P., Liu, X., Dai, M., Bao, Z., Zong, C., Chen, K., Lai, S., 2016. Evaluation of lead isotope compositions of NIST NBS 981 measured by thermal ionization mass spectrometer and multiple-collector inductively coupled plasma mass spectrometer. Solid Earth Sci. 1, 74–78. https://doi.org/10.1016/j.sesci.2016.04.001

CHAPTER 3 : MODERN ISOTOPIC RECORDS OF THE REGIONAL WATER MASSES

3.1. Introduction (français)

À travers l'étude isotopique en Nd de 33 encroûtements Fe-Mn, répartis de manière homogène dans le canal du Mozambique à des profondeurs entre 170 et 2650 m, cet axe propose un nouveau modèle 2D de la circulation moderne des masses d'eau intermédiaires et profondes. Afin d'atteindre cet objectif, il s'agit dans un premier temps, d'identifier les signatures isotopiques en Nd des masses d'eau présentes dans cette étroite zone d'étude. Le Nd est utilisé car il représente le proxy le plus adapté en raison des signatures suffisamment contrastées entre les courants de l'océan Atlantique et de l'océan Indien. La particularité de cette première étape repose donc sur la diversité des masses d'eau circulant dans le canal, avec des courants froids et peu radiogéniques qui viennent de l'océan Atlantique et des courants plus tempérés et plus radiogéniques qui arrivent au nord, issus de l'océan Indien. Basés sur des calculs de contributions, selon la méthode présentée et établie par Frank (2002), des taux d'apports peuvent être calculés pour chaque masse d'eau afin de comprendre son influence au sein du système. Dans un second temps, le rôle de la topographie est discuté, et notamment la morphologie dissymétrique du canal, marqué par une ride N-S. Cet axe tient notamment compte des récentes études hydrographiques menées en partie par Collins et al. (2016) et qui permettent de se questionner sur le rôle de la ride de Davie, structure séparant le canal en plusieurs bassins distincts sur 1200 km de long, dans la répartition des masses d'eau au sud et au nord du canal. Les analyses isotopiques en Pb viendront compléter les hypothèses proposées à travers l'isotopie du Nd. Le Pb est un proxy moins sensible pour tracer les courants (Vlastélic et al., 2001) mais son étude permettra de comparer les deux proxys étudiés et caractérisés par des temps de résidence différents.

Ce 3ème chapitre est fondé sur le prélèvement de la partie superficielle des échantillons uniquement. Il s'agit des dernières couches Fe-Mn déposées sur les encroûtements. C'est pourquoi, la résolution temporelle du modèle 2D de circulation des masses d'eau présenté ici est également discutée et critiquée dans ce chapitre.

3.1. Introduction (english)

Through the Nd isotopes study of 33 Fe-Mn crusts, homogeneously distributed in the Mozambique Channel between 170 and 2650 mbsl, this axis proposes a new 2D model of the modern circulation of the intermediate and the deep-water masses. In order to achieve this objective, the first step is to identify the Nd isotopic signatures of the water masses present in this narrow study area. Nd is used because it is the most suitable proxy due to sufficiently contrasting signatures between the Atlantic and Indian Ocean currents. Thus, the particularity lies in the diversity of the water masses in the channel, with cold and not very radiogenic currents from the Atlantic Ocean and temperate and more radiogenic currents from the Indian Ocean. Based on calculations, established by Frank (2002), input rates are determined for each water mass to understand its influence within the system. Secondly, the role of topography is discussed, in particular the asymmetrical morphology of the channel, marked by a N-S ridge. This axis takes into account the hydrographic studies carried out by Collins et al. (2016). The role of the Davie ridge is still debated. This structure separates the channel over 1200 km and may have an impact on the water masses distribution. Pb isotope analyses will complement the hypotheses from the Nd isotopes study. Pb is a less sensitive proxy for tracing currents (Vlastélic et al., 2001) but its study will allow comparison of the two proxies studied and characterised by different residence times.

This 3rd chapter is based on the sampling of the top part of the samples - the last layers deposited on the crusts. Therefore, the temporal resolution is also discussed and criticised in this chapter.

3.2. Nd isotopic signatures of the channel water masses and new 2D circulation model

- ***Paper 2*** *: Charles, C., Pelleter, E., Révillon, S., Nonnotte, P., Jorry, S.J., Kluska, J.-M., 2020. Intermediate and deep ocean current circulation in the Mozambique Channel: New insights from ferromanganese crust Nd isotopes. Marine Geology. 430, 106356.*

Marine Geology 430 (2020) 106356

Contents lists available at ScienceDirect

Marine Geology

journal homepage: www.elsevier.com/locate/margo

Intermediate and deep ocean current circulation in the Mozambique Channel: New insights from ferromanganese crust Nd isotopes

Claire Charles [a,b,*], Ewan Pelleter [a], Sidonie Révillon [b,c], Philippe Nonnotte [b], Stephan J. Jorry [a], Jean-Michel Kluska [d]

[a] IFREMER, Unité Géosciences Marines, Laboratoire Cycles Géochimiques (LCG), F 29280 Plouzané, France
[b] Univ Brest, CNRS, UMR 6538 (Laboratoire Géosciences Océan), Institut Universitaire Européen de la Mer (IUEM), Place Nicolas Copernic, 29280 Plouzané, France
[c] SEDISOR/UMR 6538 (Laboratoire Géosciences Océan), Institut Universitaire Européen de la Mer (IUEM), Place Nicolas Copernic, F 29280 Plouzané, France
[d] TOTAL Exploration and Production, CSTJF, Avenue Larribau, F 64000, Pau, France

ARTICLE INFO

Keywords:
Ferromanganese crusts
Nd isotopes
Paleoceanography
Mozambique Channel
North Atlantic Deep Water

ABSTRACT

The Mozambique Channel plays a key role in the exchange of water masses between the Indian and Atlantic Oceans, which include the North Atlantic Deep Water (NADW) inflow from the south and the North Indian Deep Water (NIDW), an aged form of the NADW spreading poleward from the northern and equatorial Indian Ocean basin. Several authors assume that the Davie Ridge acts as a topographic barrier to the northward advection of NADW, which would therefore be absent in the Comoros Basin. Other studies suggest that the NADW flows from the south of the Mozambique Channel to the Comoros Basin, indicating that the Davie Ridge may not currently constitute a blocking topographic barrier to deep water mass circulation. To address this question, we studied ferromanganese (Fe, Mn) crusts collected over 2000 km in the Mozambique Channel, from the Agulhas Plateau to the Glorieuses Islands. Neodymium (Nd) isotope compositions (ε_{Nd}) of surface scrapings range between $\varepsilon_{Nd} = -10.1$ above the Agulhas Plateau, which might reflect the NADW inflow, and more radiogenic values between $\varepsilon_{Nd} = -8.0$ and -8.2 in the Glorieuses area, highlighting the NIDW influence. However, value of $\varepsilon_{Nd} = -9.4$ measured north of the Davie Ridge cannot be explained by the sole influence of the NIDW and therefore highlights the advection of the NADW northeast of the Comoros Basin. We estimate that the contribution of the NADW through the channel is up to 68% in the Agulhas Plateau and 60% north of the Davie Ridge. These findings are consistent with previous hydrographic studies and suggest that the Davie Ridge does not currently act as topographic barrier to deep currents.

1. Introduction

Ferromanganese crusts (Fe, Mn) are marine deposits that are ubiquitous on the seafloor i.e. occur in diverse environments and at different depths. They precipitate directly from seawater on hard substrates (Hein et al., 2009) and their growth rate can vary between 0.5 and 15 mm/Ma according to the geodynamic and paleogeographic context (Kusakabe and Ku, 1984; Segl et al., 1984; Eisenhauer et al., 1992; Frank et al., 1999). As a result, the thickest crusts may represent time intervals up to 80 Ma (Frank et al., 1999). This very low precipitation rate, coupled with the fact that Fe and Mn oxyhydroxides are significant element scavengers (e.g. metals, trace elements, rare earth elements (REE); Piper, 1974; Hein et al., 2010; Lusty et al., 2018), results over time in extensive enrichment of seawater elements in the Fe-Mn crusts. These crusts therefore contain records of element cycles in the oceans (Aplin and Cronan, 1985) with each millimeter of thickness corresponding to a specific time period. They constitute ocean archives, studied since the 1980s to understand the biogeochemical cycles of metals (Koschinsky and Halbach, 1995; Koschinsky et al., 1997), and more recently, to trace global ocean current flow paths (Albarède and Goldstein, 1992; Albarède et al., 1997; Christensen et al., 1997; Frank et al., 1999). Several authors have focused on multi-element and isotopic compositions of Fe-Mn crusts from the Atlantic, Indian and Pacific Oceans. Their neodymium (Nd) isotope compositions (ε_{Nd}) have been particularly assessed (Aplin et al., 1986; Albarède et al., 1997, 1998; Frank et al., 1999). These previous global-scale studies have established the current average geochemical compositions of seawater for each geographic oceanic basin and identified major geodynamic, geochemical and

* Corresponding author.
E-mail address: claire.charles@ifremer.fr (C. Charles).

https://doi.org/10.1016/j.margeo.2020.106356
Received 5 April 2020; Received in revised form 10 August 2020; Accepted 23 September 2020
Available online 28 September 2020
0025-3227/© 2020 The Authors. Published by Elsevier B.V. This is an open access article under the CC BY-NC-ND license (http://creativecommons.org/licenses/by-nc-nd/4.0/).

climate changes over the past 15 Ma (Segl et al., 1984; Christensen et al., 1997; Ling et al., 1997; Frank and O'Nions, 1998; O'Nions et al., 1998; Frank et al., 1999; Frank et al., 2002; Hein et al., 2016). However, few analyses have been made on Fe-Mn crusts on local scale in mixing areas such as the Mozambique Channel, a strategic zone for studying the Atlantic and Indian water mass mixing (You, 2000; de Ruijter et al., 2002; van Aken et al., 2004; Collins et al., 2016; Fig. 1).

The circulation of deep currents is widely described due to the Davie Ridge (Coffin and Rabinowitz, 1987) that separates the channel into two distinct basins (i.e. the Comoros Basin in the north and the Mozambique Basin in the south; Fig. 1). According to some authors, the Davie Ridge represents a topographic obstacle to the circulation of these deep currents flowing from the Atlantic Ocean to the south and from the Indian Ocean to the north (Toole and Warren, 1993; Mantyla and Reid, 1995;

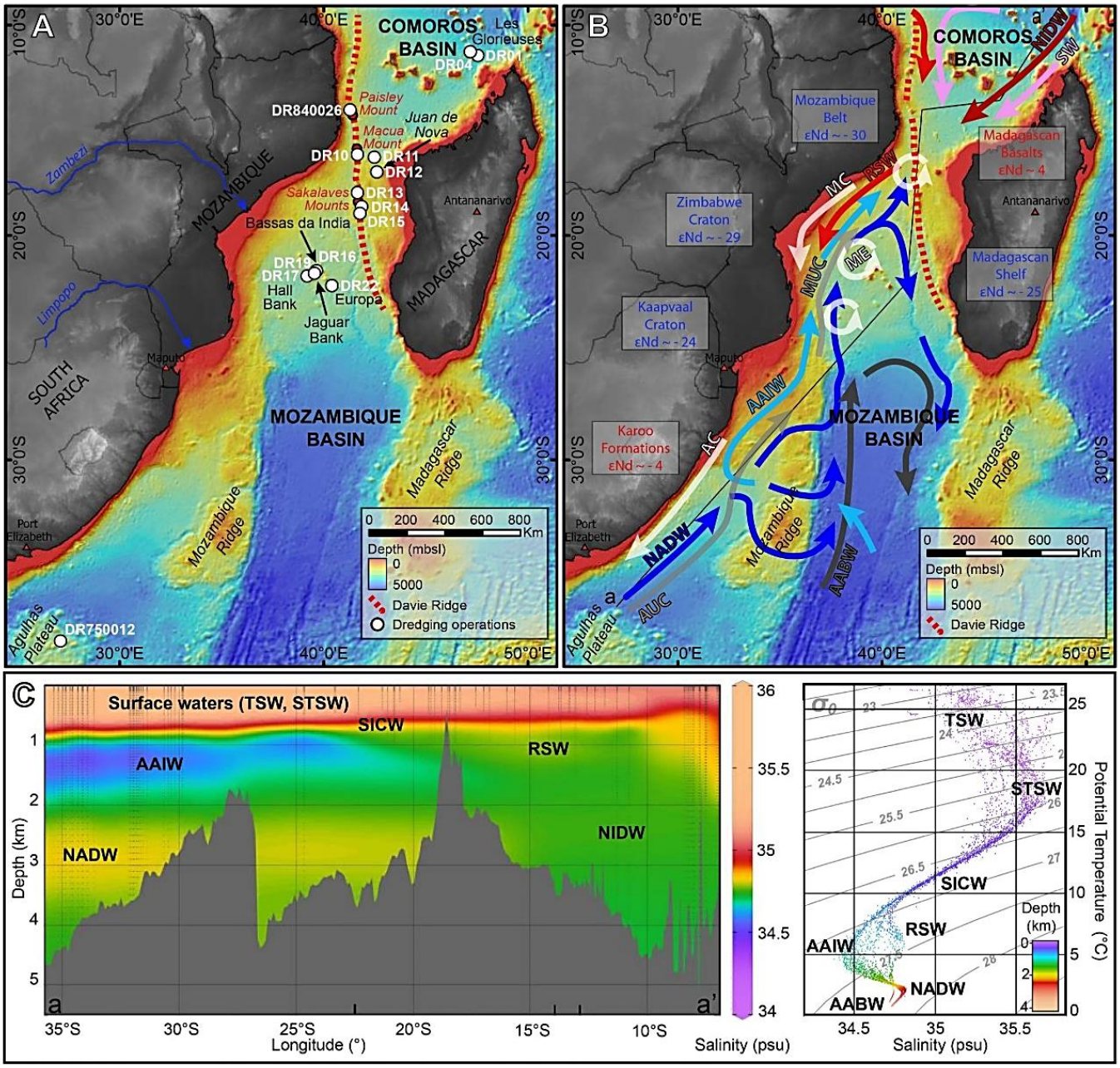

Fig. 1. (A) Bathymetry of the Mozambique Channel (data from GEBCO and PAMELA cruises) with its main structures including the Davie Ridge and the Eparses Islands. The white dots represent the dredging operations. (B) Bathymetry of the Mozambique Channel (data from GEBCO and PAMELA cruises) showing the main circulation patterns (based on Kolla et al., 1980; Fine, 1993; Toole and Warren, 1993; DiMarco et al., 2002; Lutjeharms, 2006; Ullgren et al., 2012). AABW: Antarctic Bottom Water; AAIW: Antarctic Intermediate Water; AC: Agulhas Current; AUC: Agulhas Undercurrent; MC: Mozambique Current; ME: Mozambique Eddies; MUC: Mozambique Undercurrent; NADW: North Atlantic Deep Water; NIDW: North Indian Deep Water; RSW: Red Sea Water; SW: Surface Water including TSW: Tropical Surface Water, STSW: Sub-Tropical Surface Water and SICW: South Indian Central Water. The dark line corresponds to the section located in 1C. Nd isotope signatures (ε_{Nd}) are presented for the main geological formations surrounding the channel (ε_{Nd} of Archean basement: Paquette et al., 1994; Jelsma et al., 1996; Möller et al., 1998; Kröner et al., 2000; De Waele et al., 2006; Grantham et al., 2011 and ε_{Nd} of the volcanic structures: Mahoney et al., 1991; Grousset et al., 1992; Jourdan et al., 2007). (C) Salinity section showing the distribution of the main water masses present in the Mozambique Channel, based on Conductivity Temperature Depth (CTD) profiles.

You, 2000; Fig. 1B). However, recent hydrographic data have identified deep currents from the Atlantic Ocean north of the Davie Ridge (DiMarco et al., 2002; van Aken et al., 2004; Collins et al., 2016), and thus called into question the evolution of deep currents in the Mozambique Channel as well as the role of the Davie Ridge in the distribution of these water masses.

In this study, we analyzed the Nd isotope composition of 29 crusts collected through the Mozambique Channel in order to better understand the oceanic processes in the study area. The main objectives of this paper are to (1) identify deep water masses circulation (2) interpret the actual impact of the Davie Ridge on water mass propagation to the north and (3) propose new hydrographic framework of the deep currents in the Mozambique Channel. This is the first time that such a detailed study in terms of the number of dredges and various water depths has been carried out and used for an oceanographic study on a regional scale.

2. Regional setting and geochemical approach

2.1. Geological setting

The Mozambique Channel is located in the southwestern Indian Ocean, between the East-African continental margin along Mozambique and Madagascar (Fig. 1A). It resulted from the separation of the eastern part (Madagascar, India, Antarctica and Australia) and the western part of Gondwana (Africa and South America) in the lower Jurassic (McElhinny, 1970; McKenzie and Sclater, 1971). The Antarctic-India-Madagascar structure was relocated southward along a major transform zone called the Davie Fracture Zone (DFZ) to the Upper Cretaceous (Heirtzler and Burroughs, 1971; Coffin and Rabinowitz, 1987; Gaina et al., 2013). This tectonic event is now represented by the Davie Ridge (Fig. 1A), oriented N170, which extends 1200 km east of the African continental margin (15°S) to the Madagascan marginal plateau (22°S). The ridge is punctuated by several seamounts (e.g. Paisley, Macua and Sakalaves) and separates the Comoros basin in the northeast from the deep Mozambique basin in the southwest (Fig. 1A). The major Jurassic structuring phase was followed by the separation of Madagascar and the Antarctic-India block in the Upper Cretaceous, which caused important volcanic activity in Madagascar but also in the Morondava and Majunga basins to the west of the island (Bassias, 1992; Storey et al., 1995; Rogers et al., 2000; Torsvik et al., 2000; Thompson et al., 2019; Fig. 1A). The Eparses Islands (Bassas Da India, Europa, Juan de Nova, and the Glorieuses Islands) have witnessed this volcanic activity since their formation in the Paleocene. Linked to these volcanic events, these islands and the northern part of the Madagascan continental margin are assigned a radiogenic Nd isotope signature of $\varepsilon_{Nd} \sim 4$ (Mahoney et al., 1991; Jeandel et al., 2007), whereas Madagascar presents an Archean signature in the center and in the south, characterized by an average unradiogenic value of $\varepsilon_{Nd} \sim -25$ (from $\varepsilon_{Nd} = -22$ to $\varepsilon_{Nd} = -28$; Paquette et al., 1994; Kröner et al., 2000; Fig. 1B). On the other side of the Mozambique channel, the African continental margin is assigned an unradiogenic value of $\varepsilon_{Nd} \sim -20$ (Jeandel et al., 2007). This may represent an average of Nd isotope signatures from old continental crustal sources as the Archean Kaapvaal craton ($\varepsilon_{Nd} \sim -24$; Grantham et al., 2011), Zimbabwe craton ($\varepsilon_{Nd} \sim -29$; Jelsma et al., 1996) and Mozambique belt ($\varepsilon_{Nd} \sim -30$; Möller et al., 1998; Fig. 1B) and, younger volcanic sources as the Jurassic Karoo formations with more radiogenic signature of $\varepsilon_{Nd} \sim -4$ (from $\varepsilon_{Nd} = -9$ to $\varepsilon_{Nd} = 0$; Grousset et al., 1992; Jourdan et al., 2007; Fig. 1B).

2.2. Oceanic setting

The Mozambique Channel is a complex oceanic area with (1) exchange between the water masses of the Indian and Atlantic Oceans and (2) the Davie Ridge which constitutes a topographic high ranging from several tens to 100 km in width and characterized by a basement which culminates at 300 m below sea level (mbsl) and extends to 2500 mbsl (Mougenot et al., 1986; Coffin and Rabinowitz, 1987; Fig. 1C). This ridge separates the Mozambique Channel into distinct basins (Fig. 1A). Warm Indian water masses spread from the Comoros Basin and then are dragged into the Mozambique Current (MC) in the Deep Basin (DiMarco et al., 2002; Quartly et al., 2013; Flemming and Kudrass, 2018). The deep water flows in the Mozambique Undercurrent (MUC) from the south of the Mozambique Basin to the west of the ridge (de Ruijter et al., 2002; Fig. 1B).

The MC is part of the Agulhas Current (AC), which is an essential link for heat and salt exchanges between the Indian and Atlantic Oceans (Gordon, 1986; Weijer, 1999; Lutjeharms, 2006), and is characterized by anticyclonic eddies (ME) up to 300 km in diameter that can affect the entire water column (de Ruijter et al., 2002; Halo et al., 2014; Fig. 1B). The MC transports surface water to a depth of 600 mbsl, composed of Tropical Surface Water (TSW) and Subtropical Surface Water (STSW) but also South Indian Central Water (SICW) between 200 and 600 mbsl (Fig. 1C). The intermediate waters of the MC are composed of Red Sea Water (RSW) between 900 and 1200 mbsl that enters from the north of the Mozambique Channel along the East African coast (Beal et al., 2000; Schott and McCreary, 2001; Fig. 1B, C).

The MUC and the Agulhas Undercurrent (AUC) carry Antarctic Intermediate Water (AAIW) between 800 and 1500 mbsl (Ullgren et al., 2012; Fig. 1B, C). AAIW arrives from the eastern part of the Mozambique ridge and then flows along the Mozambican coast (Fine, 1993). The North Atlantic Deep Water (NADW) is also part of the MUC, between 1500 and 3500 mbsl (Fig. 1B, C). Its inflow starts upstream of the south of Africa before entering the Mozambique Channel through the Natal Valley (Toole and Warren, 1993). The NADW flows northwards from the Mozambique Basin to the west of the Davie Ridge. Several authors consider that this water mass does not flow over the Davie Ridge and retreats south along the western edge of the ridge (Toole and Warren, 1993; Mantyla and Reid, 1995; You, 2000). Conversely, some authors identified the presence of the NADW beyond the Davie Ridge with circulation along its eastern side after a topographic blockage at 14°S (van Aken et al., 2004; Collins et al., 2016). At a depth of more than 4000 mbsl, the Antarctic Bottom Water (AABW) flows from east of the Mozambique ridge to south of the Mozambique Basin. It is then diverted, before heading south along the Madagascar Ridge (Kolla et al., 1980, Fig. 1B). Finally, north of the Mozambique Channel, the North Indian Deep Water (NIDW) flows at a depth of more than 2000 mbsl (Collins et al., 2016; Fig. 1C). It is transported from the Indian Ocean and is present in the northern part of the channel, near the Glorieuses Islands (DiMarco et al., 2002; Fig. 1B). Very few studies have examined the NIDW flow path after its arrival in northern Madagascar and its passage through the Glorieuses Islands. However, new hydrographic data, based on conductivity, temperature, pressure, dissolved oxygen and salinity measurements, allowed to identify the AAIW, NADW and NIDW water masses beyond the ridge and have proposed new circulation patterns (DiMarco et al., 2002; van Aken et al., 2004; Collins et al., 2016).

2.3. Geochemical approach

Dissolved Nd in seawater mainly originates from aerosols and continental inputs, through rivers (Goldstein et al., 1984; Goldstein and Jacobsen, 1988; Elderfield et al., 1990; Tachikawa et al., 1997; Ingri et al., 2000; Bayon et al., 2015; van der Lubbe et al., 2016). The Nd isotope composition in seawater can be modified by particulate and dissolved exchange processes along continental margins termed "boundary exchange" (Lacan and Jeandel, 2001, 2005; Rempfer et al., 2011; Pearce et al., 2013. Wilson et al., 2012). In addition, submarine groundwater discharge and benthic fluids from the pore waters of the sediments have been identified as significant sources for Nd in the contributing to REE fluxes to the oceans (Johannesson et al., 2011; Abbott et al., 2015a, 2015b; Haley et al., 2017). However, the relative contribution of these inputs to the overall Nd balance in seawater is still described according to geographic areas (Jones et al., 1994). Ocean Nd

residence time is also still debated and supposedly ranges between 600 and 2000 years (Jeandel et al., 1995; Tachikawa et al., 2003; Arsouze et al., 2009; Rempfer et al., 2011), whereas the mixing time of the deep ocean is about 1500 years (Broecker et al., 1982). While being aware of significant changes in local Nd isotope exchange processes or sources, the Nd isotope composition of intermediate and deep waters is therefore expected to be controlled predominantly by conservative mixing between water masses (Goldstein and Hemming, 2003). Nd isotopes are therefore considered as a quasi-conservative tracer of water mass chemistry with potentially great interest in paleoceanographic studies (Frank, 2002; Goldstein and Hemming, 2003). Previous studies of Fe-Mn crusts, nodules and seawater demonstrated that the Atlantic, Indian and Pacific basins each have a distinct and characteristic range in Nd isotope compositions (O'Nions et al., 1978; Piepgras et al., 1979). Consequently, Nd isotopes can be used to trace water sourcing and mixing in both the present and past oceans (Piepgras and Wasserburg, 1980, 1982, 1987; Piepgras and Jacobsen, 1988; Jeandel et al., 2013; Amakawa et al., 2019).

The variations of Nd isotope compositions are expressed as:

$$\varepsilon_{Nd} = \left(\frac{^{143}Nd/^{144}Nd\ (meas.)}{^{143}Nd/^{144}Nd\ (CHUR)} - 1 \right) \times 10^4 \quad (1)$$

where the CHUR (Chondritic Uniform Reservoir) value is 0.512638 (Jacobsen and Wasserburg, 1980). Nd isotope compositions can show significant variations related to erosion and dissolution of rocks in the source regions of water masses. The ε_{Nd} values of the Pacific Ocean range between 0 and −6 resulting from the erosion of very young volcanic rocks derived from the earth mantle mixed with continental inputs that are unradiogenic (Piepgras and Jacobsen, 1988; Shimizu et al., 1994). The water masses of the North Atlantic have ε_{Nd} values between −12 and −14 resulting from erosion of old Canadian shield continental rocks while those of the South Atlantic have ε_{Nd} values between −9 and −11, linked to the mixture between the unradiogenic values of the North Atlantic and the more radiogenic values of the Pacific (Piepgras et al., 1979; Piepgras and Wasserburg, 1982, 1987; Jeandel, 1993). Finally, the Nd isotope composition in the Indian Ocean is a result of the mixture of unradiogenic values of the Atlantic and more radiogenic values of the Pacific Ocean. Its composition ranges between ε_{Nd} = −7 and −8.5 (Bertram and Elderfield, 1993; Arsouze et al., 2007; Wilson et al., 2012). Using Nd isotopes as a tracer of ocean water masses in each ocean basin, it is possible to estimate the respective Atlantic and Pacific contributions to the Indian Ocean by a mixing between the Northwest Atlantic and the Southern Ocean. The equation for conservative Nd isotopic mixing M of the NADW and the Circumpolar Deep Water (CDW) is given by:

$$\varepsilon_{Nd\ (M)} = \frac{X_{(NADW)}\ C_{(NADW)}\ \varepsilon_{Nd\ (NADW)} + \left(1 - X_{(NADW)}\right)\ C_{(CDW)} \varepsilon_{Nd\ (CDW)}}{X_{(NADW)}\ C_{(NADW)} + \left(1 - X_{(NADW)}\right)\ C_{(CDW)}} \quad (2)$$

where ε_{Nd} and C are described as the Nd isotope composition and concentration respectively and, X as the mixing proportion. The calculation is based on a Nd isotope composition of $\varepsilon_{Nd} = -13$ and a concentration of 25 pmol/kg for the NADW (Piepgras and Wasserburg, 1982, 1987; Jeandel, 1993) and, a Nd isotope composition between $\varepsilon_{Nd} = -4$ and −6 and a concentration of 20 pmol/kg for the CDW (Piepgras and Wasserburg, 1982; Piepgras and Jacobsen, 1988; Jeandel et al., 2013). Thus, for a Nd isotope composition of $\varepsilon_{Nd} = -7$, the Indian water masses can be composed of 15% to 30% of Atlantic water masses and 70% to 85% of Pacific water masses with Atlantic $\varepsilon_{Nd} = -13$ and Pacific between $\varepsilon_{Nd} = -4$ and −6, while for a Nd isotope composition of $\varepsilon_{Nd} = -8.5$, the Indian water masses can be composed of 25% to 45% of Atlantic water masses and 55% to 75% of Pacific water masses with the same Atlantic and Pacific ε_{Nd}. These calculations are consistent with the method used by Frank et al. (2002) whereby a linear mixing relation between the two Nd end-member water masses is assumed because the Nd concentrations in the NADW and CDW do not present a systematic difference. We applied this approach to calculate NADW contributions to the Mozambique Channel. Table 1 presents a summary of Nd isotope compositions of the main water masses in the Mozambique Channel.

3. Material and methods

3.1. Fe-Mn crust sampling

This work is based on 29 Fe-Mn crust samplings. Locations, depths and other details are given in Table 2 for each sample. 27 were recovered in the Mozambique Channel during the PAMELA-MOZ1 cruise onboard the RV *L'Atalante* (Olu, 2014), as part of the PAMELA (Passive Margin Exploration Laboratory) research project. During this expedition, 22 dredging operations were carried and a total of 186 samples were recovered, including 74 Fe-Mn crusts. 2 other Fe-Mn crusts were recovered during the NOSICAA-MD06 cruise (Agulhas Plateau, sample MNHN-GS-DR75–0012; Leclaire, 1975) and the RIDA-MD39 expedition (western slope of the Davie Ridge, Paisley Mount, sample MNHN-GS-DR84–0026; Leclaire, 1984), conducted by the National Museum of Natural History (MNHN).

Finally, this study is based on 14 sampling stations distributed from the Agulhas Plateau in the south to the Glorieuses Islands north of the Davie Ridge at depths ranging from 580 and 2650 mbsl (Fig. 1A, Table 2), allowing to focus on the geochemical records of all water masses (surface, intermediate and deep).

3.2. Nd isotope measurements

After macroscopic examination, approximately 100 mg of sample were collected from scraping the surface layer of the Fe-Mn crusts. The sampling corresponds to the first 100 μm of the sample, i.e. the last elementary adsorption on Fe and Mn oxyhydroxides, and thus the modern state of water mass geochemistry (Albarède and Goldstein, 1992; Albarède et al., 1997), in the order of 20 to 80 ka due to the slow accretion rates of the studied samples ranging from 1.3 to 5.2 mm/Ma, with an average growth rate of 3.1 mm/Ma in all the samples (Bourlès et al. unpublished data). The powders were first dissolved in closed screw-top Teflon vials (Savillex) at about 100 °C for one day using 3 ml of 6 M HCl. The vials where then opened for evaporation at about 130 °C. After evaporation to dryness, approximately 2 ml of aqua regia (10 M HCl + 14 M HNO_3) was added, and the vials were capped and put back on the hot plate overnight at about 100 °C. The samples were then dried again and taken up in about 6 ml of Quartex 6 M HCl ("mother solutions"). For of Nd isotope compositions analysis, a 2 ml aliquot of the mother solution was dried, and the residue was taken up in about 0.5 ml of Quartex 14.4 M HNO_3 for one hour at 90 °C. The vials where then opened for evaporation at about 90 °C. After evaporation, 1 ml of 1 M HNO_3 was added and the samples were centrifuged. The REE fraction was separated using Eichrom® Tru spec Resin and the Nd separation was carried out using Eichrom® Ln spec Resin on volumetrically calibrated Teflon columns following an analytical procedure modified from Pin

Table 1
Water masses abbreviations used in this study together with their corresponding depth range and ε_{Nd} signatures.

Abbreviations	Water masses	Depth range (mbsl)	εNd
SICW	South Indian Central Water	200–700	−8.5 to −7[a]
RSW	Red Sea Water	800–1400	−8.5 to −7[a]
AAIW	Antarctic Intermediate Water	800–1500	−9 to −8[b]
NIDW	North Indian Deep Water	2000–3000	−8.5 to −7[a]
NADW	North Atlantic Deep Water	1500–3500	−13 to −9[c]

[a] Bertram and Elderfield (1993), Arsouze et al. (2007).
[b] Piepgras and Wasserburg (1982), Jeandel (1993), Arsouze et al. (2007), Amakawa et al. (2013).
[c] Piepgras and Wasserburg (1987), Jeandel (1993), Rickli et al. (2009), Tachikawa et al. (2017).

Table 2
International Geo Sample Number (IGSN), location, depth and ε_{Nd} values of the studied Fe-Mn crusts from the PAMELA-MOZ1 (Olu, 2014), NOSICAA-MD06 (Leclaire, 1975) and RIDA-MD39 (Leclaire, 1984) oceanographic expeditions.

Cruise	Dredge	Sample	IGSN	Location	Latitute	Longitude	Depth range (mbsl)	$^{143}Nd/^{144}Nd$	2σ (10^{-6})	εNd	Percent NADW [b]
PAMELA-MOZ-1	DR01	MOZ1-DR01-01	BFBG-155073	Glorieuses Islands	11°47'S	47°54'E	2400–2650	0.512255	4	−7.47	21–39
	DR04	MOZ1-DR04-01	BFBG-155082	Glorieuses Islands	11°28'S	47°32'E	1780–2000	0.512225	8	−8.1	29–45
	DR04	MOZ1-DR04-03	BFBG-155084	Glorieuses Islands	11°28'S	47°32'E	1780–2000	0.512227	8	−8.0	29–45
	DR04	MOZ1-DR04-04	BFBG-155085	Glorieuses Islands	11°28'S	47°32'E	1780–2000	0.512218	6	−8.2	31–47
	DR04	MOZ1-DR04-23	BFBG-169883	Glorieuses Islands	11°28'S	47°32'E	1780–2000	0.512208	4	−8.4	34–49
	DR10	MOZ1-DR10-04	BFBG-155152	Macua Mount	16°12'S	41°38'E	1000–1400	0.512226	4	−8.0	29–45
	DR10	MOZ1-DR10-05	BFBG-155153	Macua Mount	16°12'S	41°38'E	1000–1400	0.512237	6	−7.8	26–42
	DR11	MOZ1-DR11-01	BFBG-155160	Jeffrey Ridge	16°10'S	42°30'E	2400–2450	0.512180	4	−8.9	42–55
	DR11	MOZ1-DR11-03	BFBG-155162	Jeffrey Ridge	16°10'S	42°30'E	2400–2450	0.512191	4	−8.7	39–52
	DR11	MOZ1-DR11-05	BFBG-155164	Jeffrey Ridge	16°10'S	42°30'E	2400–2450	0.512197	4	−8.6	37–51
	DR11	MOZ1-DR11-07	BFBG-155166	Jeffrey Ridge	16°10'S	42°30'E	2400–2450	0.512157	8	−9.4	48–60
	DR12	MOZ1-DR12-09	BFBG-155179	Juan de Nova	17°1'S	42°36'E	1350–1650	0.512231	8	−7.9	28–44
	DR12	MOZ1-DR12-14	BFBG-155184	Juan de Nova	17°1'S	42°36'E	1350–1650	0.512245	6	−7.7	24–41
	DR12	MOZ1-DR12-V	BFBG-169884	Juan de Nova	17°1'S	42°36'E	1350–1650	0.512232	4	−7.9	27–44
	DR13	MOZ1-DR13-07	BFBG-155191	North Sakalaves Mounts	17°59'S	41°39'E	1300–1600	0.512202	6	−8.5	36–50
	DR14	MOZ1-DR14-04	BFBG-155201	Sakalaves Mounts	18°39'S	41°51'E	580–650	0.512249	4	−7.6	23–40
	DR15	MOZ1-DR15-10	BFBG-155211	South Sakalaves Mounts	18°57'S	41°45'E	1200–1250	0.512236	4	−7.8	26–43
	DR15	MOZ1-DR15-14	BFBG-155215	South Sakalaves Mounts	18°57'S	41°45'E	1200–1250	0.512247	8	−7.6	23–40
	DR16	MOZ1-DR16-05	BFBG-155220	Bassas da India	21°36'S	39°38'E	1350–1600	0.512195	4	−8.6	38–51
	DR16	MOZ1-DR16-06	BFBG-155221	Bassas da India	21°36'S	39°38'E	1350–1600	0.512172	4	−9.1	44–57
	DR17	MOZ1-DR17-01	BFBG-155224	Hall Bank	21°50'S	39°10'E	1700–1900	0.512158	6	−9.4	48–60
	DR17	MOZ1-DR17-04	BFBG-155227	Hall Bank	21°50'S	39°10'E	1700–1900	0.512175	6	−9.0	43–56
	DR19	MOZ1-DR19-01	BFBG-155233	Jaguar Bank	21°44'S	39°32'E	1000–1350	0.512257	24	−7.4	20–38
	DR22	MOZ1-DR22-01	BFBG-155243	Europa	21°18'S	40°23'E	1400–1550	0.512216	4	−8.2	32–47
	DR22	MOZ1-DR22-02	BFBG-155244	Europa	21°18'S	40°23'E	1400–1550	0.512194	6	−8.7	38–52
	DR22	MOZ1-DR22-03	BFBG-155245	Europa	21°18'S	40°23'E	1400–1550	0.512240	8	−7.8	25–42
	DR22	MOZ1-DR22-06	BFBG-155248	Europa	21°18'S	40°23'E	1400–1550	0.512221	4	−8.1	30–46
MD-39 Rida	DR84-0026	DR84-0026	MNHN-GS-DR84-0026	Paisley Mount	14°08'S	41°29'E	800–810	0.512272	4	−7.1	16–35
	DR84-0026	DR84-02		Paisley Mount	14°08'S	41°29'E	800–810	0.512272	24	−7.4[a]	20–38
	DR84-0033	DR84-09		Macua Mount	16°12'S	41°39'E	700–953	0.512274	20	−7.1[a]	16–35
MD-06 Nosicaa	DR75-0012	DR75-0012	MNHN-GS-DR75-0012	Agulhas Plateau	37°32'S	27°00'E	2550–2550	0.512119	6	−10.1	60–68
	DR75-0012	DR75-08		Agulhas Plateau	37°32'S	27°00'E	2550–2550	0.512094	26	−10.6[a]	66–73

[a] Albarède et al. (1997).
[b] Numbers are percentages of NADW calculated with Pacific water mass end-member values of $\varepsilon_{Nd} = -4$ and −6 (Frank et al., 2002).

et al. (1994). Nd fractions were loaded on double Re filaments and measured in static mode on a multicollector Thermal Ionization Mass Spectrometer (ThermoScientific Triton) at the "Pôle de Spectrométrie Océan" in Brest, France. The measured $^{143}Nd/^{144}Nd$ ratio was corrected for mass fractionation by normalizing to $^{146}Nd/^{144}Nd = 0.7219$ and the ε_{Nd} values were calculated as expressed in Eq. (1). Nd isotope composition of standard JNdi was analyzed to monitor instrumental drift. The averaged result of $^{143}Nd/^{144}Nd = 0.512088 \pm 7$ ($2\sigma \times 10^{-6}$; $n = 14$) was consistent with its certified value of $^{143}Nd/^{144}Nd = 0.512115 \pm 7$ ($2\sigma \times 10^{-6}$; Tanaka et al., 2000) corresponding to a LaJolla Nd isotope composition value of $^{143}Nd/^{144}Nd = 0.511858 \pm 7$ ($2\sigma \times 10^{-6}$; Lugmair et al., 1983), so that no instrumental bias had to be taken in account. The standard deviation of this average is ±0.13 ε_{Nd} unit and associated to each sample analysis. Blank values are below an average of 100 pg and therefore negligible in all cases.

4. Nd isotope compositions

The Nd isotope signatures from the surface layer of the Fe-Mn crusts highlight the large variability (between $\varepsilon_{Nd} = -7.1$ and -10.1) of water mass compositions (Table 2, Fig. 2). In several hydrodynamic and geochemical studies (Toole and Warren, 1993; Jeandel et al., 1995; McCave et al., 2005; Ullgren et al., 2012; Collins et al., 2016), an average water depth of 1500 mbsl is considered to separate intermediate layers (AAIW between 800 and 1500 mbsl, RSW between 900 and 1200 mbsl)

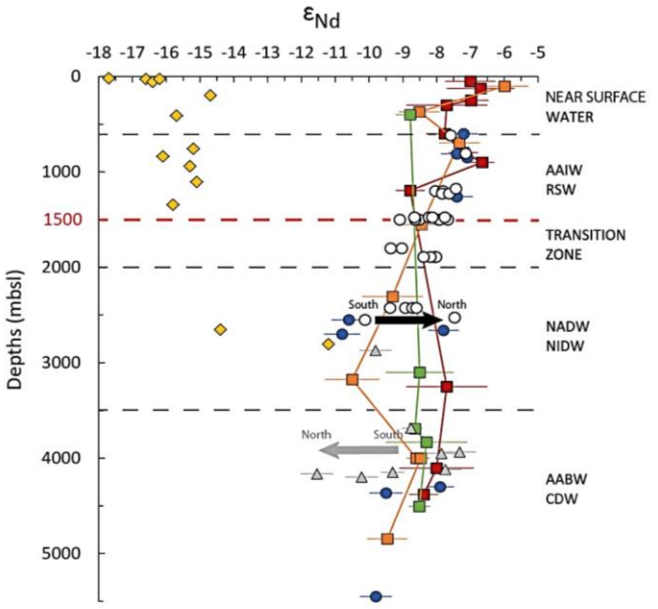

Fig. 2. Plot comparing ε_{Nd} data obtained from surface layer of Fe-Mn crusts (this study; white points) to ε_{Nd} values from the region. The yellow diamonds represent ε_{Nd} data from Zambezi sediments along the Mozambique Margin (van der Lubbe et al., 2016); the grey triangles show ε_{Nd} values from uncleaned foraminiferal coatings from the Madagascar Basin and Mascarene Basin (Wilson et al., 2012) and the blue points correspond to ε_{Nd} data from Fe-Mn nodules (Albarède et al., 1997). Seawater ε_{Nd} profiles are represented in green, orange and red respectively from the Madagascar Basin (CD1504/CD1505), the Somali Basin (CD1506/CD1507) and the Mascarene Basin (CD1502/CD1503; Bertram and Elderfield, 1993). Error bars on the data points represent 2σ. The grey arrow represents the Nd isotope variation of Wilson et al. (2012) study linked to unradiogenic Nd inputs along the Madagascan margin, whereas the black arrow corresponds to the trend of our study showing the opposite of that expected with a boundary exchange along an unradiogenic shelf. Black dotted lines and labels show the western Indian Ocean water column structure. Red dotted line corresponds to the average water depth of 1500 mbsl considered to separate intermediate and deep layers.(For interpretation of the references to color in this figure legend, the reader is referred to the web version of this article.)

from deep layers (NADW and NIDW at more than 1500–2000 mbsl). Therefore, Nd isotope composition of samples located above and below 1500 mbsl will be presented separately (Fig. 3). However, one must note that 4 dredge operations (including 9 samples) were performed both above and just below 1500 mbsl (Fig. 2). For convenience, these results will be included with those obtained on Fe-Mn crusts located strictly above 1500 mbsl; but will be discussed separately.

17 Fe-Mn crusts located above 1500 mbsl were analyzed in this study. South of the Davie Ridge, dredge 19 (DR19) is the shallowest (1000–1350 mbsl). This operation was carried out north of the Jaguar Bank and presents a sample crust with a Nd isotope composition of $\varepsilon_{Nd} = -7.4$ (Table 2, Fig. 3A). The southernmost samples, from dredge 22 (DR22; 1400–1570 mbsl), are located near Europa. For these samples, ε_{Nd} range from -7.8 to -8.7 ($n = 4$). North of these 2 dredges, near Bassas da India, samples collected with dredge 16 (DR16; 1350–1600 mbsl) show unradiogenic compositions of $\varepsilon_{Nd} = -8.6$ and -9.1. In the southern part of the Davie Ridge, south of the Sakalaves Mounts (DR15; 1200–1250 mbsl), the compositions are more radiogenic with ε_{Nd} values of -7.8 and -7.6. At the summit of the Sakalaves Mounts (DR14; 580–650 mbsl), the crust presents an $\varepsilon_{Nd} = -7.6$, whereas north of the Sakalaves Mounts (DR13; 1000–1400 mbsl), the composition is less radiogenic with a value of $\varepsilon_{Nd} = -8.5$. In the northern part of the Davie Ridge, we analyzed 2 Nd isotope compositions on 2 different crusts. The Fe-Mn crust located on the Macua Mount (DR10; 1000–1400 mbsl) shows radiogenic compositions of $\varepsilon_{Nd} = -7.8$ and -8.0, whereas the sample located on the Paisley Mount on the western slope of the Davie Ridge (DR84–0026; 810 mbsl) exhibits an isotopic composition of $\varepsilon_{Nd} = -7.1$. The analyzed samples from the southwest of Juan de Nova (DR12; 1350–1650 mbsl) show ε_{Nd} values ranging from -7.7 to -7.9 ($n = 3$).

Below 1500 mbsl, 12 Fe-Mn crusts provided Nd isotope compositions. The deepest crust was recovered on the Agulhas Plateau (DR75–0012; 2550 mbsl), 2500 km south of the Davie Ridge (Fig. 1A). It provides an ε_{Nd} value of -10.1 (Table 2, Fig. 3B). Further north, on the east of the Hall Bank (DR17; 1700–1900 mbsl), the ε_{Nd} are -9.0 and -9.4. North of the Davie Ridge, the analyzed samples from the Jeffrey Ridge (DR11; 2400–2450 mbsl) show values ranging between $\varepsilon_{Nd} = -8.6$ and -9.4 ($n = 4$), and the results from the samples located at the Glorieuses Islands (DR01; 2400–2650 mbsl, DR04; 1750–2050 mbsl) attest to more radiogenic Nd isotope compositions in the range of $\varepsilon_{Nd} = -7.5$ to -8.4 ($n = 5$).

5. Discussion

5.1. Characterization of the ε_{Nd} records

5.1.1. Impact of glacial/interglacial variability

Given the relatively slow accretion rates, the 29 studied samples span a time range between 20 and 80 ka, including the record variations of marine isotope stages (MIS) 1 (present to 14 ka), MIS 2 (14 to 29 ka), MIS 3 (29 to 57 ka), MIS 4 (57 to 71 ka) and to a lesser extent MIS 5 (71 to 130 ka). Changes in the broad patterns of ocean circulation and particles fluxes have been identified between the interglacial MIS 1, 3, 5 and the glacial stages 2, 4 (Curry and Lohmann, 1982; Boyle, 1988; Broecker and Denton, 1990; Rutberg et al., 2000; Bayon et al., 2002; Yu et al., 2008; Roberts et al., 2010; Piotrowski et al., 2004, 2005, 2012; Wei et al., 2016). In particular, Nd isotope variations of Fe-Mn oxide coatings and bulk sediment reductive leachates from southeast Atlantic cores, located near the Cape Basin, indicate cyclic changes with climate stages (Rutberg et al., 2000; Piotrowski et al., 2004, 2005, 2012): during the last glacial maximum (LGM, MIS 2) and the MIS 4 the cores recorded radiogenic ε_{Nd} values ($-6 > \varepsilon_{Nd} > -7$), while the Nd isotope signatures were unradiogenic ($-9 > \varepsilon_{Nd} > -10$) during the interglacial timescales (MIS 1, 3, 5). This variation characterized by a shift of 2 to 3 ε_{Nd} units suggests less NADW flux reached the Southern Ocean during cold stages but an increasing export of NADW during the warm climate intervals (Rutberg et al., 2000), with direct influence on the Nd isotope signature

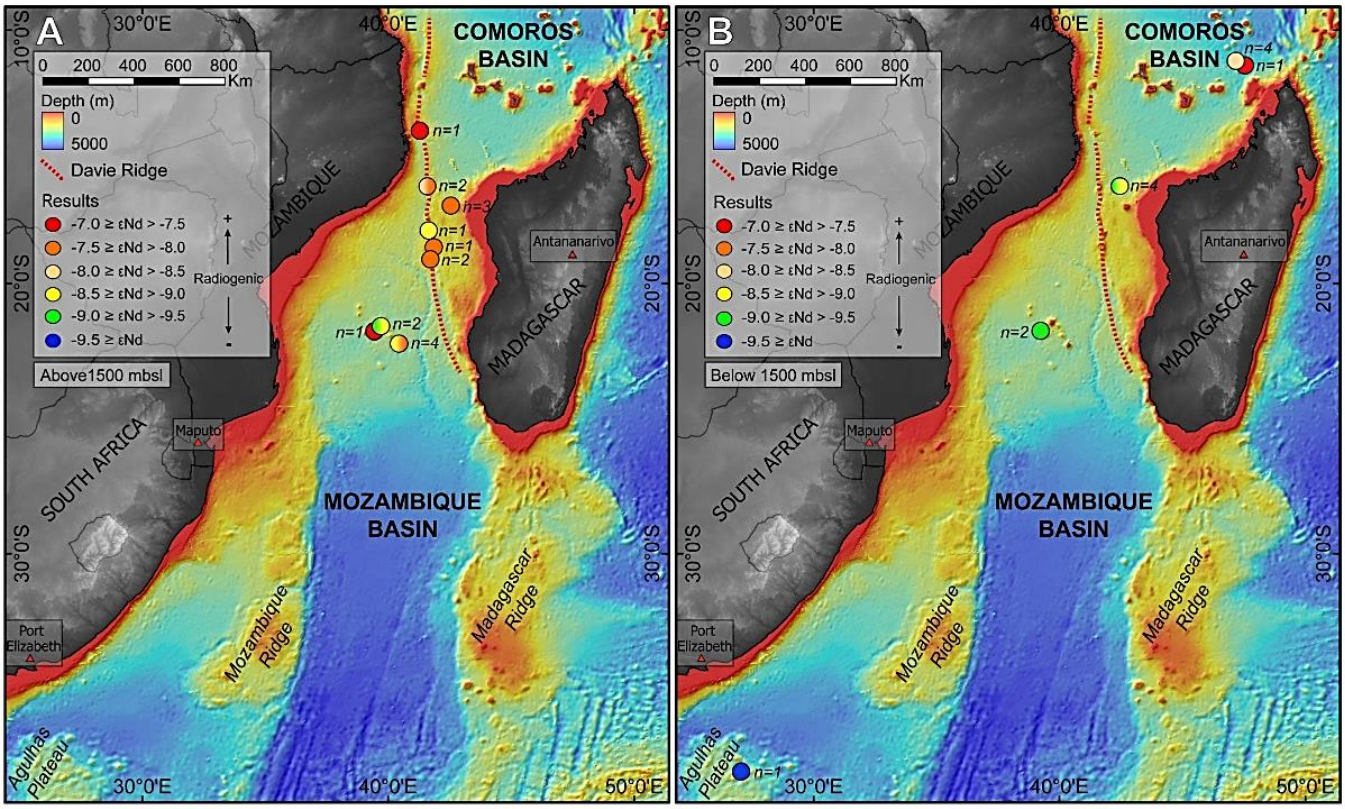

Fig. 3. (A) Bathymetry of the Mozambique Channel (data from GEBCO and PAMELA cruises) with ε_{Nd} values of the samples located above 1500 mbsl. (B) Bathymetry of the Mozambique Channel (data from GEBCO and PAMELA cruises) showing ε_{Nd} values of the samples located below 1500 mbsl. "*n*" represents the number of samples analysed per dredge.

of the Indian deep waters during the MIS (Piotrowski et al., 2009).

However, it has been demonstrated in several studies that, given their slow accumulation rates of few mm/Ma, the Nd isotope records from the outer layers of Fe-Mn oxides represent averages of several glacial/interglacial cycles (Abouchami et al., 1997; Albarède and Goldstein, 1992). The short-term changes in the patterns of ocean circulation and particle fluxes have had only minor integrated effects (Abouchami et al., 1997; Albarède and Goldstein, 1992). Insofar as the ε_{Nd} measurements of this work are going to be contrasted to present-day seawater Nd isotope signatures, it is important to notice that their analysis provides time-integrated information on the ε_{Nd} variations, which can be compared with the modern oceanic circulation (Albarède et al., 1997; Piotrowski et al., 2009; Wilson et al., 2012).

5.1.2. Influence of unradiogenic African margin on ε_{Nd} signatures

As explained in § 2.1, the African continental margin is characterized by an unradiogenic signature of $\varepsilon_{Nd} \sim -20$ (Jeandel et al., 2007), which represents an average of South African Archean cratonic rocks (Jelsma et al., 1996; Möller et al., 1998; De Waele et al., 2006; Grantham et al., 2011) and younger volcanic sources (Grousset et al., 1992; Jourdan et al., 2007; Fig. 1B). Studies in the modern ocean have suggested that inputs of river loads (van der Lubbe et al., 2016; Rahlf et al., 2020) as well as exchange between particulate and dissolved fractions along African continental margins (Rickli et al., 2010; Stichel et al., 2012b; Wilson et al., 2012) may have an important impact on the Nd isotope composition of Atlantic and Indian Oceans. In addition, recent studies have demonstrated that the pore waters can strongly control the REE compositions of the bottom waters (Haley and Klinkhammer, 2003; Schacht et al., 2010; Abbott et al., 2015a, 2015b; Du et al., 2016; Haley et al., 2017; Abbott, 2019).

In the Mozambique Channel, surface waters of the Zambezi and Limpopo discharge have unradiogenic signatures ($-14.7 > \varepsilon_{Nd} > -15.5$ and up to -22.4 respectively; Rahlf et al., 2020). This is thought to influence highly unradiogenic Nd isotope signatures ($\varepsilon_{Nd} = -18.9$ and $\varepsilon_{Nd} = -17.6$) of surface waters (<600 mbsl) linked to the AC inflow (Stichel et al., 2012b; Rahlf et al., 2020). Moreover, it has been observed that Nd isotope compositions of water masses can be modified up to a spatial variability of ~4 ε_{Nd} units due to the boundary exchange process between seawater and the unradiogenic Madagascan shelf ($\varepsilon_{Nd} \sim -25$; Paquette et al., 1994; Kröner et al., 2000), as shown by Wilson et al. (2012). Our work presents 1 sample from near surface water masses (DR14; 580–650 mbsl) and 6 other Fe-Mn crusts from intermediate waters between 800 and 1400 mbsl (DR10, DR15, DR19 and DR84–0026; Fig. 2). These dredges are spatially spread out over 900 km from the Paisley Mount (DR84–0026) to the Jaguar Bank (DR19) and under the influence of the MC, which spreads from the northern part of the Mozambique Channel and is dragged southbound. 6 of them are located north of the Zambezi (DR84–0026, DR10, DR12, DR13, DR14 and DR15) while the other 3 are situated south of the river mouth (DR16, DR19 and DR22; Fig. 1A).

Considering the hypothesis of the Zambezi River loads, the compositions of the samples located in the northern part of the channel are expected to reflect the radiogenic influence of the RSW. Conversely, the crusts located south of the river mouth should indicate unradiogenic Nd isotope signature resulting from continental Nd inputs (Stichel et al., 2012b; Rahlf et al., 2020). In the case of gradual southwards boundary exchange and/or impact of pore waters, it would involve a progressive change of ε_{Nd} signatures. If the MC acquires unradiogenic composition during its spreading along the East African margin as suggested by Wilson et al. (2012), we expect to observe a trend from radiogenic values in the northern part of the channel to unradiogenic signature in the south. However, our results show a narrow range from $\varepsilon_{Nd} = -7.1$ to

−8.0 (Fig. 2) and display no abrupt or continuous variations in the Nd isotope signature along the N-S profile. Indeed, the southernmost sample (DR19) presents a value of $\varepsilon_{Nd} = -7.4$ (Table 2, Fig. 3A), whereas it expected to have the more unradiogenic ε_{Nd} whether in the case of river inputs, boundary exchange and/or pore waters influence hypotheses. Moreover, the lowest and the highest ε_{Nd} signatures are observed from DR84–0026 ($\varepsilon_{Nd} = -7.1$) and DR10 ($\varepsilon_{Nd} = -8.0$) located in the northern part of the Mozambique Channel in a distance of 200 km from each other (Fig. 3A). As consequence, our data do not support a major influence of unradiogenic Nd inputs from the river discharges or the continental shelf.

We present 12 samples from the deep water masses (DR01, DR04, DR11, DR17 and DR75–0012; between 1700 and 2550 mbsl; Fig. 2), spatially spread out over 3500 km from the Glorieuses Islands (DR01) to the Agulhas Plateau (DR75–0012; Fig. 3B). In contrast to the crusts from the overlying water masses, these are under the influence of the NADW inflow starting upstream of the south of Africa before entering the Mozambique Channel through the Natal Valley (Toole and Warren, 1993; Fig. 1B). If the unradiogenic Nd isotope addition processes had an impact on the deep water masses, one would predict that this influence would increase as the NADW flows northward. However, the data are increasingly radiogenic towards the north, from $\varepsilon_{Nd} = -10.2$ above the Agulhas Plateau to $\varepsilon_{Nd} = -7.5$ near the Glorieuses Islands (Fig. 3B). Whereas the results of Wilson et al. (2012) present a decreasing radiogenic trend as the boundary exchange occurs, from $\varepsilon_{Nd} = -8.8$ above the Madagascar Ridge to $\varepsilon_{Nd} = -11.5$ in the northeast of the island (Fig. 2). Considering a simple boundary exchange between the African continental margin ($\varepsilon_{Nd} \sim -20$; Jeandel et al., 2007), the NADW arriving from south of Africa ($\varepsilon_{Nd} \sim -11$; Rahlf et al., 2020) and a boundary exchange rate of 28% calculated by Wilson et al. (2012), the Nd isotope composition of the crust from DR75–0012 is supposed to be $\varepsilon_{Nd} = -13.5$. Furthermore, if the interaction with the unradiogenic margin is continuous from the Agulhas Plateau to the Glorieuses Islands, the results would present Nd isotope compositions considerably lower than $\varepsilon_{Nd} = -13.5$ in all the crusts from the deep waters (DR17, DR11, DR04 and DR01). It would be the same observation in the context of unradiogenic Nd inputs from river discharges or pore waters. However, this is not apparent in our results ($\varepsilon_{Nd} = -10.2$ from the Agulhas Plateau and $\varepsilon_{Nd} = -7.1$ at the Glorieuses Islands; Fig. 3B) which are too radiogenic to be explained by the boundary exchange between the NADW and the African shelf.

Finally, the isotopic data of our work are consistent with previous studies (Fig. 2), which are focused on the conservative water mass mixing process in the same geographic area on Fe-Mn crusts (Albarède et al., 1997) and in seawater (Bertram and Elderfield, 1993). Although a slight contribution of the unradiogenic inputs from the African margin cannot be completely ruled out, we assume that our results are mainly due to water mass mixing process. The following sections will therefore discuss the identification of water masses from Nd isotope compositions and their hydrographic frameworks through the Mozambique Channel.

5.2. Intermediate layers and Indian water influence (<1500 mbsl)

Above 1500 mbsl, 1 sample provides information on the superficial water masses. Located on the Sakalaves Mounts and at shallow depths (DR14; 580–650 mbsl), this crust displays a value of $\varepsilon_{Nd} = -7.6$ likely corresponding to the Nd isotope composition of the SICW (Fig. 1C, Table 1). This is the only result on this water mass and thus it will not be discussed further here.

However, the 6 other samples are located between 800 and 1400 mbsl (DR10, DR15, DR19 and DR86–0026), illustrating the Nd isotope composition of intermediate water masses. With an range of values between $\varepsilon_{Nd} = -7.1$ and −8.0, these Fe-Mn crusts recorded Indian intermediate water (Tables 1 and 2). This intermediate layer could correspond to the RSW arriving from the north of the Mozambique Channel, following the African continental margin southward (Beal et al., 2000) to the Paisley Mount and the Macua Mount (Fig. 1). The hydrographic flow path of these Indian intermediate water masses south of the Davie Ridge (south of the Sakalaves Mounts and Jaguar Bank) could be explained by the presence of anticyclonic eddies passing through the narrowest part of the Mozambique Channel carrying saline and warm RSW southward as described previously by Ullgren et al. (2012) and Miramontes et al. (2019).

5.3. Transition zone between intermediate and deep layers

The 10 samples from the north of the Sakalaves Mounts (DR13), near Juan de Nova (DR12), Bassas da India and Europa (DR16 and DR22) present ε_{Nd} in the range of −7.7 to −9.1 (Table 2, Fig. 2). Both extremes are marked by the influence of distinct water masses. The $\varepsilon_{Nd} = -9.1$ (DR16, Bassas da India) is lower and may point out to an Atlantic inflow in the Mozambique Basin. Other values such as $\varepsilon_{Nd} = -8.7$ (DR22, Europa), −8.6 (DR16, Bassas da India) and −8.5 (DR13, North of the Sakalava Mounts) also suggest a slight influence of Atlantic currents (Table 1). North of the Davie Ridge, more radiogenic values measured on crusts located near Juan de Nova ($\varepsilon_{Nd} > -8.0$; $n = 3$) correspond to the Indian intermediate water mass inflow as described in § 5.2. However, dredge 22 shows heterogeneous isotopic compositions with one sample at $\varepsilon_{Nd} = -8.7$ that likely indicate Atlantic influence, but also 2 samples with $\varepsilon_{Nd} > -8.5$ (−8.2 and −8.1) and one crust with $\varepsilon_{Nd} > -8.0$ (−7.7) suggesting the presence of Indian water mass.

Therefore, it is imperative to understand why both Atlantic and Indian water mass inflows are recorded in the same area (Fig. 3A). Two assumptions can be considered. The first is the confrontation of the AAIW and RSW intermediate currents whose depths and thicknesses are relatively similar (Fig, 1C, Table 1). In this case, the Nd isotope variations observed would be related to mixing of the unradiogenic AAIW that enters from the south of the channel, and the more radiogenic RSW arriving from the northwest part of the Mozambique Channel (Fig. 1C). The unradiogenic results would be related to a strong AAIW influence whereas the more radiogenic values would correspond to a robust RSW inflow in the channel. However, the integrated time in these surface scraping is in the order of 30 to 80 ka due to the slow accretion rates of this studied samples ranging from 1.3 to 3.6 mm/Ma. It provides time-integrated information on the sources of Nd (Albarède et al., 1997; Frank et al., 2002) and, should streamline water mass variations mainly related to glacial and interglacial changes. In this case, the recorded isotopic compositions should be relatively homogeneous. The second hypothesis heeds the depths of the starting and ending points of dredge operations (e.g. DR16; 1600–1350 mbsl), which can lead to the recovery of Fe-Mn crusts that are under the influence of deep water masses (NADW, NIDW) and/or intermediate water masses (RSW, AAIW; Table 1, Fig. 2). Thus, within the same dredge (i.e. DR22; 1400–1550 mbsl), some samples could have recorded the isotopic composition of the intermediate currents while others could have recorded the isotopic signature of a transition zone between intermediate and deep water masses (Fig. 2). In this case, differences in the recorded Nd isotope compositions would be related to the thickness variations of the water masses in the Mozambique Channel over the last 100 ka.

5.4. Deep layers (>1500 mbsl)

The Nd isotope compositions, recorded on Fe-Mn crusts located between 1700 and 2650 mbsl, provided a significant number of results ($n = 12$) with a clear isotopic trend from the south to the north of the Mozambique Channel (Fig. 3BB). Southwestern of the Davie Ridge, the crust from the Agulhas Plateau (DR75–0012) presents an unradiogenic result of $\varepsilon_{Nd} = -10.1$ likely reflecting Atlantic deep water arrival in the Mozambique Channel (Fig. 1B, Table 1). Using the calculation of Frank et al. (2002), the contribution of the NADW is estimated at 60% in the Agulhas Plateau fixing Atlantic seawater $\varepsilon_{Nd} = -13$ and Pacific seawater $\varepsilon_{Nd} = -6$ (68% with Pacific seawater $\varepsilon_{Nd} = -4$; Table 2, Fig. 4). This

percentage is supported by the study of Rahlf et al. (2020), which estimates a mixing between a NADW fraction of up to 80–90% with the CDW eastern Cape Basin. The contribution of NADW then decreases southward, reflecting a gradual dilution with southern waters. Its influence is recorded all the way to the Hall Bank with values $\varepsilon_{Nd} = -9.0$ and −9.4 (DR17). In this area the NADW inflow is calculated between 43% and 48% (56% and 60% with Pacific seawater $\varepsilon_{Nd} = -4$; Table 2, Fig. 4). By contrast, in the north of the Mozambique Channel, near the Glorieuses Islands (DR01 and DR04), the Nd isotope compositions are more radiogenic ($-7.5 > \varepsilon_{Nd} > -8.4$; $n = 5$) corresponding to the Indian Ocean influence by the arrival of the NIDW in the Comoros Basin (Fig. 1B, Table 1). In the northern part of the channel, the contribution of the NADW is estimated between 21% and 34% (39% and 49% with Pacific seawater $\varepsilon_{Nd} = -4$; Table 2, Fig. 4). These values correspond to the contributions of Atlantic water masses in the mixing with Pacific water masses in the current Indian Ocean. Therefore, the NADW from the south of the Mozambique Channel does not seem to be present in the northern part of the Comoros Basin. However, less radiogenic compositions (up to $\varepsilon_{Nd} = -9.4$; DR11) were recorded north of the Davie Ridge, on a ridge in the Comoros Basin, 90 km north of Juan de Nova and 700 km southwest of the Glorieuses Islands (Table 2, Fig. 3B). These unradiogenic values cannot be explained solely by the presence of the NIDW in the northern part of the Mozambique Channel. The inflow of the NADW is estimated between 37% and 48% (51% and 60% with Pacific seawater $\varepsilon_{Nd} = -4$; Table 2, Fig. 4). These estimates of the Atlantic inflow show that a significant portion of the NADW crosses the Davie Ridge and flows into the northern part of the channel without reaching the Glorieuses Islands.

5.5. NADW northern boundary

This study reveals a trend based on Nd isotope compositions of Fe-Mn crusts from unradiogenic values in the south of the Africa, on the Agulhas Plateau, to more radiogenic values in the north of the Mozambique Channel (Table 2, Fig. 3). For the first time it is possible to identify and quantify the NADW influence in the Mozambique Channel to the Comoros Basin through a geochemical study of Fe-Mn crusts (Fig. 4). The only research carried out on Fe-Mn crusts in this area is that of Albarède et al. (1997), Fig. 2, indicating unradiogenic value in the southwestern part of the Mozambique Channel as presented before but an isocontour of $\varepsilon_{Nd} = -8$ upstream of the Mozambique Basin and Madagascar. This isotope limit suggests a significant restriction of the

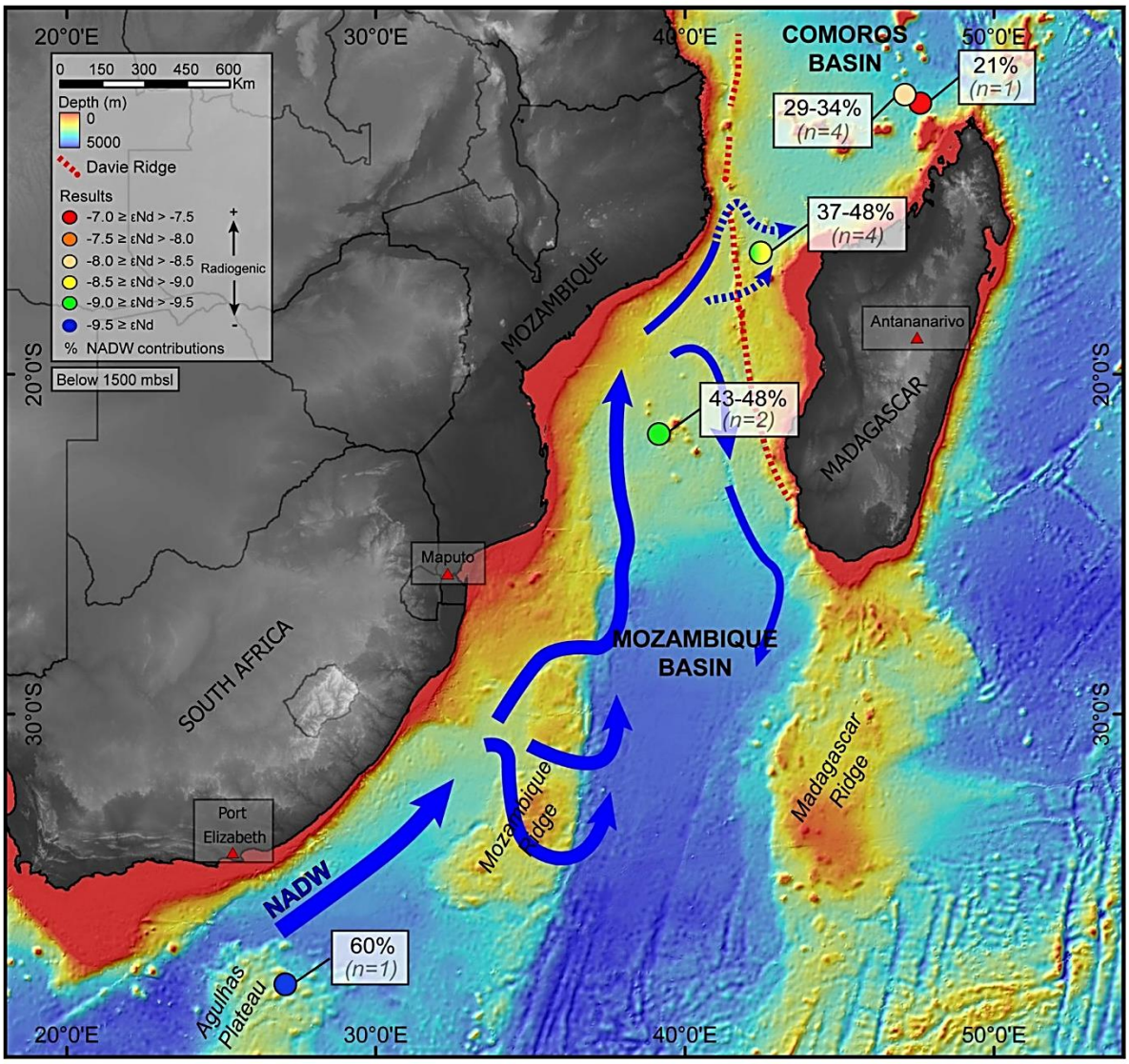

Fig. 4. Bathymetry of the Mozambique Channel (data from GEBCO and PAMELA cruises) showing Atlantic waters contributions estimated through the Mozambique Channel (for Pacific $\varepsilon_{Nd} = -6$) and the resulting circulation of NADW. The dashed arrows present a suggestion of potential NADW passages beyond the Davie Ridge.

NADW input into the Mozambique Channel which is not consistent with our results, suggesting this isotope limit further north and most importantly north of the Davie Ridge (Fig. 4). The differences in the Nd isotope values between both studies are undoubtedly related to the depth of the samples. Indeed, Albarède et al. (1997) were interested in Nd global trends in the oceans. In the centre part of the Mozambique Channel, their isotopic analyses were measured on crusts from surface layers (~600 mbsl; Fig. 2). As described in previous sections, these water masses have Nd isotope signatures from the Indian Ocean (Table 1) and are therefore naturally much more radiogenic than the results of our study, which also focuses on intermediate and deep water mass flow path.

Simultaneously, two major hydrographic studies advance scientific knowledge on the Atlantic and Indian deep currents in the Mozambique Channel. van Aken et al. (2004) noted the influence of the NADW current at depths between 1500 and 2500 mbsl in the channel. This was supported and expanded upon by the hydrographic research of Collins et al. (2016). The NADW and NIDW currents were recorded in the Comoros Basin, according to their salinity and oxygen levels. The current flow path of these deep water masses in the Mozambique Channel is therefore a visible and currently quantified phenomenon. Our study confirms the presence of the NADW in the northern part of the channel and strongly suggests a passage of the NADW beyond the Davie Ridge (Fig. 4), implying that this topographic barrier does not currently act as an impassable obstacle to the circulation of deep currents in the Mozambique Channel.

6. Summary and conclusion

Fe-Mn crusts are highly studied ocean resources in terms of their geochemical composition as archives of the chemical composition of water masses. The analysis of 29 crusts sampled in the Mozambique Channel show Nd isotope records ranging from unradiogenic values ($\varepsilon_{Nd} = -10.1$) in the Agulhas Plateau to more radiogenic values ($\varepsilon_{Nd} = -7.5$) north of the Mozambique Channel, near the Glorieuses Islands.

First, this study reveals the presence of the Indian intermediate seawater above 1500 mbsl. Secondly, the crusts dredged at depths between 1300 and 1650 mbsl show significant isotopic variations (between $\varepsilon_{Nd} = -7.7$ and -9.1), probably due to their location in a transition zone between intermediate and deep water masses with contrasted Nd isotope signatures. Finally, unradiogenic compositions are recorded beyond the Davie Ridge. These new results suggest significant contributions of the NADW flowing from the south below 1500 mbsl and crossing the Davie Ridge to be recorded in the northern part of the Mozambique Channel, in the Comoros Basin.

This unique collection of crust samples improves our understanding of the Atlantic and Indian water mass flow path in this complex area. As this key area of oceanic mixing has undergone diverse geodynamic movements, it would be interesting to carry out isotope studies on several time series distributed from the Agulhas Plateau to the Glorieuses Islands at different depths (especially in the transition zone). These future studies would allow to identify and understand major geodynamic and oceanographic events in the Mozambique Channel up to the Miocene.

Declaration of Competing Interest

The authors declare that they have no known competing financial interests or personal relationships that could have appeared to influence the work reported in this paper.

Acknowledgments

We thank the Captains, crews and onboard scientific teams of the PAMELA-MOZ01 survey onboard the R/V *L'Atalante* and, the RIDA-MD39 and the NOSICAA-MD06 surveys onboard the R/V Marion Dufresne. The oceanographic survey PAMELA-MOZ01, as well as Claire CHARLES PhD are co-funded by TOTAL and IFREMER as part of the PAMELA (Passive Margin Exploration Laboratories) scientific project. The PAMELA project is a scientific project led by Ifremer and TOTAL in collaboration with the Université de Bretagne Occidentale, Université Rennes 1, Université Pierre et Marie Curie, CNRS and IFPEN. The authors are grateful to Anne-Sophie Alix, Philippe Fernagu and Thierry Dalle Mulle for their help and the crust-sample preparation. We also thank the MNHN, Eva Moreno and Lola Johannes for allowing us to access and borrow samples from the RIDA-MD39 and NOSICAA-MD06 oceanographic expeditions belonging to the oceanic collection. We gratefully acknowledge Editor-in-Chief Michele Rebesco, Guest Editor Vittorio Maselli, Jean-Carlos Montero-Serrano and an anonymous reviewer for thorough and thoughtful comments that significantly improved the manuscript.

References

Abbott, A.N., 2019. A benthic flux from calcareous sediments results in non-conservative neodymium behavior during lateral transport: a study from the Tasman Sea. Geology 47, 363–366. https://doi.org/10.1130/G45904.1.

Abbott, A.N., Haley, B.A., McManus, J., 2015a. Bottoms up: sedimentary control of the deep north Pacific Ocean's εNd signature. Geology 43, 1035. https://doi.org/10.1130/G37114.1.

Abbott, A.N., Haley, B.A., McManus, J., Reimers, C.E., 2015b. The sedimentary flux of dissolved rare earth elements to the ocean. Geochim. Cosmochim. Acta 154, 186–200. https://doi.org/10.1016/j.gca.2015.01.010.

Abouchami, W., Goldstein, S.L., Gazer, S.J.G., Eisenhauer, A., Mangini, A., 1997. Secular changes of lead and neodymium in central Pacific seawater recorded by a Fe-Mn crust. Geochim. Cosmochim. Acta 61, 3957–3974. https://doi.org/10.1016/S0016-7037(97)00218-4.

van Aken, H.M., Ridderinkhof, H., de Ruijter, W.P.M., 2004. North Atlantic deep water in the south-western Indian Ocean. Deep Sea Res. Part Oceanogr. Res. Pap. 51, 755–776. https://doi.org/10.1016/j.dsr.2004.01.008.

Albarède, F., Goldstein, S.L., 1992. World map of Nd isotopes in sea-floor ferromanganese deposits. Geology 20, 761–763. https://doi.org/10.1130/0091-7613(1992)020<0761:WMONII>2.3.CO;2.

Albarède, F., Goldstein, S.L., Dautel, D., 1997. The neodymium isotopic composition of manganese nodules from the Southern and Indian oceans, the global oceanic neodymium budget, and their bearing on deep ocean circulation. Geochim. Cosmochim. Acta 61, 1277–1291. https://doi.org/10.1016/S0016-7037(96)00404-8.

Albarède, F., Simonetti, A., Vervoort, J.D., Blichert-Toft, J., Abouchami, W., 1998. A Hf-Nd isotopic correlation in ferromanganese nodules. Geophys. Res. Lett. 25, 3895–3898. https://doi.org/10.1029/1998GL900008.

Amakawa, H., Tazoe, H., Obata, H., Gamo, T., Sano, Y., Shen, C.-C., 2013. Neodymium isotopic composition and concentration in the Southwest Pacific Ocean. Geochem. J. 47, 409–422. https://doi.org/10.2343/geochemj.2.0260.

Amakawa, H., Yu, T.-L., Tazoe, H., Obata, H., Gamo, T., Sano, Y., Shen, C.-C., Suzuki, K., 2019. Neodymium concentration and isotopic composition distributions in the southwestern Indian Ocean and the Indian sector of the Southern Ocean. Chem. Geol. 511, 190–203. https://doi.org/10.1016/j.chemgeo.2019.01.007.

Aplin, A., Cronan, D., 1985. Ferromanganese oxide deposits from the Central Pacific Ocean, I. Encrustations from the Line Islands Archipelago. Geochim. Cosmochim. Acta 49, 427–436. https://doi.org/10.1016/0016-7037(85)90034-1.

Aplin, A., Michard, A., Albarède, F., 1986. 143Nd/144Nd in Pacific ferromanganese encrustations and nodules. Earth Planet. Sci. Lett. 81, 7–14. https://doi.org/10.1016/0012-821X(86)90096-8.

Arsouze, T., Dutay, J.-C., Lacan, F., Jeandel, C., 2007. Modeling the neodymium isotopic composition with a global ocean circulation model. Chem. Geol. 239, 165–177. https://doi.org/10.1016/j.chemgeo.2006.12.006.

Arsouze, T., Dutay, J.-C., Lacan, F., Jeandel, C., 2009. Reconstructing the Nd oceanic cycle using a coupled dynamical – biogeochemical model. Biogeosciences 6, 2829–2846. https://doi.org/10.5194/bg-6-2829-2009.

Bassias, Y., 1992. Petrological and geochemical investigation of rocks from the Davie fracture zone (Mozambique Channel) and some tectonic implications. J. Afr. Earth Sci. Middle East 15, 321–339. https://doi.org/10.1016/0899-5362(92)90018-8.

Bayon, G., German, C.R., Boella, R.M., Milton, J.A., Taylor, R.N., Nesbitt, R.W., 2002. An improved method for extracting marine sediment fractions and its application to Sr and Nd isotopic analysis. Chem. Geol. 187, 179–199. https://doi.org/10.1016/S0009-2541(01)00416-8.

Bayon, G., Toucanne, S., Skonieczny, C., André, L., Bermell, S., Cheron, S., Dennielou, B., Etoubleau, J., Freslon, N., Gauchery, T., Germain, Y., Jorry, S.J., Ménot, G., Monin, L., Ponzevera, E., Rouget, M.-L., Tachikawa, K., Barrat, J.A., 2015. Rare earth elements and neodymium isotopes in world river sediments revisited. Geochim. Cosmochim. Acta 170, 17–38. https://doi.org/10.1016/j.gca.2015.08.001.

Beal, L.M., Ffield, A., Gordon, A.L., 2000. Spreading of Red Sea overflow waters in the Indian Ocean. J. Geophys. Res. Oceans 105, 8549–8564. https://doi.org/10.1029/1999JC900306.

Bertram, C.J., Elderfield, H., 1993. The geochemical balance of the rare earth elements and neodymium isotopes in the oceans. Geochim. Cosmochim. Acta 57, 1957–1986. https://doi.org/10.1016/0016-7037(93)90087-D.

Boyle, E.A., 1988. Vertical oceanic nutrient fractionation and glacial/interglacial CO2 cycles. Nature 331, 55–56. https://doi.org/10.1038/331055a0.

Broecker, W.S., Denton, G.H., 1990. The role of ocean-atmosphere reorganizations in glacial cycles. Quat. Sci. Rev. 9, 305–341. https://doi.org/10.1016/0277-3791(90)90026-7.

Broecker, W.S., Peng, T., Beng, Z., 1982. Tracers in the Sea. Lamont-Doherty Geological Observatory, Columbia University.

Christensen, J.N., Halliday, A.N., Godfrey, L.V., Hein, J.R., Rea, D.K., 1997. Climate and Ocean dynamics and the lead isotopic records in pacific ferromanganese crusts. Science 277, 913–918. https://doi.org/10.1126/science.277.5328.913.

Coffin, M.F., Rabinowitz, P.D., 1987. Reconstruction of Madagascar and deep: evidence from the Davie fracture zone and western Somali Basin. J. Geophys. Res. Solid Earth 92, 9385–9406. https://doi.org/10.1029/JB092iB09p09385.

Collins, C., Hermes, J.C., Roman, R.E., Reason, C.J.C., 2016. First dedicated hydrographic survey of the Comoros Basin. J. Geophys. Res. Oceans 121, 1291–1305. https://doi.org/10.1002/2015JC011418.

Curry, W.B., Lohmann, G.P., 1982. Carbon Isotopic changes in benthic foraminifera from the western South Atlantic: reconstruction of glacial abyssal circulation patterns. Quat. Res. 18, 218–235. https://doi.org/10.1016/0033-5894(82)90071-0.

De Waele, B., Liégeois, J.-P., Nemchin, A.A., Tembo, F., 2006. Isotopic and geochemical evidence of proterozoic episodic crustal reworking within the irumide belt of south-central Africa, the southern metacratonic boundary of an Archaean Bangweulu Craton. Precambrian Res. 148, 225–256. https://doi.org/10.1016/j.precamres.2006.05.006.

DiMarco, S.F., Chapman, P., Nowlin, W.D., Hacker, P., Donohue, K., Luther, M., Johnson, G.C., Toole, J., 2002. Volume transport and property distributions of the Mozambique Channel. Deep Sea Res. Part II Top. Stud. Oceanogr. 49, 1481–1511. https://doi.org/10.1016/S0967-0645(01)00159-X.

Du, J., Haley, B.A., Mix, A.C., 2016. Neodymium isotopes in authigenic phases, bottom waters and detrital sediments in the Gulf of Alaska and their implications for paleo-circulation reconstruction. Geochim. Cosmochim. Acta 193, 14–35. https://doi.org/10.1016/j.gca.2016.08.005.

Eisenhauer, A., Gögen, K., Pernicka, E., Mangini, A., 1992. Climatic influences on the growth rates of Mn crusts during the late quaternary. Earth Planet. Sci. Lett. 109, 25–36. https://doi.org/10.1016/0012-821X(92)90071-3.

Elderfield, H., Upstill-Goddard, R., Sholkovitz, E.R., 1990. The rare earth elements in rivers, estuaries, and coastal seas and their significance to the composition of ocean waters. Geochim. Cosmochim. Acta 54, 971–991. https://doi.org/10.1016/0016-7037(90)90432-K.

Fine, R.A., 1993. Circulation of Antarctic intermediate water in the South Indian Ocean. Deep Sea Res. Part Oceanogr. Res. Pap. 40, 2021–2042. https://doi.org/10.1016/0967-0637(93)90043-3.

Flemming, B.W., Kudrass, H.-R., 2018. Large dunes on the outer shelf off the Zambezi Delta, Mozambique: evidence for the existence of a Mozambique Current. Geo-Mar. Lett. 38, 95–106. https://doi.org/10.1007/s00367-017-0515-5.

Frank, M., 2002. Radiogenic isotopes: tracers of past ocean circulation and erosional input. Rev. Geophys. 40, 1. https://doi.org/10.1029/2000RG000094.

Frank, M., O'Nions, R.K., 1998. Sources of Pb for Indian Ocean ferromanganese crusts: a record of Himalayan erosion? Earth planet. Sci. Lett. 158, 121–130. https://doi.org/10.1016/S0012-821X(98)00055-7.

Frank, M., O'Nions, R.K., Hein, J.R., Banakar, V.K., 1999. 60 Myr records of major elements and Pb–Nd isotopes from hydrogenous ferromanganese crusts: reconstruction of seawater paleochemistry. Geochim. Cosmochim. Acta 63, 1689–1708. https://doi.org/10.1016/S0016-7037(99)00079-4.

Frank, M., Whiteley, N., Kasten, S., Hein, J.R., O'Nions, K., 2002. North Atlantic Deep water export to the Southern Ocean over the past 14 Myr: Evidence from Nd and Pb isotopes in ferromanganese crusts. Paleoceanography 17, 12-1–12–9. https://doi.org/10.1029/2000PA000606.

Gaina, C., Torsvik, T.H., van Hinsbergen, D.J.J., Medvedev, S., Werner, S.C., Labails, C., 2013. The African Plate: a history of oceanic crust accretion and subduction since the Jurassic. Tectonophysics 604, 4–25. https://doi.org/10.1016/j.tecto.2013.05.037. Progress in understanding the South Atlantic margins.

Goldstein, S.J., Jacobsen, S.B., 1988. Rare earth elements in river waters. Earth Planet. Sci. Lett. 89, 35–47. https://doi.org/10.1016/0012-821X(88)90031-3.

Goldstein, S.L., Hemming, S.R., 2003. 6.17 - long-lived isotopic tracers in oceanography, paleoceanography, and ice-sheet dynamics. In: Holland, H.D., Turekian, K.K. (Eds.), Treatise on Geochemistry. Pergamon, Oxford, pp. 453–489. https://doi.org/10.1016/B0-08-043751-6/06179-X.

Goldstein, S.L., O'Nions, R.K., Hamilton, P.J., 1984. A Sm-Nd isotopic study of atmospheric dusts and particulates from major river systems. Earth Planet. Sci. Lett. 70, 221–236. https://doi.org/10.1016/0012-821X(84)90007-4.

Gordon, A.L., 1986. Interocean exchange of thermocline water. J. Geophys. Res. Oceans 91, 5037–5046. https://doi.org/10.1029/JC091iC04p05037.

Grantham, G.H., Manhica, A.D.S.T., Armstrong, R.A., Kruger, F.J., Loubser, M., 2011. New SHRIMP, Rb/Sr and Sm/Nd isotope and whole rock chemical data from central Mozambique and western Dronning Maud Land, Antarctica: implications for the nature of the eastern margin of the Kalahari Craton and the amalgamation of Gondwana. J. Afr. Earth Sci. 59, 74–100. https://doi.org/10.1016/j.jafrearsci.2010.08.005.

Grousset, F.E., Biscaye, P.E., Revel, M., Petit, J.-R., Pye, K., Joussaume, S., Jouzel, J., 1992. Antarctic (Dome C) ice-core dust at 18 k.y. B.P.: isotopic constraints on origins. Earth Planet. Sci. Lett. 111, 175–182. https://doi.org/10.1016/0012-821X(92)90177-W.

Haley, B.A., Klinkhammer, G.P., 2003. Complete separation of rare earth elements from small volume seawater samples by automated ion chromatography: method development and application to benthic flux. Mar. Chem. 82, 197–220. https://doi.org/10.1016/S0304-4203(03)00070-7.

Haley, B.A., Du, J., Abbott, A.N., McManus, J., 2017. The impact of benthic processes on rare earth element and neodymium isotope distributions in the oceans. Front. Mar. Sci. 4 https://doi.org/10.3389/fmars.2017.00426.

Halo, I., Backeberg, B., Penven, P., Ansorge, I., Reason, C., Ullgren, J.E., 2014. Eddy properties in the Mozambique Channel: A comparison between observations and two numerical ocean circulation models. Deep Sea Res. Part II Top. Stud. Oceanogr. 100, 38–53. https://doi.org/10.1016/j.dsr2.2013.10.015.

Hein, J.R., Conrad, T.A., Dunham, R.E., 2009. Seamount characteristics and mine-site model applied to exploration- and mining-lease-block selection for cobalt-rich ferromanganese crusts. Mar. Georesour. Geotechnol. 27, 160–176. https://doi.org/10.1080/10641190902852485.

Hein, J.R., Conrad, T.A., Staudigel, H., 2010. Seamount mineral deposits: a source of rare metals for high-technology industries. Oceanography 23, 184–189.

Hein, J.R., Conrad, T.A., Mizell, K., Banakar, V.K., Frey, F.A., Sager, W.W., 2016. Controls on Ferromanganese Crust Composition and Reconnaissance Resource Potential, Ninetyeast Ridge, Indian Ocean.

Heirtzler, J.R., Burroughs, R.H., 1971. Madagascar's paleoposition: new data from the Mozambique Channel. Science 174, 488–490. https://doi.org/10.1126/science.174.4008.488.

Ingri, J., Widerlund, A., Land, M., Gustafsson, Ö., Andersson, P., Öhlander, B., 2000. Temporal variations in the fractionation of the rare earth elements in a boreal river; the role of colloidal particles. Chem. Geol. 166, 23–45. https://doi.org/10.1016/S0009-2541(99)00178-3.

Jacobsen, S.B., Wasserburg, G.J., 1980. Sm-Nd isotopic evolution of chondrites. Earth Planet. Sci. Lett. 50, 139–155. https://doi.org/10.1016/0012-821X(80)90125-9.

Jeandel, C., 1993. Concentration and isotopic composition of Nd in the South Atlantic Ocean. Earth Planet. Sci. Lett. 117, 581–591. https://doi.org/10.1016/0012-821X(93)90104-H.

Jeandel, C., Bishop, J.K., Zindler, A., 1995. Exchange of neodymium and its isotopes between seawater and small and large particles in the Sargasso Sea. Geochim. Cosmochim. Acta 59, 535–547. https://doi.org/10.1016/0016-7037(94)00367-U.

Jeandel, C., Arsouze, T., Lacan, F., Téchiné, P., Dutay, J.-C., 2007. Isotopic Nd compositions and concentrations of the lithogenic inputs into the ocean: a compilation, with an emphasis on the margins. Chem. Geol. 239, 156–164. https://doi.org/10.1016/j.chemgeo.2006.11.013.

Jeandel, C., Delattre, H., Grenier, M., Pradoux, C., Lacan, F., 2013. Rare earth element concentrations and Nd isotopes in the Southeast Pacific Ocean. Geochem. Geophys. Geosyst. 14, 328–341. https://doi.org/10.1029/2012GC004309.

Jelsma, H.A., Vinyu, M.L., Wijbrans, J.R., Verdurmen, E.A.T., Valbracht, P.J., Davies, G. R., Valbracht, P.J., 1996. Constraints on Archaean crustal evolution of the Zimbabwe craton: a U-Pb zircon, Sm-Nd and Pb-Pb whole-rock isotope study. Contrib. Mineral. Petrol. 124, 55–70. https://doi.org/10.1007/s004100050173.

Johannesson, K.H., Chevis, D.A., Burdige, D.J., Cable, J.E., Martin, J.B., Roy, M., 2011. Submarine groundwater discharge is an important net source of light and middle REEs to coastal waters of the Indian River Lagoon, Florida, USA. Geochim. Cosmochim. Acta 75, 825–843. https://doi.org/10.1016/j.gca.2010.11.005.

Jones, C.E., Halliday, A.N., Rea, D.K., Owen, R.M., 1994. Neodymium isotopic variations in North Pacific modern silicate sediment and the insignificance of detrital REE contributions to seawater. Earth Planet. Sci. Lett. 127, 55–66. https://doi.org/10.1016/0012-821X(94)90197-X.

Jourdan, F., Bertrand, H., Schärer, U., Blichert-Toft, J., Féraud, G., Kampunzu, A.B., 2007. Major and trace element and sr, nd, hf, and pb isotope compositions of the karoo large igneous Province, Botswana–Zimbabwe: lithosphere vs mantle plume contribution. J. Petrol. 48, 1043–1077. https://doi.org/10.1093/petrology/egm010.

Kolla, V., Eittreim, S., Sullivan, L., Kostecki, J.A., Burckle, L.H., 1980. Current-controlled, abyssal microtopography and sedimentation in Mozambique Basin, southwest Indian Ocean. Mar. Geol. 34, 171–206. https://doi.org/10.1016/0025-3227(80)90071-7.

Koschinsky, A., Halbach, P., 1995. Sequential leaching of marine ferromanganese precipitates: genetic implications. Geochim. Cosmochim. Acta 59, 5113–5132. https://doi.org/10.1016/0016-7037(95)00358-4.

Koschinsky, A., Stascheit, A., Bau, M., Halbach, P., 1997. Effects of phosphatization on the geochemical and mineralogical composition of marine ferromanganese crusts. Geochim. Cosmochim. Acta 61, 4079–4094. https://doi.org/10.1016/S0016-7037(97)00231-7.

Kröner, A., Hegner, E., Collins, A.S., Windley, B.F., Brewer, T.S., Razakamanana, T., Pidgeon, R.T., 2000. Age and magmatic history of the Antananarivo block, central Madagascar, as derived from zircon geochronology and Nd isotopic systematics. Am. J. Sci. 300, 251–288. https://doi.org/10.2475/ajs.300.4.251.

Kusakabe, M., Ku, T.-L., 1984. Incorporation of Be isotopes and other trace metals into marine ferromanganese deposits. Geochim. Cosmochim. Acta 48, 2187–2193. https://doi.org/10.1016/0016-7037(84)90215-1.

Lacan, F., Jeandel, C., 2001. Tracing Papua New Guinea imprint on the central Equatorial Pacific Ocean using neodymium isotopic compositions and rare earth element patterns. Earth Planet. Sci. Lett. 186, 497–512. https://doi.org/10.1016/S0012-821X(01)00263-1.

Lacan, F., Jeandel, C., 2005. Neodymium isotopes as a new tool for quantifying exchange fluxes at the continent–ocean interface. Earth Planet. Sci. Lett. 232, 245–257. https://doi.org/10.1016/j.epsl.2005.01.004.

Leclaire, L., 1975. NOSICAA-MD06. RV Marion Dufresne. https://doi.org/10.17600/75010711.

Leclaire, L., 1984. RIDA-MD39. RV Marion Dufresne. https://doi.org/10.17600/84010511.

Ling, H.F., Burton, K.W., O'Nions, R.K., Kamber, B.S., von Blanckenburg, F., Gibb, A.J., Hein, J.R., 1997. Evolution of Nd and Pb isotopes in central Pacific seawater from ferromanganese crusts. Earth Planet. Sci. Lett. 146, 1–12. https://doi.org/10.1016/S0012-821X(96)00224-5.

van der Lubbe, H.J.L., Frank, M., Tjallingii, R., Schneider, R.R., 2016. Neodymium isotope constraints on provenance, dispersal, and climate-driven supply of Zambezi sediments along the Mozambique Margin during the past ~45,000 years. Geochem. Geophys. Geosyst. 17, 181–198. https://doi.org/10.1002/2015GC006080.

Lugmair, G.W., Shimamura, T., Lewis, R.S., Anders, E., 1983. Samarium-146 in the early solar system: evidence from neodymium in the allende meteorite. Science 222, 1015–1018. https://doi.org/10.1126/science.222.4627.1015.

Lusty, P.A.J., Hein, J.R., Josso, P., 2018. Formation and occurrence of ferromanganese crusts: earth's storehouse for critical metals. Elements 14, 313–318. https://doi.org/10.2138/gselements.14.5.313.

Lutjeharms, J.R.E., 2006. The Agulhas Current. Springer-Verlag, Berlin Heidelberg.

Mahoney, J., Nicollet, C., Dupuy, C., 1991. Madagascar basalts: tracking oceanic and continental sources. Earth Planet. Sci. Lett. 104, 350–363. https://doi.org/10.1016/0012-821X(91)90215-4.

Mantyla, A.W., Reid, J.L., 1995. On the origins of deep and bottom waters of the Indian Ocean. J. Geophys. Res. Oceans 100, 2417–2439. https://doi.org/10.1029/94JC02564.

McCave, I.N., Kiefer, T., Thornalley, D.J.R., Elderfield, H., 2005. Deep flow in the Madagascar Mascarene Basin over the last 150000 years. Philos. Trans. R. Soc. A Math. Phys. Eng. Sci. 363, 81–99.

McElhinny, M.W., 1970. Formation of the Indian Ocean. Nature 228, 977. https://doi.org/10.1038/228977a0.

McKenzie, D., Sclater, J.G., 1971. The evolution of the Indian Ocean since the late cretaceous. Geophys. J. Int. 24, 437–528. https://doi.org/10.1111/j.1365-246X.1971.tb02190.x.

Miramontes, E., Penven, P., Fierens, R., Droz, L., Toucanne, S., Jorry, S.J., Jouet, G., Pastor, L., Silva Jacinto, R., Gaillot, A., Giraudeau, J., Raisson, F., 2019. The influence of bottom currents on the Zambezi valley morphology (Mozambique Channel, SW Indian Ocean): *in situ* current observations and hydrodynamic modelling. Mar. Geol. 410, 42–55. https://doi.org/10.1016/j.margeo.2019.01.002.

Möller, A., Mezger, K., Schenk, V., 1998. Crustal age domains and the evolution of the continental crust in the Mozambique belt of Tanzania: combined Sm–Nd, Rb–Sr, and Pb–Pb isotopic evidence. J. Petrol. 39, 749–783. https://doi.org/10.1093/petroj/39.4.749.

Mougenot, D., Recq, M., Virlogeux, P., Lepvrier, C., 1986. Seaward extension of the East African Rift. Nature 321, 599. https://doi.org/10.1038/321599a0.

O'Nions, R.K., Carter, S.R., Cohen, R.S., Evensen, N.M., Hamilton, P.J., 1978. Pb, Nd and Sr isotopes in oceanic ferromanganese deposits and ocean floor basalts. Nature 273, 435–438. https://doi.org/10.1038/273435a0.

O'Nions, R.K., Frank, M., von Blanckenburg, F., Ling, H.-F., 1998. Secular variation of Nd and Pb isotopes in ferromanganese crusts from the Atlantic, Indian and Pacific Oceans. Earth Planet. Sci. Lett. 155, 15–28. https://doi.org/10.1016/S0012-821X(97)00207-0.

Olu, K., 2014. PAMELA-MOZ01 cruise. L'Atalante R/V. https://doi.org/10.17600/14001000.

Paquette, J.-L., Nédélec, A., Moine, B., Rakotondrazafy, M., 1994. U-Pb, single zircon Pb-evaporation, and Sm-Nd isotopic study of a granulite domain in SE Madagascar. J. Geol. 102, 523–538. https://doi.org/10.1086/629696.

Pearce, C.R., Jones, M.T., Oelkers, E.H., Pradoux, C., Jeandel, C., 2013. The effect of particulate dissolution on the neodymium (Nd) isotope and rare earth element (REE) composition of seawater. Earth Planet. Sci. Lett. 369–370, 138–147. https://doi.org/10.1016/j.epsl.2013.03.023.

Piepgras, D.J., Jacobsen, S.B., 1988. The isotopic composition of neodymium in the North Pacific. Geochim. Cosmochim. Acta 52, 1373–1381. https://doi.org/10.1016/0016-7037(88)90208-6.

Piepgras, D.J., Wasserburg, G.J., 1980. Neodymium isotopic variations in seawater. Earth Planet. Sci. Lett. 50, 128–138. https://doi.org/10.1016/0012-821X(80)90124-7.

Piepgras, D.J., Wasserburg, G.J., 1982. Isotopic composition of neodymium in waters from the drake passage. Science 217, 207–214.

Piepgras, D.J., Wasserburg, G.J., 1987. Rare earth element transport in the western North Atlantic inferred from Nd isotopic observations. Geochim. Cosmochim. Acta 51, 1257–1271. https://doi.org/10.1016/0016-7037(87)90217-1.

Piepgras, D.J., Wasserburg, G.J., Dasch, E.J., 1979. The isotopic composition of Nd in different ocean masses. Earth Planet. Sci. Lett. 45, 223–236. https://doi.org/10.1016/0012-821X(79)90125-0.

Pin, C., Briot, D., Bassin, C., Poitrasson, F., 1994. Concomitant separation of strontium and samarium-neodymium for isotopic analysis in silicate samples, based on specific extraction chromatography. Anal. Chim. Acta 298, 209–217. https://doi.org/10.1016/0003-2670(94)00274-6.

Piotrowski, A.M., Goldstein, S.L., Hemming, S.R., Fairbanks, R.G., 2004. Intensification and variability of ocean thermohaline circulation through the last deglaciation. Earth Planet. Sci. Lett. 225, 205–220. https://doi.org/10.1016/j.epsl.2004.06.002.

Piotrowski, A.M., Goldstein, S.L., Hemming, S.R., Fairbanks, R.G., 2005. Temporal relationships of carbon cycling and ocean circulation at Glacial boundaries. Science 307, 1933–1938. https://doi.org/10.1126/science.1104883.

Piotrowski, A.M., Banakar, V.K., Scrivner, A.E., Elderfield, H., Galy, A., Dennis, A., 2009. Indian Ocean circulation and productivity during the last glacial cycle. Earth Planet. Sci. Lett. 285, 179–189. https://doi.org/10.1016/j.epsl.2009.06.007.

Piotrowski, A.M., Galy, A., Nicholl, J.A.L., Roberts, N., Wilson, D.J., Clegg, J.A., Yu, J., 2012. Reconstructing deglacial North and South Atlantic deep water sourcing using foraminiferal Nd isotopes. Earth Planet. Sci. Lett. 357–358, 289–297. https://doi.org/10.1016/j.epsl.2012.09.036.

Piper, D.Z., 1974. Rare earth elements in ferromanganese nodules and other marine phases. Geochim. Cosmochim. Acta 38, 1007–1022. https://doi.org/10.1016/0016-7037(74)90002-7.

Quartly, G.D., de Cuevas, B.A., Coward, A.C., 2013. Mozambique Channel eddies in GCMs: a question of resolution and slippage. Ocean Model 63, 56–67. https://doi.org/10.1016/j.ocemod.2012.12.011.

Rahlf, P., Hathorne, E., Laukert, G., Gutjahr, M., Weldeab, S., Frank, M., 2020. Tracing water mass mixing and continental inputs in the southeastern Atlantic Ocean with dissolved neodymium isotopes. Earth Planet. Sci. Lett. 530, 115944. https://doi.org/10.1016/j.epsl.2019.115944.

Rempfer, J., Stocker, T.F., Joos, F., Dutay, J.-C., Siddall, M., 2011. Modelling Nd-isotopes with a coarse resolution ocean circulation model: Sensitivities to model parameters and source/sink distributions. Geochim. Cosmochim. Acta 75, 5927–5950. https://doi.org/10.1016/j.gca.2011.07.044.

Rickli, J., Frank, M., Halliday, A.N., 2009. The hafnium–neodymium isotopic composition of Atlantic seawater. Earth Planet. Sci. Lett. 280, 118–127. https://doi.org/10.1016/j.epsl.2009.01.026.

Rickli, J., Frank, M., Baker, A.R., Aciego, S., de Souza, G., Georg, R.B., Halliday, A.N., 2010. Hafnium and neodymium isotopes in surface waters of the eastern Atlantic Ocean: implications for sources and inputs of trace metals to the ocean. Geochim. Cosmochim. Acta 74, 540–557. https://doi.org/10.1016/j.gca.2009.10.006.

Roberts, N.L., Piotrowski, A.M., McManus, J.F., Keigwin, L.D., 2010. Synchronous deglacial overturning and water mass source changes. Science 327, 75–78. https://doi.org/10.1126/science.1178068.

Rogers, W.E., Hartman, W.D., Krause, K.S.K., 2000. Stratigraphic analysis of upper cretaceous rocks in the Mahajanga Basin, Northwestern Madagascar: implications for ancient and modern faunas. J. Geol. 108, 275–301.

de Ruijter, W.P.M., Ridderinkhof, H., Lutjeharms, J.R.E., Schouten, M.W., Veth, C., 2002. Observations of the flow in the Mozambique Channel: observations in the Mozambique Channel. Geophys. Res. Lett. 29, 140-1–140-3. https://doi.org/10.1029/2001GL013714.

Rutberg, R.L., Hemming, S.R., Goldstein, S.L., 2000. Reduced North Atlantic Deep Water flux to the glacial Southern Ocean inferred from neodymium isotope ratios. Nature 405, 935. https://doi.org/10.1038/35016049.

Schacht, U., Wallmann, K., Kutterolf, S., 2010. The influence of volcanic ash alteration on the REE composition of marine pore waters. J. Geochem. Explor. 106, 176–187. https://doi.org/10.1016/j.gexplo.2010.02.006. GEOFLUIDS VI: Recent Advances in Research on Fluids in Geological Processes.

Schott, F.A., McCreary, J.P., 2001. The monsoon circulation of the Indian Ocean. Prog. Oceanogr. 51, 1–123. https://doi.org/10.1016/S0079-6611(01)00083-0.

Segl, M., Mangini, A., Bonani, G., Hofmann, H.J., Nessi, M., Suter, M., Wölfli, W., Friedrich, G., Plüger, W.L., Wiechowski, A., Beer, J., 1984. 10 Be-dating of a manganese crust from Central North Pacific and implications for ocean palaeocirculation. Nature 309, 540. https://doi.org/10.1038/309540a0.

Shimizu, H., Tachikawa, K., Masuda, A., Nozaki, Y., 1994. Cerium and neodymium isotope ratios and REE patterns in seawater from the North Pacific Ocean. Geochim. Cosmochim. Acta 58, 323–333. https://doi.org/10.1016/0016-7037(94)90467-7.

Stichel, T., Frank, M., Rickli, J., Hathorne, E.C., Haley, B.A., Jeandel, C., Pradoux, C., 2012b. Sources and input mechanisms of hafnium and neodymium in surface waters of the Atlantic sector of the Southern Ocean. Geochim. Cosmochim. Acta 94, 22–37. https://doi.org/10.1016/j.gca.2012.07.005.

Storey, M., Mahoney, J.J., Saunders, A.D., Duncan, R.A., Kelley, S.P., Coffin, M.F., 1995. Timing of hot spot—related volcanism and the breakup of Madagascar and India. Science 267, 852–855. https://doi.org/10.1126/science.267.5199.852.

Tachikawa, K., Handel, C., Dupré, B., 1997. Distribution of rare earth elements and neodymium isotopes in settling particulate material of the tropical Atlantic Ocean (EUMELI site). Deep Sea Res. Part Oceanogr. Res. Pap. 44, 1769–1792. https://doi.org/10.1016/S0967-0637(97)00057-5.

Tachikawa, K., Athias, V., Jeandel, C., 2003. Neodymium budget in the modern ocean and paleo-oceanographic implications. J. Geophys. Res. Oceans 108. https://doi.org/10.1029/1999JC000285.

Tachikawa, K., Arsouze, T., Bayon, G., Bory, A., Colin, C., Dutay, J.-C., Frank, N., Giraud, X., Gourlan, A.T., Jeandel, C., Lacan, F., Meynadier, L., Montagna, P., Piotrowski, A.M., Plancherel, Y., Pucéat, E., Roy-Barman, M., Waelbroeck, C., 2017. The large-scale evolution of neodymium isotopic composition in the global modern and Holocene ocean revealed from seawater and archive data. Chem. Geol. 457, 131–148. https://doi.org/10.1016/j.chemgeo.2017.03.018.

Tanaka, T., Togashi, S., Kamioka, H., Amakawa, H., Kagami, H., Hamamoto, T., Yuhara, M., Orihashi, Y., Yoneda, S., Shimizu, H., Kunimaru, T., Takahashi, K., Yanagi, T., Nakano, T., Fujimaki, H., Shinjo, R., Asahara, Y., Tanimizu, M., Dragusanu, C., 2000. JNdi-1: a neodymium isotopic reference in consistency with LaJolla neodymium. Chem. Geol. 168, 279–281. https://doi.org/10.1016/S0009-2541(00)00198-4.

Thompson, J.O., Moulin, M., Aslanian, D., de Clarens, P., Guillocheau, F., 2019. New starting point for the Indian Ocean: second phase of breakup for Gondwana. Earth-Sci. Rev. 191, 26–56. https://doi.org/10.1016/j.earscirev.2019.01.018.

Toole, J.M., Warren, B.A., 1993. A hydrographic section across the subtropical South Indian Ocean. Deep Sea Res. Part Oceanogr. Res. Pap. 40, 1973–2019. https://doi.org/10.1016/0967-0637(93)90042-2.

Torsvik, T.H., Tucker, R.D., Ashwal, L.D., Carter, L.M., Jamtveit, B., Vidyadharan, K.T., Venkataramana, P., 2000. Late Cretaceous India-Madagascar fit and timing of break-up related magmatism. Terra Nova 12, 220–224. https://doi.org/10.1046/j.1365-3121.2000.00300.x.

Ullgren, J.E., van Aken, H.M., Ridderinkhof, H., de Ruijter, W.P.M., 2012. The hydrography of the Mozambique Channel from six years of continuous temperature, salinity, and velocity observations. Deep Sea Res. Part Oceanogr. Res. Pap. 69, 36–50. https://doi.org/10.1016/j.dsr.2012.07.003.

Wei, R., Abouchami, W., Zahn, R., Masque, P., 2016. Deep circulation changes in the South Atlantic since the Last Glacial Maximum from Nd isotope and multi-proxy records. Earth Planet. Sci. Lett. 434, 18–29. https://doi.org/10.1016/j.epsl.2015.11.001.

Weijer, W., 1999. Impact of interbasin exchange on the Atlantic overturning circulation. J. Phys. Oceanogr. 29, 19.

Wilson, D.J., Piotrowski, A.M., Galy, A., McCave, I.N., 2012. A boundary exchange influence on deglacial neodymium isotope records from the deep western Indian Ocean. Earth Planet. Sci. Lett. 341–344, 35–47. https://doi.org/10.1016/j.epsl.2012.06.009.

You, Y., 2000. Implications of the deep circulation and ventilation of the Indian Ocean on the renewal mechanism of North Atlantic Deep Water. J. Geophys. Res. Oceans 105, 23895–23926. https://doi.org/10.1029/2000JC900105.

Yu, J., Elderfield, H., Piotrowski, A.M., 2008. Seawater carbonate ion-δ13C systematics and application to glacial–interglacial North Atlantic ocean circulation. Earth Planet. Sci. Lett. 271, 209–220. https://doi.org/10.1016/j.epsl.2008.04.010.

3.3. Contribution de l'étude isotopique du Pb, apports détritiques et circulation océanique

3.3.1. Encroûtements Fe-Mn et méthodologie

Ce travail est basé sur 33 échantillons d'encroûtements Fe-Mn. Ces encroûtements Fe-Mn sont tous issus des missions PAMELA-MOZ1 (Olu, 2014), PAMELA-MOZ5 (Moulin, Evain, 2016), MD-06 Nosicaa (Leclaire, 1975) et MD-39 Rida (Leclaire, 1984). 27 échantillons proviennent de la campagne PAMELA-MOZ1, quatre sont issus de PAMELA-MOZ5, et les deux derniers ont été récupérés en accord avec le MNHN (Chapitre 2). Ce panel important d'échantillons s'étend des îles Glorieuses au nord jusqu'au plateau des Aiguilles au sud.

En effet, dans cette partie, nous intégrerons les encroûtements Fe-Mn proches des côtes africaines, issus de PAMELA-MOZ5. Ces quatre échantillons n'ont pas été mentionnés dans la partie précédente en raison de leur localisation proche, inférieure à 300 km, de la marge continentale africaine. Cette caractéristique géographique entraîne des variations en Nd liées notamment à des apports détritiques du continent, qui modifieraient la signature des échantillons et ne refléteraient pas la composition isotopique des masses d'eau.

L'utilisation du Pb permet de tracer des événements locaux, ce proxy est donc intéressant pour mettre en évidence des sources et leurs apports. Les résultats obtenus permettent ainsi de mettre en évidence des provinces isotopiques. Dans cette partie, il est donc pertinent d'analyser tous les échantillons.

La surface de ces échantillons est prélevée à l'aide d'une micro-foreuse comme vu précédemment. Les protocoles d'échantillonnage et de chimie sont décrits dans le chapitre 2. Enfin, les sessions d'analyse ont lieu au MC-ICP-MS Thermo Scientific Neptune de l'Ifremer. Le standard NIST 981 est utilisé et les rapports $^{206}Pb/^{204}Pb$, $^{207}Pb/^{204}Pb$ et $^{208}Pb/^{204}Pb$ sont mesurés puis traités selon les blancs et la potentielle dérive analytique. Une séquence « type » est décrite dans le chapitre 2 au paragraphe 2.6.2.4.

3.3.2. Distribution isotopique du Pb dans l'océan Indien

Plusieurs études notables se sont déjà intéressées à l'isotopie du Pb dans l'océan Indien à partir d'oxydes Fe-Mn (Abouchami, Goldstein, 1995 ; Frank, O'Nions, 1998 ; Vlastélic et al., 2001 ; von Blanckenburg et al.,1996). L'étude la plus récente (Vlastélic et al., 2001) repose sur l'échantillonnage de 52 encroûtements Fe-Mn, préalablement analysés pour l'isotopie du Nd par Albarède et al. (1997). Ces échantillons sont issus de profondeurs initiales qui varient de 600 à 5700 m, et sont répartis dans tous les bassins de l'océan Indien (Figure 3.1). Les encroûtements Fe-Mn provenant du canal du Mozambique sont les moins profonds (< 900 m).

La méthode de prélèvement est la même que celle utilisée au cours de cette thèse, ainsi que par Albarède et al. (1997). Elle repose sur le prélèvement d'un millimètre de poudre de la partie supérieure des échantillons, ce qui correspond aux dépôts les plus récents (Albarède et al., 1997 ; Charles et al., 2020).

Les données isotopiques en Pb de l'ensemble de ces échantillons de l'océan Indien a permis de mettre en évidence plusieurs tendances isotopiques, correspondant à des provinces géographiques bien précises (Figure 3.1 ; Vlastélic et al., 2001).

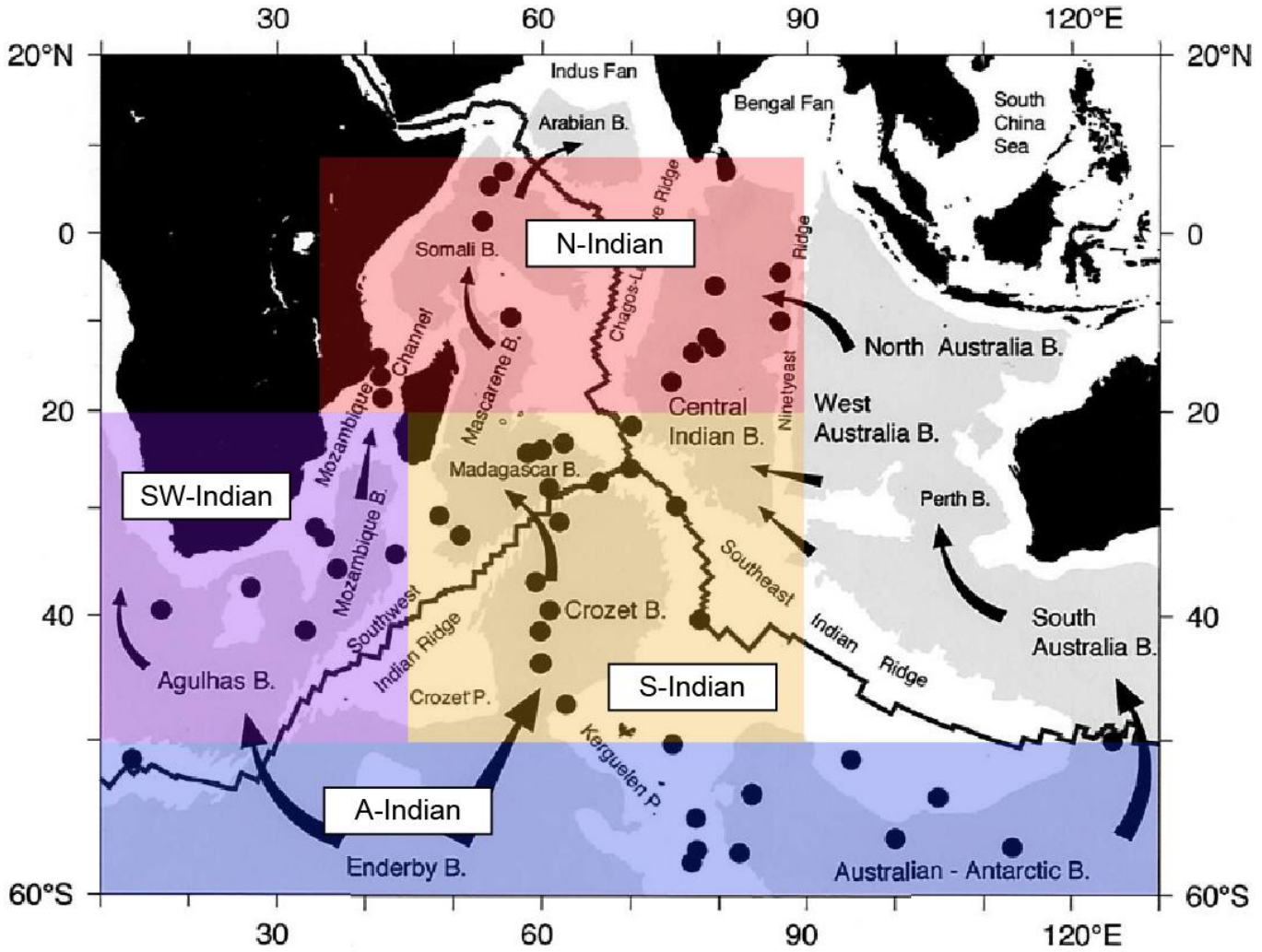

Figure 3.1. *Localisation des échantillons analysés par Vlastélic et al. (2001) ainsi que les grands domaines isotopiques définis. Les flèches montrent les voies de circulation principales des masses d'eau profondes comme définies par Mantyla et Reid (1995). Figure modifiée d'après Vlastélic et al. (2001).*

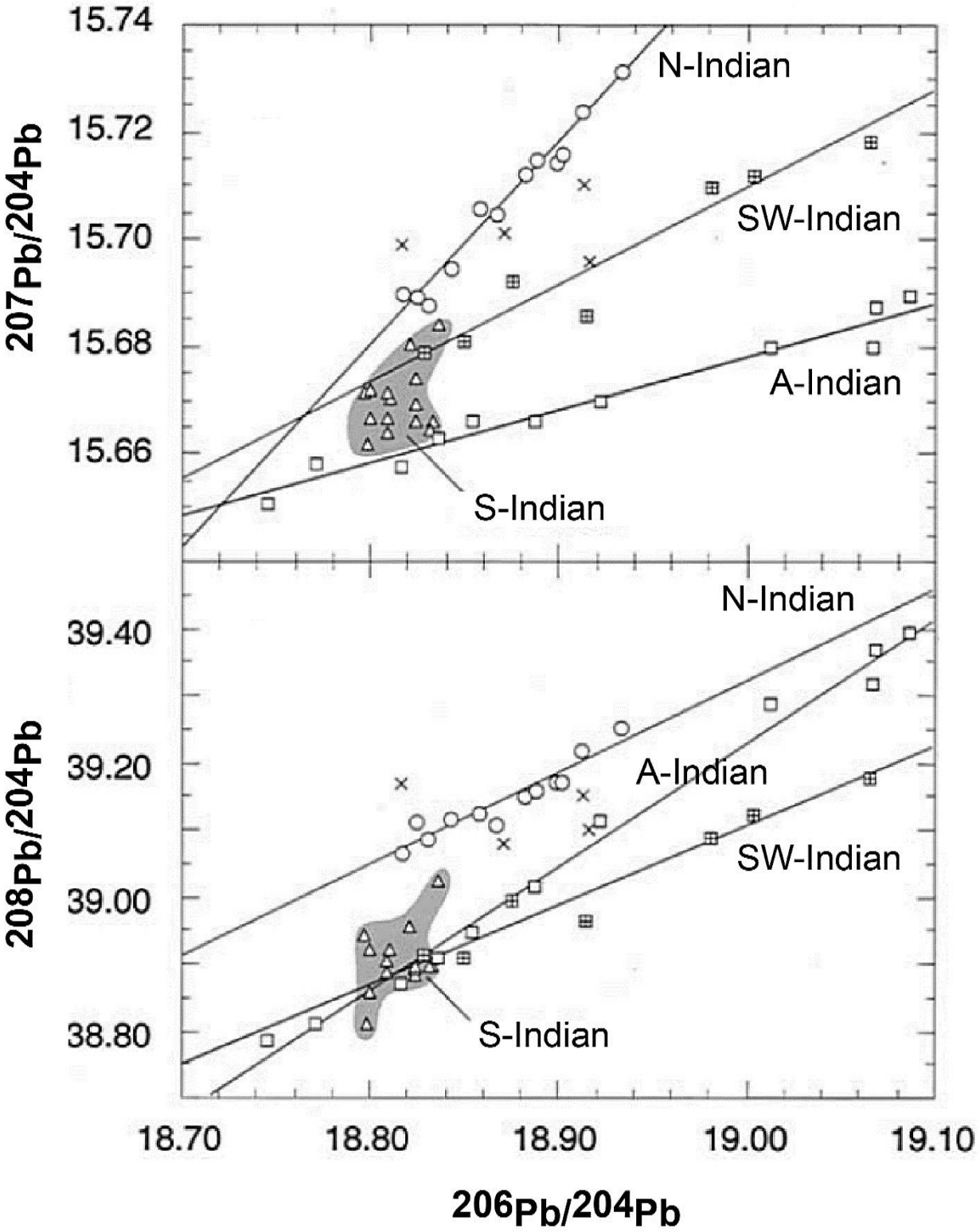

Figure 3.2. *Variations des rapports isotopiques $^{207}Pb/^{204}Pb$ vs. $^{206}Pb/^{204}Pb$ et, $^{208}Pb/^{204}Pb$ vs. $^{206}Pb/^{204}Pb$ issues Vlastélic et al. (2001). Trois lignées (N-Indian, A-Indian, SW-Indian) et un groupe de points (S-Indian) y sont définis et correspondent à différents secteurs géographiques de l'océan Indien.*

3.3.2.1. Tendances isotopiques du Pb

Les données de la composante $^{206}Pb/^{204}Pb$ varient de 18.75 à 19.09, le rapport $^{207}Pb/^{204}Pb$ montre des valeurs de 15.65 à 15.76 et enfin, les données de $^{208}Pb/^{204}Pb$ s'étendent de 38.79 à 39.40 (Vlastélic et al., 2001). Trois grandes lignées isotopiques, ainsi qu'un cluster de points, peuvent être distinguées aussi bien sur les rapports $^{207}Pb/^{204}Pb$ que le rapport $^{208}Pb/^{204}Pb$ en fonction du rapport $^{206}Pb/^{204}Pb$ (Figure 3.2).

Sur le diagramme présentant le rapport isotopique $^{207}Pb/^{204}Pb$ en fonction du rapport isotopique $^{206}Pb/^{204}Pb$ (Figure 3.2), les tendances présentent 3 pentes différentes. Elles correspondent à une variation des latitudes des encroûtements Fe-Mn analysés (Figure 3.1). Les encroûtements Fe-Mn du nord de l'océan Indien définissent une lignée très pentue alors que les échantillons Fe-Mn proche de l'Antarctique dessinent la tendance la moins pentue.

Le rapport isotopique $^{208}Pb/^{206}Pb$ calculé en fonction des rapports isotopiques $^{206}Pb/^{204}Pb$ et $^{208}Pb/^{204}Pb$ vient appuyer cette observation (Figure 3.2). Cette composante décroît du nord au sud et donc, avec la diminution de la latitude des échantillons (von Blanckenburg et al., 1996). Les échantillons dont les rapports $^{208}Pb/^{206}Pb$ sont supérieurs à 2,071 proviennent du nord de l'océan Indien alors que les rapports inférieurs à 2,071 sont mesurés dans des oxydes Fe-Mn localisés en dessous d'une latitude de 15°S Vlastélic et al., 2001).

Tous ces résultats illustrent une distribution spatiale de l'isotopie du Pb très complexe, fortement contrôlée par la latitude, et une large diversité de sources au sein même d'un seul et unique océan, qui a permis de définir des domaines isotopiques.

3.3.2.2. Réseau de domaines isotopiques

Comme le présente la figure 3.1, le domaine défini au nord de l'océan Indien « N-Indian » s'étend au-delà d'une latitude de 20°S. Il présente un rapport $^{208}Pb/^{206}Pb$ élevé qui serait lié à des apports himalayens directement hérités des interactions entre les masses d'eau et les particules des cônes sédimentaires du Bengal et de l'Indus (Frank, O'Nions, 1998 ; Vlastélic et al., 2001 ; von Blanckenburg et al., 1996). Le domaine sud-ouest Indien « SW-Indian » se trouve entre les latitudes 20°S et 50°S, et à l'ouest de 45°E. Il serait marqué par une composante très faiblement radiogénique des courants circumpolaires tels que le CDW (Circumpolar Deep Water) dérivé de l'océan Pacifique et d'une composante plus radiogénique reflétant le courant profond de l'Atlantique (NADW ; présenté dans le chapitre 1, paragraphe 1.3.2) (Abouchami et Goldstein, 1995). Le domaine sud Indien « S-Indian » correspond aux mêmes latitudes mais à l'est de 45°E, reflétant un mélange homogène des composantes principales des domaines « N-Indian » et « A-Indian » (Vlastélic et al., 2001).

Le domaine Antarctique-Indien « A-Indian » marque la frontière entre les eaux de l'Antarctique et les eaux indiennes. Il s'étend au sud de 50°S et sa signature très faiblement radiogénique proviendrait de la mer de Weddell (Abouchami, Goldstein, 1995 ; Vlastélic et al., 2001). L'étude de Vlastélic et al. (2001) est la première à définir les domaines nord Indien et sud Indien. Les provinces sud-ouest indiennes et Antarctique-Indien ont déjà été proposées et définies par Abouchami et Goldstein en 1995. Les deux études présentent des domaines similaires, tant sur le plan isotopique que sur le plan géographique.

Les quatre domaines définis indiquent donc que les échantillons y appartenant partagent des sources de Pb similaires. Cependant, d'un

domaine à l'autre, les sources changent, comme le montre l'hétérogénéité des tendances.

De plus, Vlastélic et al. (2001) ont montré qu'au sein de chaque tendance, la distribution des points peut être géographiquement contrôlée par plusieurs bassins. Ainsi, les variations au sein des lignées définies correspondent simplement à un mélange entre deux pôles isotopiques en Pb différents. Ces observations montrent que des bassins voisins, d'un même domaine, peuvent partager des signatures isotopiques de Pb proches mais également que le signal isotopique d'une source peut être exporté d'un bassin à un autre, grâce à la circulation des masses d'eau et à la topographie régionales (Abouchami, Goldstein, 1995 ; Vlastélic et al., 2001).

3.3.3. Résultats des compositions isotopiques du Pb

Les résultats des analyses isotopiques du Pb réalisées dans le cadre de cette thèse figurent dans le tableau 3.1 ci-après.

3.3.3.1. $^{206}Pb/^{204}Pb$

Les résultats de ce premier rapport isotopique présentent des valeurs allant de 18.3896 (MOZ1-DR22-06 ; Europa) à 19.3514 (MOZ5-DR05-01 ; nord de la vallée de Natal). La moyenne des résultats est de 18.8759.

La première valeur supérieure à 19 est mesurée sur l'échantillon MOZ1-DR16-06 de Bassas da India (19.0205), soit à une latitude de 21°S. Les autres données au-delà de 19 sont issues des encroûtements Fe-Mn du nord de la vallée de Natal, avec le maximum atteint à la latitude de 25°S. Une certaine corrélation est visible en fonction de la latitude : les données augmentent avec la diminution de la latitude. Cependant, des exceptions existent. L'échantillon DR75-0012 de la campagne MD-06 Nosicaa, initialement localisé sur le plateau des Aiguilles à une latitude de 37°S, présente un rapport isotopique $^{206}Pb/^{204}Pb$ de 18.8435. Quant à l'échantillon MOZ1-DR22-06 d'Europa, il montre la valeur la plus faible alors qu'il est localisé au sud de Bassas da India.

3.3.3.2. $^{207}Pb/^{204}Pb$

Le rapport isotopique $^{207}Pb/^{204}Pb$ montre un minimum de 15.6411 (MOZ1-DR22-06 ; Europa) et un maximum de 15.7881 (MOZ5-DR05-01 ; vallée de Natal). La moyenne des résultats est de 15.7006.

Les résultats inférieurs à cette moyenne sont présents dans le nord du canal du Mozambique, au-delà de la ride de Davie, alors que les résultats supérieurs à cette moyenne se retrouvent plus au sud, à partir de Bassas da India et jusque dans la vallée de Natal où le maximum est atteint. Il s'agit de la même tendance que le rapport $^{206}Pb/^{204}Pb$ en fonction de la latitude. Là encore, des exceptions existent, avec DR75-0012 qui est l'encroûtement Fe-Mn le plus au sud et qui présente une valeur en dessous de la moyenne de 15.6757 et MOZ1-DR22-06 qui montre le minimum mesuré. S'ajoutent à cela, deux anomalies de valeurs supérieures à la moyenne alors qu'il s'agit d'échantillons prélevés au niveau des îles Glorieuses (MOZ1-DR04-04 ; 15.7029) et le long de la ride de Davie (MOZ1-DR13-07 ; 15.7027).

3.3.3.3. $^{208}Pb/^{204}Pb$

Le rapport isotopique 208Pb/204Pb présente des valeurs entre 38.4746 et 39.5149. La valeur minimale est toujours portée par l'échantillon MOZ1-DR22-06 d'Europa et le minimum

Tableau 3.1. *Numéro international (IGSN), localisation, profondeur et valeurs des isotopes de Pb des encroûtements de Fe-Mn étudiés provenant des expéditions océanographiques PAMELA-MOZ1 (Olu, 2014), PAMELA-MOZ5 (Moulin, Evain, 2016), MD-06 Nosicaa (Leclaire, 1975) et MD-39 Rida (Leclaire, 1984).*

Cruise	Dredge	Sample	IGSN	Location	Latitude	Longitude	Depth range (mbsl)	$^{206}Pb/^{204}Pb$	$^{207}Pb/^{204}Pb$	$^{208}Pb/^{204}Pb$	$^{207}Pb/^{206}Pb$	$^{208}Pb/^{206}Pb$
PAMELA-MOZ-1	DR01	MOZ1-DR01-01	BFBG-155073	Glorieuses Islands	11°47'S	47°54'E	2400-2650	18.8043	15.6928	39.1267	0.8345	2.0807
	DR04	MOZ1-DR04-01	BFBG-155082	Glorieuses Islands	11°28'S	47°32'E	1780-2000	18.8146	15.6854	39.1066	0.8337	2.0785
	DR04	MOZ1-DR04-03	BFBG-155084	Glorieuses Islands	11°28'S	47°32'E	1780-2000	18.8429	15.6903	39.1451	0.8327	2.0774
	DR04	MOZ1-DR04-04	BFBG-155085	Glorieuses Islands	11°28'S	47°32'E	1780-2000	18.8446	15.7029	39.1784	0.8333	2.0790
	DR04	MOZ1-DR04-23	BFBG-169883	Glorieuses Islands	11°28'S	47°32'E	1780-2000	18.8452	15.6954	39.1626	0.8329	2.0781
	DR10	MOZ1-DR10-04	BFBG-155152	Macua Mt	16°12'S	41°38'E	1000-1400	18.8706	15.6998	39.1633	0.8320	2.0754
	DR10	MOZ1-DR10-05	BFBG-155153	Macua Mt	16°12'S	41°38'E	1000-1400	18.8412	15.6974	39.0829	0.8331	2.0743
	DR11	MOZ1-DR11-01	BFBG-155160	Jeffrey Ridge	16°10'S	42°30'E	2400-2450	18.6329	15.6737	38.8334	0.8412	2.0841
	DR11	MOZ1-DR11-03	BFBG-155162	Jeffrey Ridge	16°10'S	42°30'E	2400-2450	18.8555	15.6993	39.1038	0.8326	2.0739
	DR11	MOZ1-DR11-05	BFBG-155164	Jeffrey Ridge	16°10'S	42°30'E	2400-2450	18.8593	15.6960	39.0930	0.8323	2.0729
	DR11	MOZ1-DR11-07	BFBG-155166	Jeffrey Ridge	16°10'S	42°30'E	2400-2450	18.9000	15.6939	39.0357	0.8304	2.0654
	DR12	MOZ1-DR12-09	BFBG-155179	Juan de Nova	17°1'S	42°36'E	1350-1650	18.8314	15.6921	39.0636	0.8333	2.0744
	DR12	MOZ1-DR12-14	BFBG-155184	Juan de Nova	17°1'S	42°36'E	1350-1650	18.8762	15.6904	39.0912	0.8312	2.0709
	DR12	MOZ1-DR12-V	BFBG-169884	Juan de Nova	17°1'S	42°36'E	1350-1650	18.8317	15.6915	39.0654	0.8333	2.0744
	DR13	MOZ1-DR13-07	BFBG-155191	North Sakalaves Mts	17°59'S	41°39'E	1300-1600	18.8720	15.7027	39.0917	0.8321	2.0714
	DR14	MOZ1-DR14-04	BFBG-155201	Sakalaves Mts	18°39'S	41°51'E	580-650	18.8069	15.6949	38.9992	0.8345	2.0737
	DR15	MOZ1-DR15-10	BFBG-155211	South Sakalaves Mts	18°57'S	41°45'E	1200-1250	18.6785	15.6766	38.8594	0.8393	2.0804
	DR15	MOZ1-DR15-14	BFBG-155215	South Sakalaves Mts	18°57'S	41°45'E	1200-1250	18.8436	15.6865	39.0310	0.8325	2.0713
	DR16	MOZ1-DR16-05	BFBG-155220	Bassas da India	21°36'S	39°38'E	1350-1600	18.9417	15.7038	39.1014	0.8291	2.0643
	DR16	MOZ1-DR16-06	BFBG-155221	Bassas da India	21°36'S	39°38'E	1350-1600	19.0205	15.7258	39.2043	0.8268	2.0612
	DR17	MOZ1-DR17-01	BFBG-155224	Hall Bank	21°50'S	39°10'E	1700-1900	18.9233	15.7186	39.1200	0.8306	2.0673
	DR17	MOZ1-DR17-04	BFBG-155227	Hall Bank	21°50'S	39°10'E	1700-1900	18.9306	15.7047	39.0892	0.8296	2.0649
	DR19	MOZ1-DR19-01	BFBG-155233	Jaguar Bank	21°44'S	39°32'E	1000-1350	18.8753	15.6963	39.0480	0.8316	2.0687
	DR22	MOZ1-DR22-01	BFBG-155243	Europa	21°18'S	40°23'E	1400-1550	18.9064	15.7055	39.1119	0.8307	2.0687
	DR22	MOZ1-DR22-02	BFBG-155244	Europa	21°18'S	40°23'E	1400-1550	18.9002	15.7022	39.0906	0.8308	2.0683
	DR22	MOZ1-DR22-03	BFBG-155245	Europa	21°18'S	40°23'E	1400-1550	18.9364	15.7139	39.1382	0.8298	2.0668
	DR22	MOZ1-DR22-06	BFBG-155248	Europa	21°18'S	40°23'E	1400-1550	18.3896	15.6411	38.4746	0.8505	2.0922
PAMELA-MOZ-5	DR01	MOZ5-DR01-01	BFBG-159907	Natal valley	21°0'S	34°57'E	1450-1550	18.9641	15.7199	39.0910	0.8289	2.0613
	DR01	MOZ5-DR01-03	BFBG-159909	Natal valley	21°0'S	34°57'E	1450-1550	19.0335	15.7202	39.1621	0.8259	2.0575
	DR03	MOZ5-DR03-01	BFBG-159912	Natal valley	26°35'S	34°41'E	950-1200	19.2223	15.7677	39.4034	0.8203	2.0499
	DR05	MOZ5-DR05-01	BFBG-159913	Natal valley	25°58'S	35°12'E	170-650	19.3514	15.7881	39.5149	0.8159	2.0420
MD-39 Rida	DR84-0026	DR84-0026	MNHN-GS-DR84-0026	Paisley Mt	14°08'S	41°29'E	800-810	18.8137	15.6747	39.0303	0.8332	2.0746
MD-06 Nosicaa	DR75-0012	DR75-0012	MNHN-GS-DR75-0012	Agulhas Plateau	37°32'S	27°00'E	2550-2550	18.8435	15.6757	38.9188	0.8319	2.0654

provient de l'encroûtement Fe-Mn MOZ5-DR05-01 de la vallée de Natal. La moyenne des rapports mesurés est de 39.0855. L'hétérogénéité des résultats de ce rapport est très importante. La vallée de Natal montre toujours les valeurs les plus élevées, de 39.0910 (MOZ5-DR01-01) jusqu'au maximum mesuré.

Cependant, un échantillon (MOZ1-DR04-04) provenant des îles Glorieuses, au nord de la ride de Davie, présente une valeur de 39.1784. Il s'agit de la deuxième valeur la plus élevée. Des valeurs similaires sont également enregistrées dans d'autres dragues du nord du canal (DR01, DR10, DR11). À l'inverse, l'échantillon DR75-0012 présente encore une valeur de 38.9188 qui est en dessous de la moyenne.

3.3.3.4. $^{208}Pb/^{206}Pb$

Le rapport isotopique $^{208}Pb/^{206}Pb$ a été calculé à partir des apports $^{208}Pb/^{204}Pb$ et $^{206}Pb/^{204}Pb$. Ainsi, son maximum de 2.0922 est issu de l'échantillon MOZ1-DR22-06 d'Europa alors que son minimum de 2.0420 vient de l'encroûtement Fe-Mn MOZ5-DR05-01 de la vallée de Natal. La moyenne des valeurs de ce rapport isotopique est de 2.0707.

Dans le cas de cette composante, une disparité est très nettement visible entre les échantillons du nord du canal du Mozambique qui montrent des valeurs supérieures à la moyenne, et les encroûtements Fe-Mn provenant du sud qui présentent des valeurs bien inférieures à la moyenne (Figure 3.3).

La répartition géographique semble similaire au rapport isotopique $^{206}Pb/^{204}Pb$ qui s'apparente à la composante dominante du rapport $^{208}Pb/^{206}Pb$.

3.3.3.5. Influence de la profondeur

Pour chaque rapport étudié, il n'y a pas de corrélation globale avec la profondeur comme le montre la figure 3.3. Là encore, l'échantillon MOZ1-DR22-06 localisé à 1550 mbsl se détache des autres échantillons. Il se situe entre le pôle des échantillons des îles Glorieuses (DR01, DR04) et celui de la ride de Jeffrey (DR11).

3.3.4. Discussion

3.3.4.1. Caractérisation des signatures isotopiques du Pb

Les données isotopiques du Pb obtenues au cours de ce travail sont comparées avec les résultats des études précédentes focalisées sur l'océan Indien, particulièrement celle de Vlastelic et al. (2001).

Dans un premier temps, on note que les échantillons localisés dans le canal du Mozambique, entre les îles Glorieuses et Europa forment un cluster de points entre plusieurs lignées : « N-Indian » et « SW-Indian » (Figure 3.4A) mais aussi avec « A-Indian » (Figure 3.4 B).

Les encroûtements Fe-Mn situés à 150 km de l'embouchure du Limpopo, sont quant à eux répartis linéairement le long de la tendance « SW-Indian » que ce soit d'après le rapport isotopique $^{207}Pb/^{204}Pb$ ou $^{208}Pb/^{204}Pb$.

L'échantillon situé sur le mont Paisley (DR84-0026 ; mission MD-39 Rida) se retrouve sur la tendance « N-Indian ».

L'encroûtement Fe-Mn situé à l'extrême sud, sur le Plateau des Aiguilles (DR75-0012 ; MD-06 Nosicaa) est quant à lui positionné sur la tendance « A-Indian » (Figure 3.4A), et à la jonction des

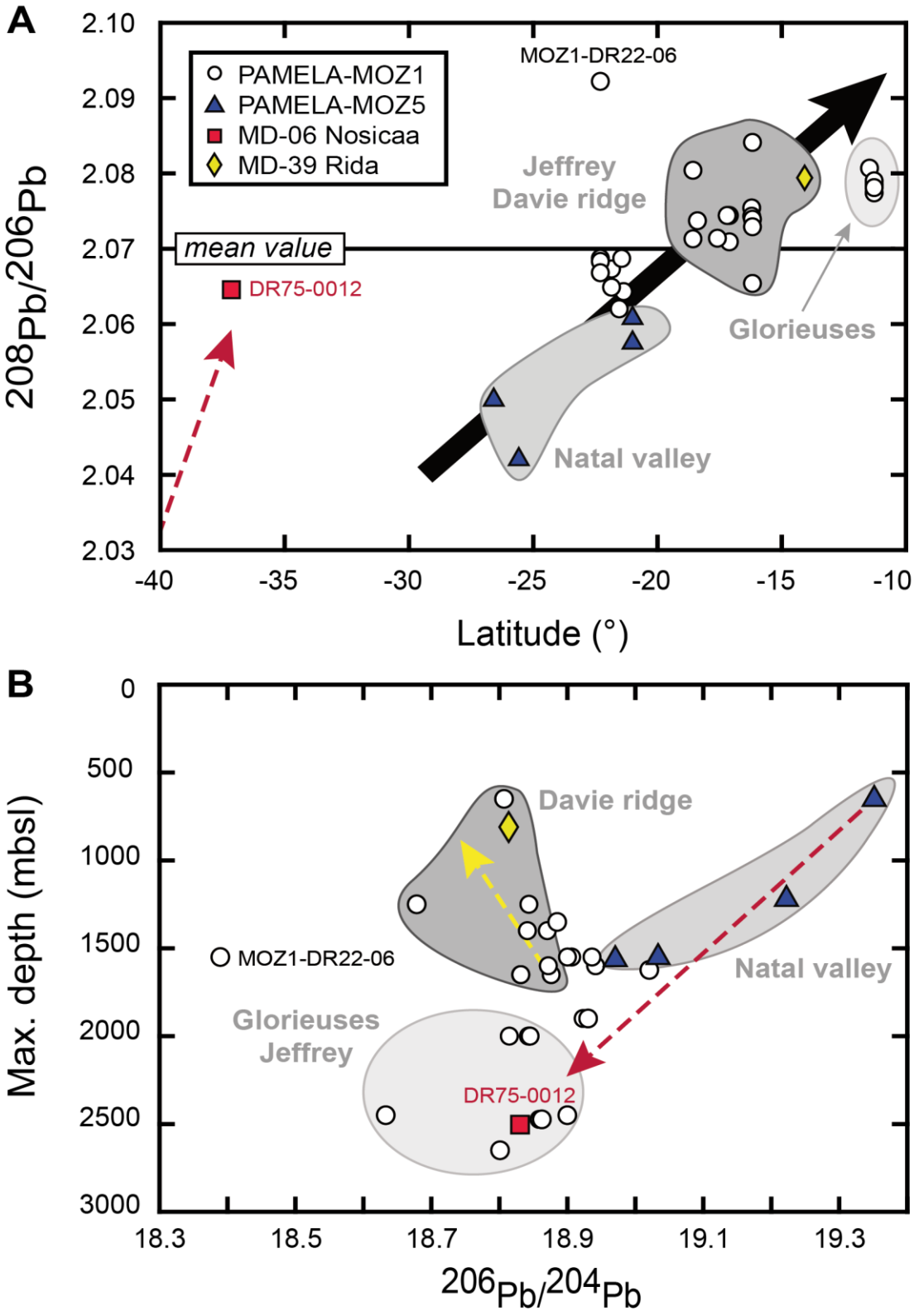

Figure 3.3. *(A) Rapport isotopique $^{208}Pb/^{206}Pb$ en fonction de la latitude montrant une tendance avec des rapports plus élevés (> 2.0707) dans le nord du canal du Mozambique. Les deux encroûtements MOZ1-DR22-06 et DR75-0012 se trouvent en dehors de cette corrélation. (B) Profondeur maximale de prélèvement des échantillons en fonction du rapport isotopique $^{206}Pb/^{204}Pb$ ne présentant pas de relation directe mais plusieurs tendances distinctes. Dans les deux graphiques, les points blancs non inclus dans un champ proviennent de la région de Bassas da India et Europa.*

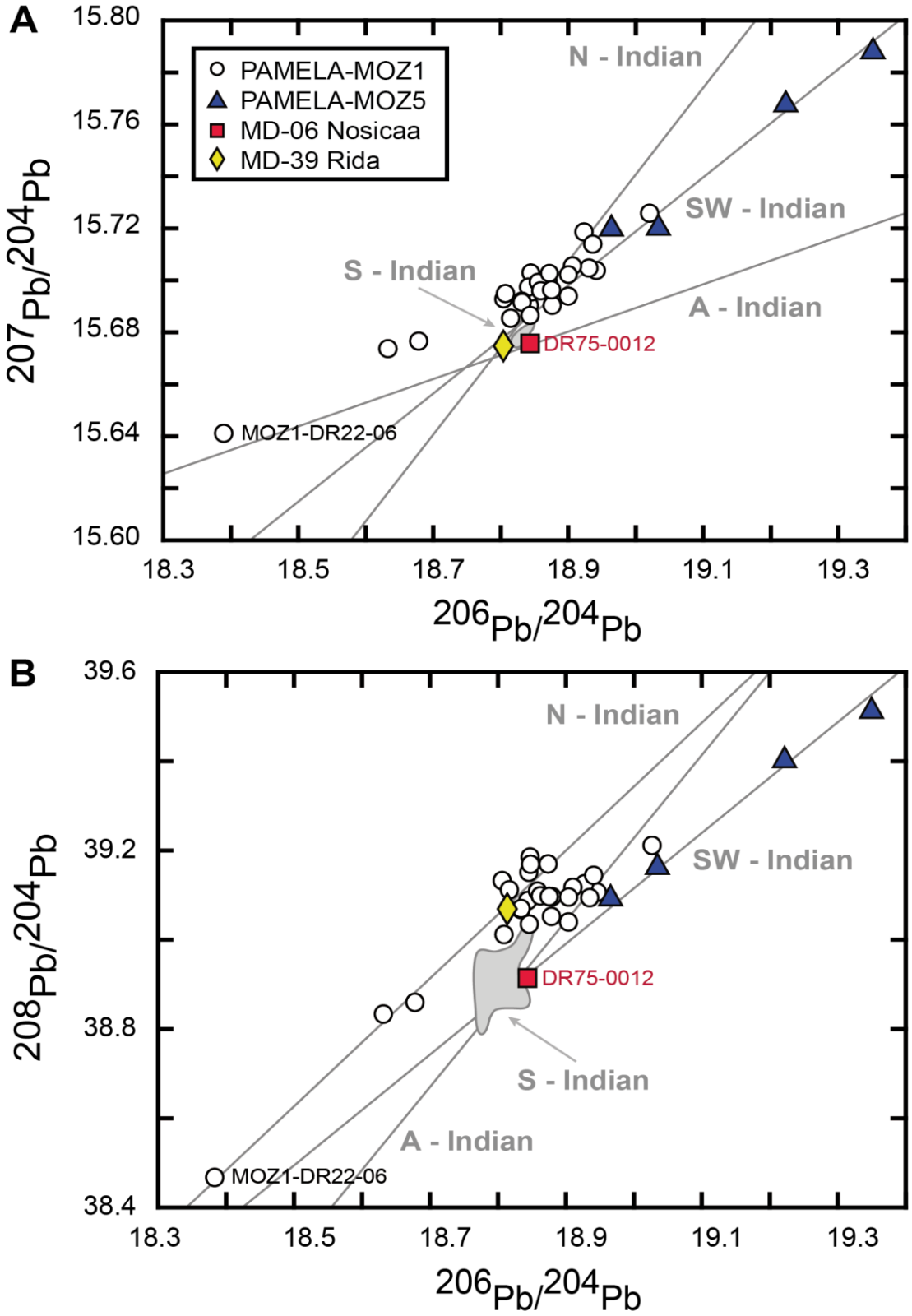

Figure 3.4. *(A) Rapport isotopique $^{207}Pb/^{204}Pb$ en fonction du rapport $^{206}Pb/^{204}Pb$. (B) Rapport isotopique $^{208}Pb/^{204}Pb$ en fonction du rapport $^{206}Pb/^{204}Pb$. Les lignées en gris sont définies d'après Vlastélic et al. (2001). Les échantillons de PAMELA-MOZ1 forment un cluster de points entre plusieurs lignées alors que les encroûtements Fe-Mn de PAMELA-MOZ5 s'alignent sur la tendance « SW-Indian ».*

tendances « A-Indian » et « SW-Indian » (Figure 3.4B).

Ainsi, la figure 3.4 montre que le canal du Mozambique enregistre des sources de Pb diverses avec des composantes plus ou moins marquées. Les enregistrements isotopiques des échantillons reflètent donc à un mélange entre plusieurs sources de Pb provenant de régions distinctes.

3.3.4.2. Signature antarctique au Plateau des Aiguilles

Cette partie est focalisée sur les échantillons au sud du canal du Mozambique : les quatre encroûtements Fe-Mn issus de la campagne PAMELA-MOZ5 et celui de MD-06 Nosicaa.

Comme vu précédemment, les encroûtements Fe-Mn du nord de la vallée de Natal (à 150 km au sud de l'embouchure du Limpopo) s'alignent parfaitement avec la tendance « SW-Indian » et sont localisés dans la région géographique correspondante, définie par Vlastélic et al. (2001). L'échantillon DR75-0012 semble se positionner sur le même alignement (Figure 3.4B). Cependant, ce n'est pas le cas sur la figure 3.3A, présentant les données isotopiques $^{208}Pb/^{206}Pb$ en fonction de la latitude. Ces observations reflètent donc une (ou plusieurs) source(s) de Pb commune(s) dans la composition isotopique des 5 encroûtements Fe-Mn mais également un apport secondaire, de composition différente, qui viendrait impacter de manière significative la signature de l'échantillon DR75-0012 localisé plus au sud du canal, sur le plateau des Aiguilles.

Cette précédente observation n'inclue qu'un seul échantillon (DR75-0012), il est donc difficile de la discuter. Cependant, d'après les lignées visibles sur la figure 3.4, ces apports seraient issue d'une source du domaine « A-Indian » dont l'isotopie est portée par la composition isotopique des masses d'eau antarctiques. Il pourrait notamment s'agir de l'influence radiogénique des basaltes antarctiques (Hart et al., 1995; Hole et al., 1993; Molzahn et al., 1996; Rocholl et al., 1995), comme illustré par Vlastélic et al. (2001). Cette hypothèse est appuyée par la figure 3.3A qui montre que l'échantillon DR75-0012 est plus au sud que les autres encroûtements mais que sa signature en $^{206}Pb/^{204}Pb$ (18.8435 ; Figure 3.3B) est similaire aux autres échantillons du canal (sauf ceux du nord de la vallée de Natal). La composition isotopique radiogénique du domaine « A-Indian », peut être propagée à travers les masses d'eau profondes de la mer de Weddell (Broecker et al., 1998; Orsi et al., 1993) qui rejoignent progressivement les courants CDW et, NADW composant principal de la circulation océanique du domaine « SW-Indian ».

3.3.4.3. Forte influence du NADW au sud-ouest du canal du Mozambique

À travers l'identification de diverses sources de Pb, se pose alors la question du transport des signatures isotopiques, que ce soit à travers les 4 grandes régions de l'océan Indien, comme le montrent notamment les échantillons de PAMELA-MOZ1 qui se positionnent entre les lignées « N-Indian » et « SW-Indian » (Figure 3.4), mais également entre plusieurs bassins d'un même domaine comme l'a identifié Vlastélic et al. (2001).

Tout comme pour l'étude isotopique du Nd vu précédemment dans le paragraphe 3.2 (Charles et al., 2021), le travail sur l'isotopie du Pb peut livrer des informations importantes sur la circulation des masses d'eau océanique dans le canal du Mozambique.

En effet, les travaux de Vlastélic et al. (2001) et Abouchami, Goldstein (1995) suggèrent que le

domaine « SW-Indian » possède une signature isotopique en Pb héritée de l'océan Atlantique. Le NADW arrivant par le sud de l'Afrique est donc considéré comme la source principale de la signature isotopique en Pb du domaine « SW-Indian ».

Ainsi, il influencerait la composition isotopique en Pb de ce domaine avec un impact de moins en moins marqué au cours de sa progression dans le canal du Mozambique.

A l'exception des échantillons DR75-0012 et MOZ1-DR22-06, une corrélation importante est visible entre la latitude des échantillons et leurs rapports isotopiques $^{208}Pb/^{206}Pb$ (Figure 3.3A). Plus le rapport isotopique $^{208}Pb/^{206}Pb$ augmente, plus la latitude augmente également. Le rapport isotopique $^{208}Pb/^{206}Pb$ étant issu pour partie du rapport isotopique $^{206}Pb/^{204}Pb$: plus le rapport $^{208}Pb/^{206}Pb$ augmente, plus le rapport $^{206}Pb/^{204}Pb$ diminue. Or, les courants de l'océan Atlantique présenteraient un rapport isotopique $^{206}Pb/^{204}Pb$ de plus en plus faible loin de leurs sources initiales.

Cette observation appuie l'hypothèse des précédentes études et montre une influence décroissante du NADW au cours de sa propagation dans le canal du Mozambique, avec

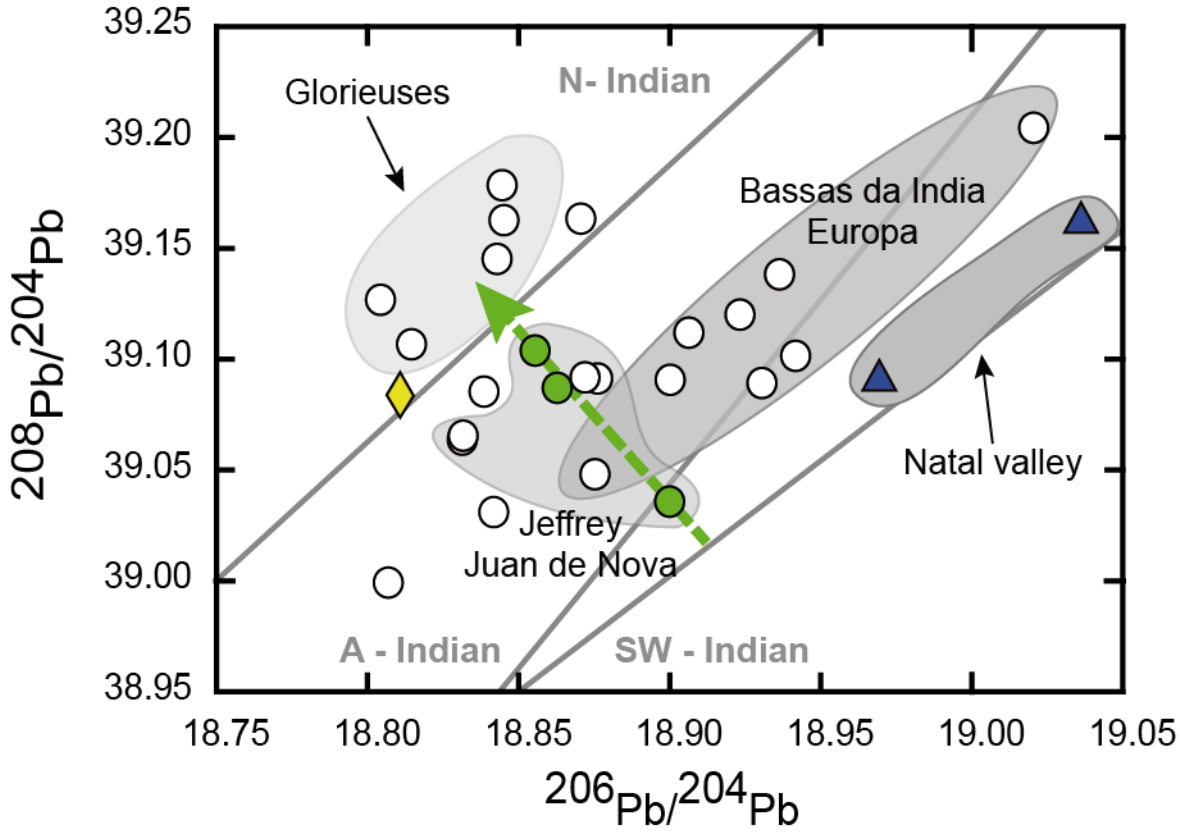

Figure 3.5. *Zoom du rapport isotopique $^{208}Pb/^{204}Pb$ en fonction du rapport $^{206}Pb/^{204}Pb$. Les lignées en gris sont définies d'après Vlastélic et al. (2001). Les échantillons de PAMELA-MOZ1 s'étendent entre plusieurs lignées alors que les encroûtements Fe-Mn de PAMELA-MOZ5 s'alignent sur la tendance « SW-Indian ». Les points verts sont issus de la drague DR11 de la ride de Jeffrey, au nord de la ride de Davie.*

les encroûtements issus de PAMELA-MOZ5 présentant les signatures $^{206}Pb/^{204}Pb$ les plus élevées.

3.3.4.4. Propagation du NADW en direction du bassin des Comores

D'après plusieurs auteurs et comme expliqué précédemment dans le paragraphe portant sur l'isotopie du Nd (Charles et al., 2021), les hauts reliefs présents dans le canal du Mozambique tels que la ride de Davie, seraient des obstacles infranchissables pour les courants profonds arrivant du sud (Mantyla and Reid, 1995; Toole, Warren, 1993; You, 2000). Les travaux de Vlastélic et al. (2001) délimite le nord du domaine « SW-Indian » à une latitude de 20°S en la justifiant notamment par la rétroflexion du NADW à l'entrée du canal du Mozambique.

Cependant, certains résultats de cette thèse viennent largement affiner ce modèle basé sur seulement 6 échantillons.

La figure 3.5 illustre un zoom de la figure 3.4B présentant le rapport isotopique $^{208}Pb/^{204}Pb$ en fonction du rapport isotopique $^{206}Pb/^{204}Pb$. Les 3 lignées de Vlastélic et al. (2001) y sont encore représentées ainsi que des ombres grises qui présentent les grandes régions du canal du Mozambique : les îles Glorieuses tout au nord, la ride de Jeffrey et Juan de Nova au nord de la ride de Davie, Bassas da India et Europa au sud de la ride de Davie et la vallée de Natal tout au sud du canal. Cette figure met en évidence les deux « pôles » isotopiques principaux du canal avec une composition isotopique typique du domaine « N-Indian », représentée par les données des encroûtements Fe-Mn issus des îles Glorieuses, et celle du domaine « SW-Indian », illustrée par les échantillons de la vallée de Natal.

En plus de ces deux « pôles » bien distincts, on observe le groupement de points « Bassas da India et Europa » qui montre une tendance parallèle à celle du domaine « SW-Indian » et des valeurs isotopiques en $^{206}Pb/^{204}Pb$ plus faibles que celles du nord de la vallée de Natal, liées à la baisse d'influence du NADW. Cette hypothèse est cohérente avec l'observation discutée dans le paragraphe 3.3.3.3.

Ce qui est plus intéressant encore, c'est le cluster de points « Jeffrey et Juan de Nova ». Il ne correspond à aucune des tendances discutées mais s'étend entre le domaine « SW-Indian » et « N-Indian ».

La drague DR11, issue de la ride de Jeffrey à une profondeur de 2400-2450 m, montre trois échantillons avec une modification graduelle de leurs compositions isotopiques depuis une signature « SW-Indian » jusqu'à une signature « N-Indian » (illustrée par la flèche verte sur la figure 3.5). L'échantillon MOZ1-DR11-07 possède un rapport isotopique $^{206}Pb/^{204}Pb$ qui est similaire, voir plus élevé, que certains points du groupe « Bassas da India et Europa ». De plus, le rapport isotopique $^{208}Pb/^{206}Pb$ de cet échantillon est inférieur à 2.071 (2.0654) qui marque la limite entre le domaine « SW-Indian » et « N-Indian ».

Ces observations montreraient que l'influence du NADW ne s'arrête pas au sud de la ride de Davie mais qu'elle persiste au nord, jusqu'à la ride de Jeffrey. L'hétérogénéité des données issues des échantillons de la drague DR11 montre une variation d'influence du NADW et donc, que la ride de Jeffrey correspondrait à la limite nord de sa propagation dans le canal du Mozambique. L'étude de Vlastélic et al. (2001) n'a sûrement pas permis d'identifier ce phénomène en raison des encroûtements Fe-Mn analysés qui sont issus des masses d'eau superficielles du canal et non pas des courants profonds (Albarède et al., 1997).

3.3.5. Résumé et conclusion

Les 33 encroûtements Fe-Mn, du canal du Mozambique, étudiés dans cette partie, présentent un set de rapports isotopiques de Pb très hétérogènes entre le nord du canal, représenté par les îles Glorieuses, et le sud représenté par un échantillon du plateau des Aiguilles. L'hétérogénéité des résultats montre que le canal du Mozambique est une région géographique particulière où plusieurs sources de Pb sont présentes. Ainsi, les enregistrements isotopiques variés des échantillons illustrent des processus de mélange entre les différentes sources.

Premièrement, ce travail révèle une corrélation entre la composante $^{208}Pb/^{206}Pb$ et la latitude des encroûtements Fe-Mn. Un échantillon, le DR75-0012 se comporte de manière différente, en dehors de la tendance. Issu du plateau des Aiguilles, il est possible qu'il reflète une signature, différente des autres échantillons, potentiellement marquée par une source de l'Antarctique apportée par les courants profonds de type CDW. Cette hypothèse montre donc des mélanges de signatures isotopiques, provenant de pôles différents, qui peuvent être déplacées à travers la circulation profonde comme le proposent Vlastélic et al. (2001). Deuxièmement, cette étude confirme les observations de Vlastélic et al. (2001) et Abouchami, Goldstein (1996) concernant l'arrivée du NADW au sud du canal du Mozambique, dans le domaine « SW-Indian ». Cependant, notre étude va plus loin, et montre que le NADW circule jusqu'au-delà de la ride de Davie, influençant notamment les signatures isotopiques en Pb des échantillons de la drague DR11 localisée proche de la ride de Jeffrey à une profondeur de 2400-2450 m, et plus particulièrement celle de l'échantillon MOZ1-DR11-07.

Là encore, cette collection unique d'encroûtements Fe-Mn permet d'améliorer nos connaissances sur le modèle de circulation des eaux intermédiaires et profondes à travers l'étude isotopique du Pb, qui est un traceur montrant des variations plus subtiles et plus fines qu'avec l'isotopie du Nd. Ce travail confirme les interprétations de l'étude isotopique du Nd, et montre que l'utilisation de deux proxys isotopiques permet de voir des phénomènes similaires à des degrés différents. Le Pb est donc un traceur très intéressant aussi bien dans l'étude de sources isotopiques locales que dans l'étude des courants océaniques à échelle régionale.

3.3.6. Références bibliographiques

Abouchami, W., Goldstein, S.L., 1995. A lead isotopic study of circum-antarctic manganese nodules. Geochim. Cosmochim. Acta 59, 1809–1820. https://doi.org/10.1016/0016-7037(95)00084-D

Albarède, F., Goldstein, S.L., Dautel, D., 1997. The neodymium isotopic composition of manganese nodules from the Southern and Indian oceans, the global oceanic neodymium budget, and their bearing on deep ocean circulation. Geochim. Cosmochim. Acta 61, 1277–1291. https://doi.org/10.1016/S0016-7037(96)00404-8

Broecker, W.S., Peacock, S.L., Walker, S., Weiss, R., Fahrbach, E., Schroeder, M., Mikolajewicz, U., Heinze, C., Key, R., Peng, T.-H., Rubin, S., 1998. How much deep water is formed in the Southern Ocean? J. Geophys. Res. Oceans 103, 15833–15843. https://doi.org/10.1029/98JC00248

Charles, C., Pelleter, E., Révillon, S., Nonnotte, P., Jorry, S.J., Kluska, J.-M., 2020. Intermediate and deep ocean current circulation in the Mozambique Channel: New insights from ferromanganese crust Nd isotopes. Mar. Geol. 430, 106356. https://doi.org/10.1016/j.margeo.2020.106356

Collins, C., Hermes, J.C., Roman, R.E., Reason, C.J.C., 2016. First dedicated hydrographic survey of the Comoros Basin. J. Geophys. Res. Oceans

121, 1291–1305. https://doi.org/10.1002/2015JC011418

Frank, M., 2002. Radiogenic isotopes: tracers of past ocean circulation and erosional input. Rev. Geophys. 40, 1–1. https://doi.org/10.1029/2000RG000094

Frank, M., O'Nions, R.K., 1998. Sources of Pb for Indian Ocean ferromanganese crusts: a record of Himalayan erosion? Earth Planet. Sci. Lett. 158, 121–130. https://doi.org/10.1016/S0012-821X(98)00055-7

Hart, S.R., Blijsztajn, J., Craddock, C., 1995. Cenozoic volcanism in Antarctica: Jones Mountains and Peter I Island. Geochim. Cosmochim. Acta 59, 3379–3388. https://doi.org/10.1016/0016-7037(95)00212-I

Hole, M.J., Kempton, P.D., Millar, I.L., 1993. Trace-element and isotopic characteristics of small-degree melts of the asthenosphere: Evidence from the alkalic basalts of the Antarctic Peninsula. Chem. Geol. 109, 51–68. https://doi.org/10.1016/0009-2541(93)90061-M

Leclaire, L., 1984. RIDA - MD39 cruise, Marion Dufresne R/V. https://doi.org/10.17600/84010511

Leclaire, L., 1975. NOSICAA - MD 06 cruise, Marion Dufresne R/V. https://doi.org/10.17600/75010711

Mantyla, A.W., Reid, J.L., 1995. On the origins of deep and bottom waters of the Indian Ocean. J. Geophys. Res. Oceans 100, 2417–2439. https://doi.org/10.1029/94JC02564

Molzahn, M., Reisberg, L., Wörner, G., 1996. Os, Sr, Nd, Pb, O isotope and trace element data from the Ferrar flood basalts, antarctica: evidence for an enriched subcontinental lithospheric source. Earth Planet. Sci. Lett. 144, 529–545. https://doi.org/10.1016/S0012-821X(96)00178-1

Moulain, M., Evain, M., 2016. PAMELA-MOZ05 cruise, Pourquoi pas ? R/V. https://doi.org/10.17600/16009500

Olu, K., 2014. PAMELA-MOZ01 cruise, L'Atalante R/V. https://doi.org/10.17600/14001000

Orsi, A.H., Nowlin, W.D., Whitworth, T., 1993. On the circulation and stratification of the Weddell Gyre. Deep Sea Res. Part Oceanogr. Res. Pap. 40, 169–203. https://doi.org/10.1016/0967-0637(93)90060-G

Rocholl, A., Stein, M., Molzahn, M., Hart, S.R., Wörner, G., 1995. Geochemical evolution of rift magmas by progressive tapping of a stratified mantle source beneath the Ross Sea Rift, Northern Victoria Land, Antarctica. Earth Planet. Sci. Lett. 131, 207–224. https://doi.org/10.1016/0012-821X(95)00024-7

Toole, J.M., Warren, B.A., 1993. A hydrographic section across the subtropical South Indian Ocean. Deep Sea Res. Part Oceanogr. Res. Pap. 40, 1973–2019. https://doi.org/10.1016/0967-0637(93)90042-2

Vlastélic, I., Abouchami, W., Galer, S.J.G., Hofmann, A.W., 2001. Geographic control on Pb isotope distribution and sources in Indian Ocean Fe-Mn deposits. Geochim. Cosmochim. Acta 65, 4303–4319. https://doi.org/10.1016/S0016-7037(01)00713-X

von Blanckenburg, F., O'nions, R.K., Heinz, J.R., 1996. Distribution and sources of pre-anthropogenic lead isotopes in deep ocean water from FeMn crusts. Geochim. Cosmochim. Acta 60, 4957–4963. https://doi.org/10.1016/S0016-7037(96)00310-9

You, Y., 2000. Implications of the deep circulation and ventilation of the Indian Ocean on the renewal mechanism of North Atlantic Deep Water. J. Geophys. Res. Oceans 105, 23895–23926. https://doi.org/10.1029/2000JC900105

3.4. Conclusion (français)

L'étude isotopique de 33 encroûtements Fe-Mn du canal du Mozambique s'est basée sur deux proxys majeurs : le Nd, avec un temps de résidence long, et le Pb dont le temps de résidence est court. Ces deux systèmes isotopiques sont donc complémentaires et permettent d'étudier aussi bien la circulation océanique à grande échelle que des variations très locales. Les échantillons étudiés se répartissent des Îles Glorieuses au nord, jusqu'au plateau des Aiguilles au sud, à des profondeurs variant de 170 m à 2650 m.

L'isotopie du Nd met en avant une tendance de plus en plus radiogénique du sud du canal jusqu'au nord du canal du Mozambique. Les résultats montrent également des valeurs peu radiogéniques au nord de la ride de Davie qui ne peuvent pas être simplement liées à une contribution du courant profond indien NIDW mais aussi au NADW. L'apport du NADW à cet endroit du canal est estimé entre 37% et 48% (avec un pôle Pacifique fixé à $\varepsilon Nd = -6$). Ce travail présente également des voies de circulation possibles à travers la ride de Davie.

L'étude isotopique du Pb vient confirmer le travail de Vlastélic et al. (2001) concernant la définition de grands domaines isotopiques dans l'océan Indien, même si notre étude permet d'affiner la limite entre le domaine « SW-Indian » et « N-Indian » semble dorénavant à revoir. Le travail mené sur le Pb est en parfaite cohérence avec le travail réalisé sur l'isotopie du Nd qui montrent, tous les deux, que la ride de Davie n'est pas une barrière infranchissable à la circulation des courants profonds et, qui proposent un nouveau modèle 2D de la circulation moderne des masses d'eau intermédiaires et profondes du canal du Mozambique.

3.4. Conclusion (english)

The isotope study of 33 Fe-Mn crusts in the Mozambique Channel was based on two major proxies: Nd, with a long residence time, and Pb, with a shorter residence time. Therefore, these two isotopic systems are complementary and make it possible to study both large-scale ocean circulation and local variations. The samples studied are distributed from the Glorieuses islands in the north to the Agulhas plateau in the south, at depths ranging from 170 mbsl to 2650 mbsl.

The Nd isotopes show an increasingly radiogenic trend from the south of the channel to the north of the Mozambique Channel. The results also illustrate low radiogenic values north of the Davie ridge, which cannot be simply related to a contribution from the Indian deep current NIDW but also from the NADW. The NADW contribution at this point is estimated to be between 37% and 48% (with a Pacific pole set at $\varepsilon Nd = -6$). This work also presents possible circulation paths through the Davie ridge.

The Pb isotopic study confirms the work of Vlastélic et al (2001) on the definition of large isotopic domains in the Indian Ocean, even if our study allows refining the limit between the "SW-Indian" and "N-Indian" domains seems to be revised. The work carried out on Pb isotopes is perfectly consistent with the work conducted on Nd isotopes; both of them indicated that the Davie ridge is not an impassable barrier to the circulation of deep currents. Moreover, we propose a new 2D model of the modern circulation of the intermediate and deep-water masses in the Mozambique Channel.

CHAPTER 4 : FE-MN CRUSTS – ARCHIVES OF VERTICAL PALEOGEODYNAMIC MOVEMENTS

Fe-Mn crusts as archives of vertical movements: new insights for the geodynamic reconstruction of the Mozambique Channel over the past 12 Ma

Will be submitted as a paper in *Earth and Planetary Science Letters*

Claire Charles[a,b*], Ewan Pelleter[a], Sidonie Révillon[b,c], Stephan J. Jorry[a], Jean-Michel Kluska[d], Didier Bourlès[e], Simon Quentin[e], Régis Braucher[e] and the ASTER team[e], Philippe Nonnotte[b], Céline Liorzou[b], Sandrine Chéron[a], Yoan Germain[a] and Jean-Alix Barrat[f]

[a] IFREMER, Unité des Géosciences Marines, 29280, Plouzané, France
[b] Univ. Brest, CNRS, UMR 6538 (Laboratoire Géosciences Océan), Institut Universitaire Européen de la Mer (IUEM), 29280, Plouzané, France
[c] SEDISOR/UMR 6538 (Laboratoire Géosciences Océan), Institut Universitaire Européen de la Mer (IUEM), 29280 Plouzané, France
[d] TOTAL Exploration and Production, CSTJF, Avenue Larribau, 64000, Pau, France
[e] CEREGE UM34, Univ. Aix Marseille, CNRS, IRD, INRAE, Coll. France, 13545, Aix en Provence, France
[f] Université de Bretagne Occidentale, CNRS, UMR 6539 (Laboratoire des Sciences de l'Environnement Marin), LIA BeBEST, Institut Universitaire Européen de la Mer (IUEM), 29280, Plouzané, France

4.1. Abstract

The Mozambique Channel is well known for its very specific location between the eastern African margin and Madagascar, in the SW Indian Ocean, where very intense currents from two oceanic domains (Indian and Atlantic) mix. Moreover, it is punctuated by seamounts and high underwater reliefs (i.e. Davie Ridge) that can influence the oceanic circulation.

Recent studies on the growth and demise of the carbonate platforms in the south of the channel and, on the development of the Glorieuses islands in the north of the channel, have raised questions about the vertical movements that have occurred in the Mozambique Channel during the Cenozoic.

The aim of this study is to assess and characterise geodynamic events recorded in the Fe-Mn crusts of the Mozambique Channel over the past 30 Ma.

For this purpose, we present a stratigraphic, mineralogical and geochemical investigation of four Fe-Mn crusts collected (1) on the summit of Macua and Paisley mounts in the NW of the channel and (2) near Europa and Hall Bank in the Mozambique Basin. A total of 61 layers were analysed, including a 21 subsample dataset of the authigenic $^{10}Be/^{9}Be$ ratio to establish the chronology. The εNd and $^{208}Pb/^{206}Pb$ values show significant amplitudes from -6.9 to -9.7 and from 2.0569 to 2.0839 respectively, and the growth rates of all the layers are comprised between 1.8 and 5.1 mm/Ma.

The isotope signatures of the four Fe-Mn crusts reflect that their geochemical contents vary between Atlantic and Indian oceans compositions. However, important increasing and decreasing trends between the Middle Miocene and the Pliocene point geochemical record changes and suggest that Fe-Mn crusts have shifted from water masses over time.

All combined results illustrate two major geodynamic events of uplift and subsidence type. Uplift is recorded between 11.7 and 3.4 Ma with a rising rate between 61 and 167 m/Ma. Subsidence event is registered from 5.1 to 1.6 Ma, with a collapse rate between 186 and 300 m/Ma.

These findings confirm previous observations based on carbonate platforms evolution and above all, provide absolute dates for the paleogeographic reconstruction of the Mozambique Channel. This is the first time that a study focused on Fe-Mn crusts, reveals and dates vertical movements of the seafloor. One more time, these geologic deposits show they are real witnesses of the past system. Bringing these two major events to light will enable us to model the paleoceanographic circulation of the Mozambique Channel over the last 30 Ma with great accuracy.

4.2. Introduction

Hydrogenetic ferromanganese (Fe-Mn) crusts are interesting records of water masses provenance and evolution through geological times, due to their ubiquitous and well-distributed presence on the entire seabed at depths of 400 to 7000 meter below sea level (mbsl). Fe-Mn oxide and hydroxide colloids precipitate directly from cold ambient seawater on indurated substrates and can integrate high contents in base, precious and strategic metals (e.g., Cu, Ni, Co, REE, Y, Pt, Nb and Zr ; Hein et al., 2010, 2000; Lusty et al., 2018). Because of their extremely slow growth (few millimetres per million years; mm/Ma; Frank et al., 2002, 1999; Konstantinova et al., 2017; Koschinsky et al., 1996; Koschinsky and Hein, 2017; Puteanus and Halbach, 1988; Segl et al., 1984), they have been known for several decades as valuable archives of paleo seawater chemistry (Frank, 2002). Precise studies focusing on long-term geochemical variations (up to 60 Ma) of hydrogenetic Fe-Mn crusts provide essential information on water masses and oceanic currents in which they have been developed, to understand their circulation paths and their mixing over time (Christensen et al., 1997; Koschinsky and Hein, 2017; Reynolds et al., 1999).

In this context, their radiogenic isotope ratios of Nd and Pb have been frequently study in order to characterise the geochemical composition of the largest oceanic basins and to understand the global oceanic mixing through time (Abouchami et al., 1997; Albarède and Goldstein, 1992; Josso et al., 2020; Mizell et al., 2020; Muiños et al., 2008). However, Fe-Mn crusts are now increasingly considered to investigate smaller areas in order to understand regional geographic and oceanographic processes with a higher resolution due to the number of samples vs. the surface of the studied area (Charles et al., 2020; Mizell et al., 2020). Recent study conducted in the Mozambique Channel which based on Nd isotopic compositions recorded in 29 Fe-Mn crusts distributed over a 2000 km transect, allowed to model present-day circulations of intermediate and deep water masses in the channel between the last 20 to 80 Ka (Charles et al., 2020). The Mozambique Channel is a strategic area to study mixing of water masses coming from two different oceanic reservoirs (i.e. Atlantic and Indian) with well-defined physical and geochemical parameters such as temperature, salinity and isotopic composition (Arsouze et al., 2007; Fine, 1993; Lutjeharms, 2006; Toole and Warren, 1993; Ullgren et al., 2012).

While significant changes can appear in local Nd isotope exchange processes or sources, the radiogenic isotope ratio of Nd dissolved in seawater is expected to be controlled mainly by conservative mixing between water masses (Goldstein and Hemming, 2003; van de Flierdt et al., 2016). For this reason, and due to its residence time between 400 and 1000 years, i.e. shorter than the homogenization time of the ocean (Jeandel et al., 1995; Rempfer et al., 2011; Tachikawa et al., 1999), the Nd represents a powerful and frequently used tracer for investigating water masses identification and mixing (Frank et al., 2002; Goldstein and Hemming, 2003; Reynolds et al., 1999). The global deep water production is essentially located in the North Atlantic Ocean from different sources such as the Norwegian-Greenland Sea (NGS) and the Labrador Sea Water (LSW) as explained by Frank (2002). The Nd isotope composition of the North Atlantic Deep Water (NADW) is about -13.5 εNd (where εNd represent the variations of Nd isotope compositions as deviation of the determined $^{143}Nd/^{144}Nd$ ratio from the chondritic uniform reservoir CHUR per 10,000 ; Jacobsen and Wasserburg, 1980) related to the constant mixing between these two different oceanic sources presenting distinct isotopic composition (NGS: -8

> εNd > -11; LSW: -14 > εNd > -17; Filippova et al., 2017; Lambelet et al., 2016; Reynolds et al., 1999). In contrast, the Pacific Ocean is characterized by a more radiogenic signature 0 > εNd > -6 related to the interaction of water masses with very young volcanic rocks (Lacan and Jeandel, 2001; Piepgras and Wasserburg, 1980; Scher et al., 2015). Finally, the Indian Ocean is a mixing basin between these two end-members, presenting intermediate Nd isotope compositions of the order of -7 > εNd > -8.5 (Arsouze et al., 2007; Bertram and Elderfield, 1993; Scher and Martin, 2008; Wilson et al., 2012).

Concurrently, the isotope composition of Pb in the Fe-Mn crusts are also considered and used as tracer for studying past water mixing for shorter length scales due to its residence time in the ocean (80 to 100 years; Cochran et al., 1983; Craig et al., 1973) lower than that of Nd. This isotopic conservative element brings different advantages to the study of the other tracers because it presents three isotope ratios. Due to this important characteristic, and considering the fact that the old cratonic shield have more radiogenic Pb compositions than the younger sedimentary and volcanic rocks (Harlavan and Erel, 2002), the sensitive Pb isotope distribution can define linear mixing trends between two major Pb sources and consequently reflect the influence of weathering local inputs (von Blanckenburg and Nägler, 2001).

Thus, through the preliminary study based on the identification of modern water masses present in the Mozambique Channel (Charles et al., 2020), it is relevant to investigate the variations of the Nd and Pb isotope signatures, as well as the major and trace element compositions, recorded in Fe-Mn crusts over the last 30 Ma. This temporal approach aims to highlight variations in geochemical records that may be related to several oceanographic upheavals (e.g., water masses mixing, increase or decrease of inputs, change of chemistry) or geodynamic movements (e.g., magmatism, subsidence and uplift phenomenon) such as those identified during the Neogene by recent tectonic, seismic and sedimentary studies in this region (Courgeon et al., 2017; Delaunay, 2018; Leroux et al., 2020; Nicholas et al., 2007; Walford et al., 2005). Based on four Fe-Mn crusts located in the north (Paisley Mount, Macua Mount) and in the south (Hall Bank, Europa) of the Mozambique Channel, the high resolution data set of the sampled layers and the absolute dating of the Fe-Mn crusts will aim: (1) to precise geochronology of specific and regional geodynamic events and (2) to estimate amplitudes and rates of seafloor uplift or subsidence at different key places of the studied area.

4.3. Geological settings

The Mozambique Channel is situated in the western part of the Indian Ocean, between the Mozambique and the Madagascar continental slopes (Figure 4.1). This broad seaway was initiated in the Early Jurassic due to the break-up of the supercontinent Gondwana in two major structures: the western part composed of the Africa and South America, and the eastern part composed of the India, Antarctica, Australia and Madagascar (Gaina et al., 2013; Leinweber and Jokat, 2012; Mahanjane, 2014). This main structuration phase was followed by stabilization and tectonic/volcanic stages as, for instance, during the separation of India and Antarctica from Madagascar around 84 Ma (Bassias, 1992), or more recently, with tectonic activity linked to the onset and development of the East African rift system (EARS) from the Oligocene up to present days (Chorowicz, 2005; Feuillet et al., 2021; Macgregor, 2015; Salman and Abdula, 1995). The asymmetric NW-SE Davie Ridge (Figure 4.1), which extends from the northern coast of

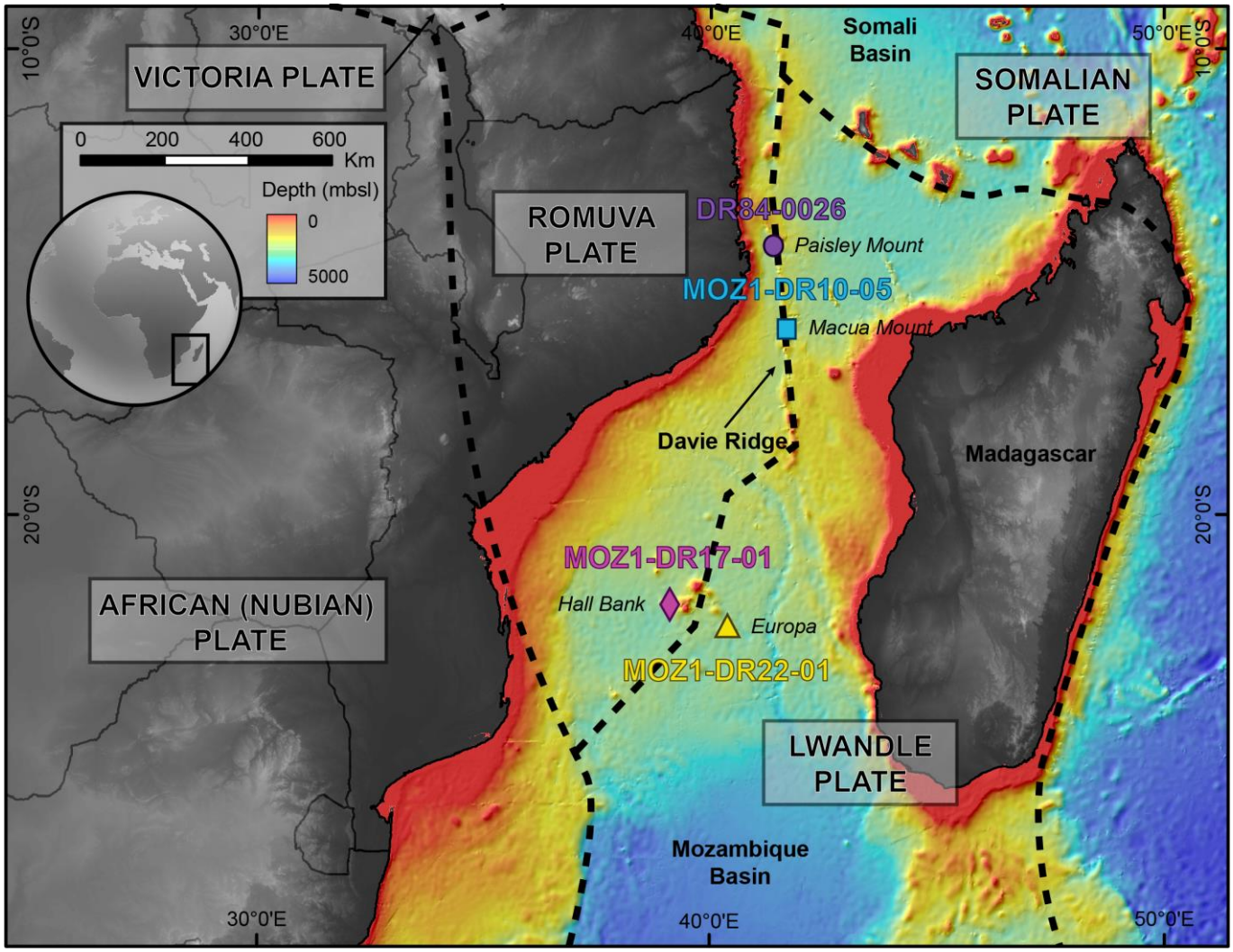

Figure 4.1. *Bathymetry of the Mozambique Channel (data from GEBCO and PAMELA cruises) with the limits of the tectonic plates of the region (dashed black lines) from Lemoine et al. (2020), Michon (2016), Saria et al. (2014), Stamps et al. (2021, 2018, 2008). The samples are represented by the purple dot (DR84-0026), the blue square (MOZ1-DR10-05), the pink diamond (MOZ1-DR17-01) and the yellow triangle (MOZ1-DR22-01).*

Mozambique to the south-western coast of Madagascar, corresponds to a fossil transform fault along which Madagascar has moved away from Africa coast and drifted towards the south between the Middle Jurassic and the Early Cretaceous (Bassias, 1992; Coffin and Rabinowitz, 1987; Franke et al., 2015; Mougenot et al., 1986; Segoufin et al., 1977). Dredge samples collected along the Davie Ridge show that isolated blocks of Precambrian basement and volcanics are preserved along this paleo-transform ridge. These volcanics include Late Cretaceous and Cenozoic lava flows (Bassias, 1992; Courgeon et al., 2016, 2017).

Since 80 Ma, Madagascar has acquired its present position and the Davie Ridge has structured the Mozambique Channel in two mains basins: the Mozambique Basin and the west Somali Basin. Recent studies, especially based on GPS measurements, seismology and structural analysis (Lemoine et al., 2020; Michon, 2016; Saria et al., 2014; Stamps et al., 2021, 2018, 2008), have proposed new kinematic models considering three minor plates (Victoria, Rovuma and Lwandle plates) in addition to the major Nubian and Somalian plates (Figure 4.1). They proposed that the southern part of the Mozambique Channel is crossed, from NE to SW, by the Rovuma-

Lwandle plate boundary, following the Quathlamba seismic axis (Déprez et al., 2013; Saria et al., 2014; Stamps et al., 2021, 2008). Analysis of the spatial distribution of active faults in the area has also revealed the presence of a 200 km - width system of faults, superimposed with the Quathlamba seismic axis (Deville et al., 2018) (Figure 4.1).

Significant volcanic events have been recorded in northern Madagascar during the Late Cretaceous (Courgeon et al., 2016; Torsvik et al., 2000, Leroux et al., 2020) although the Mozambique Channel did not present major geodynamic movement until the Oligocene, when a rapid uplift has occurred in southern Africa, directly impacting the southern region of the channel (Walford et al., 2005) followed by a structural doming in the Mozambique Basin area (Ponte, 2018). Intense volcanic activity was also described in the Comores archipelago and in southern Mozambique Channel, coupled by an extensional tectonic deformation of the Davie Fracture Zone (DFZ) (Courgeon et al., 2018, 2016; Michon, 2016). Recent studies have also focused on the long term-evolution of the isolated carbonate platforms known as the Iles Eparses and surroundings seamounts (Bassas da India, Europa, Jaguar and Hall bank, Juan de Nova and the Glorieuses Islands) which have been developed on top of volcanic structures (Courgeon et al., 2016; Jorry et al., 2016). A major drowning event has been reported during the Early Pliocene, originated from an important increasing of the subsidence at the center of the Mozambique Channel (Bassas da India area) and along the Davie Ridge (Macua and Paisley Mounts) (Courgeon et al., 2017, 2016) (Figure 4.1). All these movements seem to be linked to the development of the EARS since the Late Miocene (Chorowicz, 2005; Courgeon et al., 2018; Deville et al., 2018; Macgregor, 2015) although the dating of these tectonic and volcanic events is still debated due to the lack of absolute dates.

4.4. Oceanography

The Mozambique Channel exhibits a high number of oceanic currents. Its location on the SW of the Indian Ocean gives it the particularity of recording contrasted currents from the Atlantic and the Indian oceans. South of the Davie Ridge, the water column is mainly characterized by the North Atlantic Deep Water (NADW) whose core is located at 2500 meter below sea level (mbsl), because of its depth range of 1500-3500 mbsl, and the Antarctic Intermediate Water (AAIW) with a main influence at 1150 mbsl (depth range of 800-1500 mbsl) (Figure 4.2). Both of these currents arrive from the south of the Mozambique Basin and flow northwards along the Mozambican coast (Fine, 1993). North of the Mozambique Channel, the deep and intermediate water column is predominantly composed by the North Indian Deep Water (NIDW) whose core is located at 2500 mbsl, due to its depth range of 2000-3000 mbsl (Collins et al., 2016; DiMarco et al., 2002) and the Red Sea Water (RSW) with a main influence at 1100 mbsl (depth range of 800-1400 mbsl) (Figure 4.2) which enters in the Mozambique Channel along the East African coast towards the south (Beal et al., 2000; ; DiMarco et al., 2002; Schott and McCreary, 2001).

The water masses with low radiogenic Nd signatures ($-9 > \varepsilon Nd > -13$) come from the Atlantic Ocean and are mainly found in the deep (NADW) and intermediate (AAIW) currents (Figure 4.2). Conversely, more radiogenic ($-7 > \varepsilon Nd > -8.5$) water masses arrive north of the channel, influenced by the Indian Ocean (Figure 4.2). These Indian currents are omnipresent in the northern part of the channel from the deepest (NIDW) to the surface (TSW-STSW, SICW) waters, and mainly represented by the intermediate (RSW) and surface waters in the centre of the channel. A modern circulation model

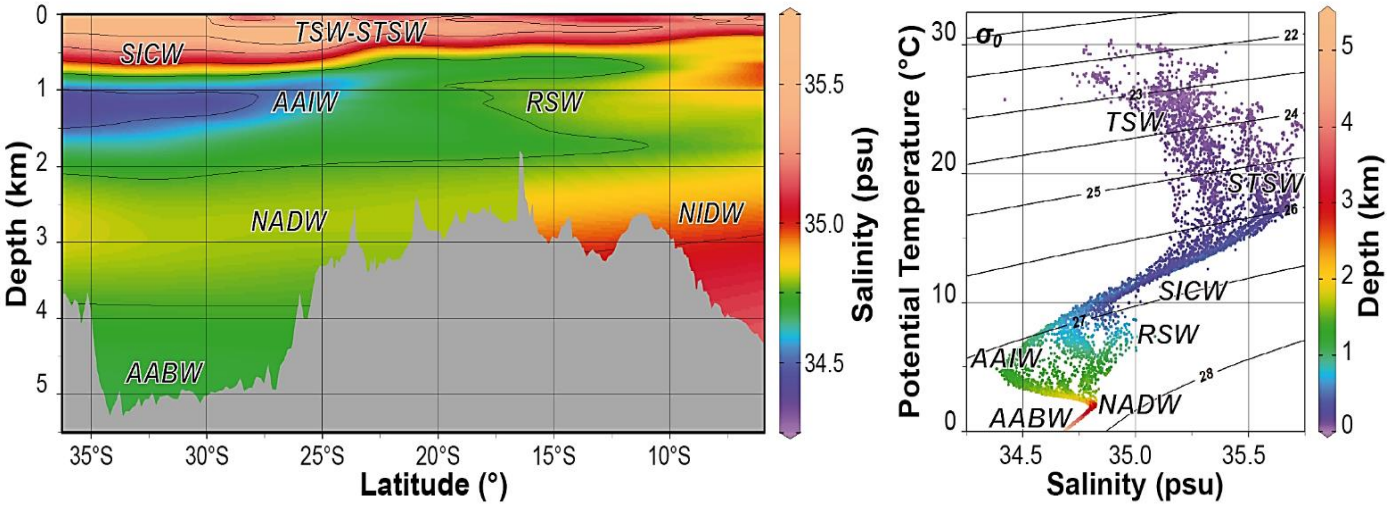

Figure 4.2. *Salinity section of the Mozambique Channel showing the distribution of its main water masses, the bathymetry is represented in grey, and T-S diagram, based on Conductivity Temperature Depth (CTD) profiles. AABW: Antarctic Bottom Water; AAIW: Antarctic Intermediate Water; NADW: North Atlantic Deep Water; NIDW: North Indian Deep Water; RSW; Red Sea Water; SICW: South Indian Centre Water; STSW; Sub-Tropical Surface Water; TSW; Tropical Surface Water.*

established by Charles et al. (2020) provides new information regarding the Nd isotope composition of all the stratigraphy of the water column whether the location north or south of the Mozambique Channel.

Until recently, little was known about the Pb isotope composition in the Indian Ocean because the impact of anthropogenic contributions considerably affected its distribution and its well-preserved signals in the oceans as it was demonstrated in the Atlantic (Véron et al., 1998, 1994; Wu and Boyle, 1997), Pacific (Flegal and Patterson, 1983) and Southern Ocean (Flegal et al., 1993). The data recently acquired by Echegoyen et al. (2014) and Lee et al. (2015) show that low ratios ($^{206}Pb/^{207}Pb$ = 1.15-1.17; $^{208}Pb/^{207}Pb$ = 2.43-2.44; $^{206}Pb/^{204}Pb$ = 18.15-18.37) appear in the shallow waters (< 1500 mbsl) of the northern Indian Ocean indicating a dominant influence of anthropogenic Pb sources. However, high ratios ($^{206}Pb/^{207}Pb$ = 1.17-1.19; $^{208}Pb/^{207}Pb$ = 2.44-2.46; $^{206}Pb/^{204}Pb$ = 18.23-18.78) were recorded in the deep layers (> 1500 mbsl) of the Southern Ocean. These high values are closer to the natural Pb isotope compositions acquired by Vlastélic et al. (2001) in Fe-Mn crusts and nodules. This last work present records in the south-western Indian Ocean (< 1500 mbsl, corresponding to the AAIW and RSW) with Pb isotope records of $^{206}Pb/^{204}Pb$ = 18.75-18.92; $^{207}Pb/^{204}Pb$ = 15.65-15.70; $^{208}Pb/^{204}Pb$ = 38.79-39.17 but also in the Mozambique Basin (> 1500 mbsl, corresponding to the NADW) with Pb isotope signals of $^{206}Pb/^{204}Pb$ = 18.83-19.06; $^{207}Pb/^{204}Pb$ = 15.68-15.72; $^{208}Pb/^{204}Pb$ = 38.91-39.18.

4.5. Samples and analytical methods

4.5.1. Fe-Mn crusts

This study is based on four Fe-Mn crusts (Figure 4.3) from the Mozambique Channel that were collected from the Europa Island in the south of the channel to the Paisley Mount in the northwest of the Davie Ridge (Figure 4.1). Three of them (MOZ1-DR10-05, MOZ1-DR17-01, MOZ1-

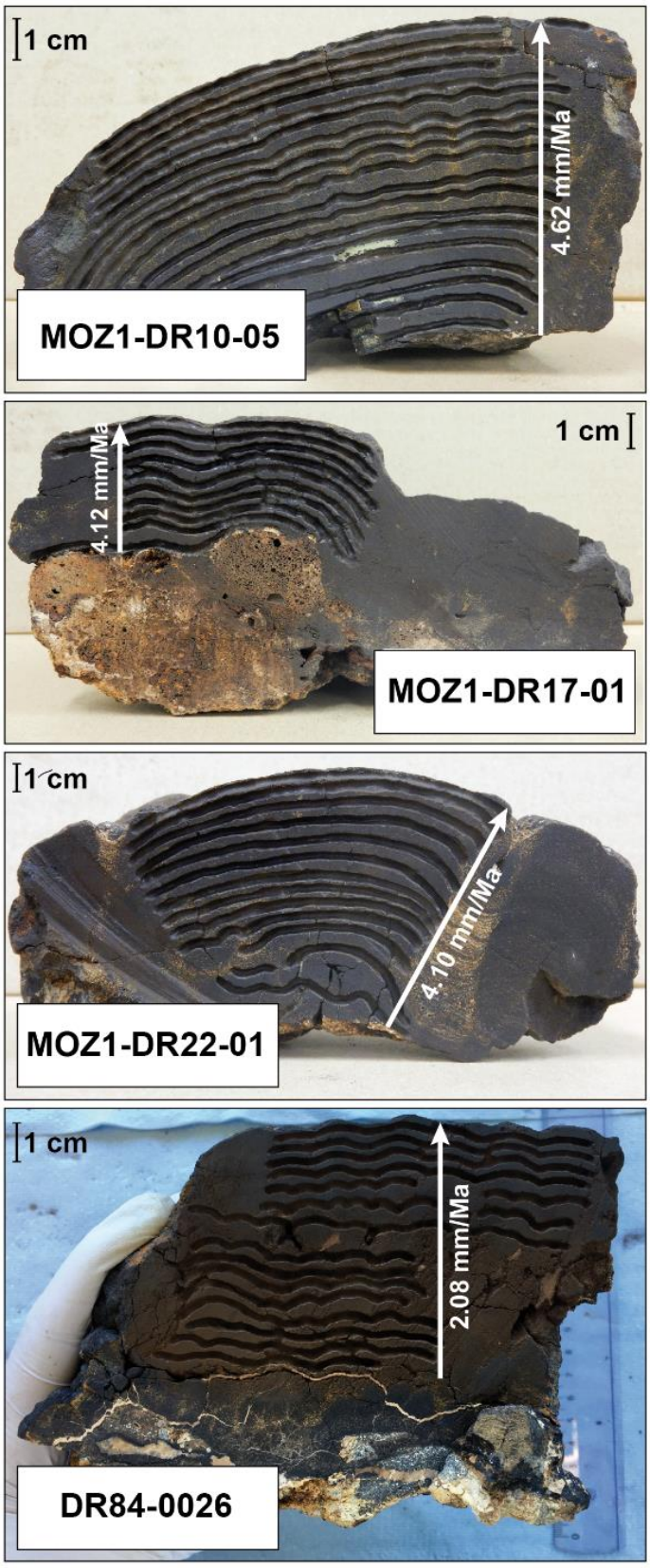

Figure 4.3. *Images of the four selected Fe-Mn crusts. They all present a planar shape and two of them (MOZ1-DR17-01; DR84-0026) show carbonate substrate.*

DR22-01) were sampled during the PAMELA-MOZ1 cruise on board the RV L'Atalante (Olu, 2014) whereas one sample (DR84-0026) was dredged during the MD-39 Rida expedition (western slope of the Davie Ridge, Paisley Mount; Leclaire, 1984) conducted by the National Museum of Natural History (MNHN).

These Fe-Mn crusts were selected for this study because their depth ranges vary from 800 (DR84-0026) and 1900 (MOZ1-DR17-01) mbsl, their thicknesses range from 34 to 72 mm and they present unaltered surface and layers (Figure 4.3). Moreover their initial locations on submarine seamounts along a wide range of latitude (Figure 4.1) and at intermediate/boundary of intermediate and deep water depths allow this work to focus if the samples moved from a water mass to another due to tectonic events in the Mozambique Channel.

The Fe-Mn crusts DR84-0026 and MOZ1-DR10-05 were recovered in the northern part of the Davie Ridge, between 800 and 1400 mbsl, which at present correspond to radiogenic Indian intermediate current such as RSW (see section 4.4).

The sample MOZ1-DR22-01 was dredged near Europa Island, between 1400 and 1550 mbsl, which corresponds to a transition zone between intermediate and deep water masses due to an important variability of the Nd isotope compositions measured at this depth range (Charles et al., 2020).

Finally, the Fe-Mn crust MOZ1-DR17-01 was recovered close to the Hall Bank, between 1700 and 1900 mbsl corresponding to the upper limit of NADW, previously presented as low radiogenic water source in the Mozambique Channel. All these details are presented in the table 4.1.

Table 4.1. *International Geo Sample Number (IGSN), location, depth and major characteristics of the four studied Fe-Mn crusts from the PAMELA-MOZ1 (Olu, 2014) and MD39-Rida (Leclaire, 1984). The water masses correspond to the modern records of the samples, the * corresponds to the transition depth defined between the intermediate and deep water by Charles et al. (2020) and GR for "Growth rate".*

Sample	MOZ1-DR10-05	MOZ1-DR17-01	MOZ1-DR22-01	DR84-0026
Cruise	PAMELA-MOZ1	PAMELA-MOZ1	PAMELA-MOZ1	MD-39 Rida
Dredge	DR10	DR17	DR22	DR84
IGSN	BFBG-155153	BFBG-155224	BFBG-155243	MNHN-GS-DR84-0026
Location	Macua Mount	Hall Bank	Europa	Paisley Mount
Latitude	16◦21'S	21◦85'S	22◦30'S	14◦08'S
Longitude	41◦38'E	39◦10'E	40◦23'E	41◦29'E
Depth range (mbsl)	1000–1400	1700–1900	1400–1550	800–810
Water mass (T_0)	RSW	NADW	Transition*/AAIW	RSW
Thickness (mm)	72	34	47	64
Average GR (mm/Ma)	4.62	4.12	4.10	2.08

4.5.2. Stratigraphic layers

After macroscopic observations, the sampled area was chosen (homogeneous layer, undamaged, and non-altered). Based on visual textural delineation, a total of 61 micro drilled layers were meticulously sampled on the four studied Fe-Mn crusts. Each powder was recovered with a clean brush and visible rock fragments and clastic minerals (such as quartz, feldspar or calcite) have been removed with precision pliers. The first sampling corresponds to the first 100 µm on the surface, i.e. the last elementary adsorption on Fe-Mn oxyhydroxides integrating between 20 and 80 ka (Albarède and Goldstein, 1992; Charles et al., 2020; Frank et al., 2002).

The other layers are carried out underneath, over the entire thickness of the Fe-Mn crusts with a resolution of 2 to 5 mm between two layers (Figure 4.3). Their width varies between 0.5 and 2 mm integrating the different states of water mass geochemistry in the order of 150 to 550 ka, due to the slow accretion rates of the four studied Fe-Mn crusts ranging from 2.08 to 4.62 mm/Ma with an average growth rate of 3.73 mm/Ma (Table 4.1). The numbering of the layers is added after the name of the sample. The number corresponds to the sampling depth (in mm) in the thickness of the Fe-Mn crust. In the case of a surface subsample, -S is noted. The samples MOZ1-DR10-05, MOZ1-DR17-01, MOZ1-DR22-01 and DR84-0026 own 20, 11, 14 and 16 layers, respectively.

4.5.3. X-ray diffraction mineralogy

X-ray diffraction (XRD) analyses were conducted with a BRUKER AXS D8 Advance diffractometer. The samples were top loaded into amorphous silica sample holders, and all analyses were run between 5° and 70°2θ, with 0.01°2θ step at 1s/step (monochromatic Cu Kα radiation, 40 kV, 30mA). Minerals were identified using Diffrac. Suite EVA software. This methodology allows to quickly identify most of the minerals present in the samples (e.g. silicates, carbonates, phosphates, oxides, and well-crystallized

oxyhydroxides). δ-MnO2 is barely visible on diffractograms even where it constitutes the main crystalline phase in most of the studied layers. Estimation of the proportion of δ-MnO2 from other crystalline phases is made on the basis of a qualitative analysis of the diffractograms i.e. ratio between "vernadite" visible peaks (37° and 66° 2θ) and peak signal of other well crystallised minerals.

4.5.4. Major, trace elements and isotopic compositions

The major and trace elements as well as Pb and Nd isotopes compositions of the Fe-Mn crusts were determined at the "Pôle Spectrométrie Océan" (PSO, Plouzané, France). All sample preparations were conducted in a Class 1000 (ISO 6) clean laboratory. A part of approximately 100 mg of each subsample was dried and subjected to a total attack with HF and HNO_3 as described in the analytical study of Charles et al. (2021). The concentrations of major elements (Fe, Mn, Al, Ca, Mg, Na, K, Ti, P) were determined by Inductively Coupled Plasma Atomic Emission Spectroscopy (ICP-AES) using a Horiba Jobin Yvon® Ultima 2 spectrometer. Aliquots of mother solutions containing the equivalent of 30 mg of powder were used for the determination of the concentrations of these elements following the procedure of Cotten et al. (1995). Instrument calibrations were made using international standards (ACE, WSE and JB2) and the relative standard deviation is ≤2%.

Aliquots of each mother solution were spiked with Tm solution (30 ng of Tm per mg of sample) and used for trace and rare earth element abundances determination, with a High-Resolution Inductively Coupled Plasma Mass Spectrometer (ThermoScientific, Thermo Electron Element XR). The details of this procedure and the measuring parameters are available in a previous analytical work focused on the characterization of eight Fe-Mn oxide standards (Charles et al., 2021).

An aliquot of 2 ml was taken for Nd and Pb column chemistry. The Pb fractions were chemically separated following conventional column chemistry procedures described in Gale (1996). The isotopic $^{206}Pb/^{204}Pb$, $^{207}Pb/^{204}Pb$ and $^{208}Pb/^{204}Pb$ ratio measurements were performed using a Neptune Multi-collector Inductively Coupled Plasma Mass Spectrometer (ThermoScientific Neptune). Pb isotope ratios were corrected for instrumental mass fractionation and machine bias by the Tl doping method of White et al. (2000), and NIST SRM981 Pb standard bracketing every 3 samples. The averaged Pb isotope reproducibility based on 87 replicate analyses of NIST SRM981 Pb is $^{206}Pb/^{204}Pb = 16.9241 \pm 6$ ($2\sigma \times 10^{-4}$), $^{207}Pb/^{204}Pb = 15.4722 \pm 5$ ($2\sigma \times 10^{-4}$) and $^{208}Pb/^{204}Pb = 36.6430 \pm 19$ ($2\sigma \times 10^{-4}$). Blank values are below an average of 50 pg and therefore negligible in all cases.

The protocol of Nd isotope analyses was detailed beforehand (Charles et al., 2020). Briefly, after the Pb extraction, the REE fraction was separated using Eichrom® Tru spec Resin. The Nd was separated from the other REE using Eichrom® Ln spec Resin following an analytical procedure modified from Pin et al. (1994). The isotopic $^{143}Nd/^{144}Nd$ ratio measurements were performed on a Multi-collector Thermal Ionization Mass Spectrometer (ThermoScientific Triton). Nd isotope composition of standard JNdi was analysed to monitor instrumental drift. The averaged result of $^{143}Nd/^{144}Nd = 0.512086 \pm 7$ ($2\sigma \times 10^{-6}$; n =16) was consistent with its certified value of $^{143}Nd/^{144}Nd = 0.512115 \pm 7$ ($2\sigma \times 10^{-6}$; Tanaka et al., 2000) corresponding to a LaJolla Nd isotope composition value of $^{143}Nd/^{144}Nd = 0.511858 \pm 7$ ($2\sigma \times 10^{-6}$; Lugmair et al., 1983). No instrumental bias had to be taken in account.

The standard deviation of this average is ± 0.13 εNd unit and associated to each sample analysis. Blank values are below an average of 100 pg and therefore negligible in all cases.

4.5.5. Be dating

Dating of the four Fe-Mn crusts were carried out on 21 layers (6 layers for MOZ1-DR10-05, MOZ1-DR17-01 and MOZ1-DR22-01; 3 layers for DR84-0026) in order to focus on the first 10 Ma (^{10}Be half-life $T_{1/2}$ = 1.387 ± 0,012 Ma according to Chmeleff et al. (2010); Korschinek et al. (2010); Nishiizumi (2007)).

The chemical preparation and the analyses were conducted in collaboration with CEREGE at the Laboratoire National des Nucléides Cosmogéniques (LN2C, France).

Approximatively 50 mg of each dry subsample were processed for authigenic Be isotope analyses according to the established and well-described protocol of Bourlès et al. (1989) revised by Simon et al. (2016). The leaching technique of Bourlès et al. (1989) allows extracting both isotopes in the phase that corresponds to the equilibrated authigenic fraction of soluble ^{10}Be and ^{9}Be.

The natural authigenic ^{9}Be concentration was measured using a graphite-furnace Atomic Absorption Spectrophotometer (AAS) with double-beam correction (ThermoScientific ICE3400®). The ^{10}Be concentration was measured after chemical preparation at the French Accelerator Mass Spectrometer (AMS) national facility ASTER (CEREGE). Chemistry blank ratios range from 10^{-13} to 10^{-14}, what is at least 3 order of magnitude lower than the sample ^{10}Be/^{9}Be ratios. Concentration values of the authigenic ^{10}Be were corrected for radioactive decay using the ^{10}Be half-life ($T_{1/2}$) presented before.

4.6. Results

4.6.1. Characterization of the studied Fe-Mn crusts

4.6.1.1. X-ray diffraction mineralogy

X-ray diffraction data indicate that the Fe-Mn crusts consist principally of poorly crystalline oxides: in the four studied Fe-Mn crusts, no distinct crystalline Mn phases, characteristic of diagenetic or hydrothermal remobilisation (e.g. 10 Å manganate, pyrolusite), were identified. It is difficult to accurately estimate the proportion of each phase. Though it is very difficult to provide a semi-quantitative estimate of the mineral phases, the diffractograms show that vernadite (δ-MnO_2) can be considered as the dominant Mn oxides phase (peaks around 2.45 and 1.42 Å). This observation is consistent with the mineralogical compositions in most marine hydrogenetic Fe-Mn oxides (Guan et al., 2017; Hein et al., 2013; Hein and Koschinsky, 2014; Mizell et al., 2020; Muiños et al., 2013). Quartz is the main allochtonous mineral phase detected in diffractograms whereas detrital minerals (e.g. plagioclase, K-feldspar) and biogenic phase (e.g. calcite) are in minor abundances when present. No diagenetic minerals such as carbonate fluorapatite (CFA) were detected on diffractograms in accordance with nonphosphatized Fe-Mn crusts (Benites et al., 2020; Mizell et al., 2020).

4.6.1.2. Major and minor elements

The concentrations of major and minor elements of the Fe-Mn crusts layers (n=61) have limited variations for Fe-Mn crusts (Table 4.2). Iron and manganese have the largest variations ranging from 14.19 (MOZ1-DR17-01 27) to 23.19 wt%

Table 4.2. *Major and trace elements mean compositions of the four studied Fe-Mn crusts.*

Sample and details	MOZ1-DR10-05 Macua Mount 16◦12'S - 41◦38'E		MOZ1-DR17-01 Hall Bank 21◦50'S - 39◦10'E		MOZ1-DR22-01 Europa 21◦18'S - 40◦23'E		DR84-0026 Paisley Mount 14◦08'S - 41◦29'E	
Subsamples	20	*SD*	11	*SD*	14	*SD*	16	*SD*
Fe (wt%)	20.48	*1.48*	17.47	*2.28*	19.46	*1.24*	19.11	*1.45*
Mn	23.70	*2.02*	20.83	*2.65*	19.41	*1.27*	20.90	*3.70*
Fe/Mn	0.87	*0.07*	0.86	*0.19*	1.01	*0.10*	0.93	*0.10*
Al	1.58	*0.56*	1.19	*0.55*	1.55	*0.43*	2.42	*1.09*
Ca	2.28	*0.56*	2.08	*0.71*	2.13	*0.16*	1.96	*0.56*
Mg	1.18	*0.29*	1.10	*0.39*	1.03	*0.04*	1.03	*0.29*
Na	1.73	*0.42*	1.64	*0.61*	1.62	*0.18*	1.60	*0.44*
K	0.69	*0.22*	0.57	*0.24*	0.79	*0.19*	1.05	*0.45*
Ti	0.65	*0.17*	0.66	*0.23*	0.65	*0.07*	0.69	*0.20*
P	0.49	*0.06*	0.40	*0.06*	0.46	*0.06*	0.44	*0.08*
Ba (ppm)	1631	*224*	1294	*76*	1501	*176*	1527	*168*
Be	8.86	*1.12*	5.46	*0.81*	8.38	*1.04*	8.81	*0.69*
Bi	9.2	*2.5*	16.6	*2.5*	8.0	*0.9*	13.5	*7.0*
Co	5617	*1293*	5800	*1099*	4436	*319*	5276	*1580*
Cr	20.2	*11.9*	52.0	*35.7*	21.5	*11.5*	17.5	*4.9*
Cs	0.29	*0.10*	0.27	*0.07*	0.26	*0.06*	0.40	*0.17*
Cu	354	*90*	373	*120*	339	*125*	432	*124*
Ga	3.0	*0.8*	2.7	*0.5*	2.9	*0.8*	4.4	*1.6*
Hf	8.36	*1.47*	5.57	*3.31*	9.74	*1.52*	10.26	*1.22*
Li	4.2	*1.2*	9.3	*15.2*	3.7	*0.7*	5.7	*2.0*
Mo	593	*71*	521	*60*	507	*99*	477	*124*
Nb	73.3	*15.5*	68.9	*8.1*	63.5	*9.8*	100.7	*18.9*
Ni	3102	*562*	3159	*708*	2607	*441*	2808	*286*
Pb	1647	*164*	1701	*152*	1645	*83*	1588	*372*
Rb	14.6	*4.2*	13.6	*4.6*	16.7	*4.5*	24.6	*9.9*
Sc	10.1	*1.7*	9.8	*1.7*	9.1	*1.0*	9.5	*1.1*
Sn	3.0	*0.5*	3.6	*0.4*	3.0	*0.4*	5.7	*0.4*
Sr	1714	*138*	1481	*114*	1518	*72*	1428	*248*
Ta	0.82	*0.23*	0.85	*0.22*	0.82	*0.21*	0.79	*0.3*
Th	70.0	*25.4*	68.6	*10.2*	60.4	*15.5*	77.5	*18.6*
Tl	48	*10*	125	*51*	31	*12*	47	*11*
U	11.8	*1.3*	10.8	*1.0*	11.4	*0.7*	10.4	*3.1*
V	875	*77*	725	*74*	798	*42*	768	*86*
W	87	*10*	80	*10*	68	*16*	78	*13*
Zn	493	*64*	652	*381*	467	*30*	457	*49*
Zr	420	*52*	329	*194*	458	*52*	377	*43*

La	250.5	*27.6*	243.6	*55.9*	215.5	*19.7*	212.2	*37.8*
Ce	1951.7	*236.9*	1957.5	*198.3*	1899.4	*303.0*	2282.6	*322.9*
Pr	59.1	*8.7*	46.0	*9.8*	51.6	*4.8*	48.9	*6.9*
Nd	228.6	*30.2*	182.4	*41.9*	192.3	*18.0*	180.9	*41.0*
Sm	43.56	*5.41*	36.49	*8.54*	37.31	*3.78*	33.25	*7.40*
Eu	9.80	*2.56*	8.57	*2.00*	9.10	*0.98*	7.85	*1.92*
Gd	44.0	*12.1*	36.8	*9.4*	39.3	*4.4*	37.4	*7.6*
Tb	6.18	*1.66*	5.50	*1.27*	5.78	*0.74*	4.81	*1.23*
Dy	36.1	*9.7*	32.8	*7.6*	35.0	*4.6*	28.0	*9.9*
Y	140.1	*36.6*	148.0	*32.1*	140.5	*30.7*	104.4	*50.6*
Ho	7.21	*2.01*	6.79	*1.48*	7.17	*1.07*	5.58	*2.22*
Er	19.78	*5.78*	19.19	*3.86*	19.73	*3.18*	15.17	*6.28*
Yb	17.62	*5.21*	17.50	*2.90*	17.95	*2.88*	14.00	*5.49*
Lu	2.56	*0.79*	2.63	*0.38*	2.62	*0.42*	2.05	*0.80*
ΣREY	2824	*225*	2744	*240*	2673	*269*	2977	*275*
La/Sm	0.89	*0.02*	1.03	*0.07*	0.89	*0.04*	1.00	*0.05*
Gd/Yb	1.27	*0.23*	1.03	*0.11*	1.11	*0.14*	1.42	*0.28*
Y/Ho	0.70	*0.10*	0.84	*0.06*	0.75	*0.07*	0.71	*0.06*
Ce/Ce*	3.91	*0.57*	4.68	*1.16*	4.38	*0.86*	5.56	*1.32*
Eu/Eu*	1.22	*0.05*	1.25	*0.02*	1.26	*0.05*	1.17	*0.05*

(MOZ1-DR10-05 14) with a mean value of 18.27 wt% and from 15.82 (DR84-0026 23) to 27.82 wt% (DR84-0026 6) with a mean value of 20.31 wt%, respectively. Fe/Mn ratios range from 0.67 to 1.22 with a mean value of 0.91 (n=61), an intermediate ratio between open-ocean seamount Fe-Mn crusts and continental margin seamount Fe-Mn crusts (Conrad et al., 2017; Hein et al., 1997; Josso et al., 2020; Mizell et al., 2020; Muiños et al., 2013).

Alumina and potassium which represent minor detrital phase (e.g. plagioclase, K-feldspar) vary from 0.75 to 3.87 wt% and 0.42 to 1.47 wt% respectively. Highest Al and K concentrations are recorded for deeper layers (> 20mm) of the hydrogenetic Fe-Mn crust dredged at Mont Paisley (DR84-0026). The three other Fe-Mn crusts (MOZ1-DR10-05; MOZ1-DR17-01; MOZ1-DR22-01) systematically exhibit Al and K contents lower than 2.40 and 1.05 wt% respectively, with the deepest layers (>20mm) exhibiting the highest concentrations. Phosphorous contents are relatively low and do not show high variability (0.32 to 0.65 wt%). The highest content is measured in the upper part of MOZ1-DR10-05, in the surface layer. The mean P concentrations of about 0.45 wt% (n=61) does not reflect any intense phosphatisation phenomenon, either in the upper (modern) or deeper (older) parts of the samples, as it can occur during intense phosphatisation events as demonstrated by Josso et al. (2019) in Tropic Seamount (NE Atlantic) Fe-Mn crusts and by Benites et al. (2020) in Rio Grande Rise (SW Atlantic).

Calcium concentrations range from 1.87 to 2.68 wt%, and highest contents are most likely related to the presence biogenic phases. Titanium do not vary significantly (0.56 to 0.87 wt%) but can be used to evaluate a potential hydrothermal impacts with the Ti index calculation (Strakovh, 1974). Ti index values range from 41 (MOZ1-DR17-01) to 85 (MOZ1-DR10-05) with a mean value of 59 (n = 61). These data fall perfectly in the range of reported values for hydrogenetic Fe-Mn crusts (Hein et al., 2013), significantly lower than those measured in hydrothermal Fe-Mn crusts (Josso et al., 2020).

4.6.1.3. Metal and trace concentrations

Cobalt, copper and nickel show minimum concentrations of 3168 (DR84-0026 20), 106 (MOZ1-DR22-01 S) and 1557 ppm (MOZ1-DR22-01 S) whereas the maximum contents are 7969 (MOZ1-DR10-05 64), 551 (DR84-0026 54) and 3865 ppm (MOZ1-DR10-05 64) respectively. Co has a mean concentrations of 4834 ppm, Cu averages 374 ppm and Ni 2617 ppm. The sum of Co + Cu + Ni shows a maximum of 1.23 wt% (MOZ1-DR10-05 64) with a mean of 0.74 wt%. These results and the Fe/Mn ratios are consistent with a predominantly hydrogenetic origin of the studied Fe-Mn crusts, and confirm geochemical compositions between those of open-ocean and continental margin Fe-Mn crusts (Koschinsky and Halbach, 1995).

Trace element show diverse abundances. Rubidium presents the narrower range of values from 5.7 to 35.5 ppm with weak standard deviations (SD) ranging from 4.2 to 9.9. Thorium, niobium and thallium show similar ranges of contents with minimum of 37.3 (MOZ1-DR10-05 8), 45.7 (MOZ1-DR10-05 5) and 11 (MOZ1-DR22-01 S) ppm, and maximum of 109.9 (MOZ1-DR10-05 51), 109.0 (DR84-0026 34) and 188.3 (MOZ1-DR17-01 11) ppm, respectively. Th mean is 69 ppm (n=61), consistent with the Th average in the Indian Fe-Mn crusts (Hein et al., 2012; Hein and Koschinsky, 2014). The SD of these three elements varies between 8.1 (Nb) and 51 (Tl) (Table 4.2). Zirconium contents are comprised between 108 (MOZ1-DR17-01 15) and 559 (MOZ1-DR17-01 32) ppm, with SD from

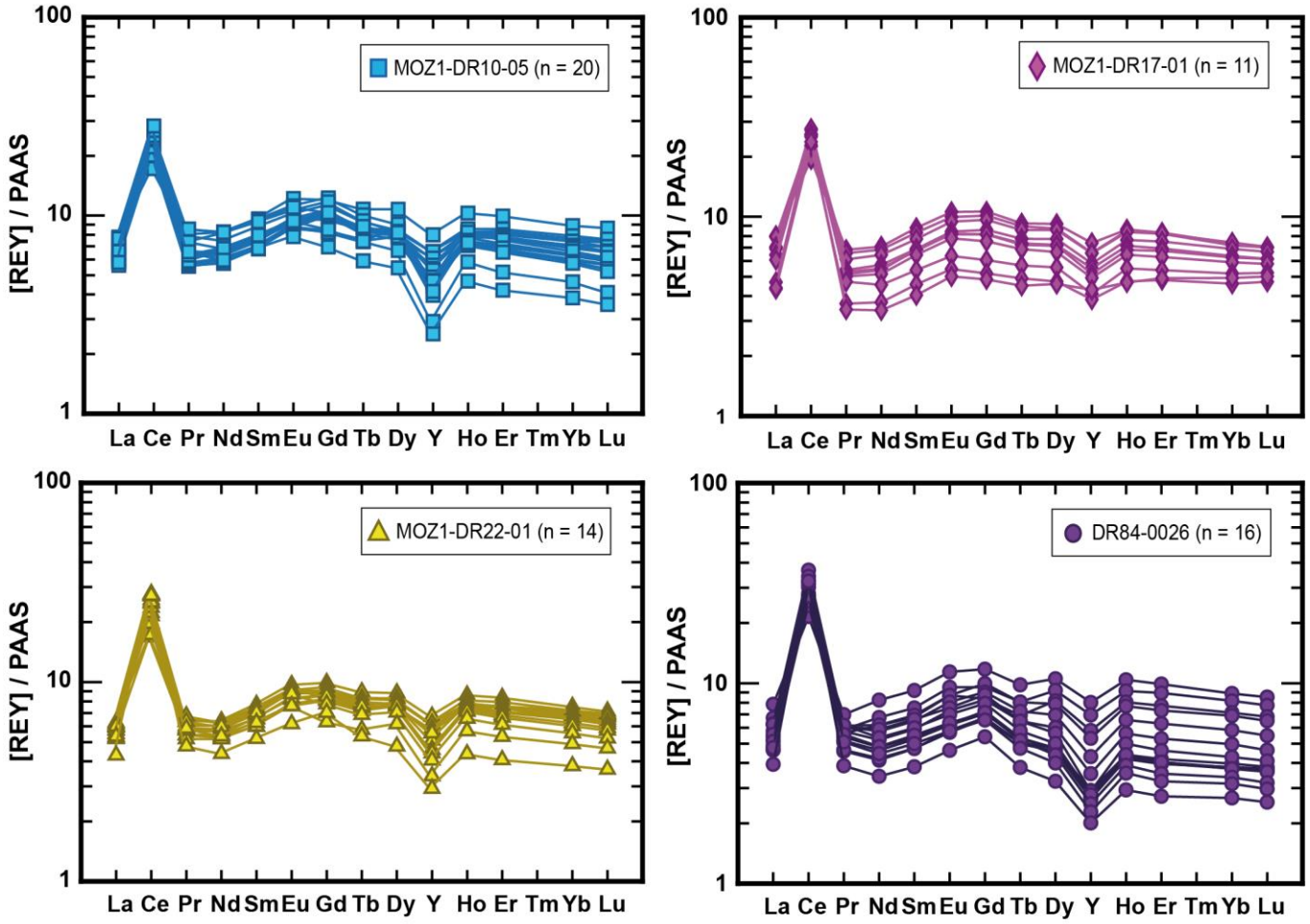

Figure 4.4. *PAAS-normalised (Taylor and McLennan, 1985) REY compositions of the four studied Fe-Mn crusts with all their respective layers (n).*

43 to 194. Zinc analyses presents values higher than the Zr, with a minimum of 375 (DR84-0026 20) and a maximum of 1727 (MOZ1-DR17-01 11) ppm and SD from 30 to 381. Finally, with the highest abundances, lead exhibits the largest set values from 1263 (DR84-0026 62) to 2368 (DR84-0026 3) ppm. The SD extend from 83 to 372 (Table 4.2). Trace elements data are consistent with those of Hein et al. (2012) acquired in Fe-Mn crusts collected from Shatsky Rise (NW Pacific).

4.6.1.4. Rare earth elements + Y

The analysed Fe-Mn layers present high contents in REY ranging from 2133 (MOZ1-DR22-01 S) to 3642 (DR84-0026 44) ppm and are controlled by very high cerium concentrations up to 2923 ppm (DR84-0026 44). The Ce means of the four Fe-Mn crusts range from 1899 to 2283 ppm (Table 4.2). According to the PAAS-normalized (Taylor and McLennan, 1985) REE and Y patterns (Figure 4.4), the Fe-Mn layers present elementary ratios such as La/Sm [$(La/Sm)_{PAAS}$ = 0.79-1.16] with means of the four Fe-Mn crusts between 0.89 (MOZ1-DR10-05 and MOZ1-DR22-01) and 1.03 (MOZ1-DR17-01), and Gd/Yb [$(Gd/Yb)_{PAAS}$ = 0.81-1.75] with means of the four Fe-Mn samples between 1.03 (MOZ1-DR17-01) and 1.42 (DR84-0026) indicating the enrichment of the heavy REE in the hydrogenetic Fe-Mn crusts (Table 4.2, Figure 4.4, 4.5).

Additionally, all three samples exhibit higher heavy REE concentrations in the deepest layers (>20mm for MOZ1-DR10-05 and MOZ1-DR22-01, and >12mm for DR84-0026) than in surface layers.

Also, the well-known anomalies such as positive Ce anomalies, calculated as the ratio of the normalized values of the element by the interpolation of the adjacent elements such as:

$$Ce/Ce^{*} = \frac{Ce_{PAAS}}{(La_{PAAS} \times Pr_{PAAS})^{1/2}} \qquad (1)$$

and negative Y anomalies are also notable on the layer patterns of the four analysed Fe-Mn crusts. Ce anomalies vary from 2.29 (MOZ1-DR10-05 1.5) to 8.65 (DR84-0026 62) in all the layers. The Fe-Mn crust DR84-0026 presents the highest mean (5.56) whereas MOZ1-DR10-05 shows the less pronounced Ce anomalies (mean = 3.91). The presence of positive Ce anomalies is caused by scavenging of Ce from seawater by hydrous Fe-Mn oxides (Elderfield et al. 1981; Goldberg et al. 1963) and its preferential retention relative to the other REE in the oxide phase through surface oxidation (Bau et al. 1996). The mean ratio $(Y/Ho)_{PAAS}$ vary from 0.70 in MOZ1-DR10-05 to 0.84 in MOZ1-DR17-01 (Table 4.2).

4.6.2. Age-depth modelling

The surface layer show similar authigenic $^{10}Be/^{9}Be$ ratios ranging from 8.6 ± 0.4 (MOZ1-DR17-01 S) to 9.6 ± 0.4 ($\times 10^{-8}$) (DR84-0026 S) which corroborate to present growth surfaces. The other measured $^{10}Be/^{9}Be$ ratios decrease in the deeper parts of the samples until 0.2 ($\times 10^{-8}$) in the layers MOZ-DR10-05 31 and MOZ1-DR22-01 31. Based on the radioactive decay of the authigenic $^{10}Be/^{9}Be$ ratio (Bourlès et al., 1989), it was possible to determine the growth rates of the

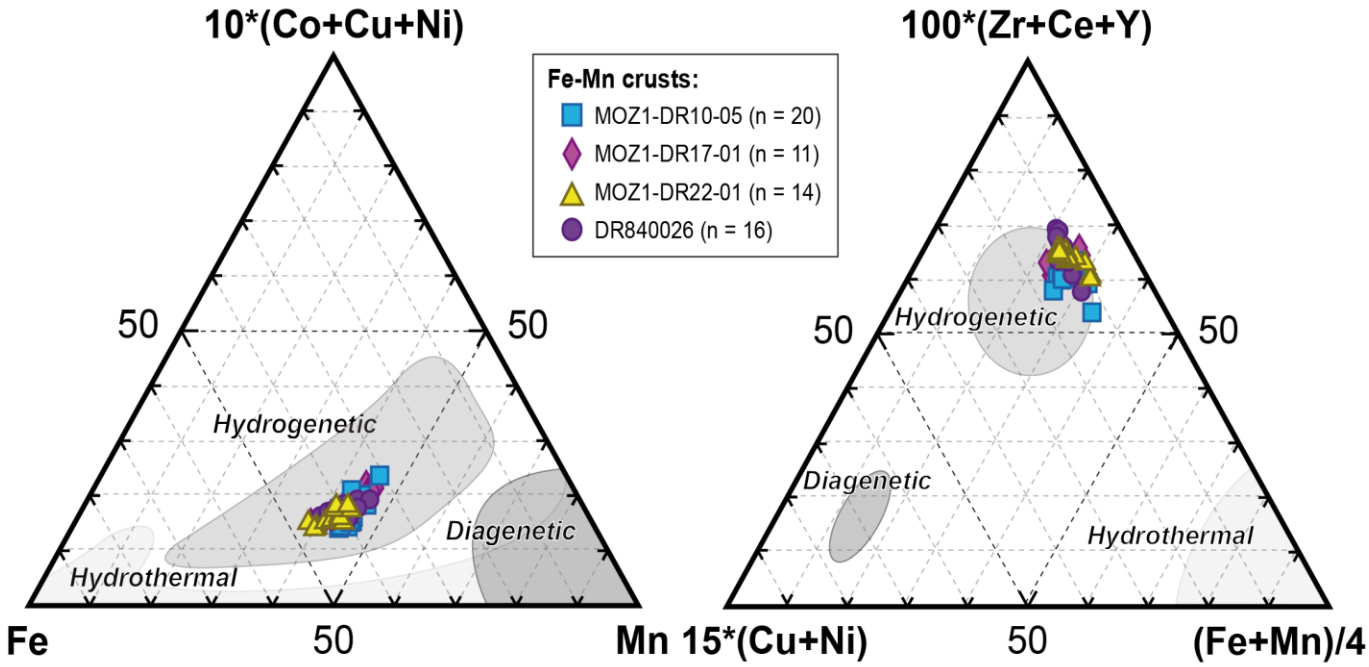

Figure 4.5. Ternary discriminative diagrams for oceanic deposits highlighting the hydrogenetic nature of all the layers (n) from each Fe-Mn crust of this work. The diagram on the left is from Bonatti et al. (1972) and the one on the right from Josso et al. (2017).

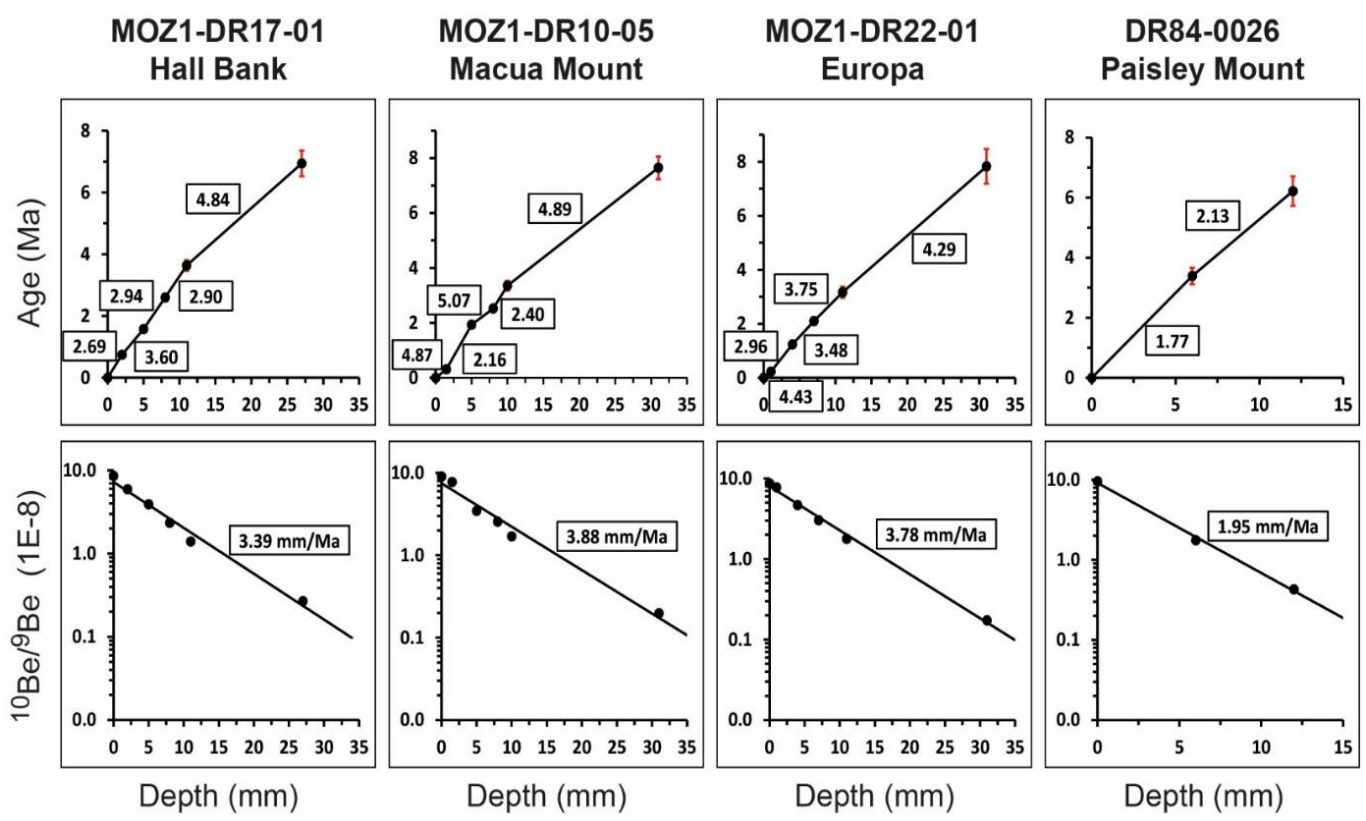

Figure 4.6. *The $^{10}Be/^{9}Be$ ratios in the crusts MOZ1-DR17-01, MOZ1-DR10-05, MOZ1-DR22-01 and DR84-0026 versus depth beneath the growth surface. The ages have been calculated from the radioactive decay of the Be in the samples. The growth rates and ages beyond the age range covered by $^{10}Be/^{9}Be$ data have been calculated using the extrapolation of the growth rates of the deepest layers whose $^{10}Be/^{9}Be$ values were measured.*

analysed layers ranging from a minimum of 1.8 (DR84-0026 6) to a maximum of 5.1 (MOZ1-DR10-05 8) mm/Ma which is typical for hydrogenetic Fe-Mn crusts (Charles et al., 2020; Christensen et al., 1997; Frank et al., 2006, 2002, 1999; Koschinsky et al., 1996; Puteanus and Halbach, 1988; Segl et al., 1984). The most significant variability in growth rate of the four Fe-Mn crusts is observed for the sample MOZ1-DR10-05, with values which vary between 2.2 (MOZ1-DR10-05 5) and 5.1 mm/Ma (MOZ1-DR10-05 8). Growth rate maximum variation by a factor 1.5 is common is the other layers. The measured ages ranging from 6.2 ± 0.5 (DR84-0026) to 7.8 ± 0.6 Ma (MOZ1-DR22-01). However, our four Fe-Mn are older than 7-8 Ma and can therefore not be dated directly with $^{10}Be/^{9}Be$ ratios in the older part.

To do this, it was possible first to calculate the growth rate between two layers in order to see the growth rate variability through time (Figure 4.6) and secondly to extrapolate, assuming constant the oldest growth rate, to the deeper layers of the samples in order to obtain the entire time series. A similar technique was used by Frank and O'Nions (1998), O'Nions et al. (1998) and Segl et al. (1984) from the initial $^{10}Be/^{9}Be$ ratio. This method results in age of 8.0 Ma for MOZ1-DR17-01, 15.6 Ma for MOZ1-DR10-05, 11.1 Ma for MOZ1-DR22-01 and 30.7 Ma for DR84-0026.

4.6.3. Nd and Pb isotope compositions

Nd and Pb isotope compositions (n=61) of the four studied Fe-Mn crusts are reported in Table 3

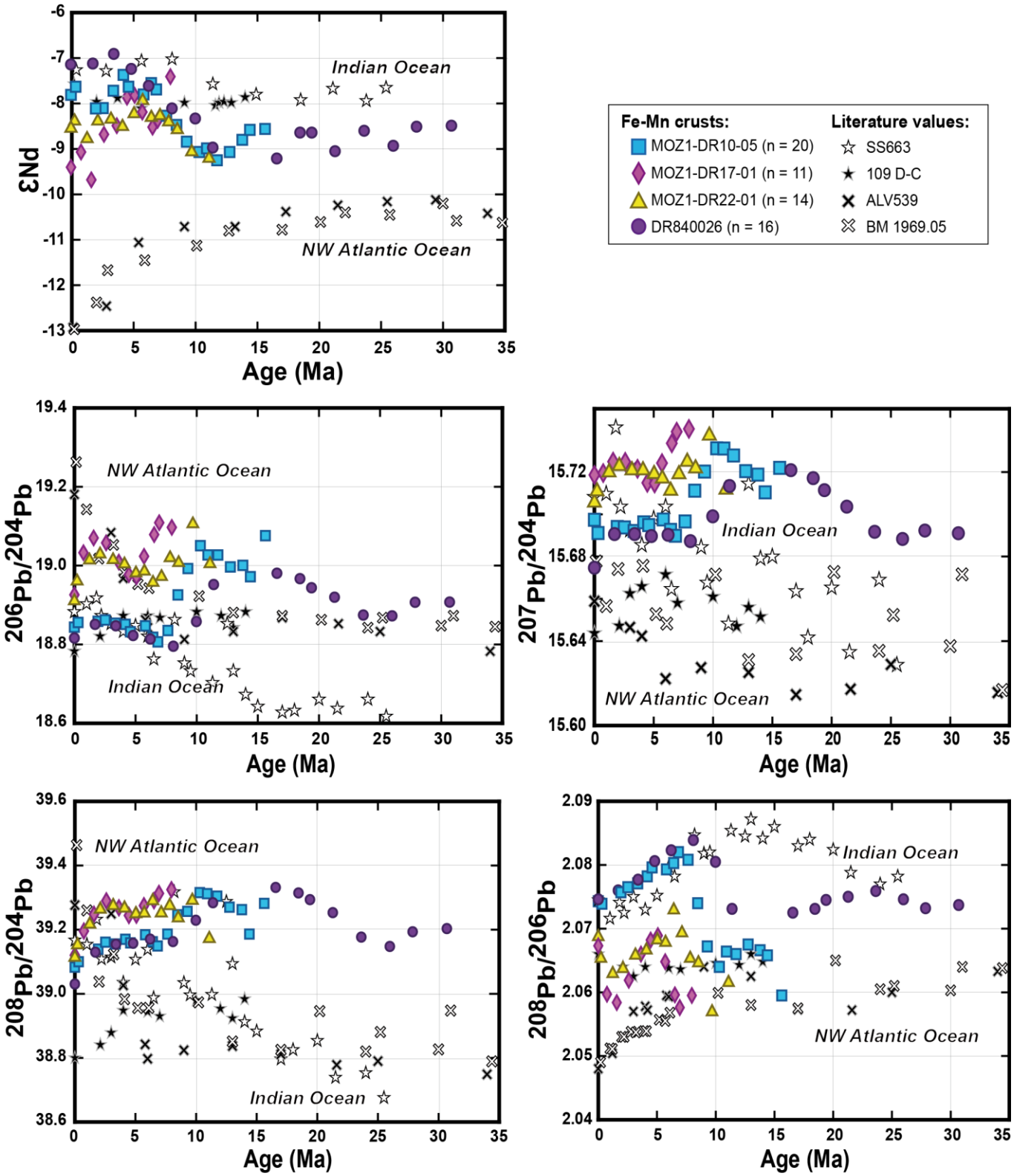

Figure 4.7. *Time series of $\varepsilon_{Nd\,(T)}$ and $^{206}Pb/^{204}Pb$, $^{207}Pb/^{204}Pb$, $^{208}Pb/^{204}Pb$, $^{208}Pb/^{206}Pb$ versus age derived from $^{10}Be/^{9}Be$ dating (**Figure 4.6**) for the four analysed Fe-Mn crusts. Error bars are included in the sample points. The time series values from the literature are shown for comparisons with SS663 isotope values from O'Nions et al. (1998) and Frank and O'Nions (1998), 109 D-C and ALV539 data from O'Nions et al. (1998) and BM 1969.5 values from Burton et al. (1997) and O'Nions et al. (1998).*

and comparison with Atlantic and Indian Ocean Fe-Mn crusts (Burton et al., 1997; Frank and O'Nions 1998; O'Nions et al., 1998; Piotrowski et al., 2000) is shown in figure 4.7.

4.6.3.1. Nd isotope data

The ε_{Nd} compositions versus Be model age of the four studied samples are mostly comprised between the NW Atlantic Fe-Mn crust (ALV539, BM1969.5) and the Indian crust (SS663, 109 D-C) compositions (Figure 4.7).

An exception is between around 7.5 and 0 Ma where the Nd compositions of the samples MOZ1-DR10-05 and DR84-0026 fit well with the Indian crust signatures (SS663, 109D-C) (Figure 4.7). However, our results are generally closer to the Indian domain, than the Atlantic domain, which is consistent with the location of the Mozambique Channel in the SW Indian Ocean. εNd values of the Fe-Mn crust MOZ1-DR10-05 vary between -9.3 (MOZ1-DR10-05 51) and -7.4 (MOZ1-DR10-05 14). These data correspond to the minimum and the maximum of a major increasing trend to more radiogenic values between 11.7 and 4.2 Ma, respectively (Figure 4.7). The Fe-Mn crusts MOZ1-DR22-01 and DR84-006 present similar increases, between 11.1 and 5.7 Ma with εNd data increasing from -9.2 (MOZ1-DR22-01 45) to -7.9 (MOZ1-DR22-01 22) for the first sample and, between 11.4 and 3.4 Ma with εNd data varying from -9.2 (DR84-0026 34) to -6.9 (DR84-0026 6) for the signature of the second sample.

Between 5 and present-day, the Fe-Mn crusts MOZ1-DR10-05, MOZ1-DR22-01 and DR84-0026 reflect some variations from -7.4 to -8.1, from -8.2 to -8.8, and from -7.2 to -6.9, respectively. However, no clear trends are highlighted and changes are not as significant as before 5 Ma. The εNd signature of the Fe-Mn crust MOZ1-DR17-01 present a different trend with an important decrease to low radiogenic data between 5.1 and 1.6 Ma with values falling from -7.8 (MOZ1-DR17-01 18) to -9.7 (MOZ1-DR17-01 5). Finally, we found that the Nd isotope data of the surface layers (the more recent records – 0 Ma) are coherent with some previous works focussing on the conservative water mass mixing process in the same geographic area on Fe-Mn crusts (Albarède et al., 1997) and in seawater (Bertram and Elderfield, 1993; van de Flierdt et al., 2016) as described by Charles et al. (2020).

For comparisons, the sample 109 D-C show a flat trend with a minimum εNd of -8.1 at 5.6 Ma and a maximum ε_{Nd} of -7.6 at 0.2 Ma. The composition of the Fe-Mn crust SS663 from the central Indian Basin vary of less than 1 εNd unit, with a discrete increase between 18.5 and 8.1 Ma with respective values of -7.9 and -7.0.

4.6.3.2. Pb isotope data

The Pb isotope ratios of the four Fe-Mn crusts are represented depending on the ages derived from $^{10}Be/^{9}Be$ dating and show significant variability in Pb isotope records (Figure 4.7).

The isotopic signatures exhibit similar trends for the $^{206}Pb/^{204}Pb$, $^{207}Pb/^{204}Pb$ and $^{208}Pb/^{204}Pb$ ratios even if the slopes can be different. These three ratios present few majors trends (increasing and decreasing). Since 26.0 Ma the record of the sample DR84-0026 presents increasingly radiogenic values from 18.8699; 15.6883 and 39.1477 to 18.9780; 15.7209 and 39.3317, respectively, at 16.6 Ma (Table 4.3). We observe that the compositions of the four Fe-Mn crusts start to decrease to less radiogenic data between 11.4 (DR84-0026) and 6.9 Ma (MOZ1-DR17-01). Then, the Pb isotope signatures of the samples MOZ1-DR10-05 and DR84-0026 stay relatively flat on the $^{206,207}Pb/^{204}Pb$ ratios, expect

one point that stand out from the trends near 0 Ma, whereas the $^{208}Pb/^{204}Pb$ values continue to decrease. The Fe-Mn crusts MOZ1-DR17-01 and MOZ1-DR22-01 both reflect radiogenic peaks (19.0676; 15.7249; 39.2899 and 19.0251; 15.7228; 39.2730 respectively) around 2 Ma (1.6-2.1 Ma) before decreasing trends (Figure 4.7).

In comparison, the $^{206}Pb/^{204}Pb$ values of the sample 109 D-C present a flat signature around 18,9 with a small decrease from 4 to 0 Ma. The Fe-Mn crust SS663 shows an important increasing trend to radiogenic values between around 26 and 2 Ma followed by a slight decline. Our samples appear to become progressively more Pacific-like, like the sample 109 D-C and as previously observed on the Pb isotope composition of the nodule 6854-6 (Cape Basin) by Frank et al. (2002).

The $^{208}Pb/^{206}Pb$ results of our samples are no more relatives to one oceanic domain than another. Like the Nd isotope signatures, two trends (increasing and decreasing) are very apparent on the diagram. The $^{208}Pb/^{206}Pb$ results of the Fe-Mn crust MOZ1-DR10-05 vary between 2.0595 (MOZ1-DR10-05 70) and 2.0820 (MOZ1-DR10-05 27). These data correspond to the minimum and the maximum of a major increasing trend between 15.6 and 6.8 Ma, respectively. The Fe-Mn crusts MOZ1-DR22-01 shows also an increasing slope with values between 2.0569 (MOZ1-DR22-01 45) and 2.0729 (MOZ1-DR22-01 25) for an age range between 9.7 and 6.4 Ma. The sample DR84-006 present a similar increase, between 11.4 and 8.1 Ma with $^{208}Pb/^{206}Pb$ data varying from 2.0725 (DR84-0026 34) to 2.0839 (DR84-0026 16) whereas its Pb isotope composition is fairly homogeneous before 11.4 Ma. The $^{208}Pb/^{206}Pb$ composition of the Fe-Mn crust MOZ1-DR17-01 present also an increasing trend. Its values are from 2.0576 at 6.9 Ma (MOZ1-DR17-01 27) to 2.0689 at 5.1 Ma (MOZ1-DR17-01 18). Unlike the ε_{Nd} trends, each $^{208}Pb/^{206}Pb$ signature of the four Fe-Mn crusts highlights decreasing slopes after the increases (Figure 4.7). These decreasing trends start between 8.1 (DR84-0026) and 5.1 (MOZ1-DR17-01) Ma. The samples DR84-0026 and MOZ1-DR10-05 present these decreases until 0 Ma whereas the MOZ1-DR17-01 and MOZ1-DR22-01 signatures decrease until 1.6-1.2 Ma before to increase again until 0 Ma.

For comparisons, the sample 109 D-C present a flat signature and, the Fe-Mn crust SS663 shows an increasing trend from 25.5 Ma (2.0782) to 13.0 Ma (2.0872) followed by a decreasing slope until around 1 Ma (2.0716), which well fit with the declining signatures of the Fe-Mn crusts MOZ1-DR10-05 and DR84-0026.

4.6.3.3. Resume

To summarize, the four studied Fe-Mn crusts record important variations of Nd (until more than 2 εNd units) and Pb isotope signatures of Mozambique Channel water masses during the past 30 Ma. The recorded compositions of the two radiogenic isotopes present similar increasing (more radiogenic) and decreasing (less radiogenic) trends. From these values, we can identify different period of changes: 1) From the Oligocene (30.7 Ma) to the Middle Miocene (11.1-11.7 Ma) with major $^{206,\ 207,\ 208}Pb/^{204}Pb$ variations recorded in the oldest sample DR84-0026 and later (15.6 Ma) in the sample MOZ1-DR10-05; 2) from the Middle Miocene (11.1-11.7 Ma) to the Pliocene (5.7-3.4 Ma) with increasing εNd and $^{208}Pb/^{206}Pb$ data and decreasing $^{206,\ 207,\ 208}Pb/^{204}Pb$ values; 3) from the Pliocene (5.1-3.4 Ma) to the Pleistocene (1.6 Ma) with decreasing signatures of εNd and $^{208}Pb/^{206}Pb$ and increasing trends of $^{206,\ 207,\ 208}Pb/^{204}Pb$; 4) from the Pleistocene (1.6 Ma) to the Holocene (0 Ma) mainly represented by decreasing $^{206,\ 207,\ 208}Pb/^{204}Pb$ and decreasing $^{208}Pb/^{206}Pb$ values.

Table 4.3. *Be, Nd and Pb isotope compositions of all layers of the four studied Fe-Mn crusts from the PAMELA-MOZ1 (Olu, 2014) and MD39-Rida (Leclaire, 1984). –S corresponds to the surface (top of the Fe-Mn crust) and the other numbers are related to their depth on the Fe-Mn crust slice. The * indicate the ^{10}Be dated layers.*

MOZ1-DR10-05	**Geochronology**				**Nd isotope compositions**			**Pb isotope compositions**					
Macua Mount	**^{10}Be/^{9}Be (10^{-8})**	**GR (mm/Ma)**	**Age (Ma)**	**Error (Ma)**	**^{143}Nd/^{144}Nd**	**2σ (10^{-6})**	**ƐNd**	**^{206}Pb/^{204}Pb**	**2σ (10^{-4})**	**^{207}Pb/^{204}Pb**	**2σ (10^{-4})**	**^{208}Pb/^{204}Pb**	**2σ (10^{-4})**
MOZ1-DR10-05 S*	9.0	-	0.0	-	0.512237	6	-7.9	18.8412	5	15.6974	6	39.0829	10
MOZ1-DR10-05 1.5*	7.8	4.9	0.31	0.02	0.512247	4	-7.6	18.8532	5	15.6911	6	39.0999	16
MOZ1-DR10-05 5*	3.4	2.2	1.93	0.08	0.512222	4	-8.1	18.8562	4	15.6940	4	39.1391	13
MOZ1-DR10-05 8*	2.6	5.1	2.5	0.1	0.512223	2	-8.1	18.8594	4	15.6938	5	39.1611	12
MOZ1-DR10-05 10*	1.7	2.4	3.4	0.2	0.512242	4	-7.7	18.8513	6	15.6921	6	39.1552	29
MOZ1-DR10-05 14			*4.2*		0.512260	6	-7.4	18.8484	4	15.6962	4	39.1699	10
MOZ1-DR10-05 16			*4.6*		0.512247	4	-7.6	18.8297	5	15.6949	5	39.1588	16
MOZ1-DR10-05 22			*5.8*		0.512238	4	-7.8	18.8448	5	15.6975	5	39.1841	14
MOZ1-DR10-05 25			*6.4*		0.512251	4	-7.5	18.8155	5	15.6926	4	39.1623	17
MOZ1-DR10-05 27			*6.8*		0.512244	4	-7.7	18.8039	5	15.6898	4	39.1490	14
MOZ1-DR10-05 31*	0.2	4.9	7.6	0.4	0.512214	4	-8.3	18.8326	7	15.6966	4	39.1862	15
MOZ1-DR10-05 35			*8.5*		0.512204	6	-8.5	18.9232	6	15.7112	4	39.2463	17
MOZ1-DR10-05 39			*9.3*		0.512185	4	-8.8	18.9900	6	15.7202	3	39.2569	11
MOZ1-DR10-05 44			*10.3*		0.512173	4	-9.1	19.0480	6	15.7312	4	39.3155	13
MOZ1-DR10-05 47			*10.9*		0.512177	4	-9.0	19.0245	10	15.7311	4	39.3120	19
MOZ1-DR10-05 51			*11.7*		0.512164	4	-9.2	19.0242	6	15.7278	4	39.3043	16
MOZ1-DR10-05 56			*12.8*		0.512173	4	-9.1	18.9940	7	15.7204	6	39.2701	32
MOZ1-DR10-05 61			*13.8*		0.512187	4	-8.8	18.9981	4	15.7188	4	39.2623	17
MOZ1-DR10-05 64			*14.4*		0.512198	4	-8.6	18.9693	6	15.7104	5	39.1860	21
MOZ1-DR10-05 70			*15.6*		0.512199	6	-8.6	19.0733	5	15.7220	4	39.2819	12
MOZ1-DR17-01 Hall Bank													
MOZ1-DR17-01 S*	8.6	-	0.0	-	0.512158	6	-9.4	18.9233	5	15.7186	5	39.1200	16
MOZ1-DR17-01 2*	5.9	2.7	0.74	0.05	0.512173	4	-9.1	19.0302	5	15.7195	5	39.1957	16
MOZ1-DR17-01 5*	3.9	3.6	1.6	0.1	0.512142	4	-9.7	19.0676	6	15.7249	6	39.2479	22

MOZ1-DR17-01 8*	2.3	2.9	2.6	0.2	0.512193	4	-8.7	19.0550	6	15.7248	6	39.2899	17
MOZ1-DR17-01 11*	1.4	2.9	3.6	0.2	0.512203	4	-8.5	19.0064	7	15.7215	7	39.2681	21
MOZ1-DR17-01 15			*4.5*		0.512235	4	-7.9	18.9746	6	15.7149	6	39.2440	22
MOZ1-DR17-01 18			*5.1*		0.512237	4	-7.8	18.9688	6	15.7146	5	39.2449	16
MOZ1-DR17-01 21			*5.7*		0.512218	4	-8.2	19.0210	7	15.7242	6	39.2746	18
MOZ1-DR17-01 25			*6.5*		0.512201	4	-8.5	19.0761	5	15.7336	4	39.2900	13
MOZ1-DR17-01 27*	0.3	4.8	6.9	0.5	0.512209	4	-8.4	19.1063	5	15.7391	4	39.3131	13
MOZ1-DR17-01 32			*8.0*		0.512258	4	-7.4	19.0944	5	15.7404	5	39.3246	12
MOZ1-DR22-01 Europa													
MOZ1-DR22-01 S*	8.6	-	0.0	-	0.512202	4	-8.5	18.9064	3	15.7055	3	39.1119	20
MOZ1-DR22-01 1*	7.7	4.4	0.23	0.01	0.512208	4	-8.4	18.9567	7	15.7108	6	39.1511	17
MOZ1-DR22-01 4*	4.7	3.0	1.24	0.07	0.512188	4	-8.8	19.0100	6	15.7198	7	39.2154	25
MOZ1-DR22-01 7*	3.0	3.5	2.1	0.1	0.512208	4	-8.4	19.0251	5	15.7228	5	39.2619	13
MOZ1-DR22-01 11*	1.8	3.7	3.2	0.2	0.512210	4	-8.3	19.0107	6	15.7208	7	39.2730	19
MOZ1-DR22-01 15			*4.1*		0.512202	4	-8.5	19.0000	7	15.7208	7	39.2657	20
MOZ1-DR22-01 19			*5.0*		0.512216	4	-8.2	18.9772	4	15.7190	4	39.2478	24
MOZ1-DR22-01 22			*5.7*		0.512231	4	-7.9	18.9816	7	15.7169	7	39.2499	30
MOZ1-DR22-01 25			*6.4*		0.512212	8	-8.3	18.9534	5	15.7111	6	39.2884	12
MOZ1-DR22-01 28			*7.1*		0.512214	6	-8.3	18.9680	5	15.7189	5	39.2505	18
MOZ1-DR22-01 31*	0.2	4.3	7.8	0.6	0.512207	6	-8.4	19.0156	4	15.7248	5	39.2732	13
MOZ1-DR22-01 34			*8.5*		0.512198	6	-8.6	19.0033	5	15.7217	7	39.2350	22
MOZ1-DR22-01 39			*9.7*		0.512173	4	-9.1	19.1016	3	15.7372	6	39.2896	58
MOZ1-DR22-01 45			*11.1*		0.512166	4	-9.2	19.0006	6	15.7116	6	39.1703	16
DR84-0026 Paisley Mount													
DR84-0026 S*	9.6	-	0.0	-	0.512272	4	-7.1	18.8137	6	15.6747	6	39.0303	16
DR84-0026 3			*1.7*		0.512273	4	-7.1	18.8485	6	15.6906	6	39.1298	16
DR84-0026 6*	1.8	1.8	3.4	0.3	0.512284	4	-6.9	18.8448	6	15.6906	7	39.1545	22

DR84-0026 9			*4.8*		0.512267	4	-7.2	18.8201	4	15.6897	4	39.1577	15
DR84-0026 12*	0.4	2.1	6.2	0.5	0.512248	4	-7.6	18.8111	7	15.6903	8	39.1705	22
DR84-0026 16			*8.1*		0.512222	4	-8.1	18.7928	6	15.6873	5	39.1628	15
DR84-0026 20			*10.0*		0.512211	4	-8.3	18.8554	5	15.6990	5	39.2292	17
DR84-0026 23			*11.4*		0.512178	6	-9.0	18.9494	6	15.7134	6	39.2839	17
DR84-0026 34			*16.6*		0.512166	4	-9.2	18.9780	7	15.7209	7	39.3317	20
DR84-0026 37			*18.4*		0.512195	2	-8.6	18.9642	5	15.7171	6	39.3143	17
DR84-0026 40			*19.4*		0.512195	2	-8.6	18.9411	7	15.7114	7	39.2936	21
DR84-0026 44			*21.3*		0.512174	4	-9.1	18.9173	5	15.7036	5	39.2530	15
DR84-0026 49			*23.6*		0.512203	4	-8.5	18.8719	8	15.6917	7	39.1767	24
DR84-0026 54			*26.0*		0.512197	4	-8.6	18.8699	5	15.6883	5	39.1477	14
DR84-0026 58			*27.9*		0.512180	12	-8.9	18.9043	6	15.6923	6	39.1932	20
DR84-0026 62			*30.7*		0.512202	6	-8.5	18.9048	19	15.6910	12	39.2034	76

4.7. Discussion

4.7.1. Characterization of the εNd records

The first step in this discussion is to understand what the isotopic records of the four studied Fe-Mn crusts really reflect and if contaminations could impact the Nd isotope signature recorded on the Fe-Mn oxides.

4.7.1.1. Phosphatisation and detrital contaminations

A particular attention is given to the P results of the oldest layers which may suggest intense phosphatisation phenomena (Benites et al., 2020; Grau and Kudrass, 1991; Halbach et al., 1989; Hein et al., 1993; Josso et al., 2019; Koschinsky et al., 1996). However, the P abundances presented before do not indicate the presence of phosphatisation in our samples (P < 0.7 wt%) which are probably too young to have registered the major episode of phosphogenesis appeared near 38 Ma (Hein et al., 1993; Josso et al., 2019) since our oldest Fe-Mn crust is dated to the Oligocene (30.7 Ma; DR84-0026). A second such event was define afterwards (between 21 and 27 Ma), however only Equatorial Pacific deposits have recorded it (Hein et al., 1993).

Vernadite is the main mineral found in the mineralogical compositions of the Fe-Mn crusts, however, detrital phases are also present even if their abundances are minor. The figure 4.8 shows that there is no clear correlation between the elements (Al, K and Mg) commonly associated with these components and the Nd isotope signatures of the Fe-Mn crusts MOZ1-DR10-05, MOZ1-DR17-01 and MOZ1-DR22-01. However, a trend stands out for the sample DR84-0026, driven by the four most radiogenic points. A potential contamination was estimated using a calculation of mixing between (1) a geochemical composition of low radiogenic Zambezi sediment (εNd = -15.5; [Nd] = 38.3 ppm; [Al] = 12.3 ppm; Bayon et al. unpublished data) and (2) the geochemical composition of the highest radiogenic Fe-Mn layer of this study (DR84-0026 6; εNd = -6.9; [Nd] = 229 ppm; [Al] = 0.84 ppm).

The mixing curve and the point of calculations show higher Al abundances than the geochemical signature of the sample DR84-0026, but similar Nd isotope values. For an input of 50% of the Zambezi sediment composition in the mixing, the resulted Nd isotope value correspond to the Nd isotope values of the layer DR84-0026 16, however, this layer shows an Al content at least twice as low as the resulted Al abundance of the mixing (Figure 4.8). No correlation exists between the Fe-Mn crust composition and the results of the mixing calculation, indicating that the Fe-Mn oxides of the samples have not recorded the geochemical signature of detrital inputs and so, the reflected records of the Fe-Mn crusts only represent the geochemical compositions of the subjacent water masses.

Potential contaminations of the Pb isotope compositions will not be considered because of the high Pb contents in the Fe-Mn crusts (Christensen et al., 1997; Dubinin et al., 2018; Hein et al., 2010; Marino et al., 2018, 2017) and in particular in our samples, ranging from 1263 (DR84-0026 62) to 2368 (DR84-0026 3) ppm.

The following section will discuss the potential influence of climate-induced marine isotope stages and/or by the very low radiogenic composition of the African continent on the Nd isotope records of the water masses registered on the Fe-Mn crusts.

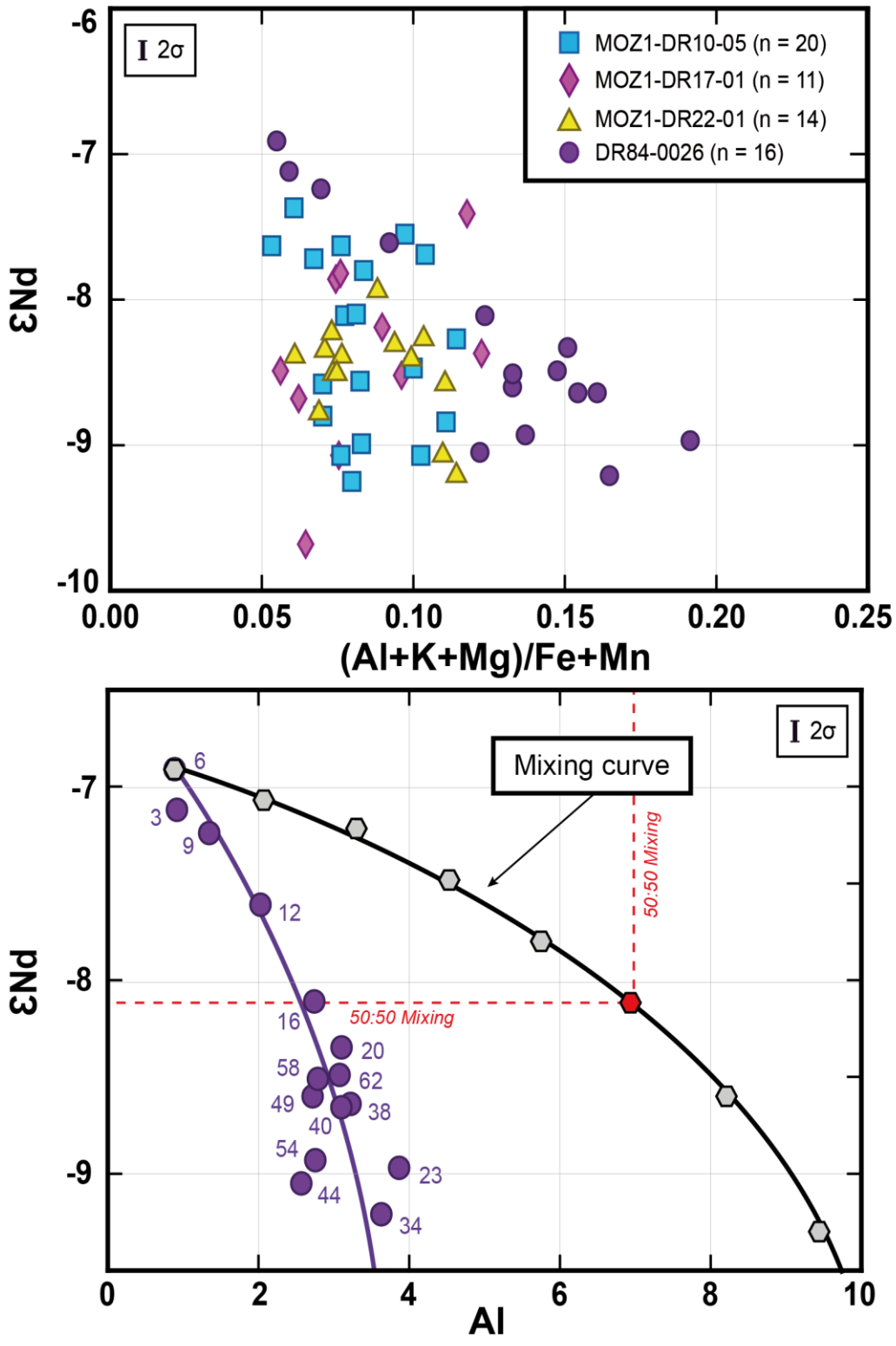

Figure 4.8. *The diagram on the top represents the Nd isotope signatures (εNd) vs. the sum of the major elements commonly associated with detrital components, normalised by Fe and Mn (due to the matrix of the Fe-Mn crusts). No correlation is visible expect for the sample DR84-0026. The diagram on the bottom illustrates a mixing calculation curve and highlights that the DR84-0026 composition shows too weak Al contents to be significantly impacted by a geochemical mixing with low radiogenic sediments containing high contents of Al.*

4.7.1.2. Impact of the glacial/interglacial cycles

Several studies have been carried out on the variations of the climatic and oceanic systems during the marine isotope stages using bulk sediments or Fe-Mn oxides (Bayon et al., 2002; Curry and Lohmann, 1982; Piotrowski et al., 2012, 2005, 2004; Rutberg et al., 2000). The geochemical compositions of the currents have been significantly modified, for example NADW have shown εNd variations of 2-3 units which would have varied the geochemical signature of the Indian deep currents (Rutberg et al., 2000).

The isotopic records measured in Fe-Mn crusts would therefore not represent the true signatures of oceanic water masses and it would be complicated to use them as archives of past oceanic circulations. However, the Fe-Mn crusts show very slow accumulation rates (from 1.77 to 4.89 in this work). Thus, the 100 µm-thick top layer incorporates a temporal resolution of 20 to 80 ka (Charles et al., 2020), while the deepest layers (between 0.5 and 2 mm thick) integrate an even longer time span from 150 to 550 ka. The isotopic compositions of Fe-Mn crusts therefore reflect condensed εNd records of these large cycles that had only minor integrated effects (Abouchami et al., 1997; Albarède and Goldstein, 1992).

4.7.1.3. Influence of the unradiogenic African margin

As explained in the section 4.3, the Mozambique Channel is located on the east of the Africa continent. Its margin presents a low radiogenic composition with Nd isotope values of εNd = -20 (Jeandel et al., 2007) corresponding of an average of distinct low radiogenic and high radiogenic Nd isotope sources. The Archean Kaapvaal craton shows εNd value of -24 (Grantham et al., 2011), the Zimbabwe craton is characterized by εNd compositions of -29 (Jelsma et al., 1996) and the results of the Mozambique Belt composition analyses show a εNd signature of -30 (Möller et al., 1998) (Figure 4.9). Conversely, the continent presents also younger sources such as the Jurassic Karoo volcanic formation (not represented on the figure 4.9), located in South Africa, with radiogenic εNd values between -9 and 0 (Grousset et al., 1992, Jourdan et al., 2007). Thanks to the dominant easterly winds, this can represent a major influence of low radiogenic εNd inputs from the river lithogenic sediments in the Mozambique Channel. The geochemistry of the regional water masses may be directly impacted due to these continental hydrological conditions (van der Lubbe et al., 2016). Moreover, it can have boundary exchange processes between particulate and dissolved fractions along the continental shelf (Rahlf et al., 2020; Rickli et al., 2010; van der Lubbe et al., 2016; Wilson et al., 2012).

As described by Roddaz et al. (2020), two main pathways of sediment inputs are responsible of the Mozambique Fan (MF) filling. Prior to the uplift of the EARS during the Eocene-Oligocene, the MF may have been fed by terrigenous sediments from north of the channel thanks to the Congo river as it might have discharged into the Indian Ocean via the Rufiji Delta in Tanzania (Stankiewicz and de Wit, 2006). The sediments would then have reached the MF through the deep Serpa Pinto Valley (Figure 4.9). The Nd isotope compositions of these sediments is constrained by a mean value of εNd = -15.6 measured in the KZR-23 core and reported in Bayon et al. (2019). Since the Miocene, the sedimentary flux came mainly from the Zambezi River through the Zambezi Valley (Droz and Mougenot, 1987; Fierens, 2019; Walford et al., 2005). The Limpopo and Zambezi discharges present very low radiogenic signatures which have been

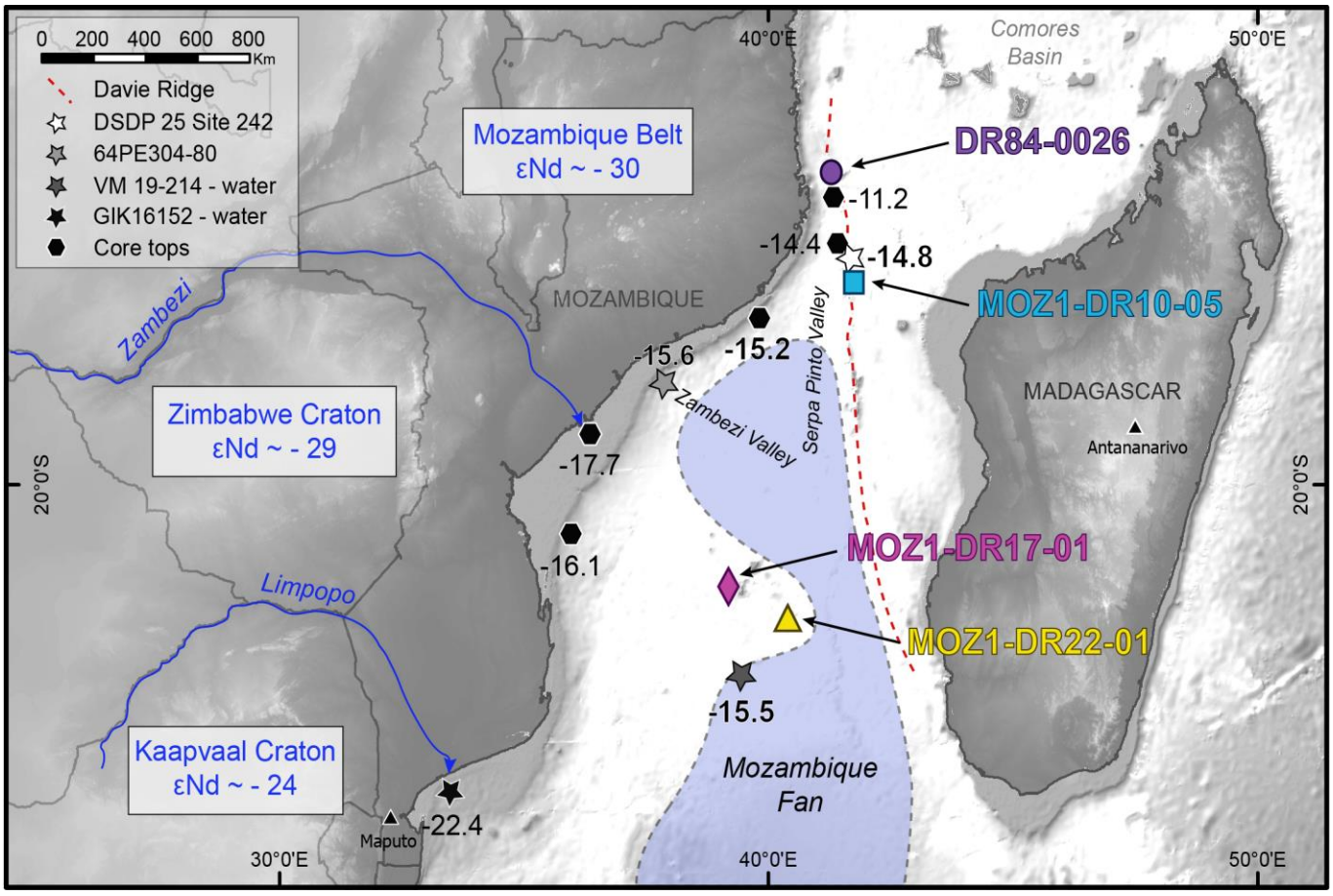

Figure 4.9. *Map of the Mozambique Channel (data from GEBCO and PAMELA cruises) showing the locations of the four Fe-Mn crusts of this study. In blue, Nd isotope signature (εNd) are presented for the main very low radiogenic formations surrounding the channel (De Waele et al., 2006; Grantham et al., 2011; Jelsma et al., 1996; Kröner et al., 2018; Möller et al., 1998; Paquette et al., 1994). The black pentagons correspond to the core tops analysed by van der Lubbe et al. (2016). The two darkest stars are surface water samples : VM 19-214 from Franzese et al. (2006) and GIK 16152 from Rahlf et al. (2020) whereas the two other stars correspond to the cores DSDP 25 Site 242 from Roddaz et al. (2020) and 64EP304-80 from van der Lubbe et al. (2016). The Mozambique Fan is represented by the blue area with dotted outline (Droz and Mougenot et al., 1987).*

studied and followed along the African continental margin through surface (<600 mbsl) waters (Franzese et al., 2006), core tops (van der Lubbe et al., 2016) and core stratigraphy, dating back as far as the Eocene (Roddaz et al., 2020; van der Lubbe et al., 2016). We present some results of these works on the figure 4.9. Concerning these cores, we only show the least radiogenic results measured until the Eocene in order to discuss the worst theory – with strongest low radiogenic εNd inputs.

Our study does not use sample from near surface waters but two Fe-Mn crusts from intermediate water masses between 800 and 1400 mbsl (MOZ1-DR10-05 and DR84-0026) have been investigated. These two samples are located on the northern part of the Davie Ridge (Figure 4.9), between the Zambezi river mouth and the Rufiji Delta. Considering the hypothesis of Congo loads until the Oligocene, the composition of the sample DR84-0026 (30.68 Ma) is expected to reflect the low radiogenic influence of this source (εNd = -

15.6; Bayon et al., 2019). The Fe-Mn crusts MOZ1-DR10-05 (15.62 Ma) is too recent to be considered in this hypothesis. The DR84-0026 εNd signature is relatively homogenous between the Oligocene and the Middle Miocene. None low radiogenic εNd inputs seem influence its composition. Moreover, this crust is located between near 800 mbsl which is not deep enough to be impacted by the deep currents transporting the low radiogenic loads to the Serpa Pinto Valley but mostly by the radiogenic RSW (constant in time). Then, if we consider gradual southwards boundary exchange, it would involve a progressive change of εNd signatures in the both Fe-Mn crusts. If the RSW acquires low radiogenic composition during its spreading along the African continental margin as suggested by Wilson et al. (2012), we expect to observe different trends between the DR84-0026 and MOZ1-DR10-05 Nd isotope signatures. However, the data of these two samples show a same increasing trend to more radiogenic values through time until εNd = -7.1 (DR84-0026) and εNd = -7.8 (MOZ1-DR10-05) which is not congruent with the Nd isotope data of the studied cores in this area either (Roddaz et al., 2020; van der Lubbe et al., 2016) (Figure 4.9). Their modern εNd data have also been discussed in Charles et al. (2020). None of our observations are consistent with a low radiogenic boundary exchange influence hypothesis.

This study also present a Fe-Mn crust from a transition zone between intermediate and deep water masses (Charles et al., 2020) which corresponds to the sample MOZ1-DR22-01 (1400-1550 mbsl), and a deeper Fe-Mn crust MOZ1-DR17-01 (1700-1900). Both of them are located between the Limpopo and Zambezi river mouths (Figure 4.9). If we consider here the hypothesis of these rivers induced low radiogenic inputs ($-22.4 < \varepsilon Nd < -15.2$; Rahlf et al., 2020; van der Lubbe et al., 2016), probably by way of the MF, it would involve a low radiogenic εNd composition of these Fe-Mn crusts since their formations. However, the MOZ1-DR22-01 signature rises to radiogenic values (Figure 4.7).

On the contrary, sample MOZ1-DR17-01 shows increasingly less radiogenic values since its formation (8.0 Ma). Being located deeper and under the NADW influence we can apply a simple boundary exchange between the African continental margin (mean εNd = -20; Jeandel et al., 2007), the NADW flowing northward in the channel with a signature of εNd = -11 constant in time; Rahlf et al., 2020) and a boundary exchange rate of 28%, calculated by Wilson et al. (2012) and presented in a previous study (Charles et al., 2020). It results Nd isotope composition of εNd = -13.5 in the south of Africa. If the interaction is continuous along the very low radiogenic margin, our results would present Nd isotope data considerably lower than εNd = -13.5.

However, none of these two samples, in particularly MOZ1-DR17-01, show Nd isotope values lower than εNd = -9.7 and any linear trend from low radiogenic to more radiogenic Nd isotope compositions is visible in the four studied Fe-Mn crusts within the latitudinal range (Figure 4.10). It would be the same observation in the context of low radiogenic Nd inputs from pore waters (Abbott, 2019; Abbott et al., 2015; Haley et al., 2017; Haley and Klinkhammer, 2003; Schacht et al., 2010).

Finally, the results are consistent with previous studies, which are focused on the conservative water mass mixing process in the same geographic area on Fe-Mn crusts (Albarède et al., 1997; Frank et al., 2002) and in seawater (Bertram and Elderfield, 1993) through time. Although a slight contribution of the low radiogenic inputs from the African margin cannot be completely dismissed, the results presented in this work mainly reflect the conservative water mass mixing process. The following sections will

therefore discuss the important Nd and Pb isotope variations recorded in our four samples since the middle Miocene which only correspond to water masses record changes.

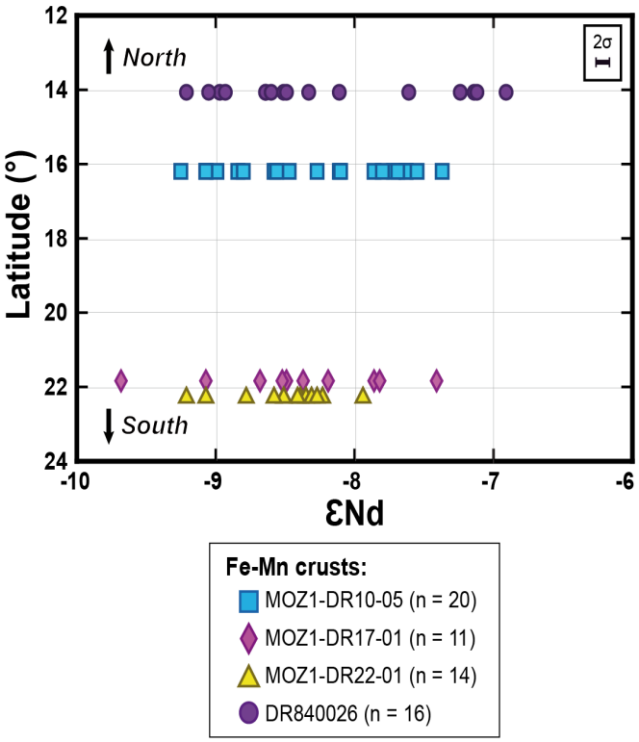

Figure 4.10. *Latitude (data from PAMELA cruises) vs. Nd isotope signatures (εNd) of all the layers of the four studied Fe-Mn crusts showing there is no linear correlation from low radiogenic values in the south (e.g. MOZ1-DR17-01) to more radiogenic values in the north of the Mozambique Channel (e.g. DR84-0026).*

4.7.2. Interpretation of the εNd records

The aim of this section is to understand the reason of the major Nd and Pb isotope variations in the studied time series during the four periods identified in the section 4.6.3 (30.6 to 11.1-11.7; 11.1-11.7 to 5.7-3.4 Ma; 5.1 to 1.6 Ma and 1.6 to 0 Ma) and illustrated in the figure 4.11. This approach implies to consider the water column in three dimensions (3D), with the NADW showing core near 2500 mbsl, and the AAIW with a core at 1150 mbsl, arriving from the south of the Mozambique Channel (Fine, 1993). In the northern part of the study area, the NIDW is found in deepest depths with a core at 2500 mbsl, and the RSW in the intermediate waters with a core at 1100 mbsl and the surface waters (< 800 mbsl) (Beal et al., 2000). Water masses with relatively similar depths can thus mix, depending on their pathways, the latitude, and the topographic barriers of the channel (i.e., Davie ridge). A particular attention should be paid to the depths and locations of the four sampled Fe-Mn crusts at the time of dredging (Figure 4.1; Table 4.1).

4.7.2.1. Physical-chemical changes of the water masses

The first hypothesis of such record variations is that the geochemical compositions and the intensity of the recorded water masses have changed over time. This hypothesis involves assessing whether major paleogeographic events have influenced chemical and physical conditions of water masses during the past 30 Ma, due to the resulted global climatic changes. Here we are going to debate the impact of the opening and closing of oceanic gateways such as the Isthmus of Panama (Burton et al., 1997; O'Nions et al., 1998) and variations in input rates of detrital material to the ocean (Abouchami et al., 1997; Frank and O'Nions, 1998; Ling et al., 1997).

Tasman strait and Drake passage. The northward displacement of Australia starts in the Early Eocene (~53 Ma) and was responsible for the entire opening of the Tasman Strait in the Late Eocene (~33.5 Ma) (Kennett, 1986; Pfuhl and McCave, 2005; Stickley et al., 2004). The complete establishment of the Drake Passage, between South America and Antarctica, was estimated around 37 Ma (Lawver and Gahagan, 2003; Scher and Martin, 2004). Both of these

events thus permit the pathway of the modern Antarctic Circumpolar Current system (ACC) during the Late Eocene (Scher and Martin, 2006), which significantly impacted the Southern Ocean structure and composition (Katz et al., 2011; Sijp and England, 2004). However, the Fe-Mn crust DR84-0026 was formed from the Oligocene (30.6 Ma), after the establishment of the ACC and thus could not record potential geochemical changes between before and after this major paleoceanographic event. In addition, during the first period (P1), this sample shows no significant change in the Nd isotope signature but only in the Pb proxy which mainly reflects local changes and so, may be linked to another explanation (Figure 4.11).

High intensity of Himalayan weathering. The second hypothesis of the Pb isotope variations recorded in the Fe-Mn crust during the P1 consists in Himalayan detrital inputs in the Indian Ocean since the Early Miocene. Indeed, a high intensity of Himalayan weathering was registered since the Oligocene (24 Ma) with a maximum erosion rate between 20 and 14 Ma (Searle, 1996). The gneisses of the Indian Shield composed of the Tethys Himalaya Belt and High Himalaya Belt have been investigated, and show high radiogenic values of the ratios $^{206}Pb/^{204}Pb$, from 18.70 to 20.23, and $^{207}Pb/^{204}Pb$, from 15.73 to 15.97 (Gariépy et al., 1985). The peaks observed in the sample DR84-0026 for the ratios $^{206,207,208}Pb/^{204}Pb$ during the P1 could quite easily record this Indian Shield signature carried by Indian oceanic currents. Moreover; the Nd isotope composition of this crust shows values between -8.5 and -9.2 (Figure 4.7, Table 4.3).

These data seem to be too low radiogenic to reflect the Indian Ocean waters as we know them today. The possible interpretation is that the low radiogenic sediments of the Bengal Fan, included the High Himalayan Crystalline of paragneisses and granites (εNd = -16) could have influence the Nd isotope composition of the Indian Ocean (Derry and France-Lanord, 1996).

However, it appears curious that the isotopic signatures of our sample differ from those of the Indian Ocean, in particular for the Fe-Mn crusts SS663 dated from the Oligocene (~ 25 Ma) (Figure 4.11) (Frank and O'Nions, 1998; O'Nions et al., 1998). The Fe-Mn crust SS663 shows an important peak of $^{208}Pb/^{206}Pb$ around 14 Ma, which does not correspond to the peak of the sample DR84-0026 recorded near 24 Ma, and does not present peak on the ratios $^{206,207,208}Pb/^{204}Pb$ whereas those of the Fe-Mn DR84-0026 crust are significant. These differences could easily be clarified by the ocean flows. Our respective samples do not come from the same area in the Indian Ocean domain, nor from the same depth. They are therefore not subject to the same currents.

The Fe-Mn crust SS663 was dredged in the central Indian Basin at more than 5000 mbsl and under the influence of the bottom current, such as the Indian Ocean Bottom Water (IOBW) transporting, in particular, Pacific geochemical records (O'Nions et al., 1998). The sample DR84-0026 studied here comes from the Paisley Mount, north of the Mozambique Channel, and was located at only 800-810 mbsl, which coincides with the onset of the Indian intermediate waters (Figure 4.1, Figure 4.2). Moreover, due to the EARS activity, different magmatic pulses have appeared in the north of the Mozambique Channel during the Oligocene (Chorowicz, 2005; Courgeon et al., 2017; Franke et al., 2015; Leroux et al., 2020; Macgregor, 2015). The Fe-Mn crust DR84-0026 may have been affected by important depth variations and thus water mass changes, whereas SS663 has only subsided by about 600 m in the past 30 Ma (Banakar and Hein, 2000) not allowing it to shift between different water masses. Thus, whereas the Pb isotope

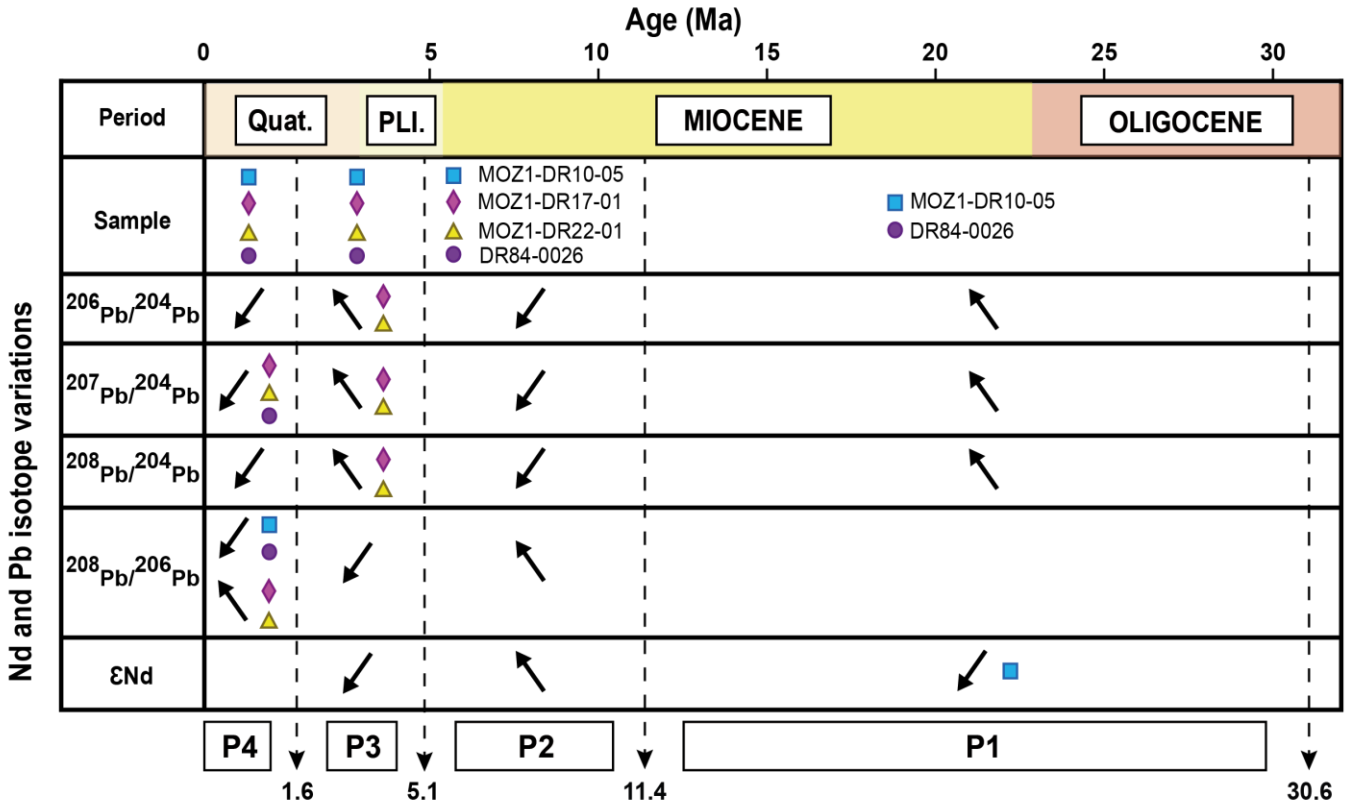

Figure 4.11. *Periods of main Nd and Pb isotope variations identified in the four time series. The arrows represent the increases (more radiogenic) and decreases (less radiogenic) in compositions. P1 is from 30.6 to 11.4 Ma; P2 from 11.4 to 5.1; P3 from 5.1 to 1.6 and P4 from 1.6 to modern time. Recent changes (P4 and P3) show more decoupled variations in the records of the four Fe-Mn crusts whereas old changes (P2, P1) are homogenous in the four samples.*

compositions recorded in the sample DR84-0026 during the P1 could correspond to the Indian Shield signature from the Himalayan weathering, it is possible that the Pb was not transported in the same way by all the water masses of the water column (due to their depths and circulation pathways) unlike the Nd which mixes much better in all regions. Thus, there may be disparities between Nd and Pb records from one sample to another.

Tethys seaway closure. Tethys Ocean have dominated the oceanic circulation until the Eocene, with an important transport of the deep, warm and saline water masses (Tethyan Indian Saline Water, TISW) from the Tethys and the Northern Indian Ocean to the Southern Ocean (Flower and Kennett, 1995, 1994; Karami et al., 2009; Ramsay et al., 1998; Woodruff and Savin, 1989) with surface waters from the Indian Ocean to the Atlantic Ocean (de la Vara et al., 2016; Hamon et al., 2013).

Since the Late Cretaceous, the intense northward displacement of the African and Indian plates have led the closure of the Tethys Basin until the Miocene (~14 Ma) (Cao et al., 2017; Cornacchia et al., 2021; Kocsis et al., 2008; Segev et al., 2017) with drastic reduction of the exchanges from around 20 Ma limited at the surface waters (Bialik et al., 2019). The Nd isotope signature of Mediterranean waters was more radiogenic and the Pb isotope composition was less radiogenic than today, due to the important volcanic contributions from Arabia and Central Mediterranean (Carminati et al., 2010; Kocsis et

al., 2008; Lustrino et al., 2011, 2009; Segev et al., 2017). Only the Fe-Mn crusts MOZ1-DR10-05 and DR84-0026 could have registered the closure of the Tethys seaway because of their ages (15.6 and 30.7 Ma, respectively). Both of these Fe-Mn crusts are located in the north of the Davie Ridge which was mostly emerged from the Eocene (~ 45 Ma) to the Oligocene (~ 26 Ma) (Bassias, 1992; Ponte, 2018). The samples were subject to surface waters flowing from the Indian Ocean to the Tethys Basin. Thus, the records before 26 Ma cannot be reflect the Tethys influence.

Since the Early Miocene (~ 23 Ma) a large-scale subsidence occurred in the Mozambique Channel (Courgeon et al., 2017, 2016; Leroux et al., 2020) and the Davie Ridge was underwater (Ponte, 2018). Due to their deeper localisations, the two Fe-Mn may have been influenced by the deep waters from the Tethys Ocean and may have recorded their reduction in the channel (Bialik et al., 2019). This could explain the significant increase of the $^{206,207,208}Pb/^{204}Pb$ ratios of the sample DR84-0026 starting at around 23 Ma until 14 Ma, at the complete closure of the Tethys seaway, even if its Nd isotope signature is more complex to explain. This hypothesis is supported by the first isotopic value of the sample MOZ1-DR10-05 showing also high radiogenic $^{206,207,208}Pb/^{204}Pb$ ratios which could correspond to the lowest influence of the Tethys waters (less radiogenic) in the Mozambique Channel at 15.6 Ma.

Indonesian seaway closure. The closure of the Indonesian seaway was a significant paleogeographic event during the end of P1 to P2. The water exchanges between the Pacific and the Indian oceans became progressively restricted for deep water circulation as early as the Middle Miocene (~ 18 to 14 Ma) because of the establishment of the modern Indonesian Island Arcs and the continuous movement of the Australian Plate (Kennett, 1985; Linthout et al., 1997; Nishimura and Suparka, 1997). However, the flows of the intermediate and surface waters continued until at least 12 Ma (Kennett, 1985), and probably until 4 Ma when the South Equatorial Current (SEC) stopped crossing the Indonesian Seaway (Cane and Molnar, 2001; Lee and Lawver, 1995; Nishimura and Suparka, 1997).

This event has also had an important influence on the chemical compositions of water masses in the Indian Ocean and it could be the cause of the high Nd and Pb variations (more radiogenic εNd and $^{208}Pb/^{206}Pb$ values vs. less radiogenic $^{206,207,208}Pb/^{204}Pb$ data) recorded in the four Fe-Mn crusts from 11.4 to 5.1 Ma. However, it has been shown by Frank et al. (2006) that the Pb isotope composition of their studied crust DODO 232D, located in the eastern equatorial Indian Ocean at 4119 mbsl, reflects more the impact of the Himalayan weathering products than the geochemical influence of the development Indonesian Island Arcs, and is the same observation for the sample SS663 located in the central Indian Basin (Frank and O'Nions, 1998; O'Nions et al., 1998). Their Nd isotope signatures are controlled by the high radiogenic Indian Ocean deep waters derived from the low radiogenic Southern Ocean waters arriving from the south along the continental margins. The location of our samples in the Mozambique Channel, even further west than the central Indian Ocean Basin to the Indonesian Island Arcs, does not seem to allow any impact of their low radiogenic Pb isotope signatures.

NADW export during the Miocene. Concerning the Nd isotope compositions of our four Fe-Mn crusts during the Miocene (P2), they increase to more and more radiogenic values (Figure 4.11). However, interpretations of Nd isotope time series from the Atlantic Ocean suggest a continuous export of the Northern Component Water (NCW) as early as 14 Ma (Frank et al.,

2002) and more recent works showed evidence for an even earlier beginning of the NCW export in the Early Oligocene (Batenburg et al., 2018; Katz et al., 2011; Scher and Martin, 2008b; Via and Thomas, 2006). With this emergence of the NCW, which evolved rapidly to its current NADW, in the southern hemisphere, the samples are expected to record water mass compositions that tend towards low radiogenic εNd data and more radiogenic $^{206,207,208}Pb/^{204}Pb$ ratios. This is not the case in our records (Figure 4.7; Table 4.3). So, this paleoceanographic change cannot explain the large variations, especially increasing Nd isotope trends towards high radiogenic values, of the Fe-Mn crusts during the P2 either.

Panama isthmus closure. The most recent tectonic event involving a major geographic change was the closure of the Central American Seaway (CAS) between the North and the South America. This uplift have been progressive from the Miocene (~ 8 Ma) to the Pliocene (~ 4 Ma) (Burton et al., 1997; Collins et al., 1996; Duque-Caro, 1990; Lunt et al., 2008) corresponding to the end of the P2 to the P3 phases (Figure 4.11). The direct consequence of such a geographic reorganisation was a restriction of the equatorial Pacific and Atlantic water exchanges (Keigwin, 1982) and thus, a more intense NADW flux in the Southern Ocean (Bell et al., 2015; Burton et al., 1997). Between 8 and 5 Ma, the signals recorded in our studied Fe-Mn crusts have continued to increase towards high radiogenic Nd values and to decrease towards low radiogenic Pb data (Figure 4.7).

Like the previous paragraph concerning the emergence of the NCW, this is contradictory to what is expected, based on the significant NADW influx in the South hemisphere. Since around 5 Ma, the Nd isotope compositions have declined for the Fe-Mn crusts MOZ1-DR10-05, MOZ1-DR17-01 and MOZ1-DR22-01. However, the increasing of the NADW (1500-3500 mbsl) input is not retained because these samples are from two different water masses (1000-1400; 1700-1900 and 1400-1550 mbsl, respectively; Table 4.1) which would not allow them to record the same water mass composition. This could have been the case if the NADW was thicker than it is now (i.e. minimum between 1000 and 1900 mbsl) but no study has demonstrated this physical change.

Northern hemisphere glaciation. The last major change discussed here concern the Northern Hemisphere Glaciation (NHG) registered from 2.7 Ma (P3 and P4 periods) and at the origin of two an expansion of a large discharge of detrital materials from the Canadian Shield to the Labrador Basin (Blaser et al., 2020; Lacan and Jeandel, 2005; Lambelet et al., 2016; Reynolds et al., 1999; von Blanckenburg and Nägler, 2001; von Blanckenburg and O'Nions, 1999). The deep Labrador Sea Water ($-14 > \varepsilon Nd > -18$) thus fed the north-western Atlantic basin with very low radiogenic Nd and high radiogenic Pb compositions.

Several studies on Fe-Mn crust time series have observed this chemical NADW change in the Atlantic (Abouchami et al., 1998; Burton et al., 1997) illustrated in the figure 4.7, in the Pacific (Abouchami et al., 1997; Christensen et al., 1997; Ling et al., 1997) and in the Indian (Frank and O'Nions, 1998) Oceans but also in the Southern Ocean from the Nd, Pb and Sr analyses of Fe-Mn micronodules, foraminifera and sediments (Winter et al., 1997).

The second consequence of the NHG is a reduced NADW export to the ACC (Bergh et al., 2021; Boyle and Keigwin, 1987, 1982; Charles and Fairbanks, 1992; Frank et al., 2002). The Fe-Mn crust MOZ1-DR17-01 located in the deep waters is the most likely to have recorded these upheavals. But its signature shows a decline towards low radiogenic Nd isotope values, similar to the Fe-Mn crust records of the NW Atlantic

(Figure 4.7) and thus it is no consistent with the NADW regression in the South. The Pb isotope values are also not consistent since they decrease like the Nd values instead of increasing like the crusts ALV539 and BM 1969.05 (Figure 4.7). This hypothesis does not explain the isotopic variations observed since 3 Ma. Moreover, the isotopic variations in this study during the P2 and P1 phase cannot reflect the high-frequency glacial and interglacial cycles (around 50 to 100 ka) that have successively occurred since the NHG because of the time integrated of the Fe-Mn resolution (see the section 4.7.1.2).

4.7.2.2. Vertically movements of the Fe-Mn crusts

As previously seen, the variations and peaks of the Pb isotopes recorded during the P1 (from 30.6 to 11.1-11.7 Ma) period can be explained by significant inputs from two distinct sources: the intense erosion of the Himalaya to the central Indian Ocean and the arrival of the Tethys currents in the northern Mozambique Channel. However, the Nd and Pb isotopic signatures registered during the P2, P3 and P4 phases have not been clarified. A second hypothesis of such variations is that the Fe-Mn crusts vertically moved from different water masses over time. This hypothesis involves assessing whether regional paleogeodynamic changes have occurred during the past 12 Ma in order to vary the depth of the samples of this work.

The four Fe-Mn crusts studied here have been selected because of their depths. For reminder, MOZ1-DR10-05 comes from between 1000 and 1400 mbsl (intermediate waters), MOZ1-DR17-01 was dredged between 1700 and 1900 mbsl (deep waters), MOZ1-DR22-01 is from the transition zone (Charles et al., 2020) located between 1400 and 1550 and finally, DR84-0026 is the shallowest with a depth between 800 and 810 mbsl (transition between surface and intermediate waters) (Table 4.1). Their depths, located close to the water mass boundaries, is the most important parameter of these samples. It allows to understand whether the Fe-Mn crusts have changed of water masses over time.

Uplift phenomenon. In order to understand the origin of the general increase εNd towards higher values and $^{206,207,208}Pb/^{204}Pb$ ratios towards lower values during the P2, this section is going to model a paleogeographic reconstruction of the Mozambique Channel.

At around 12 Ma, the Fe-Mn crusts present low radiogenic Nd signals: -9.3 for MOZ1-DR10-05 at 11.7 Ma; -9.2 for MOZ1-DR22-01 at 11.1 Ma and -9.0 recorded in DR84-0026 at 11.4 Ma (Figure 4.7; Table 4.3). These compositions do not reflect the Indian Ocean Water (IOW) signatures ($-7.5 > \varepsilon Nd > -8.0$; O'Nions et al., 1998) but are clearly similar to the composition of the Atlantic contribution in the Mozambique Channel ($-8.8 > \varepsilon Nd > -9.5$) corresponding as 50-50 mixing between the past IOW and the past NADW ($-11.0 > \varepsilon Nd > -10.5$) from Abouchami et al. (1999) and O'Nions et al. (1998).

From 11.7 Ma, the Nd isotope values increase until they reach: -7.4 for MOZ1-DR10-05 at 4.2 Ma; -7.9 for MOZ1-DR22-01 at 5.7 Ma and -6.9 in DR84-0026 at 3.4 Ma (Figure 4.7; Table 4.3). At this time, the compositions do not correspond to the NADW but to Indian intermediate waters also called RSW in the Mozambique Channel (Bertram and Elderfield, 1993; Jeandel, 1993; Lacan et al., 2012). It is interesting to note that the $^{206,207,208}Pb/^{204}Pb$ ratios also vary and show the inverse trend, towards less radiogenic values (Figure 4.7; Table 4.3). The Pb isotope data before their decline correspond to the Pb composition of the NADW whereas the Pb isotope values between 5.1 and 3.4 Ma reflect the signature of the intermediate currents (Vlastélic et

al., 2001). Both of these observations mean that the three Fe-Mn crusts have changed of water masses over time from the NADW depth (1500-3500 mbsl) between 11.1 and 11.7 Ma to the RSW depth (800-1400 mbsl) around between 5.1 and 3.4 Ma.

The only possibility of such a change is that the samples have been raised at shallower depths due to a major geodynamic event like an uplift (Figure 4.12). This phenomenon must have been generalised in the Mozambique Channel since 11.7 Ma because the three Fe-Mn crusts, located at different places, show the same trends and slopes (Figure 4.7).

Considering this geodynamic movement, three hypothesis have been tested in order to propose amplitude range and elevation rate. In all cases: (1) the range of the sample past water depths and

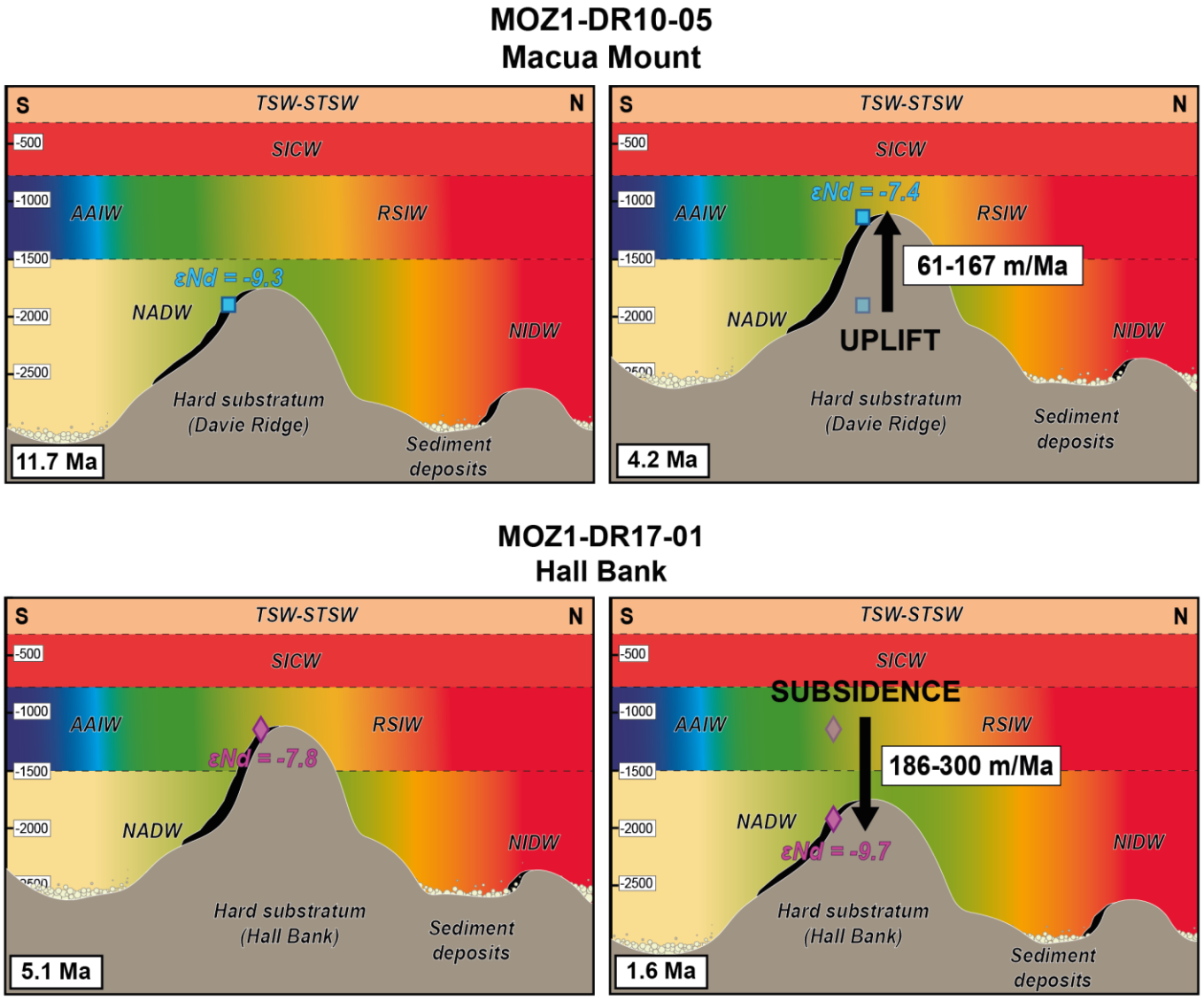

Figure 4.12. *Schematic propositions of the uplift event appeared between 11.1-11.7 and 5.7-3.4 Ma and the subsidence movement observed between 5.1 and 1.6 Ma in the Mozambique Channel. The figure is based on the examples of the sample MOZ1-DR10-05 (Macua Mount, north of the Davie Ridge) for the uplift demonstration and of the Fe-Mn crust MOZ1-DR17-01 (Hall Bank, south of the Davie Ridge) for the subsidence explanation. The colours of the water masses are identical to that on the* ***figure 4.2*** *corresponding to salinity values acquired from Conductivity Temperature Depth (CTD) profiles.*

their modern water depths after isotopic composition change as well as the time lapse between the two εNd, and (2) the bathymetric error between the starting and the ending points of dredge operations (e.g. DR10; 1000-1400 mbsl), have been considered.

The first hypothesis is based on estimated Fe-Mn crust depths issued from a linear correlation calculated between the εNd values of Fe-Mn crust surfaces and the depth of the samples from Charles et al. (2020).

The second hypothesis heeds the modern depth range of the samples (Charles et al., 2020) and the estimated depths, from the correlation, for the past depths.

The last hypothesis also considers the known modern bathymetry of the samples (Charles et al., 2020) and their estimated past depths. However, the modern depths have been re calculated integrating drowning events highlighted in the north (Glorieuses Islands, GR: 11 to 15 mm/Ma) and south (Hall Bank, GR: 29 to 39 mm/Ma) of the Mozambique Channel from (Courgeon, 2017). The results of the three hypothesis are visible on the Table 4.4.

The obtained data indicate that the Fe-Mn crusts vertically moved at least 325 m (second hypothesis; Europa Island, MOZ1-DR22-01) to a maximum of 1400 m (first hypothesis; Macua Mount, MOZ1-DR10-05). The uplift rates are relatively homogeneous in the Mozambique Channel and considering the three hypotheses. They vary from 53 m/Ma (second hypothesis; Europa Island, MOZ1-DR22-01) to 185 m/Ma (first hypothesis; Macua Mount, MOZ1-DR10-05). The values of the third hypothesis are intermediate between the values of the first one (maximum) and the second one (minimum). The second and the third hypothesis take into account the estimated bathymetry for the old unknown depths and the modern depths of the samples (Charles et al., 2020) between 5.7 and 3.4 Ma. However, carbonate platform drownings have been identified from this period (Courgeon et al., 2018) and may have impacted the depths of the samples. The third hypothesis adjust the modern depths of the Fe-Mn crusts according to the last subsidence event registered in the Mozambique Channel. That is why the results of the third hypothesis seem to be more accurate and will be used in the rest of this work. The hypothesis of a regional uplift and these calculations of movements are well supported by several studies. Previous studies have mentioned the existence of a land-bridge connecting African and Madagascar during the Cenozoic, which might explain how mammals may have crossed the Mozambique Channel to colonize Madagascar (McCall, 1997; Poux et al., 2005). Masters et al. (2021; 2006) recently combined geologic, oceanographic and biologic findings of the Mozambique Channel and finally confirmed the existence of a short-lived land bridge between African and Madagascar, between 12 and 5 Ma, which is also consistent with the presence of Miocene shallow-water carbonate platforms along the Davie Ridge at this time (Courgeon et al., 2018). This elevation could reflect different parts of the Davie Ridge, corresponding to the rise of the Fe-Mn crusts MOZ1-DR10-05 (between 465 and 1265 m) and DR84-0026 (between 960 and 1160 m) exposed above sea level. Partridge (1998) demonstrates a major uplift event between the Late Miocene and the Pliocene in the eastern part of the Africa subcontinent linked to the thermal activity of the EARS. The elevation of this uplift was estimated between 600 and 850 m, whose values are of the same order of magnitude as the results of this study. This Late Miocene doming was also identified more recently in the Mozambique Channel with sedimentology and tectonic evidences (Courgeon et al., 2017; Delaunay, 2018; Deville et al., 2018; Ponte, 2018). In addition, a study focused on the evolution of the

Table 4.4. *Amplitudes and vertical rate movements of the identified uplift (from 11.1-11.7 to 5.7-3.4 Ma) and subsidence (from 5.1 to 1.6 Ma) events in the Mozambique Channel. All the parameters are detailed in the text. [a]Mean modern depth (mbsl); [b]Estimated depth; [c]Drowning amplitude estimated from growth rates between 11 and 15 m/Ma in the north and between 29 and 39 m/Ma in the south of the channel (Courgeon 2017; Courgeon et al., 2018).*

Sample and details	MOZ1-DR10-05 Macua Mount 16◦12'S - 41◦38'E	MOZ1-DR17-01 Hall Bank 21◦50'S - 39◦10'E	MOZ1-DR22-01 Europa 21◦18'S - 40◦23'E	DR84-0026 Paisley Mount 14◦08'S - 41◦29'E
Modern depth range (mbsl)	1000-1400	1700-1900	1400-1550	810
Error (m)	400	200	150	100
		1st hypothesis		
Min ƐNd	-9.3	-9.7	-9.2	-9.0
Age (Ma)	11.7	1.6	11.1	11.4
Water mass	NADW	NADW	NADW	NADW
Estimated depth (mbsl)	2000	2200	1950	1800
Depth range (mbsl)	1800-2200	2100-2300	1875-2025	1750-1850
Max ƐNd	-7.4	-7.3	-7.9	-6.9
Age (Ma)	4.2	5.1	5.7	3.4
Water mass	RSW	RSW	RSW	RSW
Estimated depth (mbsl)	1000	950	1250	700
Depth range (mbsl)	800-1200	850-1050	1175-1325	650-750
Uplift max (m)	1400	-	850	1200
Uplift min (m)	600	-	550	1000
Subsi. max (m)	-	1450	-	-
Subsi. min (m)	-	1050	-	-
Rate max (m/Ma)	185	414	158	150
Rate min (m/Ma)	79	300	102	125
		2nd hypothesis		
Min ƐNd	-9.3	-9.7	-9.2	-9.0
Age (Ma)	11.7	1.6	11.1	11.4
Water mass	NADW	NADW	NADW	NADW
Estimated depth (mbsl)	2000	1800[a]	1950	1800
Depth range (mbsl)	1800-2200	1700-1900	1875-2025	1750-1850
Max ƐNd	-7.4	-7.3	-7.9	-6.9
Age (Ma)	4.2	5.1	5.7	3.4
Water mass	RSW	RSW	RSW	RSW
Mean modern depth (mbsl)	1200	950[b]	1475	805
Modern depth range (mbsl)	1000-1400	850-1050	1400-1550	755-855
Uplift max (m)	1200	-	625	1095
Uplift min (m)	400	-	325	895
Subsi. max (m)	-	1050	-	-
Subsi. min (m)	-	650	-	-
Rate max (m/Ma)	159	300	116	137
Rate min (m/Ma)	53	186	60	112

		3rd hypothesis		
Min ℇNd	-9.3	-9.7	-9.2	-9.0
Age (Ma)	11.7	1.6	11.1	11.4
Water mass	NADW	NADW	NADW	NADW
Estimated depth (mbsl)	2000	1800[a]	1950	1800
Depth range (mbsl)	1800-2200	1700-1900	1875-2025	1750-1850
Max ℇNd	-7.4	-7.3	-7.9	-6.9
Age (Ma)	4.2	5.1	5.7	3.4
Water mass	RSW	RSW	RSW	RSW
Mean modern depth (mbsl)	1200	950[b]	1475	805
Drowning (m)[c]	65		170	65
New modern depth (mbsl)	1135		1305	740
Modern depth range (mbsl)	935-1335	850-1050	1230-1380	690-790
Uplift max (m)	1265	-	795	1160
Uplift min (m)	465	-	495	960
Subsi. max (m)	-	1050	-	-
Subsi. min (m)	-	650	-	-
Rate max (m/Ma)	167	300	147	145
Rate min (m/Ma)	61	186	92	120

Glorieuses seamount in the northern part of the channel has also highlighted a significant Tortonian uplift phase of 425 m, dated around 9.5 and 8.9 Ma thanks to Sr isotopes and biostratigraphy coupled with stratigraphic interpretation of seismic profiles (Leroux et al., 2020). The uplift rate calculated in our study (between 61 to 167 m/Ma; Table 4.4) is completely consistent with the result presented by Leroux et al. (2020), pointing out that the uplift was generated overall the Mozambique Channel from the southern (Europa, Hall Bank) to the northern area (Davie Ridge, Glorieuses Islands).

Subsidence event. At 5.1 Ma, the Fe-Mn crust MOZ1-DR17-01 present high radiogenic Nd value of εNd = -7.8 (Figure 4.7; Table 4.3). This composition do not reflect the past NADW (-11.0 > εNd > -10.5) from Abouchami et al. (1999) and O'Nions et al. (1998) but is clearly close to the composition of the Indian Ocean Water (IOW) signatures (-7.5 > εNd > -8.0; O'Nions et al., 1998) and more precisely to the RSW in the Mozambique Channel (Bertram and Elderfield, 1993; Jeandel, 1993; Lacan et al., 2012).

From 5.1 Ma, its Nd isotope values decrease until reaching -9.4 at 0 Ma with a recorded minimum of -9.7 at 1.6 Ma (Figure 4.7; Table 4.3). At this time, the compositions do not correspond to the RSW but more likely to the NADW arriving in the channel from the south (Charles et al., 2020; Fine, 1993). Its $^{206,207,208}Pb/^{204}Pb$ ratios also vary and show trends towards more radiogenic values until around 1.6 Ma. Furthermore, the $^{206}Pb/^{204}Pb$ ratio is far from the trend of the NW Atlantic crusts (Figure 4.7).

Both of these observations mean that the Fe-Mn crust have shifted of water masses over time from the RSW depth (800-1400 mbsl) at 5.1 Ma to the NADW depth (1500-3500 mbsl) in the present-day. The most likely reason of such a change that this sample has been brought down at deeper depths due to a major geodynamic phenomenon like a subsidence between at least 5.1 and 1.6 Ma (Figure 4.12).

This event may not have been uniformly registered in the Mozambique Channel because the four Fe-Mn crusts do not show the same trends and slopes, for example the sample DR84-0026, in the north of the Davie Ridge, presents a homogenous composition since 3.4 Ma (Figure 4.7). The Fe-Mn crusts MOZ1-DR10-05, MOZ1-DR22-01 and DR84-0026 could be impacted by the subsidence, but their Nd isotope signatures do not reflect significant water mass changes. Moreover, it has been shown by Halbach and Puteanus (1984) that Mn/Fe ratio decrease during a subsidence from around 2 at the base and less than 1 at the top, related to increasing distance from the Oxygen Minimum Zone (OMZ). The Mn/Fe ratio of the sample MOZ1-DR17-01 drops from 1.4 to 0.9 between 5.1 and 1.6 Ma, whereas it is constant during this same period for the other Fe-Mn crusts.

Considering the local subsidence of the sample MOZ1-DR17-01, we propose amplitude range and decline rate calculations (Table 4.4). To do this, we assume first the range of the past depth sample and its depth after the major isotopic composition change, and secondly, the time lapse between the two εNd endmembers. Two of the hypothesis detailed before were applied.

The first one only considers estimated depths of the Fe-Mn crusts from linear correlation between Nd isotope values and water depths of the samples (Charles et al., 2020).

The second hypothesis is based on estimated depths and available modern depths (Charles et al., 2020).

The results indicate that the Fe-Mn crust MOZ1-DR17-01 collapsed at least 650 m to a maximum

of 1450 m with a subsidence rates estimated between 186 and 414 m/Ma (Table 4.4).

Previously presented, the geomorphologic work of Courgeon et al. (2017, 2016) have also identified abrupt shallow-water carbonate platforms subsidence during the Early Pliocene potentially linked to the EARS influence (Courgeon et al., 2018). These events have been recorded in the northern part of the Davie Ridge but also in the southern part of the channel, at the Hall Bank, where was dredged the sample MOZ1-DR17-01. For these two areas, Courgeon (2017) estimated subsidence amplitude of 221-317 m and 435-663 m, respectively, well supporting the results of the second hypothesis (between 650 and 1050 m). Similar observations were done at the Glorieuses area (Leroux et al., 2020). A strong subsidence phenomenon (500 m) was estimated from the Late Messinian with a movement rate evaluated around 100 m/Ma. The subsidence rate calculated in the second hypothesis (between 186 and 300 m/Ma; Figure 4.12; Table 4.4) is consistent with the result presented by Leroux et al. (2020) indicating that this subsidence event may have been more extensive than we thought. Concerning the Pb, the isotope compositions of the sample MOZ1-DR17-01 are decreased like the sample MOZ1-DR22-01 located near Europa, whereas the Fe-Mn crusts MOZ1-DR10-05 and DR84-0026 present more homogeneous composition except for the more recent values ($^{207,208}Pb/^{204}Pb$). The $^{208}Pb/^{206}Pb$ vs. age graphic presents a high correlation between these two samples and the sample SS663 from the centre of the Indian Ocean since around 7.5 Ma. At this period, Derry and France-Lanord (1996) identified a clear change of the Himalaya weathering regime from a physical erosion to one dominated by chemical weathering. This major change generates more inputs directly dissolved in the seawater, and potentially a higher diffusion of Pb in the oceans explicating the correlation between SS663, MOZ1-DR10-05 and DR84-0026 (Figure 4.7). This hypothesis indicate that these three Fe-Mn crusts are influenced by the same Pb source since around 7 Ma. Thus, we assume that Nd and Pb are not necessarily regulated by the same processes and sources, as previously seen before and demonstrated by previous studies (Frank et al., 2002, 1999).

4.8. Conclusion

This study presents new time series records for Pb and Nd isotope compositions of Fe-Mn crusts, recording major paleogeographic event (e.g. uplift, subsidence) in the Mozambique Channel, SW Indian Ocean, since the Oligocene. The high resolution geochemical investigation of four nonphosphatized Fe-Mn crusts permitted to highlight major variations, reflecting the shift of the samples from a water mass to another due to paleogeodynamic movements since the last 30 Ma, with a specific focus on the Middle Miocene to Pleistocene period. Neodymium and lead isotopic signatures show significant variations distributed in three main periods. The first period (Oligocene (30.7 Ma) to the Middle Miocene (11.7-11.1 Ma)) was mainly marked by the high influence of Pb contributions from the Himalaya and the Tethys sources in the northern water masses of the Mozambique Channel. During the second period (Middle Miocene (11.7-11.1 Ma) to Pliocene (5.7-3.4 Ma)), the increase of Nd isotope values to high radiogenic data and the decrease of Pb isotope ratios to low radiogenic signature is interpreted as the result of the rise of the four Fe-Mn crusts from NADW to RSW depths. This major change illustrates a generalised uplift in the channel from about 11.7-11.1 to 5.7-3.4 Ma. This geodynamic movement is characterized by a homogeneous elevation rate from 61 to 167 m/Ma. From Early Pliocene (5.1 Ma) to Pleistocene (1.6 Ma), a third period coincides with a subsidence (with a rate ranging from 186 to 300 m/Ma) mostly located in the

south of the channel due to decreasing Nd signatures to low radiogenic values and increasing Pb ratios to more radiogenic compositions until reflecting a transition from RSW to NADW depths. This supports and provides absolute dates for previous observations that uplift and subsidence have impacted considerably the geography of the channel from the Middle Miocene to the Pliocene (Courgeon et al., 2018, 2017, 2016; Leroux et al., 2020). Finally, our results represent high scientific interests for paleobiological reconstructions, but also and above all, for regional palaeoceanography studies. Indeed, this new paleogeographic reconstruction of the Mozambique Channel will make it possible to precisely trace the evolution of deep currents over time.

4.9. Acknowledgements

We thank the Captains, crews and onboard scientific teams of the PAMELA-MOZ01 survey onboard the R/V L'Atalante and, the MD39-Rida survey onboard the R/V Marion Dufresne. The oceanographic survey PAMELA-MOZ01, as well as Claire CHARLES PhD are co-funded by TOTAL and IFREMER as part of the PAMELA (Passive Margin Exploration Laboratories) scientific project. The PAMELA project is a scientific project led by Ifremer and TOTAL in collaboration with the Université de Bretagne Occidentale, Université Rennes 1, Université Pierre et Marie Curie, CNRS and IFPEN. The authors are grateful to Philippe FERNAGU and Thierry DALLE MULLE for their help, Coralie ANDREUCCI, Nouméa BOUTIN-PARADIS for assistance with the Be sample preparation and all the ASTER team, in particular Didier BOURLÈS, during our collaboration. The ASTER AMS national facility (CEREGE, Aix-en-Provence) is supported by INSU/CNRS, ANR through the EQUIPEX "ASTER-CEREGE" action, and IRD. We also thank the MNHN, Eva MORENO and Lola JOHANNES for allowing us to access and borrow sample from the MD39-Rida oceanographic expedition belonging to the oceanic collection.

4.10. Bibliographical references

Abbott, A.N., 2019. A benthic flux from calcareous sediments results in non-conservative neodymium behavior during lateral transport: A study from the Tasman Sea. Geology 47, 363–366. https://doi.org/10.1130/G45904.1

Abbott, A.N., Haley, B.A., McManus, J., Reimers, C.E., 2015. The sedimentary flux of dissolved rare earth elements to the ocean. Geochim. Cosmochim. Acta 154, 186–200. https://doi.org/10.1016/j.gca.2015.01.010

Abouchami, W., Galer, S.J.G., Koschinsky, A., 1999. Pb and Nd isotopes in NE Atlantic Fe–Mn crusts: Proxies for trace metal paleosources and paleocean circulation. Geochim. Cosmochim. Acta 63, 1489–1505. https://doi.org/10.1016/S0016-7037(99)00068-X

Abouchami, W., Goldstein, S.L., Gazer, S.J.G., Eisenhauer, A., Mangini, A., 1997. Secular changes of lead and neodymium in central Pacific seawater recorded by a Fe□Mn crust. Geochim. Cosmochim. Acta 61, 3957–3974. https://doi.org/10.1016/S0016-7037(97)00218-4

Albarède, F., Goldstein, S.L., 1992. World map of Nd isotopes in sea-floor ferromanganese deposits. Geology 20, 761–763. https://doi.org/10.1130/0091-7613(1992)020<0761:WMONII>2.3.CO;2

Albarède, F., Goldstein, S.L., Dautel, D., 1997. The neodymium isotopic composition of manganese nodules from the Southern and Indian oceans, the global oceanic neodymium budget, and their bearing on deep ocean circulation.

Geochim. Cosmochim. Acta 61, 1277–1291. https://doi.org/10.1016/S0016-7037(96)00404-8

Arsouze, T., Dutay, J.-C., Lacan, F., Jeandel, C., 2007. Modeling the neodymium isotopic composition with a global ocean circulation model. Chem. Geol. 239, 165–177. https://doi.org/10.1016/j.chemgeo.2006.12.006

Banakar, V.K., Hein, J.R., 2000. Growth response of a deep-water ferromanganese crust to evolution of the Neogene Indian Ocean. Mar. Geol. 162, 529–540. https://doi.org/10.1016/S0025-3227(99)00077-8

Bassias, Y., 1992. Petrological and geochemical investigation of rocks from the Davie fracture zone (Mozambique Channel) and some tectonic implications. J. Afr. Earth Sci. Middle East 15, 321–339. https://doi.org/10.1016/0899-5362(92)90018-8

Batenburg, S.J., Voigt, S., Friedrich, O., Osborne, A.H., Bornemann, A., Klein, T., Pérez-Díaz, L., Frank, M., 2018. Major intensification of Atlantic overturning circulation at the onset of Paleogene greenhouse warmth. Nat. Commun. 9, 4954. https://doi.org/10.1038/s41467-018-07457-7

Bau, M., 1996. Controls on the fractionation of isovalent trace elements in magmatic and aqueous systems: evidence from Y/Ho, Zr/Hf, and lanthanide tetrad effect. Contrib. Mineral. Petrol. 123, 323–333. https://doi.org/10.1007/s004100050159

Bayon, G., German, C.R., Boella, R.M., Milton, J.A., Taylor, R.N., Nesbitt, R.W., 2002. An improved method for extracting marine sediment fractions and its application to Sr and Nd isotopic analysis. Chem. Geol. 187, 179–199. https://doi.org/10.1016/S0009-2541(01)00416-8

Bayon, G., Schefuß, E., Dupont, L., Borges, A.V., Dennielou, B., Lambert, T., Mollenhauer, G., Monin, L., Ponzevera, E., Skonieczny, C., André, L., 2019. The roles of climate and human land-use in the late Holocene rainforest crisis of Central Africa. Earth Planet. Sci. Lett. 505, 30–41. https://doi.org/10.1016/j.epsl.2018.10.016

Beal, L.M., Ffield, A., Gordon, A.L., 2000. Spreading of Red Sea overflow waters in the Indian Ocean. J. Geophys. Res. Oceans 105, 8549–8564. https://doi.org/10.1029/1999JC900306

Bell, D.B., Jung, S.J.A., Kroon, D., Hodell, D.A., Lourens, L.J., Raymo, M.E., 2015. Atlantic Deep-water Response to the Early Pliocene Shoaling of the Central American Seaway. Sci. Rep. 5, 12252. https://doi.org/10.1038/srep12252

Benites, M., Hein, J.R., Mizell, K., Blackburn, T., Jovane, L., 2020. Genesis and Evolution of Ferromanganese Crusts from the Summit of Rio Grande Rise, Southwest Atlantic Ocean. Minerals 10, 349. https://doi.org/10.3390/min10040349

Bergh, E.W., von Koslowski, R., Compton, J.S., 2021. Variations in deep water masses along the western margin of South Africa, spanning the last two glacial terminations. Palaeogeogr. Palaeoclimatol. Palaeoecol. 562, 110148. https://doi.org/10.1016/j.palaeo.2020.110148

Bertram, C.J., Elderfield, H., 1993. The geochemical balance of the rare earth elements and neodymium isotopes in the oceans. Geochim. Cosmochim. Acta 57, 1957–1986. https://doi.org/10.1016/0016-7037(93)90087-D

Bialik, O.M., Frank, M., Betzler, C., Zammit, R., Waldmann, N.D., 2019. Two-step closure of the Miocene Indian Ocean Gateway to the Mediterranean. Sci. Rep. 9, 8842. https://doi.org/10.1038/s41598-019-45308-7

Blaser, P., Gutjahr, M., Pöppelmeier, F., Frank, M., Kaboth-Bahr, S., Lippold, J., 2020. Labrador Sea bottom water provenance and REE exchange during the past 35,000 years. Earth Planet. Sci. Lett. 542, 116299. https://doi.org/10.1016/j.epsl.2020.116299

Bonatti, E., Kraemer, T., and Rydell, H., 1972. Classification and genesis of submarine iron-manganese deposits. In: Ferromanganese deposits on the Ocean Floor, 149–161.

Bourlès, D., Raisbeck, G.M., Yiou, F., 1989. 10Be and 9Be in marine sediments and their potential for dating. Geochim. Cosmochim. Acta 53, 443–452. https://doi.org/10.1016/0016-7037(89)90395-5

Boyle, E.A., Keigwin, L., 1987. North Atlantic thermohaline circulation during the past 20,000 years linked to high-latitude surface temperature. Nature 330, 35–40. https://doi.org/10.1038/330035a0

Boyle, E.A., Keigwin, L.D., 1982. Deep Circulation of the North Atlantic over the Last 200,000 Years: Geochemical Evidence. Science 218, 784–787. https://doi.org/10.1126/science.218.4574.784

Burton, K.W., Ling, H.-F., O'Nions, R.K., 1997. Closure of the Central American Isthmus and its effect on deep-water formation in the North Atlantic. Nature 386, 382. https://doi.org/10.1038/386382a0

Cane, M.A., Molnar, P., 2001. Closing of the Indonesian seaway as a precursor to east African aridification around 3–4 million years ago. Nature 411, 157–162. https://doi.org/10.1038/35075500

Cao, W., Zahirovic, S., Flament, N., Williams, S., Golonka, J., Müller, R.D., 2017. Improving global paleogeography since the late Paleozoic using paleobiology. Biogeosciences 14, 5425–5439. https://doi.org/10.5194/bg-14-5425-2017

Carminati, E., Lustrino, M., Cuffaro, M., Doglioni, C., 2010. Tectonics, magmatism and geodynamics of Italy: What we know and what we imagine. J. Virtual Explor. 36. https://doi.org/10.3809/jvirtex.2010.00226

Charles, C., Barrat, J.-A., Pelleter, E., 2021. Trace Element Determinations in Fe-Mn Oxides by High Resolution ICP-MS after Tm Addition. Talanta 122446. https://doi.org/10.1016/j.talanta.2021.122446

Charles, C., Pelleter, E., Révillon, S., Nonnotte, P., Jorry, S.J., Kluska, J.-M., 2020. Intermediate and deep ocean current circulation in the Mozambique Channel: New insights from ferromanganese crust Nd isotopes. Mar. Geol. 430, 106356. https://doi.org/10.1016/j.margeo.2020.106356

Charles, C.D., Fairbanks, R.G., 1992. Evidence from Southern Ocean sediments for the effect of North Atlantic deep-water flux on climate. Nature 355, 416–419. https://doi.org/10.1038/355416a0

Chmeleff, J., von Blanckenburg, F., Kossert, K., Jakob, D., 2010. Determination of the 10Be half-life by multicollector ICP-MS and liquid scintillation counting. Nucl. Instrum. Methods Phys. Res. B 268, 192–199. https://doi.org/10.1016/j.nimb.2009.09.012

Chorowicz, J., 2005. The East African rift system. J. Afr. Earth Sci., Phanerozoic Evolution of Africa 43, 379–410. https://doi.org/10.1016/j.jafrearsci.2005.07.019

Christensen, J.N., Halliday, A.N., Godfrey, L.V., Hein, J.R., Rea, D.K., 1997. Climate and Ocean Dynamics and the Lead Isotopic Records in Pacific Ferromanganese Crusts. Science 277, 913–918. https://doi.org/10.1126/science.277.5328.913

Cochran, J.K., Bacon, M.P., Krishnaswami, S., Turekian, K.K., 1983. 210Po and210Pb distributions in the central and eastern Indian Ocean. Earth Planet. Sci. Lett. 65, 433–452. https://doi.org/10.1016/0012-821X(83)90180-2

Coffin, M.F., Rabinowitz, P.D., 1987. Reconstruction of Madagascar and Africa: Evidence from the Davie Fracture Zone and Western Somali Basin. J. Geophys. Res. Solid

Earth 92, 9385–9406. https://doi.org/10.1029/JB092iB09p09385

Collins, C., Hermes, J.C., Roman, R.E., Reason, C.J.C., 2016. First dedicated hydrographic survey of the Comoros Basin. J. Geophys. Res. Oceans 121, 1291–1305. https://doi.org/10.1002/2015JC011418

Collins, L.S., Coates, A.G., Berggren, W.A., Aubry, M.-P., Zhang, J., 1996. The late Miocene Panama isthmian strait. Geology 24, 687–690. https://doi.org/10.1130/0091-7613(1996)024<0687:TLMPIS>2.3.CO;2

Conrad, T., Hein, J.R., Paytan, A., Clague, D.A., 2017. Formation of Fe-Mn crusts within a continental margin environment. Ore Geol. Rev., SI:Marine mineral deposits: New resources for base, precious, and critical metals 87, 25–40. https://doi.org/10.1016/j.oregeorev.2016.09.010

Cornacchia, I., Brandano, M., Agostini, S., 2021. Miocene paleoceanographic evolution of the Mediterranean area and carbonate production changes: A review. Earth-Sci. Rev. 221, 103785. https://doi.org/10.1016/j.earscirev.2021.103785

Cotten, J., Le Dez, A., Bau, M., Caroff, M., Maury, R.C., Dulski, P., Fourcade, S., Bohn, M., Brousse, R., 1995. Origin of anomalous rare-earth element and yttrium enrichments in subaerially exposed basalts: Evidence from French Polynesia. Chem. Geol. 119, 115–138. https://doi.org/10.1016/0009-2541(94)00102-E

Courgeon, S., 2017. Cenozoic evolution of isolated carbonate platforms from the Mozambique Channel (SW Indian Ocean) : development and controls in active geodynamic settings (These de doctorat). Aix-Marseille.

Courgeon, S., Bachèlery, P., Jouet, G., Jorry, S.J., Bou, E., BouDagher-Fadel, M.K., Révillon, S., Camoin, G., Poli, E., 2018. The offshore east African rift system: new insights from the Sakalaves seamounts (Davie Ridge, SW Indian Ocean). Terra Nova 30, 380–388. https://doi.org/10.1111/ter.12353

Courgeon, S., Jorry, S.J., Camoin, G.F., BouDagher-Fadel, M.K., Jouet, G., Révillon, S., Bachèlery, P., Pelleter, E., Borgomano, J., Poli, E., Droxler, A.W., 2016. Growth and demise of Cenozoic isolated carbonate platforms: New insights from the Mozambique Channel seamounts (SW Indian Ocean). Mar. Geol. 380, 90–105. https://doi.org/10.1016/j.margeo.2016.07.006

Courgeon, S., Jorry, S.J., Jouet, G., Camoin, G., BouDagher-Fadel, M.K., Bachèlery, P., Caline, B., Boichard, R., Révillon, S., Thomas, Y., Thereau, E., Guérin, C., 2017. Impact of tectonic and volcanism on the Neogene evolution of isolated carbonate platforms (SW Indian Ocean). Sediment. Geol. 355, 114–131. https://doi.org/10.1016/j.sedgeo.2017.04.008

Craig, H., Krishnaswami, S., Somayajulu, B.L.K., 1973. 210Pb226Ra: Radioactive disequilibrium in the deep sea. Earth Planet. Sci. Lett. 17, 295–305. https://doi.org/10.1016/0012-821X(73)90194-5

Curry, W.B., Lohmann, G.P., 1982. Carbon Isotopic Changes in Benthic Foraminifera from the Western South Atlantic: Reconstruction of Glacial Abyssal Circulation Patterns. Quat. Res. 18, 218–235. https://doi.org/10.1016/0033-5894(82)90071-0

de la Vara, A., van Baak, C.G.C., Marzocchi, A., Grothe, A., Meijer, P.Th., 2016. Quantitative analysis of Paratethys sea level change during the Messinian Salinity Crisis. Mar. Geol. 379, 39–51. https://doi.org/10.1016/j.margeo.2016.05.002

De Waele, B., Liégeois, J.-P., Nemchin, A.A., Tembo, F., 2006. Isotopic and geochemical evidence of proterozoic episodic crustal reworking within the irumide belt of south-central Africa, the southern metacratonic boundary of an Archaean Bangweulu Craton. Precambrian Res.

148, 225–256. https://doi.org/10.1016/j.precamres.2006.05.006

Delaunay, A., 2018. Madagascar vertical movements (90 - 0 Ma): a double approach including onshore geomorphology and Madagascar western margins sedimentary record. https://doi.org/10.13140/RG.2.2.35631.69283

Déprez, A., Doubre, C., Masson, F., Ulrich, P., 2013. Seismic and aseismic deformation along the East African Rift System from a reanalysis of the GPS velocity field of Africa. Geophys. J. Int. 193, 1353–1369. https://doi.org/10.1093/gji/ggt085

Derry, L.A., France-Lanord, C., 1996. Neogene Himalayan weathering history and river87Sr86Sr: impact on the marine Sr record. Earth Planet. Sci. Lett. 142, 59–74. https://doi.org/10.1016/0012-821X(96)00091-X

Deville, E., Marsset, T., Courgeon, S., Jatiault, R., Ponte, J.-P., Thereau, E., Jouet, G., Jorry, S.J., Droz, L., 2018. Active fault system across the oceanic lithosphere of the Mozambique Channel: Implications for the Nubia–Somalia southern plate boundary. Earth Planet. Sci. Lett. 502, 210–220. https://doi.org/10.1016/j.epsl.2018.08.052

DiMarco, S.F., Chapman, P., Nowlin, W.D., Hacker, P., Donohue, K., Luther, M., Johnson, G.C., Toole, J., 2002. Volume transport and property distributions of the Mozambique Channel. Deep Sea Res. Part II Top. Stud. Oceanogr. 49, 1481–1511. https://doi.org/10.1016/S0967-0645(01)00159-X

Droz, L., Mougenot, D., 1987. Mozambique Upper Fan: Origin of Depositional Units1. AAPG Bull. 71, 1355–1365. https://doi.org/10.1306/703C8079-1707-11D7-8645000102C1865D

Dubinin, A.V., Rimskaya-Korsakova, M.N., Berezhnaya, E.D., Uspenskaya, T.Yu., Dara, O.M., 2018. Ferromanganese Crusts in the South Atlantic Ocean: Compositional Evolution and Specific Features of Ore Formation. Geochem. Int. 56, 1093–1108. https://doi.org/10.1134/S0016702918110034

Duque-Caro, H., 1990. Neogene stratigraphy, paleoceanography and paleobiogeography in northwest South America and the evolution of the Panama seaway. Palaeogeogr. Palaeoclimatol. Palaeoecol., Pacific Neogene event stratigraphy and paleoceanographic history 77, 203–234. https://doi.org/10.1016/0031-0182(90)90178-A

Echegoyen, Y., Boyle, E.A., Lee, J.-M., Gamo, T., Obata, H., Norisuye, K., 2014. Recent distribution of lead in the Indian Ocean reflects the impact of regional emissions. Proc. Natl. Acad. Sci. 111, 15328–15331. https://doi.org/10.1073/pnas.1417370111

Elderfield, H., Hawkesworth, C.J., Greaves, M.J., Calvert, S.E., 1981. Rare earth element geochemistry of oceanic ferromanganese nodules and associated sediments. Geochim. Cosmochim. Acta 45, 513–528. https://doi.org/10.1016/0016-7037(81)90184-8

Feuillet, N., Jorry, S., Crawford, W.C., Deplus, C., Thinon, I., Jacques, E., Saurel, J.M., Lemoine, A., Paquet, F., Satriano, C., Aiken, C., Foix, O., Kowalski, P., Laurent, A., Rinnert, E., Cathalot, C., Donval, J.-P., Guyader, V., Gaillot, A., Scalabrin, C., Moreira, M., Peltier, A., Beauducel, F., Grandin, R., Ballu, V., Daniel, R., Pelleau, P., Gomez, J., Besançon, S., Geli, L., Bernard, P., Bachelery, P., Fouquet, Y., Bertil, D., Lemarchand, A., Van der Woerd, J., 2021. Birth of a large volcanic edifice offshore Mayotte via lithosphere-scale dyke intrusion. Nat. Geosci. 14, 787–795. https://doi.org/10.1038/s41561-021-00809-x

Fierens, R., 2019. The Oligocene to Quaternary Zambezi Depositional System (Mozambique Channel, Southwest Indan Ocean) : architecture, sedimentation and forcing factors (phd thesis). Université de Bretagne occidentale - Brest.

Filippova, A., Frank, M., Kienast, M., Rickli, J., Hathorne, E., Yashayaev, I.M., Pahnke, K., 2017. Water mass circulation and weathering inputs in the Labrador Sea based on coupled Hf–Nd isotope compositions and rare earth element distributions. Geochim. Cosmochim. Acta 199, 164–184. https://doi.org/10.1016/j.gca.2016.11.024

Fine, R.A., 1993. Circulation of Antarctic intermediate water in the South Indian Ocean. Deep Sea Res. Part Oceanogr. Res. Pap. 40, 2021–2042. https://doi.org/10.1016/0967-0637(93)90043-3

Flegal, A.R., Maring, H., Niemeyer, S., 1993. Anthropogenic lead in Antarctic sea water. Nature 365, 242–244. https://doi.org/10.1038/365242a0

Flegal, A.R., Patterson, C.C., 1983. Vertical concentration profiles of lead in the Central Pacific at 15°N and 20°S. Earth Planet. Sci. Lett. 64, 19–32. https://doi.org/10.1016/0012-821X(83)90049-3

Flower, B.P., Kennett, J.P., 1995. Middle Miocene deepwater paleoceanography in the southwest Pacific: Relations with East Antarctic Ice Sheet development. Paleoceanography 10, 1095–1112. https://doi.org/10.1029/95PA02022

Flower, B.P., Kennett, J.P., 1994. The middle Miocene climatic transition: East Antarctic ice sheet development, deep ocean circulation and global carbon cycling. Palaeogeogr. Palaeoclimatol. Palaeoecol., Cenozoic Climate and Paleogeographic Changes in the Pacific Region 108, 537–555. https://doi.org/10.1016/0031-0182(94)90251-8

Frank, M., 2002. Radiogenic isotopes: tracers of past ocean circulation and erosional input. Rev. Geophys. 40, 1–1. https://doi.org/10.1029/2000RG000094

Frank, M., O'Nions, R.K., 1998. Sources of Pb for Indian Ocean ferromanganese crusts: a record of Himalayan erosion? Earth Planet. Sci. Lett. 158, 121–130. https://doi.org/10.1016/S0012-821X(98)00055-7

Frank, M., O'Nions, R.K., Hein, J.R., Banakar, V.K., 1999. 60 Myr records of major elements and Pb–Nd isotopes from hydrogenous ferromanganese crusts: reconstruction of seawater paleochemistry. Geochim. Cosmochim. Acta 63, 1689–1708. https://doi.org/10.1016/S0016-7037(99)00079-4

Frank, M., Whiteley, N., Kasten, S., Hein, J.R., O'Nions, K., 2002. North Atlantic Deep Water export to the Southern Ocean over the past 14 Myr: Evidence from Nd and Pb isotopes in ferromanganese crusts. Paleoceanography 17, 12-1-12–9. https://doi.org/10.1029/2000PA000606

Frank, M., Whiteley, N., van de Flierdt, T., Reynolds, B.C., O'Nions, K., 2006. Nd and Pb isotope evolution of deep water masses in the eastern Indian Ocean during the past 33 Myr. Chem. Geol., Special Issue in Honour of R.K. O'Nions 226, 264–279. https://doi.org/10.1016/j.chemgeo.2005.09.024

Franke, D., Jokat, W., Ladage, S., Stollhofen, H., Klimke, J., Lutz, R., Mahanjane, E.S., Ehrhardt, A., Schreckenberger, B., 2015. The offshore East African Rift System: Structural framework at the toe of a juvenile rift. Tectonics 34, 2086–2104. https://doi.org/10.1002/2015TC003922

Franzese, A.M., Hemming, S.R., Goldstein, S.L., Anderson, R.F., 2006. Reduced Agulhas Leakage during the Last Glacial Maximum inferred from an integrated provenance and flux study. Earth Planet. Sci. Lett. 250, 72–88. https://doi.org/10.1016/j.epsl.2006.07.002

Gaina, C., Torsvik, T.H., van Hinsbergen, D.J.J., Medvedev, S., Werner, S.C., Labails, C., 2013. The African Plate: A history of oceanic crust accretion and subduction since the Jurassic. Tectonophysics, Progress in understanding the South Atlantic margins 604, 4–25. https://doi.org/10.1016/j.tecto.2013.05.037

Gale, N.H., 1996. A new method for extracting and purifying lead from difficult matrices for isotopic analysis. Analytica Chimica Acta, 332, 15-21

Gariépy, C., Allègre, C.J., Rong Hua Xu, 1985. The Pb-isotope geochemistry of granitoids from the Himalaya-Tibet collision zone: implications for crustal evolution. Earth Planet. Sci. Lett. 74, 220–234. https://doi.org/10.1016/0012-821X(85)90023-8

Goldberg, E.D., Koide, M., Schmitt, R.A., Smith, R.H., 1963. Rare-Earth distributions in the marine environment. J. Geophys. Res. 1896-1977 68, 4209–4217. https://doi.org/10.1029/JZ068i014p04209

Goldstein, S.L., Hemming, S.R., 2003. 6.17 - Long-lived Isotopic Tracers in Oceanography, Paleoceanography, and Ice-sheet Dynamics, in: Holland, H.D., Turekian, K.K. (Eds.), Treatise on Geochemistry. Pergamon, Oxford, pp. 453–489. https://doi.org/10.1016/B0-08-043751-6/06179-X

Grantham, G.H., Manhica, A.D.S.T., Armstrong, R.A., Kruger, F.J., Loubser, M., 2011. New SHRIMP, Rb/Sr and Sm/Nd isotope and whole rock chemical data from central Mozambique and western Dronning Maud Land, Antarctica: Implications for the nature of the eastern margin of the Kalahari Craton and the amalgamation of Gondwana. J. Afr. Earth Sci. 59, 74–100. https://doi.org/10.1016/j.jafrearsci.2010.08.005

Grau, R., and Kudrass, H. R., 1991. Pre-eocene and younger manganese crusts from the manihiki plateau, southwest Pacific-Ocean. Marine Mining, 10(3), 231-246.

Grousset, F.E., Biscaye, P.E., Revel, M., Petit, J.-R., Pye, K., Joussaume, S., Jouzel, J., 1992. Antarctic (Dome C) ice-core dust at 18 k.y. B.P.: Isotopic constraints on origins. Earth Planet. Sci. Lett. 111, 175–182. https://doi.org/10.1016/0012-821X(92)90177-W

Guan, Y., Sun, X., Ren, Y., Jiang, X., 2017. Mineralogy, geochemistry and genesis of the polymetallic crusts and nodules from the South China Sea. Ore Geol. Rev. 89, 206–227. https://doi.org/10.1016/j.oregeorev.2017.06.020

Halbach, P., and Puteanus, D., 1989. Distribution of ferromanganese deposits. P. Halbach, G.

Haley, B.A., Du, J., Abbott, A.N., McManus, J., 2017. The Impact of Benthic Processes on Rare Earth Element and Neodymium Isotope Distributions in the Oceans. Front. Mar. Sci. 4. https://doi.org/10.3389/fmars.2017.00426

Haley, B.A., Klinkhammer, G.P., 2003. Complete separation of rare earth elements from small volume seawater samples by automated ion chromatography: method development and application to benthic flux. Mar. Chem. 82, 197–220. https://doi.org/10.1016/S0304-4203(03)00070-7

Hamon, N., Sépulchre, P., Lefebvre, V., Ramstein, G., 2013. The role of East-Tethys seaway closure in the middle Miocene climatic transition (ca. 14 Ma). Clim. Past 9, 2687–2702. https://doi.org/10.5194/cp-9-2687-2013

Harlavan, Y., Erel, Y., 2002. The release of Pb and REE from granitoids by the dissolution of accessory phases. Geochim. Cosmochim. Acta 66, 837–848. https://doi.org/10.1016/S0016-7037(01)00806-7

Hein, J.R., Conrad, T.A., Frank, M., Christl, M., Sager, W.W., 2012. Copper-nickel-rich, amalgamated ferromanganese crust-nodule deposits from Shatsky Rise, NW Pacific: SHATSKY RISE Cu-RICH Fe-Mn CRUSTS. Geochem. Geophys. Geosystems 13, n/a-n/a. https://doi.org/10.1029/2012GC004286

Hein, J.R., Conrad, T.A., Staudigel, H., 2010. Seamount Mineral Deposits: a source of rare metals for high-technology industries. Oceanography 23, 184–189.

Hein, J.R., Koschinsky, A., 2014. 13.11 - Deep-Ocean Ferromanganese Crusts and Nodules, in: Holland, H.D., Turekian, K.K. (Eds.), Treatise on Geochemistry (Second Edition). Elsevier, Oxford, pp. 273–291. https://doi.org/10.1016/B978-0-08-095975-7.01111-6

Hein , J.R. , Koschinsky, A., Bau, M., Manheim, F.T., Kang, J.-K., Roberts, L., 2000. Cobalt-Rich ferromanganese crusts in the Pacific . In: Handbook of Marine Mineral Deposits . Cronan , D. S. (ed.), 239 – 279 . Boca Raton, Florida : CRC Press .

Hein, J.R., Koschinsky, A., Halbach, P., Manheim, F.T., Bau, M., Kang, J.-K., Lubick, N., 1997. Iron and manganese oxide mineralization in the Pacific. Geol. Soc. Lond. Spec. Publ. 119, 123–138. https://doi.org/10.1144/GSL.SP.1997.119.01.09

Hein, J.R., Mizell, K., Koschinsky, A., Conrad, T.A., 2013. Deep-ocean mineral deposits as a source of critical metals for high- and green-technology applications: Comparison with land-based resources. Ore Geol. Rev. 51, 1–14. https://doi.org/10.1016/j.oregeorev.2012.12.001

Hein, J.R., Yeh, H.-W., Gunn, S.H., Sliter, W.V., Benninger, L.M., Wang, C.-H., 1993. Two Major Cenozoic Episodes of Phosphogenesis Recorded in Equatorial Pacific Seamount Deposits. Paleoceanography 8, 293–311. https://doi.org/10.1029/93PA00320

Jacobsen, S.B., Wasserburg, G.J., 1980. Sm-Nd isotopic evolution of chondrites. Earth Planet. Sci. Lett. 50, 139–155. https://doi.org/10.1016/0012-821X(80)90125-9

Jeandel, C., 1993. Concentration and isotopic composition of Nd in the South Atlantic Ocean. Earth Planet. Sci. Lett. 117, 581–591. https://doi.org/10.1016/0012-821X(93)90104-H

Jeandel, C., Arsouze, T., Lacan, F., Téchiné, P., Dutay, J.-C., 2007. Isotopic Nd compositions and concentrations of the lithogenic inputs into the ocean: A compilation, with an emphasis on the margins. Chem. Geol. 239, 156–164. https://doi.org/10.1016/j.chemgeo.2006.11.013

Jeandel, C., Bishop, J.K., Zindler, A., 1995. Exchange of neodymium and its isotopes between seawater and small and large particles in the Sargasso Sea. Geochim. Cosmochim. Acta 59, 535–547. https://doi.org/10.1016/0016-7037(94)00367-U

Jelsma, H.A., Vinyu, M.L., Wijbrans, J.R., Verdurmen, E.A.T., Valbracht, P.J., Davies, G.R., Valbracht, P.J., 1996. Constraints on Archaean crustal evolution of the Zimbabwe craton: a U-Pb zircon, Sm-Nd and Pb-Pb whole-rock isotope study. Contrib. Mineral. Petrol. 124, 55–70. https://doi.org/10.1007/s004100050173

Jorry, S.J., Camoin, G.F., Jouet, G., Roy, P.L., Vella, C., Courgeon, S., Prat, S., Fontanier, C., Paumard, V., Boulle, J., Caline, B., Borgomano, J., 2016. Modern sediments and Pleistocene reefs from isolated carbonate platforms (Iles Eparses, SW Indian Ocean): A preliminary study. Acta Oecologica, Îles Éparses (French Scattered Islands, SW Indian Ocean) as reference ecosystems for environmental research. 72, 129–143. https://doi.org/10.1016/j.actao.2015.10.014

Josso, P., Horstwood, M.S.A., Millar, I.L., Pashley, V., Lusty, P. a. J., Murton, B., 2020. Development of a Correlated Fe-Mn Crust Stratigraphy Using Pb and Nd Isotopes and Its Application to Paleoceanographic Reconstruction in the Atlantic. Paleoceanogr. Paleoclimatology 35, e2020PA003928. https://doi.org/10.1029/2020PA003928

Josso, P., Parkinson, I., Horstwood, M., Lusty, P., Chenery, S., Murton, B., 2019. Improving confidence in ferromanganese crust age models: A composite geochemical approach. Chem. Geol.

513, 108–119. https://doi.org/10.1016/j.chemgeo.2019.03.003

Josso, P., Pelleter, E., Pourret, O., Fouquet, Y., Etoubleau, J., Cheron, S., Bollinger, C., 2017. A new discrimination scheme for oceanic ferromanganese deposits using high field strength and rare earth elements. Ore Geol. Rev., SI:Marine mineral deposits: New resources for base, precious, and critical metals 87, 3–15. https://doi.org/10.1016/j.oregeorev.2016.09.003

Josso, P., Rushton, J., Lusty, P., Matthews, A., Chenery, S., Holwell, D., Kemp, S.J., Murton, B., 2020. Late Cretaceous and Cenozoic paleoceanography from north-east Atlantic ferromanganese crust microstratigraphy. Mar. Geol. 422, 106122. https://doi.org/10.1016/j.margeo.2020.106122

Jourdan, F., Bertrand, H., Schärer, U., Blichert-Toft, J., Féraud, G., Kampunzu, A.B., 2007. Major and Trace Element and Sr, Nd, Hf, and Pb Isotope Compositions of the Karoo Large Igneous Province, Botswana–Zimbabwe: Lithosphere vs Mantle Plume Contribution. J. Petrol. 48, 1043–1077. https://doi.org/10.1093/petrology/egm010

Karami, M.P., Meijer, P.T., Dijkstra, H.A., Wortel, M.J.R., 2009. An oceanic box model of the Miocene Mediterranean Sea with emphasis on the effects of closure of the eastern gateway. Paleoceanography 24. https://doi.org/10.1029/2008PA001679

Katz, M.E., Cramer, B.S., Toggweiler, J.R., Esmay, G., Liu, C., Miller, K.G., Rosenthal, Y., Wade, B.S., Wright, J.D., 2011. Impact of Antarctic Circumpolar Current Development on Late Paleogene Ocean Structure. Science 332, 1076–1079. https://doi.org/10.1126/science.1202122

Keigwin, L., 1982. Isotopic Paleoceanography of the Caribbean and East Pacific: Role of Panama Uplift in Late Neogene Time. Science 217, 350–353. https://doi.org/10.1126/science.217.4557.350

Kennett, J.P., 1986. Miocene to early Pliocene oxygen and carbon isotope stratigraphy in the Southwest Pacific, Deep Sea Drilling Project Leg 90. In: Kennett, JP; von der Borch, CC; et al. (eds.), Initial Reports of the Deep Sea Drilling Project, Washington (U.S. Govt. Printing Office), 90, 1383-1411

Kennett, J.P., (Ed.) 1985. The Miocene Ocean: Paleoceanography and Biogeography. Geological Society of America, Vol.163

Kennett, J.P., 1977. Cenozoic evolution of Antarctic glaciation, the circum-Antarctic Ocean, and their impact on global paleoceanography. J. Geophys. Res. 1896-1977 82, 3843–3860. https://doi.org/10.1029/JC082i027p03843

Kocsis, L., Vennemann, T.W., Fontignie, D., Baumgartner, C., Montanari, A., Jelen, B., 2008. Oceanographic and climatic evolution of the Miocene Mediterranean deduced from Nd, Sr, C, and O isotope compositions of marine fossils and sediments. Paleoceanography 23. https://doi.org/10.1029/2007PA001540

Konstantinova, N., Cherkashov, G., Hein, J.R., Mirão, J., Dias, L., Madureira, P., Kuznetsov, V., Maksimov, F., 2017. Composition and characteristics of the ferromanganese crusts from the western Arctic Ocean. Ore Geol. Rev. 87, 88–99. https://doi.org/10.1016/j.oregeorev.2016.09.011

Korschinek, G., Bergmaier, A., Faestermann, T., Gerstmann, U.C., Knie, K., Rugel, G., Wallner, A., Dillmann, I., Dollinger, G., von Gostomski, Ch.L., Kossert, K., Maiti, M., Poutivtsev, M., Remmert, A., 2010. A new value for the half-life of 10Be by Heavy-Ion Elastic Recoil Detection and liquid scintillation counting. Nucl. Instrum. Methods Phys. Res. Sect. B Beam Interact. Mater. At. 268, 187–191. https://doi.org/10.1016/j.nimb.2009.09.020

Koschinsky, A., Halbach, P., 1995. Sequential leaching of marine ferromanganese precipitates: Genetic implications. Geochim. Cosmochim. Acta 59, 5113–5132. https://doi.org/10.1016/0016-7037(95)00358-4

Koschinsky, A., Halbach, P., Hein, J.R., Mangini, A., 1996. Ferromanganese crusts as indicators for paleoceanographic events in the NE Atlantic. Geol. Rundsch.

Koschinsky, A., Hein, J.R., 2017. Marine Ferromanganese Encrustations: Archives of Changing Oceans. Elements 13, 177–182. https://doi.org/10.2113/gselements.13.3.177

Kröner, A., Brandl, G., Brandt, S., Klemd, R., Xie, H., 2018. Geochronological evidence for Archaean and Palaeoproterozoic polymetamorphism in the Central Zone of the Limpopo Belt, South Africa. Precambrian Res. 310, 320–347. https://doi.org/10.1016/j.precamres.2018.03.013

Lacan, F., Jeandel, C., 2005. Acquisition of the neodymium isotopic composition of the North Atlantic Deep Water. Geochem. Geophys. Geosystems 6. https://doi.org/10.1029/2005GC000956

Lacan, F., Jeandel, C., 2001. Tracing Papua New Guinea imprint on the central Equatorial Pacific Ocean using neodymium isotopic compositions and Rare Earth Element patterns. Earth Planet. Sci. Lett. 186, 497–512. https://doi.org/10.1016/S0012-821X(01)00263-1

Lacan, F., Tachikawa, K., Jeandel, C., 2012. Neodymium isotopic composition of the oceans: A compilation of seawater data. Chem. Geol. 300–301, 177–184. https://doi.org/10.1016/j.chemgeo.2012.01.019

Lambelet, M., van de Flierdt, T., Crocket, K., Rehkämper, M., Kreissig, K., Coles, B., Rijkenberg, M.J.A., Gerringa, L.J.A., de Baar, H.J.W., Steinfeldt, R., 2016. Neodymium isotopic composition and concentration in the western North Atlantic Ocean: Results from the GEOTRACES GA02 section. Geochim. Cosmochim. Acta 177, 1–29. https://doi.org/10.1016/j.gca.2015.12.019

Lawver, L.A., Gahagan, L.M., 2003. Evolution of Cenozoic seaways in the circum-Antarctic region. Palaeogeogr. Palaeoclimatol. Palaeoecol., Antarctic Cenozoic palaeoenvironments: geologic record and models 198, 11–37. https://doi.org/10.1016/S0031-0182(03)00392-4

Leclaire, L., 1984. RIDA - MD39 cruise,Marion Dufresne R/V. https://doi.org/10.17600/84010511

Lee, J.-M., Boyle, E.A., Gamo, T., Obata, H., Norisuye, K., Echegoyen, Y., 2015. Impact of anthropogenic Pb and ocean circulation on the recent distribution of Pb isotopes in the Indian Ocean. Geochim. Cosmochim. Acta 170, 126–144. https://doi.org/10.1016/j.gca.2015.08.013

Lee, T.-Y., Lawver, L.A., 1995. Cenozoic plate reconstruction of Southeast Asia. Tectonophysics, Southeast Asia Structure and Tectonics 251, 85–138. https://doi.org/10.1016/0040-1951(95)00023-2

Leinweber, V.T., Jokat, W., 2012. The Jurassic history of the Africa–Antarctica corridor — new constraints from magnetic data on the conjugate continental margins. Tectonophysics 530–531, 87–101. https://doi.org/10.1016/j.tecto.2011.11.008

Lemoine, A., Briole, P., Bertil, D., Roullé, A., Foumelis, M., Thinon, I., Raucoules, D., de Michele, M., Valty, P., Hoste Colomer, R., 2020. The 2018–2019 seismo-volcanic crisis east of Mayotte, Comoros islands: seismicity and ground deformation markers of an exceptional submarine eruption. Geophys. J. Int. 223, 22–44. https://doi.org/10.1093/gji/ggaa273

Leroux, E., Counts, J.W., Jorry, S.J., Jouet, G., Révillon, S., BouDagher-Fadel, M.K., Courgeon, S., Berthod, C., Ruffet, G., Bachèlery, P., Grenard-Grand, E., 2020. Evolution of the Glorieuses seamount in the SW Indian Ocean and surrounding deep Somali Basin since the Cretaceous. Mar. Geol. 427, 106202. https://doi.org/10.1016/j.margeo.2020.106202

Ling, H.F., Burton, K.W., O'Nions, R.K., Kamber, B.S., von Blanckenburg, F., Gibb, A.J., Hein, J.R., 1997. Evolution of Nd and Pb isotopes in Central Pacific seawater from ferromanganese crusts. Earth Planet. Sci. Lett. 146, 1–12. https://doi.org/10.1016/S0012-821X(96)00224-5

Linthout, K., Helmers, H., Sopaheluwakan, J., 1997. Late Miocene obduction and microplate migration around the southern Banda Sea and the closure of the Indonesian Seaway. Tectonophysics, Neogene Evolution of the Pacific: Tectonics of Gateways and Associated Responses 281, 17–30. https://doi.org/10.1016/S0040-1951(97)00156-X

Lubbe, H.J.L. van der, Frank, M., Tjallingii, R., Schneider, R.R., 2016. Neodymium isotope constraints on provenance, dispersal, and climate-driven supply of Zambezi sediments along the Mozambique Margin during the past ~45,000 years. Geochem. Geophys. Geosystems 17, 181–198. https://doi.org/10.1002/2015GC006080

Lugmair, G.W., Shimamura, T., Lewis, R.S., Anders, E., 1983. Samarium-146 in the Early Solar System: Evidence from Neodymium in the Allende Meteorite. Science 222, 1015–1018. https://doi.org/10.1126/science.222.4627.1015

Lunt, D.J., Valdes, P.J., Haywood, A., Rutt, I.C., 2008. Closure of the Panama Seaway during the Pliocene: implications for climate and Northern Hemisphere glaciation. Clim. Dyn. 30, 1–18. https://doi.org/10.1007/s00382-007-0265-6

Lustrino, M., Duggen, S., Rosenberg, C.L., 2011. The Central-Western Mediterranean: Anomalous igneous activity in an anomalous collisional tectonic setting. Earth-Sci. Rev. 104, 1–40. https://doi.org/10.1016/j.earscirev.2010.08.002

Lustrino, M., Morra, V., Fedele, L., Franciosi, L., 2009. Beginning of the Apennine subduction system in central western Mediterranean: Constraints from Cenozoic "orogenic" magmatic activity of Sardinia, Italy. Tectonics 28. https://doi.org/10.1029/2008TC002419

Lusty, P.A.J., Hein, J.R., Josso, P., 2018. Formation and Occurrence of Ferromanganese Crusts: Earth's Storehouse for Critical Metals. Elements 14, 313–318. https://doi.org/10.2138/gselements.14.5.313

Lutjeharms, J.R.E., 2006. The Agulhas Current. Springer-Verlag, Berlin Heidelberg.

Macgregor, D., 2015. History of the development of the East African Rift System: A series of interpreted maps through time. J. Afr. Earth Sci. 101, 232–252. https://doi.org/10.1016/j.jafrearsci.2014.09.016

Mahanjane, E.S., 2014. The Davie Fracture Zone and adjacent basins in the offshore Mozambique Margin – A new insights for the hydrocarbon potential. Mar. Pet. Geol. 57, 561–571. https://doi.org/10.1016/j.marpetgeo.2014.06.015

Marino, E., González, F.J., Lunar, R., Reyes, J., Medialdea, T., Castillo-Carrión, M., Bellido, E., Somoza, L., 2018. High-Resolution Analysis of Critical Minerals and Elements in Fe–Mn Crusts from the Canary Island Seamount Province (Atlantic Ocean). Minerals 8, 285. https://doi.org/10.3390/min8070285

Marino, E., González, F.J., Somoza, L., Lunar, R., Ortega, L., Vázquez, J.T., Reyes, J., Bellido, E., 2017. Strategic and rare elements in Cretaceous-Cenozoic cobalt-rich ferromanganese crusts from seamounts in the Canary Island Seamount Province (northeastern tropical Atlantic). Ore Geol. Rev., SI:Marine mineral deposits: New

resources for base, precious, and critical metals 87, 41–61. https://doi.org/10.1016/j.oregeorev.2016.10.005

Masters, J.C., de Wit, M.J., Asher, R.J., 2006. Reconciling the origins of Africa, India and Madagascar with vertebrate dispersal scenarios. Folia Primatol. Int. J. Primatol. 77, 399–418. https://doi.org/10.1159/000095388

Masters, J.C., Génin, F., Zhang, Y., Pellen, R., Huck, T., Mazza, P.P.A., Rabineau, M., Doucouré, M., Aslanian, D., 2021. Biogeographic mechanisms involved in the colonization of Madagascar by African vertebrates: Rifting, rafting and runways. J. Biogeogr. 48, 492–510. https://doi.org/10.1111/jbi.14032

Masters, J.C., Génin, F., Zhang, Y., Pellen, R., Huck, T., Mazza, P.P.A., Rabineau, M., Doucouré, M., Aslanian, D., 2021. Biogeographic mechanisms involved in the colonization of Madagascar by African vertebrates: Rifting, rafting and runways. J. Biogeogr. 48, 492–510. https://doi.org/10.1111/jbi.14032

Michon, L., 2016. The volcanism of the Comoros archipelago integrated at a regional scale, in: Bachelery, Patrick, Lénat, Jean-François, Muro, D., Andrea, Michon, Laurent (Eds.), Active Volcanoes of the Southwest Indian Ocean: Piton de La Fournaise and Karthala, Active Volcanoes of the World. Springer-Verlag, pp. 233–244.

Mizell, K., Hein, J.R., Lam, P.J., Koppers, A.A.P., Staudigel, H., 2020. Geographic and Oceanographic Influences on Ferromanganese Crust Composition Along a Pacific Ocean Meridional Transect, 14 N to 14S. Geochem. Geophys. Geosystems 21, e2019GC008716. https://doi.org/10.1029/2019GC008716

Möller, A., Mezger, K., Schenk, V., 1998. Crustal Age Domains and the Evolution of the Continental Crust in the Mozambique Belt of Tanzania: Combined Sm–Nd, Rb–Sr, and Pb–Pb Isotopic Evidence. J. Petrol. 39, 749–783. https://doi.org/10.1093/petroj/39.4.749

Mougenot, D., Recq, M., Virlogeux, P., Lepvrier, C., 1986. Seaward extension of the East African Rift. Nature 321, 599. https://doi.org/10.1038/321599a0

Muiños, S.B., Frank, M., Maden, C., Hein, J.R., van de Flierdt, T., Lebreiro, S.M., Gaspar, L., Monteiro, J.H., Halliday, A.N., 2008. New constraints on the Pb and Nd isotopic evolution of NE Atlantic water masses. Geochem. Geophys. Geosystems 9, Q02007. https://doi.org/10.1029/2007GC001766

Muiños, S.B., Hein, J.R., Frank, M., Monteiro, J.H., Gaspar, L., Conrad, T., Pereira, H.G., Abrantes, F., 2013. Deep-sea Fe-Mn Crusts from the Northeast Atlantic Ocean: Composition and Resource Considerations. Mar. Georesources Geotechnol. 31, 40–70. https://doi.org/10.1080/1064119X.2012.661215

Nicholas, C.J., Pearson, P.N., McMillan, I.K., Ditchfield, P.W., Singano, J.M., 2007. Structural evolution of southern coastal Tanzania since the Jurassic. J. Afr. Earth Sci. 48, 273–297. https://doi.org/10.1016/j.jafrearsci.2007.04.003

Nishiizumi, K., Imamura, M., Caffee, M.W., Southon, J.R., Finkel, R.C., McAninch, J., 2007. Absolute calibration of 10Be AMS standards. Nucl. Inst Methods Phys. Res. B 2, 403–413. https://doi.org/10.1016/j.nimb.2007.01.297

Nishimura, S., Suparka, S., 1997. Tectonic approach to the Neogene evolution of Pacific-Indian Ocean seaways. Tectonophysics, Neogene Evolution of the Pacific: Tectonics of Gateways and Associated Responses 281, 1–16. https://doi.org/10.1016/S0040-1951(97)00155-8

Olu, K., 2014. PAMELA-MOZ01 cruise,L'Atalante R/V. https://doi.org/10.17600/14001000

O'Nions, R.K., Frank, M., von Blanckenburg, F., Ling, H.-F., 1998. Secular variation of Nd and Pb isotopes in ferromanganese crusts from the Atlantic, Indian and Pacific Oceans. Earth Planet. Sci. Lett. 155, 15–28. https://doi.org/10.1016/S0012-821X(97)00207-0

Paquette, J.-L., Nédélec, A., Moine, B., Rakotondrazafy, M., 1994. U-Pb, Single Zircon Pb-Evaporation, and Sm-Nd Isotopic Study of a Granulite Domain in SE Madagascar. J. Geol. 102, 523–538. https://doi.org/10.1086/629696

Partridge, T.C., 1998. Of diamonds, dinosaurs and diastrophism : 150 million years of landscape evolution in southern Africa. South Afr. J. Geol. 101, 167–184. https://doi.org/10.10520/EJC-947b4efa3

Pfuhl, H.A., McCave, I.N., 2005. Evidence for late Oligocene establishment of the Antarctic Circumpolar Current. Earth Planet. Sci. Lett. 235, 715–728. https://doi.org/10.1016/j.epsl.2005.04.025

Piepgras, D.J., Wasserburg, G.J., 1980. Neodymium isotopic variations in seawater. Earth Planet. Sci. Lett. 50, 128–138. https://doi.org/10.1016/0012-821X(80)90124-7

Pin, C., Briot, D., Bassin, C., Poitrasson, F., 1994. Concomitant separation of strontium and samarium-neodymium for isotopic analysis in silicate samples, based on specific extraction chromatography. Anal. Chim. Acta 298, 209–217. https://doi.org/10.1016/0003-2670(94)00274-6

Piotrowski, A.M., Galy, A., Nicholl, J.A.L., Roberts, N., Wilson, D.J., Clegg, J.A., Yu, J., 2012. Reconstructing deglacial North and South Atlantic deep water sourcing using foraminiferal Nd isotopes. Earth Planet. Sci. Lett. 357–358, 289–297. https://doi.org/10.1016/j.epsl.2012.09.036

Piotrowski, A.M., Goldstein, S.L., Hemming, S.R., Fairbanks, R.G., 2005. Temporal Relationships of Carbon Cycling and Ocean Circulation at Glacial Boundaries. Science 307, 1933–1938. https://doi.org/10.1126/science.1104883

Piotrowski, A.M., Goldstein, S.L., Hemming, S.R., Fairbanks, R.G., 2004. Intensification and variability of ocean thermohaline circulation through the last deglaciation. Earth Planet. Sci. Lett. 225, 205–220. https://doi.org/10.1016/j.epsl.2004.06.002

Piotrowski, A.M., Lee, D.-C., Christensen, J.N., Burton, K.W., Halliday, A.N., Hein, J.R., Günther, D., 2000. Changes in erosion and ocean circulation recorded in the Hf isotopic compositions of North Atlantic and Indian Ocean ferromanganese crusts. Earth Planet. Sci. Lett. 181, 315–325. https://doi.org/10.1016/S0012-821X(00)00205-3

Ponte, J.-P., 2018. La marge africaine du canal du Mozambique, le système turbiditique du Zambèze : une approche « Source to Sink » au Méso – Cénozoïque (phd thesis). Université Rennes 1.

Poux, C., Madsen, O., Marquard, E., Vieites, D.R., de Jong, W.W., Vences, M., 2005. Asynchronous Colonization of Madagascar by the Four Endemic Clades of Primates, Tenrecs, Carnivores, and Rodents as Inferred from Nuclear Genes. Syst. Biol. 54, 719–730. https://doi.org/10.1080/10635150500234534

Puteanus, D., Halbach, P., 1988. Correlation of Co concentration and growth rate — A method for age determination of ferromanganese crusts. Chem. Geol. 69, 73–85. https://doi.org/10.1016/0009-2541(88)90159-3

Rahlf, P., Hathorne, E., Laukert, G., Gutjahr, M., Weldeab, S., Frank, M., 2020. Tracing water mass mixing and continental inputs in the southeastern Atlantic Ocean with dissolved neodymium

isotopes. Earth Planet. Sci. Lett. 530, 115944. https://doi.org/10.1016/j.epsl.2019.115944

Ramsay, A.T.S., Smart, C.W., Zachos, J.C., 1998. A Model of early to middle Miocene Deep Ocean circulation for the Atlantic and Indian Oceans. Geol. Soc. Lond. Spec. Publ. 131, 55–70. https://doi.org/10.1144/GSL.SP.1998.131.01.04

Rempfer, J., Stocker, T.F., Joos, F., Dutay, J.-C., Siddall, M., 2011. Modelling Nd-isotopes with a coarse resolution ocean circulation model: Sensitivities to model parameters and source/sink distributions. Geochim. Cosmochim. Acta 75, 5927–5950. https://doi.org/10.1016/j.gca.2011.07.044

Reynolds, B.C., Frank, M., O'Nions, R.K., 1999. Nd- and Pb-isotope time series from Atlantic ferromanganese crusts: implications for changes in provenance and paleocirculation over the last 8 Myr. Earth Planet. Sci. Lett. 173, 381–396. https://doi.org/10.1016/S0012-821X(99)00243-5

Rickli, J., Frank, M., Baker, A.R., Aciego, S., de Souza, G., Georg, R.B., Halliday, A.N., 2010. Hafnium and neodymium isotopes in surface waters of the eastern Atlantic Ocean: Implications for sources and inputs of trace metals to the ocean. Geochim. Cosmochim. Acta 74, 540–557. https://doi.org/10.1016/j.gca.2009.10.006

Roddaz, M., Nauton-Fourteu, M., Santos, R.V., Dantas, E.L., Calves, G., 2020. Controls on the provenance of late Eocene to Quaternary Mozambique Channel shales (DSDP 25 Site 242). Mar. Geol. 421, 106090. https://doi.org/10.1016/j.margeo.2019.106090

Rutberg, R.L., Hemming, S.R., Goldstein, S.L., 2000. Reduced North Atlantic Deep Water flux to the glacial Southern Ocean inferred from neodymium isotope ratios. Nature 405, 935. https://doi.org/10.1038/35016049

Salman, G., Abdula, I., 1995. Development of the Mozambique and Ruvuma sedimentary basins, offshore Mozambique. Sediment. Geol. 96, 7–41. https://doi.org/10.1016/0037-0738(95)00125-R

Saria, E., Calais, E., Stamps, D.S., Delvaux, D., Hartnady, C.J.H., 2014. Present-day kinematics of the East African Rift. J. Geophys. Res. Solid Earth 119, 3584–3600. https://doi.org/10.1002/2013JB010901

Schacht, U., Wallmann, K., Kutterolf, S., 2010. The influence of volcanic ash alteration on the REE composition of marine pore waters. J. Geochem. Explor., GEOFLUIDS VI: Recent Advances in Research on Fluids in Geological Processes 106, 176–187. https://doi.org/10.1016/j.gexplo.2010.02.006

Scher, H.D., Martin, E.E., 2008a. Oligocene deep water export from the North Atlantic and the development of the Antarctic Circumpolar Current examined with neodymium isotopes. Paleoceanography 23. https://doi.org/10.1029/2006PA001400

Scher, H.D., Martin, E.E., 2008b. Oligocene deep water export from the North Atlantic and the development of the Antarctic Circumpolar Current examined with neodymium isotopes. Paleoceanography 23. https://doi.org/10.1029/2006PA001400

Scher, H.D., Martin, E.E., 2006. Timing and Climatic Consequences of the Opening of Drake Passage. Science 312, 428–430. https://doi.org/10.1126/science.1120044

Scher, H.D., Martin, E.E., 2004. Circulation in the Southern Ocean during the Paleogene inferred from neodymium isotopes. Earth Planet. Sci. Lett. 228, 391–405. https://doi.org/10.1016/j.epsl.2004.10.016

Scher, H.D., Whittaker, J.M., Williams, S.E., Latimer, J.C., Kordesch, W.E.C., Delaney, M.L., 2015. Onset of Antarctic Circumpolar Current 30 million years ago as Tasmanian Gateway aligned

with westerlies. Nature 523, 580–583. https://doi.org/10.1038/nature14598

Schott, F.A., McCreary, J.P., 2001. The monsoon circulation of the Indian Ocean. Prog. Oceanogr. 51, 1–123. https://doi.org/10.1016/S0079-6611(01)00083-0

Searle, M.P., 1996. Cooling history, erosion, exhumation and kinematics of the Himalaya-Karakoram-Tibet orogenic belt. Pp. 110–137 in: Asian Tectonics. (Yin, A. and Harrison, M.A., editors). Cambridge University Press, Cambridge, UK.

Segev, A., Avni, Y., Shahar, J., Wald, R., 2017. Late Oligocene and Miocene different seaways to the Red Sea–Gulf of Suez rift and the Gulf of Aqaba–Dead Sea basins. Earth-Sci. Rev. 171, 196–219. https://doi.org/10.1016/j.earscirev.2017.05.004

Segl, M., Mangini, A., Bonani, G., Hofmann, H.J., Nessi, M., Suter, M., Wölfli, W., Friedrich, G., Plüger, W.L., Wiechowski, A., Beer, J., 1984. 10 Be-dating of a manganese crust from Central North Pacific and implications for ocean palaeocirculation. Nature 309, 540. https://doi.org/10.1038/309540a0

Segoufin, J., Leclaire, L., Clochiatti, M., 1977. Les structures du canal de Mozambique. Le problème de la Ride de Davie. Apports récents à la Géologie du Gondwana, Annales Soc. Géol. Nord, Villeneuve d'Ascq, t. XCVII (1977), 309-314

Sijp, W.P., England, M.H., 2004. Effect of the Drake Passage Throughflow on Global Climate. J. Phys. Oceanogr. 34, 1254–1266. https://doi.org/10.1175/1520-0485(2004)034<1254:EOTDPT>2.0.CO;2

Simon, Q., Thouveny, N., Bourlès, D.L., Valet, J.-P., Bassinot, F., Ménabréaz, L., Guillou, V., Choy, S., Beaufort, L., 2016. Authigenic 10Be/9Be ratio signatures of the cosmogenic nuclide production linked to geomagnetic dipole moment variation since the Brunhes/Matuyama boundary. J. Geophys. Res. Solid Earth 121, 7716–7741. https://doi.org/10.1002/2016JB013335

Stamps, D.S., Calais, E., Saria, E., Hartnady, C., Nocquet, J.-M., Ebinger, C.J., Fernandes, R.M., 2008. A kinematic model for the East African Rift. Geophys. Res. Lett. 35. https://doi.org/10.1029/2007GL032781

Stamps, D.S., Kreemer, C., Fernandes, R., Rajaonarison, T.A., Rambolamanana, G., 2021. Redefining East African Rift System kinematics. Geology 49, 150–155. https://doi.org/10.1130/G47985.1

Stamps, D.S., Saria, E., Kreemer, C., 2018. A Geodetic Strain Rate Model for the East African Rift System. Sci. Rep. 8, 732. https://doi.org/10.1038/s41598-017-19097-w

Stankiewicz, J., de Wit, M.J., 2006. A proposed drainage evolution model for Central Africa—Did the Congo flow east? J. Afr. Earth Sci. 44, 75–84. https://doi.org/10.1016/j.jafrearsci.2005.11.008

Stickley, C.E., Brinkhuis, H., Schellenberg, S.A., Sluijs, A., Röhl, U., Fuller, M., Grauert, M., Huber, M., Warnaar, J., Williams, G.L., 2004. Timing and nature of the deepening of the Tasmanian Gateway. Paleoceanography 19. https://doi.org/10.1029/2004PA001022

Tachikawa, K., Jeandel, C., Roy-Barman, M., 1999. A new approach to the Nd residence time in the ocean: the role of atmospheric inputs. Earth Planet. Sci. Lett. 170, 433–446. https://doi.org/10.1016/S0012-821X(99)00127-2

Tanaka, T., Togashi, S., Kamioka, H., Amakawa, H., Kagami, H., Hamamoto, T., Yuhara, M., Orihashi, Y., Yoneda, S., Shimizu, H., Kunimaru, T., Takahashi, K., Yanagi, T., Nakano, T., Fujimaki, H., Shinjo, R., Asahara, Y., Tanimizu,

M., Dragusanu, C., 2000. JNdi-1: a neodymium isotopic reference in consistency with LaJolla neodymium. Chem. Geol. 168, 279–281. https://doi.org/10.1016/S0009-2541(00)00198-4

Taylor, S.R., McLennan, S.M., 1985. The continental crust: Its composition and evolution. United States: N. p., 1985. Web.

Toole, J.M., Warren, B.A., 1993. A hydrographic section across the subtropical South Indian Ocean. Deep Sea Res. Part Oceanogr. Res. Pap. 40, 1973–2019. https://doi.org/10.1016/0967-0637(93)90042-2

Torsvik, T.H., Tucker, R.D., Ashwal, L.D., Carter, L.M., Jamtveit, B., Vidyadharan, K.T., Venkataramana, P., 2000. Late Cretaceous India-Madagascar fit and timing of break-up related magmatism. Terra Nova 12, 220–224. https://doi.org/10.1046/j.1365-3121.2000.00300.x

Ullgren, J.E., van Aken, H.M., Ridderinkhof, H., de Ruijter, W.P.M., 2012. The hydrography of the Mozambique Channel from six years of continuous temperature, salinity, and velocity observations. Deep Sea Res. Part Oceanogr. Res. Pap. 69, 36–50. https://doi.org/10.1016/j.dsr.2012.07.003

van de Flierdt, T., Griffiths, A.M., Lambelet, M., Little, S.H., Stichel, T., Wilson, D.J., 2016. Neodymium in the oceans: a global database, a regional comparison and implications for palaeoceanographic research. Philos. Trans. R. Soc. Math. Phys. Eng. Sci. 374, 20150293. https://doi.org/10.1098/rsta.2015.0293

Véron, A.J., Church, T.M., Flegal, A.R., 1998. Lead Isotopes in the Western North Atlantic: Transient Tracers of Pollutant Lead Inputs. Environ. Res. 78, 104–111. https://doi.org/10.1006/enrs.1998.3856

Véron, A.J., church, T.M., Patterson, C.C., Flegal, A.R., 1994. Use of stable lead isotopes to characterize the sources of anthropogenic lead in North Atlantic surface waters. Geochim. Cosmochim. Acta 58, 3199–3206. https://doi.org/10.1016/0016-7037(94)90047-7

Via, R.K., Thomas, D.J., 2006. Evolution of Atlantic thermohaline circulation: Early Oligocene onset of deep-water production in the North Atlantic. Geology 34, 441–444. https://doi.org/10.1130/G22545.1

Vlastélic, I., Abouchami, W., Galer, S.J.G., Hofmann, A.W., 2001. Geographic control on Pb isotope distribution and sources in Indian Ocean Fe-Mn deposits. Geochim. Cosmochim. Acta 65, 4303–4319. https://doi.org/10.1016/S0016-7037(01)00713-X

von Blanckenburg, F., Nägler, T.F., 2001. Weathering versus circulation-controlled changes in radiogenic isotope tracer composition of the Labrador Sea and North Atlantic Deep Water. Paleoceanography 16, 424–434. https://doi.org/10.1029/2000PA000550

von Blanckenburg, F., O'Nions, R.K., 1999. Response of beryllium and radiogenic isotope ratios in Northern Atlantic Deep Water to the onset of northern hemisphere glaciation. Earth Planet. Sci. Lett. 167, 175–182. https://doi.org/10.1016/S0012-821X(99)00028-X

Walford, H.L., White, N.J., Sydow, J.C., 2005. Solid sediment load history of the Zambezi Delta. Earth Planet. Sci. Lett. 238, 49–63. https://doi.org/10.1016/j.epsl.2005.07.014

White, W.M., Albaréde, F., Telouk, P., 2000. High-precision analysis of Pb isotope ratios by multi-collector ICP-MS. Chem.Geol. 167,257–270

Wilson, D.J., Piotrowski, A.M., Galy, A., McCave, I.N., 2012. A boundary exchange influence on deglacial neodymium isotope records from the deep western Indian Ocean.

Earth Planet. Sci. Lett. 341–344, 35–47. https://doi.org/10.1016/j.epsl.2012.06.009

Winter, B.L., Johnson, C.M., Clark, D.L., 1997. Strontium, neodymium, and lead isotope variations of authigenic and silicate sediment components from the Late Cenozoic Arctic Ocean: Implications for sediment provenance and the source of trace metals in seawater. Geochim. Cosmochim. Acta 61, 4181–4200. https://doi.org/10.1016/S0016-7037(97)00215-9

Woodruff, F., Savin, S.M., 1989. Miocene deepwater oceanography. Paleoceanography 4, 87–140. https://doi.org/10.1029/PA004i001p00087

Wu, J., Boyle, E.A., 1997. Lead in the western North Atlantic Ocean: Completed response to leaded gasoline phaseout. Geochim. Cosmochim. Acta 61, 3279–3283. https://doi.org/10.1016/S0016-7037(97)89711-6

CHAPTER 5 : DEEP PALEOCEANOGRAPHY OF THE CHANNEL OVER THE LAST 20 MA

5.1. Résumé (français)

Le canal du Mozambique a connu de nombreux bouleversements géodynamiques depuis le Crétacé supérieur (Castelino et al., 2015 ; Charles et al., in prep. ; Leinweber et al., 2013 ; Ponte, 2019 ; Walford et al., 2005). Couplés aux événements paléogéographiques majeurs recensés à la surface du globe depuis plus de 30 Ma, notamment grâce aux encroutements Fe-Mn (Frank et al., 2002), ces phénomènes ont impacté la circulation et l'évolution des masses d'eau, dans et entre, les grands bassins océaniques. C'est pourquoi, après avoir identifié un uplift et une subsidence dans le chapitre précédent, il s'agira maintenant de comprendre l'influence de ces phénomènes sur la circulation des masses d'eau profondes dans le canal du Mozambique. Cet axe est basé sur l'étude de 3 encroûtements Fe-Mn situés dans les masses d'eau profondes (>1780 m): MOZ1-DR04-23 (archipel des Glorieuses – extrême nord du canal), MOZ1-DR11-01 (ride de Jeffrey – milieu du canal, nord de la ride de Davie) et DR75-0012 (Plateau des Aiguilles – extrême sud du canal). Un total de 52 prélèvements est analysé dont 18 permettent d'établir une géochronologie à partir du rapport isotopique $^{10}Be/^{9}Be$. Les taux de croissance des échantillons s'étendent de 2.0 à 8.9 mm/Ma. Les données isotopiques reflètent que εNd varie entre -7.9 et -10.5 et que les rapports $^{206,207,208}Pb/^{204}Pb$ s'étendent respectivement de 18.7928 à 19.1063, de 15.6747 à 15.7404 et de 39.0303 à 39.3317.

La reconstruction paléocéanographique indique que le NADW a fortement circulé dans le canal du Mozambique, jusqu'à l'archipel des Glorieuses jusqu'à 12.4 Ma (apport ~81-87%) avant de considérablement diminuer. Notre étude établit un lien direct entre cette réduction du NADW au nord du canal et l'uplift enregistré à partir de 11.7 Ma dont la conséquence a été une surrection majeure de la ride de Davie.

5.1. Abstract (english)

The Mozambique Channel has been subject to numerous geodynamic upheavals since the Late Cretaceous (Castelino et al., 2015; Charles et al., in prep.; Leinweber et al., 2013; Ponte, 2018; Walford et al., 2005). Coupled with the major paleogeographic events recorded at the surface of the globe for more than 30 Ma, notably using Atlantic and Indian Fe-Mn crusts (Frank et al., 2002), these phenomena have impacted the circulation and evolution of water masses, within and between the major oceanic basins. That is why, after identification of an uplift and a subsidence in the previous chapter, we shall now understand the influence of these paleogeodynamic events on the deep-water mass circulation in the Mozambique Channel. This axis is based on the study of 3 Fe-Mn crusts initially located in deep water masses (>1780 mbsl): MOZ1-DR04-23 (Glorieuses archipelago – northern end of the channel), MOZ1-DR11-01 (Jeffrey Ridge – middle of the channel, north of the Davie Ridge) and DR75-0012 (Agulhas Plateau – southern end of the channel). 52 samples were analysed, 18 of which were used to establish a geochronology from the $^{10}Be/^{9}Be$ isotope ratio. The growth rates of the samples range from 2.0 to 8.9 mm/Ma. The isotopic data reflect that εNd varies between -7.9 to -10.5 and that the $^{206,207,208}Pb/^{204}Pb$ ratios range from 18.7928 to 19.1063, from 15.6747 to 15.7404 and from 39.0303 to 39.3317 respectively.

The palaeoceanographic reconstruction indicates that the NADW circulated strongly in the Mozambique Channel up to the Glorieuses Archipelago until 12.4 Ma (~81-87% contribution) before decreasing considerably. Our study establishes a direct link between the NADW reduction, in north of the channel, and the uplift recorded from 11.7 Ma onwards, the consequence of which was a major surge in the Davie Ridge.

5.2. Introduction

The Indian Ocean is a key area for studying Atlantic and Pacific water mass exchanges (Fine, 1993; Schott et al., 2009; Thomas et al., 2003; van Aken et al., 2004; You, 2000; Zachos et al., 2001). However, these mixing of water masses have evolved over time due to major paleogeographic changes to the origin of many reorganization of ocean circulation patterns (Frank et al., 2002), such as the opening of the Tasman Strait and the Drake Passage during the Eocene (Barker and Burrell, 1977; Kennett and von der Borch, 1986; Pfuhl and McCave, 2005; Scher and Martin, 2004; Stickley et al., 2004; Weissel and Hayes, 1972). Additionally, the Miocene is a well-known period of intense climatic and oceanographic variations (Holbourn et al., 2013b, 2013a; Kennett, 1985; Pagani et al., 2010; Shevenell and Kennett, 2004; Verducci et al., 2009; Woodruff and Savin, 1991; Zachos et al., 2001). Numerous geological events occurred at this time, and could have affected the Indian deep-water circulation.

First, the definite closure of the Tethys Seaway was established at around 14 Ma with the sealing of the eastern gateway (Cornacchia et al., 2021; Hsü et al., 1977). The Tethys Basin had an important role as intermediary between the Atlantic, Indian and Southern Ocean water mass transfers (de la Vara et al., 2016; Karami et al., 2009), notably with the Tethyan Indian Saline Water (TISW) first exported in the northern Indian Ocean and secondly transported to the Southern Ocean (Woodruff and Savin, 1989; Wright et al., 2018). Secondly, the exchanges of deep waters between the Pacific and Indian Oceans became progressively low due to the constant northward movement of the Australian Plate and the evolving Indonesian Island Arcs (Linthout et al., 1997). The complete closure of this seaway is still debated between 10 and 4 Ma (Linthout et al., 1997; Nishimura and Suparka, 1997) even if some paleoceanographic researches suggest that from 4.4 Ma, the South Equatorial Current (SEC) could not flow through the Indonesian Seaway (Lee and Lawver, 1995). From this period, the Indian surface water temperature drastically cooled while the western Pacific Ocean temperature increased (Cane and Molnar, 2001). Finally, the closing of the Central American Seaway (CAS) between the North and the South America was estimated between 8 and 4 Ma (Burton et al., 1997; Haug and Tiedmann, 1998). Linked to this important upheaval, the North Hemisphere Glaciation (NHG) started at about 3 Ma (Raymo, 1994) with a major oceanographic consequence: the significant reduction of the North Atlantic Deep Water (NADW) export to the Southern Ocean (Boyle and Keigwin, 1987; Frank et al., 2002).

In order to reconstruct the paleoceanography since the Early Cenozoic, many studies worked on geochemical proxies such as the isotopes of Nd and Pb from the Fe-Mn crusts or marine sediments (Charles et al., 2020; Christensen et al., 1997; Frank et al., 2002; Josso et al., 2020; Mizell et al., 2020; O'Nions et al., 1998; Piotrowski et al., 2005; Rutberg et al., 2020; Scher and Martin, 2004). These two water mass tracers are interesting to focus on due to their oceanic residence time, which allows them particular characteristics. The oceanic residence time of the Nd is estimated between 600 and 2000 years (Amakawa et al., 2000), about the circulation time of the global ocean. Thus, the Nd has a quasi-conservative behaviour allowing the distinction between present and past water masses of the oceans. The Pb presents a shorter average residence time of about 80 years (Schaule and Patterson, 1981). In contrast to Nd, local input sources from the surrounding continents strongly modify its composition, which can vary a lot over short length scales (Frank and O'Nions, 1998; von Blanckenburg and Nägler, 2001; von Blanckenburg and O'Nions, 1999).

Consequently, the oceanic basins present their own geochemical composition (Bertram and Elderfield, 1993; Jeandel et al., 1995; Vance et al., 2004). The use and combination of the Nd and Pb as geochemical proxies provides large details about paleoceanography and paleogeography, which are essential to improve the scientific climate, oceanic and geologic reconstructions.

Frank et al. (2006, 2002) and O'Nions et al. (1998), studied time series of Nd and Pb isotopes from several Fe-Mn crusts from the Indian Ocean (Figure 5.1). Two come from the centre of the Ocean (SS663; 109D-C) and two are from the eastern part of the Indian Ocean (232D; 13KD-1). The samples were dated using profiles of the ratio of the radioactive cosmogenic isotope ^{10}Be to stable ^{9}Be. Whereas the samples from the centre of the Indian Ocean show small variations over the last 20 Ma, the isotopic signatures of the two other Fe-Mn crusts are more complicated to understand. Data of Pb isotope highlight a strong impact of the Oligocene Himalayan erosion on the deep currents of the east of the Indian Ocean. The Nd and Pb values also show a combined influence of the Indonesian Island Arcs formation as well as the closing of the Indonesian seaway on the circulation and geochemical evolution of the intermediate and deep-water masses since the Miocene until present-day.

In this chapter (later submitted as a paper), we are going to complete this previous research, established in the Indian Ocean, by reconstructing the Nd and Pb isotope variations of the deep-water masses in the south-western (SW) part of the

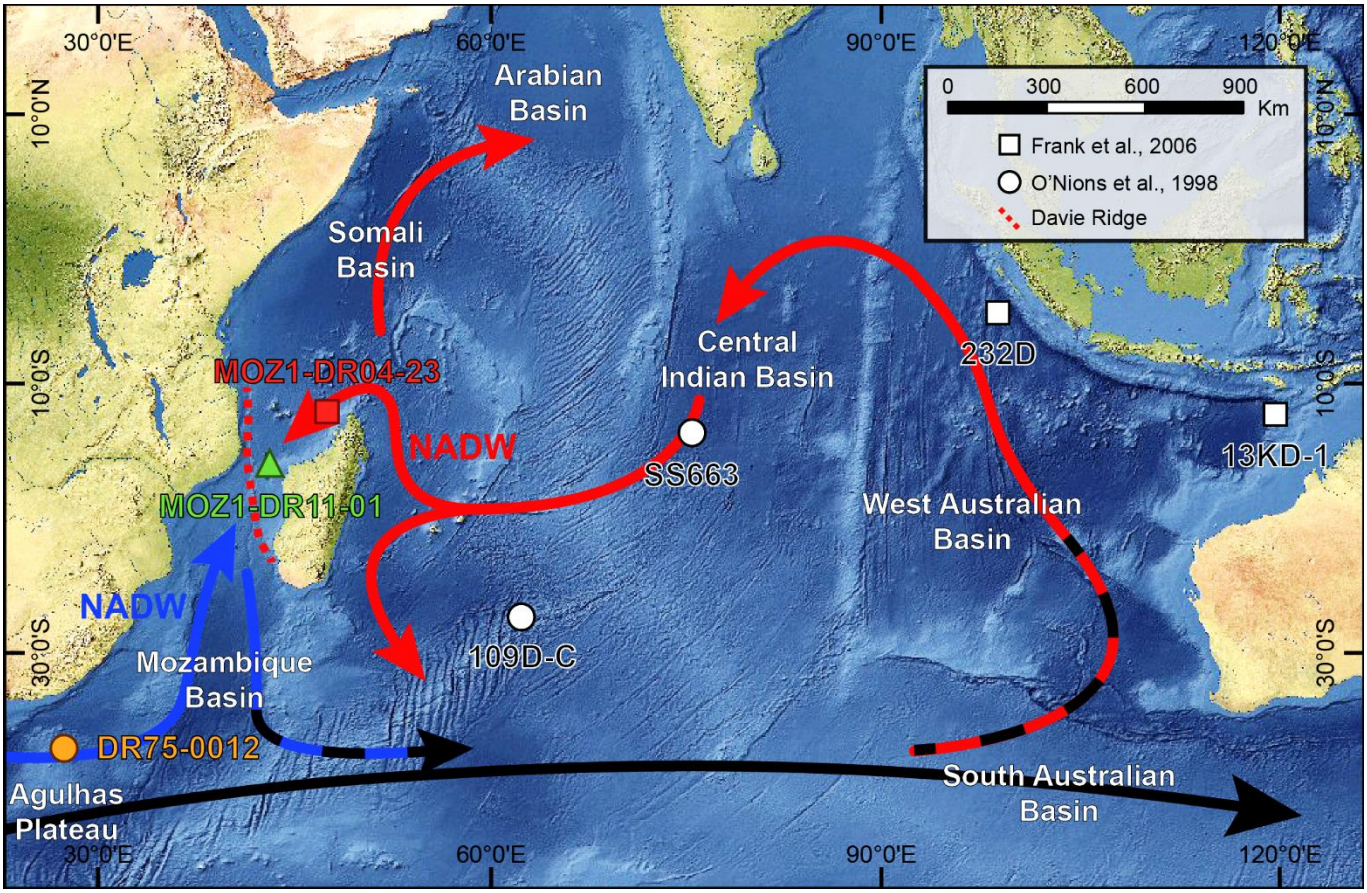

Figure 5.1. *Map of localisations of the samples 232D and 13KD-1 from Frank et al. (2006), SS663 and 109D-C from O'Nions et al. (1998) and, the Fe-Mn crusts studied in this work: MOZ1-DR04-23, MOZ1-DR11-01 and DR75-0012 dredged in the Mozambique Channel (SW Indian Ocean). The arrows indicate the main deep-water flow patterns according to Mantyla and Reid (1995).*

Indian Ocean. To do that, three Fe-Mn crusts were selected, all from the deep-waters. One is from the Agulhas Plateau located SW of the Africa continent, where the NADW arrive before to enter in the Mozambique Channel (Figure 5.1). A second crust is from the Jeffrey Ridge situated west of Madagascar and north of the main structure of the channel: the Davie Ridge, which may have blocked the deep currents over time (Chapter 4; Charles et al., in prep.). The last Fe-Mn is from the Glorieuses Island in the Comoros Basin, north of the Mozambique Channel (Figure 5.1). The Mozambique Channel is an interesting area due to the mixture of the water masses from the Atlantic into the Indian Ocean. North Atlantic Deep Current (NADW), which arrive near the Agulhas Plateau, presents low radiogenic compositions of Nd between -9 and -11, whereas the North Indian Deep Current (NIDW) from the Glorieuses Islands is characterized by more radiogenic Nd isotope signatures from -7 to -8.5 (Albarède and Goldstein, 1992; Bertram and Elderfield, 1993; Charles et al., 2020; Jeandel, 1993; Lacan et al., 2012; Rahlf et al., 2020; van de Flierdt et al., 2016).

Considering (1) the flows and (2) the chemical characteristics of the deep currents as well as (3) the geodynamic events appeared in the Mozambique Channel, the aim of this study is to develop a reconstruction of long-term variations of circulation patterns in the Mozambique Channel, SW Indian Ocean, since the Middle-Miocene.

5.3. Geological context

The Mozambique Channel is located in the SW Indian Ocean, bounded by the Mozambique continental slope to the west and the Madagascar continental margin to the east. Its present structure results from the break-up of the western part (South America and Africa) and the eastern part (Madagascar, Indian and Australia) of Gondwana super continent occurring between the Early Jurassic and the Early Cretaceous (Castelino et al., 2015; Coffin and Rabinowitz, 1987; Gaina et al., 2013; Leinweber and Jokat, 2012; Thompson et al., 2019). During this rifting, Madagascar was drifted southwards from Tanzania along a major transform zone: the Davie Fracture Zone (Coffin and Rabinowitz, 1987; Davis et al., 2016; Heirtzler and Burroughs, 1971).

Today, the Davie Ridge represents the witness of this major paleogeodynamic event with an orientation of N170 and a length of 1200 km from the east African to the SW Madagascar margins. This structure splits the Mozambique Channel in two distinct parts. (1) The Somali Basin in the north, which opened during southward drift of Madagascar (Ségoufin and Patriat, 1980; Davies et al., 2016). This old basin hosts the Comoros and the Glorieuses volcanic archipelagos since 10 Ma (Berthod et al., 2021; Emerick and Duncan, 1982; Michon, 2016; Nougier et al., 1986; Tzevahirtzian et al., 2021) which marked the northern boundary of the channel. (2) The Mozambique Basin in the south, which is one of the first oceanic basins of the Indian Ocean. It is bounded to the east by Madagascar and the Madagascar Ridge and, to the west by the Mozambique Ridge (Jacques et al., 2019). Further south at around 37°S, the Agulhas Plateau is situated SW of the Mozambique Ridge. This structure is about 750km long and 400km wide and, rises about 2500m above the surrounding ocean floor (Gohl and Uenzelmann-Neben, 2001).

Over time, several geodynamic phenomenon have affected the geography of the Mozambique Channel such as the development and the propagation of the East African Rift System (EARS) during the Paleogene (Chorowicz, 2005; Franke et al., 2015; McGregor, 2015; Mahanjane, 2014; Stamps et al., 2021). It certainly initiated a

major uplift event during the Oligocene (Leroux et al., 2020; Walford et al., 2005) at the origin of the emergence and the erosion of the Davie Ridge between at least 36 and 30 Ma (Courgeon et al., 2017; Masters et al., 2021). Then, an alternation of geodynamic vertical movements were identified thanks to seismology profiles, geomorphological interpretations, biostratigraphic reconstructions and Fe-Mn crust isotopic analyses. A first subsidence event was identified from the Late Oligocene to the Middle-Miocene (Leroux et al., 2020; McGrew, 1983), then a generalised uplift impacted the channel from Middle-Miocene to the Pliocene (Charles et al., in prep.; Delaunay, 2018) and finally, a subsidence phenomenon was highlighted during the Pliocene thanks to the study of Fe-Mn crusts and old carbonate platforms systems (Charles et al., in prep.; Courgeon et al., 2018).

5.4. Materials

The three Fe-Mn crusts (Figure 5.2) of this work were recovered in the Mozambique Channel during the PAMELA-MOZ1 cruise on board the RV L'Atalante (Olu, 2014) and the MD-06 Nosicaa expedition on board the RV Marion Dufresne (Leclaire, 1975) conducted by the National Museum of Natural History (MNHN). They all present a massive texture.

The northernmost sample MOZ1-DR04-23 is from the archipelago of the Glorieuses Islands and was dredged between 1780 and 2000 mbsl. The sample MOZ1-DR11-01 is from the Jeffrey Ridge emplaced north of the Davie Ridge and was recovered between 2400 and 2450 mbsl. Both of these samples have clearly well-defined millimetre scale Fe-Mn oxides layers represented by lighter coloured stratigraphic lines, however MOZ1-DR11-01 shows allochthones clasts between 40 and 70 mm of depth (Figure 5.2).

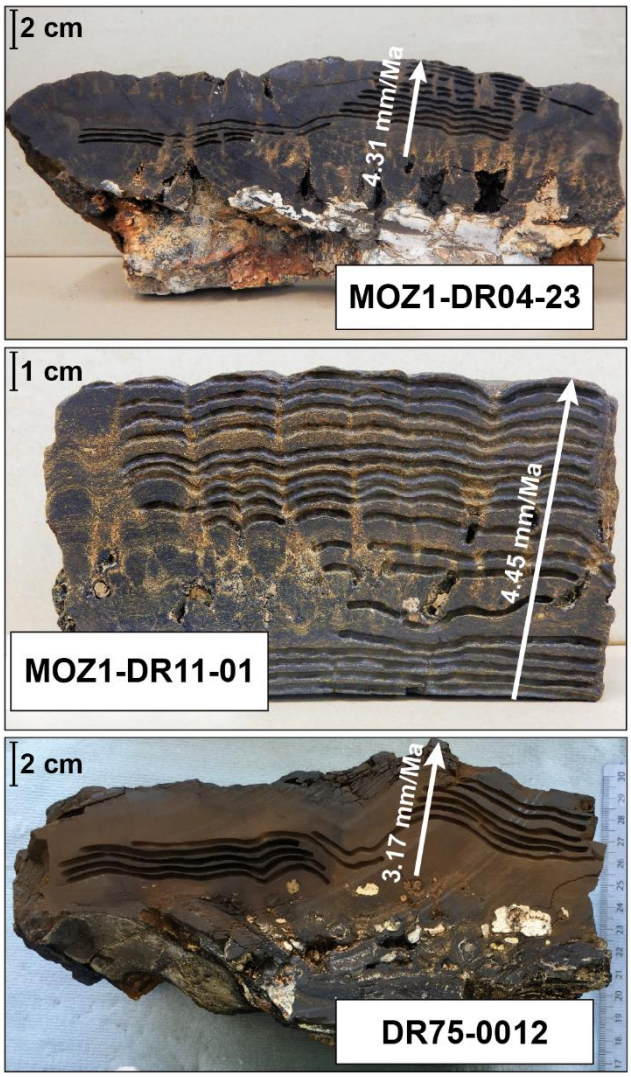

Figure 5.2. *Images of the three selected Fe-Mn crusts. They all present a planar shape and two of them (MOZ1-DR04-23, DR75-0012) show polygenic breach substrates.*

The southernmost sample DR75-0012 comes from the Agulhas Plateau at a depth of 2550 mbsl. Its colour is darker brown and the Fe-Mn oxides layers are discrete and difficult to distinct with naked eye. Their depths and locations offer the possibility to focus on the deep-water masses evolution from the low latitudes corresponding to the NIDW circulation to the high latitudes of the channel represented by the NADW. The three Fe-Mn crusts have respective thicknesses of 75, 83 and 50 mm (Figure 5.2, Table 5.1) and present

Table 5.1. *International Geo Sample Number (IGSN), location, depth and major characteristics of the studied Fe-Mn crusts from the PAMELA-MOZ1 (Olu, 2014) and MD-06 Nosicaa (Leclaire, 1975). The water masses correspond to the modern records of the analysed samples by Charles et al. (2020).*

Sample	MOZ1-DR04-23	MOZ1-DR11-01	DR75-0012
Cruise	PAMELA-MOZ1	PAMELA-MOZ1	MD- 06 Nosicaa
Dredge	DR04	DR11	DR75
IGSN	BFBG-169883	BFBG-155160	MNHN-GS-DR75-0012
Location	Glorieuses Islands	Jeffrey Ridge	Agulhas Plateau
Latitude	11◦28'S	16◦10'S	37◦32'S
Longitude	47◦32'E	42◦30'E	27◦00'E
Depth range (mbsl)	1780-2000	2400-2450	2550
Water mass (T_0)	NIDW	NIDW	NADW
Thickness (mm)	75	83	50
Layers	20	19	13
Average growth rate (mm/Ma)	4.31	4.45	3.17

unaltered surface and layers (Figure 5.2). All these details are presented in the table 5.1.

Based on visual textural delineation, 52 layers were meticulously sampled using a hand-held micro drill to obtain sub-samples along a profile perpendicular to the Fe-Mn oxides. All the process was presented in the study of Charles et al. (in prep.). Respectively 20, 19 and 13 layers were performed on MOZ1-DR04-23, MOZ1-DR11-01and DR75-0012 Fe-Mn crusts. The numbering of the layers is noted after the name of the sample. The number corresponds to the sampling depth (mm) in the thickness of the Fe-Mn crust. In the case of a surface subsample, -S is added.

The top sampling corresponds to the first 100 µm on the surface integrating between 20 and 80 ka (Charles et al., in prep., 2020; Frank et al., 2002). The other layers were performed underneath, over the entire thickness of the Fe-Mn crusts with a resolution of 2 to 5 mm between two layers (Figure 5.2). Their width varies between 0.5 and 2 mm integrating the different states of water mass geochemistry in the order of 150 to 550 ka, due to the slow accretion rates of the three Fe-Mn crusts. Charles et al. (in prep.) presented a Be-proxy age method, which was applied in this work to determine the chronology of the samples. Their mean growth rates vary between 3.17 (DR75-0012) to 4.45 (MOZ11-DR11-01) mm/Ma.

5.5. Methods

5.5.1. Mineralogy

The quantitative mineralogy of layers representative of the main macro layers was acquired using X-ray diffraction (XRD). Analyses were conducted with a BRUKER AXS D8 Advance diffractometer at the Laboratoire des

Cycles Géochimiques at IFREMER (Plouzané, France). Approximately 100 mg of each powdered and homogenised layer were top loaded into amorphous silica sample holders. All analyses were run between 5° and 70° 2θ, in steps of 0.01° 2θ at 1 s/step (monochromatic Cu Kα radiation, 40 kV, 30 mA). Minerals were identified using Diffrac suite EVA software. This methodology allows rapidly identifying most of the mineral species present in the studied Fe-Mn crusts (e.g. silicates, carbonates, phosphates, oxides, and well-crystallized oxyhydroxides). δ-MnO2 is barely visible on diffractograms even where it constitutes the main crystalline phase in most of studied samples. Estimation of the proportion of δ-MnO2 from other crystalline phases is made on the basis of a qualitative analysis of the diffractograms i.e. ratio between "vernadite" visible peaks (37° and 66° 2θ) and peak signal of other well crystallised minerals.

5.5.2. Geochemistry

All the following geochemical and analytical procedures were performed at the "Pôle Spectrométrie Océan" (PSO, Plouzané, France) from 100 mg of each layers. The preparation of the mother solutions is detailed by Charles et al. (2021). Major elements contents were determined by Inductively Coupled Plasma Atomic Emission Spectroscopy (ICP-AES) as described by Charles et al. (in prep.) following the method of Cotton et al. (1995). After Tm addition, trace and rare earth element (REE) concentrations were measured with a High-Resolution Inductively Coupled Plasma Mass Spectrometer (HR-ICP-MS). The procedure is described in the study of Charles et al. (2021) on the characterization of Fe-Mn oxide standards.

Isotopy. Chemical separation and purification methods for Nd and Pb are the same than those presented in the study of Charles et al. (2020), based on the Nd analytical procedure from Pin et al. (1994) and on the Pb chemistry procedure described in Gale (1996). Nd isotopes were measured by Thermal Ionisation Mass Spectrometry (TIMS) whereas Pb isotope ratios were measured by Multi-Collector Inductively Coupled Mass Spectrometry (MC-ICP-MS) using a Tl-doping method (White et al., 2000).

$^{10}Be/^{9}Be$ measurements were performed on 18 layers (6 layers for MOZ1-DR04-23; 9 layers for MOZ1-DR11-01; 3 layers for DR75-0012) to focus on the first 10 Ma of the studied Fe-Mn crusts (^{10}Be half-life T1/2 = 1.387 ± 0,012 Ma according to Chmeleff et al. (2010), Korschinek et al. (2010) and Nishiizumi et al. (2007)). The procedure is described by Charles et al. (2022) according to the protocol of Bourlès et al. (1989) and Simon et al. (2016). ^{9}Be concentrations were measured using an Atomic Absorption Spectrophotometer (AAS) and ^{10}Be contents were measured at the French Accelerator Mass Spectrometer (AMS) national facility ASTER (CEREGE).

5.6. Results

5.6.1. Petrology and mineralogy

The studied Fe-Mn crusts consist mainly of poorly crystalline oxides. The results of X-ray diffraction (Appendix 5 – MOZ1-DR04-23) present no distinct crystalline Mn phase characteristic of diagenetic or hydrothermal remobilisation (e.g. 10 Å manganate, pyrolusite). Though it is very difficult to provide a semi-quantitative estimate of the mineral phases, the diffractograms show that δ-MnO_2 (possibly Fe-vernadite) can be considered as the dominant Mn oxides phase with detectable peaks around 2.45 and 1.42 Å. Quartz is the main allochtonous mineral phase detected, whereas other detrital

minerals such as plagioclase and K-feldspar and biogenic phase (e.g. calcite) are in low contents (when present). These three Fe-Mn crusts do not present diagenetic minerals such as carbonate fluorapatite (CFA). These results are in accordance with nonphosphatized geochemistry samples (Benites et al., 2020; Mizell et al., 2020).

5.6.2. Age-depth modelling

$^{10}Be/^{9}Be$ analyses for 18 layers of the samples are presented in the figure 5.3, showing the $^{10}Be/^{9}Be$ profiles for the three Fe-Mn crusts, and in the table 5.2. The Be ratios of the surfaces of the samples MOZ1-DR04-23 and DR75-0012 present respective values of 6.7 and 7.6 $\times 10^{-8}$. These data are in good agreement with other surface values in the Indian Ocean including the Fe-Mn crusts 13KD-1 and 232D (Frank et al., 2006; von Blanckenburg et al., 1996) and marine sediments (Bourlès et al., 1989), indicating that the topmost layer reflects the actual growth surface.

5.6.2.1. $^{10}Be/^{9}Be$ extrapolated

The decrease in Be ratio with depth in the Fe-Mn crust MOZ1-DR04-23 corresponds to an average growth rate of 3.91 mm/Ma and an age of 16.2 Ma at a depth of 70 mm. The methodology consist of an extrapolation of the last measured growth rate (layer MOZ1-DR04-23 11; 5.10 mm/Ma) to the next layers until MOZ1-DR04-23 30 whose $^{10}Be/^{9}Be$ ratio has been measured. Its growth rate is 4.5 mm/Ma and is then extrapolated to the base of the Fe-Mn crust. This procedure is justified because there are no structural changes visible in the Fe-Mn crust (Figure 5.2) and because the measured growth rates do not reflect major fluctuation.

This methodology is as close to reality as possible because it is the last growth rate that is considered and the intervals in which it is applied are relatively small (short period).

The same extrapolation is done for the crust DR75-0012. Even though, the average growth rate of the Fe-Mn crust DR75-0012 is 2.7 mm/Ma, we preferred using the last rate calculated from Be isotopes (i.e. 3.4 mm/Ma at 6.7 Ma) to provide an age of 15.2 Ma (Table 5.2).

Table 5.2. *Results of $^{10}Be/^{9}Be$ isotope analyses and age determination with the extrapolation of the last measured growth rate (GR) for the three studied Fe-Mn crusts. –S indicates the surface layer and the other numbers are related to their depths on the Fe-Mn crust slice. The * show the layers whose Be isotopes have been measured.*

MOZ1-DR04-23 Glorieuses Islands	**$^{10}Be/^{9}Be$ (10^{-8})**	**GR (mm/Ma)**	**Age (Ma)**	**Error (Ma)**
MOZ1-DR04-23 S*	6.7	-	0.0	-
MOZ1-DR04-23 2*	4.3	2.3	0.88	0.05
MOZ1-DR04-23 5*	3.1	4.6	1.53	0.08
MOZ1-DR04-23 7*	2.3	3.1	2.2	0.1
MOZ1-DR04-23 11*	1.5	5.1	3.0	0.2
MOZ1-DR04-23 15			*3.7*	
MOZ1-DR04-23 18			*4.3*	
MOZ1-DR04-23 22			*5.1*	
MOZ1-DR04-23 26			*5.9*	
MOZ1-DR04-23 30*	0.2	4.5	7.2	0.4
MOZ1-DR04-23 33			*7.9*	
MOZ1-DR04-23 38			*9.0*	
MOZ1-DR04-23 41			*9.7*	
MOZ1-DR04-23 45			*10.6*	
MOZ1-DR04-23 48			*11.3*	
MOZ1-DR04-23 53			*12.4*	
MOZ1-DR04-23 58			*13.5*	
MOZ1-DR04-23 62			*14.4*	
MOZ1-DR04-23 68			*15.3*	
MOZ1-DR04-23 70			*16.2*	

MOZ1-DR11-01				
Jeffrey Ridge				
MOZ1-DR11-01 S*	7.4	-	0.0	-
MOZ1-DR11-01 2*	6.5	8.9	0.23	0.01
MOZ1-DR11-01 6*	3.5	6.0	0.98	0.08
MOZ1-DR11-01 11*	2.3	5.1	1.9	0.2
MOZ1-DR11-01 14*	1.5	3.6	2.7	0.2
MOZ1-DR11-01 19*	1.0	6.1	3.5	0.2
MOZ1-DR11-01 21*	0.7	2.9	4.2	0.3
MOZ1-DR11-01 25*	0.5	7.8	4.7	0.3
MOZ1-DR11-01 28*	0.4	3.7	5.5	0.4
MOZ1-DR11-01 32			*6.6*	
MOZ1-DR11-01 39			*8.5*	
MOZ1-DR11-01 45			*10.1*	
MOZ1-DR11-01 49			*11.2*	
MOZ1-DR11-01 59			*13.9*	
MOZ1-DR11-01 67			*16.1*	
MOZ1-DR11-01 70			*16.9*	
MOZ1-DR11-01 74			*18.0*	
MOZ1-DR11-01 77			*18.8*	
MOZ1-DR11-01 80			*19.6*	
DR75-0012				
Agulhas Plateau				
DR750-012 S*	7.6	-	0.0	-
DR75-0012 3			*1.5*	
DR75-0012 8*	1.0	2.0	4.0	0.3
DR75-0012 12			*6.1*	
DR75-0012 17*	0.3	3.4	6.7	0.4
DR75-0012 21			*7.9*	
DR75-0012 23			*8.4*	
DR75-0012 28			*9.9*	
DR75-0012 34			*11.7*	
DR75-0012 37			*12.6*	
DR75-0012 40			13.4	
DR75-0012 43			*14.3*	
DR75-0012 46			*15.2*	

The chronology of the Fe-Mn crust MOZ1-DR11-01 was more difficult to establish due to its measured surface $^{10}Be/^{9}Be$ ratio (5.8×10^{-8}) lower than that measured at a depth of 2 mm (6.5×10^{-8}) (Figure 5.3, Table 5.2). This result is not in accordance with the fact that the initial authigenic $^{10}Be/^{9}Be$ ratio (top of the sample) is the starting point for radioactive decay losses (Chapter 2). From these results, several questions may arise.

We have to understand why the surface measurement is lower than that measured at a depth of 2 mm. The sampling is meticulously done on the surface of the botryoidal texture in order to obtain a maximum of powder. The first hypothesis to consider is that the surface of MOZ1-DR11-01 reflects areas of erosion. This would have made it possible to sample lower and older layers. This hypothesis should not be forgotten because even if a petrographic analysis is carried out beforehand, it is still possible to hit weathered parts of the surface sample during sampling. The second hypothesis is to consider a problem or an error during the analytical process. Although this hypothesis can never be rejected, it seems unlikely as this sample was processed together with other samples showing no discrepancies. This sample would need to be re-analysed to validate the data.

Considering an eroded surface, the higher ratio (6.5×10^{-8} from the layer MOZ1-DR11-01 2) was first chosen as the initial authigenic $^{10}Be/^{9}Be$ ratio. The obtained age for the surface layer is oldest than 0 Ma (0.23 Ma). It results an average growth rate of 5.23 mm/Ma and an age of 19.7 Ma at a depth of 80 mm with an extrapolation of the last measured growth rate (layer MOZ1-DR11-01 28; 3.70 mm/Ma) to the base of the sample. However, this choice implies that MOZ1-DR11-01 2 corresponds to the surface and it is clear on the Fe-Mn crust MOZ1-DR11-01 (Figure 5.2) that matter overhangs the layer MOZ1-DR11-01 2. Therefore, in a second step, the $^{10}Be/^{9}Be$ ratio on the surface was estimated according to the equation of the line passing through the measured

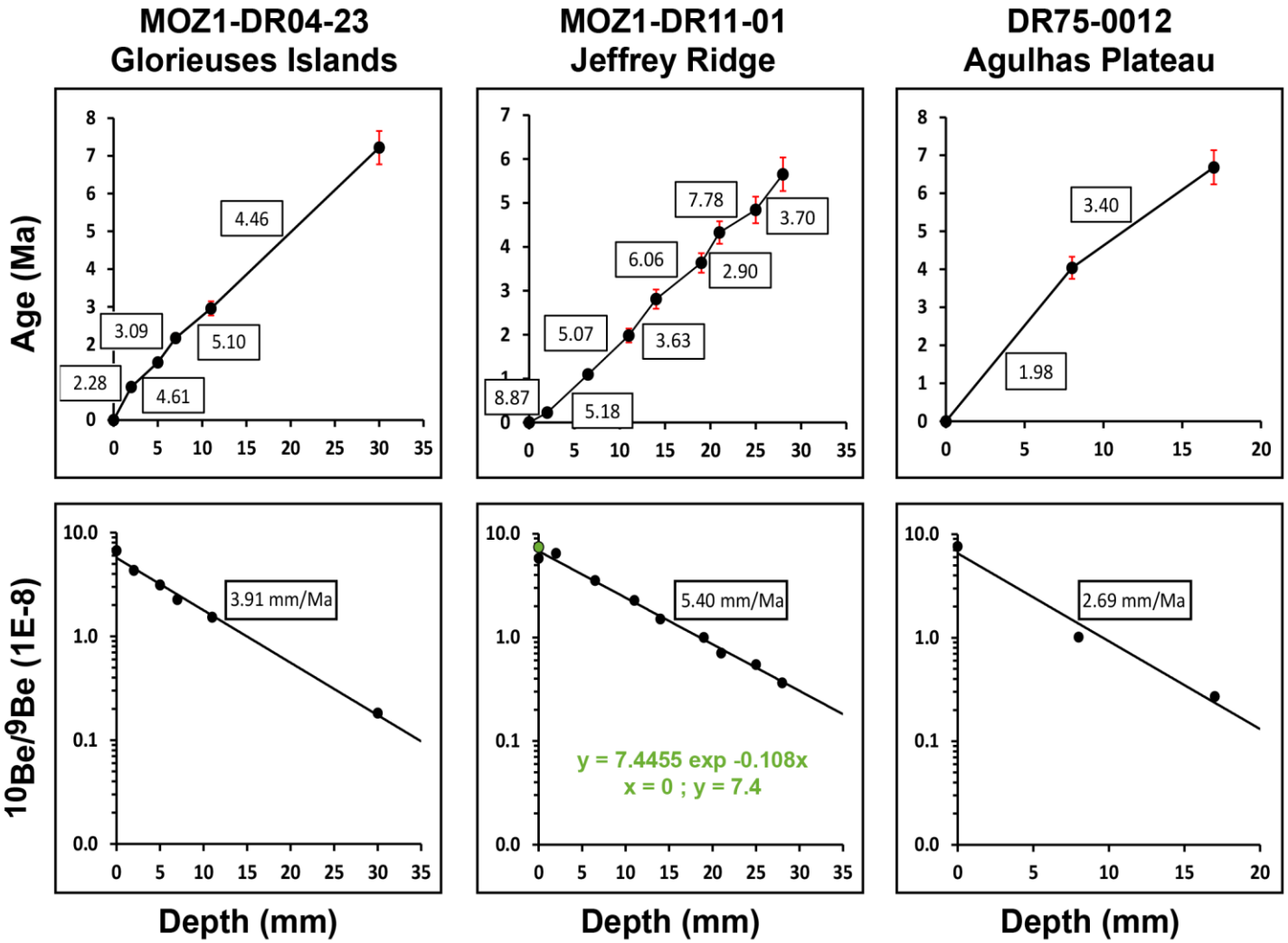

Figure 5.3. *The $^{10}Be/^{9}Be$ ratios in the crusts MOZ1-DR04-23, MOZ1-DR11-01 and DR75-0012 versus depth beneath the growth surfaces. The ages have been calculated from the radioactive decay of the Be in the samples. The growth rates and ages beyond the age ranges covered by $^{10}Be/^{9}Be$ values were calculated using the extrapolation of the growth rates of the deepest layers whose $^{10}Be/^{9}Be$ values were measured.*

$^{10}Be/^{9}Be$ ratios (without the erroneous surface value). It results a ratio of 7.4×10^{-8} (Figure 5.3), an average growth rate of 5.50 mm/Ma and an age of 19.6 Ma (Table 5.2). This estimate and its results are the most consistent and finally this choice was considered for the age model of the Fe-Mn crust MOZ1-DR11-01.

5.6.2.2. Other methods

However, an independent method was developed by Manheim (1986) to estimate growth rates (GR) of Fe-Mn crusts beyond 10 Ma, based on their Co concentration. In figure 5.4, the age-depth relationship of the three studied Fe-Mn crusts are presented considering Co-content equations of:

(1) Manheim (1986), where [Co] is the Co concentration in wt%:

$$GR\ (mm/Ma) = \frac{0.68}{[Co]^{1.67}} \qquad (1)$$

(2) Manheim and Lane-Bostwick (1988), where [Co] is the Co concentration in wt% and, [Fe] and [Mn] the Fe and Mn concentrations also in wt%:

$$GR\ (mm/Ma) = \frac{0.68}{\left([Co] \times \left(\frac{50}{[Fe] + [Mn]}\right)\right)^{1.67}} \quad (2)$$

(3) Frank et al. (1999), where [Co] is the Co concentration in wt%:

$$GR\ (mm/Ma) = \frac{0.25}{[Co]^{2.69}} \qquad (3)$$

The obtained ages are compared with the «$^{10}Be/^{9}Be$ extrapolated» chronology established before (section 5.6.2.1).

The equation of Manheim, Lane-Bostwick (1988) appears to provide older ages for the three Fe-Mn crusts (MOZ1-DR04-23: 35.4 Ma; MOZ1-DR11-01: 28.7 Ma; DR75-0012: 18.4 Ma) than the extrapolation and calibration methods (Figure 5.4). It can be link to the high Fe and Mn contents taken in account, which certainly decrease the growth rates and inflate the ages. In the case of the Fe-Mn crust DR75-0012, the oldest age (22.3 Ma) is estimated from the equation developed by Frank et al. (1999) (Figure 5.4). For this sample, the equation is no adaptable because the layer DR75-0012 2 present a Co abundance of more than 1%, whereas Frank et al. (1999) tested this equation for Co-poor Fe-Mn crust. However, they did not finally retain this relationship for their chronologies.

The equation derived from Co-content of Manheim (1986) presents the closest Co-chronology to $^{10}Be/^{9}Be$ extrapolated chronology (MOZ1-DR04-23: 21.8 Ma; MOZ1-DR11-01: 13.2 Ma; DR75-0012: 13.4 Ma) (Figure 5.4). Knowing that Co-flux is assumed to have been constant and seeing the growth rates acquired from the equation of Manheim (1986) are the most similar with those from the $^{10}Be/^{9}Be$ analyses, this relationship was used to calculate «$^{10}Be/^{9}Be$ calibrated» chronology. It involves applying the age model acquired from the $^{10}Be/^{9}Be$ analyses in the upper part of the Fe-Mn crusts and continuing with an age model calculated from the Manheim (1986) equation (1) in the lower part of the Fe-Mn crusts (where no $^{10}Be/^{9}Be$ ratios were analysed). The results of the «$^{10}Be/^{9}Be$ calibrated» Co chronology are visible on the figure 5.4. The ages of the samples MOZ1-DR04-23, MOZ1-DR11-01 and DR75-0012 are respectively 19.2, 15.8 and 15.0 Ma. The resulted chronology of the Fe-Mn crust DR75-0012 is

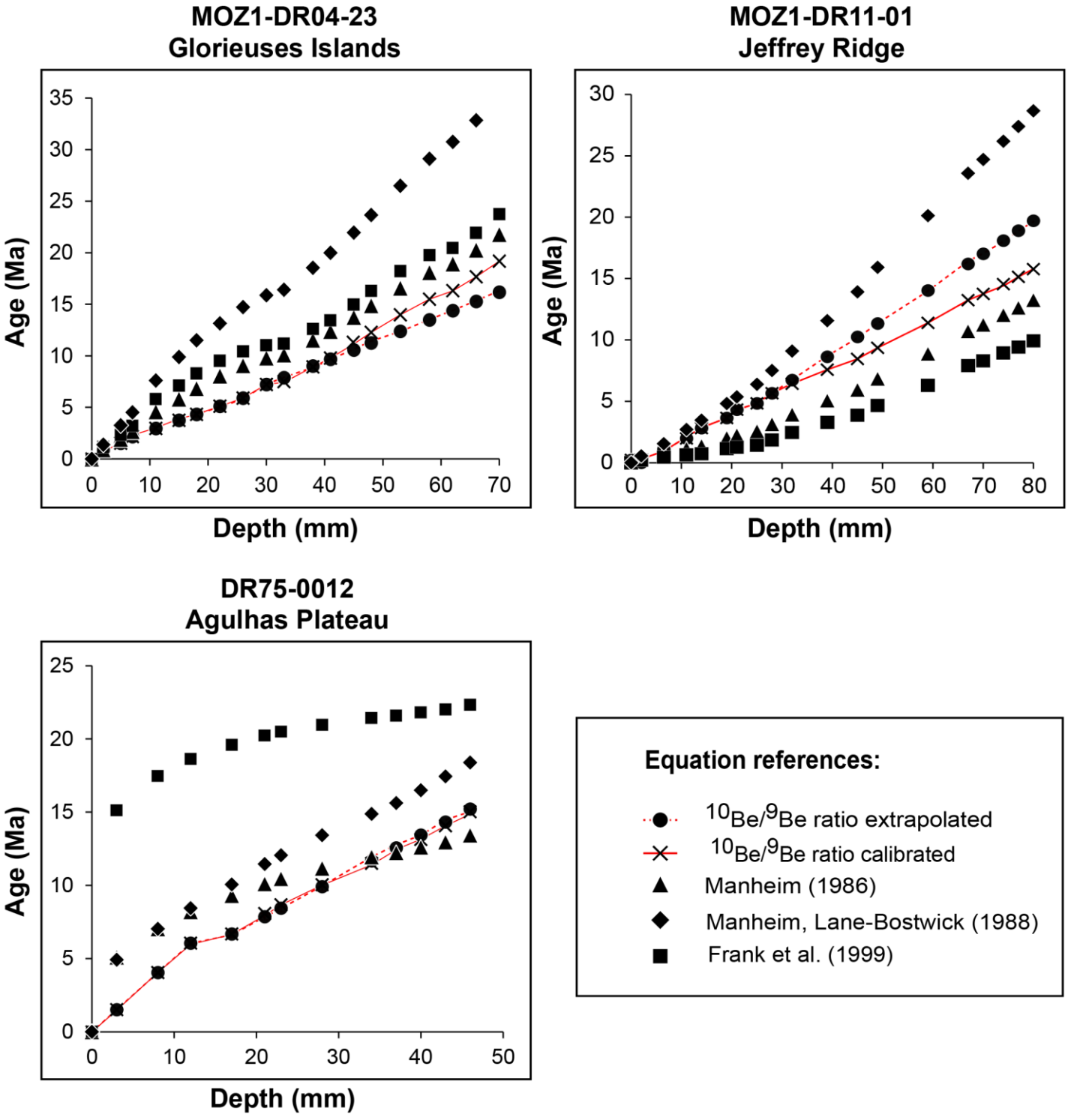

Figure 5.4. *Evaluation of the relationship between the ages (Ma) and the depths (mm) for the studied Fe-Mn crusts presenting a combination of $^{10}Be/^{9}Be$ and Co based calculations. The dashed line corresponds to the chronology acquired by extrapolation of the last growth rate from $^{10}Be/^{9}Be$ measurements, whereas the solid line is the $^{10}Be/^{9}Be$ calibrated Co chronology. The other data are Co chronology established with different equations from Frank et al. (1999), Manheim (1986) and Manheim and Lane-Bostwick (1988).*

satisfying. However, the ages obtained for the two other samples are either higher (MOZ1-DR04-23) or lower (MOZ1-DR11-01) than the «^{10}Be/^{9}Be extrapolated» chronology. Due to the lack of a homogenous observation (over, under, similar) resulted from this methodology, the model age finally adopted consists of the «^{10}Be/^{9}Be extrapolated» chronology.

Although the dating with Be isotopes is absolute for the first part of the chronologies, the final ages have to be considered with caution. The extrapolation methodology cannot account for occurrence of hiatuses in the oldest parts of the Fe-Mn crusts and the recently protocol developed with the Os isotope evolution (Klemm et al., 2008, 2005) has not yet been applied to the studied samples.

5.6.3. Major and minor elements

The concentrations of major and minor elements of the Fe-Mn crusts layers (n=52) have limited variations for Fe-Mn crusts (Table 5.3). Iron and manganese have the largest variations ranging from 13.31 (MOZ1-DR11-01 14) to 23.73 wt% (DR75-0012 12) with a mean value of 18.86 wt% and from 9.80 (MOZ1-DR11-01 14) to 27.72 wt% (DR75-0012 3) with a mean value of 16.49 wt%, respectively. Fe/Mn ratios range from 0.84 to 1.89 with a mean value of 1.18 (n=52), an intermediate ratio between open-ocean seamount Fe-Mn crusts and continental margin seamount Fe-Mn crusts (Conrad et al., 2017; Hein et al., 1997; Josso et al., 2020; Mizell et al., 2020b; Muiños et al., 2013).

Alumina and potassium which represent minor detrital phase (e.g. plagioclase, K-feldspar) vary from 0.84 to 3.62 wt% and from 0.37 to 1.40 wt% respectively. Highest Al and K concentrations are recorded for deeper layers (> 45mm) of the hydrogenetic Fe-Mn crusts dredged at the Glorieuses Islands (MOZ1-DR04-23 68, Al_{max} = 3.29, K_{max} = 1.06) and Jeffrey Ridge (MOZ1-DR11-01 45, Al_{max} = 3.62, K_{max} = 1.40). The third Fe-Mn crust systematically exhibit Al and K contents lower than 2.61 and 0.79 wt% respectively (DR75-0012 37). Phosphorous contents are relatively low and do not show high variability (from 0.25 to 0.60 wt%). The highest content is measured in the surface layer of DR75-0012. The mean P concentrations of about 0.37 wt% (n=52) does not reflect any intense phosphatisation phenomenon either in the upper (modern) or deeper (older) parts of the samples as observed by Benites et al. (2020) in the SW Atlantic or Josso et al. (2019) the NE Atlantic Fe-Mn crusts and dated to the Late Eocene. Calcium concentrations range from 1.22 to 3.52 wt% with a mean of 1.83 wt%, and the highest contents are most likely related to the presence biogenic phases. Titanium present a variation from 0.44 to 2.19 wt% and can be used to evaluate a potential hydrothermal impacts with the Ti index calculation (Strakovh, 1974). Ti index values range from 16 (MOZ1-DR04-23 33) to 72 (DR75-0012 8) with an average value of 52 (n = 52). These data fall perfectly in the range of reported data for hydrogenetic Fe-Mn crusts (Figure 5.5), significantly lower than in hydrothermal Fe-Mn crusts presented values up to more than 4000 (Josso et al., 2020).

Table 5.3. *Chemical characterisation of the three studied Fe-Mn crusts. The data correspond to the means of the elements. The standard deviations (SD) are also provided to represent a complete vision of the ranges.*

Sample and details	MOZ1-DR04-23 Glorieuses Islands 11◦28'S - 47◦32'E		MOZ1-DR11-01 Jeffrey Ridge 16◦10'S - 42◦30'E		DR75-0012 Agulhas Plateau 37◦32'S - 27◦00'E	
Subsamples	20	*SD*	19	*SD*	13	*SD*
Fe (wt%)	19.78	*1.72*	16.64	*1.42*	20.15	*2.56*
Mn	17.62	*1.78*	14.24	*2.24*	17.06	*5.00*
Fe/Mn	1.14	*0.21*	1.19	*0.15*	1.23	*0.20*
Al	2.16	*0.60*	2.27	*0.54*	1.90	*0.68*
Ca	2.03	*0.37*	1.64	*0.22*	1.76	*0.65*
Mg	1.02	*0.06*	0.91	*0.09*	0.95	*0.16*
Na	1.52	*0.14*	1.62	*0.21*	1.48	*0.10*
K	0.74	*0.16*	0.87	*0.22*	0.60	*0.17*
Ti	0.90	*0.35*	0.56	*0.08*	0.68	*0.19*
P	0.40	*0.03*	0.31	*0.03*	0.41	*0.09*
Ba (ppm)	1330	*215*	1359	*228*	1214	*167*
Be	8.35	*1.61*	6.44	*1.81*	9.16	*1.46*
Bi	5.7	*1.0*	11.5	*2.1*	14.0	*5.7*
Co	3950	*693*	2603	*536*	3610	*2362*
Cr	21.4	*4.8*	20.6	*4.7*	18.9	*5.6*
Cs	0.46	*0.22*	0.45	*0.11*	0.41	*0.16*
Cu	429	*102*	531	*166*	471	*77*
Ga	4.5	*1.1*	5.2	*1.0*	3.6	*1.0*
Hf	12.78	*1.81*	3.42	*1.54*	10.38	*1.98*
Li	8.7	*3.4*	9.0	*6.4*	5.8	*2.0*
Mo	400	*76*	396	*108*	447	*139*
Nb	93.4	*19.3*	61.6	*12.9*	56.1	*10.3*
Ni	2046	*422*	1820	*390*	1549	*603*
Pb	1188	*70*	1196	*174*	1472	*454*
Rb	16.4	*5.1*	21.7	*5.9*	16.0	*6.7*
Sc	10.6	*1.1*	8.9	*0.7*	10.1	*0.8*
Sn	3.0	*0.3*	3.3	*1.6*	4.3	*0.6*
Sr	1045	*67*	1013	*110*	1019	*254*
Ta	2.21	*1.11*	0.71	*0.28*	0.60	*0.10*
Th	73.4	*22.9*	57.4	*19.5*	46.7	*14.4*
Tl	19	*10*	63	*34*	53	*16*
U	9.1	*1.0*	7.8	*0.8*	9.3	*2.5*
V	580	*50*	572	*85*	703	*129*
W	55	*9*	54	*12*	60	*20*
Zn	516	*149*	535	*123*	462	*67*
Zr	576	*67*	244	*91*	379	*39*

La	236.7	*24.3*	228.3	*35.2*	240.5	*59.6*
Ce	1844.6	*200.9*	1768.2	*335.9*	1503.4	*205.1*
Pr	56.1	*9.4*	45.7	*8.2*	55.4	*8.6*
Nd	215.7	*33.2*	178.7	*28.6*	235.5	*57.0*
Sm	40.53	*6.02*	35.52	*5.87*	42.53	*8.99*
Eu	9.61	*1.44*	7.81	*2.23*	9.17	*3.33*
Gd	41.3	*5.3*	33.0	*9.1*	42.7	*17.1*
Tb	5.93	*0.80*	4.88	*1.35*	5.91	*2.28*
Dy	35.3	*4.4*	28.6	*7.7*	37.0	*14.7*
Y	125.5	*14.4*	114.4	*16.7*	146.3	*43.9*
Ho	6.95	*0.79*	5.70	*1.51*	7.28	*2.96*
Er	18.77	*1.89*	15.53	*4.12*	19.41	*7.76*
Yb	17.20	*1.42*	14.11	*3.68*	17.18	*6.77*
Lu	2.53	*0.18*	2.12	*0.55*	2.46	*0.98*
ΣREY	2657	*258*	2489	*404*	2376	*396*
La/Sm	0.91	*0.06*	1.00	*0.07*	0.87	*0.05*
Gd/Yb	1.20	*0.09*	1.17	*0.13*	1.24	*0.07*
Y/Ho	0.70	*0.05*	0.73	*0.09*	0.72	*0.02*
Ce/Ce*	3.89	*0.41*	4.17	*0.35*	3.19	*0.36*
Eu/Eu*	1.24	*0.02*	1.24	*0.02*	1.19	*0.03*

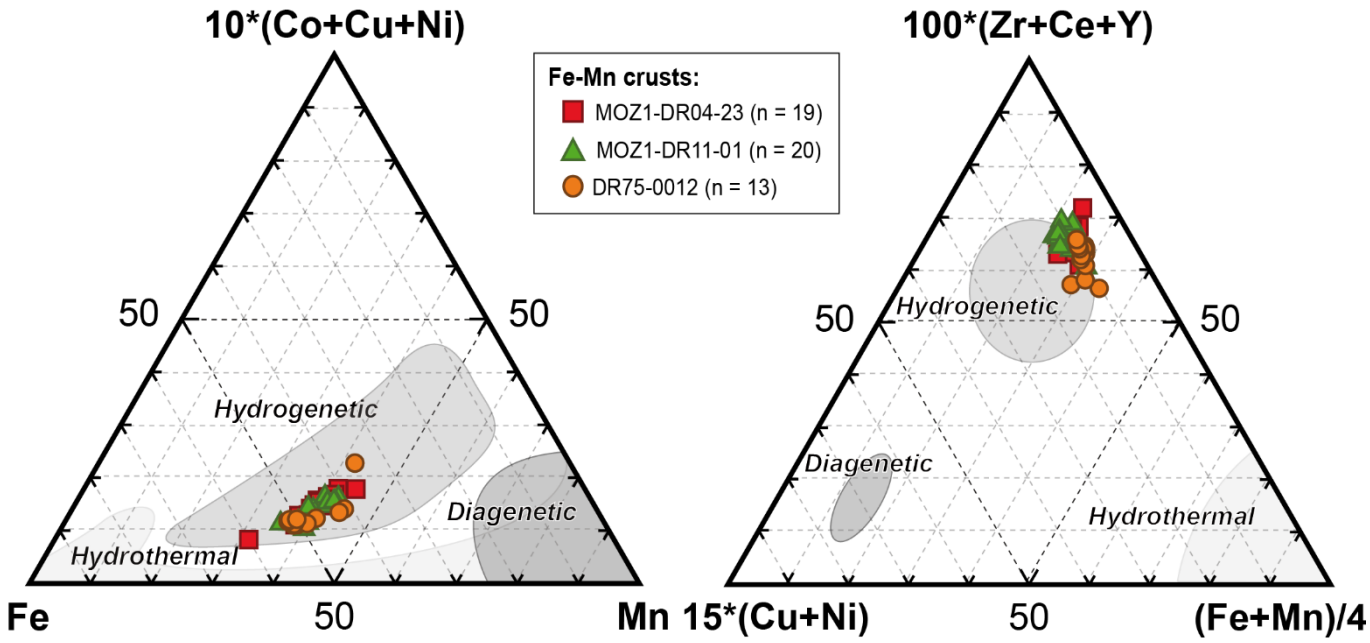

Figure 5.5. *Ternary discriminative diagrams for oceanic deposits highlighting the hydrogenetic nature of all the layers (n) from each Fe-Mn crust of this work. The diagram on the left is from Bonatti et al. (1972) and the one on the right is from Josso et al. (2017).*

5.6.4. Metal and trace elements

Cobalt shows minimum contents of 1981 (MOZ1-DR04-23 33), 1624 (MOZ1-DR11-01 14) and 1990 ppm (DR75-0012 37) whereas the maximum are 5088 (MOZ1-DR04-23 11), 3296 (MOZ1-DR11-01 67) and 10897 ppm (DR75-0012 3) respectively. This metal has a mean concentration of 3372 ppm (n=52). Copper presents minimum contents of 624 (MOZ1-DR04-23 70), 300 (MOZ1-DR11-01 S) and 275 ppm (DR75-0012 S) whereas the maximum are 229 (MOZ1-DR04-23 S), 729 (MOZ1-DR11-01 77) and 597 ppm (DR75-0012 8) respectively. Its average concentration is 476 ppm (n=52). Nickel exhibits minimum contents of 968 (MOZ1-DR04-23 33), 1037 (MOZ1-DR11-01 14) and 1270 ppm (DR75-0012 43) whereas the maximum are 2926 (MOZ1-DR04-23 70), 2543 (MOZ1-DR11-01 59) and 3762 ppm (DR75-0012 3) respectively. It presents a mean value of 1981 ppm (n=52). The sum of Co + Cu + Ni shows a maximum of 1.48 wt% (DR75-0012 3) with a mean of 0.57 wt%. These results and the Fe/Mn ratios are consistent with a predominantly hydrogenetic origin of the three studied Fe-Mn crusts (Figure 5.5), and confirm geochemical compositions between those of open-ocean and continental margin Fe-Mn crusts (Koschinsky and Halbach, 1995).

Trace elements present various abundances. Rubidium shows the narrower range of values from 5.1 (DR75-0012 3) to 35.9 ppm (MOZ1-DR11-01 45) with small standard deviations (SD) between 5.1 and 6.7. Thorium, niobium and thallium present three similar intervals of values, with minimum contents of 28.0 (DR75-0012 8), 38.4 (DR75-0012 8) and 6 ppm (MOZ1-DR04-23 30), and maximum concentrations of 113.5 (MOZ1-DR04-23 68), 118.6 (MOZ1-DR04-23 68) and 117 ppm (MOZ1-DR11-01 80), respectively. Th mean is 61 ppm (n=52), coherent with the Th average in the Indian Fe-Mn crusts (Hein et al., 2012; Hein and Koschinsky, 2014). The higher SD of these three elements is 34 for Tl (MOZ1-DR11-01). The results of zirconium are comprised between 125 (MOZ1-DR11-01 80) and 773 ppm (MOZ1-DR04-23 33) with SD from 39 to 91. With closer variability than Zr, zinc shows values from 344 (MOZ1-DR11-01 45) to 1077 ppm (MOZ1-DR04-23 33) and SD between 67 and 149. Lead results exhibit the largest set of values with a minimum of 870 ppm (MOZ1-DR11-01 25) and a maximum of 2300 ppm (DR75-0012 3) showing SD that extends to 454 for the Fe-Mn crust DR75-0012 (Table 5.3). Trace elements data are consistent with those of Hein et al. (2012) acquired in Fe-Mn crusts collected from Shatsky Rise (NW Pacific).

5.6.5. Rare earth elements + Y

The analysed Fe-Mn layers highlight high concentrations in REY ranging from 1830 (DR75-0012 37) to 3333 ppm (MOZ1-DR11-01 74) with a mean value of 2526 ppm (n=52). These contents are controlled by very high cerium values up to 2446 ppm (MOZ1-DR11-01 74) and an average value of 1731 ppm (n=52). The Ce means of the three Fe-Mn crusts vary between 1503 (DR75-0012) and 1845 ppm (MOZ1-DR04-13).

According to the PAAS-normalized (Pourmand et al., 2012; Taylor and McLennan, 1985) REE and Y patterns (Figure 5.6), the Fe-Mn layers present elementary ratios such as La/Sm [$(La/Sm)_{PAAS}$ = 0.79-1.13] with means between 0.87 (DR75-0012) and 1.00 (MOZ1-DR11-01), and Gd/Yb [$(Gd/Yb)_{PAAS}$ = 1.03-1.40] with means of the three Fe-Mn samples between 1.17 (MOZ1-DR11-01) and 1.24 (DR75-0012) indicating the enrichment of the heavy REE in the hydrogenetic Fe-Mn crusts (Table 5.3, Figure 5.5, 5.6). Additionally, MOZ1-DR04-23 and MOZ1-DR11-01 show higher heavy REE contents in the

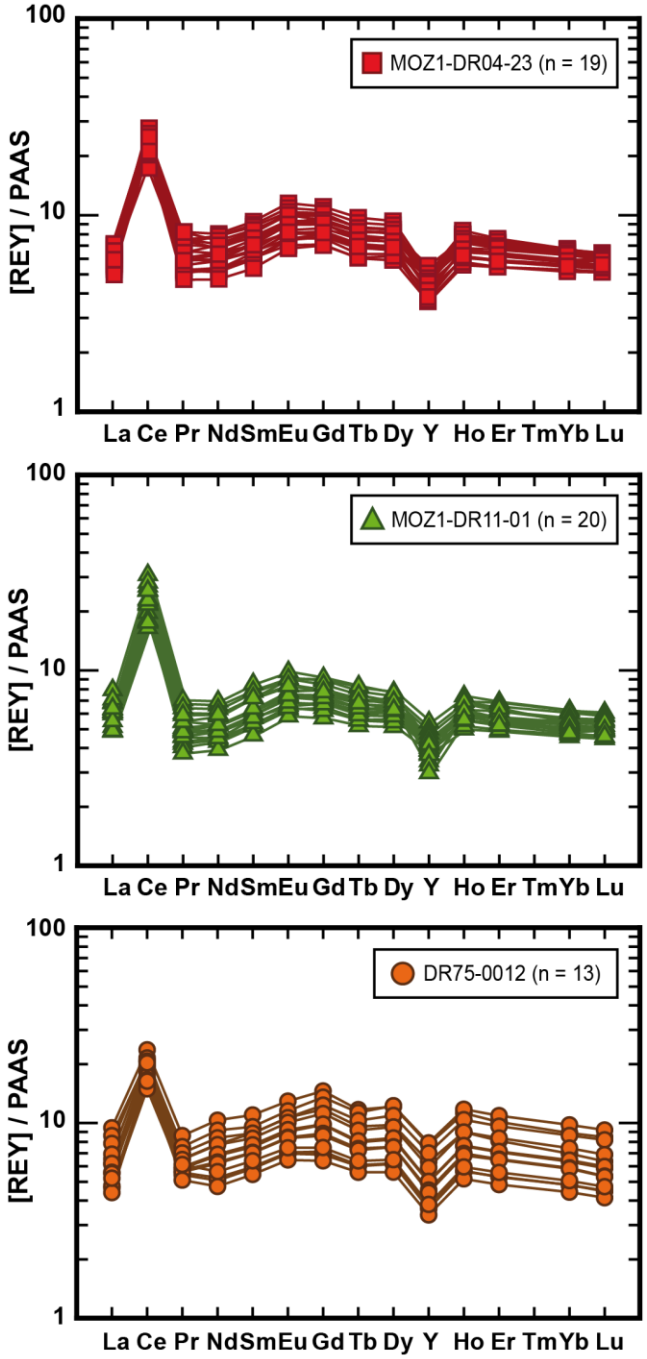

Figure 5.6. *PAAS-normalised (Pourmand et al., 2012; Taylor and McLennan, 1985) REY compositions of the three studied Fe-Mn crusts with all their respective layers (n).*

deepest layers (> 26 mm and > 59 mm, respectively) than in surface layers. The sample DR75-0012 do not present this observation. Its higher concentrations in heaver REE are located near the surface (< 8 mm). The Ce anomaly was calculated as:

$$Ce/Ce^{*} = \frac{Ce_{PAAS}}{(La_{PAAS} \times Pr_{PAAS})^{1/2}} \qquad (4)$$

Ce anomalies vary from 2.53 (DR75-0012 S) to 4.80 (MOZ1-DR11-01 45) in all the layers. The Fe-Mn crust MOZ1-DR11-01 shows the highest mean (4.17) whereas DR75-0012 presents the less pronounced Ce anomaly mean (3.19). The presence of positive Ce anomalies is caused by scavenging of Ce from seawater by hydrous Fe-Mn oxides (Elderfield et al. 1981; Goldberg et al. 1963) and its preferential retention relative to the other REE in the oxide phase through surface oxidation (Bau, 1996). Finally, small Y anomaly is also present in the samples, the ratio $(Y/Ho)_{PAAS}$ vary from 0.57 to 0.87 both values in MOZ1-DR17-01.

5.6.6. Nd and Pb isotope compositions

Neodymium and lead isotope compositions (n=52) of the three studied Fe-Mn crusts are reported in table 5.4. Comparisons with Atlantic and Indian Ocean Fe-Mn crust signatures (Burton et al., 1997; Frank and O'Nions, 1998; O'Nions et al., 1998) are also visible in Figure 5.7.

5.6.6.1. Neodymium

The εNd results compositions versus Be model age of the three Fe-Mn crusts are comprised between the NW Atlantic crust (ALV539, BM1969.5) and the Indian crust (SS663, 109 D-C) compositions over all time (Figure 5.7). The results are comprised between a minimum of -10.5 (DR75-0012 8) and a maximum of -7.9

Table 5.4. *Nd and Pb isotope compositions of all the layers of the three studied Fe-Mn crusts from the PAMELA-MOZ1 (Olu, 2014) and MD06-Nosicaa (Leclaire, 1975). -S corresponds to the surface (top of the Fe-Mn crust) and the other numbers are related to their depth on the Fe-Mn crust slice. The * indicate the ^{10}Be dated layers.*

MOZ1-DR04-23	**Nd isotope compositions**			**Pb isotope compositions**					
Glorieuses Islands	**^{143}Nd/^{144}Nd**	**2σ (10^{-6})**	**εNd**	**^{206}Pb/^{204}Pb**	**2σ (10^{-4})**	**^{207}Pb/^{204}Pb**	**2σ (10^{-4})**	**^{208}Pb/^{204}Pb**	**2σ (10^{-4})**
MOZ1-DR04-23 S*	0.512208	4	-8.4	18.8452	3	15.6954	4	39.1626	89
MOZ1-DR04-23 2*	0.512209	4	-8.4	18.8850	3	15.7000	4	39.2270	60
MOZ1-DR04-23 5*	0.512200	4	-8.5	18.8899	4	15.7041	4	39.2414	17
MOZ1-DR04-23 7*	0.512210	4	-8.3	18.8862	4	15.6990	5	39.1958	67
MOZ1-DR04-23 11*	0.512219	4	-8.2	18.8818	3	15.7002	5	39.2625	71
MOZ1-DR04-23 15	0.512212	4	-8.3	18.8726	3	15.7006	3	39.2314	7
MOZ1-DR04-23 18	0.512227	4	-8.0	18.8950	4	15.7071	4	39.2545	26
MOZ1-DR04-23 22	0.512234	8	-7.9	18.9130	5	15.7096	4	39.2713	25
MOZ1-DR04-23 26	0.512220	4	-8.2	18.8935	4	15.7007	5	39.2296	25
MOZ1-DR04-23 30*	0.512206	4	-8.4	18.8697	5	15.7052	5	39.2456	28
MOZ1-DR04-23 33	0.512197	6	-8.6	18.8811	4	15.7089	4	39.2772	24
MOZ1-DR04-23 38	0.512196	4	-8.6	18.9125	5	15.7135	5	39.3835	15
MOZ1-DR04-23 41	0.512176	6	-9.0	18.8975	4	15.7141	3	39.3128	6
MOZ1-DR04-23 45	0.512188	8	-8.8	18.8994	3	15.7149	3	39.2794	22
MOZ1-DR04-23 48	0.512175	4	-9.0	18.9674	4	15.7252	4	39.3272	14
MOZ1-DR04-23 53	0.512153	4	-9.5	18.9810	5	15.7273	4	39.3410	13
MOZ1-DR04-23 58	0.512166	4	-9.2	18.9403	5	15.7213	4	39.3038	14
MOZ1-DR04-23 62	0.512175	4	-9.0	18.9314	5	15.7208	4	39.3155	13
MOZ1-DR04-23 68	0.512181	4	-8.9	18.9353	6	15.7211	4	39.3251	15
MOZ1-DR04-23 70	0.512188	4	-8.8	18.9341	6	15.7200	4	39.3153	13
MOZ1-DR11-01									
Jeffrey Ridge									
MOZ1-DR11-01 S*	0.512180	4	-8.9	18.6329	3	15.6737	4	38.8334	12
MOZ1-DR11-01 2*	0.512149	6	-9.5	18.8703	3	15.6974	3	39.1227	10
MOZ1-DR11-01 6*	0.512131	6	-9.9	18.9021	5	15.7044	5	39.1631	14
MOZ1-DR11-01 11*	0.512130	16	-9.9	18.9550	4	15.7117	4	39.2339	11
MOZ1-DR11-01 14*	0.512117	16	-10.2	18.9547	5	15.7123	5	39.2505	15
MOZ1-DR11-01 19*	0.512142	6	-9.7	18.9081	4	15.7078	4	39.2191	11
MOZ1-DR11-01 21*	0.512153	16	-9.5	18.8959	3	15.7091	3	39.2083	8
MOZ1-DR11-01 25*	0.512145	4	-9.6	18.9062	4	15.7111	4	39.2172	9
MOZ1-DR11-01 28*	0.512154	6	-9.4	18.9908	4	15.7232	4	39.2876	11
MOZ1-DR11-01 32	0.512148	4	-9.6	18.9879	5	15.7187	5	39.2695	18
MOZ1-DR11-01 39	0.512175	4	-9.0	18.9727	5	15.7207	4	39.2791	12
MOZ1-DR11-01 45	0.512157	4	-9.4	18.9812	3	15.5676	3	39.2793	12
MOZ1-DR11-01 49	0.512138	4	-9.8	18.9740	5	15.7194	4	39.2585	11
MOZ1-DR11-01 59	0.512130	4	-9.9	19.0382	5	15.7315	5	39.3225	14

MOZ1-DR11-01 67	0.512138	4	-9.8	19.0267	5	15.7276	4	39.3195	12
MOZ1-DR11-01 70	0.512140	4	-9.7	19.0144	5	15.7255	5	39.2973	14
MOZ1-DR11-01 74	0.512146	4	-9.6	19.0333	5	15.7256	4	39.3021	13
MOZ1-DR11-01 77	0.512142	14	-9.7	19.0016	4	15.7182	5	39.2357	16
MOZ1-DR11-01 80	0.512160	4	-9.3	19.0090	4	15.7182	4	39.2235	12
DR75-0012 Agulhas Plateau									
DR750-012 S*	0.512119	6	-10.1	18.8435	4	15.6757	4	38.9188	12
DR75-0012 3	0.512124	2	-10.0	18.8871	4	15.6811	5	38.9448	15
DR75-0012 8*	0.512100	2	-10.5	18.9621	6	15.6960	6	39.0429	18
DR75-0012 12	0.512115	2	-10.2	18.9574	6	15.6960	5	39.0285	16
DR75-0012 17*	0.512121	2	-10.1	18.9901	5	15.7017	6	39.0718	19
DR75-0012 21	0.512127	2	-10.0	18.9630	6	15.6961	7	39.0402	19
DR75-0012 23	0.512129	2	-9.9	18.9622	9	15.6955	8	39.0483	24
DR75-0012 28	0.512129	3	-9.9	18.9596	7	15.6957	7	39.0515	22
DR75-0012 34	0.512135	3	-9.8	18.9740	6	15.7022	6	39.0725	20
DR75-0012 37	0.512133	2	-9.9	18.9701	7	15.6997	7	39.0642	21
DR75-0012 40	0.512132	3	-9.9	18.9562	10	15.6963	10	39.0454	29
DR75-0012 43	0.512133	2	-9.9	18.9329	7	15.6907	7	39.0132	20
DR75-0012 46	0.512136	1	-9.8	18.9250	8	15.6896	8	39.0012	23

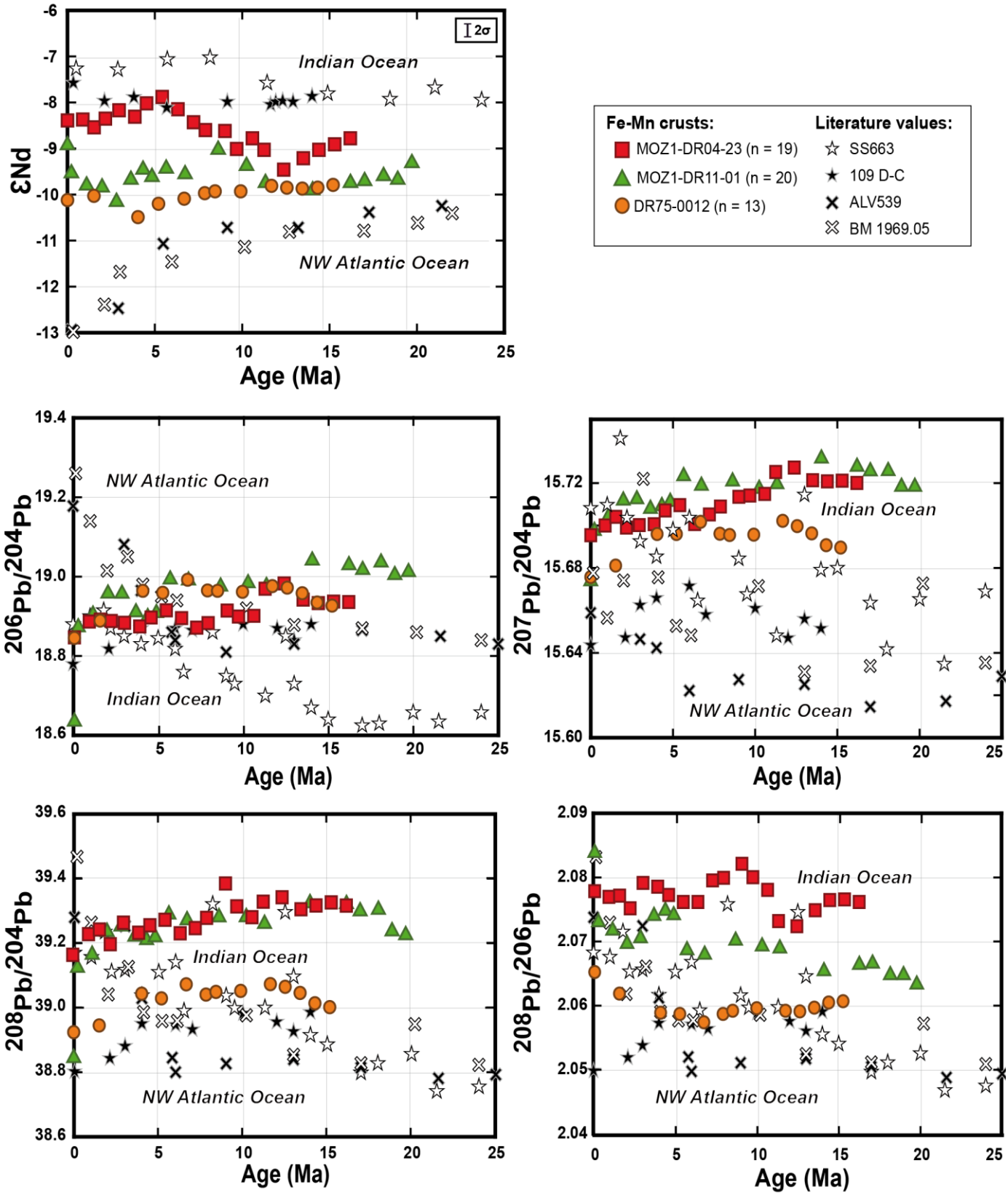

Figure 5.7. *Time series of $\varepsilon_{Nd\ (T)}$ and $^{206}Pb/^{204}Pb$, $^{207}Pb/^{204}Pb$, $^{208}Pb/^{204}Pb$, $^{208}Pb/^{206}Pb$ versus ages derived from $^{10}Be/^{9}Be$ dating (**Figure 5.3**) for the three analysed Fe-Mn crusts. Error bars are included in the sample points. The time series values from the literature are shown for comparisons with SS663 isotope values from O'Nions et al. (1998) and Frank and O'Nions (1998); 109 D-C and ALV539 data from O'Nions et al. (1998); and BM 1969.5 values from Burton et al. (1997) and O'Nions et al. (1998).*

(MOZ1-DR04-23 22). The isotopic signatures are very close at 12.4 Ma with a narrow set of values from -9.5 to -9.9, and furthest away between 5.1 and 4.0 Ma showing a greater range of values from the minimum and the maximum cited before. The compositions of MOZ1-DR11-01 and DR75-0012 are closer to the Atlantic domain than the Indian domain between 19.1 and 12. 4 Ma. For the Fe-Mn crust DR75-0012, this observation is consistent with its location near Agulhas Plateau, south of the African continent, under the NADW influence (Figure 5.1). After 12.4 Ma, the three isotopic signatures diverge. The sample MOZ1-DR04-23 tends towards increasingly radiogenic values, until it reaches the Indian signature (109D-C) at 5.1 Ma (εNd = -7.9) and then stays relatively flat to present-day (εNd = -8.4). The Fe-Mn crust MOZ1-DR11-01 follows MOZ1-DR04-23 to 8.6 Ma (εNd = -9.0) before moving up to low radiogenic signature. Between 8.6 and 1.1 Ma, its trend seems similar to the sample DR75-0012 even if the composition of this last is less radiogenic. MOZ1-DR11-01 and DR75-0012 both reflect the same decrease than the NW Atlantic compositions until 2.8 Ma. For the last 2 Ma, the sample DR75-0012 shows an homogeneous signature (-10.0 > εNd > -10.1) whereas MOZ1-DR11-01 increases to more radiogenic values (-10.2 to -8.9). In comparisons, the other Fe-Mn crusts from Indian Ocean vary of less than 1 εNd unit. Sample 109 D-C show a smooth signature with εNd data varying from -8.1 to -7.6 since 5.6 Ma, and the composition of the sample SS663, from the central Indian Basin, present a discrete increase between 18.5 (εNd = -7.9) and 8.1 Ma (εNd = -7.0).

5.6.6.2. Lead

The $^{206}Pb/^{204}Pb$, $^{207}Pb/^{204}Pb$, $^{208}Pb/^{204}Pb$ and $^{208}Pb/^{206}Pb$ isotope ratios of the three studied Fe-Mn crusts are represented depending on the ages derived from $^{10}Be/^{9}Be$ dating (Figure 5.7).

$^{206}Pb/^{204}Pb$ and $^{208}Pb/^{204}Pb$

The results show few variations of the $^{206}Pb/^{204}Pb$ and $^{208}Pb/^{204}Pb$ signatures. The ratios vary between 18.6329 (MOZ1-DR11-01 S, present-day) and 19.0382 (MOZ1-DR11-01 59, 14 Ma), and between 38.8334 (MOZ1-DR11-01 S, present-day) and 39.3835 (MOZ1-DR04-23 38, 9 Ma), respectively. The three samples present weak decreases in both of cases, between old and recent layers (Figure 5.7). In the case of the $^{208}Pb/^{204}Pb$ values, MOZ1-DR04-23 and MOZ1-DR11-01 present very close compositions (mean = 39.28 and 39.23, respectively), whereas the Fe-Mn crust DR75-0012 shows lower data (mean = 39.02).

$^{207}Pb/^{204}Pb$

The ratio $^{207}Pb/^{204}Pb$ also highlights similar trends of the samples MOZ1-DR04-23 and MOZ1-DR11-01 with respective present-day minimum of 15.6954 and 15.6737, and maximum of 15.7273 (MOZ1-DR04-23 53, 12.4 Ma) and 15.7315 (MOZ1-DR11-01 59, 11.4 Ma). However, MOZ1-DR11-01 presents a high peak of 15.7232 at 5.7 Ma whereas the signature of MOZ1-DR04-23 is at 15.7007 near to the DR75-0012 composition (15.7017). The DR75-0012 signature corresponds in three distinct trends: an increase between 15.2 (DR75-0012 46, 15.6896) and 11.7 Ma (DR75-0012 34, 15.7022), a dip until 6.8 Ma (DR75-0012 17, 15.7017) and an important decrease until present-day (DR75-0012 S, 15.6757). The three samples present global decrease of the ratio between old and recent layers.

$^{208}Pb/^{206}Pb$

$^{208}Pb/^{206}Pb$ values show three different isotopic signatures. The sample MOZ1-DR04-23 has a range of data from 2.0726 (MOZ1-DR04-23 53,

12.4 Ma) to 2.0802 (MOZ1-DR04-23 33, 9.0 Ma). All its results are higher than 2.071, $^{208}Pb/^{206}Pb$ ratio separating the Southwest Indian domain and the North Indian domain defined according to Vlastélic et al. (2001). In contrast, the sample DR75-0012 shows a set of values between 2.0575 (DR75-0012 17, 6.7 Ma) and 2.0654 (DR75-0012 S, present-day), with a smooth signature between 15.2 and 6.7 Ma. Between these two extreme signatures, the Fe-Mn crust MOZ1-DR11-01 presents an increasing trend from 2.0634 (MOZ1-DR11-01 80, 19.7 Ma) to 2.0841 (MOZ1-DR11-01 S, actually), with an isotopic composition below 2.071 between 19.7 and 5.7 Ma.

5.7. Discussion

All the element results are consistent with observations from Indian Ocean crusts (Hein et al., 2016) and more generally in the hydrogenetic Fe-Mn oxides. Both the minor and major element characteristics of the three studied samples indicate a hydrogenetic origin (Figure 5.5) and no phosphatisation phenomenon have been recorded in all the Fe-Mn layers. Moreover, we assume that minor contributions of low radiogenic detrital inputs from the African continent and/or Madagascar do not influence the Nd and Pb isotope compositions of the studied Fe-Mn crusts (Charles et al., in prep.). Isotopic results are derived from a conservative mixing process providing time-integrated information on the water masses compositions (Abouchami et al., 1997; Albarède and Goldstein, 1992; Charles et al., 2020).

5.7.1. South of the channel: Agulhas Plateau

The Nd record of the sample DR75-0012 shows only small variations (mean = -10.0, SD = 0.20, n= 13) likely reflecting a constant arrival of the NADW in the south of the Mozambique Channel. The lower radiogenic peak (εNd = -10.5) stands out from the trend at 4.0 Ma (Figure 5.7, Table 5. 4).

According to the calculation of Frank et al. (2002), we estimated the contribution of the NADW through the Mozambique Channel over time, fixing Atlantic seawater εNd = −13 and Pacific seawater εNd = −6 (also tested with Pacific seawater εNd = −4; Table 5.5).

It appears that NADW inputs have always been intense, since 15.2 Ma (86-90%) to presently (60-68%). The maximum influence is recorded between 7.9 and 6.7 Ma (88-91%) and the minimum is registered between 1.5 and present-day (59-69%). These values are in concordance with those of Rahlf et al. (2020), which estimates mixing between the NADW and the CDW in the Cape Basin up to 80–90%. The decreasing inflow since 1.5 Ma, also visible on the figure 5.7 in comparison to the NW Atlantic crust signatures. The Northern Hemisphere Glaciation started from 3 Ma. This major upheaval firstly changed the NADW composition to a lower radiogenic Nd signature (Abouchami et al., 1998; Burton et al., 1997; Frank and O'Nions, 1998) and secondly reduced its export to the ACC (Boyle and Keigwin, 1987, 1982; Charles and Fairbanks, 1992; Frank et al., 2002). This reduction seems to be recorded in DR75-0012 from 1.5 Ma (Table 5.5).

The Pb isotope composition of DR75-0012 is compared with available data of other Fe-Mn crusts from the different oceans (Abouchami et al., 1997; Burton et al., 1997; Frank et al., 2002; Frank and O'Nions, 1998; Ling et al., 1997; O'Nions et al., 1998; Figure 5.8). The domain of the Southern Ocean includes also the southern Indian Ocean (with the data of the Fe-Mn crust 109D-C). This domain is intermediate between the NW Atlantic and Pacific domains. The North Indian domain, comprising the data of the crust

Table 5.5. *Calculations of the NADW and the NIDW inputs at three different locations of the Mozambique Channel (Glorieuses Islands, Jeffrey Ridge and Agulhas Plateau) over time. Numbers are percentages of NADW calculated with Pacific water mass end-member values of εNd = -4 and -6 (Frank et al., 2002).*

Sample	Age (Ma)	ƐNd	NADW		NIDW	
MOZ1-DR04-23			**Pacific water mass end-member**			
Glorieuses Islands			**εNd = -4**	**εNd = -6**	**εNd = -4**	**εNd = -6**
MOZ1-DR04-23 S*	0.0	-8.4	34%	49%	51%	66%
MOZ1-DR04-23 2*	0.88	-8.4	34%	49%	51%	66%
MOZ1-DR04-23 5*	1.53	-8.5	38%	52%	48%	62%
MOZ1-DR04-23 7*	2.2	-8.3	36%	51%	49%	64%
MOZ1-DR04-23 11*	3.0	-8.2	34%	50%	50%	66%
MOZ1-DR04-23 15	3.9	-8.3	41%	56%	44%	59%
MOZ1-DR04-23 18	4.5	-8.0	40%	57%	43%	60%
MOZ1-DR04-23 22	5.4	-7.9	38%	56%	44%	62%
MOZ1-DR04-23 26	6.3	-8.2	45%	61%	39%	55%
MOZ1-DR04-23 30*	7.2	-8.4	53%	67%	33%	47%
MOZ1-DR04-23 33	7.9	-8.6	57%	70%	30%	43%
MOZ1-DR04-23 38	9.0	-8.6	57%	70%	30%	43%
MOZ1-DR04-23 41	9.7	-9.0	65%	76%	24%	35%
MOZ1-DR04-23 45	10.6	-8.8	61%	73%	27%	39%
MOZ1-DR04-23 48	11.3	-9.0	68%	78%	22%	32%
MOZ1-DR04-23 53	12.4	-9.5	81%	87%	13%	19%
MOZ1-DR04-23 58	13.5	-9.2	77%	85%	15%	23%
MOZ1-DR04-23 62	14.4	-9.0	74%	83%	17%	26%
MOZ1-DR04-23 68	15.3	-8.9	72%	81%	19%	28%
MOZ1-DR04-23 70	16.2	-8.8	70%	80%	20%	30%
MOZ1-DR11-01						
Jeffrey Ridge						
MOZ1-DR11-01 S*	0.0	-8.9	42%	55%	45%	58%
MOZ1-DR11-01 2*	0.23	-9.5	50%	62%	38%	50%
MOZ1-DR11-01 6*	1.09	-9.9	58%	67%	33%	42%
MOZ1-DR11-01 11*	2.0	-9.9	59%	69%	31%	41%
MOZ1-DR11-01 14*	2.8	-10.2	64%	73%	28%	36%
MOZ1-DR11-01 19*	3.6	-9.7	59%	69%	31%	41%
MOZ1-DR11-01 21*	4.3	-9.5	66%	75%	25%	34%
MOZ1-DR11-01 25*	4.8	-9.6	70%	78%	22%	30%
MOZ1-DR11-01 28*	5.7	-9.4	69%	78%	22%	31%
MOZ1-DR11-01 32	6.7	-9.6	74%	81%	19%	26%
MOZ1-DR11-01 39	8.6	-9.0	65%	76%	24%	35%
MOZ1-DR11-01 45	10.25	-9.4	74%	82%	19%	26%
MOZ1-DR11-01 49	11.3	-9.8	80%	87%	13%	20%

MOZ1-DR11-01 59	14.0	-9.9	85%	90%	10%	15%
MOZ1-DR11-01 67	16.2	-9.8	84%	89%	12%	16%
MOZ1-DR11-01 70	17.0	-9.7	83%	89%	11%	17%
MOZ1-DR11-01 74	18.1	-9.6	82%	88%	12%	18%
MOZ1-DR11-01 77	18.9	-9.7	85%	90%	10%	15%
MOZ1-DR11-01 80	19.7	-9.3	78%	86%	14%	22%
DR75-0012 Agulhas Plateau						
DR750-012 S*	0.0	-10.1	60%	68%	32%	40%
DR75-0012 3	1.5	-10.0	59%	69%	31%	41%
DR75-0012 8*	4.0	-10.5	87%	90%	10%	13%
DR75-0012 12	5.2	-10.2	84%	88%	12%	16%
DR75-0012 17*	6.7	-10.1	88%	91%	9%	12%
DR75-0012 21	7.9	-10.0	88%	91%	9%	12%
DR75-0012 23	8.4	-9.9	86%	90%	10%	14%
DR75-0012 28	9.9	-9.9	85%	90%	10%	15%
DR75-0012 34	11.7	-9.8	83%	88%	12%	17%
DR75-0012 37	12.6	-9.9	85%	90%	10%	15%
DR75-0012 40	13.4	-9.9	85%	90%	10%	15%
DR75-0012 43	14.3	-9.9	86%	90%	10%	14%
DR75-0012 46	15.2	-9.8	86%	90%	10%	14%

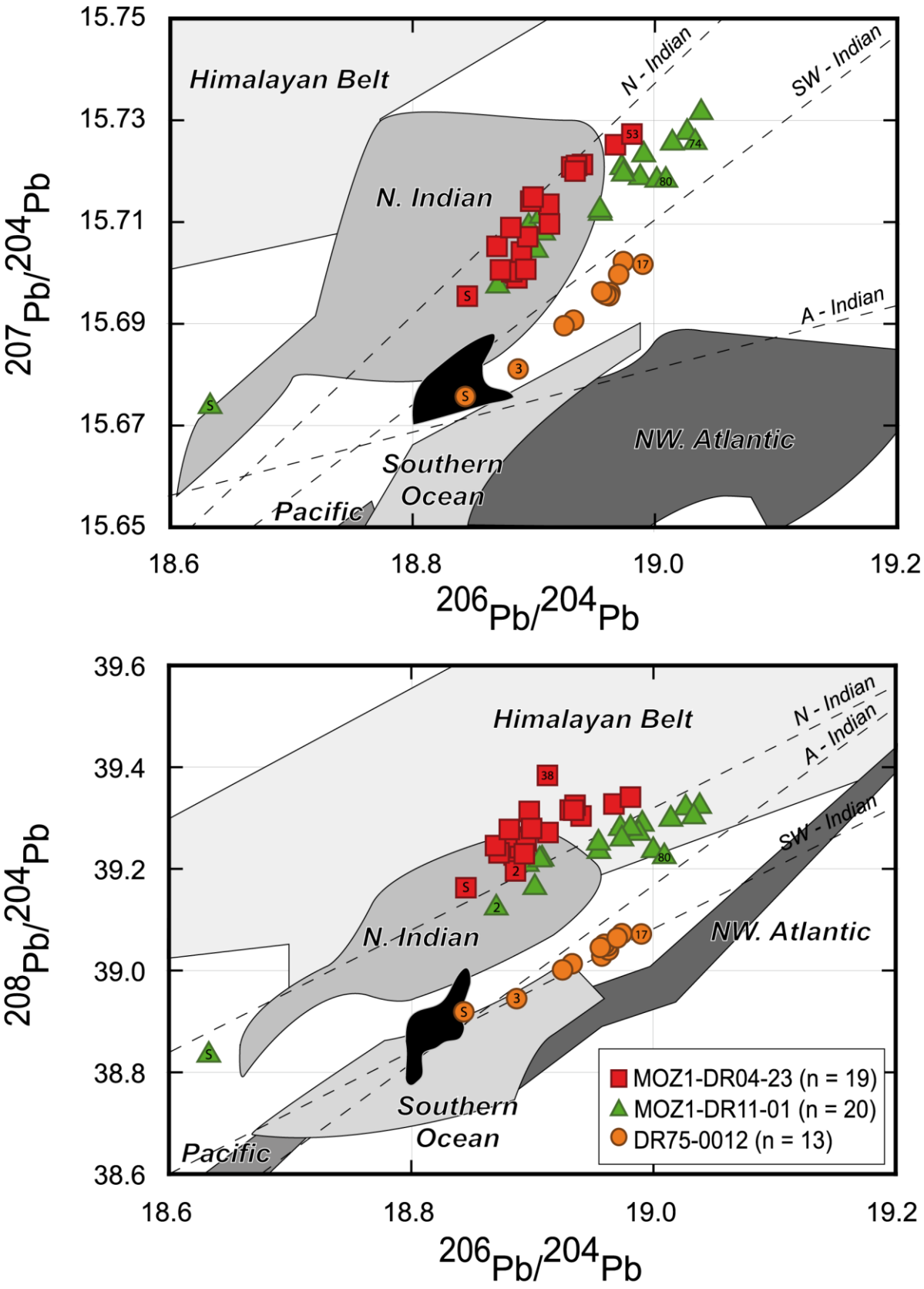

Figure 5.8. *Comparison of the Pb isotope ratios of crusts MOZ1-DR04-23, MOZ1-DR11-01 and DR75-0012 with other available Fe-Mn crusts time series results and the isotopic composition of the Himalayan Belt composed of granites. Defined domains are from Abouchami et al. (1997), Burton et al. (1997), Frank and O'Nions (1998), Frank et al. (2002), Ling et al. (1997) and O'Nions et al. (1998). The dashed lines and black area (S-*Indian*) represent also oceanographic domains from Vlastélic et al. (2001).*

109D-C, is characterized with higher values of $^{207}Pb/^{204}Pb$ and $^{208}Pb/^{204}Pb$ ratios.

The Fe-Mn crust DR75-0012, from Agulhas Plateau, shows $^{208}Pb/^{204}Pb$ vs. $^{206}Pb/^{204}Pb$ and $^{207}Pb/^{204}Pb$ vs. $^{206}Pb/^{204}Pb$ linear trends between the N. Indian and the Southern Ocean / NW Atlantic domains (Figure 5.8).

The $^{208}Pb/^{204}Pb$ vs. $^{206}Pb/^{204}Pb$ points are aligned with the SW-Indian line, although the recent layers of this Fe-Mn crusts getting closer to the intersection of the SW-Indian, A-Indian and S-Indian lines.

The $^{207}Pb/^{204}Pb$ vs. $^{206}Pb/^{204}Pb$ trend of this Fe-Mn crust is shown between the SW-Indian and A-Indian lines defined by Vlastélic et al. (2001). Its oldest layers (n=8) are close to the SW-Indian line and from 5.2 Ma, recent data become closer to the A-Indian line and the S-Indian domain. The more recent values reflect the last 1.5 Ma (DR75-0012 S and DR75-0012 3) and confirm the reduction of the NADW, previously seen with the Nd isotope data and percentages. The sample have recorded a strong influence of the Southern Ocean composition since 1.5 Ma (minimum percentages of the NADW inputs), whereas its oldest layers mainly reflect the SW-Indian domain composition with at least 84-88% of NADW (Table 5.5).

Moreover, the results of $^{208}Pb/^{206}Pb$ are all lower than 2.071 (Figure 5.7). Vlastélic et al. (2001) defined 2.071 as a boundary between the SW-Indian and N-Indian domains (see figure 3.1 in the Chapter 3). All these Nd and Pb compiled observations indicate the important NADW presence in the SW-Indian domain since 15.2 Ma (86-90%), and its reduced inflow since 1.5 Ma (60-68%) causing less amount of NADW entering in the Mozambique Channel.

5.7.2. North of the channel: Glorieuses Islands

The Nd signature of the sample MOZ1-DR04-23 presents two major variations at 12.4 Ma (MOZ1-DR04-23 53; εNd = -9.5) and at 5.4 Ma (MOZ1-DR04-23 22; εNd = -7.9), likely reflecting the NADW and the NIDW influence, respectively. The lower radiogenic peak (εNd = -9.5) is near to the DR75-0012 composition and reflects a NADW influence of 81-87% (Table 5.5). This contribution is almost as strong as the one estimated in the sample DR75-0012 at 12.6 Ma (DR75-0012 37; 85-90%). Inversely, the high radiogenic peak at 5.4 Ma (εNd = -7.9) reach out the Fe-Mn crust compositions of the Indian Ocean (SS663, 109D-C; Figure 5.7). At this period, the input of NADW decreases to 38-56% and the NIDW influence is consequently estimated more intense (44-62%).

The Pb isotope signatures of MOZ1-DR04-23 are compared with available data of other Fe-Mn crusts from the different oceans (Abouchami et al., 1997; Burton et al., 1997; Frank and O'Nions, 1998; Frank et al., 2002; Ling et al., 1997; O'Nions et al., 1998; Figure 5.8). It appears that the layers of MOZ1-DR04-23, from the Glorieuses Islands, are mainly situated in the N-Indian domain defined with the ratios $^{207}Pb/^{204}Pb$ vs. $^{206}Pb/^{204}Pb$. The layer from a depth of 53 mm is the furthest point from the domain and correspond at the period of the stronger NADW arrival (12.4 Ma) even if the point does not reach out the SW-Indian line. The younger layers came closer to the N-Indian domain and signature, probably linked to the increasing influence of the Indian water masses after 12.4 Ma (NIDW from 13-19% at 12.4 Ma to 51-66% presently). Moreover, the results of $^{208}Pb/^{206}Pb$ are all higher than 2.071 (Figure 5.7), indicating that the Pb isotope composition of MOZ1-DR04-23 well corresponds to the N-Indian domain defined by Vlastélic et al. (2001). This observation is

consistent with the location of this Fe-Mn crust in the north of the Mozambique Channel, near the Glorieuses Islands (Figure 5.1).

The strong influence of an Indian component is also visible with the data of $^{208}Pb/^{204}Pb$ ratio. However, the layer MOZ1-DR04-23 38 (9.0 Ma) is also far away from the N-Indian domain and plotted in the domain of the Himalayan Belt composition. This layer was also identified with the highest $^{208}Pb/^{206}Pb$ value (2.0824), which may reflects the discharge of low radiogenic (Derry and France-Lanord, 1996) Himalayan weathering products. Frank and O'nions (1998) also highlighted this phenomenon in the Fe-Mn crust SS663 with a maximum value of the $^{208}Pb/^{206}Pb$ ratio of 2.088 at about 13 Ma to 7.4 Ma. This could be explain by an intense erosion rate of the Himalayan granites estimated between 20 and 14 Ma (Searle, 1996). The sample SS663 would have recorded the signature of the Himalayan contribution earlier than MOZ1-DR04-23 because of its location directly downstream of the Himalayan inputs supplied by the Ganges River (Frank et al., 2006).

5.7.3. Paleocirculation of the deep currents

The sample MOZ1-DR11-01 from the Jeffrey Ridge, north of the Davie Ridge, present a Nd isotope signature, before 12 Ma, similar to the DR75-0012. Between 16.2 and 14.0 Ma, both reflect the NADW influence with the same estimated contributions: 85-90% (MOZ1-DR11-01 59, 14.0 Ma) and 86-90% (DR75-0012 43, 14.3 Ma). This first observation indicates that, since at least 16.2 Ma, the NADW flowed in a northward direction, beyond the Davie Ridge and even to the Glorieuses Archipelago where its influence is estimated up to 81-87% at 12.4 Ma (MOZ1-DR04-23 53). The NIDW does not seem to have much influence at this time (13-19%), probably blocked by the very intense Atlantic water mass. During this period, the Atlantic current thus appears to control the deep oceanographic circulation of the entire Mozambique Channel (Figure 5.9).

From 11.3 Ma, the sample MOZ1-DR11-01 reflects a diminution of the NADW input with εNd data until -9 at 8.6 Ma and a contribution about 65-76% (MOZ1-DR11-01 39). This reduction appears at the same period that the one estimated in the Glorieuses Archipelago with the sample MOZ1-DR04-23, indicating that the NADW is less intense in the north of the channel since 11.3 Ma. However, no NADW reduction is visible in the Nd isotope record of the sample DR75-0012 (Table 5.5; Figure 5.7). The diminution of the NADW in the north may thus be a consequence of a regional upheaval in the centre and in the north of the Mozambique Channel. A major generalised uplift was identified and dated between the Middle-Miocene (11.7-11.1 Ma) and the Early Pliocene (5.7-3.4 Ma) by Charles et al. (in prep.) thanks to the isotopic analyses of three Fe-Mn crusts: MOZ1-DR22-01 from Europa island and, MOZ1-DR10-05 and DR86-0024 from the Davie Ridge (Leclaire, 1984; Olu, 2014).

This study well supports several previous studies (Courgeon et al., 2018, 2017; Delaunay, 2018; Masters et al., 2021, 2006; McCall, 1997; Ponte et al., 2019; Poux et al., 2005). The amplitude of this geodynamic event have been estimated between 465 and 1265 m (Charles et al., in prep.). With such an elevation, the Davie Ridge may have gradually reduced the northward Atlantic deep waters evolution in the Mozambique Channel, allowing the NIDW intensification in the northern part of the channel (MOZ1-DR04-23 38, 30-43%). The isotopic changes recorded in the Fe-Mn crusts MOZ1-DR04-23 and MOZ1-DR11-01 cannot reflect variation of the sample depths from the NADW to Indian intermediate

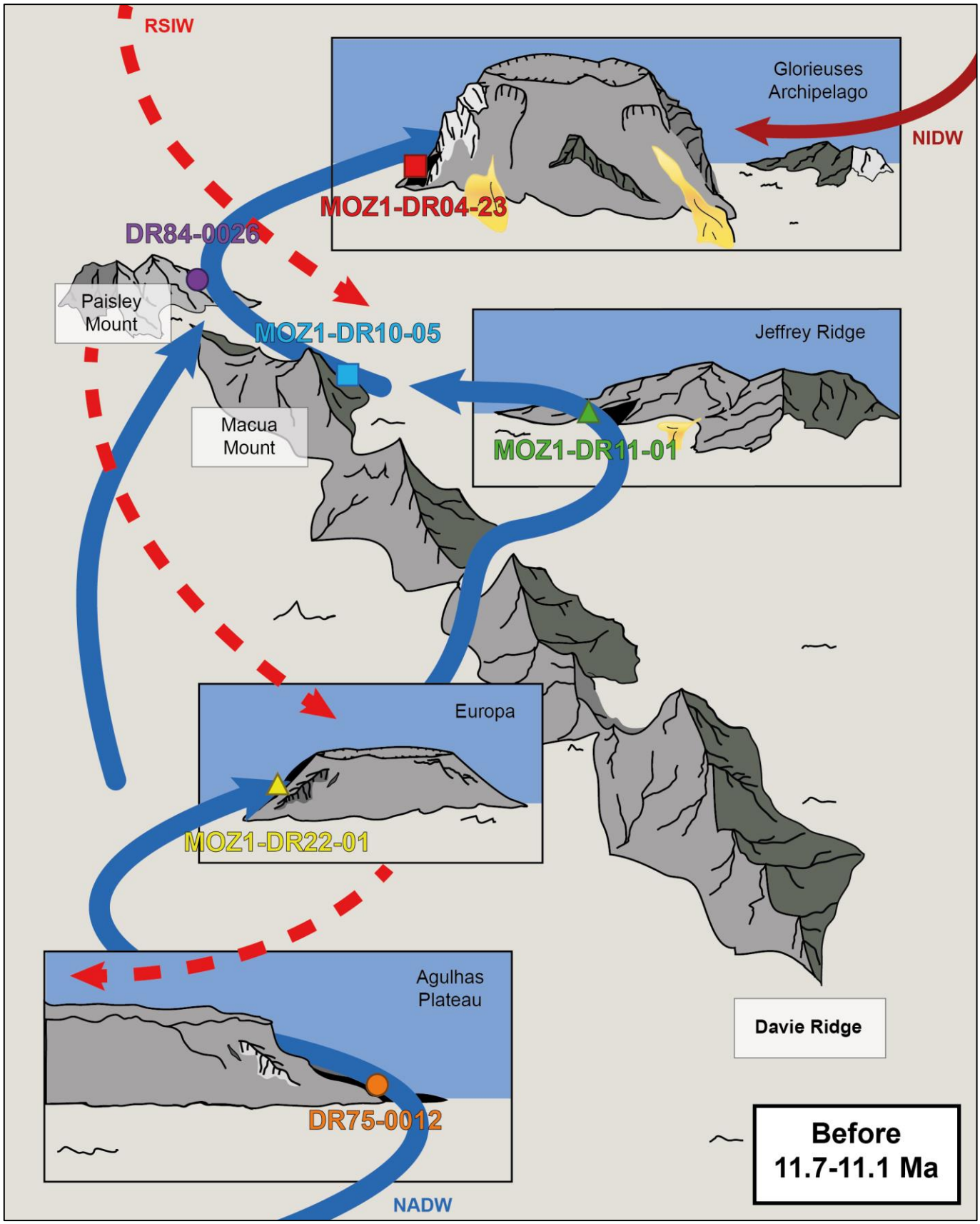

Figure 5.9. *Paleoceanographic reconstruction of the deep-water masses (NADW, NIDW) in the Mozambique Channel before the major uplift event appeared during the Middle Miocene (11.7-11.1 Ma) and identified near Europa island (MOZ1-DR22-01) and in the northern part of the Davie ridge (DR84-0026 and MOZ1-DR10-05) according to Charles et al. (in prep.).*

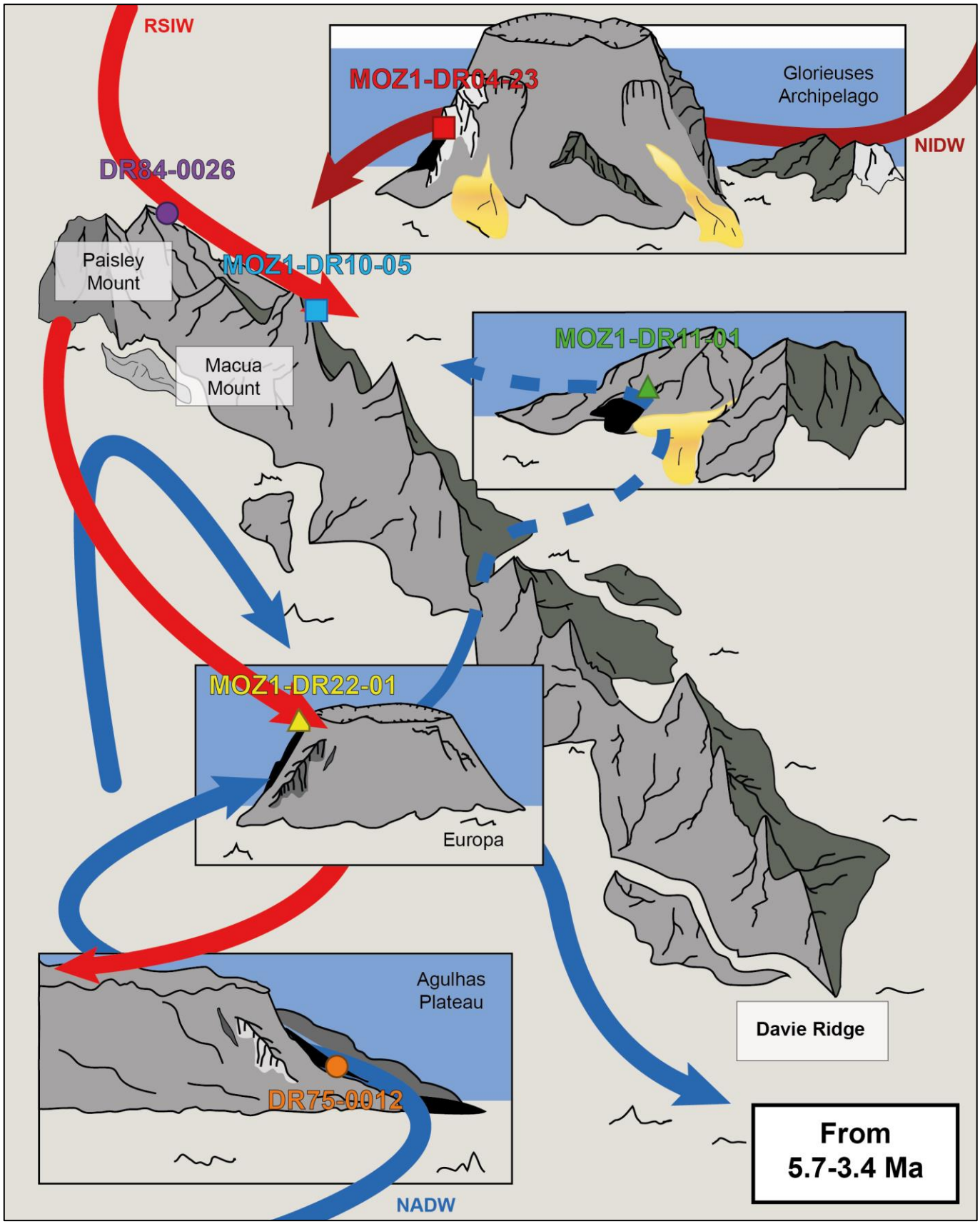

Figure 5.10. *Paleoceanographic reconstruction of the deep-water masses (NADW, NIDW) in the Mozambique Channel from the Early Pliocene (5.7-3.4 Ma), after the major geodynamic uplift identified near Europa island (MOZ1-DR22-01) and in the northern part of the Davie ridge (DR84-0026 and MOZ1-DR10-05) according to Charles et al. (in prep.).*

water (RSIW), because the present-day depths of these Fe-Mn crusts are 1780-2000 mbsl and 2400-2450 mbsl, respectively (Table 5.1). If the samples had also undergone this uplift, their old depths would have been even greater, and in no case, they would have been influenced by the RSIW (Figure 5.7). The decline of the NADW arrival and the increase of the NIDW in the north of the channel would therefore be indirect consequences of the uplift phenomenon that occurred in the Middle Miocene (11.7-11.1 Ma) (Figure 5.10).

At the end of the uplift in the Early Pliocene (5.7-3.4 Ma), MOZ1-DR04-23 indicates similar values with the Indian Ocean compositions (εNd = -7.9 at 5.4 Ma; Figure 5.7) reflecting the sole influence of the NIDW, until present-day (MOZ1-DR04-23 S, 51-66%). This is supported by the study of the Nd isotope composition of Fe-Mn crusts in the Glorieuses Archipelago by Charles et al. (2020), which estimated the NADW contribution about 21-39% presently. These values correspond to the contribution of Atlantic water masses in the mixing with Pacific water masses in the current Indian Ocean. Therefore, the NADW from the south of the Mozambique Channel does not seem to be present in the Glorieuses Archipelago (Charles et al., 2020; Figure 5.10). However, the sample MOZ1-DR11-01 of the Jeffrey Ridge presents a trend similar to the DR75-0012 with significant contributions of the NADW (between 69-78% at 5.7 Ma to 42-55% presently; Table 5.5). These results show that the NADW has never stopped circulating at the Jeffrey Ridge, north of the Davie Ridge, even if its influence was reduced and not enough strong to reach the Glorieuses Archipelago (Figure 5.10).

5.8. Conclusion

This work highlights new time series records for Pb and Nd isotope compositions of Atlantic and Indian water masses in the Mozambique Channel, SW Indian Ocean, since the Miocene (19.7 Ma). The high resolution of geochemical analyse of three deep Fe-Mn crusts from the south (Agulhas Plateau) to the north (Glorieuses Archipelago) of the channel allow to identify major variations of the regional water masses signatures. Lead and neodymium isotope records present important changes from the Middle Miocene (11.3 Ma) to the Early Pliocene (5.4 Ma). Before the Middle Miocene, the Mozambique Channel was dominated by the NADW circulation from the South to the North with a strong influence. However, since 11.3 Ma, our results reflects a gradual diminution of the NADW arrival in the Glorieuses Archipelago we interpret as an indirect consequence of a major uplift phenomenon (11.7-11.1 to 5.7-3.4 Ma) previously identified and dated by Charles et al. (in prep.). This uplift has certainly raised the Davie Ridge of at least 465 m, and thus, reducing the NADW gateway to the north of the channel. At the end of the uplift, the NADW does not seem to appear in the Glorieuses Archipelago even if a small contribution continue to reach the Jeffrey Ridge, north of the Davie Ridge. This study presents a reconstruction of the deep-water masses flowing in SW Indian Ocean over the last 20 Ma, contributing to complete the work already carried out in the central and eastern Indian Ocean (Frank and O'Nions, 1998; Frank et al., 2006, 2002). Moreover, these new results allow relating currents evolution with the geodynamic history of the Mozambique, which continues to provide new geographic information.

5.9. Acknowledgements

We thank the Captains, crews and onboard scientific teams of the PAMELA-MOZ01 survey onboard the R/V L'Atalante and, the MD06-Nosicaa survey onboard the R/V Marion Dufresne. The oceanographic survey PAMELA-MOZ01, as well as Claire CHARLES PhD are co-

funded by TOTAL and IFREMER as part of the PAMELA (Passive Margin Exploration Laboratories) scientific project. The PAMELA project is a scientific project led by Ifremer and TOTAL in collaboration with the Université de Bretagne Occidentale, Université Rennes 1, Université Pierre et Marie Curie, CNRS and IFPEN. The authors are grateful to Philippe FERNAGU and Thierry DALLE MULLE for their help, Coralie ANDREUCCI, Nouméa BOUTIN-PARADIS for assistance with the Be sample preparation and all the ASTER team, in particular Didier BOURLÈS, during our collaboration. The ASTER AMS national facility (CEREGE, Aix-en-Provence) is supported by INSU/CNRS, ANR through the EQUIPEX "ASTER-CEREGE" action, and IRD. We also thank the MNHN, Eva MORENO and Lola JOHANNES for allowing us to access and borrow sample from the MD06-Nosicaa oceanographic expedition belonging to the oceanic collection.

5.10. Bibliographical references

Abouchami, W., Goldstein, S.L., Gazer, S.J.G., Eisenhauer, A., Mangini, A., 1997. Secular changes of lead and neodymium in central Pacific seawater recorded by a Fe-Mn crust. Geochim. Cosmochim. Acta 61, 3957–3974. https://doi.org/10.1016/S0016-7037(97)00218-4

Albarède, F., Goldstein, S.L., 1992. World map of Nd isotopes in sea-floor ferromanganese deposits. Geology 20, 761–763. https://doi.org/10.1130/0091-7613(1992)020<0761:WMONII>2.3.CO;2

Amakawa, H., Alibo, D.S., Nozaki, Y., 2000. Nd isotopic composition and REE pattern in the surface waters of the eastern Indian Ocean and its adjacent seas. Geochim. Cosmochim. Acta 64, 1715–1727. https://doi.org/10.1016/S0016-7037(00)00333-1

Barker, P.F., Burrell, J., 1977. The opening of Drake Passage. Mar. Geol., Circum-Antartic Marine Geology 25, 15–34. https://doi.org/10.1016/0025-3227(77)90045-7

Bau, M., 1996. Controls on the fractionation of isovalent trace elements in magmatic and aqueous systems: evidence from Y/Ho, Zr/Hf, and lanthanide tetrad effect. Contrib. Mineral. Petrol. 123, 323–333. https://doi.org/10.1007/s004100050159

Benites, M., Hein, J.R., Mizell, K., Blackburn, T., Jovane, L., 2020. Genesis and Evolution of Ferromanganese Crusts from the Summit of Rio Grande Rise, Southwest Atlantic Ocean. Minerals 10, 349. https://doi.org/10.3390/min10040349

Berthod, C., Médard, E., Di Muro, A., Hassen Ali, T., Gurioli, L., Chauvel, C., Komorowski, J.-C., Bachèlery, P., Peltier, A., Benbakkar, M., Devidal, J.-L., Besson, P., Le Friant, A., Deplus, C., Nowak, S., Thinon, I., Burckel, P., Hidalgo, S., Feuillet, N., Jorry, S., Fouquet, Y., 2021. Mantle xenolith-bearing phonolites and basanites feed the active volcanic ridge of Mayotte (Comoros archipelago, SW Indian Ocean). Contrib. Mineral. Petrol. 176, 75. https://doi.org/10.1007/s00410-021-01833-1

Bertram, C.J., Elderfield, H., 1993. The geochemical balance of the rare earth elements and neodymium isotopes in the oceans. Geochim. Cosmochim. Acta 57, 1957–1986. https://doi.org/10.1016/0016-7037(93)90087-D

Bonatti, E., Kraemer, T., and Rydell, H., 1972. Classification and genesis of submarine iron-manganese deposits. In: Ferromanganese deposits on the Ocean Floor, 149–161

Bourlès, D., Raisbeck, G.M., Yiou, F., 1989. 10Be and 9Be in marine sediments and their potential for dating. Geochim. Cosmochim. Acta 53, 443–452. https://doi.org/10.1016/0016-7037(89)90395-5

Boyle, E.A., Keigwin, L., 1987. North Atlantic thermohaline circulation during the past 20,000 years linked to high-latitude surface temperature. Nature 330, 35–40. https://doi.org/10.1038/330035a0

Boyle, E.A., Keigwin, L.D., 1982. Deep Circulation of the North Atlantic over the Last 200,000 Years: Geochemical Evidence. Science 218, 784–787. https://doi.org/10.1126/science.218.4574.784

Burton, K.W., Ling, H.-F., O'Nions, R.K., 1997. Closure of the Central American Isthmus and its effect on deep-water formation in the North Atlantic. Nature 386, 382. https://doi.org/10.1038/386382a0

Cane, M.A., Molnar, P., 2001. Closing of the Indonesian seaway as a precursor to east African aridification around 3–4 million years ago. Nature 411, 157–162. https://doi.org/10.1038/35075500

Castelino, J.A., Reichert, C., Klingelhoefer, F., Aslanian, D., Jokat, W., 2015. Mesozoic and Early Cenozoic sediment influx and morphology of the Mozambique Basin. Mar. Pet. Geol. 66, 890–905. https://doi.org/10.1016/j.marpetgeo.2015.07.028

Charles, C., Barrat, J.-A., Pelleter, E., 2021. Trace Element Determinations in Fe-Mn Oxides by High Resolution ICP-MS after Tm Addition. Talanta 122446. https://doi.org/10.1016/j.talanta.2021.122446

Charles, C., Pelleter, E., Révillon, S., Nonnotte, P., Jorry, S.J., Kluska, J.-M., 2020. Intermediate and deep ocean current circulation in the Mozambique Channel: New insights from ferromanganese crust Nd isotopes. Mar. Geol. 430, 106356. https://doi.org/10.1016/j.margeo.2020.106356

Charles, C.D., Fairbanks, R.G., 1992. Evidence from Southern Ocean sediments for the effect of North Atlantic deep-water flux on climate. Nature 355, 416–419. https://doi.org/10.1038/355416a0

Chmeleff, J., von Blanckenburg, F., Kossert, K., Jakob, D., 2010. Determination of the 10Be half-life by multicollector ICP-MS and liquid scintillation counting. Nucl. Instrum. Methods Phys. Res. B 268, 192–199. https://doi.org/10.1016/j.nimb.2009.09.012

Chorowicz, J., 2005. The East African rift system. J. Afr. Earth Sci., Phanerozoic Evolution of Africa 43, 379–410. https://doi.org/10.1016/j.jafrearsci.2005.07.019

Christensen, J.N., Halliday, A.N., Godfrey, L.V., Hein, J.R., Rea, D.K., 1997. Climate and Ocean Dynamics and the Lead Isotopic Records in Pacific Ferromanganese Crusts. Science 277, 913–918. https://doi.org/10.1126/science.277.5328.913

Coffin, M.F., Rabinowitz, P.D., 1987. Reconstruction of Madagascar and Africa: Evidence from the Davie Fracture Zone and Western Somali Basin. J. Geophys. Res. Solid Earth 92, 9385–9406. https://doi.org/10.1029/JB092iB09p09385

Conrad, T., Hein, J.R., Paytan, A., Clague, D.A., 2017. Formation of Fe-Mn crusts within a continental margin environment. Ore Geol. Rev., SI:Marine mineral deposits: New resources for base, precious, and critical metals 87, 25–40. https://doi.org/10.1016/j.oregeorev.2016.09.010

Cornacchia, I., Brandano, M., Agostini, S., 2021. Miocene paleoceanographic evolution of the Mediterranean area and carbonate production changes: A review. Earth-Sci. Rev. 221, 103785. https://doi.org/10.1016/j.earscirev.2021.103785

Cotten, J., Le Dez, A., Bau, M., Caroff, M., Maury, R.C., Dulski, P., Fourcade, S., Bohn, M., Brousse, R., 1995. Origin of anomalous rare-earth element and yttrium enrichments in subaerially exposed basalts: Evidence from French

Polynesia. Chem. Geol. 119, 115–138. https://doi.org/10.1016/0009-2541(94)00102-E

Courgeon, S., Bachèlery, P., Jouet, G., Jorry, S.J., Bou, E., BouDagher-Fadel, M.K., Révillon, S., Camoin, G., Poli, E., 2018. The offshore east African rift system: new insights from the Sakalaves seamounts (Davie Ridge, SW Indian Ocean). Terra Nova 30, 380–388. https://doi.org/10.1111/ter.12353

Courgeon, S., Jorry, S.J., Jouet, G., Camoin, G., BouDagher-Fadel, M.K., Bachèlery, P., Caline, B., Boichard, R., Révillon, S., Thomas, Y., Thereau, E., Guérin, C., 2017. Impact of tectonic and volcanism on the Neogene evolution of isolated carbonate platforms (SW Indian Ocean). Sediment. Geol. 355, 114–131. https://doi.org/10.1016/j.sedgeo.2017.04.008

Davis, J.K., Lawver, L.A., Norton, I.O., Gahagan, L.M., 2016. New Somali Basin magnetic anomalies and a plate model for the early Indian Ocean. Gondwana Res. 34, 16–28. https://doi.org/10.1016/j.gr.2016.02.010

de la Vara, A., van Baak, C.G.C., Marzocchi, A., Grothe, A., Meijer, P.Th., 2016. Quantitative analysis of Paratethys sea level change during the Messinian Salinity Crisis. Mar. Geol. 379, 39–51. https://doi.org/10.1016/j.margeo.2016.05.002

Delaunay, A., 2018. Madagascar vertical movements (90 - 0 Ma): a double approach including onshore geomorphology and Madagascar western margins sedimentary record. https://doi.org/10.13140/RG.2.2.35631.69283

Derry, L.A., France-Lanord, C., 1996. Neogene Himalayan weathering history and river87Sr86Sr: impact on the marine Sr record. Earth Planet. Sci. Lett. 142, 59–74. https://doi.org/10.1016/0012-821X(96)00091-X

Elderfield, H., Hawkesworth, C.J., Greaves, M.J., Calvert, S.E., 1981. Rare earth element geochemistry of oceanic ferromanganese nodules and associated sediments. Geochim. Cosmochim. Acta 45, 513–528. https://doi.org/10.1016/0016-7037(81)90184-8

Emerick, C.M., Duncan, R.A., 1982. Age progressive volcanism in the Comores Archipelago, western Indian Ocean and implications for Somali plate tectonics. Earth Planet. Sci. Lett. 60, 415–428. https://doi.org/10.1016/0012-821X(82)90077-2

Fine, R.A., 1993. Circulation of Antarctic intermediate water in the South Indian Ocean. Deep Sea Res. Part Oceanogr. Res. Pap. 40, 2021–2042. https://doi.org/10.1016/0967-0637(93)90043-3

Frank, M., O'Nions, R.K., 1998. Sources of Pb for Indian Ocean ferromanganese crusts: a record of Himalayan erosion? Earth Planet. Sci. Lett. 158, 121–130. https://doi.org/10.1016/S0012-821X(98)00055-7

Frank, M., O'Nions, R.K., Hein, J.R., Banakar, V.K., 1999. 60 Myr records of major elements and Pb–Nd isotopes from hydrogenous ferromanganese crusts: reconstruction of seawater paleochemistry. Geochim. Cosmochim. Acta 63, 1689–1708. https://doi.org/10.1016/S0016-7037(99)00079-4

Frank, M., Whiteley, N., Kasten, S., Hein, J.R., O'Nions, K., 2002. North Atlantic Deep Water export to the Southern Ocean over the past 14 Myr: Evidence from Nd and Pb isotopes in ferromanganese crusts. Paleoceanography 17, 12-1-12–9. https://doi.org/10.1029/2000PA000606

Frank, M., Whiteley, N., van de Flierdt, T., Reynolds, B.C., O'Nions, K., 2006. Nd and Pb isotope evolution of deep water masses in the eastern Indian Ocean during the past 33 Myr. Chem. Geol., Special Issue in Honour of R.K. O'Nions 226, 264–279. https://doi.org/10.1016/j.chemgeo.2005.09.024

Franke, D., Jokat, W., Ladage, S., Stollhofen, H., Klimke, J., Lutz, R., Mahanjane, E.S., Ehrhardt, A., Schreckenberger, B., 2015. The offshore East African Rift System: Structural framework at the toe of a juvenile rift. Tectonics 34, 2086–2104. https://doi.org/10.1002/2015TC003922

Gaina, C., Torsvik, T.H., van Hinsbergen, D.J.J., Medvedev, S., Werner, S.C., Labails, C., 2013. The African Plate: A history of oceanic crust accretion and subduction since the Jurassic. Tectonophysics, Progress in understanding the South Atlantic margins 604, 4–25. https://doi.org/10.1016/j.tecto.2013.05.037

Gale, N.H., 1996. A new method for extracting and purifying lead from difficult matrices for isotopic analysis. Analytica Chimica Acta, 332, 15-21

Gohl, K., Uenzelmann-Neben, G., 2001. The crustal role of the Agulhas Plateau, southwest Indian Ocean: evidence from seismic profiling. Geophys. J. Int. 144, 632–646. https://doi.org/10.1046/j.1365-246x.2001.01368.x

Goldberg, E.D., Koide, M., Schmitt, R.A., Smith, R.H., 1963. Rare-Earth distributions in the marine environment. J. Geophys. Res. 1896-1977 68, 4209–4217. https://doi.org/10.1029/JZ068i014p04209

Haug, G.H., Tiedemann, R., 1998. Effect of the formation of the Isthmus of Panama on Atlantic Ocean thermohaline circulation. Nature 393, 673. https://doi.org/10.1038/31447

Hein, J.R., Conrad, T., Mizell, K., Banakar, V.K., Frey, F.A., Sager, W.W., 2016. Controls on ferromanganese crust composition and reconnaissance resource potential, Ninetyeast Ridge, Indian Ocean.

Hein, J.R., Conrad, T.A., Frank, M., Christl, M., Sager, W.W., 2012. Copper-nickel-rich, amalgamated ferromanganese crust-nodule deposits from Shatsky Rise, NW Pacific: SHATSKY RISE Cu-RICH Fe-Mn CRUSTS. Geochem. Geophys. Geosystems 13, n/a-n/a. https://doi.org/10.1029/2012GC004286

Hein, J.R., Koschinsky, A., 2014. 13.11 - Deep-Ocean Ferromanganese Crusts and Nodules, in: Holland, H.D., Turekian, K.K. (Eds.), Treatise on Geochemistry (Second Edition). Elsevier, Oxford, pp. 273–291. https://doi.org/10.1016/B978-0-08-095975-7.01111-6

Hein, J.R., Koschinsky, A., Halbach, P., Manheim, F.T., Bau, M., Kang, J.-K., Lubick, N., 1997. Iron and manganese oxide mineralization in the Pacific. Geol. Soc. Lond. Spec. Publ. 119, 123–138. https://doi.org/10.1144/GSL.SP.1997.119.01.09

Heirtzler, J.R., Burroughs, R.H., 1971. Madagascar's Paleoposition: New Data from the Mozambique Channel. Science 174, 488–490. https://doi.org/10.1126/science.174.4008.488

Holbourn, A., Kuhnt, W., Clemens, S., Prell, W., Andersen, N., 2013a. Middle to late Miocene stepwise climate cooling: Evidence from a high-resolution deep water isotope curve spanning 8 million years. Paleoceanography 28, 688–699. https://doi.org/10.1002/2013PA002538

Holbourn, A., Kuhnt, W., Frank, M., Haley, B.A., 2013b. Changes in Pacific Ocean circulation following the Miocene onset of permanent Antarctic ice cover. Earth Planet. Sci. Lett. 365, 38–50. https://doi.org/10.1016/j.epsl.2013.01.020

Hsü, K.J., Montadert, L., Bernoulli, D., Cita, M.B., Erickson, A., Garrison, R.E., Kidd, R.B., Mèlierés, F., Müller, C., Wright, R., 1977. History of the Mediterranean salinity crisis. Nature 267, 399–403. https://doi.org/10.1038/267399a0

Jacques, G., Hauff, F., Hoernle, K., Werner, R., Uenzelmann-Neben, G., Garbe-Schönberg, D., Fischer, M., 2019. Nature and origin of the

Mozambique Ridge, SW Indian Ocean. Chem. Geol. 507, 9–22. https://doi.org/10.1016/j.chemgeo.2018.12.027

Jeandel, C., 1993. Concentration and isotopic composition of Nd in the South Atlantic Ocean. Earth Planet. Sci. Lett. 117, 581–591. https://doi.org/10.1016/0012-821X(93)90104-H

Jeandel, C., Bishop, J.K., Zindler, A., 1995. Exchange of neodymium and its isotopes between seawater and small and large particles in the Sargasso Sea. Geochim. Cosmochim. Acta 59, 535–547. https://doi.org/10.1016/0016-7037(94)00367-U

Josso, P., Horstwood, M.S.A., Millar, I.L., Pashley, V., Lusty, P. a. J., Murton, B., 2020. Development of a Correlated Fe-Mn Crust Stratigraphy Using Pb and Nd Isotopes and Its Application to Paleoceanographic Reconstruction in the Atlantic. Paleoceanogr. Paleoclimatology 35, e2020PA003928. https://doi.org/10.1029/2020PA003928

Josso, P., Parkinson, I., Horstwood, M., Lusty, P., Chenery, S., Murton, B., 2019. Improving confidence in ferromanganese crust age models: A composite geochemical approach. Chem. Geol. 513, 108–119. https://doi.org/10.1016/j.chemgeo.2019.03.003

Josso, P., Pelleter, E., Pourret, O., Fouquet, Y., Etoubleau, J., Cheron, S., Bollinger, C., 2017. A new discrimination scheme for oceanic ferromanganese deposits using high field strength and rare earth elements. Ore Geol. Rev., SI:Marine mineral deposits: New resources for base, precious, and critical metals 87, 3–15. https://doi.org/10.1016/j.oregeorev.2016.09.003

Josso, P., Rushton, J., Lusty, P., Matthews, A., Chenery, S., Holwell, D., Kemp, S.J., Murton, B., 2020. Late Cretaceous and Cenozoic paleoceanography from north-east Atlantic ferromanganese crust microstratigraphy. Mar. Geol. 422, 106122. https://doi.org/10.1016/j.margeo.2020.106122

Karami, M.P., Meijer, P.T., Dijkstra, H.A., Wortel, M.J.R., 2009. An oceanic box model of the Miocene Mediterranean Sea with emphasis on the effects of closure of the eastern gateway. Paleoceanography 24. https://doi.org/10.1029/2008PA001679

Kennett, J.P., 1985. The Miocene Ocean: Paleoceanography and Biogeography. Geological Society of America.

Kennett, J.P., and von der Borch, C.C., 1986. Southwest Pacific Cenozoic paleoceanography. In Kennett, J.P., von der Borch, C.C., et al., Init. Repts. DSDP, 90 (Pt. 2): Washington (U.S. Govt. Printing Office), 1493-1517.

Klemm, V., Frank, M., Levasseur, S., Halliday, A.N., Hein, J.R., 2008. Seawater osmium isotope evidence for a middle Miocene flood basalt event in ferromanganese crust records. Earth Planet. Sci. Lett. 273, 175–183. https://doi.org/10.1016/j.epsl.2008.06.028

Klemm, V., Levasseur, S., Frank, M., Hein, J.R., Halliday, A.N., 2005. Osmium isotope stratigraphy of a marine ferromanganese crust. Earth Planet. Sci. Lett. 238, 42–48. https://doi.org/10.1016/j.epsl.2005.07.016

Korschinek, G., Bergmaier, A., Faestermann, T., Gerstmann, U.C., Knie, K., Rugel, G., Wallner, A., Dillmann, I., Dollinger, G., von Gostomski, Ch.L., Kossert, K., Maiti, M., Poutivtsev, M., Remmert, A., 2010. A new value for the half-life of 10Be by Heavy-Ion Elastic Recoil Detection and liquid scintillation counting. Nucl. Instrum. Methods Phys. Res. Sect. B Beam Interact. Mater. At. 268, 187–191. https://doi.org/10.1016/j.nimb.2009.09.020

Koschinsky, A., Halbach, P., 1995. Sequential leaching of marine ferromanganese precipitates: Genetic implications. Geochim. Cosmochim.

Acta 59, 5113–5132. https://doi.org/10.1016/0016-7037(95)00358-4

Lacan, F., Tachikawa, K., Jeandel, C., 2012. Neodymium isotopic composition of the oceans: A compilation of seawater data. Chem. Geol. 300–301, 177–184. https://doi.org/10.1016/j.chemgeo.2012.01.019

Leclaire, L., 1984. RIDA - MD39 cruise, Marion Dufresne R/V. https://doi.org/10.17600/84010511

Leclaire, L., 1975. NOSICAA - MD 06 cruise, Marion Dufresne R/V. https://doi.org/10.17600/75010711

Lee, T.-Y., Lawver, L.A., 1995. Cenozoic plate reconstruction of Southeast Asia. Tectonophysics, Southeast Asia Structure and Tectonics 251, 85–138. https://doi.org/10.1016/0040-1951(95)00023-2

Leinweber, V.T., Jokat, W., 2012. The Jurassic history of the Africa–Antarctica corridor — new constraints from magnetic data on the conjugate continental margins. Tectonophysics 530–531, 87–101. https://doi.org/10.1016/j.tecto.2011.11.008

Leinweber, V.T., Klingelhoefer, F., Neben, S., Reichert, C., Aslanian, D., Matias, L., Heyde, I., Schreckenberger, B., Jokat, W., 2013. The crustal structure of the Central Mozambique continental margin — Wide-angle seismic, gravity and magnetic study in the Mozambique Channel, Eastern Africa. Tectonophysics 599, 170–196. https://doi.org/10.1016/j.tecto.2013.04.015

Leroux, E., Counts, J.W., Jorry, S.J., Jouet, G., Révillon, S., BouDagher-Fadel, M.K., Courgeon, S., Berthod, C., Ruffet, G., Bachèlery, P., Grenard-Grand, E., 2020. Evolution of the Glorieuses seamount in the SW Indian Ocean and surrounding deep Somali Basin since the Cretaceous. Mar. Geol. 427, 106202. https://doi.org/10.1016/j.margeo.2020.106202

Ling, H.F., Burton, K.W., O'Nions, R.K., Kamber, B.S., von Blanckenburg, F., Gibb, A.J., Hein, J.R., 1997. Evolution of Nd and Pb isotopes in Central Pacific seawater from ferromanganese crusts. Earth Planet. Sci. Lett. 146, 1–12. https://doi.org/10.1016/S0012-821X(96)00224-5

Linthout, K., Helmers, H., Sopaheluwakan, J., 1997. Late Miocene obduction and microplate migration around the southern Banda Sea and the closure of the Indonesian Seaway. Tectonophysics, Neogene Evolution of the Pacific: Tectonics of Gateways and Associated Responses 281, 17–30. https://doi.org/10.1016/S0040-1951(97)00156-X

Macgregor, D., 2015. History of the development of the East African Rift System: A series of interpreted maps through time. J. Afr. Earth Sci. 101, 232–252. https://doi.org/10.1016/j.jafrearsci.2014.09.016

Mahanjane, E.S., 2014. The Davie Fracture Zone and adjacent basins in the offshore Mozambique Margin – A new insights for the hydrocarbon potential. Mar. Pet. Geol. 57, 561–571. https://doi.org/10.1016/j.marpetgeo.2014.06.015

Manheim, F.T., 1986. Marine Cobalt Resources. Science 232, 600–608. https://doi.org/10.1126/science.232.4750.600

Manheim, F.T., Lane-Bostwick, C.M., 1988. Cobalt in ferromanganese crusts as a monitor of hydrothermal discharge on the Pacific sea floor. Nature 335, 59. https://doi.org/10.1038/335059a0

Mantyla, A.W., Reid, J.L., 1995. On the origins of deep and bottom waters of the Indian Ocean. J. Geophys. Res. Oceans 100, 2417–2439. https://doi.org/10.1029/94JC02564

Masters, J.C., Génin, F., Zhang, Y., Pellen, R., Huck, T., Mazza, P.P.A., Rabineau, M., Doucouré, M., Aslanian, D., 2021. Biogeographic mechanisms involved in the colonization of Madagascar by African vertebrates: Rifting,

rafting and runways. J. Biogeogr. 48, 492–510. https://doi.org/10.1111/jbi.14032

Masters, J.C., Wit, M.J. de, Asher, R.J., 2006. Reconciling the Origins of Africa, India and Madagascar with Vertebrate Dispersal Scenarios. Folia Primatol. (Basel) 77, 399–418. https://doi.org/10.1159/000095388

McCall, R.A., 1997. Implications of recent geological investigations of the Mozambique Channel for the mammalian colonization of Madagascar. Proc. R. Soc. Lond. B Biol. Sci. 264, 663–665. https://doi.org/10.1098/rspb.1997.0094

McGrew, H., 1983. Oil and gas developments in central and southern Africa in 1982, Am. Assoc. Pet. Geol. Bull., 67, 1723-1794

Michon, L., 2016. The volcanism of the Comoros archipelago integrated at a regional scale, in: Bachelery, Patrick, Lénat, Jean-François, Muro, D., Andrea, Michon, Laurent (Eds.), Active Volcanoes of the Southwest Indian Ocean: Piton de La Fournaise and Karthala, Active Volcanoes of the World. Springer-Verlag, pp. 233–244.

Mizell, K., Hein, J.R., Koschinsky, A., Hayes, S.M., 2020a. Effects of Phosphatization on the Mineral Associations and Speciation of Pb in Ferromanganese Crusts. ACS Earth Space Chem. 4, 1515–1526. https://doi.org/10.1021/acsearthspacechem.0c00037

Mizell, K., Hein, J.R., Lam, P.J., Koppers, A.A.P., Staudigel, H., 2020b. Geographic and Oceanographic Influences on Ferromanganese Crust Composition Along a Pacific Ocean Meridional Transect, 14 N to 14S. Geochem. Geophys. Geosystems 21, e2019GC008716. https://doi.org/10.1029/2019GC008716

Muiños, S.B., Hein, J.R., Frank, M., Monteiro, J.H., Gaspar, L., Conrad, T., Pereira, H.G., Abrantes, F., 2013. Deep-sea Fe-Mn Crusts from the Northeast Atlantic Ocean: Composition and Resource Considerations. Mar. Georesources Geotechnol. 31, 40–70. https://doi.org/10.1080/1064119X.2012.661215

Nishiizumi, K., Imamura, M., Caffee, M.W., Southon, J.R., Finkel, R.C., McAninch, J., 2007. Absolute calibration of 10Be AMS standards. Nucl. Inst Methods Phys. Res. B 2, 403–413. https://doi.org/10.1016/j.nimb.2007.01.297

Nishimura, S., Suparka, S., 1997. Tectonic approach to the Neogene evolution of Pacific-Indian Ocean seaways. Tectonophysics, Neogene Evolution of the Pacific: Tectonics of Gateways and Associated Responses 281, 1–16. https://doi.org/10.1016/S0040-1951(97)00155-8

Nougier, J., Cantagrel, J.M., Karche, J.P., 1986. The Comores archipelago in the western Indian Ocean: volcanology, geochronology and geodynamic setting. J. Afr. Earth Sci. 1983 5, 135–145. https://doi.org/10.1016/0899-5362(86)90003-5

Olu, K., 2014. PAMELA-MOZ01 cruise,L'Atalante R/V. https://doi.org/10.17600/14001000

O'Nions, R.K., Frank, M., von Blanckenburg, F., Ling, H.-F., 1998. Secular variation of Nd and Pb isotopes in ferromanganese crusts from the Atlantic, Indian and Pacific Oceans. Earth Planet. Sci. Lett. 155, 15–28. https://doi.org/10.1016/S0012-821X(97)00207-0

Pagani, M., Liu, Z., LaRiviere, J., Ravelo, A.C., 2010. High Earth-system climate sensitivity determined from Pliocene carbon dioxide concentrations. Nat. Geosci. 3, 27–30. https://doi.org/10.1038/ngeo724

Pfuhl, H.A., McCave, I.N., 2005. Evidence for late Oligocene establishment of the Antarctic Circumpolar Current. Earth Planet. Sci. Lett. 235, 715–728. https://doi.org/10.1016/j.epsl.2005.04.025

Pin, C., Briot, D., Bassin, C., Poitrasson, F., 1994. Concomitant separation of strontium and samarium-neodymium for isotopic analysis in silicate samples, based on specific extraction chromatography. Anal. Chim. Acta 298, 209–217. https://doi.org/10.1016/0003-2670(94)00274-6

Piotrowski, A.M., Goldstein, S.L., Hemming, S.R., Fairbanks, R.G., 2005. Temporal Relationships of Carbon Cycling and Ocean Circulation at Glacial Boundaries. Science 307, 1933–1938. https://doi.org/10.1126/science.1104883

Ponte, J.-P., Robin, C., Guillocheau, F., Popescu, S., Suc, J.-P., Dall'Asta, M., Melinte-Dobrinescu, M.C., Bubik, M., Dupont, G., Gaillot, J., 2019. The Zambezi delta (Mozambique channel, East Africa): High resolution dating combining bio-orbital and seismic stratigraphies to determine climate (palaeoprecipitation) and tectonic controls on a passive margin. Mar. Pet. Geol. 105, 293–312. https://doi.org/10.1016/j.marpetgeo.2018.07.017

Pourmand, A., Dauphas, N., Ireland, T.J., 2012. A novel extraction chromatography and MC-ICP-MS technique for rapid analysis of REE, Sc and Y: Revising CI-chondrite and Post-Archean Australian Shale (PAAS) abundances. Chem. Geol. 291, 38–54. https://doi.org/10.1016/j.chemgeo.2011.08.011

Poux, C., Madsen, O., Marquard, E., Vieites, D.R., de Jong, W.W., Vences, M., 2005. Asynchronous Colonization of Madagascar by the Four Endemic Clades of Primates, Tenrecs, Carnivores, and Rodents as Inferred from Nuclear Genes. Syst. Biol. 54, 719–730. https://doi.org/10.1080/10635150500234534

Rahlf, P., Hathorne, E., Laukert, G., Gutjahr, M., Weldeab, S., Frank, M., 2020. Tracing water mass mixing and continental inputs in the southeastern Atlantic Ocean with dissolved neodymium isotopes. Earth Planet. Sci. Lett. 530, 115944. https://doi.org/10.1016/j.epsl.2019.115944

Raymo, M.E., 1994. The Initiation of Northern Hemisphere Glaciation. Annu. Rev. Earth Planet. Sci. 22, 353–383. https://doi.org/10.1146/annurev.ea.22.050194.002033

Rutberg, R.L., Hemming, S.R., Goldstein, S.L., 2000. Reduced North Atlantic Deep Water flux to the glacial Southern Ocean inferred from neodymium isotope ratios. Nature 405, 935. https://doi.org/10.1038/35016049

Schaule, B.K., Patterson, C.C., 1981. Lead concentrations in the northeast Pacific: evidence for global anthropogenic perturbations. Earth Planet. Sci. Lett. 54, 97–116. https://doi.org/10.1016/0012-821X(81)90072-8

Scher, H.D., Martin, E.E., 2004. Circulation in the Southern Ocean during the Paleogene inferred from neodymium isotopes. Earth Planet. Sci. Lett. 228, 391–405. https://doi.org/10.1016/j.epsl.2004.10.016

Schott, F.A., Xie, S.-P., McCreary, J.P., 2009. Indian Ocean circulation and climate variability. Rev. Geophys. 47, RG1002. https://doi.org/10.1029/2007RG000245

Searle, M.P., 1996. Cooling history, erosion, exhumation and kinematics of the Himalaya-Karakoram-Tibet orogenic belt. Pp. 110–137 in: Asian Tectonics. (Yin, A. and Harrison, M.A., editors). Cambridge University Press, Cambridge, UK

Ségoufin, J., Patriat, P., 1980. Existence d'anomalies mésozoïques dans le bassin de Somalie; implications pour les relations Afrique-Antarctique-Madagascar. C. R. Acad. Sci. Paris, Ser.2, 2918: 85-88

Shevenell, A., Kennett, J.P., 2004. Paleoceanographic Change During the Middle Miocene Climate Revolution: An Antarctic Stable

Isotope Perspective. Shevenell AE Kennett JP 2004 Paleocenographic Change Middle Miocene Clim. Revolut. Antarct. Stable Isot. Perspect. Kennett JP Warn. Eds Cenozoic South. Ocean Tecton. Sediment. Clim. Change Aust. Antarct. Geophys. Monogr. Ser. 151 Am. Geophys. Union Wash. US Pp 235-252 ISBN 9780875904160 151. https://doi.org/10.1029/151GM14

Simon, Q., Thouveny, N., Bourlès, D.L., Valet, J.-P., Bassinot, F., Ménabréaz, L., Guillou, V., Choy, S., Beaufort, L., 2016. Authigenic 10Be/9Be ratio signatures of the cosmogenic nuclide production linked to geomagnetic dipole moment variation since the Brunhes/Matuyama boundary. J. Geophys. Res. Solid Earth 121, 7716–7741. https://doi.org/10.1002/2016JB013335

Stamps, D.S., Kreemer, C., Fernandes, R., Rajaonarison, T.A., Rambolamanana, G., 2021. Redefining East African Rift System kinematics. Geology 49, 150–155. https://doi.org/10.1130/G47985.1

Stickley, C.E., Brinkhuis, H., Schellenberg, S.A., Sluijs, A., Röhl, U., Fuller, M., Grauert, M., Huber, M., Warnaar, J., Williams, G.L., 2004. Timing and nature of the deepening of the Tasmanian Gateway. Paleoceanography 19. https://doi.org/10.1029/2004PA001022

Strakhov, N. M., 1974. Exhalations from the mid_ocean ridges as a source of ore elements in oceanic sediments. Litol. Polezn. Iskop, (3), 20-37

Taylor, S.R., McLennan, S.M., 1985. The continental crust: Its composition and evolution.

Thomas, D.J., Bralower, T.J., Jones, C.E., 2003. Neodymium isotopic reconstruction of late Paleocene-early Eocene thermohaline circulation. Earth Planet. Sci. Lett. 209, 309–322. https://doi.org/10.1016/S0012-821X(03)00096-7

Thompson, J.O., Moulin, M., Aslanian, D., de Clarens, P., Guillocheau, F., 2019. New starting point for the Indian Ocean: Second phase of breakup for Gondwana. Earth-Sci. Rev. 191, 26–56. https://doi.org/10.1016/j.earscirev.2019.01.018

Tzevahirtzian, A., Zaragosi, S., Bachèlery, P., Biscara, L., Marchès, E., 2021. Submarine morphology of the Comoros volcanic archipelago. Mar. Geol. 432, 106383. https://doi.org/10.1016/j.margeo.2020.106383

van Aken, H.M., Ridderinkhof, H., de Ruijter, W.P.M., 2004. North Atlantic deep water in the south-western Indian Ocean. Deep Sea Res. Part Oceanogr. Res. Pap. 51, 755–776. https://doi.org/10.1016/j.dsr.2004.01.008

van de Flierdt, T., Griffiths, A.M., Lambelet, M., Little, S.H., Stichel, T., Wilson, D.J., 2016. Neodymium in the oceans: a global database, a regional comparison and implications for palaeoceanographic research. Philos. Trans. R. Soc. Math. Phys. Eng. Sci. 374, 20150293. https://doi.org/10.1098/rsta.2015.0293

Vance, D., Scrivner, A.E., Beney, P., Staubwasser, M., Henderson, G.M., Slowey, N.C., 2004. The use of foraminifera as a record of the past neodymium isotope composition of seawater. Paleoceanography 19. https://doi.org/10.1029/2003PA000957

Verducci, M., Foresi, L.M., Scott, G.H., Sprovieri, M., Lirer, F., Pelosi, N., 2009. The Middle Miocene climatic transition in the Southern Ocean: Evidence of paleoclimatic and hydrographic changes at Kerguelen plateau from planktonic foraminifers and stable isotopes. Palaeogeogr. Palaeoclimatol. Palaeoecol. 280, 371–386. https://doi.org/10.1016/j.palaeo.2009.06.024

Vlastélic, I., Abouchami, W., Galer, S.J.G., Hofmann, A.W., 2001. Geographic control on Pb isotope distribution and sources in Indian Ocean

Fe-Mn deposits. Geochim. Cosmochim. Acta 65, 4303–4319. https://doi.org/10.1016/S0016-7037(01)00713-X

von Blanckenburg, F., Belshaw, N.S., O'Nions, R.K., 1996. Separation of 9Be and cosmogenic 10Be from environmental materials and SIMS isotope dilution analysis. Chem. Geol. 129, 93–99. https://doi.org/10.1016/0009-2541(95)00157-3

von Blanckenburg, F., Nägler, T.F., 2001. Weathering versus circulation-controlled changes in radiogenic isotope tracer composition of the Labrador Sea and North Atlantic Deep Water. Paleoceanography 16, 424–434. https://doi.org/10.1029/2000PA000550

von Blanckenburg, F., O'Nions, R.K., 1999. Response of beryllium and radiogenic isotope ratios in Northern Atlantic Deep Water to the onset of northern hemisphere glaciation. Earth Planet. Sci. Lett. 167, 175–182. https://doi.org/10.1016/S0012-821X(99)00028-X

Walford, H.L., White, N.J., Sydow, J.C., 2005. Solid sediment load history of the Zambezi Delta. Earth Planet. Sci. Lett. 238, 49–63. https://doi.org/10.1016/j.epsl.2005.07.014

Weissel, J.K. and Hayes, D.E., 1972. Magnetic anomalies in the Southeast Indian Ocean, in Antarctic Oceanology II - The Antarctic - New Zealand Sector, D.E. Hayes (ed.), Am. Geophys. Union., Ant. Res. Ser., 19: 165-196.

White, W.M., Albaréde, F., Telouk, P., 2000. High-precision analysis of Pb isotope ratios by multi-collector ICP-MS. Chem.Geol. 167,257–270

Woodruff, F., Savin, S., 1991. Mid-Miocene isotope stratigraphy in the deep sea: High-resolution correlations, paleoclimatic cycles, and sediment preservation. Paleoceanography 6, 755–806. https://doi.org/10.1029/91PA02561

Woodruff, F., Savin, S.M., 1989. Miocene deepwater oceanography. Paleoceanography 4, 87–140. https://doi.org/10.1029/PA004i001p00087

Wright, N.M., Scher, H.D., Seton, M., Huck, C.E., Duggan, B.D., 2018. No Change in Southern Ocean Circulation in the Indian Ocean From the Eocene Through Late Oligocene. Paleoceanogr. Paleoclimatology 33, 152–167. https://doi.org/10.1002/2017PA003238

You, Y., 2000. Implications of the deep circulation and ventilation of the Indian Ocean on the renewal mechanism of North Atlantic Deep Water. J. Geophys. Res. Oceans 105, 23895–23926. https://doi.org/10.1029/2000JC900105

Zachos, J., Pagani, M., Sloan, L., Thomas, E., Billups, K., 2001. Trends, Rhythms, and Aberrations in Global Climate 65 Ma to Present. Science 292, 686–693. https://doi.org/10.1126/science.1059412

CHAPITRE 6 : SYNTHÈSE, CONCLUSIONS ET PERSPECTIVES

6.1. Introduction

Ce chapitre final vise à synthétiser et à discuter les résultats obtenus tout au long de cette thèse ainsi qu'à aborder quelques perspectives scientifiques soulevées par cette étude.

La zone d'étude est située entre l'est du continent africain et l'ouest de Madagascar, ce qui correspond à un couloir maritime constitué de masses d'eau arrivant du sud de l'océan Atlantique et du nord de l'océan Indien. De par ses particularités océanographiques et géographiques, le canal du Mozambique constitue un lieu tout à fait unique pour comprendre la courantologie régionale et son évolution passée. Ainsi, les objectifs de ce travail étaient (1) d'identifier les masses d'eau océaniques circulant dans le canal du Mozambique, (2) de retracer leur évolution au cours des derniers 30 Ma et (3) de comprendre l'impact des bouleversements climatiques et géographiques à échelle mondiale et régionale sur la composition géochimique des masses d'eau et sur leur circulation.

Grâce à plusieurs missions océanographiques (Leclaire, 1975, 1984 ; Moulin, Evain, 2016 ; Olu, 2014), un panel exceptionnel de 33 encroûtements Fe-Mn a été dragué avec des intervalles les plus réguliers possibles le long des 1600 km que constituent le canal du Mozambique, assurant une répartition spatiale (X, Y) idéale des échantillons pour cette étude. Ils correspondent à des profondeurs variant de 170 à 2650 m permettant ainsi d'étudier les signatures de toutes les masses d'eau de la région (surfaces, intermédiaires et profondes). Les traceurs isotopiques étudiés correspondent au Nd et au Pb, qui sont des proxys hautement utilisés et étudiés pour la caractérisation des masses d'eau dans les différents bassins océaniques (Albarède et al., 1997; Christensen et al., 1997; Frank, 2002; Frank et al., 2002; Frank, O'Nions, 1998; Ling et al., 1997; O'Nions et al., 1998; Rehkämper et al., 2004). De par l'érosion et la dissolution des roches continentales, chaque domaine océanique possède une signature isotopique en Nd qui lui est propre. Quant au Pb, il s'agit d'un proxy isotopique moins sensible pour tracer les courants mais qui peut refléter des apports élémentaires locaux ainsi que leurs sources. Son utilisation permet également de comparer ses tendances à celles du Nd, malgré les temps de résidence différents de ces deux traceurs isotopiques.

Plusieurs axes d'analyses ont été choisis et étudiés. Il s'agissait dans un premier temps d'échantillonner et d'analyser la surface des 33 encroûtements Fe-Mn, afin d'acquérir une vision 3D des masses d'eau et de leurs signatures isotopiques (Chapitre 3). Cet axe permettait ainsi d'établir la courantologie moderne du canal. Le second axe d'analyse visait à établir des séries temporelles sur quatre encroûtements Fe-Mn, dont les profondeurs sont proches de limites isotopiques en Nd des courants, afin d'étudier des changements de masses d'eau (Chapitre 4). Enfin, le dernier axe permettait d'étudier les séries temporelles de trois encroûtements Fe-Mn profonds (> 1780 m) (Chapitre 5). Ces échantillons étant choisis pour leurs localisations à trois endroits clés du canal (jalon nord ; centre – nord de la ride de Davie ; jalon sud), ils permettaient de comprendre et d'établir la paléocéanographie de la région.

Ainsi, dans ce chapitre, les conclusions principales de cette thèse viennent répondre à des questions soulevées dans le chapitre 1 mais également dans les discussions scientifiques amenées au cours du manuscrit. Certaines interrogations demeurent et seront donc présentées avec les perspectives, à la fin de ce chapitre.

6.2. Que reflète la signature géochimique des encroûtements Fe-Mn ?

Les encroûtements Fe-Mn constituent des archives condensées de l'évolution géochimique des océans au cours du temps. Plusieurs protocoles ont été établis et présentés dans le chapitre 2 afin d'analyser la minéralogie et la géochimie élémentaire et isotopique des oxydes de Fe-Mn.

- **Charles, C.**, Barrat, J.-A., Pelleter, E., 2021. Trace Element Determinations in Fe-Mn Oxides by High Resolution ICP-MS after Tm Addition. Talanta 122446.

Cependant, cette conclusion ne reviendra pas sur les analyses minéralogiques et géochimiques (majeurs, traces) (développement analytique ; Charles et al., 2021). Bien qu'il s'agisse d'un travail majeur et indispensable pour s'assurer de la bonne caractérisation des signatures isotopiques (Nd, Pb) de l'eau de mer, il mérite une étude d'envergure entièrement dédiée compte tenu du côté exceptionnel du jeu de données (perspectives - paragraphe 6.6.2).

6.3. Identification et modèle de circulation des masses d'eau subactuelles dans le canal du Mozambique

Cette étude repose sur l'analyse isotopique du Nd de la surface des 33 échantillons de la thèse (170-2650 m de profondeur), intégrant une large résolution temporelle de 20 000 à 80 000 ans.

6.3.1. Quelles sont les principales masses d'eau dans la région et quelles sont leurs signatures isotopiques en Nd ?

La composition isotopique des masses d'eau présentes dans le canal du Mozambique varie entre de valeurs très faiblement radiogéniques (εNd = -10.1) au Plateau des Aiguilles jusqu'à des valeurs plus radiogéniques (εNd = -7.1) au mont Paisley. Les résultats ont permis d'identifier les signatures isotopiques en Nd des masses d'eau présentent dans le canal, avec :

(1) une masse d'eau superficielle (> 700 m) caractérisée par une signature fortement radiogénique (εNd = -7.6) correspondant au SICW ;

(2) une masse d'eau indienne intermédiaire (> 1500 m) similaire au RSW présentant une signature isotopique en Nd également très radiogénique (-7.1 > εNd > -8.0) ;

(3) une zone de transition isotopique caractérisée d'une part par sa profondeur (axe Z), entre les masses d'eau intermédiaires et profondes (de 1300 à 1650 m ; -7.7 > εNd > -9.1), et d'autre part d'après les zones de mélange de deux masses d'eau profondes aux signatures contrastées (NADW, NIDW – voir ci-dessous ; axes X et Y) ;

(4) des masses d'eau profondes aux compositions isotopiques contrastées reflétant NIDW (εNd up to -7.5) et le NADW (εNd = -10.1) (Figure 6.1).

Il a ainsi été possible d'établir une cartographie 2D des courants dans le canal du Mozambique (avec leurs signatures isotopiques en Nd et leurs variations), mais également de les étudier en 3D grâce aux profondeurs variées des encroûtements analysés.

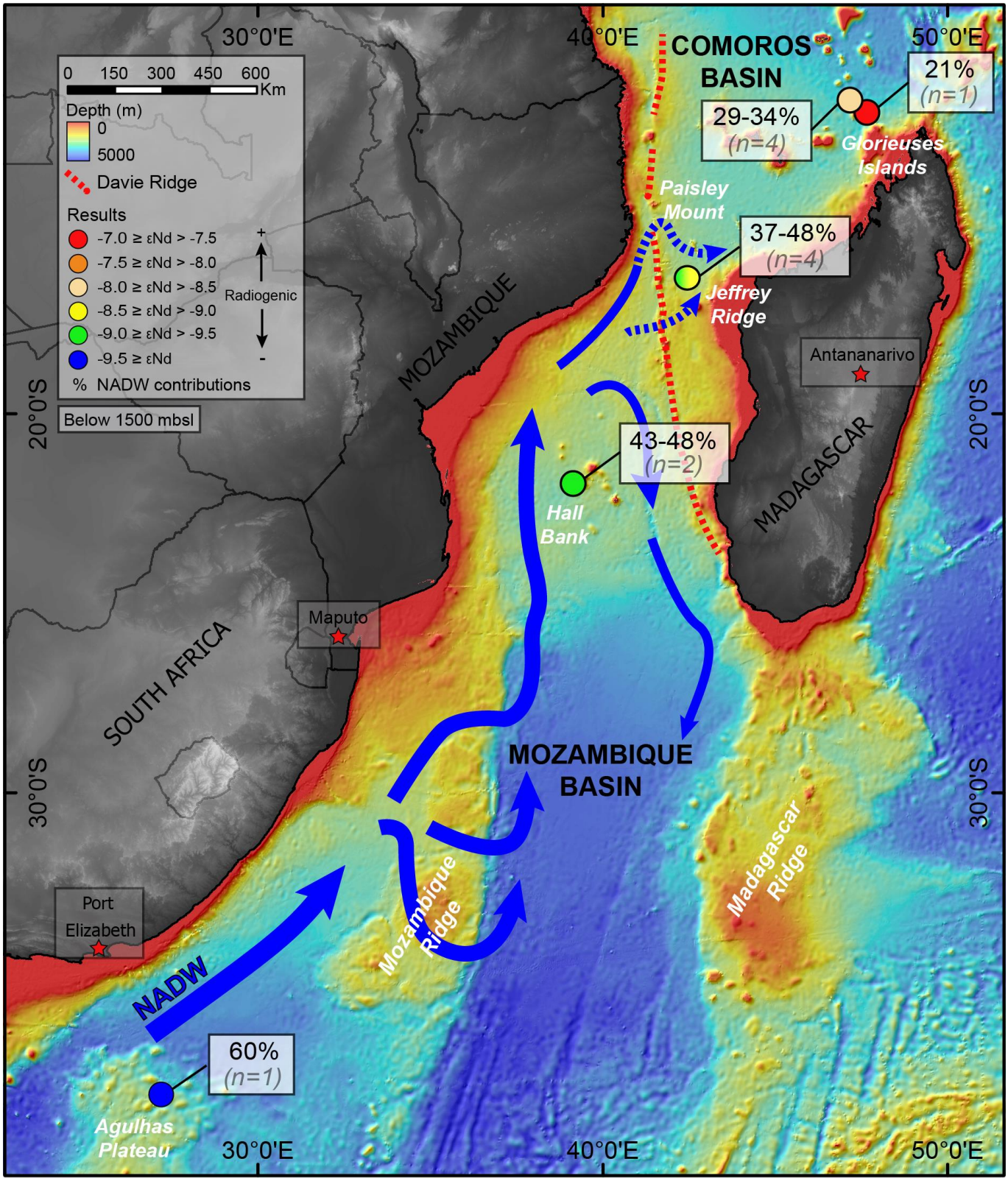

Figure 6.1. *Bathymétrie du canal du Mozambique (données issues de GEBCO et des missions océanographiques PAMELA) montrant les estimations de contributions du NADW et sa circulation dans le canal du Mozambique. Les flèches en pointillés représentes les potentiels passages topographiques de la ride de Davie permettant la propagation du NADW dans le bassin des Comores. Il s'agit d'une figure synthèse issue du papier Charles et al. (2020), modifiée et replacée ici par souci de confort pour le lecteur.*

6.3.2. Quelle est la circulation moderne des courants profonds ?

A travers la corrélation des résultats isotopiques en Nd et en Pb, un nouveau modèle océanographique a été établi apportant des informations inédites sur l'évolution des courants profonds dans le canal du Mozambique (Figure 6.1). Il montre que le NADW circule au sud du continent africain, et a été enregistré au niveau du Plateau des Aiguilles. Le courant Atlantique évolue ensuite dans le canal du Mozambique, par le sud, en direction du nord, où il traverse la ride du Mozambique avant d'atteindre le bassin profond du Mozambique et, dans un second temps, la région du Banc du Hall. Au nord, se trouve la ride de Davie. Cette structure marque la séparation entre le sud et le nord du canal, le séparant en deux bassins : le bassin profond du Mozambique et le bassin des Comores, où le NADW (up to $\varepsilon Nd = -9.4$) circule jusqu'à 90 km au nord de Juan de Nova et 700 km au sud des Îles Glorieuses. Cependant, c'est le NIDW qui est le courant profond majoritaire du bassin des Comores. Il s'étend depuis les Îles Glorieuses, en direction du sud, où il rencontre et domine le NADW au niveau de la ride de Jeffrey (16°S).

6.3.3. La ride de Davie joue-t-elle un rôle de barrière topographique dans l'évolution des masses d'eau profondes?

Plusieurs auteurs ayant étudié la géodynamique du canal du Mozambique présentent la ride de Davie comme une barrière topographique à la circulation des masses d'eau profondes de la région (Mantyla, Reid, 1995; Toole, Warren, 1993; You, 2000).

Cependant, le travail de cette thèse vient apporter de nouvelles estimations quant à la propagation des courants profonds dans le canal. La contribution du NADW au niveau du Plateau des Aiguilles a été estimée à 60% (Figure 6.1). Cette estimation est appuyée par le travail de Rahlf et al. (2020) qui démontre le mélange du NADW et du CDW à l'est de Cape Basin, au sud de l'Afrique. Sa contribution diminue ensuite progressivement avec son expansion vers le nord, jusqu'à atteindre entre 43 et 48% d'influence au Banc du Hall et entre 37 et 48% à la ride de Jeffrey, juste au nord de la ride de Davie (16°S).

Au niveau de la ride de Jeffrey, il rencontre le NIDW dont l'influence est majoritaire, avec une contribution estimée entre 52 et 63%. Ces observations et quantifications viennent en support des résultats hydrographiques de Collins et al. (2016), enregistrant le NIDW et le NADW dans le bassin des Comores.

Cette thèse confirme que la ride de Davie ne s'apparente pas à un obstacle géographique empêchant la circulation des courants profonds dans le nord du canal du Mozambique, et suggère que des couloirs topographiques sont présents le long de cette ride pour permettre l'évolution du courant NADW vers le nord (Figure 6.1).

- **Charles, C.**, Pelleter, E., Révillon, S., Nonnotte, P., Jorry, S.J., Kluska, J.-M., 2020. Intermediate and deep ocean current circulation in the Mozambique Channel: New insights from ferromanganese crust Nd isotopes. Marine Geology. 430, 106356.

6.4. Géodynamique du canal du Mozambique : identification et datation de mouvements verticaux à partir de 12 Ma

Le premier axe de recherche (paragraphe 6.2) a identifié la circulation moderne des masses d'eau présentes dans le canal du Mozambique et leurs signatures isotopiques en Nd. Les étudier a

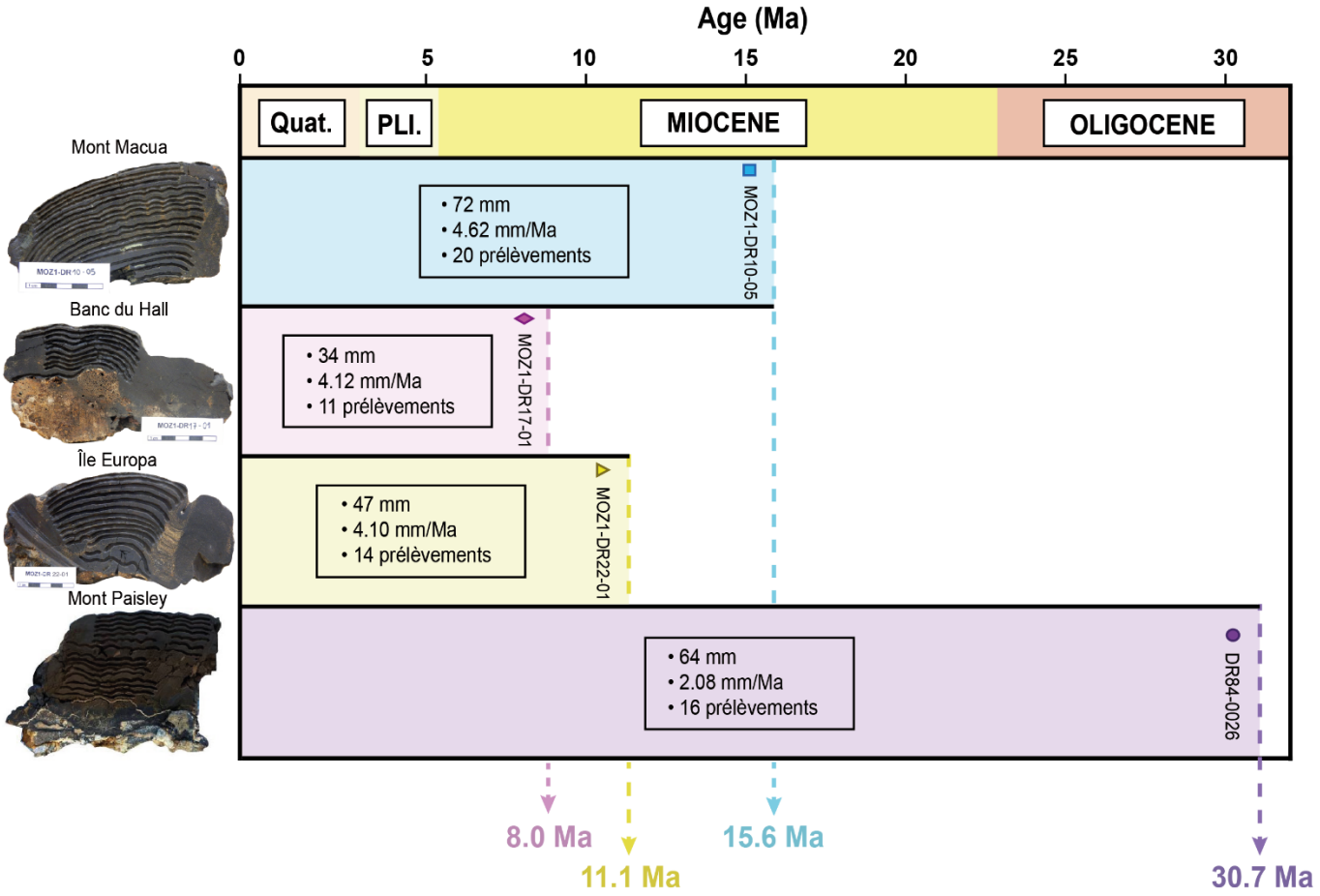

Figure 6.2. *Figure synthétique présentant les quatre encroûtements Fe-Mn utilisés dans la reconstruction paléogéodynamique du canal du Mozambique et leurs principales caractéristiques (épaisseur, taux de croissance, nombre de lamines prélevées et âge).*

également révélé des différences de εNd (jusqu'à plus de 2 unités) entre des masses d'eau profondes et intermédiaires.

De telles différences pourraient permettre d'identifier des changements de bathymétrie des encroûtements Fe-Mn dans une région où de nombreux auteurs ont mis en évidence des phases d'uplift et de subsidence depuis le début du Miocène (~ 23 Ma ; e.g. Courgeon et al., 2017, 2016; Leroux et al., 2020 ; Ponte, 2018 ; Walford et al., 2005).

Ainsi, quatre encroûtements Fe-Mn ont été sélectionnés, en fonction de leurs profondeurs modernes (800 à 1900 m), afin d'identifier de potentiels mouvements verticaux à partir des variations leurs signatures isotopiques en Nd.

6.4.1. Quelle est la résolution temporelle des encroûtements Fe-Mn étudiés pour les reconstructions géodynamiques ?

Les quatre encroûtements Fe-Mn échantillonnés et analysés pour la reconstruction paléogéographique du canal du Mozambique ont des âges estimés à 15.6 Ma (MOZ1-DR10-05, Mont Macua), 8.0 Ma (MOZ1-DR17-01, Banc du Hall), 11.1 Ma (MOZ1-DR22-01, Île Europa) et 30.7 Ma (DR84-0026, Mont Paisley) (Figure 6.2). Leur résolution temporelle est comprise entre 150

000 et 550 000 ans par strate (avec un total de lamines prélevées de 20, 11, 14 et 16, respectivement).

6.4.2. Des bouleversements géographiques ont-ils été enregistrés dans le canal du Mozambique ? Si oui, lesquels ?

Des variations significatives ont été révélées dans les signatures isotopiques (Nd, Pb) des quatre encroûtements Fe-Mn ici analysés. Elles montrent trois grandes périodes de bouleversements :

(1) depuis l'Oligocène (30.7 Ma) au Miocène moyen (11.1-11.7 Ma) avec des changements majeurs dans les compositions isotopiques en Pb des échantillons DR84-0026 et MOZ1-DR10-05 ;

(2) entre le Miocène moyen (11.1-11.7 Ma) et le Pliocène (5.7-3.4) avec des enregistrements isotopiques en Nd de plus en plus radiogéniques et en Pb de moins en moins radiogéniques sur les quatre séries temporelles étudiées ;

(3) entre le début du Pliocène (5.7-3.4 Ma) et le Pléistocène (1.6 Ma) avec des variations isotopiques en Nd de moins en moins radiogéniques et de plus en plus radiogénique en Pb, principalement visibles sur l'échantillon MOZ1-DR17-01.

L'étude de ces variations a montré que les encroûtements Fe-Mn étudiés ont changé de position dans la colonne d'eau au cours du temps, passant d'une masse d'eau à une autre, aux propriétés géochimiques différentes, grâce à des mouvements verticaux locaux.

Plusieurs événements paléogéographiques majeurs ont ainsi été identifiés, et datés depuis l'Oligocène. Entre 30.7 et 11.1 Ma, de fortes influences isotopiques en Pb, issues des produits détritiques de la structure himalayenne, apportés par les courants indiens, et des apports élémentaires du bassin de la Téthys, transportés par d'anciens courants méditerranéens, ont été enregistrées au niveau du Mont Macua, au nord du canal du Mozambique et de la ride de Davie (Figure 6.3).

A partir de 11.7 Ma, les enregistrements en Nd reflètent d'abord un phénomène d'uplift puis de subsidence. Le premier secoue la géodynamique du canal jusqu'à 3.4 Ma (Figure 6.3). Il est identifié aussi bien au sud qu'au nord de la région, avec une surélévation importante de la ride de Davie. Grâce aux datations absolues, aux valeurs isotopiques en Nd et aux connaissances acquises lors du chapitre 3, il a été possible de calculer le taux de croissance de ce phénomène qui est estimé entre 61 à 167 m/Ma, engendrant une amplitude entre 465 et 1265 m. Quant à la subsidence, elle affecte le bassin profond du Mozambique entre 5.1 et 1.6 Ma (Figure 6.3). Nous avons estimé son taux de d'affaissement entre 186 et 300 m/Ma, soit une amplitude comprise entre 650 et 1050 m.

Ces estimations ont pu être comparées à des résultats obtenus de manières indépendantes. Elles montrent une parfaite cohérence avec les données d'études précédentes estimant : (1) un uplift entre 850 m au sud (Partridge, 1998) et 425-600 m au nord (Îles Glorieuses ; Leroux et al., 2020 ; Partridge, 1998) et (2) une subsidence comprise entre 435 et 663 m au sud (Bank du Hall ; Courgeon, 2017), entre 221 et 317 m au nord de la ride de Davie (Courgeon, 2017) et jusqu'à 500 m aux Îles Glorieuses (Leroux et al., 2020).

L'identification de ces deux phénomènes, leurs datations absolues et les calculs associés, viennent compléter des études préalablement menées sur la

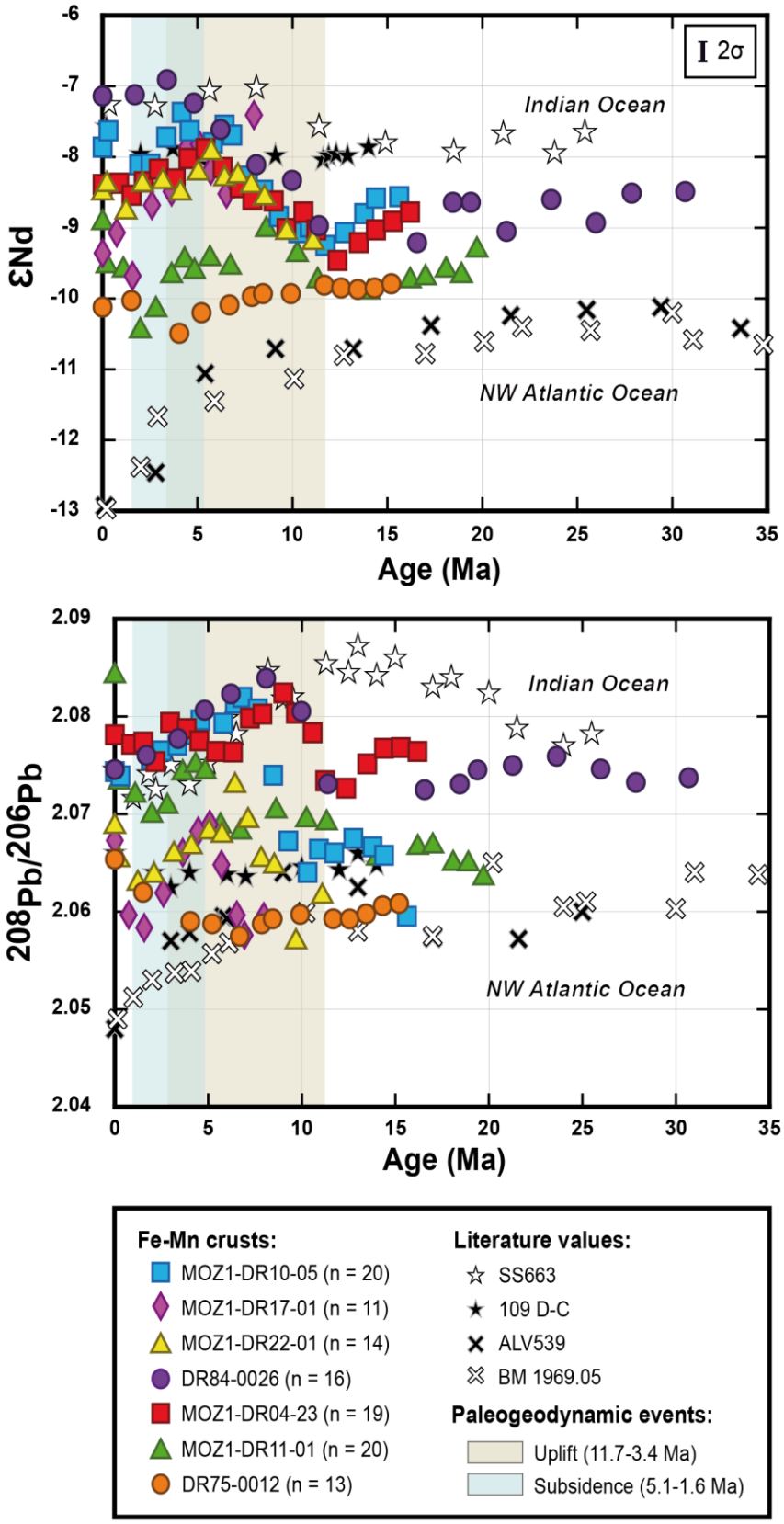

Figure 6.3. *Figure synthétique des signatures isotopiques $\varepsilon_{Nd\ (T)}$ et $^{208}Pb/^{206}Pb$ en fonction du temps. La marge d'erreur est incluse dans les points. Des signatures provenant d'études précédentes ont été ajoutées pour comparaisons : SS663 de O'Nions et al. (1998) et Frank, O'Nions (1998); 109 D-C et ALV539 de O'Nions et al. (1998) et, BM 1969.5 de Burton et al. (1997) and O'Nions et al. (1998).*

géodynamique de la région entre le Miocène et le Pliocène (Charles et al., in prep).

Ainsi, à partir d'encroûtements Fe-Mn minutieusement sélectionnés d'après leurs profondeurs et leurs localisations, dans des régions aux masses d'eau dont les propriétés isotopiques sont bien différenciées, il est possible d'identifier, d'estimer et de dater des mouvements verticaux.

C'est la première fois que de tels objets géologiques sont utilisés pour de telles reconstructions géodynamiques.

6.4.3. Quelle pourrait être l'incidence de tels mouvements verticaux sur la circulation des masses d'eau régionales au cours du temps ?

Ces bouleversements bathymétriques peuvent avoir des conséquences majeures en impactant considérablement les voies de circulation habituelles de courants océaniques.

En effet, l'échantillon DR84-0026, localisé au nord de la ride de Davie et analysé dans le chapitre 4, révèle que sa signature isotopique en Nd, au Miocène, est celle d'une masse d'eau fortement influencée par une composition peu radiogénique de type NADW. Ce qui indique que ce courant circulait intensément au nord du canal il y a plus de 12 Ma. Or, les recherches effectuées sur la circulation moderne (Chapitre 3) reflètent que la signature isotopique des masses d'eau profondes au nord du canal, n'est aujourd'hui pas si différente de celle des courants intermédiaires indiens (RSW), indiquant la circulation du NIDW. La corrélation de ces résultats indique donc des changements topographiques, comme synthétisé dans le paragraphe précédent, mais également océanographiques.

Ainsi, les élévations de topographie (uplift) peuvent créer des obstacles et indirectement, des déviations des masses d'eau. A l'inverse, les affaissements de topographie (subsidence) peuvent ouvrir de nouvelles voies de propagation des courants. C'est donc tout un système océanographique qui peut se retrouver modifié.

6.5. Reconstruction océanographique des courants profonds du canal du Mozambique : un modèle évolutif sur 20 Ma

Le second axe de recherche (paragraphe 6.3), basé sur quatre encroûtements Fe-Mn localisés à des profondeurs très variées, a permis d'identifier, de caractériser et de dater deux phénomènes géodynamiques majeurs ayant impacté la topographie du canal du Mozambique depuis 11.7 Ma.

Le troisième axe d'étude vise à retracer l'évolution des courants profonds au cours du temps à partir de trois encroûtements Fe-Mn situés dans les masses d'eau profondes (> 1780 m) et répartis à trois endroits clés du canal (jalon nord ; centre – nord de la ride de Davie ; jalon sud). L'objectif ici était d'identifier la circulation profonde avant et après les bouleversements géodynamiques mis préalablement en évidence.

6.5.1. Quelle est la résolution temporelle des encroûtements Fe-Mn étudiés pour les reconstructions océanographiques ?

Les trois encroûtements Fe-Mn échantillonnés et analysés pour la reconstruction paléocéanographique du canal du Mozambique ont des âges estimés à 16.2 Ma (MOZ1-DR04-23, Îles Glorieuses), 19.7 Ma (MOZ1-DR11-01, Ride de Jeffrey) et 15.2 Ma (DR75-0012, Plateau des Aiguilles) (Figure 6.4). Leur résolution

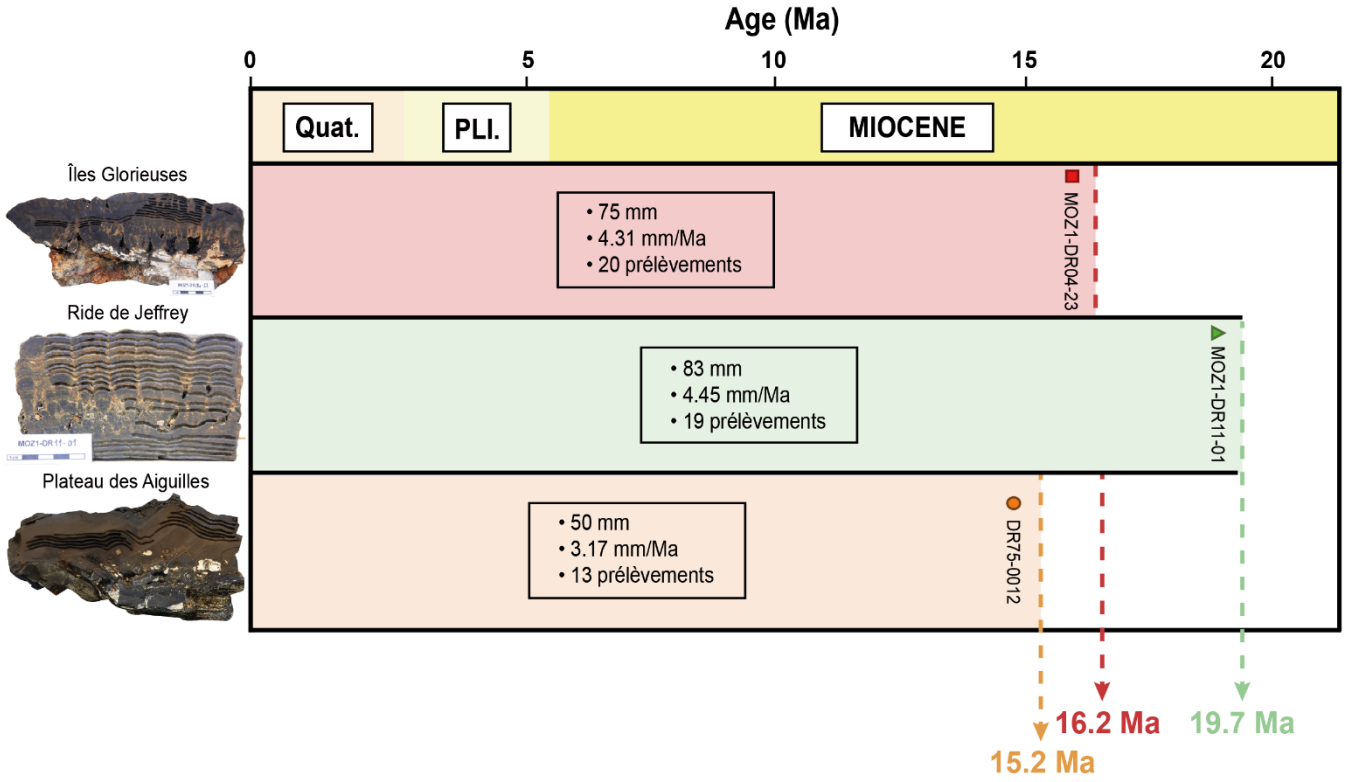

Figure 6.4. *Figure synthétique présentant les trois encroûtements Fe-Mn utilisés dans la reconstruction paléocéanographiques du canal du Mozambique et leurs principales caractéristiques (épaisseur, taux de croissance, nombre de lamines prélevées et âge).*

temporelle est comprise entre 150 000 et 550 000 mille ans par strate prélevée (avec un total de lamines prélevées de 20, 19 et 13, respectivement).

6.5.2. Comment ont évolué les signatures isotopiques des courants profonds au cours des 20 derniers Ma ?

Au sud du canal du Mozambique, la composition géochimique du NADW est restée relativement constante et peu radiogénique en Nd au cours du Néogène (εNd = -9.8 à 15.2 Ma) et du Quaternaire (εNd = -10.1 à l'actuel) (Figure 6.3).

Bien que la glaciation de l'hémisphère nord, débutée il y 3 Ma, ait modifié significativement les propriétés du NADW, et notamment son isotopie, vers une composante Nd plus faiblement radiogénique (εNd = -13 à l'actuel ; Abouchami et al., 1997; Burton et al., 1997; Frank, O'Nions, 1998), ce changement de composition ne se reflète pas dans le canal du Mozambique (en raison d'une diminution de l'export du NADW vers l'océan Austral).

Depuis l'Oligocène, le NIDW, au nord du canal, présente une géochimie beaucoup plus radiogénique, semblable à celle du NIDW enregistrée à l'est et au centre de l'océan Indien (Frank, O'Nions, 1998 ; O'Nions et al., 1998) (Figure 6.4).

Cependant, une source de Pb très peu radiogénique est enregistrée au niveau des Îles

Glorieuses vers 9.0 Ma ($^{208}Pb/^{206}Pb$ = 2.0824) (Figure 6.4). Elle reflèterait un apport important des produits granitiques issus de l'altération de l'Himalaya (Derry, France-Lanord, 1996), dont l'érosion fut estimée très intense entre 20 et 14 Ma (Searle, 1996).

6.5.3. Quelles sont les conséquences de l'uplift sur le transport des masses d'eau profondes au cours des 12 derniers Ma ?

La circulation océanique des courants profonds du canal du Mozambique a été significativement modifiée entre le Miocène (11.7 Ma) et le Pliocène (3.4 Ma).

Avant 11.7 Ma, le NADW dominait la courantologie du canal, depuis le sud jusqu'au nord, avec une forte influence, estimée entre 81 et 87% à 12.4 Ma, et similaire à celle mesurée au Plateau des Aiguilles (83-88%). Cependant, à partir de cette période, sa présence dans l'archipel des Îles Glorieuses diminue graduellement en raison de la mise en place progressive de l'uplift identifié et daté précédemment (11.7-3.4 Ma) (Figure 6.3, 6.5).

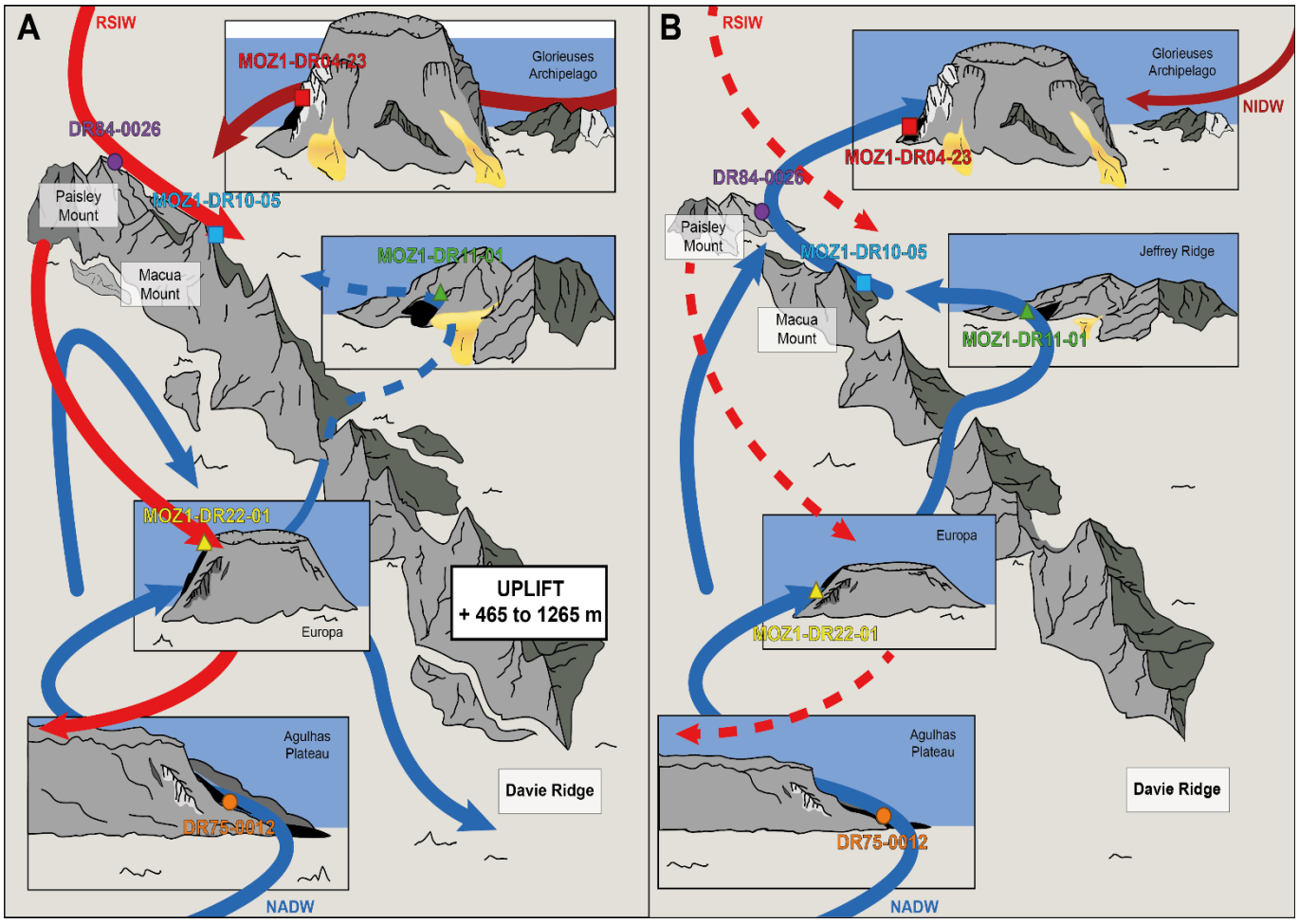

Figure 6.5. *Reconstruction paléocéanographique des courants profonds Atlantique (NADW) et Indien (NIDW) du canal du Mozambique. La figure (A) illustre la situation au Pliocène (3.4 Ma), après la mise en place de l'uplift généralisé dans la région, alors que la figure B correspond à la reconstruction paléocourantologique au Miocène (11.7 Ma), avant ce bouleversement géodynamique. Il s'agit d'une figure synthèse issue du chapitre 5 et modifiée.*

La contribution du NADW est alors estimée avec un minimum de 38% à 5.4 Ma. Au cours de ce phénomène, la ride de Davie s'est surélevée d'une amplitude estimée entre 465 et 1265 m, réduisant ainsi la circulation du NADW dans le bassin des Comores (Figure 6.5), avec un minimum d'apport de 34% à 3.0 Ma.

Il continue cependant à atteindre la ride de Jeffrey, nord de la ride de Davie, à hauteur de 64% minimum à 2.8 Ma contre 85% minimum juste avant l'uplift (14.0 Ma).

Malgré ces bouleversements paléogéographiques majeurs, la ride de Davie n'a jamais été suffisante pour limiter complètement l'évolution du courant NADW au nord du canal du Mozambique, et son mélange avec le NIDW (Figure 6.5).

6.6. Perspectives

6.6.1. Etendre la fiabilité des modèles d'âge des encroûtements Fe-Mn étudiés au-delà de 12 Ma

Dans cette étude, nous avons démontré que les encroûtements Fe-Mn étudiés se sont formés progressivement entre le Paléogène et le Quaternaire, dans le canal du Mozambique, en enregistrant l'évolution des compositions géochimiques des masses d'eau présentes dans la région.

Afin de réaliser des reconstructions paléogéographiques et paléocéanographiques, ils ont été échantillonnés et analysés, notamment afin d'obtenir leurs datations et d'établir des chronologies. Pour cela, l'isotopie du Be a été hautement utilisée. Cependant, celle-ci ne permet pas d'obtenir des âges absolus au-delà de 12 Ma (Chmeleff et al., 2010 ; Korschinek et al., 2010).

Pour pallier à cette limite, le choix a été fait d'extrapoler les taux de croissance mesurés, par rapports aux datations acquises par analyses isotopiques du Be, pour établir des chronologies supérieures à 10 Ma (Chapitres 4 et 5). Cependant, d'autres méthodes de datations existent et méritent d'être approfondies, afin de comparer les modèles d'âges obtenus et d'optimiser ainsi le facteur temporel des reconstructions.

6.6.1.1. Chronologie par datation empirique

La datation à partir du cobalt est basée sur le flux constant de cet élément et de sa concentration directement dépendant du taux de croissance (Frank et al., 1999; Manheim, 1986; Puteanus, Halbach, 1988). Cette méthode est utilisée fréquemment dans les reconstructions paléocéanographiques et indépendamment des autres techniques (David et al., 2001 ; Frank et al., 1999 ; Hu et al., 2012 ; Ling et al., 2005 ; Marino et al., 2017).

Dans le cadre de cette thèse, des datations ont été réalisées sur les encroûtements Fe-Mn MOZ1-DR04-23, MOZ1-DR11-01 et DR75-0012, à partir des équations développées par Manheim (1986), Manheim, Lane-Bostwick (1988) et Frank et al. (1999) (Chapitre 5). Ces résultats et comparaisons ont permis de développer une méthode de datations, à partir de l'isotopie du Be et de la méthode de Manheim (1986) lors que des datations absolues ne sont pas disponibles.

Bien que la méthode de datation à partir de la concentration en cobalt doit être considérée avec précaution en raison des lacunes de dépôts, il s'agit d'une technique de datation qui peut aider à préciser les âges des encroûtements Fe-Mn au-delà de 10 Ma (Frank et al., 2002), notamment en étant couplée à l'isotopie du Be.

Ainsi, il serait pertinent de tester les équations discutées dans le chapitre 5, sur les autres encroûtements Fe-Mn, notamment ceux utilisés pour les reconstructions paléogéographiques (MOZ1-DR10-05, MOZ1-DR17-01, MOZ1-DR22-01 et DR84-0026). Une nouvelle équation fiable pourrait être développée et de nouveaux modèles d'âges pourraient ainsi renforcer les contraintes temporelles des mouvements géodynamiques (uplift, subsidence) identifiés.

6.6.1.2. Chronologie par datation indirecte

Afin de pallier aux limites de la méthode précédente, une technique prometteuse a été développée à partir de l'isotopie de l'osmium (Klemm et al., 2005). Elle est basée sur la comparaison de l'évolution globale de l'isotopie de l'Os dans les encroûtements et celle dans l'eau de mer (Burton et al., 1999 ; Klemm et al., 2005 ; Peucker-Ehrenbrink, Ravizza, 2012, 2000).

Là encore, il serait intéressant de procéder aux analyses isotopiques de l'Os de certains échantillons utilisés en séries temporelles afin de fixer avec justesse certains âges plus vieux que 10 Ma, tout en tenant en compte de potentielles lacunes qui seront désormais discernables. Une première sélection des échantillons a été réalisée.

Les encroûtements Fe-Mn estimés plus jeune que 10 Ma ont naturellement été écartés. Les échantillons ayant enregistrés l'uplift tels que MOZ1-DR10-05 (Mont Macua, 15.6 Ma) et DR84-0026 (Mont Paisley, 30.7 Ma) semblent très intéressants à analyser et notamment le DR84-0026 puisqu'il s'étend jusqu'à l'Oligocène.

L'encroûtement Fe-Mn MOZ1-DR04-23 (Îles Glorieuses, 16.2 Ma) serait également un bon candidat puisqu'il enregistre la diminution graduelle du NADW dans le bassin des Comores à partir de 11.7 Ma. Il s'agit également d'un échantillon très intéressant pour évaluer de potentiels phénomènes volcaniques régionaux.

6.6.2. Identifier des événements locaux par étude minéralogique et géochimique haute résolution de deux encroûtements Fe-Mn

Au cours de cette thèse, deux échantillons ont révélé une minéralogie et une géochimie différentes des autres encroûtements Fe-Mn. Leurs caractéristiques soulèvent plusieurs interrogations qui n'ont pas pu être approfondies.

Il s'agit de MOZ1-DR04-23 et de MOZ5-DR03-01. Le premier, MOZ1-DR04-23 (16.2 Ma), provient des Îles Glorieuses, localisé à grandes profondeurs, cet échantillon a permis de mettre en lumière la circulation des courants profonds dans le bassin des Comores (Chapitre 5).

Quant au second, MOZ5-DR03-01 (19.7 Ma), il a été dragué au large du continent africain, au nord de la vallée de Natal, à 110 km des côtes les plus proches et à une profondeur entre 950 et 1200 m (Figure 6.6). Les résultats des analyses de cet encroûtement Fe-Mn n'ont pas été présentés dans les chapitres précédents dans la mesure les enregistrements reflètent des phénomènes qui dépassent du cadre initial de la thèse.

Dans cette partie, nous proposons de poursuivre les études sur ces deux encroûtements Fe-Mn afin d'identifier et de caractériser des événements, très locaux, enregistrés à travers leur minéralogie et géochimie. Les analyses de minéralogie quantitatives ont dans un premier temps été effectuées par XRD à l'IFREMER comme présentées préalablement (Chapitre 5).

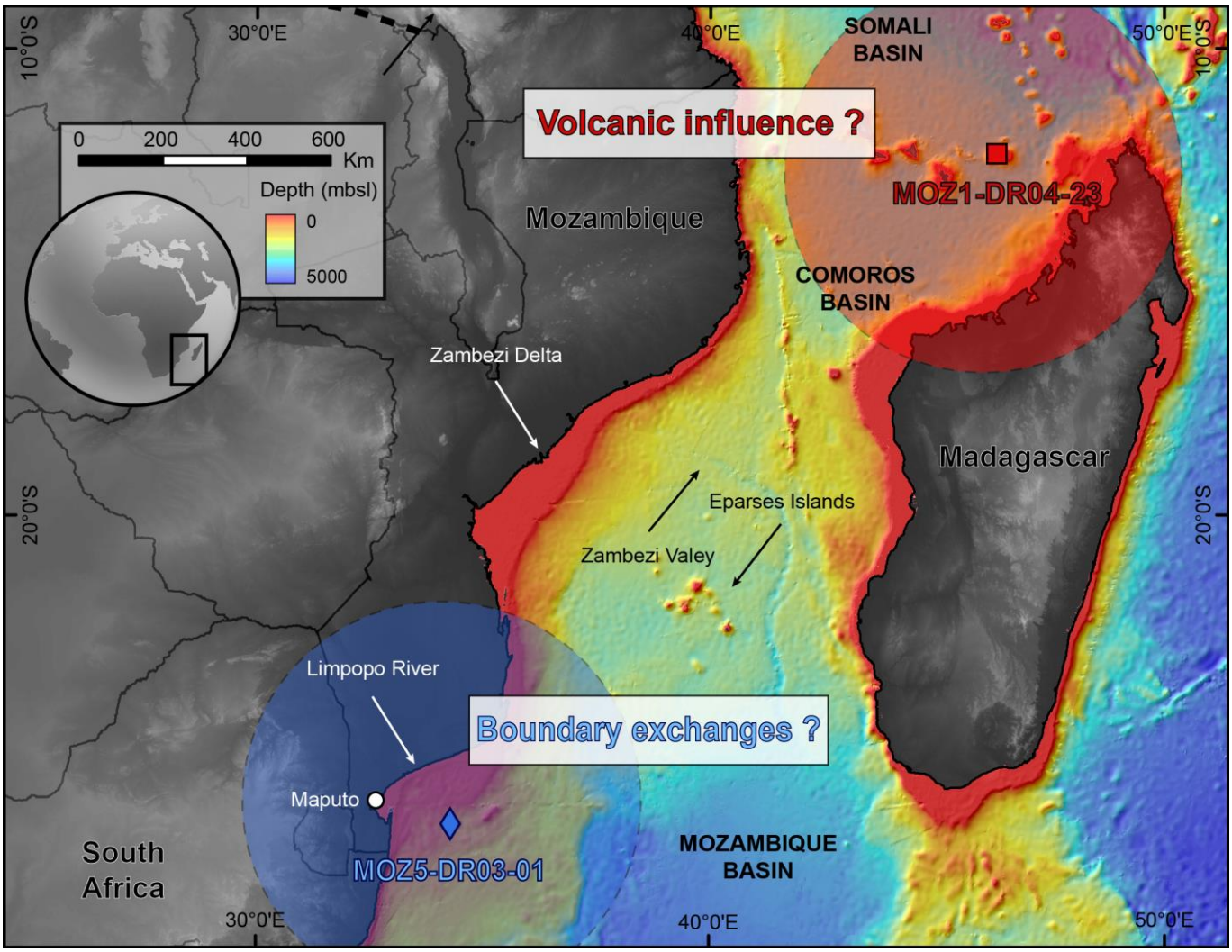

Figure 6.6. *Bathymétrie du canal du Mozambique (données issues de GEBCO et des missions océanographiques PAMELA) présentant la localisation des encroûtements Fe-Mn MOZ1-DR04-23 (Îles Glorieuses, 16.2 Ma) et MOZ5-DR03-01 (Vallée de Natal, 19.7 Ma) ainsi que les zones d'influence de potentiels phénomènes locaux enregistrés dans leurs compositions minéralogiques et géochimiques.*

La suite des analyses pétrographiques et minéralogiques a été menée en collaboration avec TOTAL-CSTJF. L'étude pétrographique de lames minces (40*60 mm ; Annexe 7) polies et recouvertes de carbone (25 nm d'épaisseur) a été réalisée afin de soumettre les échantillons à des analyses précises incluant l'étude des textures et des distributions d'éléments associés.

Des cartographies minéralogiques automatisées utilisant l'instrument FEG-SEM Qemscan ® (QUANTA 650, FEI) ont été réalisées sur les sections des échantillons (résolution 20 µm/pixel) et sur des zoom (résolution 2 µm/pixel). Les acquisitions de données FEG-SEM comprennent l'imagerie par électrons secondaires, électrons rétrodiffusés (BSE) (résolution 250 nm) et la cartographie par spectroscopie dispersive en énergie (EDS) (résolution 2 µm).

Enfin, le logiciel Nanomin (FEI, Hillsboro, OR, USA) a été utilisé pour analyser les données SEM-EDS afin de produire des cartes minéralogiques et chimiques des encroûtements

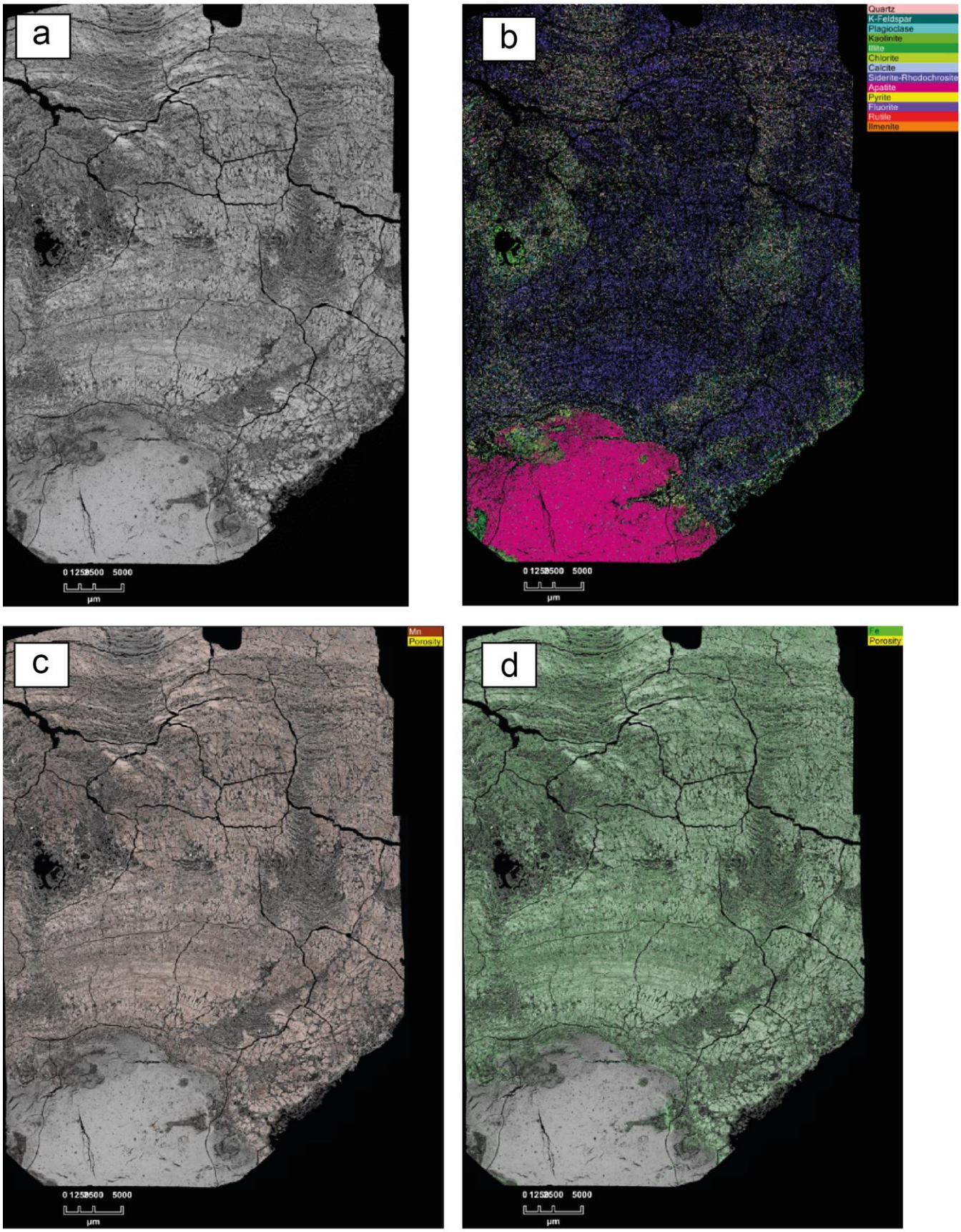

Figure 6.7. *Images et cartographies minéralogiques de la lame mince MOZ1-DR04-23 E réalisées avec le FEG-SEM Qemscan ®. a) acquisition BSE ; b) acquisition EDS montrant les principales phases minéralogiques (Nanomin - FEI, Hillsboro, OR, USA) ; c) acquisition BSE et les oxydes Mn ; d) acquisition BSE et les oxydes Fe.*

et de définir des caractéristiques texturales.

En ce qui concerne les analyses élémentaires et isotopiques (Nd, Pb, Be), elles ont déjà été réalisées selon les mêmes protocoles déjà présentés (Chapitre 2), et en même temps que les autres échantillons de la thèse.

6.6.2.1. Encroûtement Fe-Mn MOZ1-DR04-23 : événements volcaniques

Les premières analyses minéralogiques effectuées par XRD montrent que MOZ1-DR04-23 contient du quartz, en tant que principal minéral allochtone, ainsi que des feldspaths plagioclases et des feldspaths potassiques, en plus des oxydes Fe-Mn (Annexe 5). Ces résultats sont confirmés par les acquisitions et cartographies minéralogiques effectuées au FEG-SEM Qemscan ® (Figure 6.7 ; Annexe 7).

Par exemple, la composition totale de la lame mince MOZ1-DR04-23 E reflète du quartz (7%), les feldspaths potassiques (5%), les feldspaths plagioclases (3%) mais également des phases de pyrite, d'ilménite et de rutile en moindre teneur (< 0.5%).

D'autres lames minces de l'échantillon MOZ1-DR04-23 montrent également la présence de muscovite (< 0.5%). En ce qui concerne les données élémentaires, elles montrent des lamines de l'échantillon MOZ1-DR04-23 riches en aluminium (3.3% ; MOZ1-DR04-23 62 et 68 ; 14.4 et 15.3 Ma) et en titane (jusqu'à 2.2 % ; MOZ1-DR04-23 30, 33 et 38 ; 7.2 à 9.0 Ma), ainsi que deux corrélations entre ces deux éléments (Figure 6.8), ce qui pourrait refléter

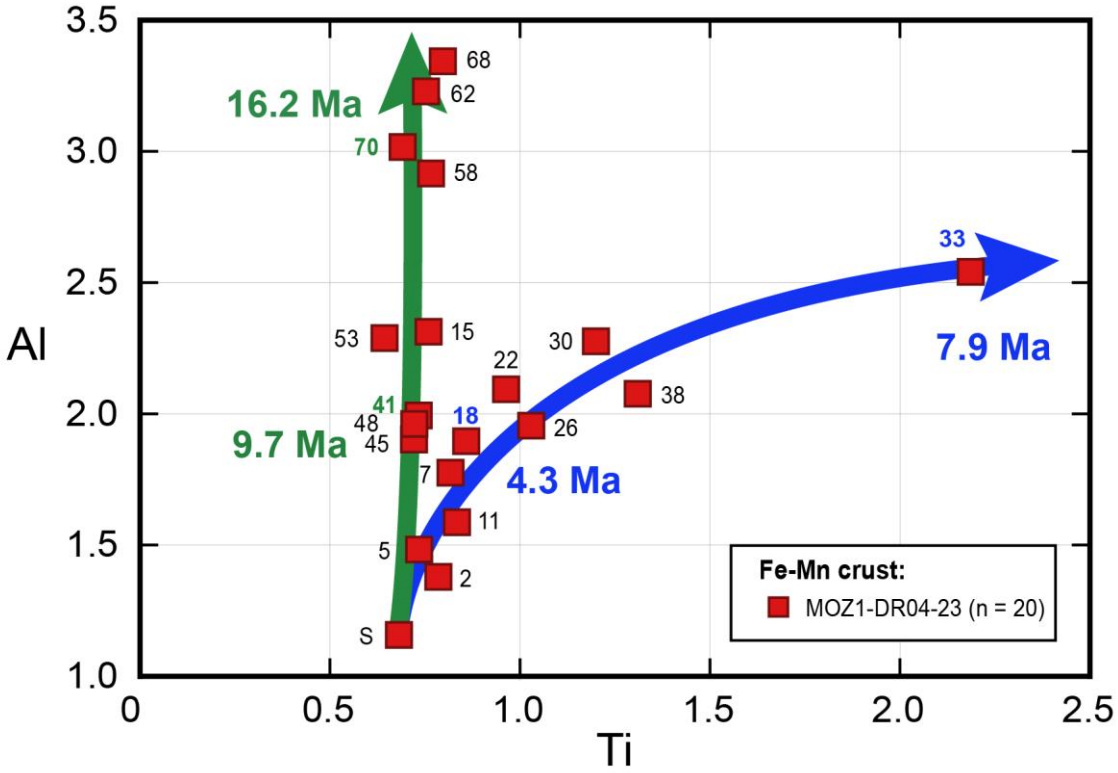

Figure 6.8. *Graphique des concentrations en Al en fonction des concentrations en Ti dans l'encroûtement Fe-Mn MOZ1-DR04-23. Les numéros au niveau de chaque point correspondent à la profondeur (mm) de la lamine prélevée dans l'encroûtement Fe-Mn, ceux en gras et en couleurs correspondent aux lamines dont les datations sont indiquées. Les deux flèches indiquent de potentiels influences de phénomènes volcaniques et/ou d'apports sédimentaires, et les âges associés.*

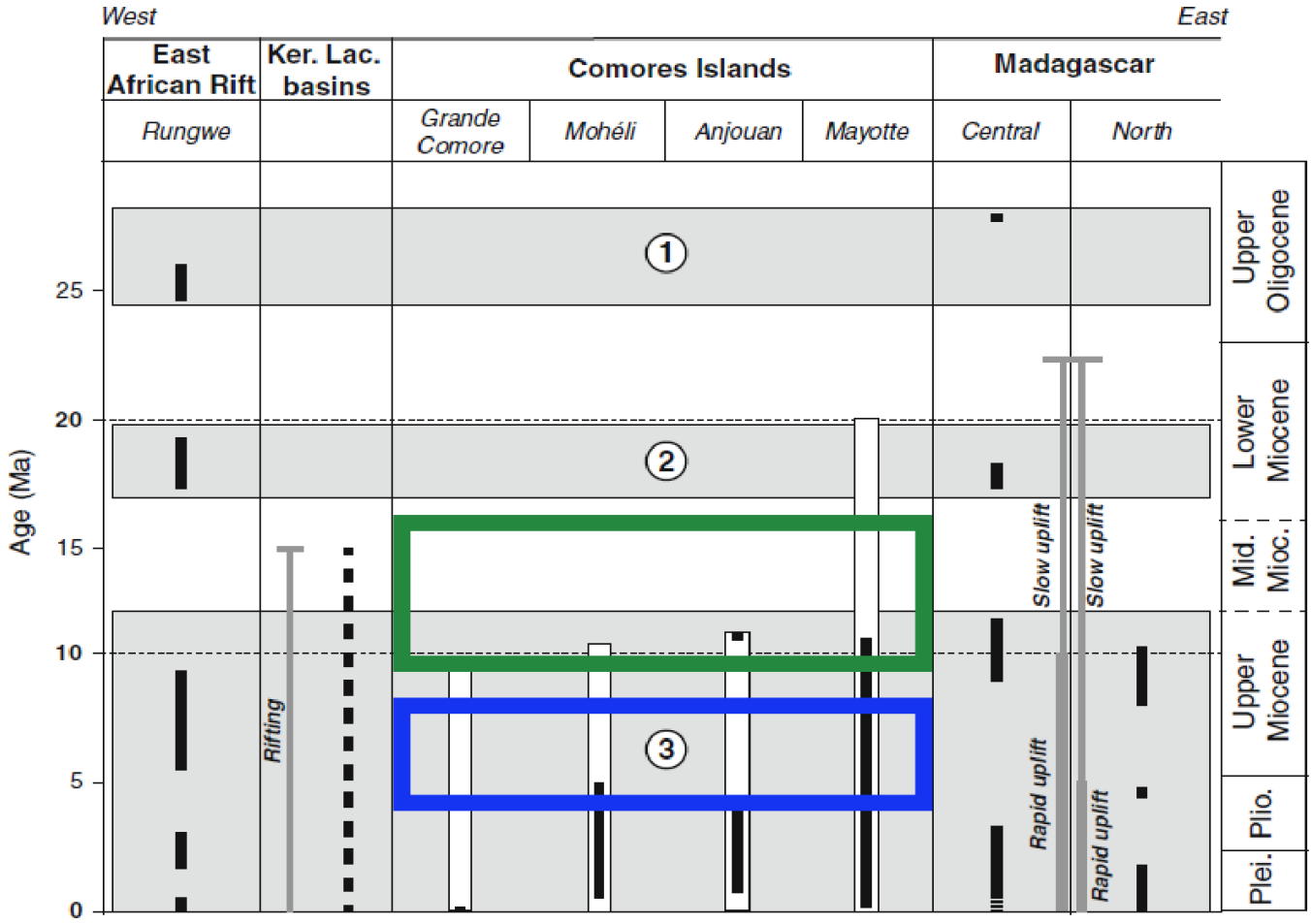

Figure 6.9. *Synthèse des phénomènes volcaniques (barres noires) dans l'archipel des Comores et dans les régions environnantes. Les barres blanches représentent les activités nouvellement estimées. Les numéros 1, 2 et 3 correspondent aux différentes périodes de volcanisme. Les encadrés représentent de potentiels phénomènes volcaniques enregistrés dans l'encroûtement Fe-Mn MOZ1-DR04-23, provenant de la région des Îles Glorieuses (**Figure 6.8**). Image modifiée, d'après Michon (2016).*

l'enregistrement d'apports détritiques riches en Al, à définir, et/ou des phénomènes volcaniques d'âges et de propriétés chimiques différents.

Il serait pertinent de s'intéresser aux zooms étudiés lors des acquisitions minéralogiques afin de pointer les zones d'abondances de ces minéraux et éléments. Une fois corrélées avec la chronologie de l'encroûtement Fe-Mn MOZ1-DR04-23, cela permettrait de s'intéresser à l'identification et à la caractérisation de potentiels phénomènes volcaniques (Figure 6.9) au cours des 16 derniers Ma. Dans un second temps, les analyses isotopiques en en Os pourraient significativement compléter ce travail en indiquant des événements magmatiques. Enfin, il serait aussi très intéressant de réaliser des analyses de Pb à haute résolution, avec un LA-MC-ICP-MS (Josso et al., 2020). Cette technique permettrait de mettre en évidence des variations géochimiques très fines aux âges préalablement choisis.

6.6.2.2. Encroûtement Fe-Mn MOZ5-DR03-01: « boundary exchanges »

Le second échantillon discuté est MOZ5-DR03-01 et provient du nord de la vallée de Natal. Les

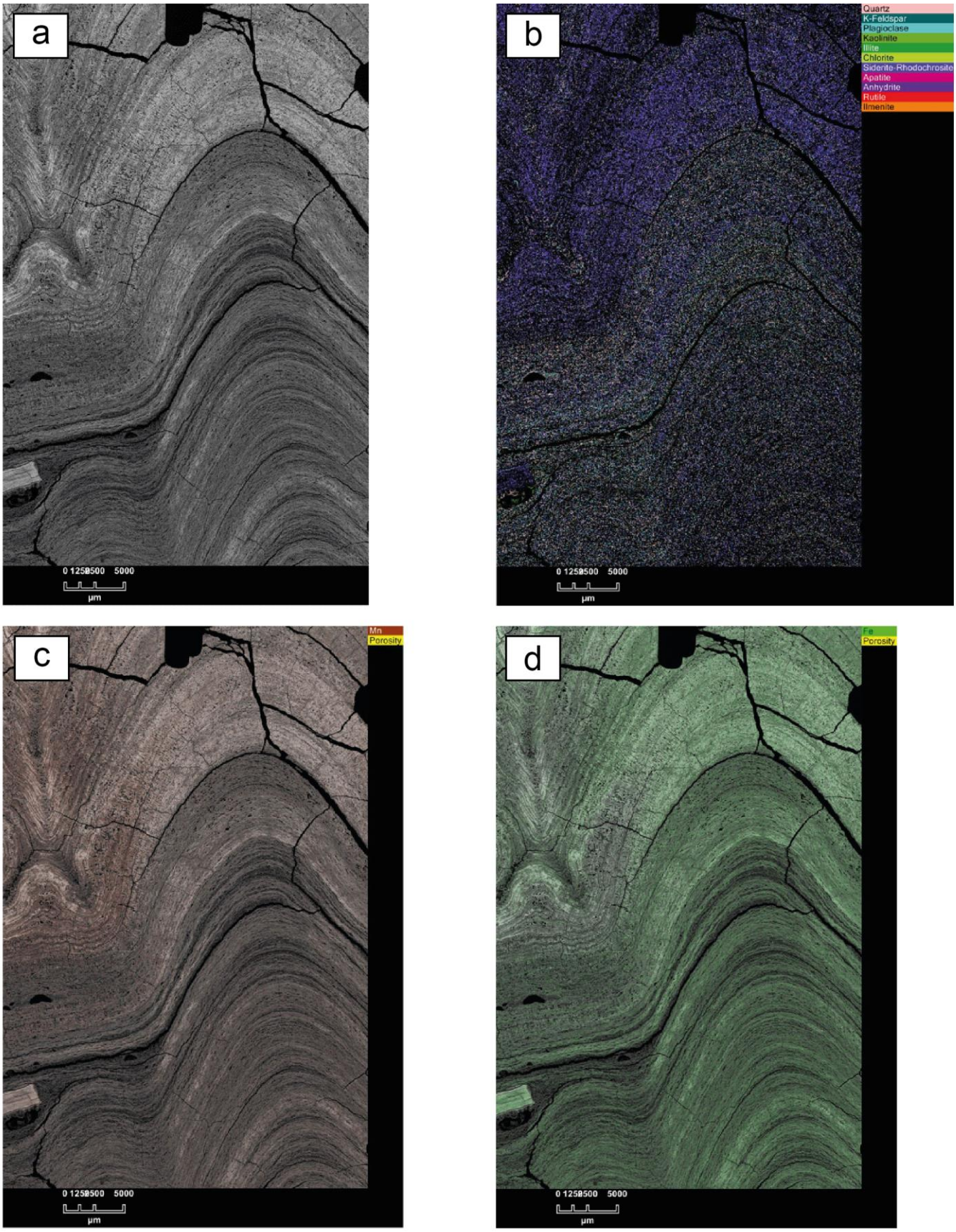

Figure 6.10. *Images et cartographies minéralogiques de la lame mince MOZ5-DR03-01 B réalisées avec le FEG-SEM Qemscan ®. a) acquisition BSE ; b) acquisition EDS montrant les principales phases minéralogiques (Nanomin - FEI, Hillsboro, OR, USA) ; c) acquisition BSE et les oxydes Mn ; d) acquisition BSE et les oxydes Fe.*

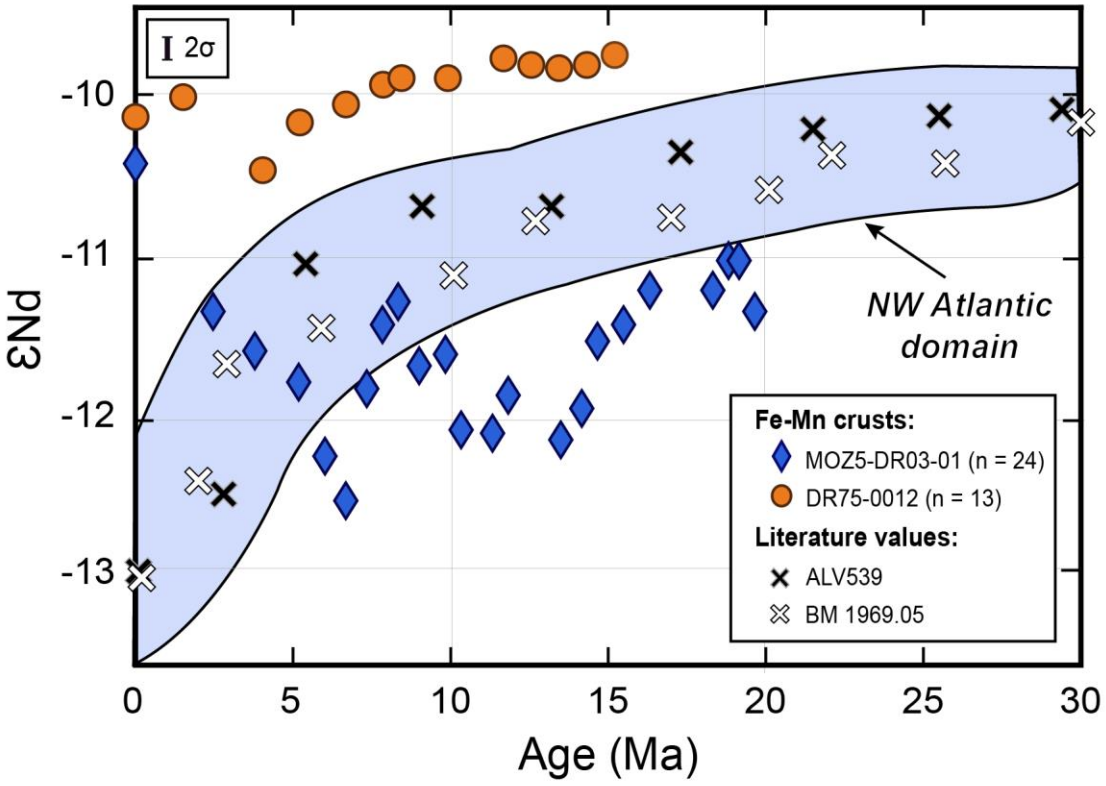

Figure 6.11. *Signature isotopique en Nd ($\varepsilon_{Nd\,(T)}$) en fonction de l'âge, acquis à partir du rapport isotopique $^{10}Be/^{9}Be$, des encroûtements Fe-Mn MOZ5-DR03-01 et DR75-0012 issus de cette étude. Les données des encroûtements Fe-Mn ALV539 et BM 1969.05 proviennent des travaux de Burton et al. (1997) et de O'Nions et al. (1998).*

résultats préliminaires issus de la XRD montrent une minéralogie commune aux autres encroûtements, avec la présence de quartz, feldspaths plagioclases et feldspaths potassiques en plus des oxydes Fe-Mn majoritaires (Annexe 6). Les acquisitions au FEG-SEM Qemscan ® confirment ces phases minéralogiques présentes à 11%, 6% et 5%, respectivement, dans la lame mince MOZ5-DR03-01 B (Figure 6.10 ; Annexe 7). Elles révèlent aussi la faible présence de minéraux tels que de la dolomite (<0.5%) ou de l'anhydrite (dans une seconde lame mince de l'échantillon) (<0.01%).

En ce qui concerne les données élémentaires, l'encroûtement Fe-Mn MOZ5-DR03-01 ne montre pas de valeurs qui ressortent par rapport aux autres échantillons.

Cependant, sa composition isotopique en Nd est très différente de celles préalablement étudiées (Chapitres 4 et 5). Celle-ci est très peu radiogénique (-10.2 > εNd > -12.5) et est marquée par de grandes variations (jusqu'à 2 εNd) (Figure 6.11). La signature montre son minimum à 6.7 Ma avant de remonter vers des valeurs plus radiogéniques.

Comme le montre la Figure 6.11, la composition isotopique en Nd de cet échantillon, est nettement moins radiogénique et moins homogène que celle de l'échantillon DR75-012, localisé plus au sud du canal du Mozambique (Plateau des Aiguilles), ou encore, celles des encroûtements Fe-Mn situés au nord-ouest de l'océan Atlantique (ALV539 ; BM 1969.05 ; Burton et al., 1997 ; O'Nions et al., 1998).

De tels changements isotopiques en si peu de temps ne semblent pas refléter la composition isotopique d'origine de la masse d'eau dans lequel l'encroûtement Fe-Mn s'est formé (AAIW ; -8 > εNd > -9 ; Amakawa et al., 2013; Arsouze et al., 2007; Jeandel, 1993; Piepgras, Wasserburg, 1982) mais laissent penser que l'histoire de cet échantillon est complètement différente des autres, et n'est pas liée aux mêmes processus géochimiques.

L'une des hypothèses pour expliquer cette signature particulière pourrait être que des minéraux allochtones, identifiés par leurs hautes concentrations en Al et K, pourraient avoir des quantités significatives de Nd avec une signature très peu radiogénique qui pourrait contaminer la signature initiale de l'échantillon. Cependant, aucune corrélation n'est observable entre ses concentrations en Al et K, et sa signature isotopique en Nd.

Compte tenu de la localisation de MOZ5-DR03-01 à moins de 150 km des côtes africaines et à une profondeur inférieure à 1200 m, il serait intéressant de travailler sur les échanges géochimiques entre le domaine terrestre africain très peu radiogénique (εNd < -20 ; Jeandel et al., 2007) et les masses d'eau circulant proches de la marge.

Ce travail permettrait de déterminer si des interactions existent (boundary exchanges ?) et dans quelles mesures elles peuvent impacter la signature isotopique de MOZ5-DR03-01.

L'étude des proxys isotopiques de l'Os et de l'hafnium (Hf) pourrait également approfondir cette piste. Dans ce cadre, l'isotopie de l'Hf pourrait indiquer des sources d'apports détritiques. Par exemple, les apports de croûte continentale, qu'ils soient éoliens ou apportées par des rivières environnantes telles que le Limpopo (Figure 6.6), possèdent des valeurs peu radiogéniques en Hf (-6 > εHf > -12). En revanche, les apports volcaniques possèdent des compositions isotopiques en Hf beaucoup plus radiogénique (εHf à partir de +13) (David et al., 2001 ; Godfrey et al., 1997 ; Piotrowski et al., 2000).

Grâce à ces données et leur mise en parallèle avec la chronologie de l'échantillon MOZ5-DR03-01, il serait possible de mettre en évidence des périodes de haute et de faible érosion du continent, des sources de flux détritiques, mais également de calculer des taux d'apports sédimentaires dans la vallée de Natal.

6.6.3. Modélisation océanographique

La dernière perspective développée dans ce manuscrit concerne la modélisation numérique des modèles courantologiques établis préalablement (Chapitre 5). En effet, il s'agirait de modéliser la courantologie et la géographie du canal du Mozambique en intégrant les nouvelles observations paléogéographiques. Les deux modèles établiraient une évolution de la circulation des courants avant et après l'uplift (11.7-3.4 Ma). Ils pourraient prendre en compte, les données paléocéanographiques et paléogéographiques de cette thèse, avec :

(1) les contributions des courants profonds (NADW, NIDW), estimées depuis 15.2 Ma au Plateau des Aiguilles (DR75-0012), 19.7 Ma au niveau de la ride de Jeffrey (MOZ1-DR11-01) et 16.2 aux Îles Glorieuses (MOZ1-DR04-23),

(2) les variations bathymétriques identifiées à différents endroits du canal (Ride de Davie, Banc du Hall, Île Europa), et estimées entre 465 et 1265 m pour l'uplift (Figure 6.5) et entre 650 et 1050 pour la subsidence,

Il s'agirait également de prendre en considération les grands bouleversements géographiques déjà identifiés et datés dans d'autres travaux tels que:

(3) le volcanisme dans le bassin des Comores (Figure 6.9) et la formation des reliefs associés à partir de 30 Ma (Debeuf, 2004 ; Emerick, Duncan, 1982 ; Hajash, Amastrong, 1972 ; Michon, 2016 ; Montaggioni, Nougier, 1981 ; Nougier et al., 1986 ; Pelleter et al., 2014),

Enfin, il serait pertinent de se rapprocher des équipes de modélisation des masses d'eau afin d'introduire :

(4) des données physiques dans nos modèles comme la température, la salinité, la densité, le taux d'oxygène et la vélocité des courants océaniques étudiés (Figure 6.12),

(5) et des données climatiques concernant la région du canal : le vent (sa force, son orientation), la présence d'eddies (leurs diamètres, leurs orientation), l'influence des glaciations et des déglaciations (ex. Glaciation de l'Hémisphère Nord et la réduction du NADW vers le Sud (Bergh et al., 2021; Boyle, Keigwin, 1987, 1982; Charles, Fairbanks, 1992; Frank et al., 2002).

Ces modèles numériques permettraient de comparer nos observations et de compléter nos données. Il serait notamment possible de calculer des contributions le long de sections nord-sud, à des points précis, différents de ceux que nous connaissons déjà. Nous aurions alors une idée quantitative de l'évolution du NADW dans la totalité du canal. Un des points également importants, serait de travailler avec précision, à haute résolution, sur la topographie de la ride de Davie. Cette étude pourrait indiquer des zones de cette structure qui auraient été émergées ou encore, des endroits de passages pour les courants profonds, tels que des failles dans la topographie (Figure 6.5, 6.12).

Enfin, ces modèles numériques permettraient de visualiser l'influence de phénomènes à grande échelle sur le système local qu'est le canal du Mozambique, et de les intégrer à des reconstructions plus conséquentes comme un modèle de circulation de l'océan Indien (e.g. Frank et al., 2006) et un modèle de circulation des courants mondiaux tenant compte des travaux effectués dans chaque bassin océanique.

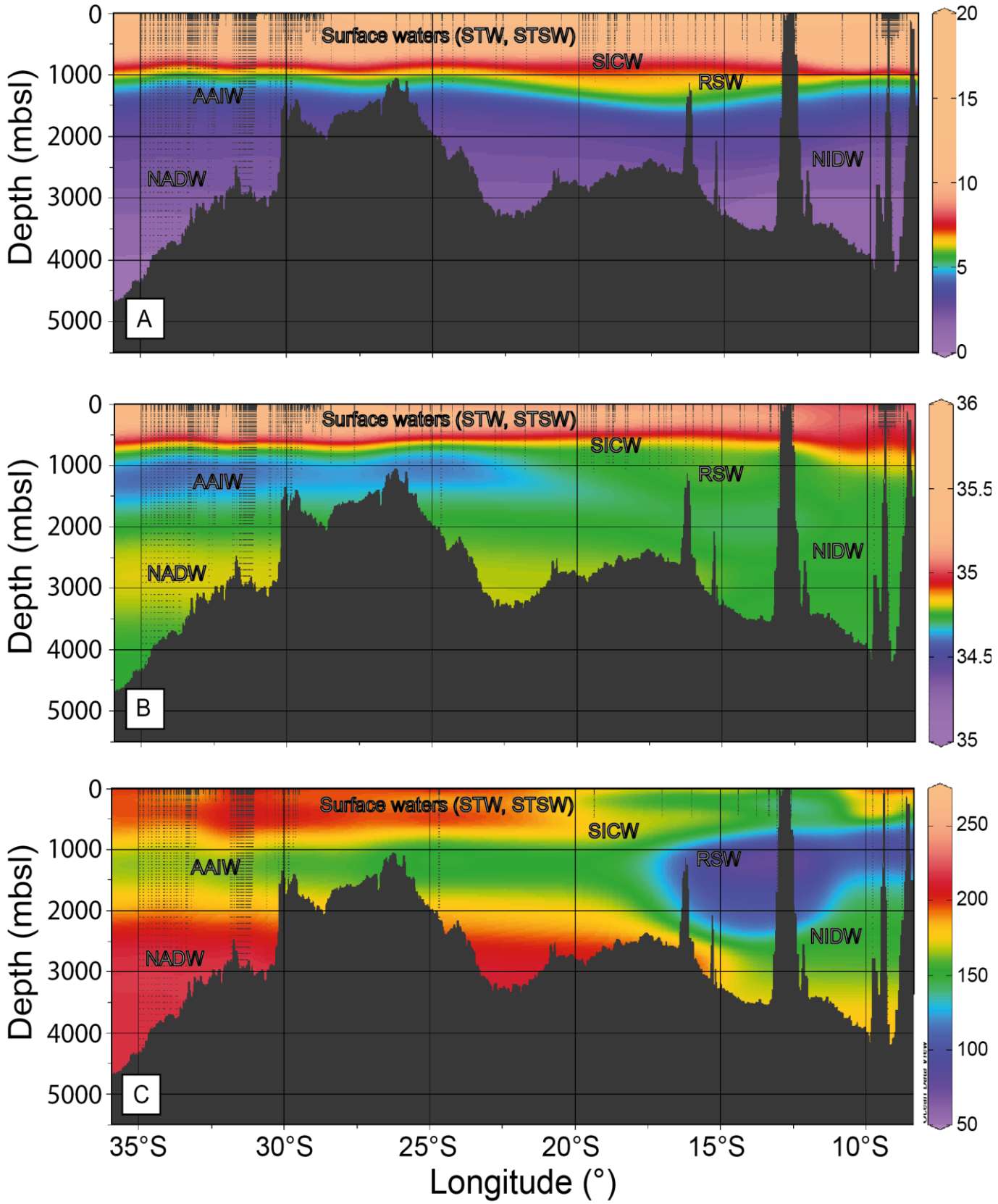

Figure 6.12. *Sections correspondantes à la distribution des principales masses d'eau du canal du Mozambique, d'après les profils Conductivité-Température-Profondeur (CTD). A : Données de température (°C) ; B : Données de salinité (psu) ; C : Données en oxygène dissous (ml/l). La bathymétrie du canal du Mozambique est issue des données GEBCO 2014 et des campagnes PAMELA)*

6.7. Références bibliographiques

Abbott, A.N., 2019. A benthic flux from calcareous sediments results in non-conservative neodymium behavior during lateral transport: A study from the Tasman Sea. Geology 47, 363–366. https://doi.org/10.1130/G45904.1

Abbott, A.N., Haley, B.A., McManus, J., 2015a. Bottoms up: Sedimentary control of the deep North Pacific Ocean's εNd signature. Geology 43, 1035–1035. https://doi.org/10.1130/G37114.1

Abbott, A.N., Haley, B.A., McManus, J., Reimers, C.E., 2015b. The sedimentary flux of dissolved rare earth elements to the ocean. Geochim. Cosmochim. Acta 154, 186–200. https://doi.org/10.1016/j.gca.2015.01.010

Abouchami, W., Goldstein, S.L., Gazer, S.J.G., Eisenhauer, A., Mangini, A., 1997. Secular changes of lead and neodymium in central Pacific seawater recorded by a Fe□Mn crust. Geochim. Cosmochim. Acta 61, 3957–3974. https://doi.org/10.1016/S0016-7037(97)00218-4

Albarède, F., Goldstein, S.L., Dautel, D., 1997. The neodymium isotopic composition of manganese nodules from the Southern and Indian oceans, the global oceanic neodymium budget, and their bearing on deep ocean circulation. Geochim. Cosmochim. Acta 61, 1277–1291. https://doi.org/10.1016/S0016-7037(96)00404-8

Amakawa, H., Tazoe, H., Obata, H., Gamo, T., Sano, Y., Shen, C.-C., 2013. Neodymium isotopic composition and concentration in the Southwest Pacific Ocean. Geochem. J. 47, 409–422. https://doi.org/10.2343/geochemj.2.0260

Arsouze, T., Dutay, J.-C., Lacan, F., Jeandel, C., 2007. Modeling the neodymium isotopic composition with a global ocean circulation model. Chem. Geol. 239, 165–177. https://doi.org/10.1016/j.chemgeo.2006.12.006

Bergh, E.W., von Koslowski, R., Compton, J.S., 2021. Variations in deep water masses along the western margin of South Africa, spanning the last two glacial terminations. Palaeogeogr. Palaeoclimatol. Palaeoecol. 562, 110148. https://doi.org/10.1016/j.palaeo.2020.110148

Boyle, E.A., Keigwin, L., 1987. North Atlantic thermohaline circulation during the past 20,000 years linked to high-latitude surface temperature. Nature 330, 35–40. https://doi.org/10.1038/330035a0

Boyle, E.A., Keigwin, L.D., 1982. Deep Circulation of the North Atlantic over the Last 200,000 Years: Geochemical Evidence. Science 218, 784–787. https://doi.org/10.1126/science.218.4574.784

Burton, K.W., Bourdon, B., Birck, J.-L., Allègre, C.J., Hein, J.R., 1999. Osmium isotope variations in the oceans recorded by FeMn crusts. Earth Planet. Sci. Lett. 171, 185–197. https://doi.org/10.1016/S0012-821X(99)00139-9

Burton, K.W., Ling, H.-F., O'Nions, R.K., 1997. Closure of the Central American Isthmus and its effect on deep-water formation in the North Atlantic. Nature 386, 382. https://doi.org/10.1038/386382a0

Cao, W., Zahirovic, S., Flament, N., Williams, S., Golonka, J., Müller, R.D., 2017. Improving global paleogeography since the late Paleozoic using paleobiology. Biogeosciences 14, 5425–5439. https://doi.org/10.5194/bg-14-5425-2017

Charles, C., Pelleter, E., Révillon, S., Nonnotte, P., Jorry, S.J., Kluska, J.-M., 2020. Intermediate and deep ocean current circulation in the Mozambique Channel: New insights from ferromanganese crust Nd isotopes. Mar. Geol. 430, 106356. https://doi.org/10.1016/j.margeo.2020.106356

Charles, C.D., Fairbanks, R.G., 1992. Evidence from Southern Ocean sediments for the effect of North Atlantic deep-water flux on climate. Nature 355, 416–419. https://doi.org/10.1038/355416a0

Chmeleff, J., von Blanckenburg, F., Kossert, K., Jakob, D., 2010. Determination of the 10Be half-life by multicollector ICP-MS and liquid scintillation counting. Nucl. Instrum. Methods Phys. Res. B 268, 192–199. https://doi.org/10.1016/j.nimb.2009.09.012

Christensen, J.N., Halliday, A.N., Godfrey, L.V., Hein, J.R., Rea, D.K., 1997. Climate and Ocean Dynamics and the Lead Isotopic Records in Pacific

Ferromanganese Crusts. Science 277, 913–918. https://doi.org/10.1126/science.277.5328.913

Collins, C., Hermes, J.C., Roman, R.E., Reason, C.J.C., 2016. First dedicated hydrographic survey of the Comoros Basin. J. Geophys. Res. Oceans 121, 1291–1305. https://doi.org/10.1002/2015JC011418

Cornacchia, I., Brandano, M., Agostini, S., 2021. Miocene paleoceanographic evolution of the Mediterranean area and carbonate production changes: A review. Earth-Sci. Rev. 221, 103785. https://doi.org/10.1016/j.earscirev.2021.103785

Courgeon, S., 2017. Cenozoic evolution of isolated carbonate platforms from the Mozambique Channel (SW Indian Ocean) : development and controls in active geodynamic settings (These de doctorat). Aix-Marseille.

Courgeon, S., Bachèlery, P., Jouet, G., Jorry, S.J., Bou, E., BouDagher-Fadel, M.K., Révillon, S., Camoin, G., Poli, E., 2018. The offshore east African rift system: new insights from the Sakalaves seamounts (Davie Ridge, SW Indian Ocean). Terra Nova 30, 380–388. https://doi.org/10.1111/ter.12353

Courgeon, S., Jorry, S.J., Camoin, G.F., BouDagher-Fadel, M.K., Jouet, G., Révillon, S., Bachèlery, P., Pelleter, E., Borgomano, J., Poli, E., Droxler, A.W., 2016. Growth and demise of Cenozoic isolated carbonate platforms: New insights from the Mozambique Channel seamounts (SW Indian Ocean). Mar. Geol. 380, 90–105. https://doi.org/10.1016/j.margeo.2016.07.006

Courgeon, S., Jorry, S.J., Jouet, G., Camoin, G., BouDagher-Fadel, M.K., Bachèlery, P., Caline, B., Boichard, R., Révillon, S., Thomas, Y., Thereau, E., Guérin, C., 2017. Impact of tectonic and volcanism on the Neogene evolution of isolated carbonate platforms (SW Indian Ocean). Sediment. Geol. 355, 114–131. https://doi.org/10.1016/j.sedgeo.2017.04.008

David, K., Frank, M., O'Nions, R.K., Belshaw, N.S., Arden, J.W., 2001. The Hf isotope composition of global seawater and the evolution of Hf isotopes in the deep Pacific Ocean from Fe–Mn crusts. Chem. Geol. 178, 23–42. https://doi.org/10.1016/S0009-2541(00)00427-7

Debeuf, D., 2004. Etude de l'évolution volcano-structurale et magmatique de Mayotte (Archipel des Comores, Océan Indien): Approches structurale, pétrographique, géochimique et géochronologique. Unpublished Ph.D. thesis, Université de La Réunion, 243 pp

Derry, L.A., France-Lanord, C., 1996. Neogene Himalayan weathering history and river87Sr86Sr: impact on the marine Sr record. Earth Planet. Sci. Lett. 142, 59–74. https://doi.org/10.1016/0012-821X(96)00091-X

Emerick, C.M., Duncan, R.A., 1982. Age progressive volcanism in the Comores Archipelago, western Indian Ocean and implications for Somali plate tectonics. Earth Planet. Sci. Lett. 60, 415–428. https://doi.org/10.1016/0012-821X(82)90077-2

Frank, M., 2002. Radiogenic isotopes: tracers of past ocean circulation and erosional input. Rev. Geophys. 40, 1–1. https://doi.org/10.1029/2000RG000094

Frank, M., O'Nions, R.K., 1998. Sources of Pb for Indian Ocean ferromanganese crusts: a record of Himalayan erosion? Earth Planet. Sci. Lett. 158, 121–130. https://doi.org/10.1016/S0012-821X(98)00055-7

Frank, M., O'Nions, R.K., Hein, J.R., Banakar, V.K., 1999. 60 Myr records of major elements and Pb–Nd isotopes from hydrogenous ferromanganese crusts: reconstruction of seawater paleochemistry. Geochim. Cosmochim. Acta 63, 1689–1708. https://doi.org/10.1016/S0016-7037(99)00079-4

Frank, M., Whiteley, N., Kasten, S., Hein, J.R., O'Nions, K., 2002. North Atlantic Deep Water export to the Southern Ocean over the past 14 Myr: Evidence from Nd and Pb isotopes in ferromanganese crusts. Paleoceanography 17, 12-1-12–9. https://doi.org/10.1029/2000PA000606

Frank, M., Whiteley, N., van de Flierdt, T., Reynolds, B.C., O'Nions, K., 2006. Nd and Pb isotope evolution of deep water masses in the eastern Indian Ocean during the past 33 Myr. Chem. Geol., Special Issue in Honour of R.K. O'Nions 226, 264–279. https://doi.org/10.1016/j.chemgeo.2005.09.024

Godfrey, L.V., Lee, D.-C., Sangrey, W.F., Halliday, A.N., Salters, V.J.M., Hein, J.R., White, W.M., 1997.

The Hf isotopic composition of ferromanganese nodules and crusts and hydrothermal manganese deposits: Implications for seawater Hf. Earth Planet. Sci. Lett. 151, 91–105. https://doi.org/10.1016/S0012-821X(97)00106-4

Hajash, A., Armstrong, R.L., 1972. Paleomagnetic and radiometric evidence for the age of the Comores Islands, west central Indian Ocean. Earth Planet. Sci. Lett. 16, 231–236. https://doi.org/10.1016/0012-821X(72)90195-1

Haley, B.A., Klinkhammer, G.P., 2003. Complete separation of rare earth elements from small volume seawater samples by automated ion chromatography: method development and application to benthic flux. Mar. Chem. 82, 197–220. https://doi.org/10.1016/S0304-4203(03)00070-7

Hu, R., Chen, T., Ling, H., 2012. Late Cenozoic history of deep water circulation in the western North Pacific: Evidence from Nd isotopes of ferromanganese crusts. Chin. Sci. Bull. 57, 4077–4086. https://doi.org/10.1007/s11434-012-5322-9

Jeandel, C., 1993. Concentration and isotopic composition of Nd in the South Atlantic Ocean. Earth Planet. Sci. Lett. 117, 581–591. https://doi.org/10.1016/0012-821X(93)90104-H

Jeandel, C., Arsouze, T., Lacan, F., Téchiné, P., Dutay, J.-C., 2007. Isotopic Nd compositions and concentrations of the lithogenic inputs into the ocean: A compilation, with an emphasis on the margins. Chem. Geol. 239, 156–164. https://doi.org/10.1016/j.chemgeo.2006.11.013

Josso, P., Horstwood, M.S.A., Millar, I.L., Pashley, V., Lusty, P. a. J., Murton, B., 2020. Development of a Correlated Fe-Mn Crust Stratigraphy Using Pb and Nd Isotopes and Its Application to Paleoceanographic Reconstruction in the Atlantic. Paleoceanogr. Paleoclimatology 35, e2020PA003928. https://doi.org/10.1029/2020PA003928

Josso, P., Parkinson, I., Horstwood, M., Lusty, P., Chenery, S., Murton, B., 2019. Improving confidence in ferromanganese crust age models: A composite geochemical approach. Chem. Geol. 513, 108–119. https://doi.org/10.1016/j.chemgeo.2019.03.003

Josso, P., Pelleter, E., Pourret, O., Fouquet, Y., Etoubleau, J., Cheron, S., Bollinger, C., 2017. A new discrimination scheme for oceanic ferromanganese deposits using high field strength and rare earth elements. Ore Geol. Rev., SI:Marine mineral deposits: New resources for base, precious, and critical metals 87, 3–15. https://doi.org/10.1016/j.oregeorev.2016.09.003

Klemm, V., Levasseur, S., Frank, M., Hein, J.R., Halliday, A.N., 2005. Osmium isotope stratigraphy of a marine ferromanganese crust. Earth Planet. Sci. Lett. 238, 42–48. https://doi.org/10.1016/j.epsl.2005.07.016

Kocsis, L., Vennemann, T.W., Fontignie, D., Baumgartner, C., Montanari, A., Jelen, B., 2008. Oceanographic and climatic evolution of the Miocene Mediterranean deduced from Nd, Sr, C, and O isotope compositions of marine fossils and sediments. Paleoceanography 23. https://doi.org/10.1029/2007PA001540

Korschinek, G., Bergmaier, A., Faestermann, T., Gerstmann, U.C., Knie, K., Rugel, G., Wallner, A., Dillmann, I., Dollinger, G., von Gostomski, Ch.L., Kossert, K., Maiti, M., Poutivtsev, M., Remmert, A., 2010. A new value for the half-life of 10Be by Heavy-Ion Elastic Recoil Detection and liquid scintillation counting. Nucl. Instrum. Methods Phys. Res. Sect. B Beam Interact. Mater. At. 268, 187–191. https://doi.org/10.1016/j.nimb.2009.09.020

Koschinsky, A., Hein, J.R., 2017. Marine ferromanganese encrustations: Archives of changing oceans. Elements. https://doi.org/10.2113/gselements.13.3.177

Leclaire, L., 1984. RIDA - MD39 cruise, Marion Dufresne R/V. https://doi.org/10.17600/84010511

Leclaire, L., 1975. NOSICAA - MD 06 cruise, Marion Dufresne R/V. https://doi.org/10.17600/75010711

Leroux, E., Counts, J.W., Jorry, S.J., Jouet, G., Révillon, S., BouDagher-Fadel, M.K., Courgeon, S., Berthod, C., Ruffet, G., Bachèlery, P., Grenard-Grand, E., 2020. Evolution of the Glorieuses seamount in the SW Indian Ocean and surrounding deep Somali Basin since the Cretaceous. Mar. Geol. 427, 106202. https://doi.org/10.1016/j.margeo.2020.106202

Ling, H.F., Burton, K.W., O'Nions, R.K., Kamber, B.S., von Blanckenburg, F., Gibb, A.J., Hein, J.R., 1997. Evolution of Nd and Pb isotopes in Central Pacific seawater from ferromanganese crusts. Earth Planet. Sci. Lett. 146, 1–12. https://doi.org/10.1016/S0012-821X(96)00224-5

Ling, H.-F., Jiang, S.-Y., Frank, M., Zhou, H.-Y., Zhou, F., Lu, Z.-L., Chen, X.-M., Jiang, Y.-H., Ge, C.-D., 2005. Differing controls over the Cenozoic Pb and Nd isotope evolution of deepwater in the central North Pacific Ocean. Earth Planet. Sci. Lett. 232, 345–361. https://doi.org/10.1016/j.epsl.2004.12.009

Manheim, F.T., 1986. Marine Cobalt Resources. Science 232, 600–608. https://doi.org/10.1126/science.232.4750.600

Manheim, F.T., Lane-Bostwick, C.M., 1988. Cobalt in ferromanganese crusts as a monitor of hydrothermal discharge on the Pacific sea floor. Nature 335, 59. https://doi.org/10.1038/335059a0

Mantyla, A.W., Reid, J.L., 1995. On the origins of deep and bottom waters of the Indian Ocean. J. Geophys. Res. Oceans 100, 2417–2439. https://doi.org/10.1029/94JC02564

Marino, E., González, F.J., Somoza, L., Lunar, R., Ortega, L., Vázquez, J.T., Reyes, J., Bellido, E., 2017. Strategic and rare elements in Cretaceous-Cenozoic cobalt-rich ferromanganese crusts from seamounts in the Canary Island Seamount Province (northeastern tropical Atlantic). Ore Geol. Rev., SI:Marine mineral deposits: New resources for base, precious, and critical metals 87, 41–61. https://doi.org/10.1016/j.oregeorev.2016.10.005

Masters, J.C., Génin, F., Zhang, Y., Pellen, R., Huck, T., Mazza, P.P.A., Rabineau, M., Doucouré, M., Aslanian, D., 2021. Biogeographic mechanisms involved in the colonization of Madagascar by African vertebrates: Rifting, rafting and runways. J. Biogeogr. 48, 492–510. https://doi.org/10.1111/jbi.14032

Masters, J.C., Wit, M.J. de, Asher, R.J., 2006. Reconciling the Origins of Africa, India and Madagascar with Vertebrate Dispersal Scenarios. Folia Primatol. (Basel) 77, 399–418. https://doi.org/10.1159/000095388

McCall, R.A., 1997. Implications of recent geological investigations of the Mozambique Channel for the mammalian colonization of Madagascar. Proc. R. Soc. Lond. B Biol. Sci. 264, 663–665. https://doi.org/10.1098/rspb.1997.0094

Michon, L., 2016. The volcanism of the Comoros archipelago integrated at a regional scale, in: Bachelery, Patrick, Lénat, Jean-François, Muro, D., Andrea, Michon, Laurent (Eds.), Active Volcanoes of the Southwest Indian Ocean: Piton de La Fournaise and Karthala, Active Volcanoes of the World. Springer-Verlag, pp. 233–244.

Montaggioni, L.F., Nougier, J., 1981. Les enclaves de roches detritiques dans les Volcans d'Anjouan (Archipel des Comores); Origine et interpretation dans le cadre de l'evolution du Canal de Mozambique. Bull. Société Géologique Fr. S7-XXIII, 595–601. https://doi.org/10.2113/gssgfbull.S7-XXIII.6.595

Moulin, M., Evain, M., 2016. PAMELA-MOZ05 cruise, Pourquoi pas ? R/V. https://doi.org/10.17600/16009500

Nougier, J., Cantagrel, J.M., Karche, J.P., 1986. The Comores archipelago in the western Indian Ocean: volcanology, geochronology and geodynamic setting. J. Afr. Earth Sci. 1983 5, 135–145. https://doi.org/10.1016/0899-5362(86)90003-5

Olu, K., 2014. PAMELA-MOZ01 cruise, L'Atalante R/V. https://doi.org/10.17600/14001000

O'Nions, R.K., Frank, M., von Blanckenburg, F., Ling, H.-F., 1998. Secular variation of Nd and Pb isotopes in ferromanganese crusts from the Atlantic, Indian and Pacific Oceans. Earth Planet. Sci. Lett. 155, 15–28. https://doi.org/10.1016/S0012-821X(97)00207-0

Partridge, T.C., 1998. Of diamonds, dinosaurs and diastrophism : 150 million years of landscape evolution in southern Africa. South Afr. J. Geol. 101, 167–184. https://doi.org/10.10520/EJC-947b4efa3

Pelleter, A.-A., Caroff, M., Cordier, C., Bachelery, P., Nehlig, P., Debeuf, D., Arnaud, N., 2014. Melilite-bearing lavas in Mayotte (France): An insight into the mantle source below the Comores. Lithos 208–209, 281–297. https://doi.org/10.1016/j.lithos.2014.09.012

Peucker-Ehrenbrink, B., Ravizza, G., 2012. Chapter 8 - Osmium Isotope Stratigraphy, in: Gradstein, F.M., Ogg, J.G., Schmitz, M.D., Ogg, G.M. (Eds.), The Geologic Time Scale. Elsevier, Boston, pp. 145–166. https://doi.org/10.1016/B978-0-444-59425-9.00008-1

Peucker-Ehrenbrink, B., Ravizza, G., 2000. The marine osmium isotope record. Terra Nova 12, 205–219. https://doi.org/10.1046/j.1365-3121.2000.00295.x

Piepgras, D.J., Wasserburg, G.J., 1982. Isotopic Composition of Neodymium in Waters from the Drake Passage. Science 217, 207–214.

Piotrowski, A.M., Lee, D.-C., Christensen, J.N., Burton, K.W., Halliday, A.N., Hein, J.R., Günther, D., 2000. Changes in erosion and ocean circulation recorded in the Hf isotopic compositions of North Atlantic and Indian Ocean ferromanganese crusts. Earth Planet. Sci. Lett. 181, 315–325. https://doi.org/10.1016/S0012-821X(00)00205-3

Poux, C., Madsen, O., Marquard, E., Vieites, D.R., de Jong, W.W., Vences, M., 2005. Asynchronous Colonization of Madagascar by the Four Endemic Clades of Primates, Tenrecs, Carnivores, and Rodents as Inferred from Nuclear Genes. Syst. Biol. 54, 719–730. https://doi.org/10.1080/10635150500234534

Puteanus, D., Halbach, P., 1988. Correlation of Co concentration and growth rate — A method for age determination of ferromanganese crusts. Chem. Geol. 69, 73–85. https://doi.org/10.1016/0009-2541(88)90159-3

Rahlf, P., Hathorne, E., Laukert, G., Gutjahr, M., Weldeab, S., Frank, M., 2020. Tracing water mass mixing and continental inputs in the southeastern Atlantic Ocean with dissolved neodymium isotopes. Earth Planet. Sci. Lett. 530, 115944. https://doi.org/10.1016/j.epsl.2019.115944

Rehkämper, M., Frank, M., Hein, J.R., Halliday, A., 2004. Cenozoic marine geochemistry of thallium deduced from isotopic studies of ferromanganese crusts and pelagic sediments. Earth Planet. Sci. Lett. 219, 77–91. https://doi.org/10.1016/S0012-821X(03)00703-9

Rickli, J., Frank, M., Baker, A.R., Aciego, S., de Souza, G., Georg, R.B., Halliday, A.N., 2010. Hafnium and neodymium isotopes in surface waters of the eastern Atlantic Ocean: Implications for sources and inputs of trace metals to the ocean. Geochim. Cosmochim. Acta 74, 540–557. https://doi.org/10.1016/j.gca.2009.10.006

Searle, M.P., 1996. Cooling history, erosion, exhumation and kinematics of the Himalaya-Karakoram-Tibet orogenic belt. Pp. 110–137 in: Asian Tectonics. (Yin, A. and Harrison, M.A., editors). Cambridge University Press, Cambridge, UK.

Segev, A., Avni, Y., Shahar, J., Wald, R., 2017. Late Oligocene and Miocene different seaways to the Red Sea–Gulf of Suez rift and the Gulf of Aqaba–Dead Sea basins. Earth-Sci. Rev. 171, 196–219. https://doi.org/10.1016/j.earscirev.2017.05.004

Stichel, T., Frank, M., Rickli, J., Hathorne, E.C., Haley, B.A., Jeandel, C., Pradoux, C., 2012. Sources and input mechanisms of hafnium and neodymium in surface waters of the Atlantic sector of the Southern Ocean. Geochim. Cosmochim. Acta 94, 22–37. https://doi.org/10.1016/j.gca.2012.07.005

Toole, J.M., Warren, B.A., 1993. A hydrographic section across the subtropical South Indian Ocean. Deep Sea Res. Part Oceanogr. Res. Pap. 40, 1973–2019. https://doi.org/10.1016/0967-0637(93)90042-2

Wilson, D.J., Piotrowski, A.M., Galy, A., McCave, I.N., 2012. A boundary exchange influence on deglacial neodymium isotope records from the deep western Indian Ocean. Earth Planet. Sci. Lett. 341–344, 35–47. https://doi.org/10.1016/j.epsl.2012.06.009

You, Y., 2000. Implications of the deep circulation and ventilation of the Indian Ocean on the renewal mechanism of North Atlantic Deep Water. J. Geophys. Res. Oceans 105, 23895–23926. https://doi.org/10.1029/2000JC900105

CHAPTER 6 : SUMMARY, CONCLUSIONS AND PERSPECTIVES

6.1. Introduction

This final chapter aims to synthesize and discuss the results obtained throughout this thesis as well as to address some scientific perspectives raised by this study.

The study area is located between the east of the African continent and the west of Madagascar, which corresponds to a maritime corridor made up of water masses arriving from the southern Atlantic Ocean and the northern Indian Ocean. Due to its oceanographic and geographical particularities, Mozambique Channel is a very unique place to understand regional currents and their past evolution. Thus, the objectives of this work were (1) to identify the oceanic water masses circulating in the Mozambique Channel, (2) to trace their evolution over the last 30 Ma and (3) to understand the impact of climatic and geographical changes on a global and regional scale on the geochemical composition of water masses and their circulation.

Thanks to several oceanographic missions (Leclaire, 1975, 1984 ; Moulin, Evain, 2016 ; Olu, 2014 an exceptional panel of 33 Fe-Mn crusts was dredged in a homogeneous manner in the channel. They correspond to depths ranging from 170 to 2650 m thus making it possible to study the signatures of all water masses in the region (surface, intermediate and deep). The isotopic tracers studied correspond to Nd and Pb, which are highly used and studied proxies for the characterization of water masses in the various ocean basins. (Albarède et al., 1997; Christensen et al., 1997; Frank, 2002; Frank et al., 2002; Frank et O'Nions, 1998; Ling et al., 1997; O'Nions et al., 1998; Rehkämper et al., 2004). Due to the erosion and dissolution of continental rocks, each oceanic domain has its own unique Nd isotopic signature. As for Pb, it is a less sensitive isotopic proxy for tracing currents but which can reflect local elemental inputs as well as their sources. Its use also makes it possible to compare its trends with those of Nd, despite the different residence times of these two isotopic tracers.

Several axis of analysis were chosen and studied. The first step was to sample and analyse the surface of the 33 Fe-Mn crusts, in order to acquire a 3D vision of water masses and their isotopic signatures. This axis allowed to establish the modern currentology of the Channel. The second axis of analysis aimed to establish time series on four Fe-Mn crusts, whose depths are close to isotopic limits in Nd of currents, in order to study changes in water masses. Finally, the last axis allowed to study the time series of three deep Fe-Mn crusts (> 1780 m). These samples being chosen for their locations at three key locations in the channel (north milestone; centre – north of the Davie ridge; south milestone), they made it possible to understand and establish the paleoceanography of the region.

Thus, in this chapter, the main conclusions of this thesis answer questions raised in chapter 1, but which were also motivated by the scientific discussions brought about throughout the manuscript. Some questions remain and will therefore be presented with the perspectives, at the end of this chapter.

6.2. What does the geochemical signature of Fe-Mn crusts reflect?

Several protocols have been established and presented in chapter 2 to analyse the mineralogy and elemental and isotopic geochemistry of Fe-Mn oxides.

- **Charles, C.**, Barrat, J.-A., Pelleter, E., 2021. Trace Element Determinations in Fe-Mn

Oxides by High Resolution ICP-MS after Tm Addition. Talanta 122446.

However, this conclusion will not go back on the mineralogical and geochemical analyses (major, traces) (analytical development; Charles et al., 2021). Although this is a major and essential work to ensure the correct characterization of isotopic signatures (Nd, Pb) of seawater, it deserves a comprehensive study entirely dedicated to the exceptional side of the dataset.

6.3. Identification and circulation model of modern water masses in the Mozambique Channel

This study is based on the complete panel of the 33 samples of the thesis (170-2650 m deep), and their modern geochemical compositions, integrating 20 000 to 80 000 years.

6.3.1. What are the main water masses in the Mozambique Channel and what are their Nd isotope signatures?

The isotopic composition of the water masses present in the Mozambique Channel varies between very low radiogenic values (εNd = -10.1) at the Agulhas Plateau to more radiogenic values (εNd = -7.1) at Mount Paisley. The results made it possible to identify the Nd isotopic signatures of the water masses present in the channel, with:

(1) a surface water mass (> 700 m) characterized by a strongly radiogenic signature (εNd = -7.6) corresponding to SICW;

(2) an intermediate Indian water mass (> 1500 m) similar to the RSW with an Nd isotopic signature that is also very radiogenic (-7.1 > εNd > -8.0) ;

(3) an isotopic transition zone located between intermediate and deep water masses (from 1300 to 1650 m ; -7.7 > εNd > -9.1) ;

(4) deep water masses with contrasting isotopic compositions reflecting NIDW (εNd up to -7.5) and NADW (εNd = -10.1) (Figure 6.1).

It was thus possible to establish a 2D cartography of the currents in the Mozambique Channel (with their isotopic signatures in Nd and their variations), but also to study them in 3D thanks to the varied depths of the crusts analysed.

6.3.2. What is the modern circulation of deep currents in the Mozambique Channel?

Through the correlation of isotopic results in Nd and Pb, a new oceanographic model has been established providing unprecedented information on the evolution of deep currents in the Mozambique Channel (Figure 6.1).

It shows that NADW circulates in the south of the African continent, and was recorded at the Agulhas Plateau. The Atlantic current then moves through the Mozambique Channel from the the south towards the north, where it crosses the Mozambique Ridge before reaching the Deep Mozambique Basin and, in a second time, the Hall Bank region. To the north is the Davie Ridge. This structure marks separation between the south and north of the channel, separating it into two basins: the deep Mozambique Basin and the Comoros basin, where the NADW (up to εNd = -9.4) circulates up to 90 km north of Juan de Nova and 700 km south of the Glorious Islands. However, it is the NIDW which is the major deep current in the Comoros Basin. It extends from the Glorious Islands, in a southerly direction, where it meets and dominates the NADW at the level of Jeffrey Ridge (16°S).

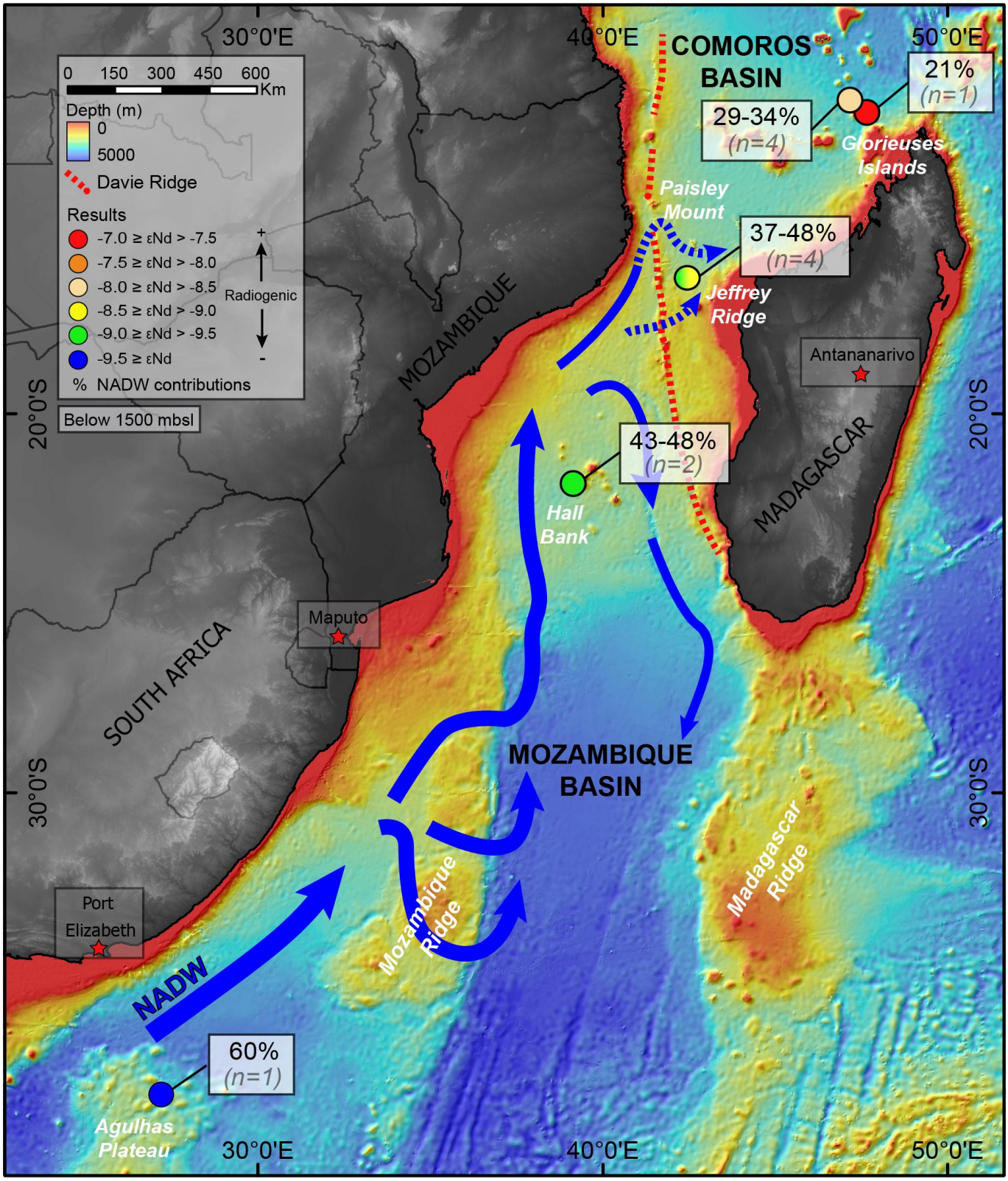

Figure 6.1. *Mozambique Channel bathymetry (data from GEBCO and PAMELA oceanographic missions) showing estimated contributions from NADW and its circulation in the Mozambique Channel. The dotted arrows represent the potential topographic passages of the Davie Ridge allowing the propagation of NADW in the Comoros Basin. This is a summary figure from the paper Charles et al. (2020), modified and relocated here for the convenience of the reader.*

6.3.3. Does the Davie Ridge act as a topographic barrier in the modern evolution of deep water masses?

Several authors who have studied the geodynamics of Mozambique Channel present the Davie Ridge as a topographic barrier to the circulation of deep water masses in the region. (Mantyla, Reid, 1995; Toole, Warren, 1993; You, 2000).

However, the work of this thesis comes to bring new estimates as for the propagation of deep currents in the channel. The contribution of NADW to the Agulhas Plateau has been estimated at 60% (Figure 6.1). This estimate is supported by the work of Rahlf et al. (2020) which demonstrates the mixing of NADW and CDW east of Cape Basin, in southern Africa. Its contribution then gradually decreases with its northward expansion, until it reaches between 43 and 48% influence at the Hall Bank and between 37 and 48% at Jeffrey Ridge, just north of the Davie Ridge (16°S). At the level of Jeffrey Ridge, it meets the NIDW whose influence is the majority, with an estimated contribution of between 52 and 63%. These observations and quantifications support the hydrographic results of Collins et al. (2016), recording NIDW and NADW in the Comoros Basin.

This thesis confirms that the Davie Ridge is not a geographical obstacle preventing the circulation of deep currents in the northern part of the Mozambique Channel, and suggests that topographic passages are present along this ridge to allow the evolution of the NADW current northward (Figure 6.1).

- **Charles, C.**, Pelleter, E., Révillon, S., Nonnotte, P., Jorry, S.J., Kluska, J.-M., 2020. Intermediate and deep ocean current circulation in the Mozambique Channel: New insights from ferromanganese crust Nd isotopes. Marine Geology. 430, 106356.

6.4. Geodynamics of the Mozambique Channel: recording and identification of vertical movements from 12 Ma

The first axis of research (paragraph 6.3) identified the modern circulation of water masses present in Mozambique Channel and their isotopic signatures in Nd. Studying them also revealed differences in εNd (up to more than 2 units) between deep and intermediate water masses.

Such differences could make it possible to identify changes in the bathymetry of Fe-Mn crusts in a region where many authors have highlighted uplift and subsidence phases since the beginning of the Miocene (~ 23 Ma; e.g. Courgeon et al., 2017, 2016; Leroux et al., 2020; Ponte, 2018; Walford et al., 2005).

Thus, four Fe-Mn crusts were selected, according to their modern depths (800 to 1900 m), in order to identify potential vertical movements from the variations of their isotopic signatures in Nd.

6.4.1. What is the temporal resolution of Fe-Mn crusts studied for paleogeodynamic reconstructions?

The four Fe-Mn crusts sampled and analysed for the paleogeographic reconstruction of the Mozambique Channel have estimated ages of 15.6 Ma (MOZ1-DR10-05, Mount Macua), 8.0 Ma (MOZ1-DR17-01, Hall Bank), 11.1 Ma (MOZ1-DR22-01, Europa Island) et 30.7 Ma (DR84-0026, Mount Paisley) (Figure 6.2). Their temporal resolution is between 150 000 and 550

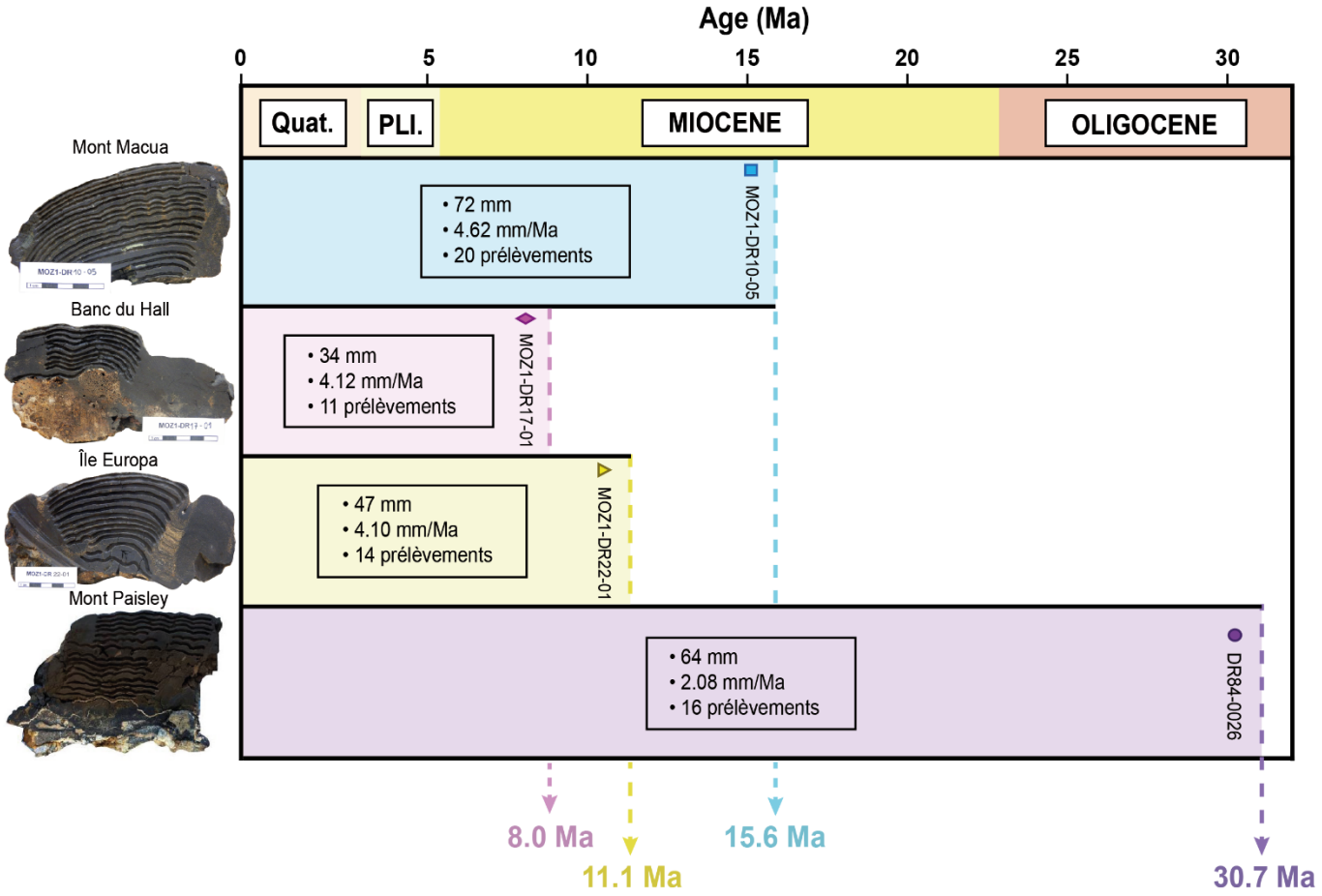

Figure 6.2. *Synthetic figure showing the four Fe-Mn crusts used in the paleogeodynamic reconstruction of the Mozambique Channel and their main characteristics (thickness, growth rate, number of laminae sampled and age).*

000 years per stratum (with a total of laminae sampled of 20, 11, 14 and 16, respectively).

6.4.2. Have geographic changes been recorded in the Mozambique Channel? If yes, which ones?

Significant variations were revealed in the isotopic signatures (Nd, Pb) of the four Fe-Mn crusts analysed here. They show three major periods of upheaval:

(1) from the Oligocene (30.7 Ma) to the middle Miocene (11.1-11.7 Ma) with major changes in the Pb isotopic compositions of samples DR84-0026 and MOZ1-DR10-05;

(2) between the Middle Miocene (11.1-11.7 Ma) and the Pliocene (5.7-3.4) with increasingly radiogenic Nd isotopic records and less and less radiogenic Pb over the four time series studied;

(3) between the beginning of the Pliocene (5.7-3.4 Ma) and the Pleistocene (1.6 Ma) with isotopic variations in Nd less and less radiogenic and more and more radiogenic in Pb, mainly visible on sample MOZ1-DR17-01.

The study of these variations has shown that Fe-Mn crusts studied have changed position in the water column over time, moving from one mass of water to another, with different geochemical properties, thanks to local vertical movements.

Several major paleogeographic events have thus been identified and dated since the Oligocene. Between 30.7 and 11.1 Ma, strong isotopic influences in Pb, resulting from detrital products of the Himalayan structure, brought by Indian currents, and elementary contributions from the Tethys basin, transported by ancient Mediterranean currents, were recorded at the level of Mount Macua, north of the Mozambique Channel and the Davie Ridge (Figure 6.3).

From 11.7 Ma, Nd recordings first reflect an uplift and then a subsidence phenomenon. The first shakes the channel geodynamics up to 3.4 Ma (Figure 6.3). It is identified both in the south and in the north of the region, with a significant elevation of the Davie ridge. Using absolute dating, isotopic values in Nd and the knowledge acquired in chapter 3, it was possible to calculate the growth rate of this phenomenon which is estimated between 61 to 167 m/Ma. As for subsidence, it affects the deep basin of Mozambique between 5.1 and 1.6 Ma (Figure 6.3). We estimated its subsidence rate between 186 and 300 m/Ma.

These movement estimates could be compared with results obtained independently. They show perfect consistency with data from previous studies estimated: (1) an unplift between 850 m in the south (Partridge, 1998) and 425-600 in the north (Îles Glorieuses; Leroux et al., 2020; Partridge, 1998) and (2) a subsidence between 435 and 663 m in the south (Hall Bank; Courgeon et al., 2017), between 221 and 317 m north of the Davie Ridge (Courgeon, 2017) and up to 500 m near the Îles Glorieuses (Leroux et al., 2020).

The identification of these two phenomena, their absolute dating and the associated calculations, complement previously conducted studies on the geodynamics of the region between the Miocene and the Pliocene (Charles et al., in prep).

Thus, from carefully selected Fe-Mn crusts according to their depths and their locations, in regions with water masses whose isotopic properties are well differentiated, it is possible to identify, estimate and date vertical movements.

This is the first time that such geological objects have been used for geodynamic reconstructions.

6.4.3. What might be the impact of such vertical movements on the circulation of regional water masses?

These bathymetric upheavals can have major consequences by considerably impacting the usual circulation routes of ocean currents.

Indeed, sample DR84-0026, located north of the Davie Ridge and analysed in chapter 4 reveals that its isotopic signature in Nd, in the Miocene, is that of a water mass strongly influenced by a low radiogenic composition of NADW type. This indicates that this current was circulating intensely north of the channel more than 12 Ma ago. However, research on modern circulation (chapter 3) reflects that the isotopic signature of deep water masses north of the channel is not today so different from that of the Indian intermediate currents (RSW), indicating the circulation of the NIDW. The correlation of these results therefore indicates topographic changes, as summarized in the previous paragraph, but also oceanographic changes.

Thus, topographic elevations (uplift) can create obstacles and indirectly, deviations of water masses. Conversely, topographic subsidence can open up new routes for the propagation of currents. It is therefore an entire oceanographic system that can be modified.

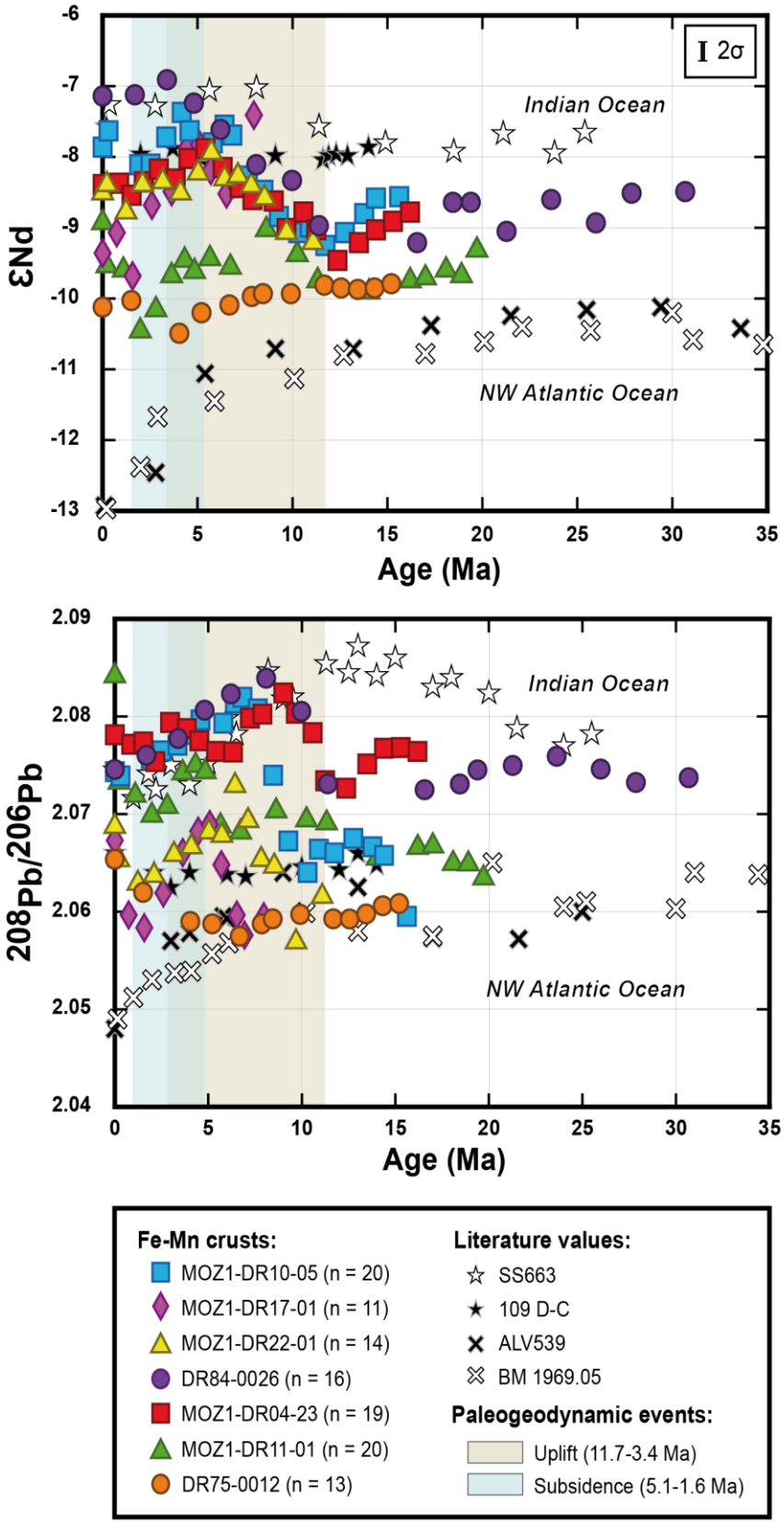

Figure 6.3. *Synthetic figure of the isotopic signatures εNd (T) and 208Pb/206Pb over time. The margin of error is included in the points. Signatures from previous studies have been added for comparison: SS663 from O'Nions et al. (1998) and Frank, O'Nions (1998); 109 D-C and ALV539 from O'Nions et al. (1998) and, BM 1969.5 from Burton et al. (1997) and O'Nions et al. (1998).*

6.5. Paleoceanographic reconstruction of the deep currents of Mozambique Channel: an evolutionary model over 30 Ma

The second axis of research (paragraph 6.3), based on four Fe-Mn crusts located at very varied depths, has made it possible to identify, characterize and date two major geodynamic phenomena that have impacted the topography of the Mozambique Channel since 11.7 Ma.

The third axis of study aims to trace the evolution of deep currents over time from three Fe-Mn crusts located in deep water masses (> 1780 m) and distributed at three key locations in the channel (milestone North; centre – north of the Davie Ridge; south milestone). The objective here was to identify the deep circulation before and after the geodynamic upheavals previously highlighted.

6.5.1. What is the temporal resolution of Fe-Mn crusts studied for paleoceanographic reconstructions?

The three Fe-Mn crusts sampled and analysed for the paleoceanographic reconstruction of the Mozambique Channel have estimated ages of 16.2 Ma (MOZ1-DR04-23, Glorious Islands), 19.7 Ma (MOZ1-DR11-01, Jeffrey Ridge) et 15.2 Ma (DR75-0012, Agulhas Plateau) (Figure 6.4). Their temporal resolution is between 150 000 and 550 000 years per stratum sampled (with a total of laminae sampled of 20, 19 and 13, respectively).

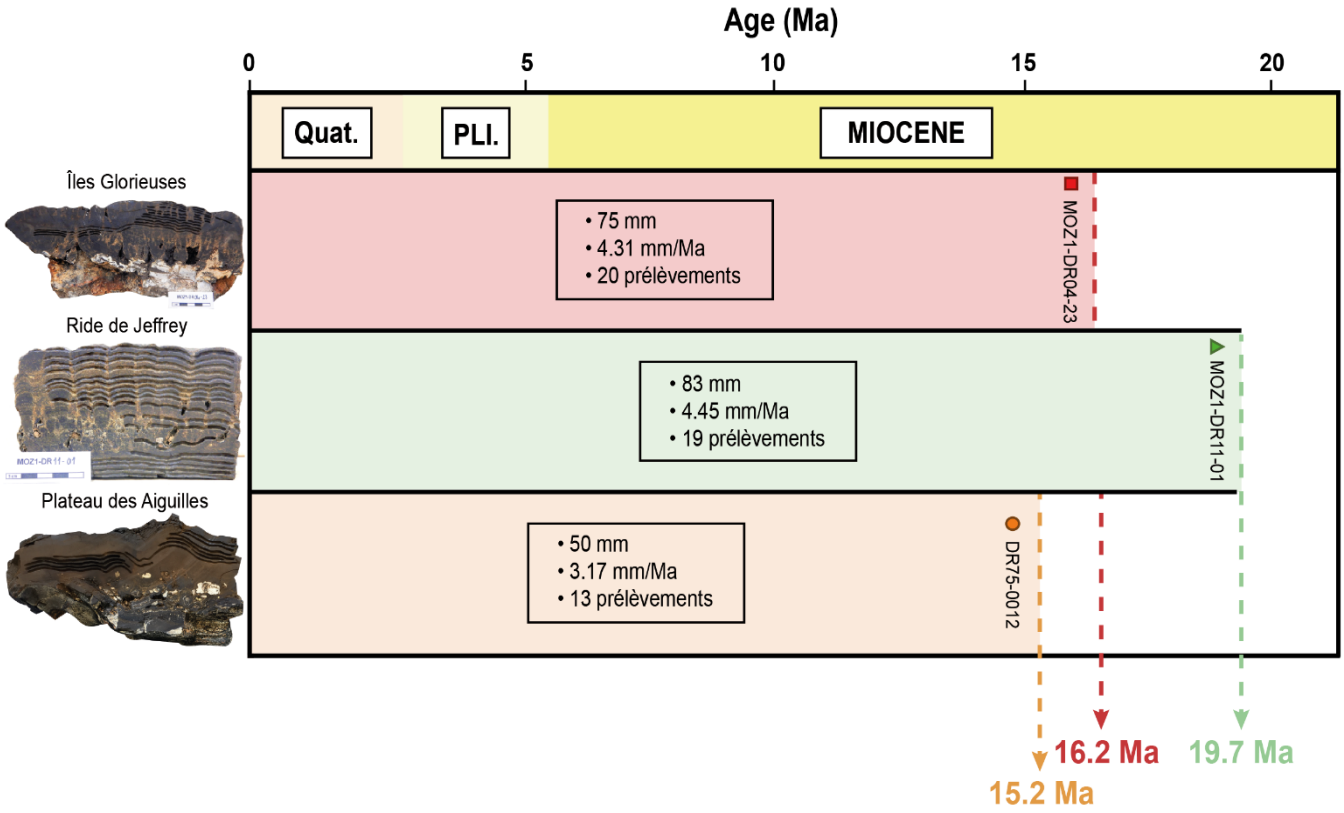

Figure 6.4. *Synthetic figure presenting the four Fe-Mn crusts used in the paleogeodynamic reconstruction of the Mozambique Channel and their main characteristics (thickness, growth rate, number of laminae sampled and age).*

6.5.2. How did the isotopic signatures of the deep currents of the Mozambique Channel evolve during the 20 Ma?

South of the Mozambique Channel, the geochemical composition of NADW remained relatively constant and not very radiogenic in Nd during the Neogene (εNd = -9.8 to 15.2 Ma) and the Quaternary (εNd = -10.1 to the present) (Figure 6.3).

Although the glaciation of the northern hemisphere, which began 3 Ma ago, significantly modified the properties of NADW, and in particular its isotopy, towards a more weakly radiogenic Nd component (εNd = -13 to the present ; Abouchami et al., 1997; Burton et al., 1997; Frank and O'Nions, 1998), this change in composition is not reflected in the Mozambique Channel (due to a decrease in NADW export to the Southern Ocean).

The NIDW, north of the channel, has a much more radiogenic geochemistry, similar to that of NIDW recorded in the east and middle of the Indian Ocean (Frank, O'Nions, 1998; O'Nions et al., 1998) (Figure 6.4).

However, a weak radiogenic Pb source is recorded at the level of the Glorious Islands around 9.0 Ma ($^{208}Pb/^{206}Pb$ = 2.0824) (Figure

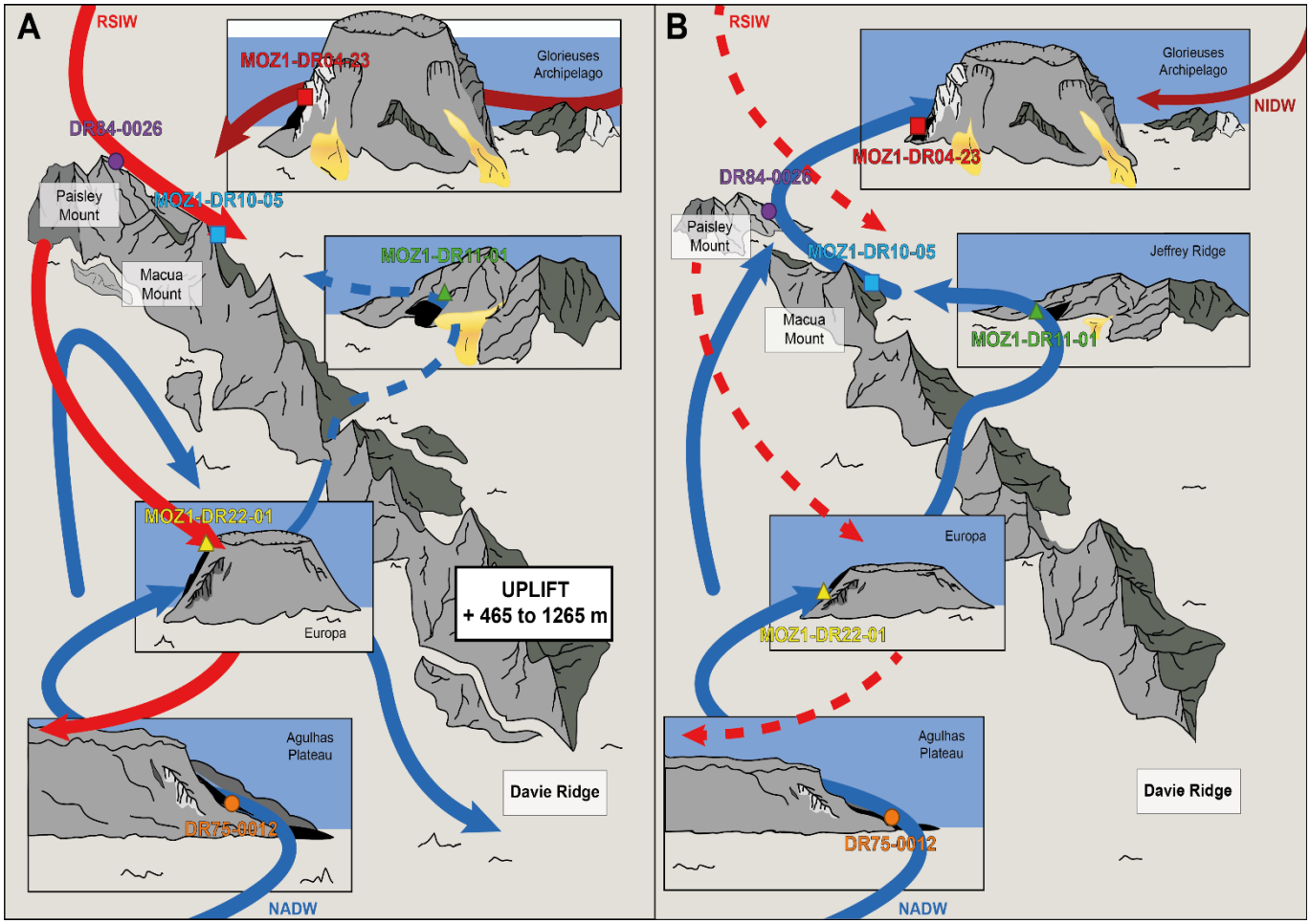

Figure 6.5. *Paleoceanographic reconstruction of the deep Atlantic (NADW) and Indian (NIDW) currents of the Mozambique Channel. Figure (A) illustrates the situation in the Pliocene (3.4 Ma), after the establishment of the generalized uplift in the region, while figure B corresponds to the current reconstruction in the Miocene (11.7 Ma), before this geodynamic upheaval. This is a summary figure from chapter 5 and modified.*

6.4). It would reflect a significant contribution of granitic products from the alteration of the Himalayas (Derry et France-Lanord, 1996), whose erosion was estimated to be very intense between 20 and 14 Ma (Searle, 1996).

6.5.3. What are the consequences of the uplift on the transport of deep water masses in the Mozambique Channel during the last 12 Ma?

The ocean circulation of the deep currents of the Mozambique Channel was significantly modified between the Miocene (11.7 Ma) and the Pliocene (3.4 Ma).

Before 11.7 Ma, the NADW dominated currentology of the channel, from the south to the north, with a strong influence, estimated between 81 and 87% at 12.4 Ma, and similar to that measured at the Agulhas Plateau (83-88%). However, from this period, its presence in the archipelago of the Glorious Islands gradually decreases due to the progressive establishment of the uplift identified and dated previously (11.7-3.4 Ma) (Figure 6.3, 6.5).

The contribution of NADW is then estimated with a minimum of 38% at 5.4 Ma. During this phenomenon, the Davie ridge increased by an estimated amplitude between 465 and 1265 m, thus reducing the circulation of NADW in the Comoros basin (Figure 6.5), with a minimum input of 34% at 3.0 Ma.

However, it continues to reach the Jeffrey Ridge, north of the Davie Ridge, at a minimum of 64% at 2.8 Ma against a minimum of 85% just before the uplift (14.0 Ma).

Despite these major paleogeographic upheavals, the Davie Ridge was never sufficient to completely limit the evolution of the NADW current north of the Mozambique Channel, and its mixing with the NIDW (Figure 6.5).

6.6. Perspectives

6.6.1. Improve the reliability of age models of Fe-Mn crusts studied beyond 12 Ma

In this study, we demonstrated that the studied Fe-Mn crusts formed gradually between the Paleogene and the Quaternary, in the Mozambique Channel, by recording the evolution of the geochemical compositions of the water masses present in the region. In order to carry out paleogeographic and paleoceanographic reconstructions, they were sampled and analysed, in particular in order to obtain their dating and to establish chronologies. For this, the Be isotopy has been widely used. However, it does not allow to obtain reliable absolute ages beyond 12 Ma (Chmeleff et al., 2010 ; Korschinek et al., 2010). To compensate for this limitation, the choice was made to extrapolate the growth rates measured, in relation to the dating acquired by isotopic analyses of the Be, to establish chronology greater than 10 Ma (Chapters 4 and 5). However, other dating methods exist and deserve further study, in order to compare the age models obtained and thus optimize the temporal factor of the reconstructions.

6.6.1.1. Chronology by empirical dating

Dating from cobalt is based on the constant flux of this element and its concentration directly dependent on the growth rate (Frank et al., 1999; Manheim, 1986; Puteanus et Halbach, 1988). This method is frequently used in paleoceanographic reconstructions and independently of other techniques. (David et al., 2001 ; Frank et al., 1999

; Hu et al., 2012 ; Ling et al., 2005 ; Marino et al., 2017).

As part of this thesis, dating was carried out on Fe-Mn crusts MOZ1-DR04-23, MOZ1-DR11-01 and DR75-0012, from the equations developed by Manheim (1986), Manheim and Lane-Bostwick (1988) and Frank et al. (1999) (Chapter 5). These results and comparisons have made it possible to develop a dating method, based on the Be isotopy and Manheim (1986) method when absolute dating is not available.

Although the method of dating from cobalt concentration should be considered with caution due to gaps in deposition, it is a dating technique that can help specify the ages of Fe-Mn crusts beyond of 10 Ma (Frank et al., 2002), in particular by being coupled to the isotopy of Be.

Thus, it would be relevant to test the equations discussed in chapter 5, on other Fe-Mn crusts, especially those used for paleogeographic reconstructions (MOZ1-DR10-05, MOZ1-DR17-01, MOZ1-DR22-01 and DR84-0026). A new reliable equation could be developed and new age models could thus reinforce the temporal constraints of geodynamic movements (uplift, subsidence) identified.

6.6.1.2. Chronology by indirect dating

In order to overcome the limitations of previous method, a promising technique has been developed from the isotopy of osmium (Klemm et al., 2005). It is based on the comparison of global evolution of the isotopy of Os in crusts and in seawater. (Burton et al., 1999 ; Klemm et al., 2005 ; Peucker-Ehrenbrink and Ravizza, 2012, 2000).

Here again, it would be interesting to carry out isotopic analyses of the Os of certain samples used in time series in order to accurately fix certain ages older than 10 Ma, while taking into account potential gaps that will now be discernible. A first selection of samples has been made.
The Fe-Mn crusts estimated to be younger than 10 Ma have naturally been discarded. Samples that have recorded uplift such as MOZ1-DR10-05 (Mount Macua, 15.6 Ma) and DR84-0026 (Mount Paisley, 30.7 Ma) seem very interesting to analyse, and in particular DR84-0026 since it extends up to in the Oligocene.

The Fe-Mn crust MOZ1-DR04-23 (Glorious Islands, 16.2 Ma) The Fe-Mn crust MOZ1-DR04-23 (Glorious Islands, 16.2 Ma) would also be a good candidate since it records the gradual decrease of NADW in the Comoros basin from 11.7 Ma. It is also a very interesting sample to evaluate potential regional volcanic phenomena.

6.6.2. Identify local events by high resolution mineralogical and geochemical study of two Fe-Mn crusts

During this thesis, two samples revealed a different mineralogy and geochemistry from other Fe-Mn crusts. Their characteristics raise several questions that could not be further explored. These are MOZ1-DR04-23 and MOZ5-DR03-01.

The first, MOZ1-DR04-23 (16.2 Ma), comes from the Glorious Islands, located at great depths, this sample has shed light on the circulation of deep currents in Comoros basin (Chapter 5). As for the second, MOZ5-DR03-01 (19.7 Ma), it was dredged off the African continent, north of the Natal Valley, 110 km from the nearest coast and at a depth between 950 and 1200 m (Figure 6.6). The results of the analyses of this Fe-Mn crust were not presented in the previous chapters insofar as the recordings reflect phenomena that go beyond the initial scope of the thesis.

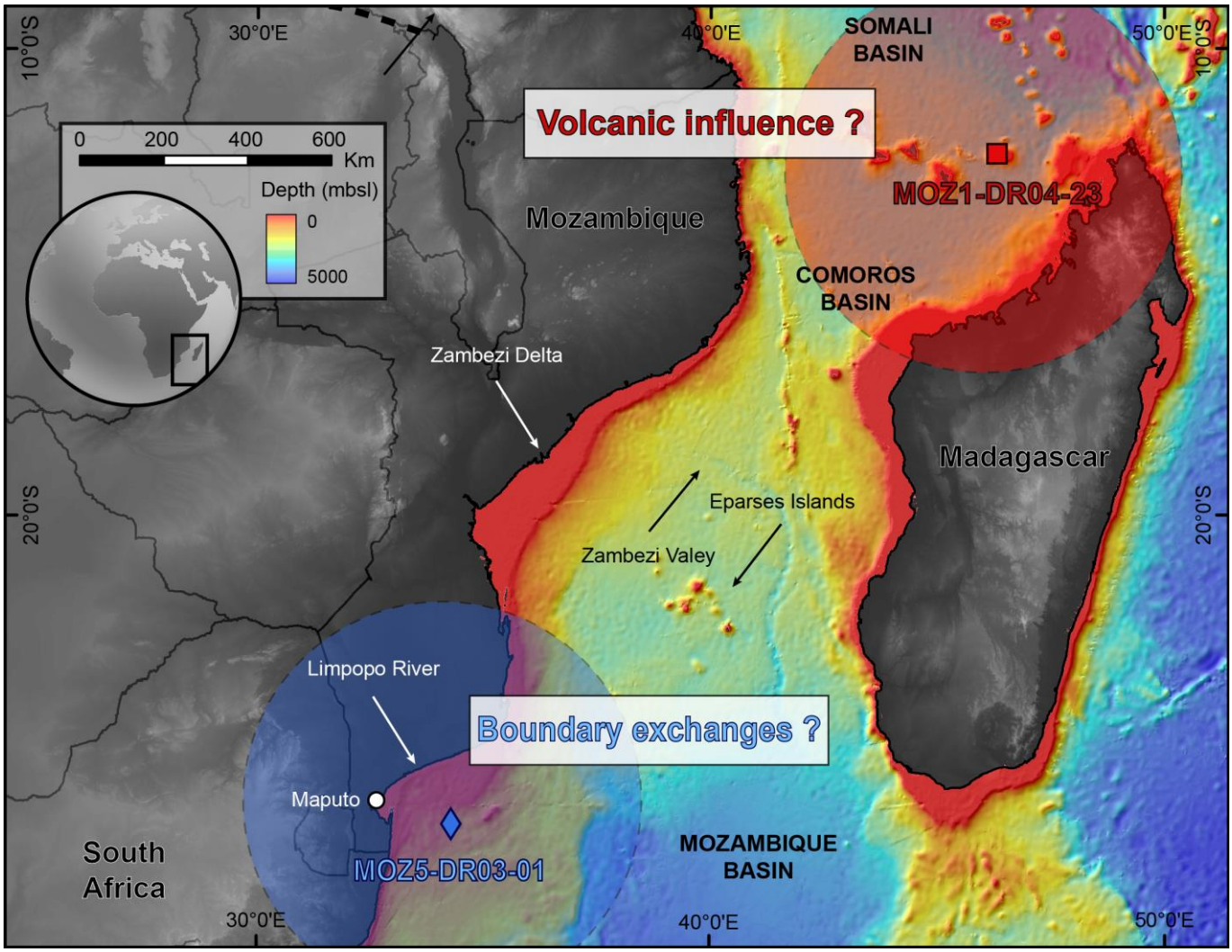

Figure 6.6. *Bathymetry of the Mozambique Channel (data from GEBCO and PAMELA oceanographic missions) showing the location of Fe-Mn crusts MOZ1-DR04-23 (Glorious Islands, 16.2 Ma) and MOZ5-DR03-01 (Natal Valley, 19.7 Ma) as well as the zones of influence of potential local phenomena recorded in their mineralogical and geochemical compositions.*

In this part, we propose to continue the studies on these two Fe-Mn crusts in order to identify and characterize very local events, recorded through their mineralogy and geochemistry. Quantitative mineralogy analyses were first carried out by XRD at IFREMER as presented previously (Chapter 5).

Further petrographic and mineralogical analyses were carried out in collaboration with TOTAL-CSTJF. The petrographic study of thin sections (40*60 mm; Appendix 7) polished and covered with carbon (25 nm thick) was carried out in order to submit samples to precise analyses including the study of textures and distributions of associated elements. Automated mineralogical maps using the FEG-SEM Qemscan ® (QUANTA 650, FEI) were carried out on the sections of the samples (resolution 20 µm/pixel) and on the zooms (resolution 2 µm/pixel). FEG-SEM data acquisitions include secondary electron, backscattered electron (BSE) imaging (250 nm resolution) and energy dispersive spectroscopy (EDS) mapping (2 µm resolution). Finally, Nanomin software (FEI, Hillsboro, OR, USA) was used to analyse the SEM-EDS data to produce mineralogical and chemical maps of the crusts and to define textural characteristics. For

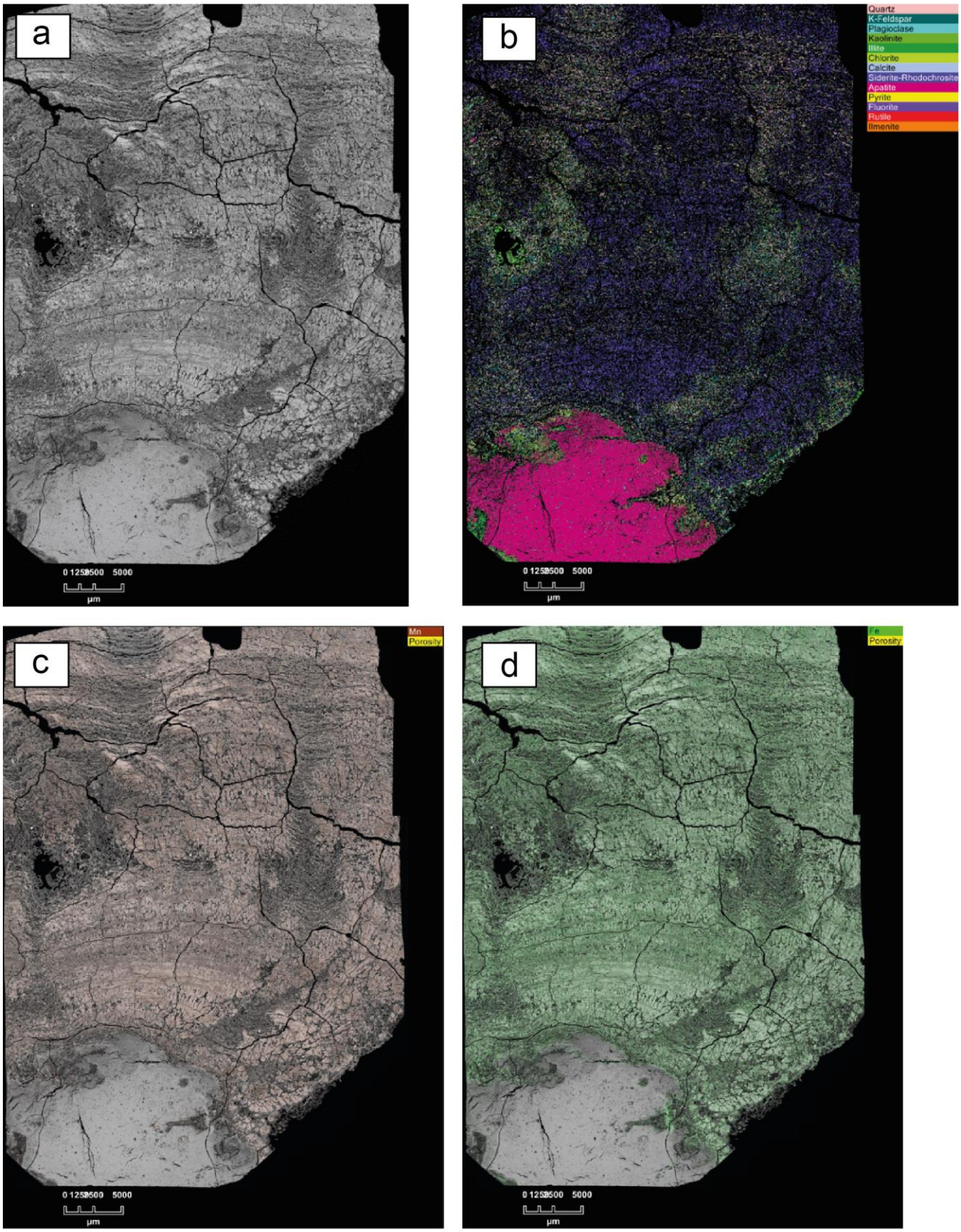

Figure 6.7. *Images and mineralogical maps of the MOZ1-DR04-23 E thin section made with the FEG-SEM Qemscan ®. a) BSE acquisition; b) EDS acquisition showing the main mineralogical phases (Nanomin - FEI, Hillsboro, OR, USA); c) BSE acquisition and Mn oxides; d) BSE acquisition and Fe oxides.*

elementary and isotopic analyses (Nd, Pb, Be), they have already been carried out according to the same protocols already presented (Chapter 2), and at the same time as the other samples of the thesis.

6.6.2.1. Fe-Mn crust MOZ1-DR04-23: volcanic events

The first mineralogical analyses carried out by XRD show that MOZ1-DR04-23 contains quartz, as the main allochtonous mineral, as well as plagioclase feldspars and potassium feldspars, in addition to Fe-Mn oxides (Appendix 5). These results are confirmed by the acquisitions and mineralogical mappings carried out with FEG-SEM Qemscan ® (Figure 6.7; Appendix 7).

For example, the total composition of the MOZ1-DR04-23 E thin section reflects quartz (7%), potassium feldspars (5%), plagioclase feldspars (3%) but also phases of pyrite, ilmenite and lower rutile content (< 0.5%).

Other thin sections of sample MOZ1-DR04-23 also show the presence of muscovite (< 0.5%).

Regarding elementary data, they show laminae of sample MOZ1-DR04-23 rich in aluminium (3.3% ; MOZ1-DR04-23 62 and 68 ; 14.4 and 15.3 Ma) and in titanium (up to 2.2 % ; MOZ1-DR04-23 30, 33 and 38 ; 7.2 to 9.0 Ma), as well as two correlations between these two elements (Figure 6.8), which could reflect the recording of Al rich detrital inputs and/or volcanic phenomena of different ages and chemical properties.

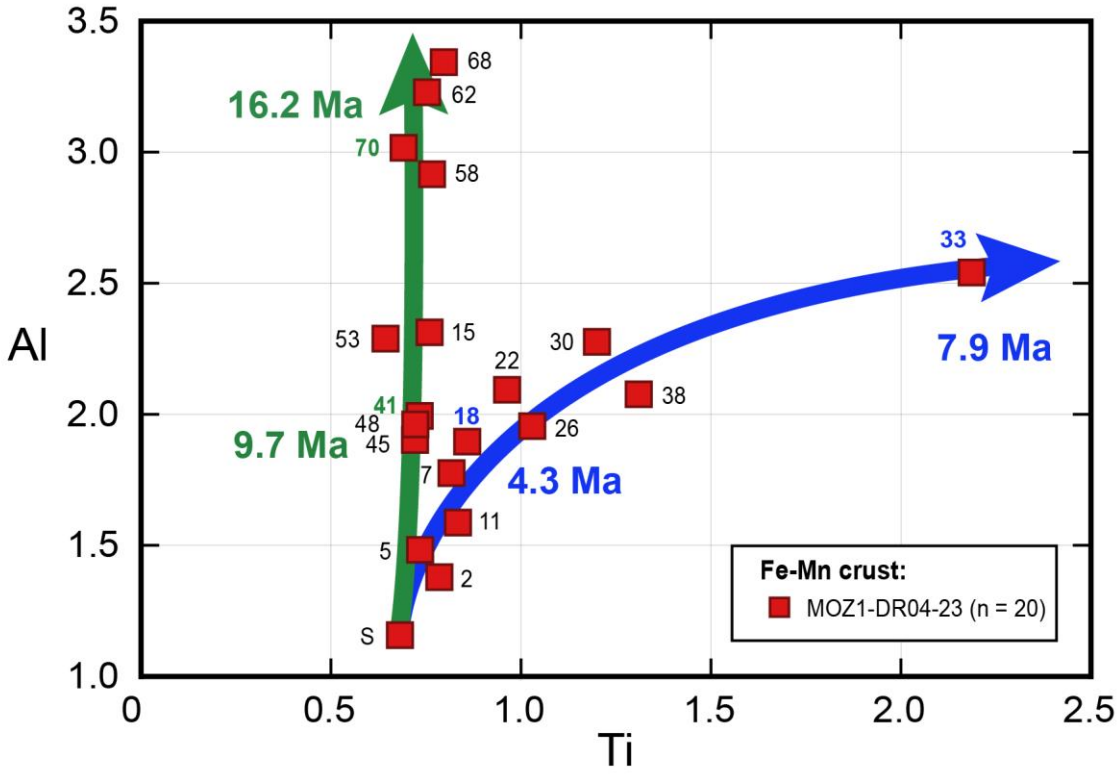

Figure 6.8. *Plot of Al concentrations versus Ti concentrations in the Fe-Mn crust MOZ1-DR04-23. The numbers at each point correspond to the depth (mm) of the lamina sampled on the Fe-Mn crust, those in bold and in colour correspond to the laminae with the dates indicated. The two arrows indicate potential volcanic and/or sedimentary influences and associated ages.*

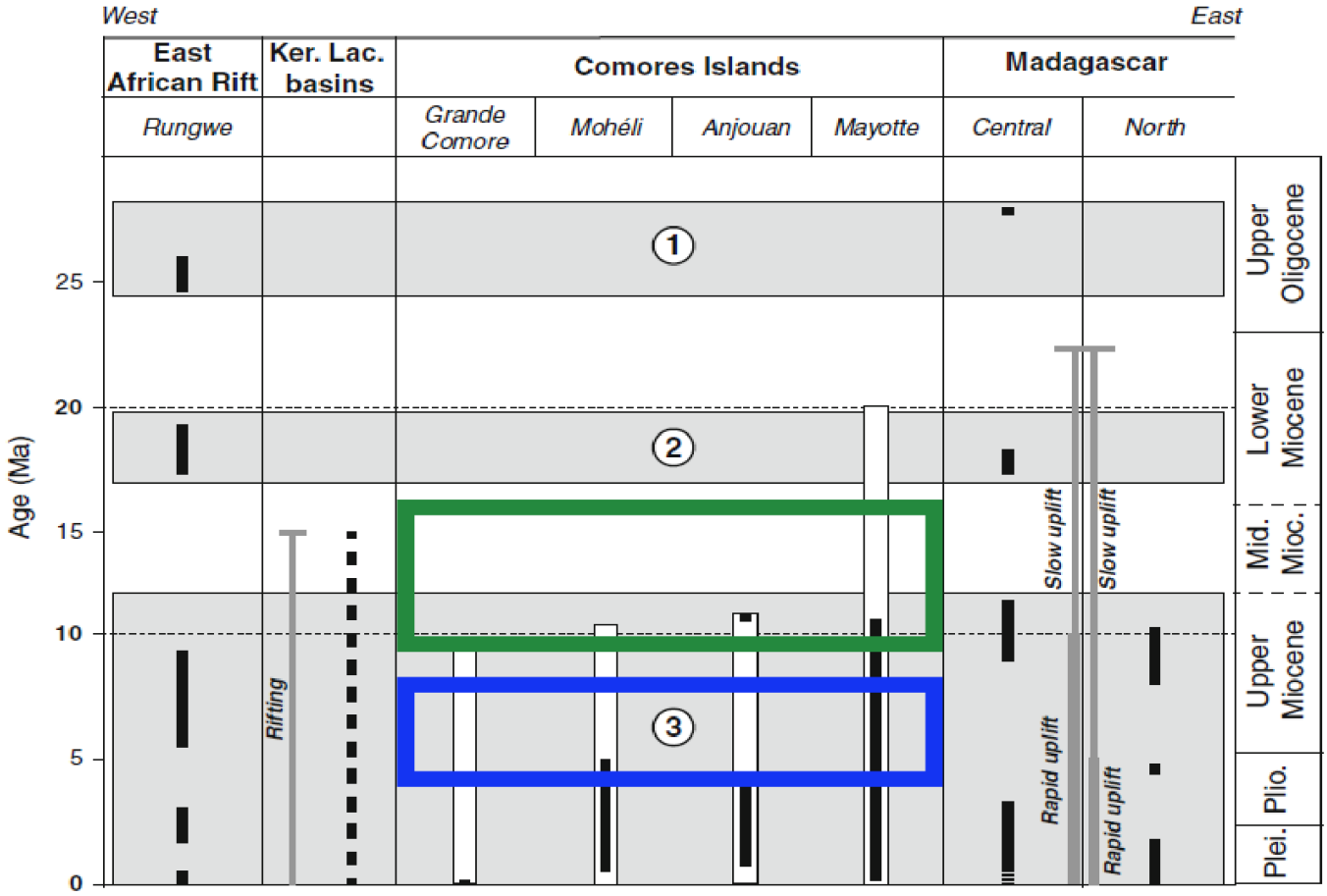

Figure 6.9. *Synthesis of volcanic phenomena (black bars) in the Comoros archipelago and in the surrounding regions. White bars represent newly estimated activities. Numbers 1, 2 and 3 correspond to the different periods of volcanism. The boxes represent potential volcanic phenomena recorded in the Fe-Mn crust MOZ1-DR04-23, from the Glorious Islands region (**Figure 6.8**). Modified image, according to Michon (2016).*

Regarding elementary data, they show laminae of sample MOZ1-DR04-23 rich in aluminum (3.3% ; MOZ1-DR04-23 62 and 68 ; 14.4 and 15.3 Ma) and in titanium (up to 2.2 % ; MOZ1-DR04-23 30, 33 and 38 ; 7.2 to 9.0 Ma), as well as two correlations between these two elements (Figure 6.8), which could reflect the recording of two volcanic phenomena of different ages and chemical properties.

It would be relevant to focus on the zooms studied during mineralogical acquisitions in order to point out the areas of abundance of these minerals and elements. Once correlated with the chronology of the Fe-Mn crust MOZ1-DR04-23, this would make it possible to focus on the identification and characterization of potential volcanic phenomena (Figure 6.9) during the 16 Ma. In a second time, Os isotope analyses could significantly complete this work by indicating magmatic events. Finally, it would also be very interesting to carry out high-resolution Pb analyses with an LA-MC-ICP-MS (Josso et al., 2020). This technique would allow the identification of very fine geochemical variations at previously selected ages.

6.6.2.2. Fe-Mn crust MOZ5-DR03-01: « boundary exchanges »

The second sample discussed is MOZ5-DR03-01 and comes from the northern Natal Valley. The preliminary results from the XRD show a

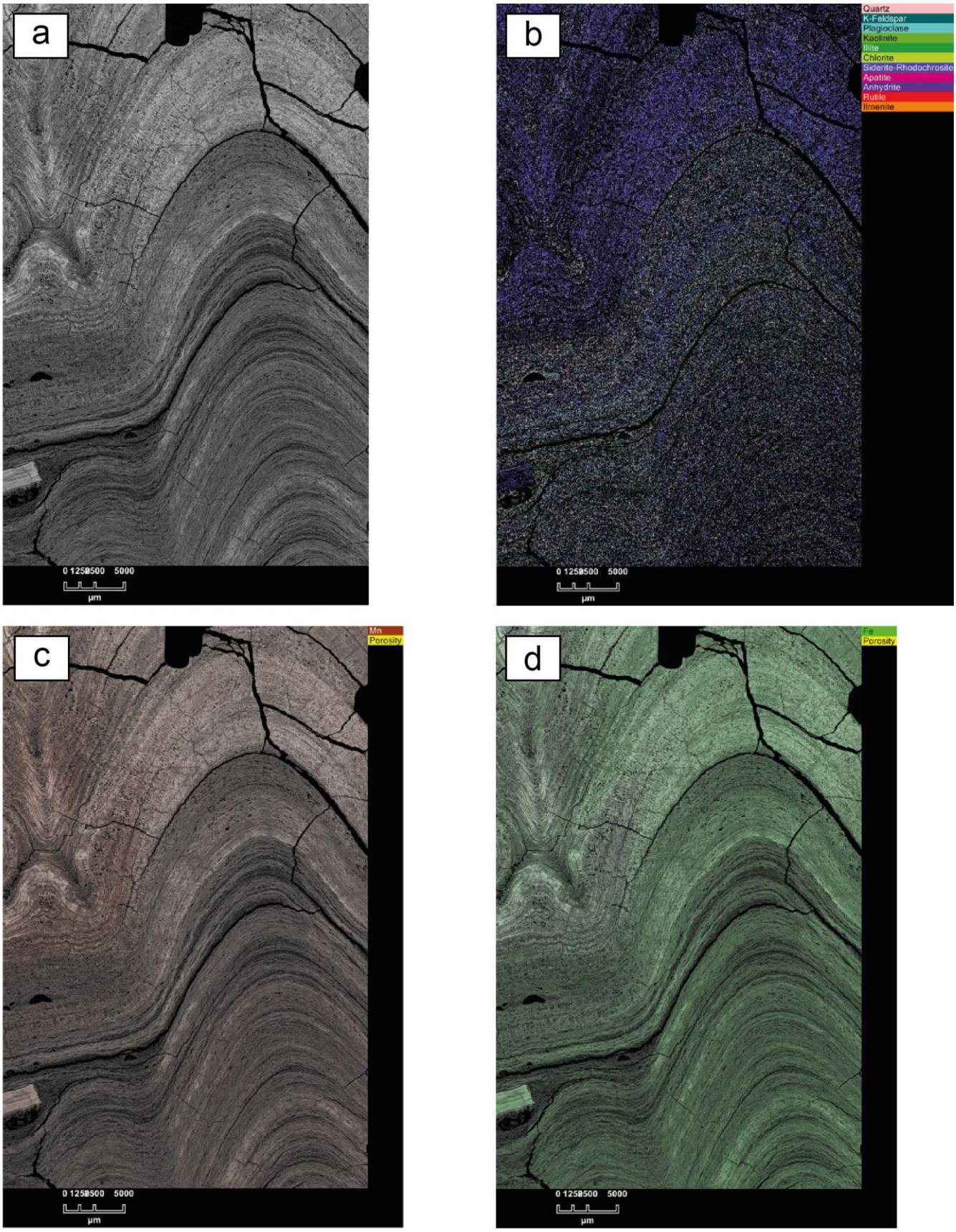

Figure 6.10. *Images and mineralogical maps of the MOZ5-DR03-01 B thin section produced with the FEG-SEM Qemscan ®. a) BSE acquisition; b) EDS acquisition showing the main mineralogical phases (Nanomin - FEI, Hillsboro, OR, USA) ; c) BSE acquisition and Mn oxides; d) BSE acquisition and Fe oxides.*

mineralogy common to the other crusts, with the presence of quartz, plagioclase feldspars and potassium feldspars in addition to the majority Fe-Mn oxides (Appendix 6).

The FEG-SEM Qemscan ® acquisitions confirm these mineralogical phases present at 11%, 6% and 5%, respectively, in the thin section MOZ5-DR03-01 B (Figure 6.10; Appendix 7). They also reveal the low presence of minerals such as dolomite (<0.5%) or anhydrite (in a second thin section of the sample) (<0.01%).

Regarding the elementary data, the Fe-Mn crust MOZ5-DR03-01 does not show values that stand out compared to the other samples. However, its isotopic composition in Nd is very different from those previously studied (Chapters 4 and 5). This one is less radiogenic (-10.2 > εNd > -12.5) and is marked by great variations (up to 2 εNd) (Figure 6.11). The signature shows its minimum at 6.7 Ma before going up to more radiogenic values. As shown in Figure 6.11, the isotopic composition in Nd of this sample is significantly less radiogenic and less homogeneous than that of sample DR75-012, located further south of the Mozambique Channel (Agulhas Plateau), or even those of the Fe-Mn crusts located northwest Atlantic Ocean (ALV539; BM 1969.05; Burton et al., 1997; O'Nions et al., 1998). Such isotopic changes in such a short time do not seem to reflect the original isotopic composition of the water mass in which the Fe-Mn crust formed (AAIW; -8 > εNd > -9 ; Amakawa et al., 2013; Arsouze et al., 2007; Jeandel, 1993; Piepgras, Wasserburg, 1982) but suggest that the history of this sample is completely different from the others, and is not linked to the same geochemical processes.

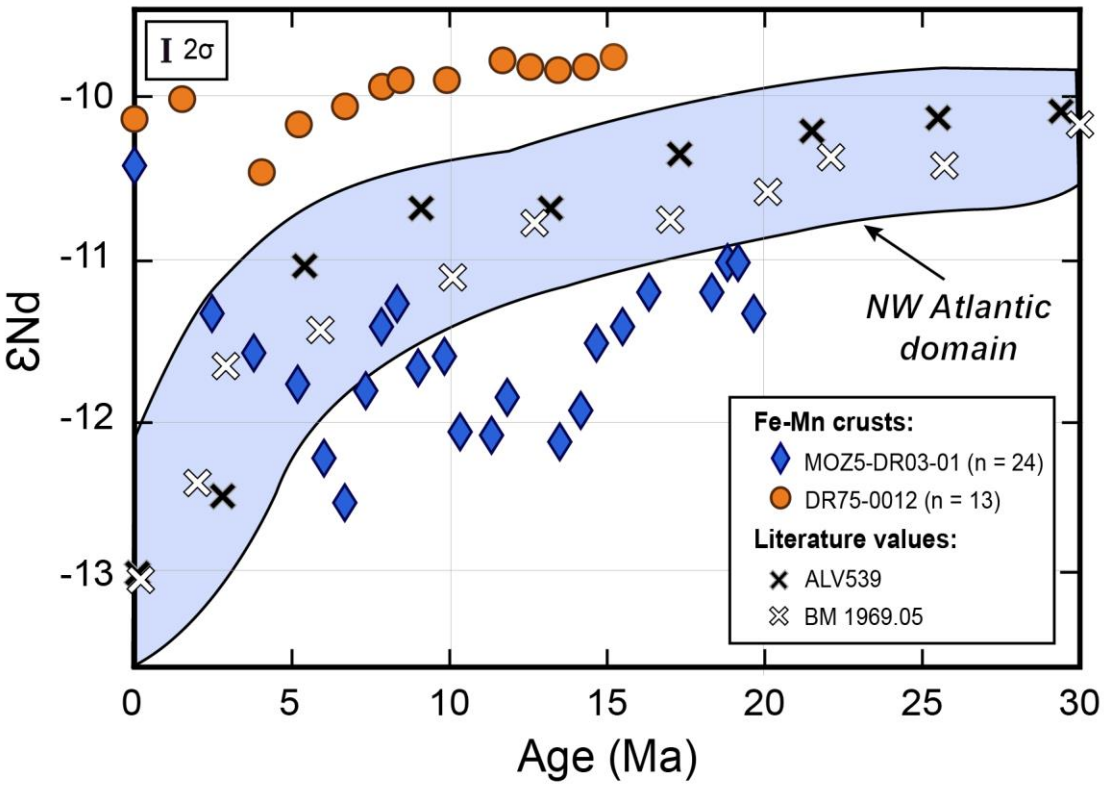

Figure 6.11. *Nd isotopic signature ($\varepsilon_{Nd\,(T)}$) according to the age, acquired from the $^{10}Be/^{9}Be$, isotopic ratio, of the Fe-Mn crusts MOZ5-DR03-01 and DR75-0012 from this study. The data for the Fe-Mn ALV539 and BM 1969.05 crusts come from the work of Burton et al. (1997) and of O'Nions et al. (1998).*

One of the hypotheses to explain this particular signature could be that elements such as aluminium or potassium have contaminated the Nd composition and its isotopy. However, no correlation is observable. Given the location of MOZ5-DR03-01 less than 150 km from the African coast and at a depth of less than 1200 m, it would be interesting to work on the geochemical exchanges between the very little radiogenic African terrestrial domain (ƐNd < -20 ; Jeandel et al., 2007) and water masses circulating near the margin.

This work would make it possible to determine whether interactions exist (boundary exchanges?) and to what extent they can impact the isotopic signature of MOZ5-DR03-01.

The study of the isotopic proxies of Os and hafnium (Hf) could also deepen this track. In this context, the isotopy of Hf could indicate sources of detrital inputs. For example, inputs from continental crust, whether wind or brought by surrounding rivers such as the Limpopo (Figure 6.6), have low radiogenic values in Hf (-6 > εHf> -12). In contrast, volcanic inputs have much more radiogenic Hf isotopic compositions (εHf from +13) (David et al., 2001; Godfrey et al., 1997; Piotrowski et al., 2000). Using these data and their comparison with the chronology of sample MOZ5-DR03-01, it would be possible to identify periods of high and low erosion of the continent, sources of detrital flows, but also to calculate sediment intake rates in the Natal Valley.

6.6.3. Oceanographic modelling

The last perspective developed in this manuscript concerns the numerical modelling of previously established currentological models (chapter 5). Indeed, it would be to model the currentology and geography of the Mozambique Channel by integrating new paleogeographic observations. The two models would establish an evolution of the circulation of currents before and after the uplift (11.7-3.4 Ma). They could take into account the paleoceanographic and paleogeographic data of this thesis, with:

(1) the contributions of deep currents (NADW, NIDW), estimated since 15.2 Ma at the Agulhas Plateau (DR75-0012), 19.7 Ma at the level of the Jeffrey Ridge (MOZ1-DR11-01 and 16.2 at the Glorious Islands (MOZ1-DR04-23),

(2) the bathymetric variations identified at different locations in the channel (Davie Ridge, Hall Bank, Europa Island), and estimated between 465 and 1265 m for the uplift (Figure 6.5) and between 650 and 1050 for the subsidence,

It would also take into account the major geographical upheavals already identified and dated in other works such as:

(3) volcanism in the Comoros Basin (Figure 6.9) and the formation of associated reliefs from 30 Ma (Debeuf, 2004 ; Emerick, Duncan, 1982 ; Hajash, Amastrong, 1972 ; Michon, 2016 ; Montaggioni, Nougier, 1981 ; Nougier et al., 1986 ; Pelleter et al., 2014),

Finally, it would be relevant to get closer to the water masses modelling teams in order to introduce:

(4) physical data in our models such as temperature, salinity, density, oxygen level and velocity of the ocean currents studied (Figure 6.12),

(5) and climatic data concerning the canal region: the wind (its strength, its orientation), the presence of eddies (their diameters, their orientation), the influence of glaciations and

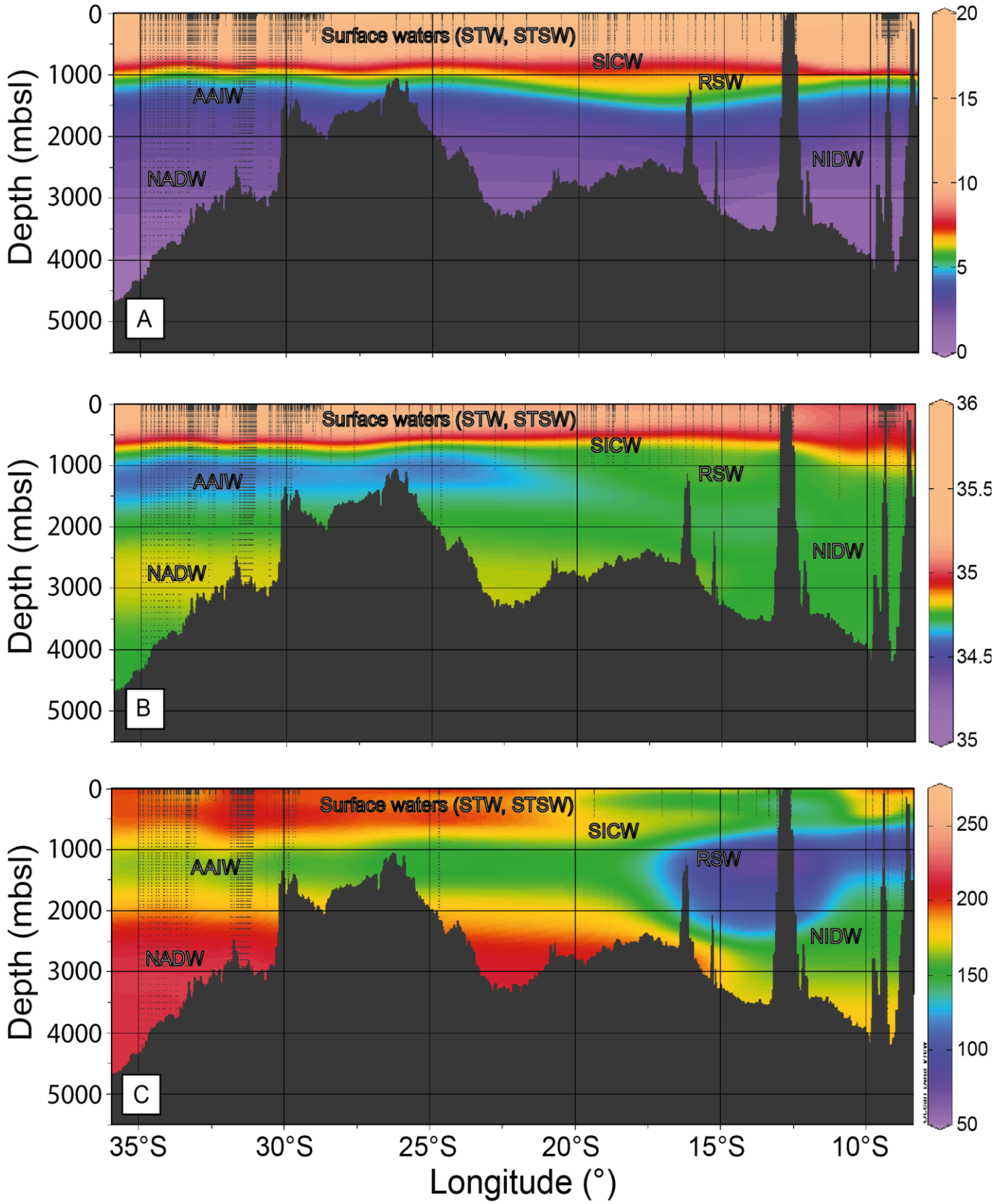

Figure 6.12. *Sections corresponding to distribution of the main water masses of Mozambique Channel, according to the Conductivity-Temperature-Depth (CTD) profiles. A: Temperature data (°C); B: Salinity data (psu) ; C: Dissolved oxygen data (ml/l). The bathymetry of Mozambique Channel is taken from GEBCO 2014 data and PAMELA campaigns.*

(6) deglaciations (e.g. Glaciation of the Northern Hemisphere and reduction of the NADW towards the South (Bergh et al., 2021; Boyle, Keigwin, 1987, 1982; Charles, Fairbanks, 1992; Frank et al., 2002).

These numerical models would allow us to compare our observations and complete our data. In particular, it would be possible to calculate contributions along north-south sections, at precise points, different from those we already know. We would then have a quantitative idea of the evolution of NADW in the entire channel. One of the equally important points would be to work with precision, at high resolution, on the topography of the Davie ridge. Modelling could help find places of passages such as faults in the structure, where deep currents could flow (Figure 6.5, 6.12).

Finally, these numerical models would make it possible to visualize the influence of large-scale phenomena on the local system that is the Mozambique Channel, and to integrate them into larger reconstructions such as a circulation model of the Indian Ocean (e.g. Frank et al., 2006) and a global current circulation model taking into account the work done in each ocean basin.

6.7. Bibliographical references

Abbott, A.N., 2019. A benthic flux from calcareous sediments results in non-conservative neodymium behavior during lateral transport: A study from the Tasman Sea. Geology 47, 363–366. https://doi.org/10.1130/G45904.1

Abbott, A.N., Haley, B.A., McManus, J., 2015a. Bottoms up: Sedimentary control of the deep North Pacific Ocean's εNd signature. Geology 43, 1035–1035. https://doi.org/10.1130/G37114.1

Abbott, A.N., Haley, B.A., McManus, J., Reimers, C.E., 2015b. The sedimentary flux of dissolved rare earth elements to the ocean. Geochim. Cosmochim. Acta 154, 186–200. https://doi.org/10.1016/j.gca.2015.01.010

Abouchami, W., Goldstein, S.L., Gazer, S.J.G., Eisenhauer, A., Mangini, A., 1997. Secular changes of lead and neodymium in central Pacific seawater recorded by a Fe□Mn crust. Geochim. Cosmochim. Acta 61, 3957–3974. https://doi.org/10.1016/S0016-7037(97)00218-4

Albarède, F., Goldstein, S.L., Dautel, D., 1997. The neodymium isotopic composition of manganese nodules from the Southern and Indian oceans, the global oceanic neodymium budget, and their bearing on deep ocean circulation. Geochim. Cosmochim. Acta 61, 1277–1291. https://doi.org/10.1016/S0016-7037(96)00404-8

Amakawa, H., Tazoe, H., Obata, H., Gamo, T., Sano, Y., Shen, C.-C., 2013. Neodymium isotopic composition and concentration in the Southwest Pacific Ocean. Geochem. J. 47, 409–422. https://doi.org/10.2343/geochemj.2.0260

Arsouze, T., Dutay, J.-C., Lacan, F., Jeandel, C., 2007. Modeling the neodymium isotopic composition with a global ocean circulation model. Chem. Geol. 239, 165–177. https://doi.org/10.1016/j.chemgeo.2006.12.006

Bergh, E.W., von Koslowski, R., Compton, J.S., 2021. Variations in deep water masses along the western margin of South Africa, spanning the last two glacial terminations. Palaeogeogr. Palaeoclimatol. Palaeoecol. 562, 110148. https://doi.org/10.1016/j.palaeo.2020.110148

Boyle, E.A., Keigwin, L., 1987. North Atlantic thermohaline circulation during the past 20,000 years linked to high-latitude surface temperature. Nature 330, 35–40. https://doi.org/10.1038/330035a0

Boyle, E.A., Keigwin, L.D., 1982. Deep Circulation of the North Atlantic over the Last 200,000 Years: Geochemical Evidence. Science 218, 784–787. https://doi.org/10.1126/science.218.4574.784

Burton, K.W., Bourdon, B., Birck, J.-L., Allègre, C.J., Hein, J.R., 1999. Osmium isotope variations in the oceans recorded by FeMn crusts. Earth Planet. Sci.

Lett. 171, 185–197. https://doi.org/10.1016/S0012-821X(99)00139-9

Burton, K.W., Ling, H.-F., O'Nions, R.K., 1997. Closure of the Central American Isthmus and its effect on deep-water formation in the North Atlantic. Nature 386, 382. https://doi.org/10.1038/386382a0

Cao, W., Zahirovic, S., Flament, N., Williams, S., Golonka, J., Müller, R.D., 2017. Improving global paleogeography since the late Paleozoic using paleobiology. Biogeosciences 14, 5425–5439. https://doi.org/10.5194/bg-14-5425-2017

Charles, C., Pelleter, E., Révillon, S., Nonnotte, P., Jorry, S.J., Kluska, J.-M., 2020. Intermediate and deep ocean current circulation in the Mozambique Channel: New insights from ferromanganese crust Nd isotopes. Mar. Geol. 430, 106356. https://doi.org/10.1016/j.margeo.2020.106356

Charles, C.D., Fairbanks, R.G., 1992. Evidence from Southern Ocean sediments for the effect of North Atlantic deep-water flux on climate. Nature 355, 416–419. https://doi.org/10.1038/355416a0

Chmeleff, J., von Blanckenburg, F., Kossert, K., Jakob, D., 2010. Determination of the 10Be half-life by multicollector ICP-MS and liquid scintillation counting. Nucl. Instrum. Methods Phys. Res. B 268, 192–199. https://doi.org/10.1016/j.nimb.2009.09.012

Christensen, J.N., Halliday, A.N., Godfrey, L.V., Hein, J.R., Rea, D.K., 1997. Climate and Ocean Dynamics and the Lead Isotopic Records in Pacific Ferromanganese Crusts. Science 277, 913–918. https://doi.org/10.1126/science.277.5328.913

Collins, C., Hermes, J.C., Roman, R.E., Reason, C.J.C., 2016. First dedicated hydrographic survey of the Comoros Basin. J. Geophys. Res. Oceans 121, 1291–1305. https://doi.org/10.1002/2015JC011418

Cornacchia, I., Brandano, M., Agostini, S., 2021. Miocene paleoceanographic evolution of the Mediterranean area and carbonate production changes: A review. Earth-Sci. Rev. 221, 103785. https://doi.org/10.1016/j.earscirev.2021.103785

Courgeon, S., 2017. Cenozoic evolution of isolated carbonate platforms from the Mozambique Channel (SW Indian Ocean) : development and controls in active geodynamic settings (These de doctorat). Aix-Marseille.

Courgeon, S., Bachèlery, P., Jouet, G., Jorry, S.J., Bou, E., BouDagher-Fadel, M.K., Révillon, S., Camoin, G., Poli, E., 2018. The offshore east African rift system: new insights from the Sakalaves seamounts (Davie Ridge, SW Indian Ocean). Terra Nova 30, 380–388. https://doi.org/10.1111/ter.12353

Courgeon, S., Jorry, S.J., Camoin, G.F., BouDagher-Fadel, M.K., Jouet, G., Révillon, S., Bachèlery, P., Pelleter, E., Borgomano, J., Poli, E., Droxler, A.W., 2016. Growth and demise of Cenozoic isolated carbonate platforms: New insights from the Mozambique Channel seamounts (SW Indian Ocean). Mar. Geol. 380, 90–105. https://doi.org/10.1016/j.margeo.2016.07.006

Courgeon, S., Jorry, S.J., Jouet, G., Camoin, G., BouDagher-Fadel, M.K., Bachèlery, P., Caline, B., Boichard, R., Révillon, S., Thomas, Y., Thereau, E., Guérin, C., 2017. Impact of tectonic and volcanism on the Neogene evolution of isolated carbonate platforms (SW Indian Ocean). Sediment. Geol. 355, 114–131. https://doi.org/10.1016/j.sedgeo.2017.04.008

David, K., Frank, M., O'Nions, R.K., Belshaw, N.S., Arden, J.W., 2001. The Hf isotope composition of global seawater and the evolution of Hf isotopes in the deep Pacific Ocean from Fe–Mn crusts. Chem. Geol. 178, 23–42. https://doi.org/10.1016/S0009-2541(00)00427-7

Debeuf, D., 2004. Etude de l'évolution volcano-structurale et magmatique de Mayotte (Archipel des Comores, Océan Indien): Approches structurale, pétrographique, géochimique et géochronologique. Unpublished Ph.D. thesis, Université de La Réunion, 243 pp

Derry, L.A., France-Lanord, C., 1996. Neogene Himalayan weathering history and river87Sr86Sr: impact on the marine Sr record. Earth Planet. Sci. Lett. 142, 59–74. https://doi.org/10.1016/0012-821X(96)00091-X

Emerick, C.M., Duncan, R.A., 1982. Age progressive volcanism in the Comores Archipelago, western Indian Ocean and implications for Somali plate

tectonics. Earth Planet. Sci. Lett. 60, 415–428. https://doi.org/10.1016/0012-821X(82)90077-2

Frank, M., 2002. Radiogenic isotopes: tracers of past ocean circulation and erosional input. Rev. Geophys. 40, 1–1. https://doi.org/10.1029/2000RG000094

Frank, M., O'Nions, R.K., 1998. Sources of Pb for Indian Ocean ferromanganese crusts: a record of Himalayan erosion? Earth Planet. Sci. Lett. 158, 121–130. https://doi.org/10.1016/S0012-821X(98)00055-7

Frank, M., O'Nions, R.K., Hein, J.R., Banakar, V.K., 1999. 60 Myr records of major elements and Pb–Nd isotopes from hydrogenous ferromanganese crusts: reconstruction of seawater paleochemistry. Geochim. Cosmochim. Acta 63, 1689–1708. https://doi.org/10.1016/S0016-7037(99)00079-4

Frank, M., Whiteley, N., Kasten, S., Hein, J.R., O'Nions, K., 2002. North Atlantic Deep Water export to the Southern Ocean over the past 14 Myr: Evidence from Nd and Pb isotopes in ferromanganese crusts. Paleoceanography 17, 12-1-12–9. https://doi.org/10.1029/2000PA000606

Frank, M., Whiteley, N., van de Flierdt, T., Reynolds, B.C., O'Nions, K., 2006. Nd and Pb isotope evolution of deep water masses in the eastern Indian Ocean during the past 33 Myr. Chem. Geol., Special Issue in Honour of R.K. O'Nions 226, 264–279. https://doi.org/10.1016/j.chemgeo.2005.09.024

Godfrey, L.V., Lee, D.-C., Sangrey, W.F., Halliday, A.N., Salters, V.J.M., Hein, J.R., White, W.M., 1997. The Hf isotopic composition of ferromanganese nodules and crusts and hydrothermal manganese deposits: Implications for seawater Hf. Earth Planet. Sci. Lett. 151, 91–105. https://doi.org/10.1016/S0012-821X(97)00106-4

Hajash, A., Armstrong, R.L., 1972. Paleomagnetic and radiometric evidence for the age of the Comores Islands, west central Indian Ocean. Earth Planet. Sci. Lett. 16, 231–236. https://doi.org/10.1016/0012-821X(72)90195-1

Haley, B.A., Klinkhammer, G.P., 2003. Complete separation of rare earth elements from small volume seawater samples by automated ion chromatography: method development and application to benthic flux. Mar. Chem. 82, 197–220. https://doi.org/10.1016/S0304-4203(03)00070-7

Hu, R., Chen, T., Ling, H., 2012. Late Cenozoic history of deep water circulation in the western North Pacific: Evidence from Nd isotopes of ferromanganese crusts. Chin. Sci. Bull. 57, 4077–4086. https://doi.org/10.1007/s11434-012-5322-9

Jeandel, C., 1993. Concentration and isotopic composition of Nd in the South Atlantic Ocean. Earth Planet. Sci. Lett. 117, 581–591. https://doi.org/10.1016/0012-821X(93)90104-H

Jeandel, C., Arsouze, T., Lacan, F., Téchiné, P., Dutay, J.-C., 2007. Isotopic Nd compositions and concentrations of the lithogenic inputs into the ocean: A compilation, with an emphasis on the margins. Chem. Geol. 239, 156–164. https://doi.org/10.1016/j.chemgeo.2006.11.013

Josso, P., Horstwood, M.S.A., Millar, I.L., Pashley, V., Lusty, P. a. J., Murton, B., 2020. Development of a Correlated Fe-Mn Crust Stratigraphy Using Pb and Nd Isotopes and Its Application to Paleoceanographic Reconstruction in the Atlantic. Paleoceanogr. Paleoclimatology 35, e2020PA003928. https://doi.org/10.1029/2020PA003928

Josso, P., Parkinson, I., Horstwood, M., Lusty, P., Chenery, S., Murton, B., 2019. Improving confidence in ferromanganese crust age models: A composite geochemical approach. Chem. Geol. 513, 108–119. https://doi.org/10.1016/j.chemgeo.2019.03.003

Josso, P., Pelleter, E., Pourret, O., Fouquet, Y., Etoubleau, J., Cheron, S., Bollinger, C., 2017. A new discrimination scheme for oceanic ferromanganese deposits using high field strength and rare earth elements. Ore Geol. Rev., SI:Marine mineral deposits: New resources for base, precious, and critical metals 87, 3–15. https://doi.org/10.1016/j.oregeorev.2016.09.003

Klemm, V., Levasseur, S., Frank, M., Hein, J.R., Halliday, A.N., 2005. Osmium isotope stratigraphy of a marine ferromanganese crust. Earth Planet. Sci. Lett. 238, 42–48. https://doi.org/10.1016/j.epsl.2005.07.016

Kocsis, L., Vennemann, T.W., Fontignie, D., Baumgartner, C., Montanari, A., Jelen, B., 2008. Oceanographic and climatic evolution of the Miocene Mediterranean deduced from Nd, Sr, C, and O isotope compositions of marine fossils and sediments. Paleoceanography 23. https://doi.org/10.1029/2007PA001540

Korschinek, G., Bergmaier, A., Faestermann, T., Gerstmann, U.C., Knie, K., Rugel, G., Wallner, A., Dillmann, I., Dollinger, G., von Gostomski, Ch.L., Kossert, K., Maiti, M., Poutivtsev, M., Remmert, A., 2010. A new value for the half-life of 10Be by Heavy-Ion Elastic Recoil Detection and liquid scintillation counting. Nucl. Instrum. Methods Phys. Res. Sect. B Beam Interact. Mater. At. 268, 187–191. https://doi.org/10.1016/j.nimb.2009.09.020

Koschinsky, A., Hein, J.R., 2017. Marine ferromanganese encrustations: Archives of changing oceans. Elements. https://doi.org/10.2113/gselements.13.3.177

Leclaire, L., 1984. RIDA - MD39 cruise, Marion Dufresne R/V. https://doi.org/10.17600/84010511

Leclaire, L., 1975. NOSICAA - MD 06 cruise, Marion Dufresne R/V. https://doi.org/10.17600/75010711

Leroux, E., Counts, J.W., Jorry, S.J., Jouet, G., Révillon, S., BouDagher-Fadel, M.K., Courgeon, S., Berthod, C., Ruffet, G., Bachèlery, P., Grenard-Grand, E., 2020. Evolution of the Glorieuses seamount in the SW Indian Ocean and surrounding deep Somali Basin since the Cretaceous. Mar. Geol. 427, 106202. https://doi.org/10.1016/j.margeo.2020.106202

Ling, H.F., Burton, K.W., O'Nions, R.K., Kamber, B.S., von Blanckenburg, F., Gibb, A.J., Hein, J.R., 1997. Evolution of Nd and Pb isotopes in Central Pacific seawater from ferromanganese crusts. Earth Planet. Sci. Lett. 146, 1–12. https://doi.org/10.1016/S0012-821X(96)00224-5

Ling, H.-F., Jiang, S.-Y., Frank, M., Zhou, H.-Y., Zhou, F., Lu, Z.-L., Chen, X.-M., Jiang, Y.-H., Ge, C.-D., 2005. Differing controls over the Cenozoic Pb and Nd isotope evolution of deepwater in the central North Pacific Ocean. Earth Planet. Sci. Lett. 232, 345–361. https://doi.org/10.1016/j.epsl.2004.12.009

Manheim, F.T., 1986. Marine Cobalt Resources. Science 232, 600–608. https://doi.org/10.1126/science.232.4750.600

Manheim, F.T., Lane-Bostwick, C.M., 1988. Cobalt in ferromanganese crusts as a monitor of hydrothermal discharge on the Pacific sea floor. Nature 335, 59. https://doi.org/10.1038/335059a0

Mantyla, A.W., Reid, J.L., 1995. On the origins of deep and bottom waters of the Indian Ocean. J. Geophys. Res. Oceans 100, 2417–2439. https://doi.org/10.1029/94JC02564

Marino, E., González, F.J., Somoza, L., Lunar, R., Ortega, L., Vázquez, J.T., Reyes, J., Bellido, E., 2017. Strategic and rare elements in Cretaceous-Cenozoic cobalt-rich ferromanganese crusts from seamounts in the Canary Island Seamount Province (northeastern tropical Atlantic). Ore Geol. Rev., SI:Marine mineral deposits: New resources for base, precious, and critical metals 87, 41–61. https://doi.org/10.1016/j.oregeorev.2016.10.005

Masters, J.C., Génin, F., Zhang, Y., Pellen, R., Huck, T., Mazza, P.P.A., Rabineau, M., Doucouré, M., Aslanian, D., 2021. Biogeographic mechanisms involved in the colonization of Madagascar by African vertebrates: Rifting, rafting and runways. J. Biogeogr. 48, 492–510. https://doi.org/10.1111/jbi.14032

Masters, J.C., Wit, M.J. de, Asher, R.J., 2006. Reconciling the Origins of Africa, India and Madagascar with Vertebrate Dispersal Scenarios. Folia Primatol. (Basel) 77, 399–418. https://doi.org/10.1159/000095388

McCall, R.A., 1997. Implications of recent geological investigations of the Mozambique Channel for the mammalian colonization of Madagascar. Proc. R. Soc. Lond. B Biol. Sci. 264, 663–665. https://doi.org/10.1098/rspb.1997.0094

Michon, L., 2016. The volcanism of the Comoros archipelago integrated at a regional scale, in: Bachelery, Patrick, Lénat, Jean-François, Muro, D., Andrea, Michon, Laurent (Eds.), Active Volcanoes of the Southwest Indian Ocean: Piton de La Fournaise and Karthala, Active Volcanoes of the World. Springer-Verlag, pp. 233–244.

Montaggioni, L.F., Nougier, J., 1981. Les enclaves de roches detritiques dans les Volcans d'Anjouan (Archipel des Comores); Origine et interpretation dans le cadre de l'evolution du Canal de Mozambique. Bull. Société Géologique Fr. S7-XXIII, 595–601. https://doi.org/10.2113/gssgfbull.S7-XXIII.6.595

Moulin, M., Evain, M., 2016. PAMELA-MOZ05 cruise, Pourquoi pas ? R/V. https://doi.org/10.17600/16009500

Nougier, J., Cantagrel, J.M., Karche, J.P., 1986. The Comores archipelago in the western Indian Ocean: volcanology, geochronology and geodynamic setting. J. Afr. Earth Sci. 1983 5, 135–145. https://doi.org/10.1016/0899-5362(86)90003-5

Olu, K., 2014. PAMELA-MOZ01 cruise, L'Atalante R/V. https://doi.org/10.17600/14001000

O'Nions, R.K., Frank, M., von Blanckenburg, F., Ling, H.-F., 1998. Secular variation of Nd and Pb isotopes in ferromanganese crusts from the Atlantic, Indian and Pacific Oceans. Earth Planet. Sci. Lett. 155, 15–28. https://doi.org/10.1016/S0012-821X(97)00207-0

Partridge, T.C., 1998. Of diamonds, dinosaurs and diastrophism : 150 million years of landscape evolution in southern Africa. South Afr. J. Geol. 101, 167–184. https://doi.org/10.10520/EJC-947b4efa3

Pelleter, A.-A., Caroff, M., Cordier, C., Bachelery, P., Nehlig, P., Debeuf, D., Arnaud, N., 2014. Melilite-bearing lavas in Mayotte (France): An insight into the mantle source below the Comores. Lithos 208–209, 281–297. https://doi.org/10.1016/j.lithos.2014.09.012

Peucker-Ehrenbrink, B., Ravizza, G., 2012. Chapter 8 - Osmium Isotope Stratigraphy, in: Gradstein, F.M., Ogg, J.G., Schmitz, M.D., Ogg, G.M. (Eds.), The Geologic Time Scale. Elsevier, Boston, pp. 145–166. https://doi.org/10.1016/B978-0-444-59425-9.00008-1

Peucker-Ehrenbrink, B., Ravizza, G., 2000. The marine osmium isotope record. Terra Nova 12, 205–219. https://doi.org/10.1046/j.1365-3121.2000.00295.x

Piepgras, D.J., Wasserburg, G.J., 1982. Isotopic Composition of Neodymium in Waters from the Drake Passage. Science 217, 207–214.

Piotrowski, A.M., Lee, D.-C., Christensen, J.N., Burton, K.W., Halliday, A.N., Hein, J.R., Günther, D., 2000. Changes in erosion and ocean circulation recorded in the Hf isotopic compositions of North Atlantic and Indian Ocean ferromanganese crusts. Earth Planet. Sci. Lett. 181, 315–325. https://doi.org/10.1016/S0012-821X(00)00205-3

Poux, C., Madsen, O., Marquard, E., Vieites, D.R., de Jong, W.W., Vences, M., 2005. Asynchronous Colonization of Madagascar by the Four Endemic Clades of Primates, Tenrecs, Carnivores, and Rodents as Inferred from Nuclear Genes. Syst. Biol. 54, 719–730. https://doi.org/10.1080/10635150500234534

Puteanus, D., Halbach, P., 1988. Correlation of Co concentration and growth rate — A method for age determination of ferromanganese crusts. Chem. Geol. 69, 73–85. https://doi.org/10.1016/0009-2541(88)90159-3

Rahlf, P., Hathorne, E., Laukert, G., Gutjahr, M., Weldeab, S., Frank, M., 2020. Tracing water mass mixing and continental inputs in the southeastern Atlantic Ocean with dissolved neodymium isotopes. Earth Planet. Sci. Lett. 530, 115944. https://doi.org/10.1016/j.epsl.2019.115944

Rehkämper, M., Frank, M., Hein, J.R., Halliday, A., 2004. Cenozoic marine geochemistry of thallium deduced from isotopic studies of ferromanganese crusts and pelagic sediments. Earth Planet. Sci. Lett. 219, 77–91. https://doi.org/10.1016/S0012-821X(03)00703-9

Rickli, J., Frank, M., Baker, A.R., Aciego, S., de Souza, G., Georg, R.B., Halliday, A.N., 2010. Hafnium and neodymium isotopes in surface waters of the eastern Atlantic Ocean: Implications for sources and inputs of trace metals to the ocean. Geochim. Cosmochim. Acta 74, 540–557. https://doi.org/10.1016/j.gca.2009.10.006

Searle, M.P., 1996. Cooling history, erosion, exhumation and kinematics of the Himalaya-Karakoram-Tibet orogenic belt. Pp. 110–137 in: Asian Tectonics. (Yin, A. and Harrison, M.A., editors). Cambridge University Press, Cambridge, UK.

Segev, A., Avni, Y., Shahar, J., Wald, R., 2017. Late Oligocene and Miocene different seaways to the Red

Sea–Gulf of Suez rift and the Gulf of Aqaba–Dead Sea basins. Earth-Sci. Rev. 171, 196–219. https://doi.org/10.1016/j.earscirev.2017.05.004

Stichel, T., Frank, M., Rickli, J., Hathorne, E.C., Haley, B.A., Jeandel, C., Pradoux, C., 2012. Sources and input mechanisms of hafnium and neodymium in surface waters of the Atlantic sector of the Southern Ocean. Geochim. Cosmochim. Acta 94, 22–37. https://doi.org/10.1016/j.gca.2012.07.005

Toole, J.M., Warren, B.A., 1993. A hydrographic section across the subtropical South Indian Ocean. Deep Sea Res. Part Oceanogr. Res. Pap. 40, 1973–2019. https://doi.org/10.1016/0967-0637(93)90042-2

Wilson, D.J., Piotrowski, A.M., Galy, A., McCave, I.N., 2012. A boundary exchange influence on deglacial neodymium isotope records from the deep western Indian Ocean. Earth Planet. Sci. Lett. 341–344, 35–47. https://doi.org/10.1016/j.epsl.2012.06.009

You, Y., 2000. Implications of the deep circulation and ventilation of the Indian Ocean on the renewal mechanism of North Atlantic Deep Water. J. Geophys. Res. Oceans 105, 23895–23926. https://doi.org/10.1029/2000JC900105

APPENDICES

APPENDIX 1.

Details of the oceanographic cruises

Cruise	Num. dredge	Start	Hour	End	Hour
PAMELA-MOZ1	MOZ1-DR01	28/09/2014	04:07:48	28/09/2014	04:38:40
PAMELA-MOZ1	MOZ1-DR04	30/09/2014	15:30:10	30/09/2014	16:05:56
PAMELA-MOZ1	MOZ1-DR10	11/10/2014	20:40:28	11/10/2014	21:25:54
PAMELA-MOZ1	MOZ1-DR11	12/10/2014	05:05:26	12/10/2014	05:46:39
PAMELA-MOZ1	MOZ1-DR12	13/10/2014	05:30:42	13/10/2014	06:20:48
PAMELA-MOZ1	MOZ1-DR13	14/10/2014		14/10/2014	06:18:14
PAMELA-MOZ1	MOZ1-DR14	14/10/2014	20:50:00	14/10/2014	21:25:03
PAMELA-MOZ1	MOZ1-DR15	15/10/2014	11:38:43	15/10/2014	12:25:55
PAMELA-MOZ1	MOZ1-DR16	19/10/2014	17:01:22	19/10/2014	17:46:00
PAMELA-MOZ1	MOZ1-DR17	20/10/2014	11:47:39	20/10/2014	12:19:29
PAMELA-MOZ1	MOZ1-DR19	21/10/2014	12:42:38	21/10/2014	13:22:38
PAMELA-MOZ1	MOZ1-DR22	22/10/2014	09:12:28	22/10/2014	09:45:48
PAMELA-MOZ5	MOZ5-DR01	31/03/2016	07:13:00	31/03/2016	07:52:20
PAMELA-MOZ5	MOZ5-DR03	31/03/2016	18:05:59	31/03/2016	19:12:59
PAMELA-MOZ5	MOZ5-DR05	01/04/2016	11:00:43	01/04/2016	11:44:31
MD-39 Rida	DR84-0026	14/05/1984		14/05/1984	
MD-06 Nosicaa	DR75-0012	1975		1975	

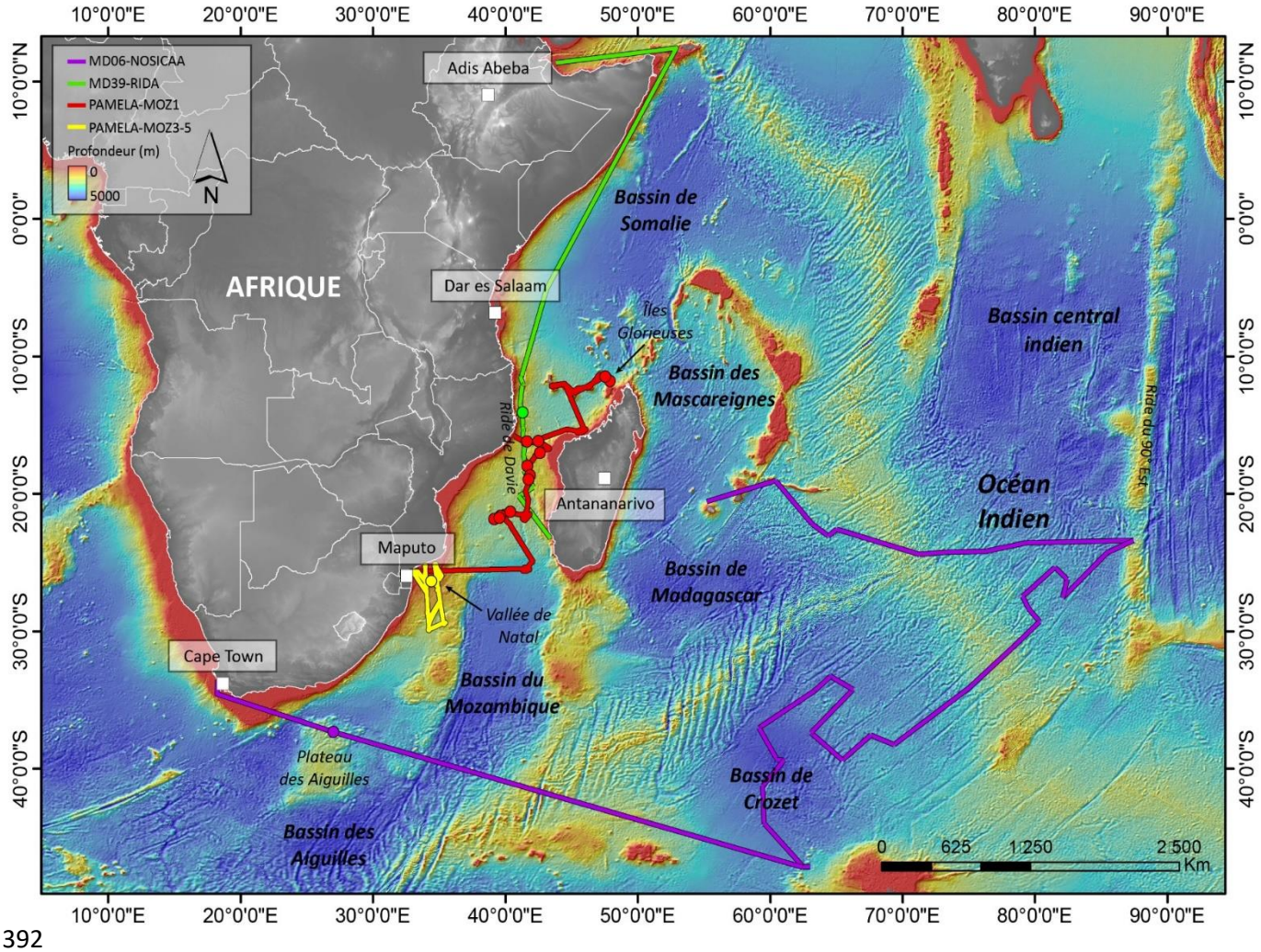

Start Lat.	Start Long.	End Lat.	End long.	Deep1 (mbsl)	Deep2 (mbsl)	Distance (m)
11°47'S	47°54'E	11°48S	47°54E	2400	2650	1166
11°28'S	47°32'E	11°28'S	47°32'E	2000	1780	516
16°12'S	41°38'E	16°12'S	41°40'E	1000	1400	1711
16°10'S	42°30'E	16°12'S	42°31'E	2400	2450	1445
17°01'S	42°36'E	17°01'S	42°37'E	1650	1350	830
17°59'S	41°39'E	17°59'S	41°39'E	1300	1600	729
18°39'S	41°51'E	18°39'S	41°51'E	650	580	722
18°57'S	41°45'E	18°57'S	41°45'E	1200	1250	529
21°36'S	39°36'E	21°37'S	39°39'E	1600	1350	1378
21°50'S	39°10'E	21°50'S	39°11'E	1700	1900	732
21°44'S	39°32'E	21°45'S	39°33'E	1000	1350	529
22°18'S	40°23'E	22°18'S	40°23'E	1400	1550	492
21°01'S	34°58'E	21°01'S	34°59'E	1550	1450	1283
26°35'S	34°41'E	26°36'S	34°40'E	1200	950	1389
25°58'S	35°12'E	25°57'S	35°13'E	170	650	819
14°08'S	41°29'E	14°09'S	41°28'E	810	800	584
37°32'S	27°00'E	37°32'S	27°00'E	2550	2550	-

APPENDIX 2.

List and details of the 33 Fe-Mn crusts of this study

Cruise	Dredge	Sample	IGSN
PAMELA-MOZ1	DR01	MOZ1-DR01-01	BFBG-155073
PAMELA-MOZ1	DR04	MOZ1-DR04-01	BFBG-155082
PAMELA-MOZ1	DR04	MOZ1-DR04-03	BFBG-155084
PAMELA-MOZ1	DR04	MOZ1-DR04-04	BFBG-155085
PAMELA-MOZ1	DR04	MOZ1-DR04-23	BFBG-169883
PAMELA-MOZ1	DR10	MOZ1-DR10-04	BFBG-155152
PAMELA-MOZ1	DR10	MOZ1-DR10-05	BFBG-155153
PAMELA-MOZ1	DR11	MOZ1-DR11-01	BFBG-155160
PAMELA-MOZ1	DR11	MOZ1-DR11-03	BFBG-155162
PAMELA-MOZ1	DR11	MOZ1-DR11-05	BFBG-155164
PAMELA-MOZ1	DR11	MOZ1-DR11-07	BFBG-155166
PAMELA-MOZ1	DR12	MOZ1-DR12-09	BFBG-155179
PAMELA-MOZ1	DR12	MOZ1-DR12-14	BFBG-155184
PAMELA-MOZ1	DR12	MOZ1-DR12-V	BFBG-169884
PAMELA-MOZ1	DR13	MOZ1-DR13-07	BFBG-155191
PAMELA-MOZ1	DR14	MOZ1-DR14-04	BFBG-155201
PAMELA-MOZ1	DR15	MOZ1-DR15-10	BFBG-155211
PAMELA-MOZ1	DR15	MOZ1-DR15-14	BFBG-155215
PAMELA-MOZ1	DR16	MOZ1-DR16-05	BFBG-155220
PAMELA-MOZ1	DR16	MOZ1-DR16-06	BFBG-155221
PAMELA-MOZ1	DR17	MOZ1-DR17-01	BFBG-155224
PAMELA-MOZ1	DR17	MOZ1-DR17-04	BFBG-155227
PAMELA-MOZ1	DR19	MOZ1-DR19-01	BFBG-155233
PAMELA-MOZ1	DR22	MOZ1-DR22-01	BFBG-155243
PAMELA-MOZ1	DR22	MOZ1-DR22-02	BFBG-155244
PAMELA-MOZ1	DR22	MOZ1-DR22-03	BFBG-155245
PAMELA-MOZ1	DR22	MOZ1-DR22-06	BFBG-155248
PAMELA-MOZ5	DR01	MOZ5-DR01-01	BFBG-159907
PAMELA-MOZ5	DR01	MOZ5-DR01-03	BFBG-159909
PAMELA-MOZ5	DR03	MOZ5-DR03-01	BFBG-159912
PAMELA-MOZ5	DR05	MOZ5-DR05-01	BFBG-159913
MD-39 Rida	DR84-0026	DR84-0026	MNHN-GS-DR84-0026
MD-06 Nosicaa	DR75-0012	DR75-0012	MNHN-GS-DR75-0012

Location	Latitude	Longitude	Depth range (mbsl)	Type of sample
Glorieuses Islands	11°47’S	47°54’E	2400-2650	Surface
Glorieuses Islands	11°28’S	47°32’E	1780-2000	Surface
Glorieuses Islands	11°28’S	47°32’E	1780-2000	Surface
Glorieuses Islands	11°28’S	47°32’E	1780-2000	Surface
Glorieuses Islands	11°28’S	47°32’E	1780-2000	Surface + TS
Macua Mount	16°12’S	41°38’E	1000-1400	Surface
Macua Mount	16°12’S	41°38’E	1000-1400	Surface + TS
Jeffrey Ridge	16°10’S	42°30’E	2400-2450	Surface + TS
Jeffrey Ridge	16°10’S	42°30’E	2400-2450	Surface
Jeffrey Ridge	16°10’S	42°30’E	2400-2450	Surface
Jeffrey Ridge	16°10’S	42°30’E	2400-2450	Surface
Juan de Nova	17°1’S	42°36’E	1350-1650	Surface
Juan de Nova	17°1’S	42°36’E	1350-1650	Surface
Juan de Nova	17°1’S	42°36’E	1350-1650	Surface
North Sakalaves Mounts	17°59’S	41°39’E	1300-1600	Surface
Sakalaves Mounts	18°39’S	41°51’E	580-650	Surface
South Sakalaves Mounts	18°57’S	41°45’E	1200-1250	Surface
South Sakalaves Mounts	18°57’S	41°45’E	1200-1250	Surface
Bassas da India	21°36’S	39°38’E	1350-1600	Surface
Bassas da India	21°36’S	39°38’E	1350-1600	Surface
Hall Bank	21°50’S	39°10’E	1700-1900	Surface + TS
Hall Bank	21°50’S	39°10’E	1700-1900	Surface
Jaguar Bank	21°44’S	39°32’E	1000-1350	Surface
Europa	21°18’S	40°23’E	1400-1550	Surface + TS
Europa	21°18’S	40°23’E	1400-1550	Surface
Europa	21°18’S	40°23’E	1400-1550	Surface
Europa	21°18’S	40°23’E	1400-1550	Surface
North Natal Valley	21°01'S	34°58'E	1550-1450	Surface
North Natal Valley	21°01'S	34°58'E	1550-1450	Surface
North Natal Valley	26°35'S	34°41'E	950-1200	Surface + TS
North Natal Valley	25°58'S	35°12'E	170-650	Surface
Paisley Mount	14°08’S	41°29’E	800-810	Surface + TS
Agulhas Plateau	37°32’S	27°00’E	2550-2550	Surface + TS

TS = Time series

APPENDIX 3.

Presentation of the sampled and analysed time series

Appendix 3.

MOZ1-DR04-23

Sample name:	MOZ1-DR04-23		
IGSN:	BFBG-169883		
Cruise:	PAMELA-MOZ-1		
Reference:	Olu, 2014		
Dredge:	DR04		
Location:	Îles Glorieuses	11°28’S	47°32’E
Depth range (mbsl):	1780-2000		
Water mass (T_0):	NIDW		
Thickness (mm):	75		
Sampled layers:	20		

Growth rate (mm/Ma):

Min :	2.28	0.9 Ma
Mean :	4.31	
Max :	5.10	3.0 Ma

Age (Ma):	16.2 Ma
Epoch:	Early Miocene

εNd :

Min :	-9.5	12.4 Ma
Mean :	-8.6	
Max :	-7.9	5.1 Ma

$^{206}Pb/^{204}Pb$:

Min :	18.8452	0 Ma
Mean :	18.9056	
Max :	18.9810	12.4 Ma

$^{207}Pb/^{204}Pb$:

Min :	15.6954	0 Ma
Mean :	15.7104	
Max :	15.7273	12.4 Ma

$^{208}Pb/^{204}Pb$:

Min :	39.1626	0 Ma
Mean :	39.2751	
Max :	39.3835	9.0 Ma

MOZ1-DR10-05

Sample name:	MOZ1-DR10-05		
IGSN:	BFBG-155153		
Cruise:	PAMELA-MOZ-1		
Reference:	Olu, 2014		
Dredge:	DR10		
Location:	Macua Mount	16°12'S	41°38'E
Depth range (mbsl):	1000-1400		
Water mass (T_0):	RSW		
Thickness (mm):	72		
Sampled layers:	20		

Growth rate (mm/Ma):			
	Min :	2.16	1.9 Ma
	Mean :	4.62	
	Max :	5.07	2.5 Ma
Age (Ma):		15.2 Ma	
Epoch:		Middle Miocene	

εNd :			
	Min :	-9.3	11.7 Ma
	Mean :	-8.3	
	Max :	-7.4	4.2 Ma
$^{206}Pb/^{204}Pb$:			
	Min :	18.8039	6.8 Ma
	Mean :	18.9145	
	Max :	19.0733	15.6 Ma
$^{207}Pb/^{204}Pb$:			
	Min :	15.6898	6.8 Ma
	Mean :	15.7065	
	Max :	15.7312	10.3 Ma
$^{208}Pb/^{204}Pb$:			
	Min :	39.0829	0 Ma
	Mean :	39.2042	
	Max :	39.3155	10.3 Ma

MOZ1-DR11-01

Sample name:	MOZ1-DR11-01		
IGSN:	BFBG-155160		
Cruise:	PAMELA-MOZ-1		
Reference:	Olu, 2014		
Dredge:	DR11		
Location:	Jeffrey Ridge	16°10'S	42°30'E
Depth range (mbsl):	2400-2450		
Water mass (T_0):	NIDW		
Thickness (mm):	83		
Sampled layers:	19		

Growth rate (mm/Ma):			
	Min :	2.90	4.3 Ma
	Mean :	4.45	
	Max :	7.78	4.8 Ma
Age (Ma):		19.7 Ma	
Epoch:		Early Miocene	

εNd :			
	Min :	-10.2	2.8 Ma
	Mean :	-9.6	
	Max :	-8.9	0 Ma
$^{206}Pb/^{204}Pb$:			
	Min :	18.6329	0 Ma
	Mean :	18.9503	
	Max :	19.0382	14.0 Ma
$^{207}Pb/^{204}Pb$:			
	Min :	15.5676	10.3 Ma
	Mean :	15.7143	
	Max :	15.7315	14.0 Ma
$^{208}Pb/^{204}Pb$:			
	Min :	38.8334	0 Ma
	Mean :	39.2275	
	Max :	39.3225	14.0 Ma

MOZ1-DR17-01

Sample name:	MOZ1-DR17-01		
IGSN:	BFBG-155224		
Cruise:	PAMELA-MOZ-1		
Reference:	Olu, 2014		
Dredge:	DR17		
Location:	Hall Bank	21°50'S	39°10'E
Depth range (mbsl):	1700-1900		
Water mass (T_0):	NADW		
Thickness (mm):	34		
Sampled layers:	11		

Growth rate (mm/Ma):			
	Min :	2.69	0.7 Ma
	Mean :	4.12	
	Max :	4.84	6.9 Ma
Age (Ma):		8.0 Ma	
Epoch:		Late Miocene	

εNd :			
	Min :	-9.7	1.6 Ma
	Mean :	-8.4	
	Max :	-7.4	8.0 Ma
$^{206}Pb/^{204}Pb$:			
	Min :	18.9233	0 Ma
	Mean :	19.0294	
	Max :	19.1063	6.9 Ma
$^{207}Pb/^{204}Pb$:			
	Min :	15.7146	5.1 Ma
	Mean :	15.7251	
	Max :	15.7404	8.0 Ma
$^{208}Pb/^{204}Pb$:			
	Min :	39.1200	0 Ma
	Mean :	39.2557	
	Max :	39.3246	8.0 Ma

MOZ1-DR22-01

Sample name:	MOZ1-DR22-01		
IGSN:	BFBG-155243		
Cruise:	PAMELA-MOZ-1		
Reference:	Olu, 2014		
Dredge:	DR22		
Location:	Europa	21°18'S	40°23'E
Depth range (mbsl):	1400-1550		
Water mass (T_0):	Transition/AAIW		
Thickness (mm):	47		
Sampled layers:	14		

Growth rate (mm/Ma):

Min :	2.96	1.2 Ma
Mean :	4.10	
Max :	4.43	0.2 Ma

Age (Ma):	11.1 Ma
Epoch:	Middle Miocene

εNd :

Min :	-9.2	11.0 Ma
Mean :	-8.5	
Max :	-7.9	5.7 Ma

$^{206}Pb/^{204}Pb$:

Min :	18.9064	0 Ma
Mean :	18.9936	
Max :	19.1016	9.7 Ma

$^{207}Pb/^{204}Pb$:

Min :	15.7055	0 Ma
Mean :	15.7197	
Max :	15.7372	9.7 Ma

$^{208}Pb/^{204}Pb$:

Min :	39.1119	0 Ma
Mean :	39.2345	
Max :	39.2896	9.7 Ma

DR75-0012

Sample name:	DR75-0012		
IGSN:	MNHN-GS-DR75-0012		
Cruise:	MD-06 Nosicaa		
Reference:	Leclaire, 1975		
Dredge:	DR75-0012		
Location:	Agulhas Plateau	37°32'S	27°00'E
Depth range (mbsl):	2550-2550		
Water mass (T_0):	NADW		
Thickness (mm):	50		
Sampled layers:	13		

Growth rate (mm/Ma):			
	Min :	1.98	4.0 Ma
	Mean :	3.17	
	Max :	3.40	6.7 Ma
Age (Ma):		15.2 Ma	
Epoch:		Middle Miocene	

εNd :			
	Min :	-10.5	4.0 Ma
	Mean :	-10.0	
	Max :	-9.8	15.2 Ma
$^{206}Pb/^{204}Pb$:			
	Min :	18.8435	0 Ma
	Mean :	18.9376	
	Max :	18.9901	6.7 Ma
$^{207}Pb/^{204}Pb$:			
	Min :	15.6757	0 Ma
	Mean :	15.6922	
	Max :	15.7022	11.2 Ma
$^{208}Pb/^{204}Pb$:			
	Min :	38.9188	0 Ma
	Mean :	39.0187	
	Max :	39.0725	11.2 Ma

DR84-0026

Sample name:	DR84-0026		
IGSN:	MNHN-GS-DR84-0026		
Cruise:	MD-39 Rida		
Reference:	Leclaire, 1984		
Dredge:	DR84-0026		
Location:	Paisley Mount	14°08'S	41°29E
Depth range (mbsl):	800-810		
Water mass (T_0):	RSW		
Thickness (mm):	64		
Sampled layers:	16		

Growth rate (mm/Ma):			
	Min :	1.77	3.4 Ma
	Mean :	2.08	
	Max :	2.13	6.2 Ma
Age (Ma):		30.7 Ma	
Epoch:		Oligocene	

εNd :			
	Min :	-9.2	16.6 Ma
	Mean :	-8.3	
	Max :	-6.9	3.4 Ma
$^{206}Pb/^{204}Pb$:			
	Min :	18.7928	8.1 Ma
	Mean :	18.8805	
	Max :	18.9780	16.6 Ma
$^{207}Pb/^{204}Pb$:			
	Min :	15.6747	0 Ma
	Mean :	15.6886	
	Max :	15.7209	16.6 Ma
$^{208}Pb/^{204}Pb$:			
	Min :	39.0303	0 Ma
	Mean :	39.2076	
	Max :	39.3317	16.6 Ma

MOZ5-DR03-01

Sample name:	MOZ5-DR03-01		
IGSN:	BFBG-159912		
Cruise:	PAMELA-MOZ-5		
Reference:	Moulin, Evain, 2016		
Dredge:	DR03		
Location:	North of Natal Valley	26°35'S	34°41E
Depth range (mbsl):	950-1200		
Water mass (T_0):	AAIW		
Thickness (mm):	100		
Sampled layers:	24		

Growth rate (mm/Ma):			
	Min :	1.22	2.5 Ma
	Mean :	5.54	
	Max :	6.1	6.7 Ma
Age (Ma):		19.7 Ma	
Epoch:		Late Miocene	

εNd :			
	Min :	-12.5	6.7 Ma
	Mean :	-11.6	
	Max :	-10.4	0 Ma
$^{206}Pb/^{204}Pb$:			
	Min :		8.1 Ma
	Mean :	19.5246	
	Max :		16.6 Ma
$^{207}Pb/^{204}Pb$:			
	Min :		0 Ma
	Mean :	15.8219	
	Max :		16.6 Ma
$^{208}Pb/^{204}Pb$:			
	Min :		0 Ma
	Mean :	39.6745	
	Max :		16.6 Ma

APPENDIX 4.

Locations of the 8 thin sections sampled on the Fe-Mn crusts
MOZ1-DR04-23 and MOZ5-DR03-01

Appendix 4.

MOZ1-DR04-23

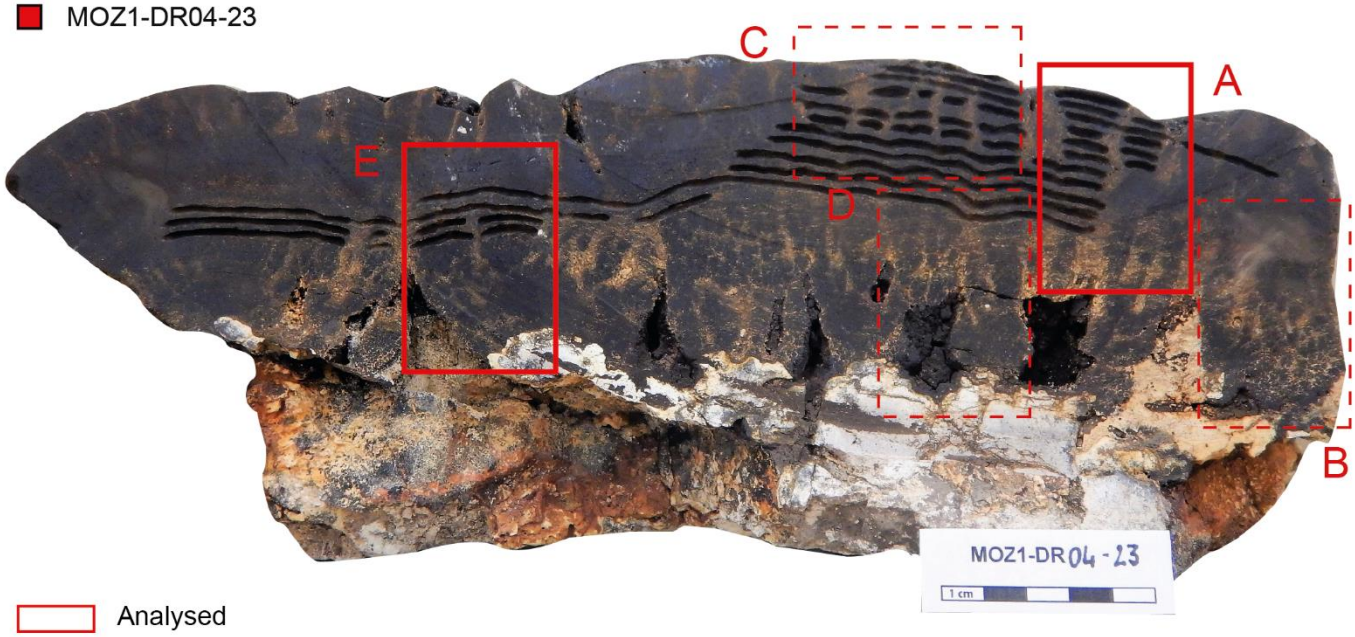

Analysed

Not analysed

MOZ5-DR03-01

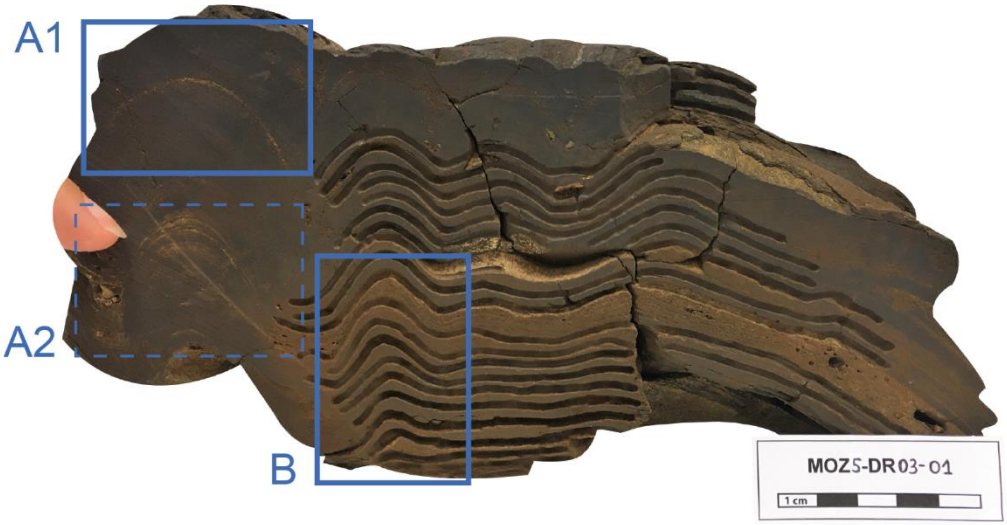

Analysed

Not analysed

APPENDIX 5.

XRD patterns of the sample MOZ1-DR04-23

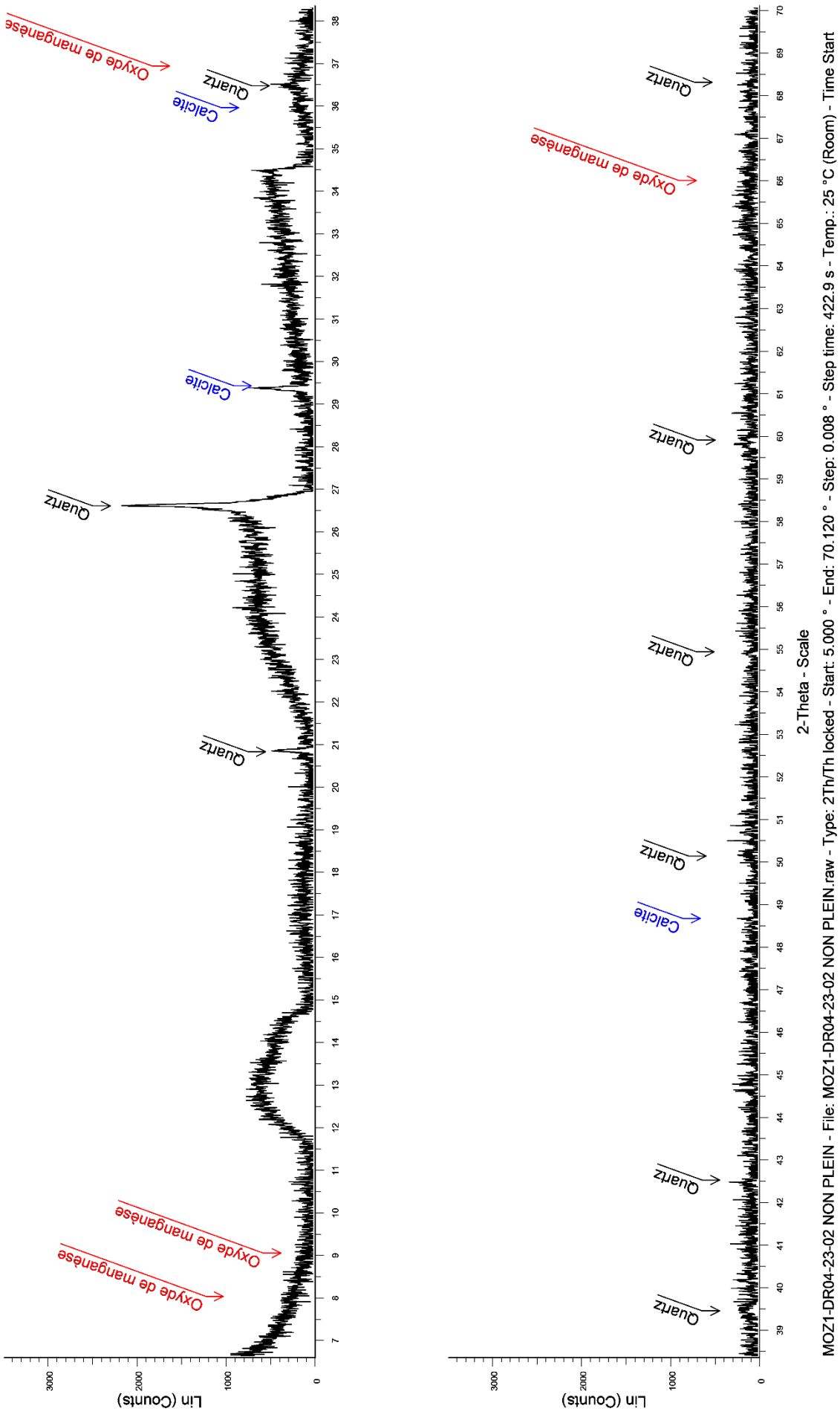
Oxyde de manganèse
Calcite
Quartz
Oxyde de manganèse
Oxyde de manganèse
Quartz
Calcite
Quartz
Quartz
Lin (Counts)
2-Theta - Scale
MOZ1-DR04-23-02 NON PLEIN - File: MOZ1-DR04-23-02 NON PLEIN.raw - Type: 2Th/Th locked - Start: 5.000 ° - End: 70.120 ° - Step: 0.008 ° - Step time: 422.9 s - Temp.: 25 °C (Room) - Time Start

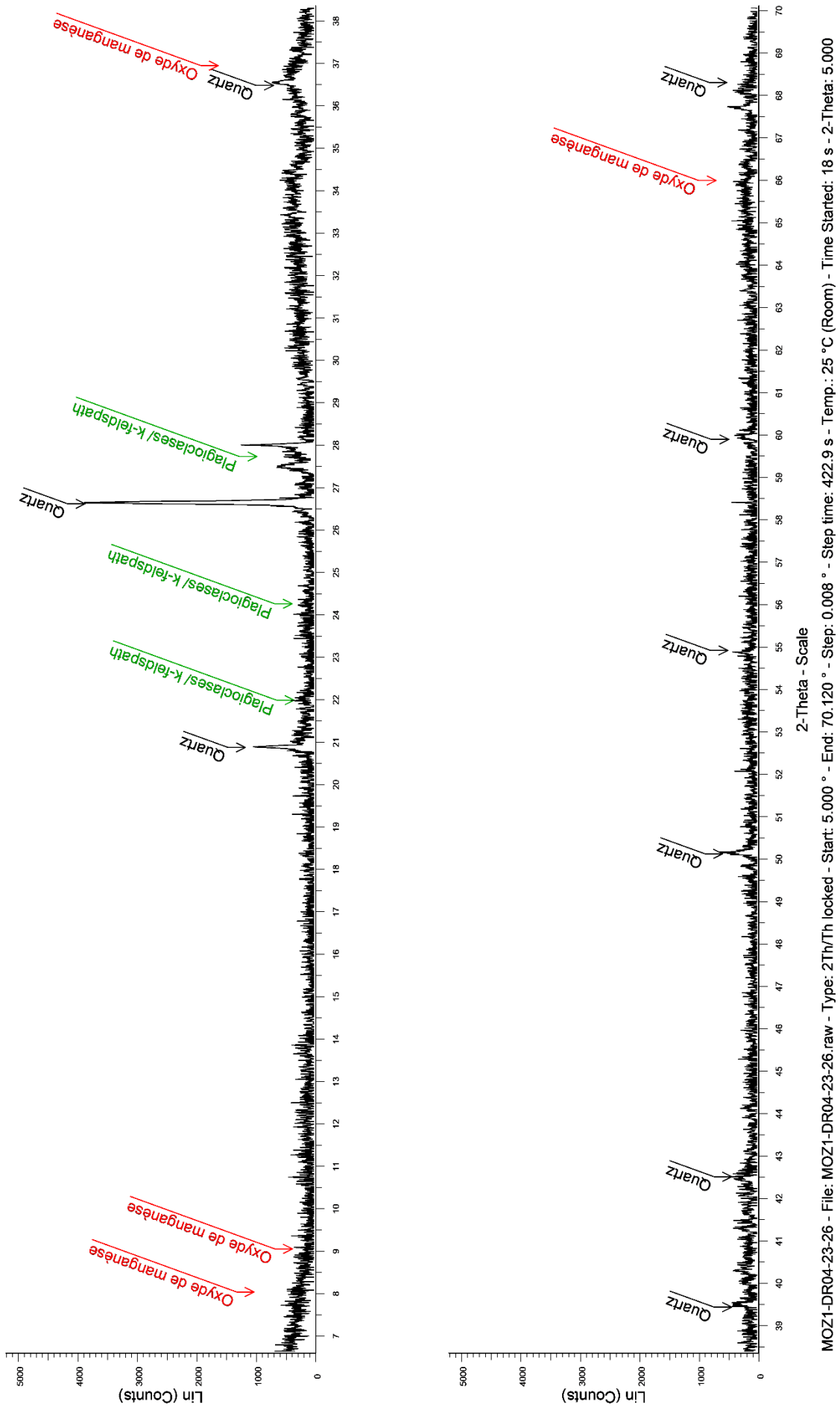
Lin (Counts)
2-Theta - Scale
Quartz
Oxyde de manganèse
Plagioclases/ k-feldspath
MOZ1-DR04-23-26 - File: MOZ1-DR04-23-26.raw - Type: 2Th/Th locked - Start: 5.000 ° - End: 70.120 ° - Step: 0.008 ° - Step time: 422.9 s - Temp.: 25 °C (Room) - Time Started: 18 s - 2-Theta: 5.000

APPENDIX 6.

XRD patterns of the sample MOZ5-DR03-01

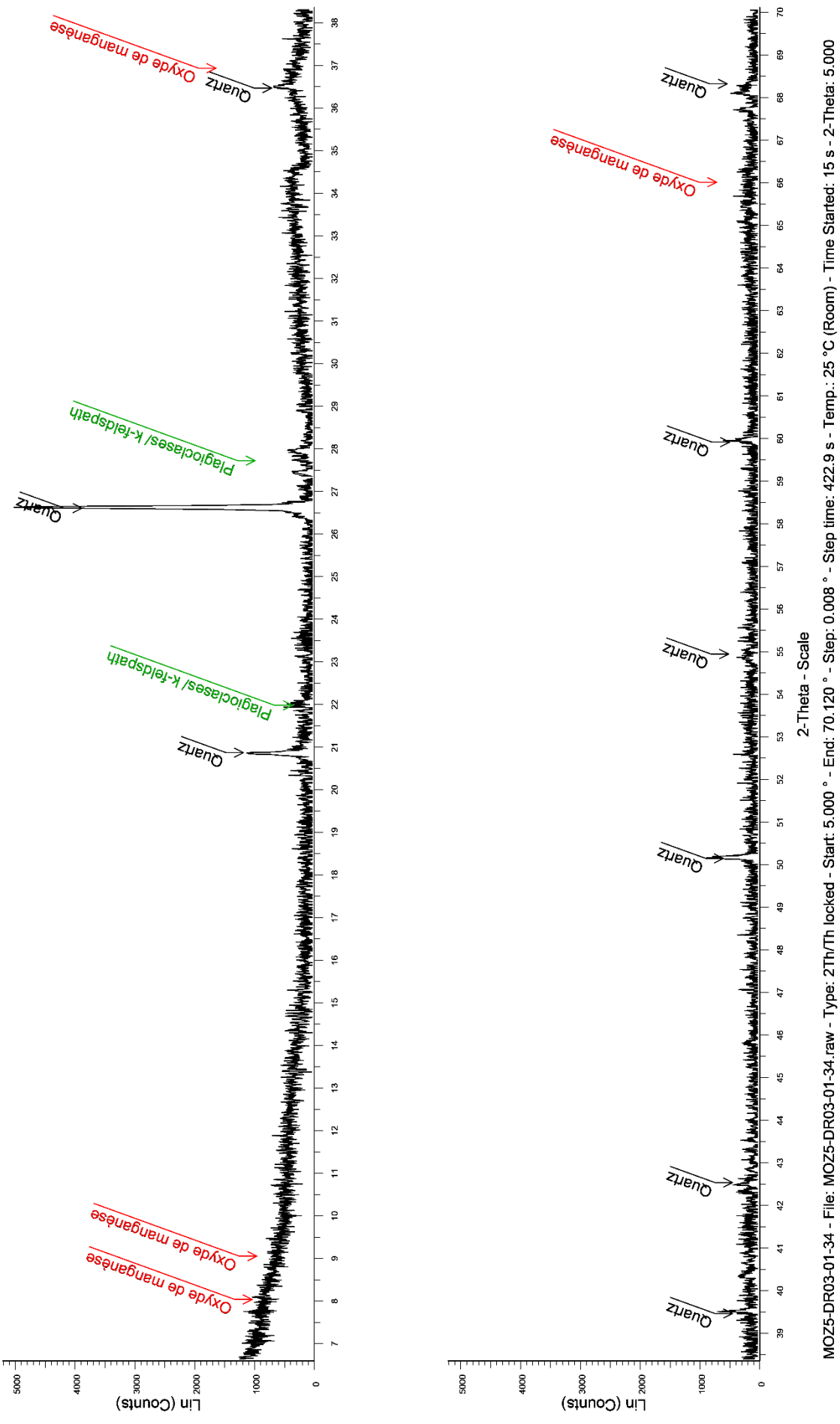
Quartz
Oxyde de manganèse
Plagioclases/ k-feldspath
Lin (Counts)
2-Theta - Scale
MOZ5-DR03-01-34 - File: MOZ5-DR03-01-34.raw - Type: 2Th/Th locked - Start: 5.000 ° - End: 70.120 ° - Step: 0.008 ° - Step time: 422.9 s - Temp.: 25 °C (Room) - Time Started: 15 s - 2-Theta: 5.000

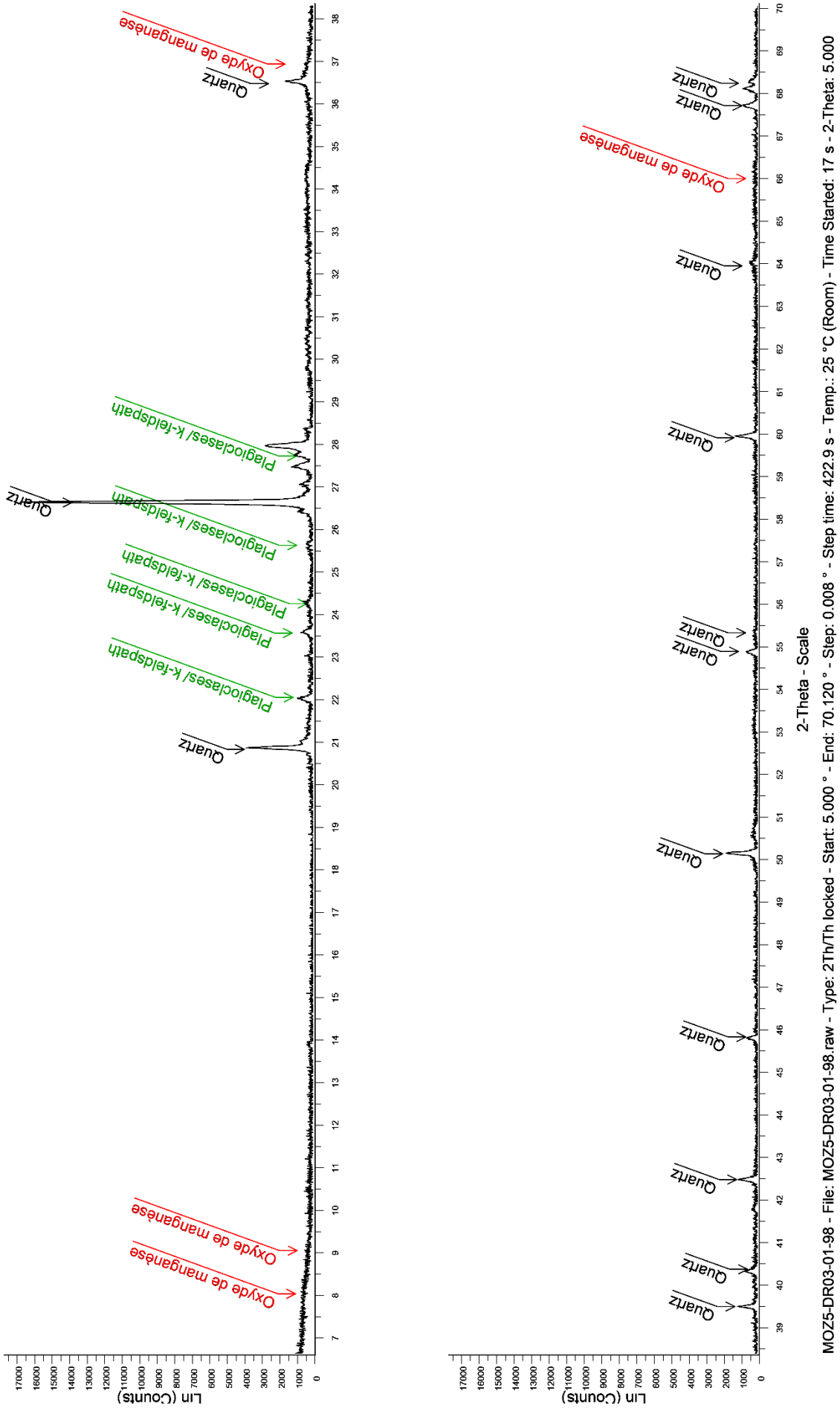
Oxyde de manganèse
Quartz
Plagioclases/ k-feldspath
Lin (Counts)
2-Theta - Scale
MOZ5-DR03-01-98 - File: MOZ5-DR03-01-98.raw - Type: 2Th/Th locked - Start: 5.000 ° - End: 70.120 ° - Step: 0.008 ° - Step time: 422.9 s - Temp.: 25 °C (Room) - Time Started: 17 s - 2-Theta: 5.000

APPENDIX 7.

Mineralogical results of the 4 thin sections from the Fe-Mn crusts
MOZ1-DR04-23 and MOZ5-DR03-01 - FEG-SEM Qemscan ®

Appendix 7.

MOZ1-DR04-23 A

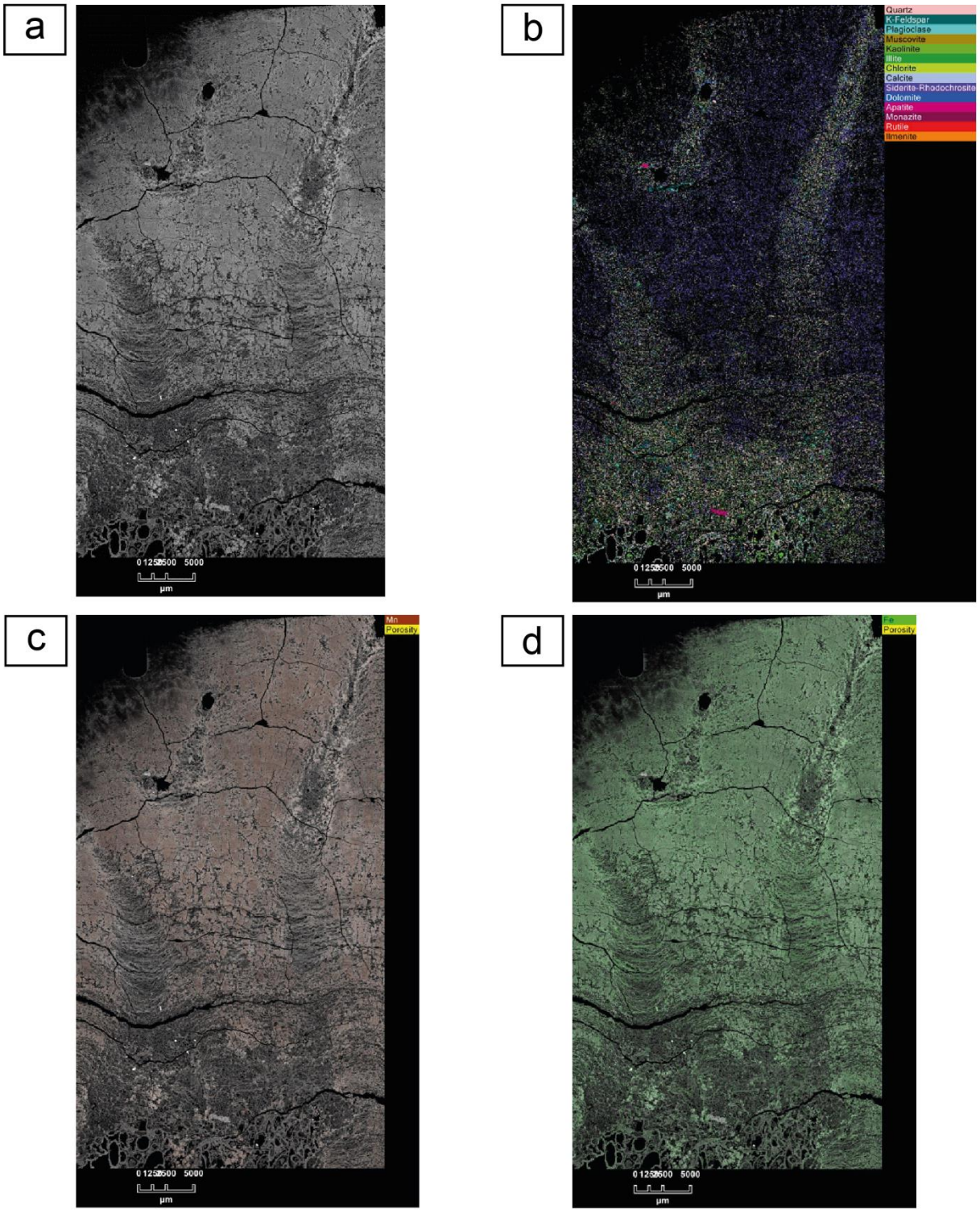

MOZ1-DR04-03 E

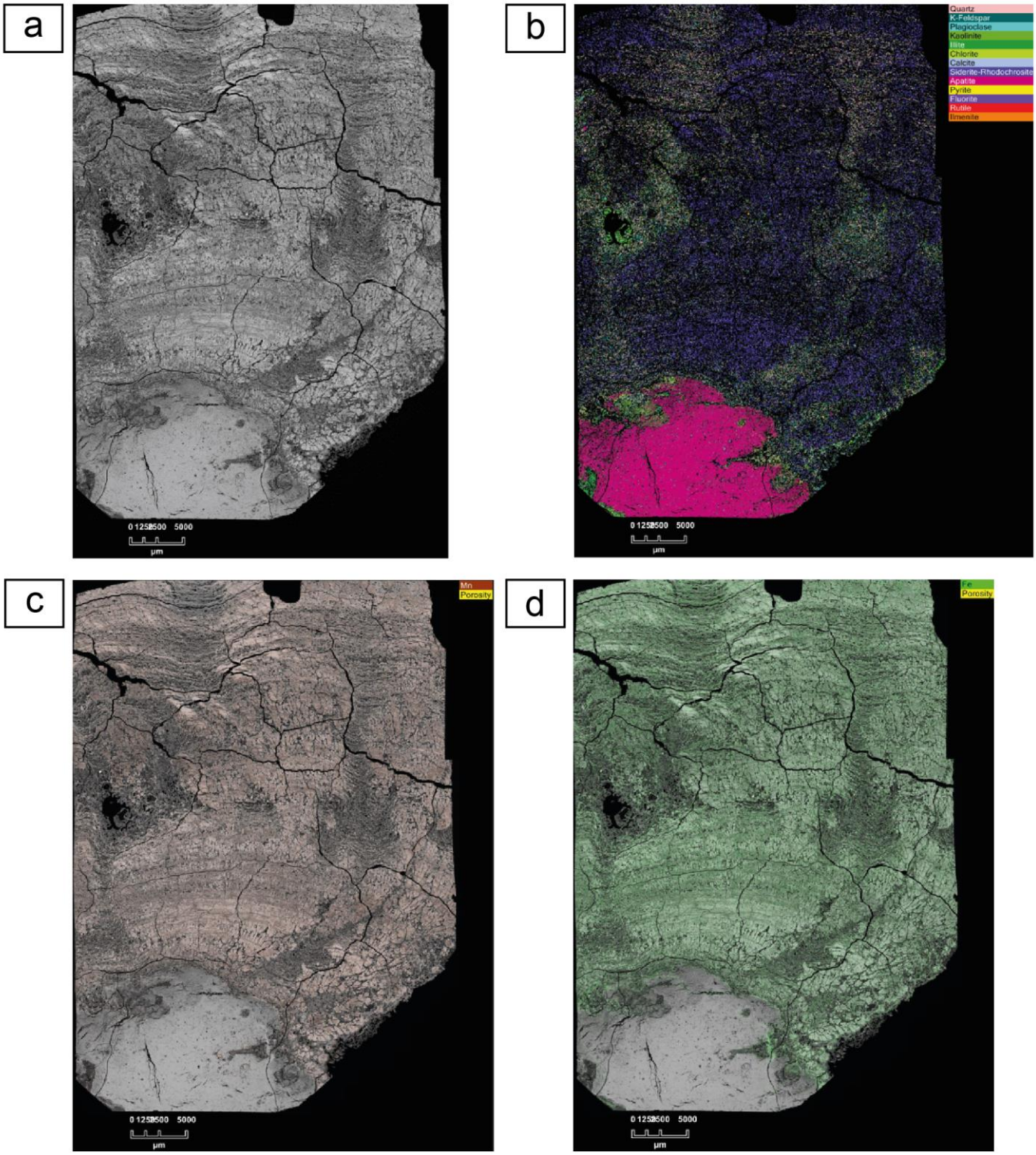

MOZ5-DR03-01 A1

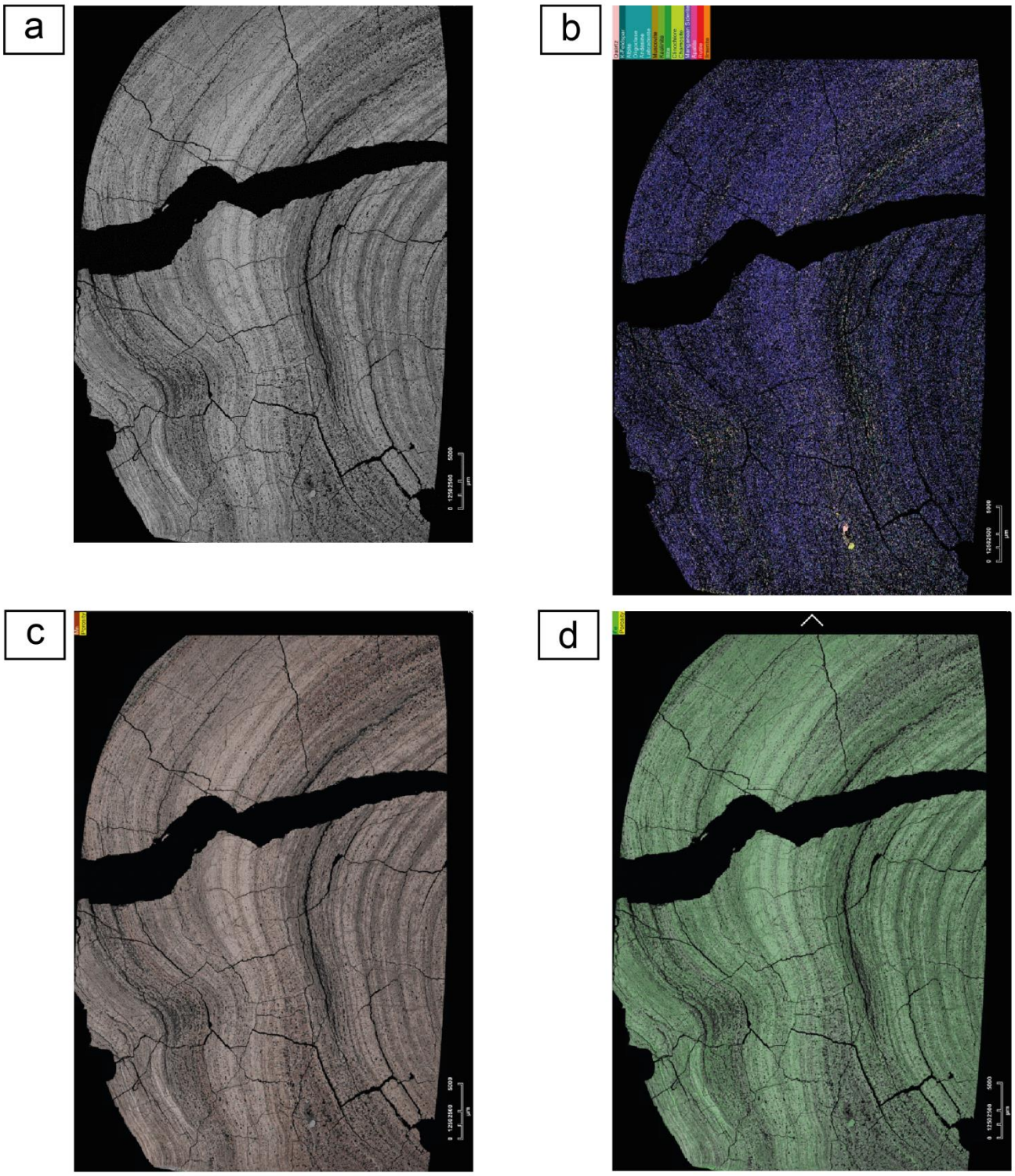

MOZ5-DR03-01 B

a

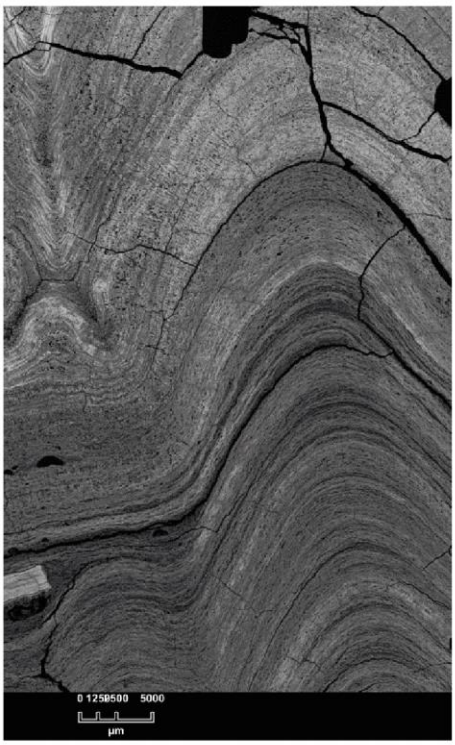

b

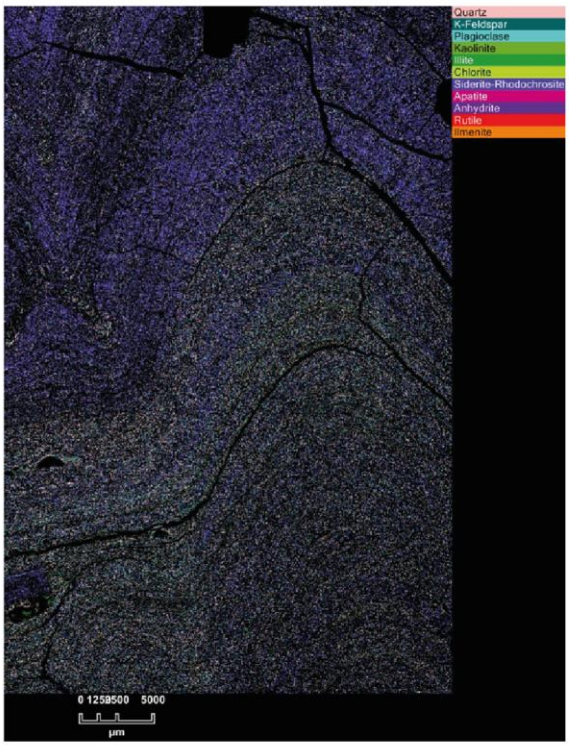

c

d

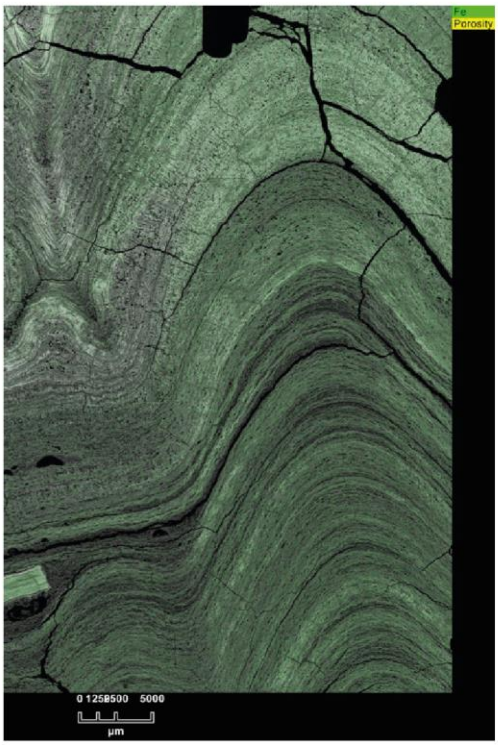

APPENDIX 8.

C. CHARLES *et al.*, 2019. Paleoceanographic and paleogeographic reconstruction of the Mozambique Channel through geochemical study of Fe-Mn crusts. *Seminar PAMELA*. November 2019, Pau, France. Poster

Appendix 8.

PALEOCEANOGRAPHIC AND PALEOGEOGRAPHIC RECONSTRUCTION OF THE MOZAMBIQUE CHANNEL THROUGH THE GEOCHEMICAL STUDY OF FE-MN CRUSTS

PAMELA – PAssive Margins Exploration LAboratories

Charles C. [1,2] [a], Pelleter E. [1], Révillon S. [2,3], Nonnotte P. [2], Agranier A. [2], Guéguen B. [2,4], Bourlès D. [5], Chailan O. [6], ASTER Team [5] and the MOZ1 and MOZ3/5 science parties

[1] Ifremer [2] CNRS, Univ Brest, UMR 6538 [3] SEDISOR [4] CNRS, Univ Brest, UMS 3113
[5] Aix-Marseille Univ., CNRS, IRD, INRA, Coll France, UM34 CEREGE [6]Total Exploration and Production

Setting

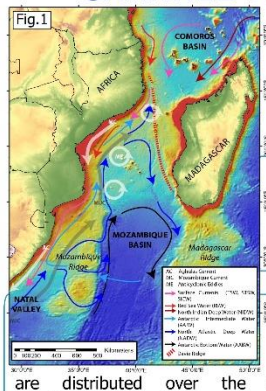

The Mozambique Channel is located in the southwestern Indian Ocean, between the East African continental margin of Mozambique and Madagascar (**Fig.1**). It plays a key role in the intense mixing of water masses between the **Indian and Atlantic Oceans** with several bottom currents flowing between about 2000 and 3500 mbsl. At depth, the circulation of currents (**Fig.1**) is widely discussed due to the **Davie ridge**[a, b] that separates the canal into two distinct basins.

Fe-Mn crusts

Fe-Mn crusts are marine deposits that are distributed over the seafloor. They **precipitate directly from seawater**[c] and their **growth rate** varies according to the geodynamic context (1 to 6 mm/Ma).

These characteristics allow them to record the chemical composition of the water masses over time. In this respect, with thicknesses of up to 20 cm (**Fig.2**), they constitute **archives of the ocean chemistry over time** and are therefore valuable tools for paleocurrent studies and paleogeographic reconstructions[d].

Methodology

50 Fe-Mn crusts were dredged during PAMELA-MOZ1[e], PAMELA-MOZ3/5[f], RIDA cruises on either side of the Davie Ridge (**Fig.3**)
• **32 surface** scrapings samples→ investigation of **subcurrent** Nd isotopes composition of water masses • **8 time series**→ investigation of water masses changes during the **Cenozoic**.

Multi-elements analyses are performed by HR-ICP-MS and Nd isotopes are measured using TIMS at the PSO (Pôle de Spectrométrie Océan) in Plouzané, France. The dating is based on the radioactive decay of the authigenic 10Be/9Be ratio[g] measured at ASTER located at CEREGE, Aix-en-Provence, France.

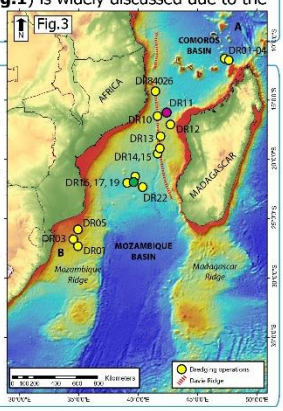

1. Subcurrent trends

High Nd isotopes variability on the same geographic area :
• crusts located above 1500 mbsl : εNd varies from more radiogenic composition in the north (-7 → RSW) to unradiogenic composition in the south (-11 → AAIW). Mix of Indian and Atlantic intermediate currents around Bassas Da India (**Fig.4, Fig.6**).

• crusts located below 1500 mbsl : εNd varies from more radiogenic composition in the north (-7.5 → NIDW) to unradiogenic composition in the south (-10.2 → NADW). From all these results, the contribution of the NADW through the Mozambique channel was estimated (**Fig.5, Fig.7**).

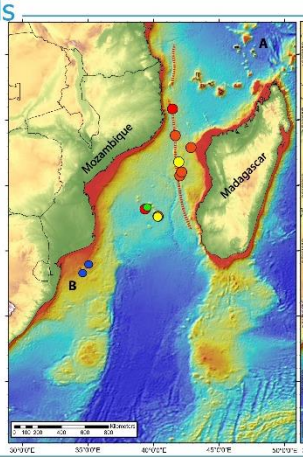

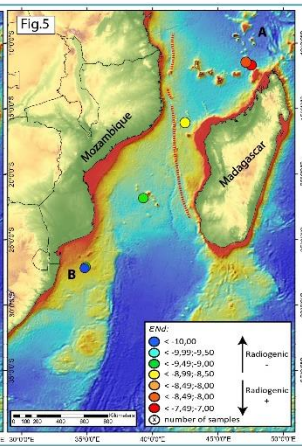

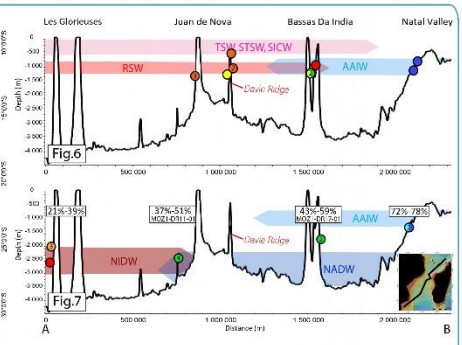

The contribution of the NADW is estimated at up to 51% north of the Davie Ridge (**Fig.7**). This is in agreement with the studies of Collins[b] → the Davie Ridge does not currently act as a topographic barrier to bottom currents.

2. Time series

• MOZ1-DR11-01 : larger NADW (or proto-NADW) influence from 15 Ma to 9 Ma ; εNd = -9.7 at 13 Ma) (**Fig.8**). The contribution of NADW in the Comoros Basin is estimated between 82% and 88% at roughly 13 Ma. The Davie Ridge did not stop the exchange between Atlantic and Indian deep water masses during the last 18 Ma.
• MOZ1-DR17-01 : From 11 Ma to 4 Ma, εNd agrees with a NIDW influence (-8.1 < εNd < -7.0) whereas from 4 Ma to present, εNd point to a NADW influence (εNd=-9.4 ;**Fig.8**) → subsidence event during the Pliocene (**Fig.9**) as proposed by Courgeon[h].

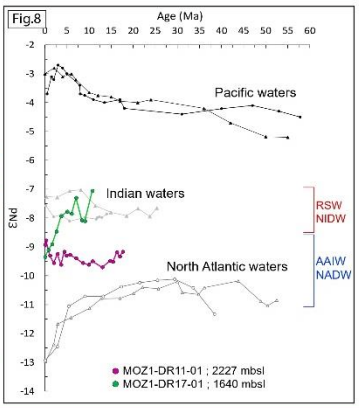

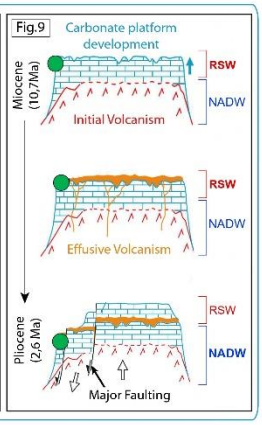

Perspectives

• Geochemistry : to conclude with isotopic (Nd, Pb) and element analyses of all time series samples. Os isotopes measurements → Os isotopes could be used as **chronological tool** for the acquisition of ages greater than 14 Ma.

• Mineralogy : micron scale analyses of (1) surface of the samples → **erosion** linked to the water masses dynamic (2) time series samples → characterization of authigenic minerals, and **allochthonous minerals** (e.g. volcanic clasts).

References

(a) Coffin, M.F., Rabinowitz, P.D., 1987. Reconstruction of Madagascar and Africa: Evidence from the Davie Fracture Zone and Western Somali Basin. J. Geophys. Res. Solid Earth 92, 9385–9406 ; (b) Collins, C., Hermes, J.C., Roman, R.E., Reason, C.J.C., 2016. First dedicated hydrographic survey of the Comoros Basin. J. Geophys. Res. Oceans 121, 1291–1305 ; (c) Koschinsky, A., Halbach, P., 1995. Sequential leaching of marine ferromanganese precipitates: Genetic implications. Geochim. Cosmochim. Acta 59, 5113–5132 ; (d) Frank, M., 2002. Radiogenic isotopes: tracers of past ocean circulation and erosional input. Rev. Geophys. 40, 1-1 ; (e) Ola Karine, 2014. PAMELA-MOZ01 cruise, L'Atalante R/V ; (f) Moulin Maryline, Ewain Mikael, 2016. PAMELA-MOZ05 cruise,Pourquoi pas? R/V ; (g) Bourlès, D., Raisbeck, G.M., Yiou, F., 1989. 10Be and 9Be in marine sediments and their potential for dating. Geochim. Cosmochim. Acta 53, 443–452 ; (h) Courgeon, S., Jorry, S.J., Camoin, G.F., Boudagher-Fadel, M.K., Jouet, G., Révillon, S., Bachèlery, P., Pelleter, E., Borgomano, J., Poli, E., Droxler, A.W., 2016. Growth and demise of Cenozoic isolated carbonate platforms: New insights from the Mozambique Channel seamounts (SW Indian Ocean). Mar. Geol. 380, 90–105.

[a] corresponding author : claire.charles@ifremer.fr

PAMELA SEMINAR - CSTJF PAU - NOVEMBER 21-22, 2019

APPENDIX 9.

C. CHARLES *et al.*, 2019. Paleoceanographic and paleogeographic reconstruction of the Mozambique Channel through geochemical study of Fe-Mn crusts. *Seminar PAMELA*. November 2019, Pau, France. Oral presentation

Appendix 9.

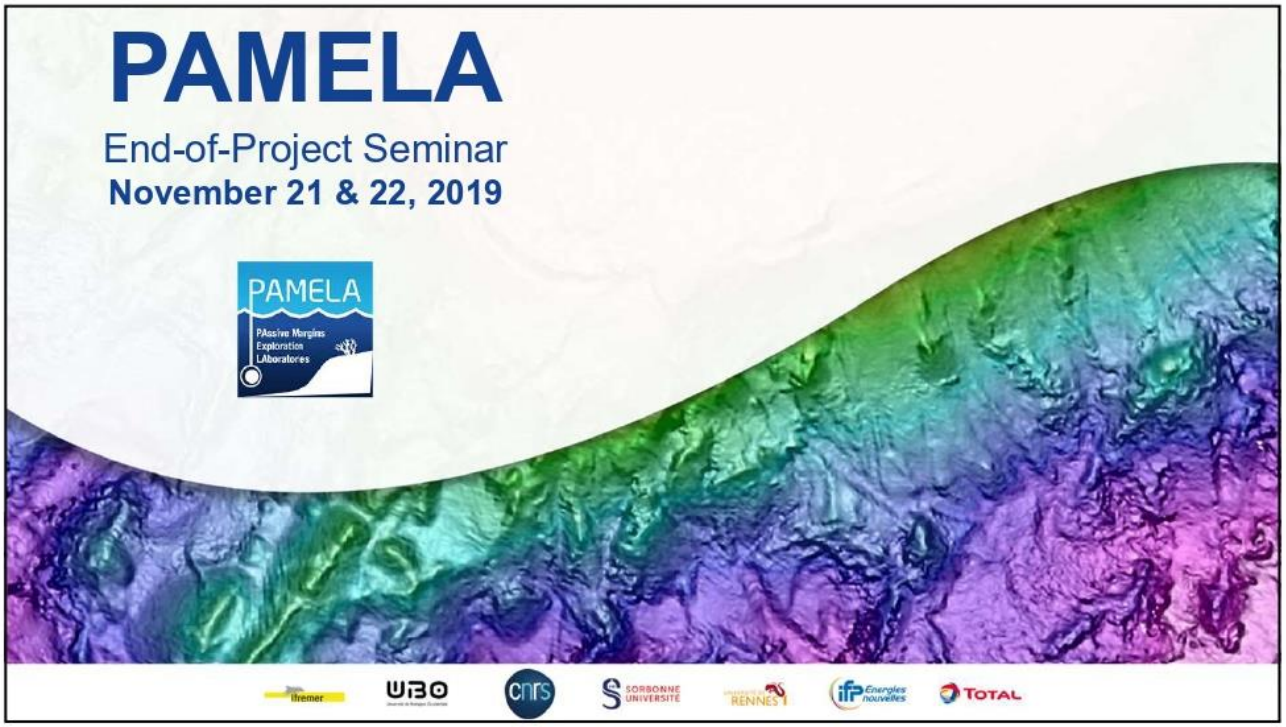
PAMELA
End-of-Project Seminar
November 21 & 22, 2019
PAMELA
PAssive Margins
Exploration
LAboratories

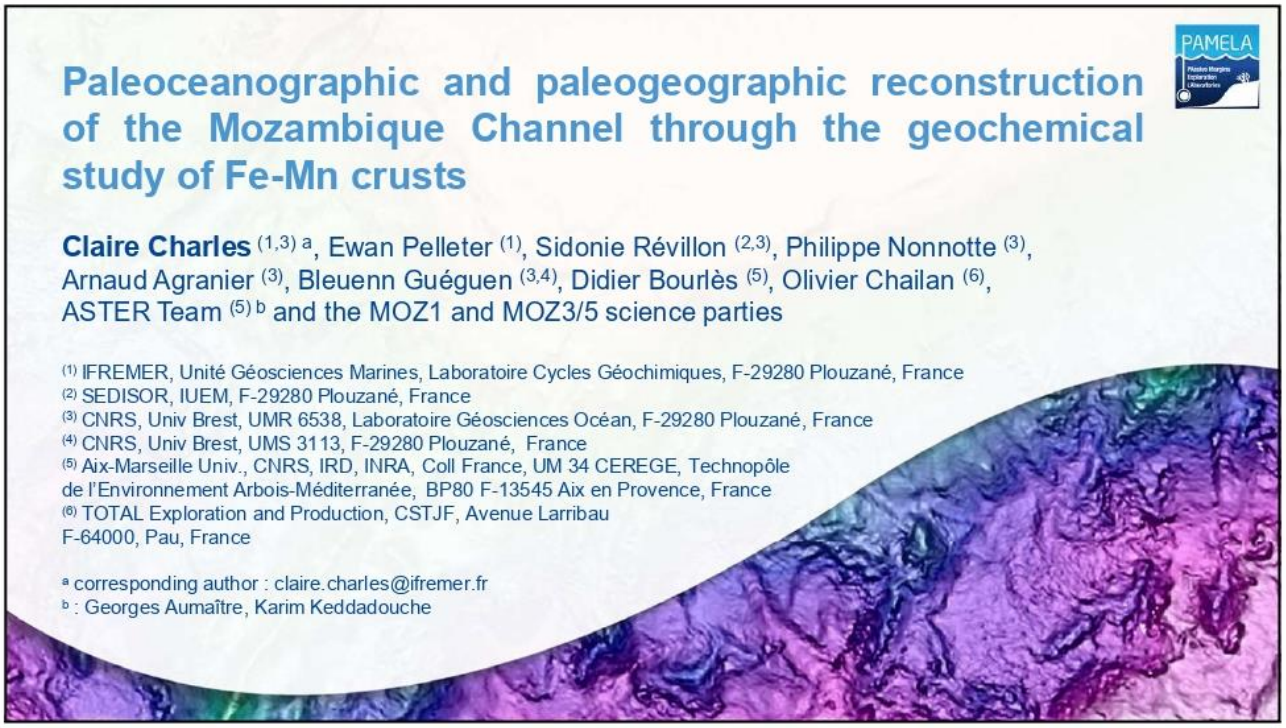
Paleoceanographic and paleogeographic reconstruction of the Mozambique Channel through the geochemical study of Fe-Mn crusts
PAMELA
Claire Charles (1,3) a, Ewan Pelleter (1), Sidonie Révillon (2,3), Philippe Nonnotte (3), Arnaud Agranier (3), Bleuenn Guéguen (3,4), Didier Bourlès (5), Olivier Chailan (6), ASTER Team (5) b and the MOZ1 and MOZ3/5 science parties
(1) IFREMER, Unité Géosciences Marines, Laboratoire Cycles Géochimiques, F-29280 Plouzané, France
(2) SEDISOR, IUEM, F-29280 Plouzané, France
(3) CNRS, Univ Brest, UMR 6538, Laboratoire Géosciences Océan, F-29280 Plouzané, France
(4) CNRS, Univ Brest, UMS 3113, F-29280 Plouzané, France
(5) Aix-Marseille Univ., CNRS, IRD, INRA, Coll France, UM 34 CEREGE, Technopôle de l'Environnement Arbois-Méditerranée, BP80 F-13545 Aix en Provence, France
(6) TOTAL Exploration and Production, CSTJF, Avenue Larribau F-64000, Pau, France
a corresponding author : claire.charles@ifremer.fr
b : Georges Aumaître, Karim Keddadouche

Why focusing on Fe-Mn crusts ?

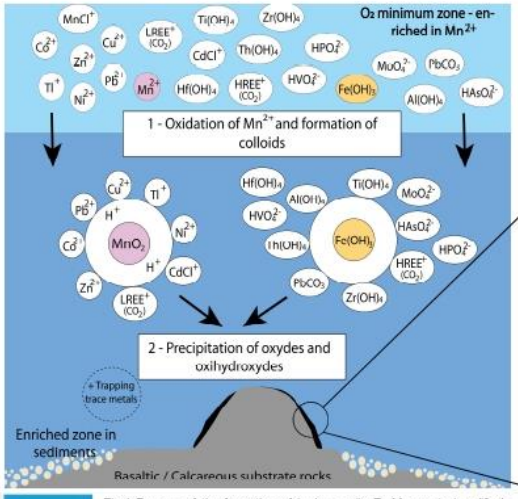

Fig.1 Process of the formation of hydrogenetic Fe-Mn crusts (modified, according to Koschinsky, Halbach, 1995)

Growth rate :
1 to 7mm/Ma

Up to 80 Ma !!

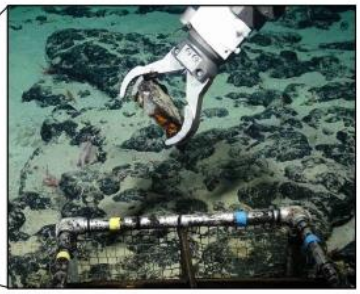

Fig.2 Zoom : ROV sampling Fe-Mn crusts on seamount (according to Bloodworth, BGS)

Fig.3 Fe-Mn crusts from Mozambique Channel (PAMELA-MOZ1; Olu, 2014 and PAMELA-MOZ3/5 ; Moulin and Evain, 2016)

Previous geochemical studies and objectives

1. Surface study

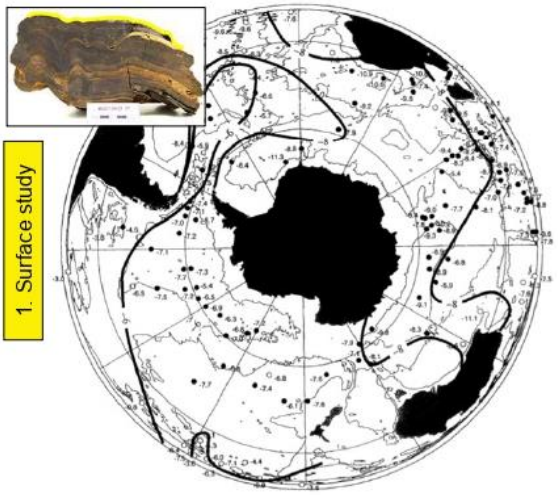

Fig.4 Nd isotopic values representation (Albarède *et al.*, 1997; Mercator projection)

2. Time serie study

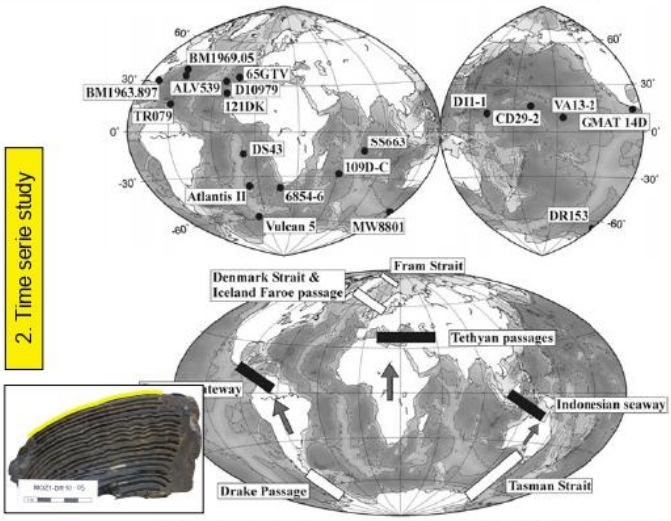

Fig.5 Location of major paleogeographic events (arrows : tectonic directions – in black the closures and in white the openings – modified, according to Frank *et al.*, 2002)

Oceanographic cruises and samples

Oceanographic cruises : **MD39 RIDA** (1984, MNHN),
PAMELA MOZ1 (2014), **PAMELA MOZ3/5** (2016)

- 16 dredging operations
- **31 ferromanganese crusts ; 8 time series**
- Location from the Glorieuses Islands to the Natal Valley
- Depth between 500 mbsl and 2500 mbsl

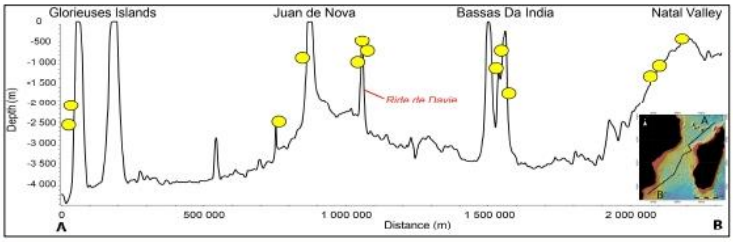

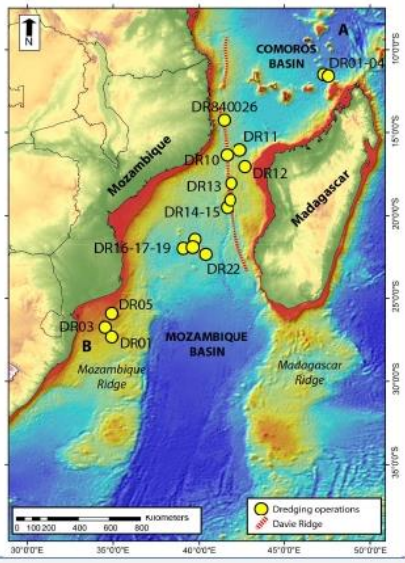

PAMELA End-of-Project Seminar – November 21 & 22, 2019 – CSTJF Pau 5

Elements and isotopic analyses

Element	Radiogenic isotopes	Parents isotopes	Half-life	Primordial isotope	Residence time, years	Input sources
Nd	^{143}Nd	^{147}Sm	106 Gyr	^{144}Nd	600-2000	Erosion of continental crust

$$\varepsilon Nd = \left[\frac{\left(\frac{^{143}Nd}{^{144}Nd}Ech.\right) - \left(\frac{^{143}Nd}{^{144}Nd}CHUR\right)}{\left(\frac{^{143}Nd}{^{144}Nd}CHUR\right)}\right]$$

* 10 000 avec $\left(\frac{^{143}Nd}{^{144}Nd}CHUR\right) = 0{,}512638$

-14 εNd -3

\- Radiogenic +

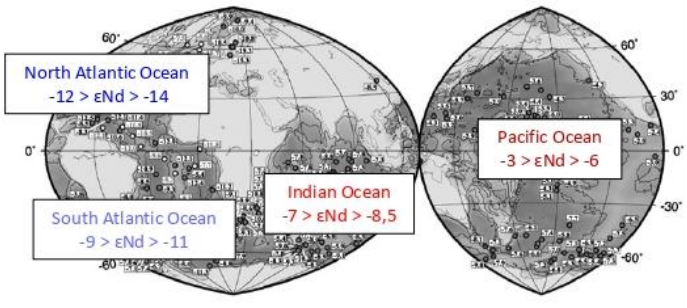

Fig.6 Distribution of Nd isotopes values in the different world oceans (Jeandel, 1993 ; Jeandel *et al.*, 1995 ; Albarède *et al.*, 1998 ; Tachikawa *et al.*, 1999, 1999 ; Frank, 2002)

PAMELA End-of-Project Seminar – November 21 & 22, 2019 – CSTJF Pau 6

Elements and isotopic analyses

Element	Radiogenic isotopes	Parents isotopes	Half-life	Primordial isotope	Residence time, years	Input sources
Nd	^{143}Nd	^{147}Sm	106 Gyr	^{144}Nd	600-2000	Erosion of continental crust (ECC)
Be	^{10}Be	Cosmogenic	1,5 Myr	^{9}Be	200-1000	^{10}Be : Atmo. fallout ^{9}Be : ECC

Dating up to 13Ma

$$\varepsilon Nd = \left[\frac{\left(\frac{143Nd}{144Nd}Ech.\right) - \left(\frac{143Nd}{144Nd}CHUR\right)}{\left(\frac{143Nd}{144Nd}CHUR\right)}\right]$$

* 10 000 avec $\left(\frac{143Nd}{144Nd}CHUR\right) = 0{,}512638$

-14 εNd -3

\- Radiogenic +

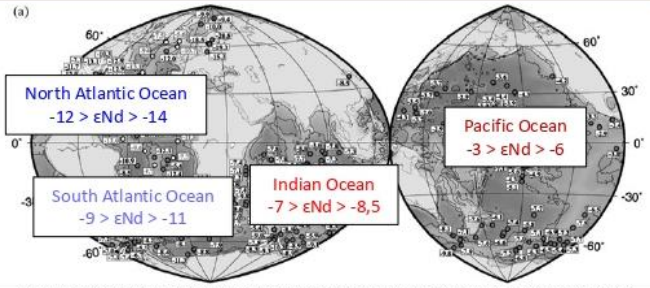

Fig.6 Distribution of Nd isotopes values in the different world oceans (Jeandel, 1993 ; Jeandel *et al.*, 1995 ; Albarède *et al.*, 1998 ; Tachikawa *et al.*, 1999, 1999 ; Frank, 2002)

Oceanographic and geodynamic recontructions

1. Surface study

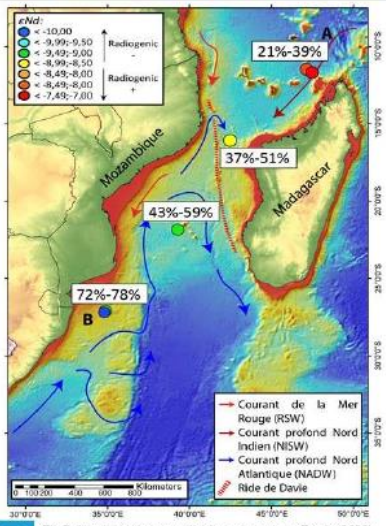

Fig.7 Atlantic waters contributions, based on Frank (2002) study, through the MC and the resulting circulation of NADW.

2. Time serie study

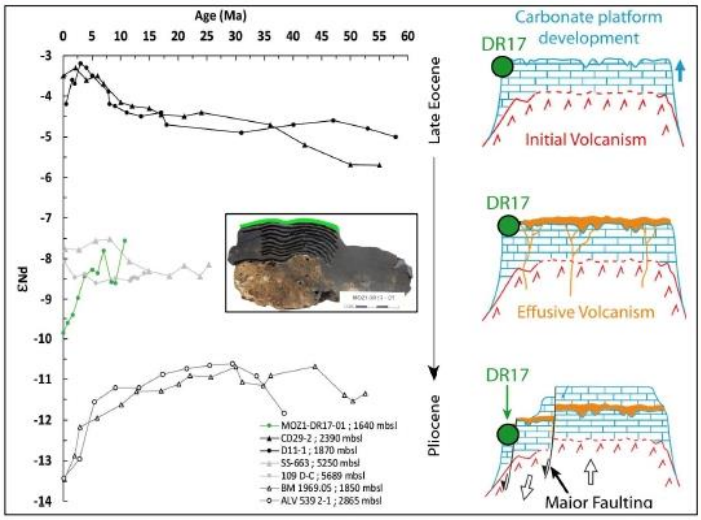

Fig.8 εNd results of the MOZ1-DR17-01 crust with the ^{10}Be dating and the hypothesis that the MOZ1-DR17-01 crust would be a witness of a subsidence phenomenon around Bassas Da India during the Pliocene as proposed by Courgeon et al., (2016).

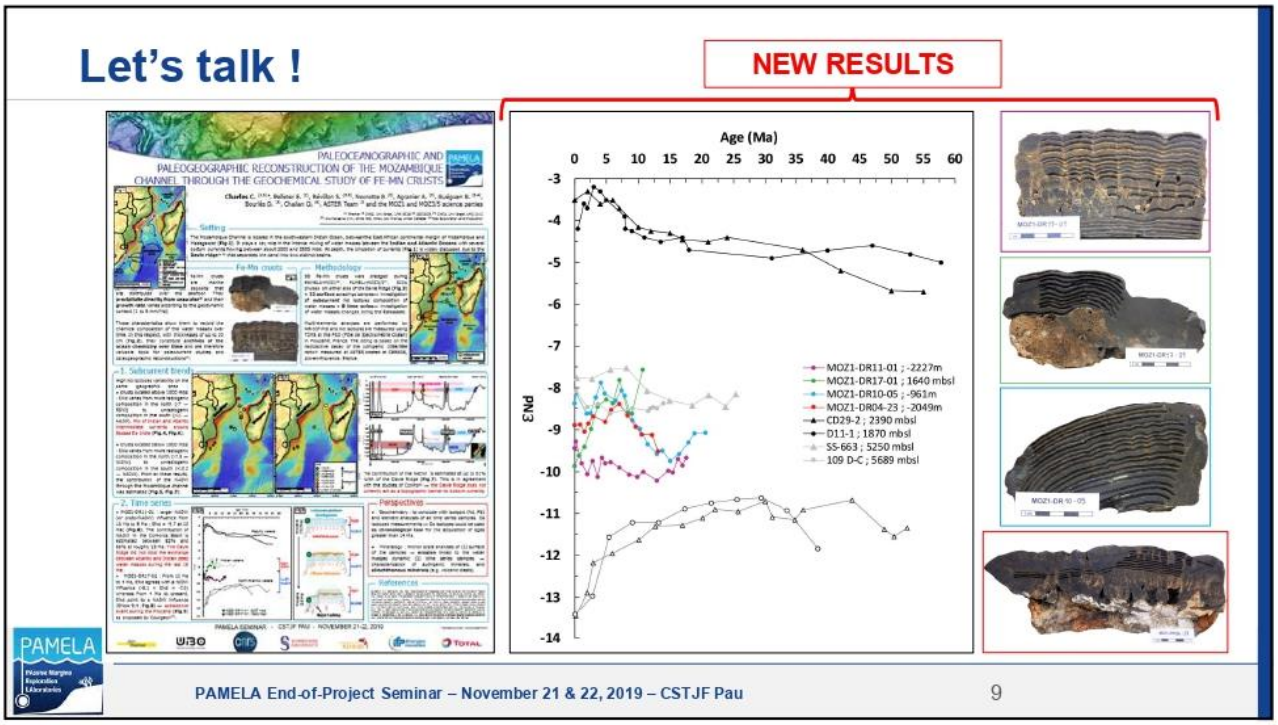
Let's talk !
NEW RESULTS
PALEOCEANOGRAPHIC AND PALEOGEOGRAPHIC RECONSTRUCTION OF THE MOZAMBIQUE CHANNEL THROUGH THE GEOCHEMICAL STUDY OF FE-MN CRUSTS
Age (Ma)
0 5 10 15 20 25 30 35 40 45 50 55 60
-3 -4 -5 -6 -7 -8 -9 -10 -11 -12 -13 -14
εNd
MOZ1-DR11-01 ; -2227m
MOZ1-DR17-01 ; 1640 mbsl
MOZ1-DR10-05 ; -961m
MOZ1-DR04-23 ; -2049m
CD29-2 ; 2390 mbsl
D11-1 ; 1870 mbsl
SS-663 ; 5250 mbsl
109 D-C ; 5689 mbsl
PAMELA
PAMELA End-of-Project Seminar – November 21 & 22, 2019 – CSTJF Pau
9

APPENDIX 10.

C. CHARLES *et al.*, 2019. Paleoceanographic and paleogeodynamic reconstruction of the Mozambique Channel – Contribution of Nd isotopes in ferromanganese crusts. *European Geosciences Union.* April 2019, Vienna, Austria. Oral presentation

Appendix 10.

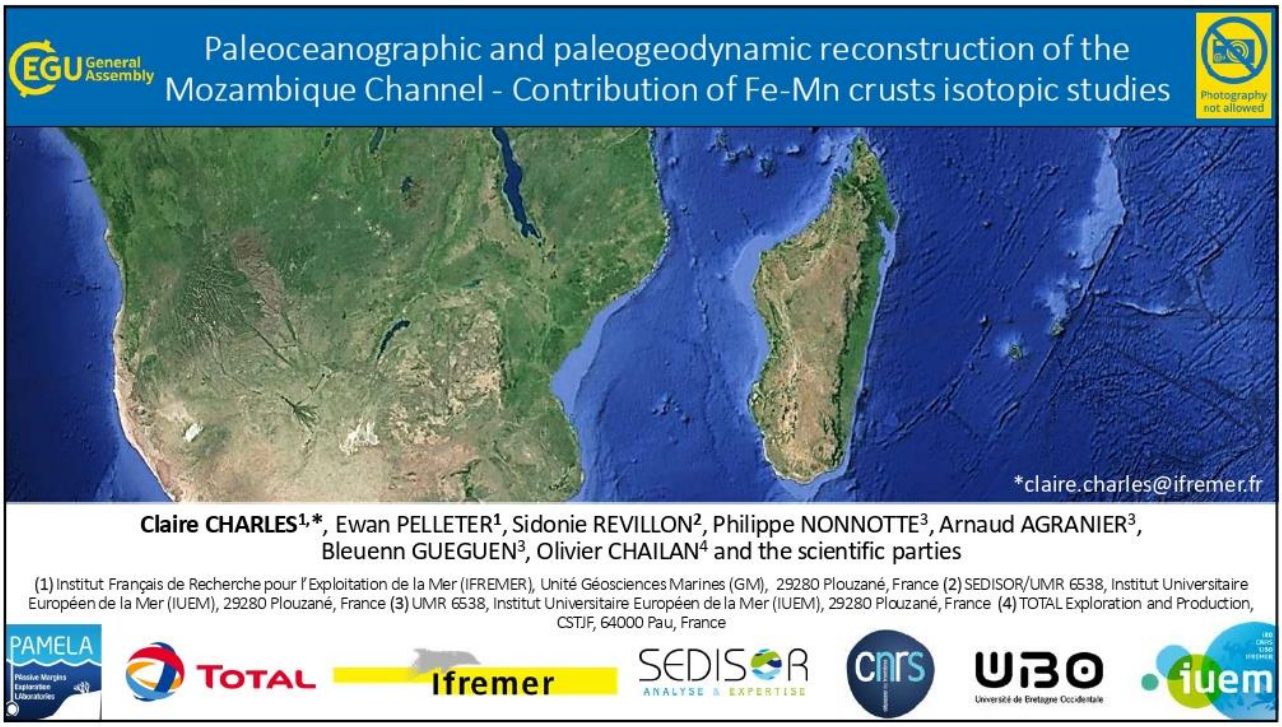
Paleoceanographic and paleogeodynamic reconstruction of the Mozambique Channel - Contribution of Fe-Mn crusts isotopic studies
Photography not allowed
*claire.charles@ifremer.fr
Claire CHARLES[1,*], Ewan PELLETER[1], Sidonie REVILLON[2], Philippe NONNOTTE[3], Arnaud AGRANIER[3], Bleuenn GUEGUEN[3], Olivier CHAILAN[4] and the scientific parties
(1) Institut Français de Recherche pour l'Exploitation de la Mer (IFREMER), Unité Géosciences Marines (GM), 29280 Plouzané, France (2) SEDISOR/UMR 6538, Institut Universitaire Européen de la Mer (IUEM), 29280 Plouzané, France (3) UMR 6538, Institut Universitaire Européen de la Mer (IUEM), 29280 Plouzané, France (4) TOTAL Exploration and Production, CSTJF, 64000 Pau, France

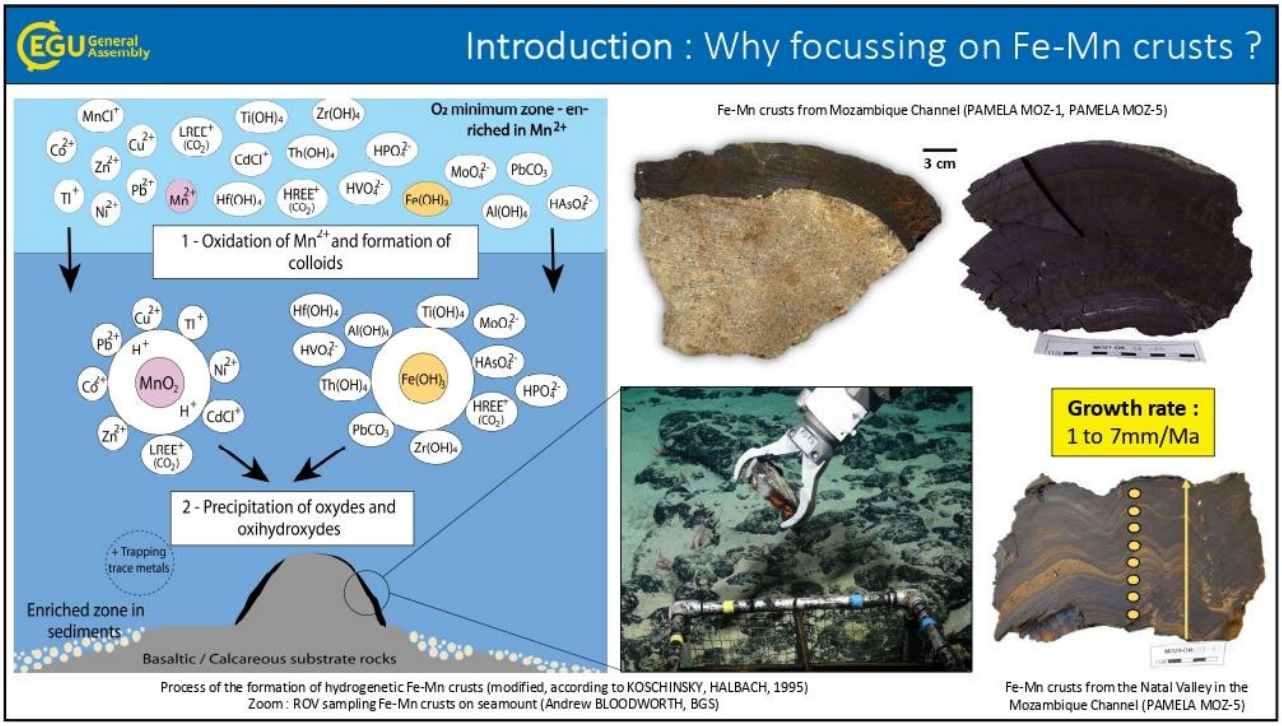
Introduction : Why focussing on Fe-Mn crusts ?
O2 minimum zone - enriched in Mn2+
1 - Oxidation of Mn2+ and formation of colloids
2 - Precipitation of oxydes and oxihydroxydes
+ Trapping trace metals
Enriched zone in sediments
Basaltic / Calcareous substrate rocks
Process of the formation of hydrogenetic Fe-Mn crusts (modified, according to KOSCHINSKY, HALBACH, 1995)
Zoom : ROV sampling Fe-Mn crusts on seamount (Andrew BLOODWORTH, BGS)
Fe-Mn crusts from Mozambique Channel (PAMELA MOZ-1, PAMELA MOZ-5)
3 cm
Growth rate : 1 to 7mm/Ma
Fe-Mn crusts from the Natal Valley in the Mozambique Channel (PAMELA MOZ-5)

Introduction : Previous geochemical studies and objectives

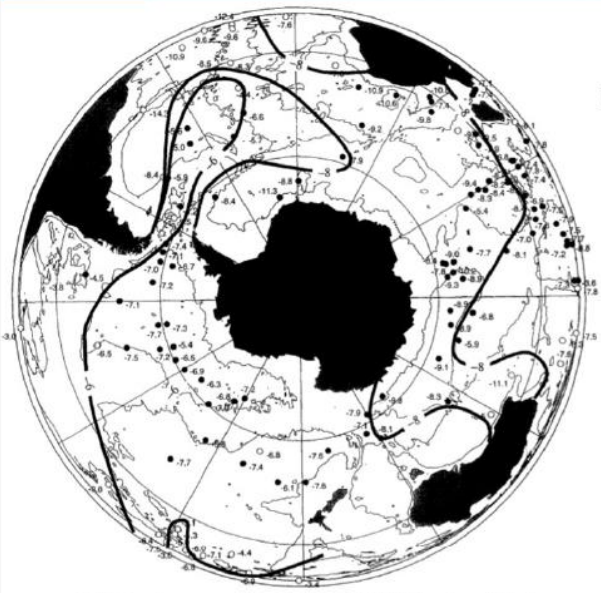

Nd isotopic values representation (Albarède *et al.*, 1997; Mercator projection)

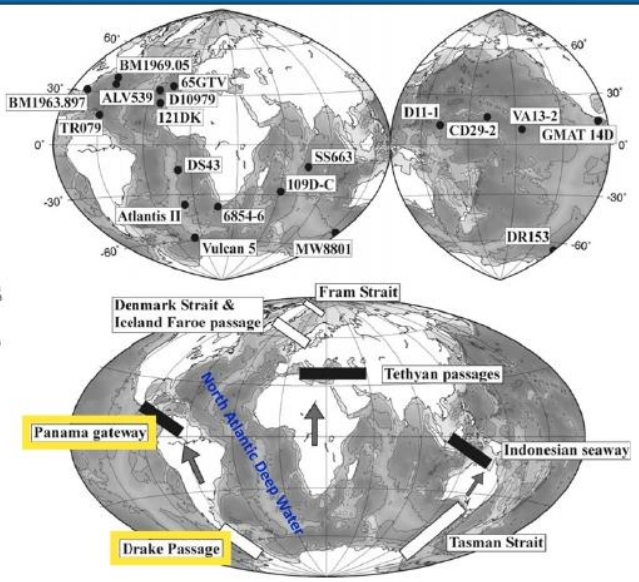

Location of major paleogeographic events (arrows : tectonic directions in black the closures and in white the openings – modified, according to Frank *et al.*, 2002)

3

Regional context : Mozambique Channel oceanography

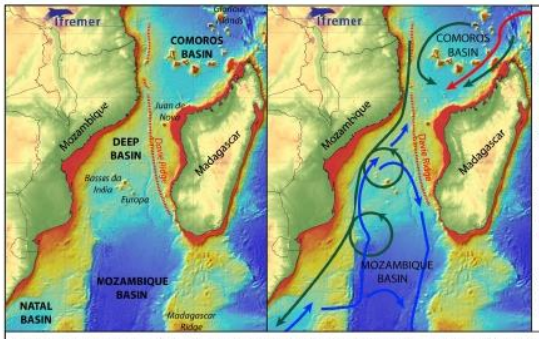

Davie Ridge : – – –

Surface waters (STSW-TSW) : →

Pacifique Ocean *(not represented here)*
- ƐNd : -3 à -6

North Indian Deep Water (NIDW) : →
- ƐNd : -7 à -8,5

North Atlantic Deep Water (NADW) : →
- ƐNd : -10 à -14

Mozambique Channel bathymetry showing the main circulation patterns (according to van Aken et al., 2004; Ullgren et al., 2012) and Nd isotopic domains (Piepgras et al., 1979 ; Goldstein and O'Nions, 1981 ; Albarède and Goldstein, 1982)

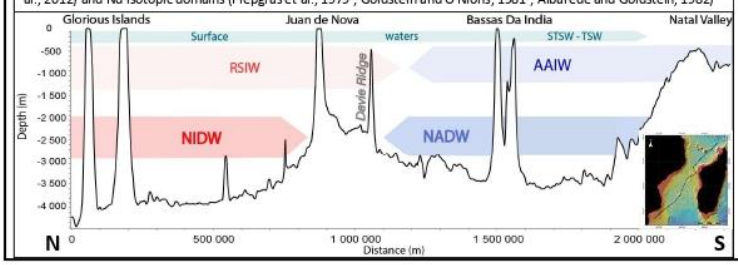

Mix of Indian and Atlantic currents

Surface waters or superficiel currents :
- Subtropical Surface Water (STSW)
- Courant du Mozambique (TSW)

Intermediate currents :
- Antarctic Intermediate Water (AAIW)
- Red Sea Intermediate Water (RSIW)

Deep currents :
- North Atlantic Deep Water (NADW)
- North Indian Deep Water (NIDW)

↓

Role of the Davie Ridge?

4

Methodology : sampling and isotopic geochemistry

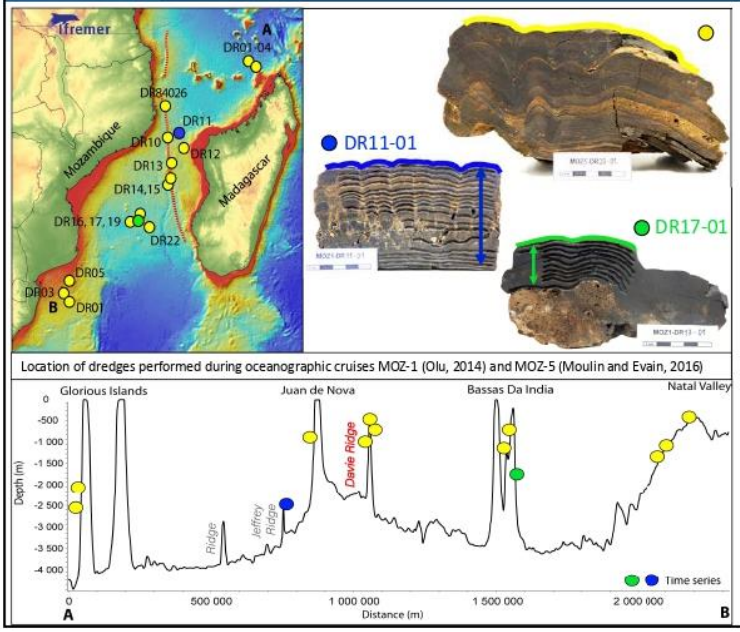

Surface scrapings on 31 crusts + 2 additional samples : **surface and time series** scrapings

REEs separation through **chromatography columns** → Separation of light and heavy rare-earth éléments → **Nd recovery**

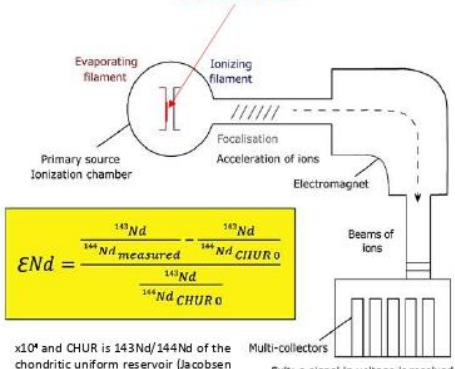

$$\varepsilon Nd = \frac{\frac{^{143}Nd}{^{144}Nd_{measured}} - \frac{^{143}Nd}{^{144}Nd_{CHUR\,0}}}{\frac{^{143}Nd}{^{144}Nd_{CHUR\,0}}}$$

x10⁴ and CHUR is 143Nd/144Nd of the chondritic uniform reservoir (Jacobsen and Wasserburg, 1980)

5

Results / Discussion : surface scrapings isotopic studies

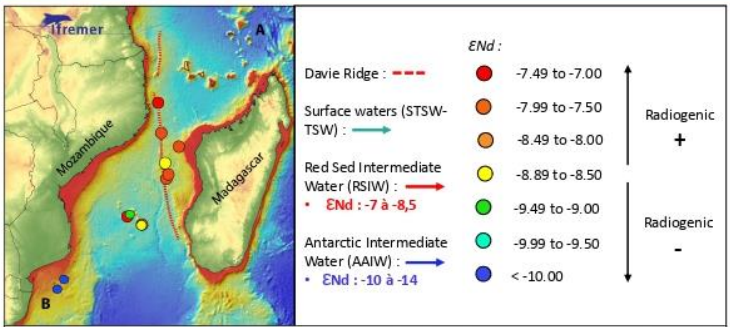

Isotopic values for samples above 1500 meters (map) and Nd isotopic domains (O'Nions et al., 1978 ; Piepgras et al., 1979 ; Goldstein and O'Nions, 1981 ; Albarède and Goldstein, 1982)

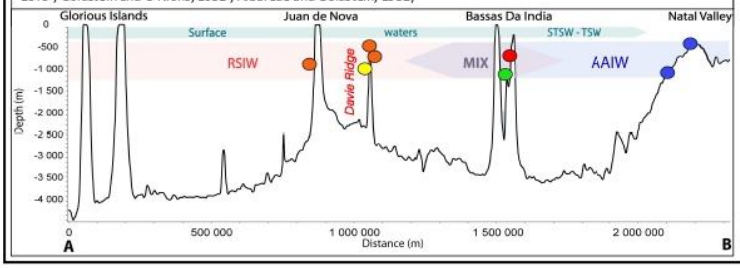

High εNd variability on the same geographic area → separation of the results in two groups : < 1500 m and > 1500 m

εNd results : heterogeneous → **very radiogenic** samples (-7, north) to **unradiogenic** samples (-11, south)

- High radiogenic values from the Paisley Mount to Bassas Da India → **RSIW**
- Unradiogenic samples in the south → the **AAIW** flow from the Valley Natal to Bassas Da India

Mix of Indian and Atlantic intermediate currents around Bassas Da India

6

Results / Discussion : surface scrapings isotopic studies

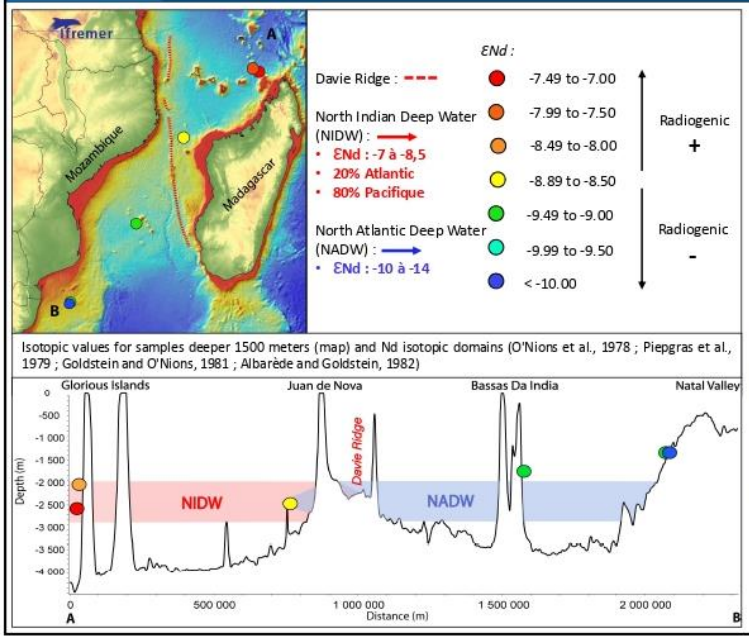

Isotopic values for samples deeper 1500 meters (map) and Nd isotopic domains (O'Nions et al., 1978 ; Piepgras et al., 1979 ; Goldstein and O'Nions, 1981 ; Albarède and Goldstein, 1982)

High εNd variability on the same geographic area → separation of the results in two groups : < 1500 m and > 1500 m

εNd trend from **radiogenic** samples in the north (-7.5 → NIDW) to **unradiogenic** samples in the south (-10.2 → NADW)

Calculation of the current inputs → new model

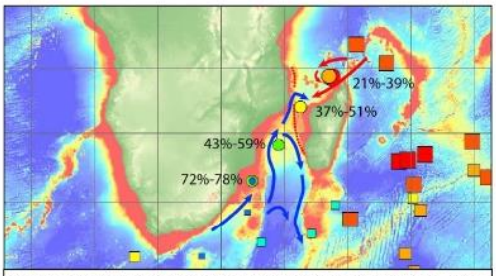

The squares correspond to previous study values (Goldstein, O'nions, 1981; Ben Othman et al., 1989; Albarède et al., 1997; Frank, 2002)

Results / Discussion : DR11-01 as a tracer of ocean currents

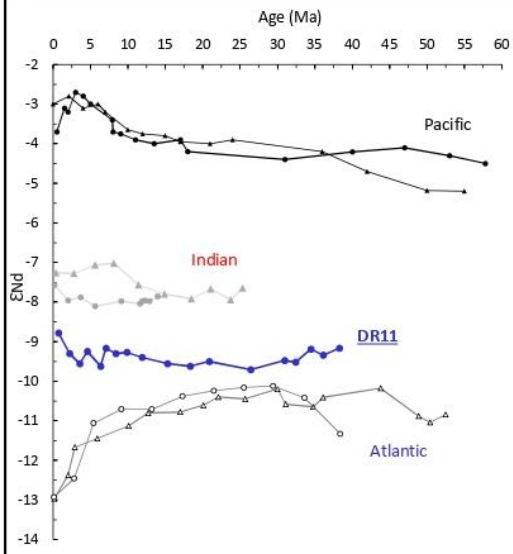

Nd isotopic trends from Pacifique, Indian and Atlantic deep waters (according to BURTON et al., 1997; O'NIONS et al., 1998; FRANK et al., 1999) and Nd isotopic trend from the sample DR11-01

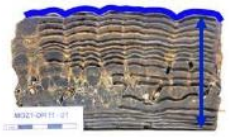

DR11 Sample is located on the north of the Davie Ridge at a depth of approx. 2200 m → explain the deep water circulation in time

40-22 Ma : NADW estimate between 72% and 88% → Important proto-NADW circulation beyond the Davie Ridge → 26 Ma : wide passage

22- 1 Ma : Increasingly low (proto-)NADW circulation beyond the Davie Ridge → 1 Ma NADW estimate between 40% and 54%

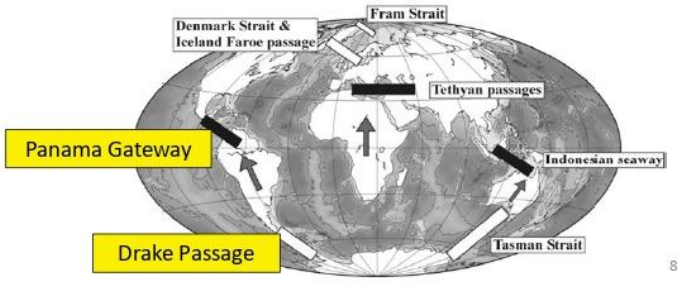

8

Results / Discussion : DR17-01 as a marker of vertical movement

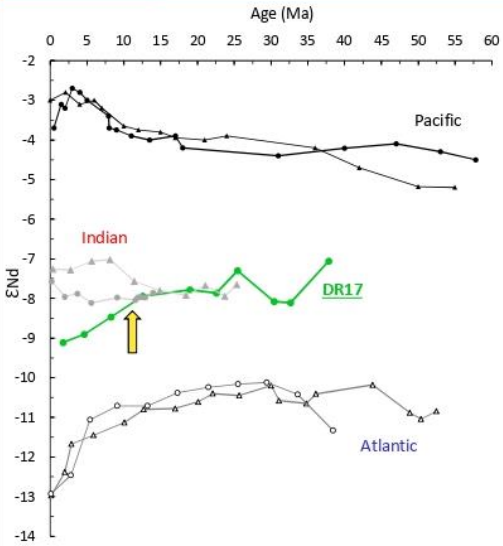

Nd isotopic trends from Pacifique, Indian and Atlantic deep waters (according to BURTON et al., 1997; O'NIONS et al., 1998; FRANK et al., 1999) and Nd isotopic trend from the sample DR17-01

DR17 Sample is located near Bassas da India, south of the Davie Ridge at a depth of approx. 1600 m → intermediate currents

38-12 Ma : εNd values of Indian intermediate water → **RSIW**

12-1 Ma : DR17 trend becomes less radiogenic until values between the Indian and Atlantic domains (-9.1)

Water masses changement → vertical movement

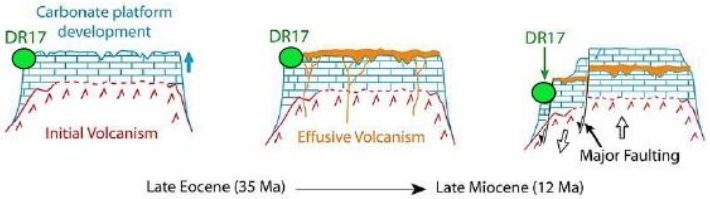

Vertical movement of the DR17 sample - faulting and subsidence phenomenon (modified, according to COURGEON et al., 2017)

9

Conclusion

Present circulation :

1. The RSIW intermediate current flows from the north of the Mozambique Channel to Bassas Da India where it mixes with the AAIW intermediate current

2. The **Davie Ridge does not prevent the circulation of deep currents** in the Mozambique Channel. The NADW is recorded in the north of the ride, towards Juan de Nova

Past circulation :

1. The **Davie Ridge has never been an impassable barrier** to the flow of deep currents. About 25 Ma the NADW influence on the north side of the ride were maximum

2. More recently the NADW was less recorded in the north of the ride. This reduction is related to **major geodynamic events** such as the circulation of the Antarctic Circumpolar Current and the closure of the Panama Gateway

Geodynamic :

1. Vertical movements were recorded with the DR17 sample near Bassas da India. This geodynamic began on **Late Miocene** and can be related to **progressive subsidence** and faulting on carbonate platform (Courgeon et al., 2017) → $^{10}Be/^{9}Be$ based dating

10

Appendix 1

Growth rate calculation according to **Manheim and Lane Bostwick (1988)** :

1. This method assumes that the flow of Co on an Mn oxide is constant over a given period of time due to the very short residence time of the Co.
2. If the Co flux is constant then the Co concentration will be directly dependent on the growth rate of the sample.

$$GR\ (mm/Ma) = \frac{0{,}68}{\left([Co] \times \left(\frac{50}{[Fe]+[Mn]}\right)\right)^{1{,}67}}$$

This is an empirical method !!

→ We are working on a new study based on the absolute dating from the **Be cosmogenic nucleides**

12

Appendix 2

Isotopic values at -11 in the Natal Basin for samples in lower than 1500m depths ?

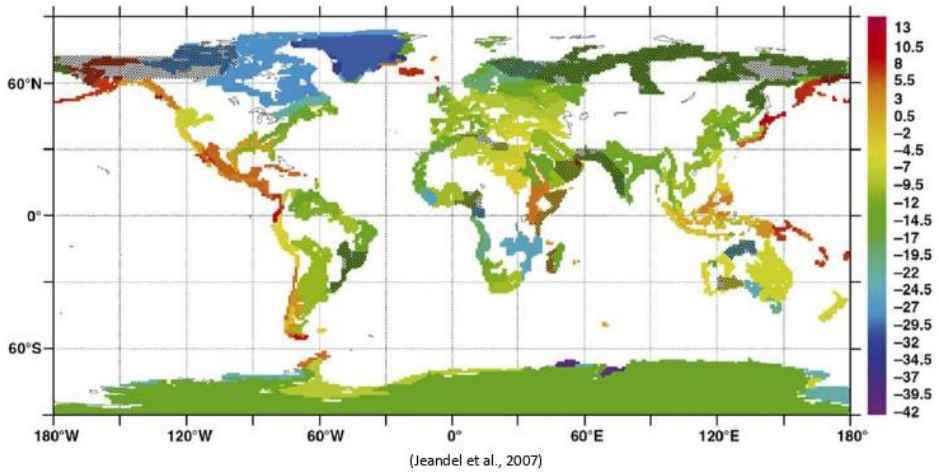

(Jeandel et al., 2007)

Unradiogenic values for the African East coast → εNd = -23

Exchange coast/ocean → could play a significant role in the Natal Basin εNd values

13

APPENDIX 11.

C. CHARLES *et al.*, 2020. Paleoceanographic reconstruction of the Mozambique Channel through the Fe-Mn crusts geochemical study. *Goldschmidt Conference.* June 2020, Honolulu, Hawaii, USA. Oral presentation

Appendix 11.

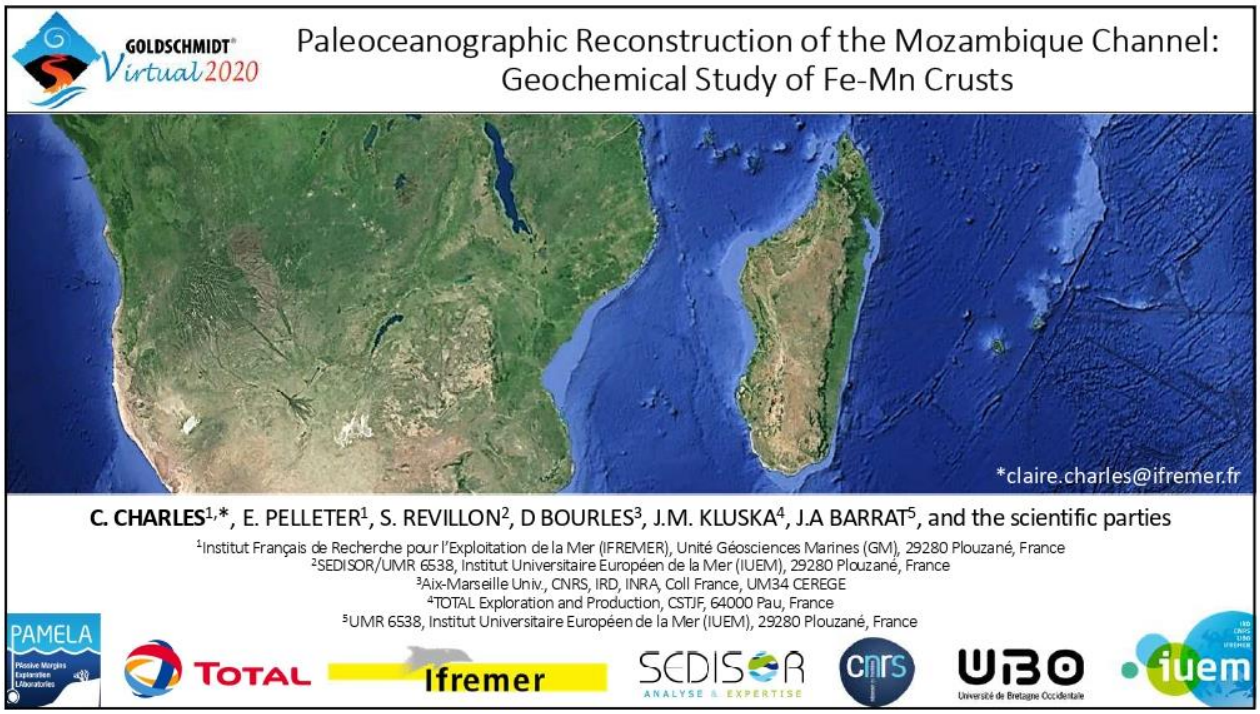
GOLDSCHMIDT Virtual 2020
Paleoceanographic Reconstruction of the Mozambique Channel: Geochemical Study of Fe-Mn Crusts
*claire.charles@ifremer.fr
C. CHARLES[1,*], E. PELLETER[1], S. REVILLON[2], D BOURLES[3], J.M. KLUSKA[4], J.A BARRAT[5], and the scientific parties
[1]Institut Français de Recherche pour l'Exploitation de la Mer (IFREMER), Unité Géosciences Marines (GM), 29280 Plouzané, France
[2]SEDISOR/UMR 6538, Institut Universitaire Européen de la Mer (IUEM), 29280 Plouzané, France
[3]Aix-Marseille Univ., CNRS, IRD, INRA, Coll France, UM34 CEREGE
[4]TOTAL Exploration and Production, CSTJF, 64000 Pau, France
[5]UMR 6538, Institut Universitaire Européen de la Mer (IUEM), 29280 Plouzané, France
PAMELA
TOTAL
Ifremer
SEDISOR
cnrs
UBO
iuem

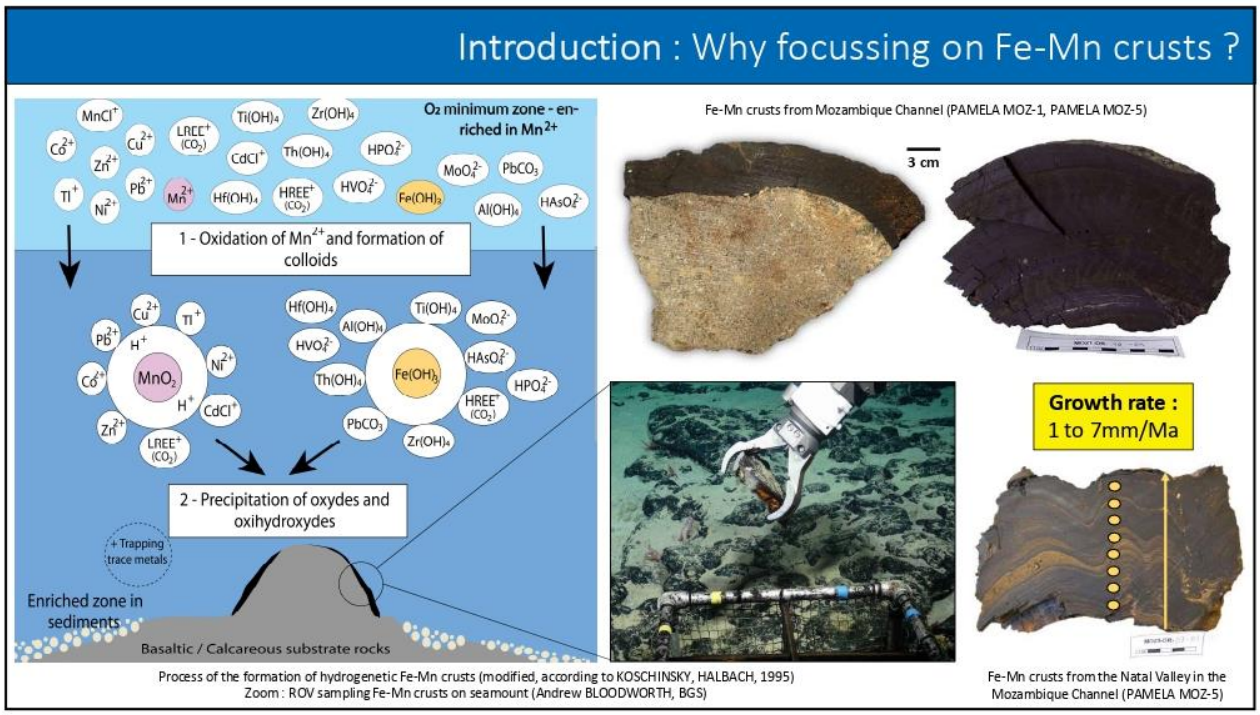
Introduction : Why focussing on Fe-Mn crusts ?
O2 minimum zone - enriched in Mn2+
1 - Oxidation of Mn2+ and formation of colloids
2 - Precipitation of oxydes and oxihydroxydes
+ Trapping trace metals
Enriched zone in sediments
Basaltic / Calcareous substrate rocks
Process of the formation of hydrogenetic Fe-Mn crusts (modified, according to KOSCHINSKY, HALBACH, 1995)
Zoom : ROV sampling Fe-Mn crusts on seamount (Andrew BLOODWORTH, BGS)
Fe-Mn crusts from Mozambique Channel (PAMELA MOZ-1, PAMELA MOZ-5)
3 cm
Growth rate : 1 to 7mm/Ma
Fe-Mn crusts from the Natal Valley in the Mozambique Channel (PAMELA MOZ-5)

Introduction : Previous geochemical studies and objectives

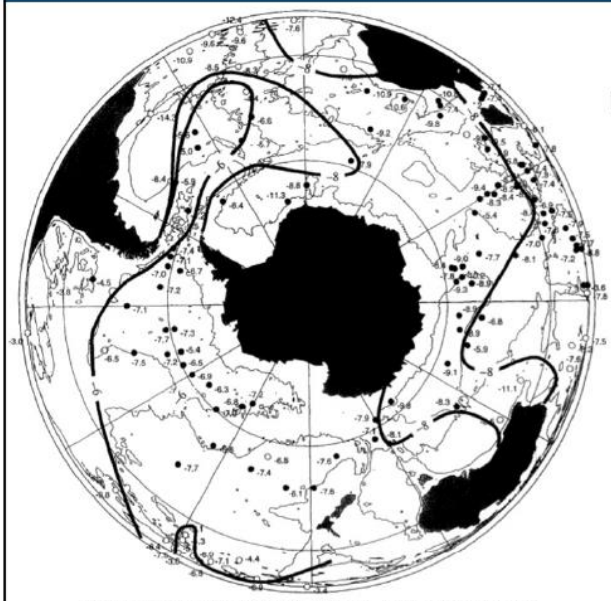

Nd isotopic values representation (Albarède *et al.*, 1997; Mercator projection)

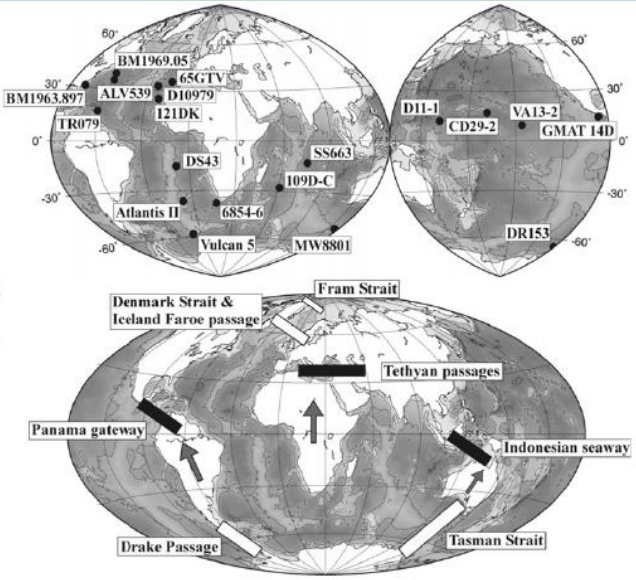

Location of major paleogeographic events (arrows : tectonic directions in black the closures and in white the openings – modified, according to Frank et al., 2002)

3

Regional context : Mozambique Channel oceanography

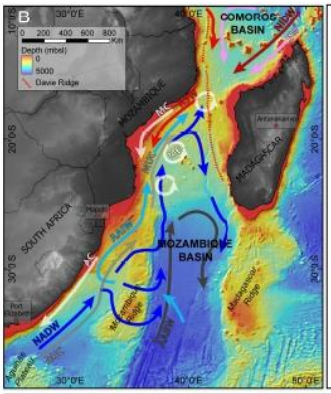

Davie Ridge : ■ ■ ■ ■

Pacifique Ocean
(not represented here)
- εNd : -3 to -6

North Indian Deep Water (NIDW) :
- **εNd : -7 to -8,5**

North Atlantic Deep Water (NADW) :
- **εNd : -10 to -14**

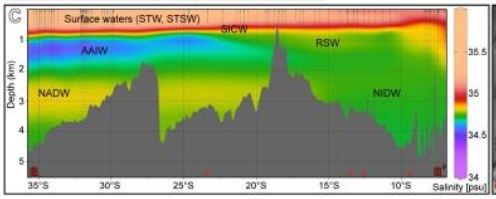

Mix of Indian and Atlantic currents

Surface waters or superficiel currents :
- Subtropical Surface Water (STSW)
- Courant du Mozambique (TSW)

Intermediate currents :
- Antarctic Intermediate Water (AAIW)
- Red Sea Intermediate Water (RSIW)

Deep currents :
- North Atlantic Deep Water (NADW)
- North Indian Deep Water (NIDW)

Role of the Davie Ridge?

4

Methodology : sampling and isotopic geochemistry

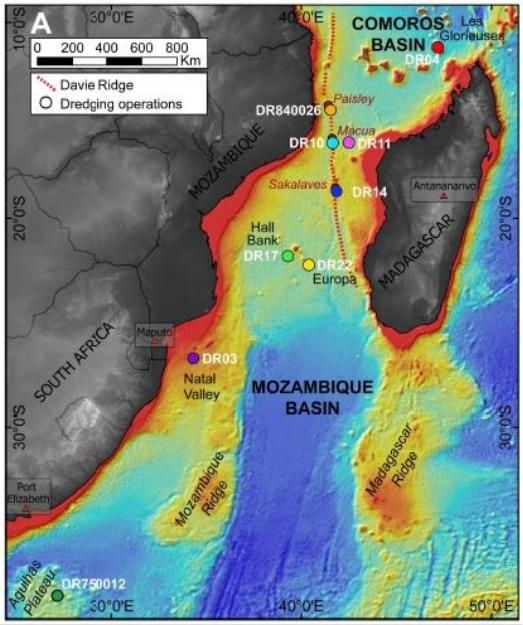

9 crusts : **surface and time serie** scrapings
41 $^{10}Be/^{9}Be$ datations

REEs separation through **chromatography columns** → Separation of light and heavy rare-earth elements → **Nd recovery**

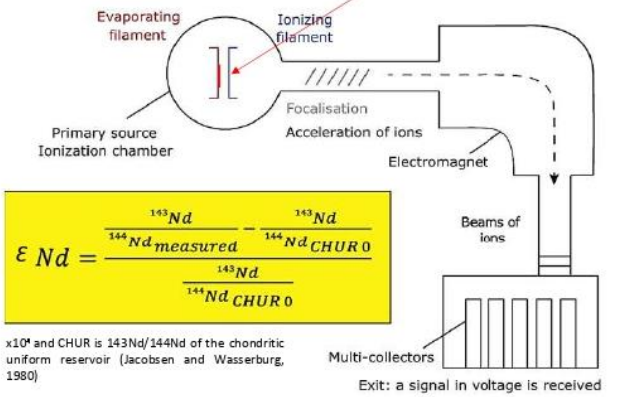

$$\varepsilon Nd = \frac{\frac{^{143}Nd}{^{144}Nd_{measured}} - \frac{^{143}Nd}{^{144}Nd_{CHUR\,0}}}{\frac{^{143}Nd}{^{144}Nd_{CHUR\,0}}}$$

x10⁴ and CHUR is 143Nd/144Nd of the chondritic uniform reservoir (Jacobsen and Wasserburg, 1980)

5

DR11-01 as a tracer of ocean currents

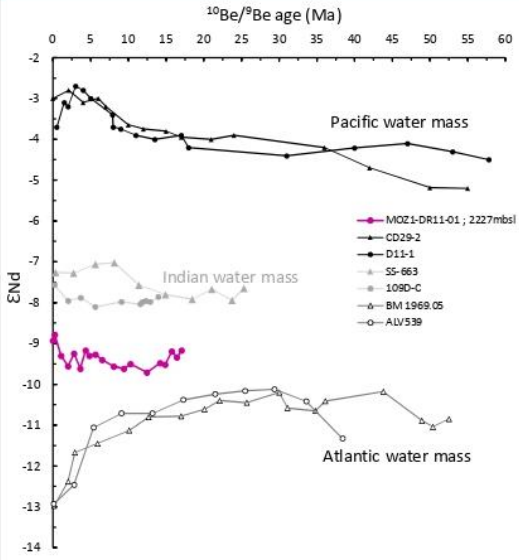

Nd isotope trends from Pacifique, Indian and Atlantic deep waters (according to BURTON et al., 1997; O'NIONS et al., 1998; FRANK et al., 1999) and Nd isotopic trend from the sample DR11-01

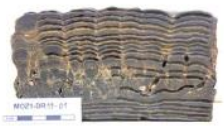

DR11-01 Sample is located on the north of the Davie Ridge at a depth of approx. 2200 m → explain the deep water circulation in time

13 Ma : NADW estimate between 81% and 87% → Important proto-**NADW** circulation beyond the Davie Ridge → wide passage

2 Ma: Increasingly low (proto-)**NADW** circulation beyond the Davie Ridge → 0.2 Ma **NADW** estimate between 40% and 53%

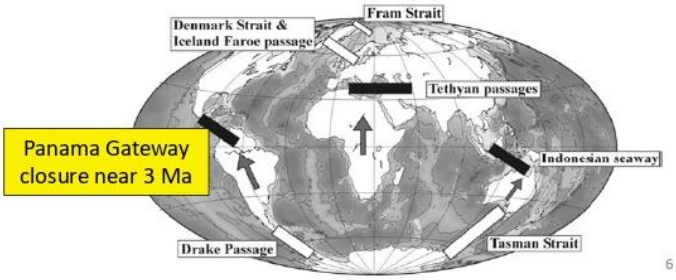

6

DR17-01 as a marker of subsidence

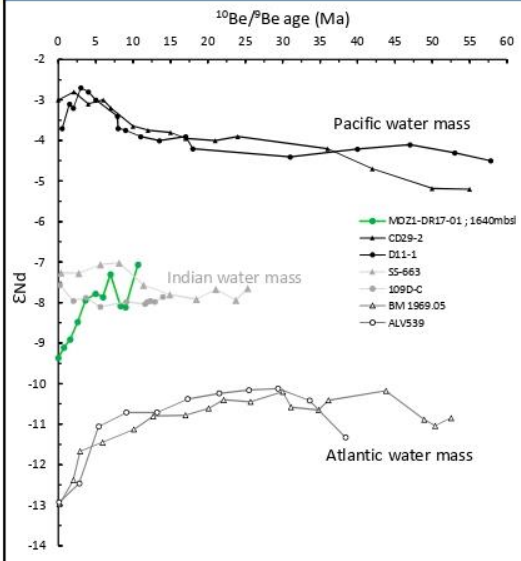

Nd isotope trends from Pacifique, Indian and Atlantic deep waters (according to BURTON et al., 1997; O'NIONS et al., 1998; FRANK et al., 1999) and Nd isotopic trend from the sample DR17-01

DR17-01 Sample is located near Bassas da India, south of the Davie Ridge at a depth of approx. 1600 m → intermediate currents

11-5 Ma : εNd values of Indian intermediate water → **RSIW**

5 Ma : DR17 trend becomes less radiogenic until values between the Indian and Atlantic domains (εNd = -9.1)

Water masses changement → vertical movement
Subsidence

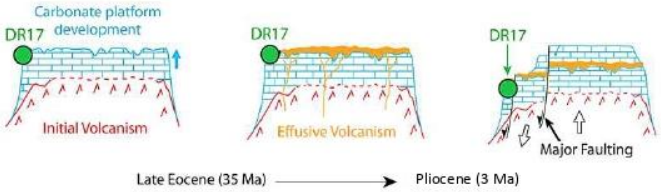

Vertical movement of the DR17 sample - faulting and subsidence phenomenon (modified, according to COURGEON et al., 2017)

7

DR10-05 and DR22-01 as markers of uplift

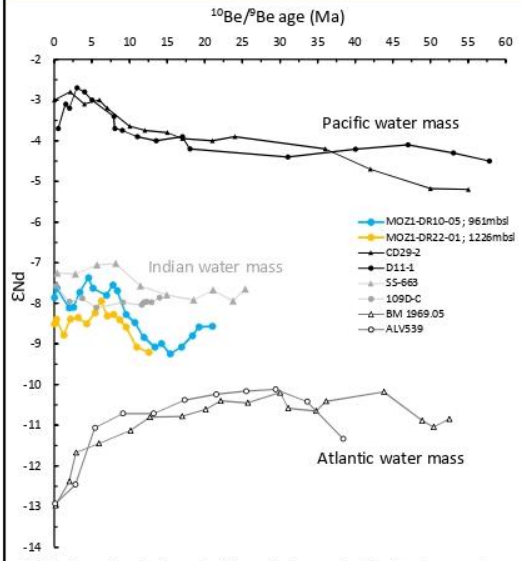

Nd isotope trends from Pacifique, Indian and Atlantic deep waters (according to BURTON et al., 1997; O'NIONS et al., 1998; FRANK et al., 1999) and Nd isotopic trend from the sample DR10-05 and DR22-01

DR10-05 Sample is located on the Macua Mount, on the Davie Ridge at a depth of approx. 961 m → surface currents

DR22-01 Sample is located near Europoa, south of the Davie Ridge at a depth of approx. 1226 m → intermediate currents

16-12 Ma : εNd values of Atlantique deep water → **NADW** estimated to 82% → samples located at more than 1500 mbsl

12-8 Ma : topographic change in the channel (general movement) and the Davie Ridge rises up → the crusts record Indian surface currents (-8 < εNd < -7)

Water masses changement → vertical elevation
Uplift

8-0 Ma : topographic change near Europa (local movement) → the DR22 sample drops into a transition zone (intermediate currents)

8

DR04-23 as a tracer of NADW diminution

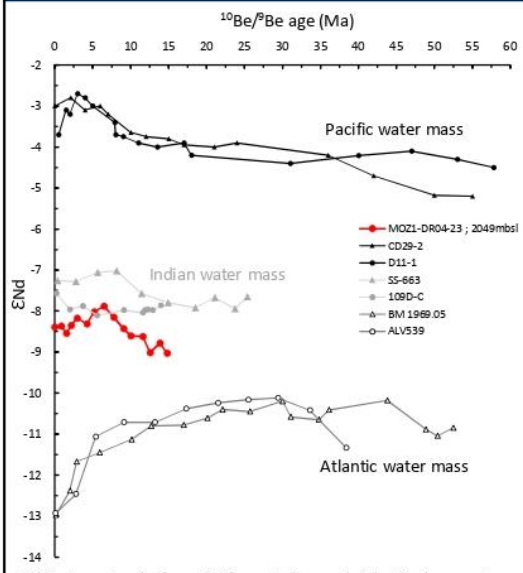

Nd isotope trends from Pacifique, Indian and Atlantic deep waters (according to BURTON et al., 1997; O'NIONS et al., 1998; FRANK et al., 1999) and Nd isotopic trend from the sample DR04-23

DR04-23 Sample is located on Les Glorieuses, in the Comores Bassin at a depth of approx. 2049 m → deep currents

15 Ma : εNd values of Atlantique deep water → **NADW** estimated to 78% → the deep Davie Ridge allows a wide passage of the NADW

15-6 Ma : topographic change → the Davie Ridge rises up (DR10) → reduced passage and reduced NADW inputs (until 38% vs. 62% of NIDW)

These observations confirm the hypothesis of vertical phenomena in the Mozambique Channel between 15 and 6 Ma with direct consequences on the circulation of deep currents.

9

DR03-01 as a marker of geochemical exchange

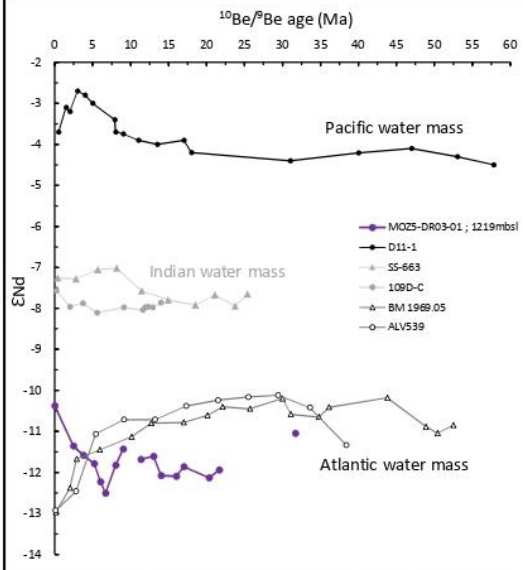

Nd isotope trends from Pacifique, Indian and Atlantic deep waters (according to BURTON et al., 1997; O'NIONS et al., 1998; FRANK et al., 1999) and Nd isotopic trend from the sample DR03-01

DR03-01 Sample is located in the Natal Valley, close to the African coast, at a depth of approx. 1219 m

Isotopic trend much **less radiogenic** than other crusts → close to the pure Atlantic water masse values – some values are even more negative (between 31 and 5 Ma – NADW inputs > 100%)

Sample with a very different story from the others → other phenomenon than a simple mixing of different currents

Geochemical exchanges (isotopic) between the African east coast which is unradiogenic (εNd > -22 *Jeandel et al., 2007*) **and the Atlantic water masses arriving from the south.**

10

Conclusion

Present circulation :

1. The RSW intermediate current flow from the north of the Mozambique Channel to Europa where it mixes with the AAIW intermediate current

2. The **Davie Ridge does not prevent the circulation of deep currents** in the Mozambique Channel. The NADW is recorded in the north of the Davie Ridge

Geodynamic :

1. Vertical movements were recorded. A **upflit** phenomenon was identified between 15 and 6 Ma (DR22, DR10) while a more local **subsidence** was recorded in the southern part of the channel, near Bassas da India, from 5 Ma (DR17)

Past circulation :

1. The **Davie Ridge has never been an impassable barrier** to the flow of deep currents. About 15 Ma the NADW influence on the north side of the ride were maximum (DR11, DR04)

2. Between 6 and 0.2 Ma the NADW was less recorded in the north of the Davie Ridge. This reduction was (1) a direct consequence of **local vertical movements** identified between 15 and 6 Ma (reduced NADW passage) and (2) more recently, related to **major geodynamic events** such as the circulation of the Antarctic Circumpolar Current and the closure of the Panama Gateway

Geochemical exchanges :

1. Identification of geochemical exchanges between the African east coast which is unradiogenic ($\varepsilon Nd > -22$) and the Atlantic water masses arriving from the south (Natal Valley) → Jeandel et al., 2007

10

APPENDIX 12.

C. CHARLES *et al.*, 2021. Vertical movements recorded in Fe-Mn crusts: what interest in resource exploration? *Goldschmidt Conference.* July 2021, Lyon, France. Oral presentation

Appendix 12.

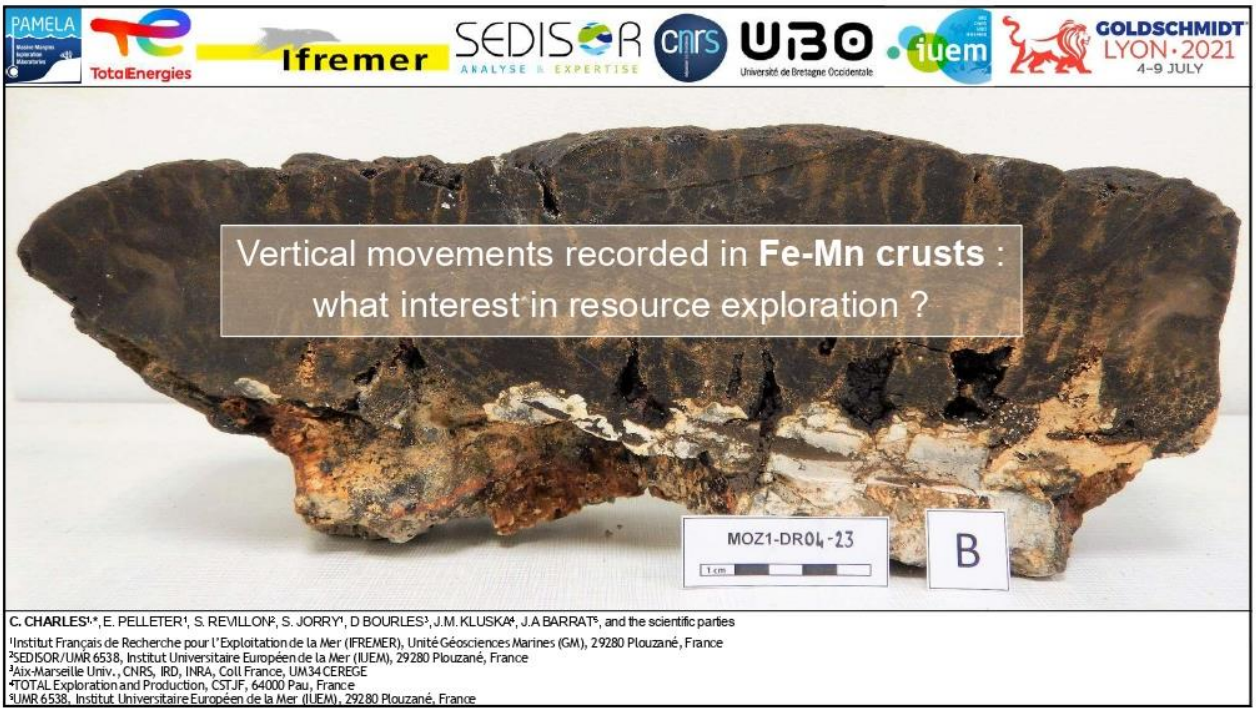
PAMELA
TotalEnergies
Ifremer
SEDISOR
ANALYSE & EXPERTISE
cnrs
UBO
Université de Bretagne Occidentale
iuem
GOLDSCHMIDT
LYON · 2021
4–9 JULY
Vertical movements recorded in Fe-Mn crusts :
what interest in resource exploration ?
MOZ1-DR04-23
B
C. CHARLES[1,*], E. PELLETER[1], S. REVILLON[2], S. JORRY[1], D BOURLES[3], J.M. KLUSKA[4], J.A BARRAT[5], and the scientific parties
[1]Institut Français de Recherche pour l'Exploitation de la Mer (IFREMER), Unité Géosciences Marines (GM), 29280 Plouzané, France
[2]SEDISOR/UMR 6538, Institut Universitaire Européen de la Mer (IUEM), 29280 Plouzané, France
[3]Aix-Marseille Univ., CNRS, IRD, INRA, Coll France, UM34 CEREGE
[4]TOTAL Exploration and Production, CSTJF, 64000 Pau, France
[5]UMR 6538, Institut Universitaire Européen de la Mer (IUEM), 29280 Plouzané, France

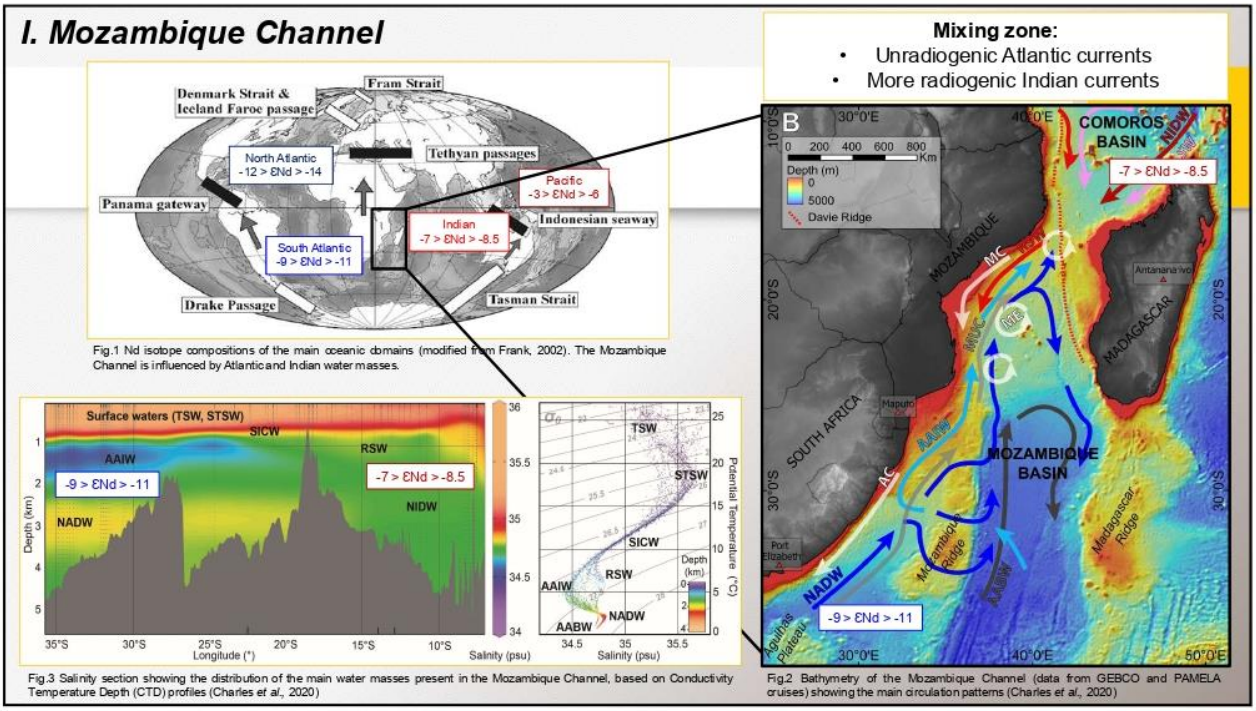
I. Mozambique Channel
Mixing zone:
• Unradiogenic Atlantic currents
• More radiogenic Indian currents
Denmark Strait & Iceland Faroe passage
Fram Strait
Tethyan passages
North Atlantic -12 > εNd > -14
Pacific -3 > εNd > -6
Panama gateway
Indonesian seaway
Indian -7 > εNd > -8.5
South Atlantic -9 > εNd > -11
Drake Passage
Tasman Strait
Fig.1 Nd isotope compositions of the main oceanic domains (modified from Frank, 2002). The Mozambique Channel is influenced by Atlantic and Indian water masses.
Surface waters (TSW, STSW)
SICW
AAIW
RSW
-9 > εNd > -11
-7 > εNd > -8.5
NIDW
NADW
Depth (km)
Longitude (°)
Salinity (psu)
TSW
STSW
SICW
RSW
AAIW
NADW
AABW
Potential Temperature (°C)
Fig.3 Salinity section showing the distribution of the main water masses present in the Mozambique Channel, based on Conductivity Temperature Depth (CTD) profiles (Charles et al., 2020)
COMOROS BASIN
-7 > εNd > -8.5
MOZAMBIQUE
MC
MADAGASCAR
Antananarivo
SOUTH AFRICA
Maputo
AAIW
AC
MOZAMBIQUE BASIN
Port Elizabeth
Mozambique Ridge
Madagascar Ridge
NADW
-9 > εNd > -11
Agulhas Plateau
Davie Ridge
Depth (m)
Km
Fig.2 Bathymetry of the Mozambique Channel (data from GEBCO and PAMELA cruises) showing the main circulation patterns (Charles et al., 2020)

I. Mozambique Channel

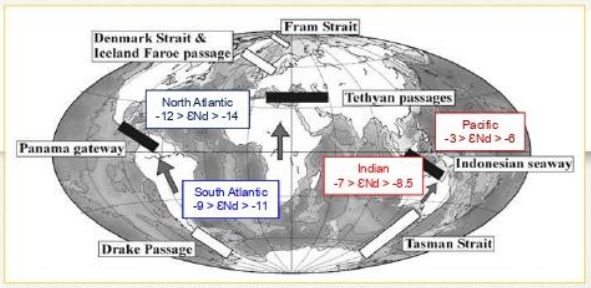

Fig.1 Nd isotope compositions of the main oceanic domains (modified from Frank, 2002). The Mozambique Channel is influenced by Atlantic and Indian water masses.

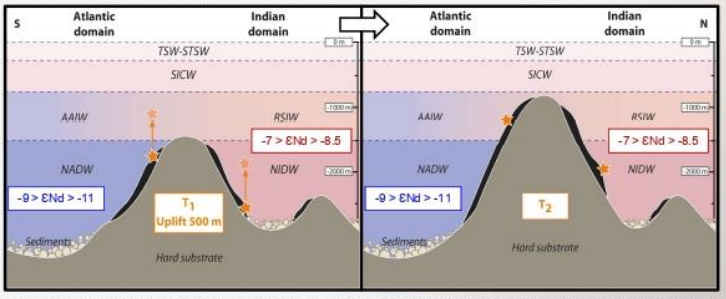

Fig.4 Example of a vertical movements (here uplift) which can influence the position (depth) of the Fe-Mn crusts within the different water masses of the channel.

Mixing zone:
- Unradiogenic Atlantic currents
- More radiogenic Indian currents

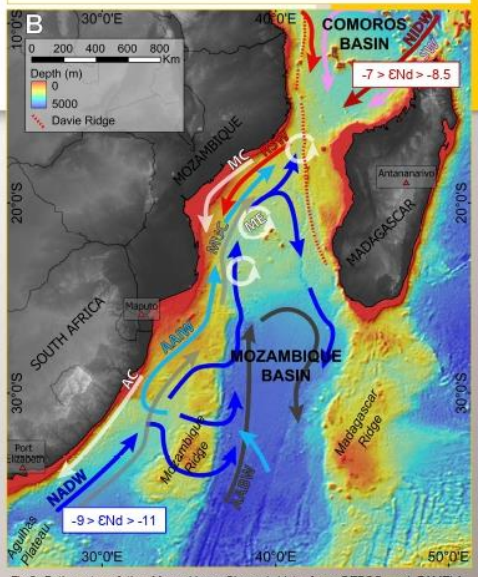

Fig.2 Bathymetry of the Mozambique Channel (data from GEBCO and PAMELA cruises) showing the main circulation patterns (Charles *et al.*, 2020)

II. Fe-Mn crusts

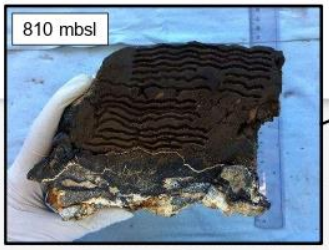

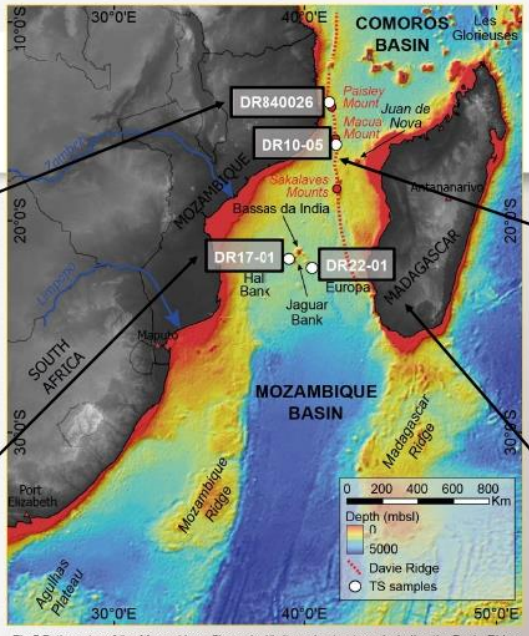

Fig.5 Bathymetry of the Mozambique Channel with its main structures including the Davie Ridge and the Eparses Islands. The white dots represent the 4 studied time serie samples.

II. Fe-Mn crusts

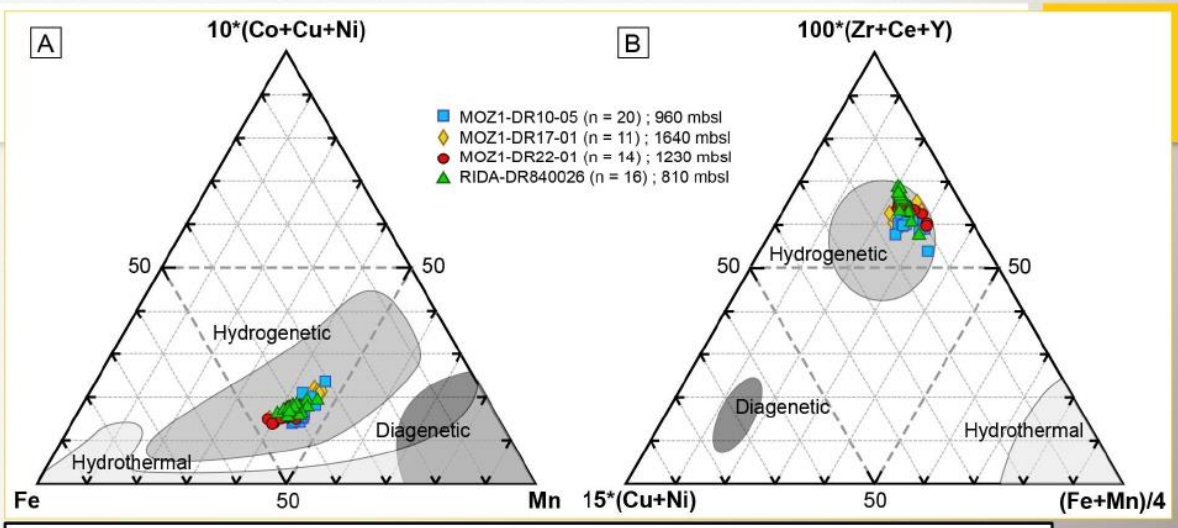

Analyses :

- Nd isotope compositions
- Major and trace elements
- $^{10}Be/^{9}Be$ datings (n = 21)

Fig 6. Classification of the 4 studied Fe-Mn crusts - schemes according to Bonatti, 1972 (A) and Josso et al., 2017 (B).

III. Nd isotope compositions

Paleogeodynamic reconstruction from the 4 studied Fe-Mn crusts :

→ Two major geodynamic movements recorded in the 4 Fe-Mn crusts at 12 and 6 Ma.

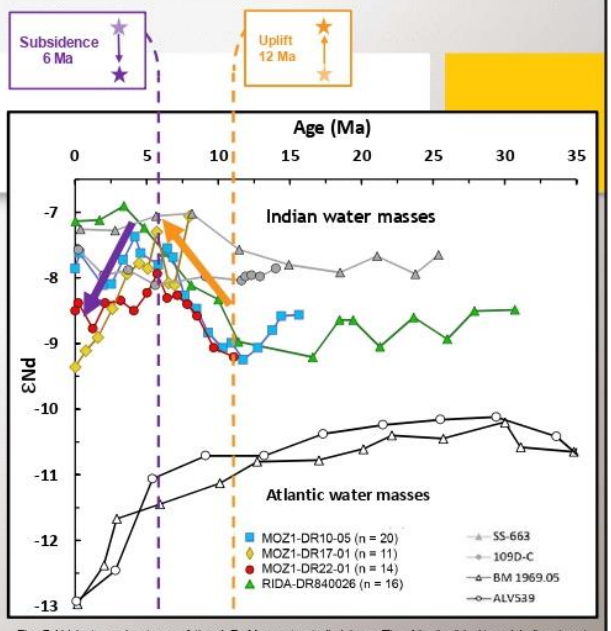

Fig. 7 Nd isotope signatures of the 4 Fe-Mn crusts studied here. The Atlantic (black) and Indian (grey) signatures are used as reference points.

III. Nd isotope compositions

Sample	RIDA - DR840026	MOZ1-DR10-05	MOZ1-DR22-01
Depth	810 m	960 m	1230 m
Local.	Mont Paisley	Mont Macua	Europa
Uplift	Min. 690 m	Min. 539 m	Min. 274 m
Rate	86 m/Ma	71 m/Ma	51 m/Ma

Sample	MOZ1-DR17-01
Depth	1640 m
Local.	Banc du Hall
Subsidence	Min. 640 m
Rate	112 m/Ma

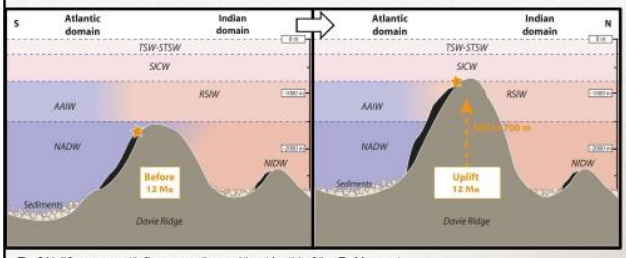

Fig.8 Uplift movement influence on the position (depth) of the Fe-Mn crusts.

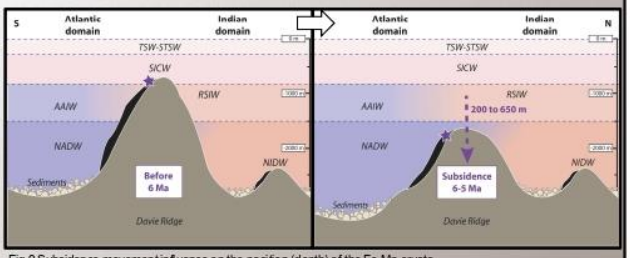

Fig.9 Subsidence movement influence on the position (depth) of the Fe-Mn crusts.

Uplift at 12 Ma

Subsidence at 6 Ma

IV. Element concentrations

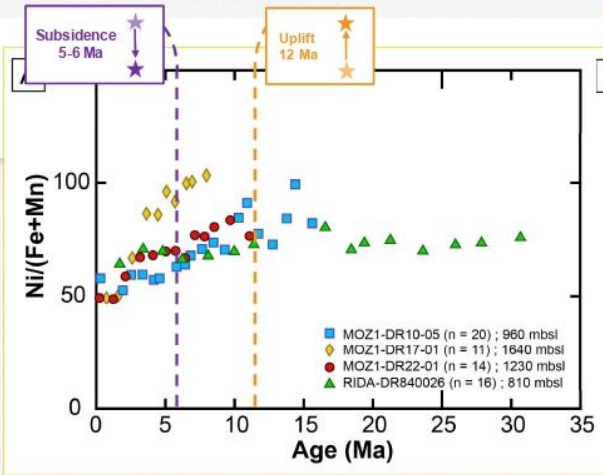

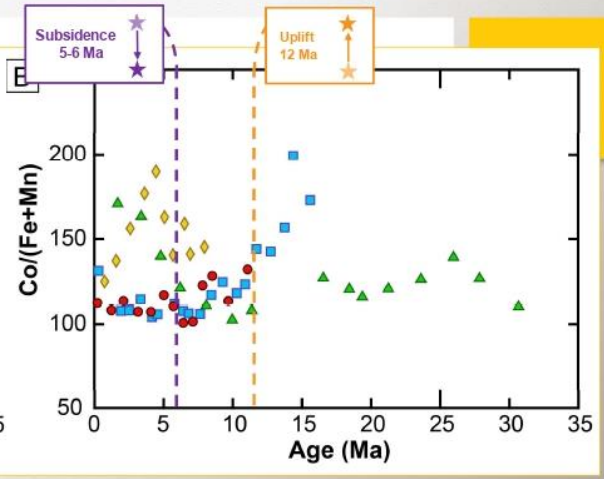

[Ni] ppm	min	2362	1840	1783	2423
	max	4452	3772	3108	3432

[Co] ppm	min	4137	4682	3875	3594
	max	8939	7611	4942	8288

Observations :

- Ni : decrease in concentrations after the uplift and after the subsidence for **MOZ1-DR17-01**
- Co : increase and decrease in concentrations, no control of the bathymetric changes

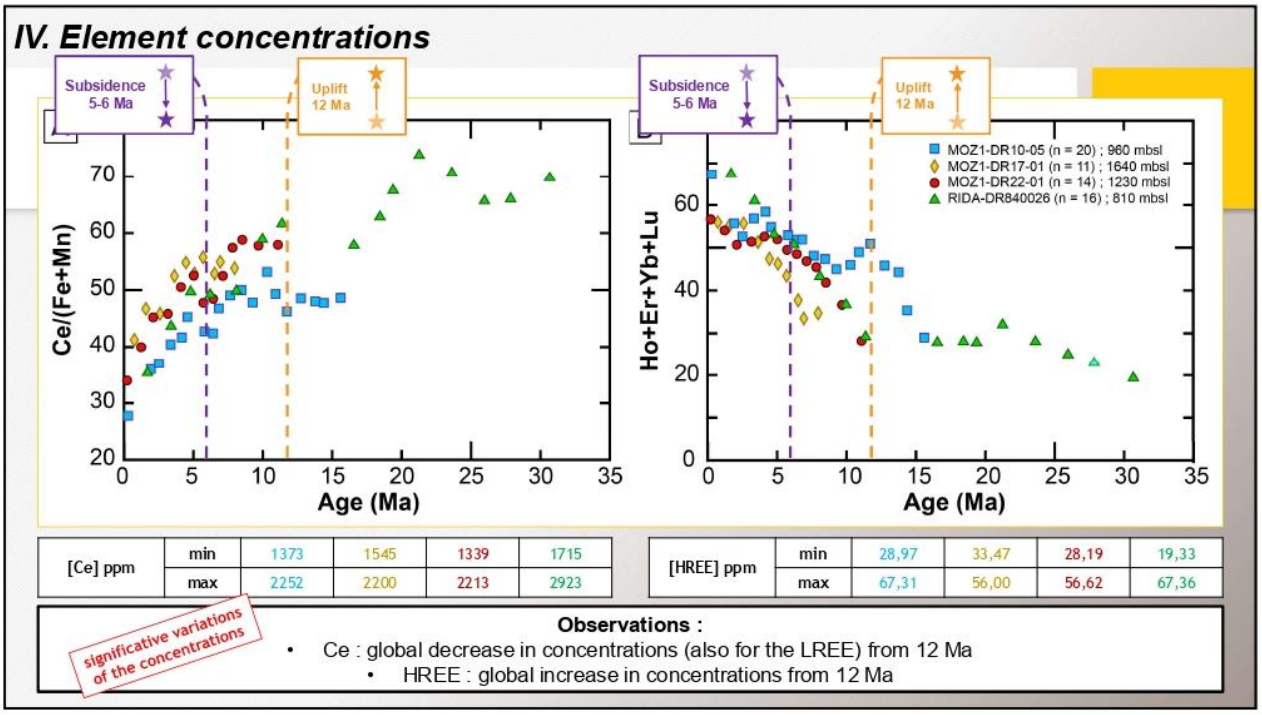

[Ce] ppm	min	1373	1545	1339	1715
	max	2252	2200	2213	2923

[HREE] ppm	min	28,97	33,47	28,19	19,33
	max	67,31	56,00	56,62	67,36

significative variations of the concentrations

Observations :

- Ce : global decrease in concentrations (also for the LREE) from 12 Ma
- HREE : global increase in concentrations from 12 Ma

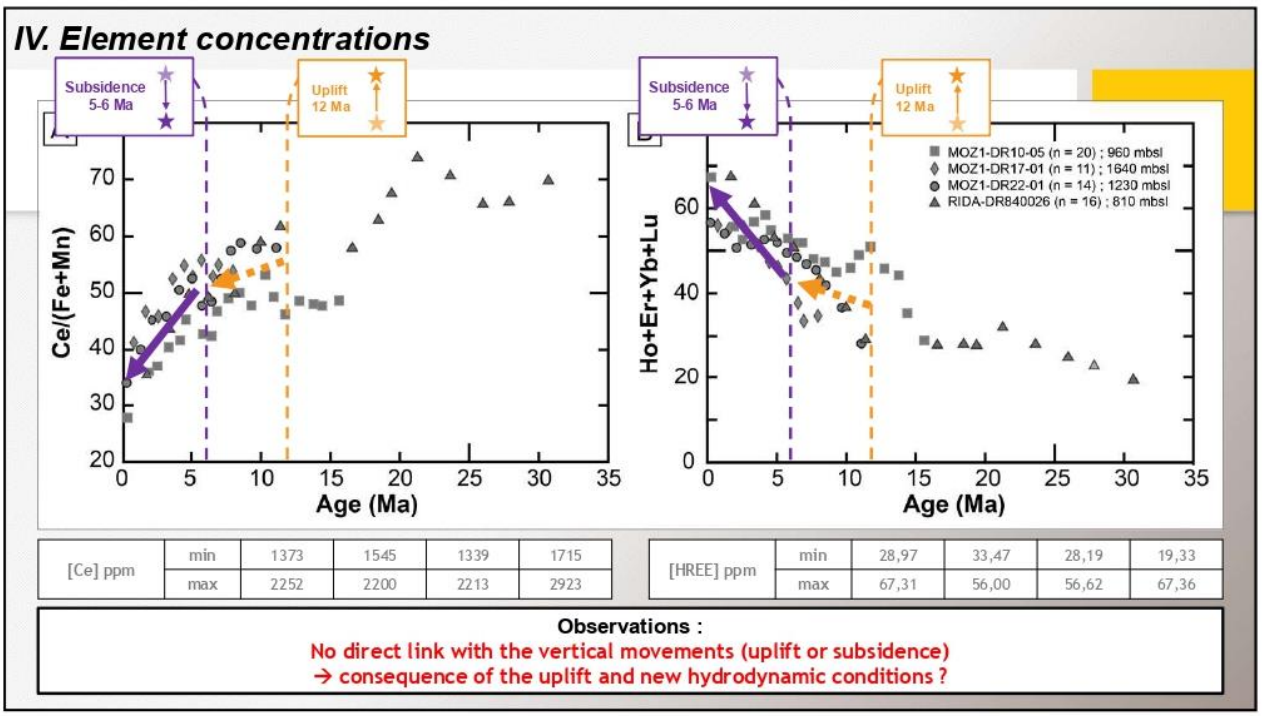

[Ce] ppm	min	1373	1545	1339	1715
	max	2252	2200	2213	2923

[HREE] ppm	min	28,97	33,47	28,19	19,33
	max	67,31	56,00	56,62	67,36

Observations :

No direct link with the vertical movements (uplift or subsidence)

→ consequence of the uplift and new hydrodynamic conditions ?

V. Conclusion

- Identification and datations of an **uplift** (12 Ma) and a **subsidence** (around 6 Ma) through the Nd isotope geochemistry of 4 Fe-Mn crusts from the Mozambique Channel
- No clear increasing or decreasing trends of economic metals (Co, Ni) linked to the identified vertical movements → concentrations variations may be control by local impacts
- However, REE seem to be sensitive to hydrodynamic changes (until the uplift → indirect consequence ?)
- The recorded signatures from the Fe-Mn crusts of the Mozambique Channel show high HREE concentrations in the **intermediate water masses** (1000-1500 mbsl) whereas Ce concentrations decrease

claire.charles@ifremer.fr

DOCTORAT SCIENCES BRETAGNE DE LA MER LOIRE ET DU LITTORAL

UBO Université de Bretagne Occidentale

Titre : Reconstructions paléocéanographiques et paléogéographiques du Canal du Mozambique (Océan Indien): apport de l'étude isotopique des encroûtements Fe-Mn

Mots clés : canal du Mozambique ; encroûtements Fe-Mn ; isotopie Nd, Pb ; NADW ; NIDW ; uplift

Résumé : Le canal du Mozambique, localisé à l'est du craton africain et à l'ouest de la marge continentale de Madagascar, abrite d'intenses mélanges de masses d'eau des océans Atlantique et Indien qui soulèvent des interrogations, à savoir si et comment elles ont circulé au cours du temps, en s'adaptant à la géodynamique du canal. L'analyse géochimique (éléments majeurs, traces ; isotopie Nd, Pb) et la datation absolue (isotopie Be) de 33 encroûtements Fe-Mn, répartis depuis le Plateau des Aiguilles au sud jusqu'au bassin des Comores au nord, permet ici d'établir des séries temporelles afin d'étudier l'évolution des courants régionaux jusqu'à 30.7Ma. Depuis 80 000ans, le NADW circule jusqu'à la ride de Jeffrey alors que dans l'archipel des Comores, le NIDW est majoritaire. Cependant, ce modèle océanographique n'a pas toujours fonctionné ainsi. Dès sa mise en place, le NADW a eu une forte influence jusqu'aux Îles Glorieuses. Entre 11.7 et 3.4Ma, un soulèvement bouleversa la géodynamique du canal, entrainant une élévation de la ride de Davie. Le NADW diminua au nord, jusqu'à se retirer du bassin des Comores, au profit de l'augmentation du NIDW. Entre 5.1 et 1.6 Ma, une subsidence, enregistrée au centre du canal, modifia à son tour la bathymétrie et l'océanographie du secteur. La géochimie révèle également des apports élémentaires téthysiens et himalayens dans les courants profonds. Ainsi, grâce à une étude haute résolution des courants profonds du canal du Mozambique ce doctorat complète les modèles océanographiques de l'océan Indien et innove dans les reconstructions géodynamiques grâce à l'utilisation des encroutements Fe-Mn dans la caractérisation de mouvements verticaux.

Title : Paleoceanographic and paleogeographic reconstructions of the Mozambique Channel (Indian Ocean): contribution of the isotopic study of Fe-Mn crusts

Kew-words : Fe-Mn crusts ; Mozambique channel ; NADW ; NIDW ; Nd, Pb isotopes ; uplift

Abstract: The Mozambique Channel, located east of the African craton and west of the Madagascar continental margin, hosts intense mixing of water masses from the Atlantic and Indian Oceans, raising questions about whether and how they have circulated over time, adapting to the geodynamics of the channel. Geochemical analysis (major and trace elements; Nd and Pb isotopes) and absolute dating (Be isotope) of 33 Fe-Mn crusts, distributed from the Agulhas Plateau in the south to the Comoros Basin in the north, will be used to establish time series to study the evolution of regional currents up to 30.7Ma. For the past 80 000 years, the NADW has been flowing as far as the Jeffrey Ridge, whereas in the Comoros Archipelago, the NIDW is in the majority. However, this oceanographic model has not always worked this way. Since its formation, the NADW has had a strong influence as far as the Glorious Islands. Between 11.7 and 3.4Ma, an uplift disturbed the geodynamics of the channel, raising the Davie Ridge. The NADW decreased in the north, until it retired from the Comoros Basin, to the benefit of the NIDW expansion. Between 5.1 and 1.6 Ma, subsidence was recorded in the centre of the channel, which modified the bathymetry and oceanography of the area. Geochemistry also reveals Tethyan and Himalayan elemental inputs into the deep currents. Thus, thanks to a high-resolution study of the deep currents of the Mozambique Channel, this PhD completes the oceanographic models of the Indian Ocean and innovates in geodynamic reconstructions using Fe-Mn encrustations in the characterisation of vertical movements.